Waqar Ahmed

M. J. Jackson

# EMERGING NANOTECHNOLOGIES FOR MANUFACTURING

For information on all Elsevier publications
visit our website at elsevierdirect.com

Working together to grow
libraries in developing countries

www.elsevier.com | www.bookaid.org | www.sabre.org

ELSEVIER    BOOK AID International    Sabre Foundation

# Series Editor's Preface

This book aims to achieve the most difficult of combinations – simultaneous breadth and depth. As a collection of chapters written by individual experts, it manages to convey some of the coherence of the field, despite the fact that it is already vast. The opening chapter is introductory, but the remainder of the book deals with specialized topics at the cutting edge. Different chapters adopt somewhat different styles according to the nature of their subject matter. For example, Chapter 3 on advanced characterization techniques first explains them and then describes various applications in the manner of case studies. Other chapters are a delight even just to dip into – for example, Chapter 4 describes fascinating forests of nanowires and other more exotic structures that can be produced nowadays.

Because of the vastness of the field, it is almost impossible for any one person to be already acquainted with the topics selected for inclusion. Therefore, every nanotechnologist is likely to find something new and interesting in this book. The reader will also become aware that even if the end product of a manufacturing process is a microdevice, nanotechnology is nevertheless involved in the fabrication. Several chapters, while not concerned with manufacture per se, deal with matters closely related to nanomanufacturing (or nanofacture as it is nowadays called). Thus, Chapter 9 deals with the safety of nanoparticles, an aspect that should certainly not be neglected.

An interesting feature of this book is the fact that the contributors are working in a diverse set of institutes in many different parts of the world. This very graphically underlines the extraordinary multidisciplinarity of nanotechnology, as well as the fact that it is already a truly global technology.

Jeremy Ramsden
Cranfield University, United Kingdom

# Foreword

For a number of years, nanotechnology has attracted considerable widespread attention from both scientists and industrialists. A great deal of research has been carried out with a range of interesting phenomena and applications emerging. The focus of this book is to present emerging nanotechnologies that are likely to be highly suitable for manufacturing products on a large scale and economically. This book contains contributions from international experts. Despite the wide range of areas, in-depth coverage of the topics has been a major objective of this book. It is widely believed that nanotechnology will cause a new revolution in fields such as medicine, materials, energy, electronics and agriculture. Therefore, to capitalize on this translation of nanotechnologies into manufactured products on a large scale in an economic manner will be critical.

In Chapter 1, the various approaches to nanotechnology and its transition to nanomanufacturing are described. Chapter 2 covers the use of nanotechnology in enhancing the performance of gas sensors. For a better understanding of the effects of nanomaterial on the functionality of various products, it is important to characterize nanostructures, and various techniques employed for this purpose are described in Chapter 3. In order to use nanotechnology to manufacture products, various techniques are used to pattern thin films and several self-assembly techniques are described in Chapter 4. Numerous new applications of carbon nanotubes are emerging and in Chapter 5 various routes for the synthesis of carbon nanotubes are discussed. Chapter 6 highlights the use of nanoparticles in biological specimens and it is highly likely that these will have important applications in medicine. Another important technology for manufacturing products is nano- and micromachining which is highlighted in Chapter 7. At the nanoscale, there are often very complex relationships among input design parameters and process or product outputs. It would be prohibitively time consuming to perform all of the combinatorially possible experiments in order to comprehend these relationships. However, statistical design of experiment is a technique that can be used to efficiently explore the relationships and develop greater understanding. Consequently, it is becoming increasingly central to the advancement of nanotechnology and nanomanufacturing and this topic is discussed in Chapter 8. There is considerable

debate going on about the environmental and health impact of nanotechnology, therefore, Chapter 9 describes issues involved in use of nanotechnology from a health and safety perspective. The impact of nanotechnology will be judged by many on its ability to generate commercial income; Chapter 10 describes commercialization issues involved in translating nanotechnology to manufactured products. Chapter 11 describes soft-lithographic techniques which have advantages over photolithography because they are inexpensive, simple and ideally suited for manufacturing products with micro- and nanoscale features. In Chapter 12, the applications of nanoscale diamond for RF-MEMS devices are discussed. The use of nanostructured coating on tools for micromachining is described in Chapter 13. Numerous new applications of nanoparticles are emerging and in Chapter 14, the techniques involved in the synthesis of metal oxide nanopowders to impart new functionality are described.

*Waqar Ahmed*
*Mark J. Jackson*

# Contributors

**W. Ahmed**
School of Computing, Engineering and Physical Sciences, Faculty of Science and Technology, University of Central Lancashire, Preston, UK.

**I.A. Appavoo**
Nanoscience and Nanotechnology Initiative, National University of Singapore, Singapore.

**T. Athar**
Indian Institute of Chemical Technology, Hyderabad, India.

**A.-M. Azad**
Department of Chemical Engineering, University of Toledo, Toledo, OH, USA.

**S. Balachandran**
Department of Electrical Engineering, University of South Florida, Tampa, FL, USA.

**D. Brabazon**
**H. Gomez**
Department of Mechanical Engineering, University of South Florida, Tampa, FL, USA.

**R.G. Handy**
Center for Advanced Manufacturing, MET, College of Technology, Purdue University, West Lafayette, IN, USA.

**M.J. Jackson**
Center for Advanced Manufacturing, MET, College of Technology, Purdue University, West Lafayette, IN, USA.

**S. Jeedigunta**
Department of Electrical Engineering, University of South Florida, Tampa, FL, USA.

**E. Kohn**
Institute of Electron Devices and Circuits, University of Ulm, Ulm, Germany.

**M.G. Krishna**
School of Physics, University of Hyderabad, Hyderabad, India.

**A. Kumar**
Department of Mechanical Engineering, University of South Florida, Tampa, FL, USA.

**P. Kumar**
School of Physics, University of Hyderabad, Hyderabad, India.

**J. Kusterer**
Institute of Electron Devices and Circuits, University of Ulm, Ulm, Germany.

**M. Mann**
Cambridge University Engineering Department, Cambridge, UK.

**B. Milne**
Cambridge University Engineering Department, Cambridge, UK.

**H.B. Nembhard**
Harold and Inge Marcus Department of Industrial and Manufacturing Engineering, Pennsylvania State University, PA, USA.

**A. Raffer**
**G.M. Robinson**
Micro Machinists, L.L.C., Purdue Research Park, West Lafayette, IN, USA.

MET, College of Technology, Purdue University, West Lafayette, IN, USA.

**M. Rodriguez**
Center for Advanced Manufacturing, MET, College of Technology, Purdue University, West Lafayette, IN, USA.

**K. Subramani**
Institute for Nanoscale Science and Technology (INSAT), University of Newcastle upon Tyne, Newcastle upon Tyne, UK.

**K. Teo**
AIXTRON Ltd. Nanoinstruments, Swavesey, Cambridge, UK.

**I. Ul Hassan**
Dhofar University, College of Arts and Applied Sciences, Department of Science and Mathematics, Salalah, Sultanate of Oman.

**T. Weller**
Department of Electrical Engineering, University of South Florida, Tampa, FL, USA.

**M.D. Whitfield**
Micro Machinists, L.L.C., Purdue Research Park, West Lafayette, IN, USA.

MET, College of Technology, Purdue University, West Lafayette, IN, USA.

**M. D. Whitt**
Center for Advanced Manufacturing, MET, College of Technology, Purdue University, West Lafayette, IN, USA.

**C. Yuangyai**
Harold and Inge Marcus Department of Industrial and Manufacturing Engineering, The Pennsylvania State University, PA, USA.

**Y. Zhang**
Nanoscience and Nanotechnology Initiative, National University of Singapore Division of Bioengineering, Faculty of Engineering, National University of Singapore, Singapore.

# Nanotechnology to Nanomanufacturing

W. Ahmed[1], M.J. Jackson[2] and I.Ul Hassan[3]

[1]*School of Computing, Engineering and Physical Sciences, Faculty of Science and Technology, University of Central Lancashire, Preston, UK*
[2]*Center for Advanced Manufacturing, MET, College of Technology, Purdue University, West Lafayette, IN, USA*
[3]*Dhofar University, College of Arts and Applied Sciences, Department of Mathematics and Sciences, Salalah, Sultanate of Oman*

## CONTENTS

## ABSTRACT

Nanotechnology is a term that is used to describe the science and technology related to the control and manipulation of matter and devices on a scale less than 100 nm in dimension. It involves a multidisciplinary approach involving fields such as applied physics, materials science, chemistry, biology, surface science, robotics, engineering, electrical engineering and biomedical engineering. At this scale the properties of matter is dictated and there are few boundaries between scientific disciplines. Generally, two main approaches have been used in nanotechnology. These are known as the 'bottom-up' and 'top-down' approaches. The former involves building up from atoms into molecules to assemble nanostructures, materials and devices. The latter involves making structures and devices from larger entities without specific

control at the atomic level. Progress in both approaches has been accelerated in recent years with the development and application of highly sensitive equipment. For example, instruments such as atomic force microscope (AFM), scanning tunnelling microscope (STM), electron beam lithography, molecular beam epitaxy, etc., have become available to push forward development in this exciting new field. These instruments allow observation and manipulation of novel nanostructures. Considerable research is being carried throughout the world in developing nanotechnology, and many new applications have emerged. However, a related term is nanomanufacturing, used to describe industrial scale manufacture of nanotechnology-based objects at high rate, low cost and reliability. In this paper we discuss the opportunities and challenges facing the transition from nanotechnology to nanomanufacturing. Tools, templates and processes are currently being developed that will enable high volume manufacturing of components and structures on a nanoscale and these are reviewed. These advancements will accelerate the development of commercial products and enable the creations of a new generation of applications in various different commercial sectors including drug delivery, cosmetics, biomedical implants, electronics, optical components, automotive and aerospace parts.

## 1.1 INTRODUCTION

Although nanotechnology has been around since the beginning of time, the discovery of nanotechnology has been attributed to Richard Feynman[1] who presented a paper called 'There is Plenty of Room at the Bottom' on 29 December 1959 at the annual meeting of the American Physical Society. Feynman talked about the storage of information on a very small scale, writing and reading in atoms, about miniaturization of the computer, building tiny machines, tiny factories and electronic circuits with atoms. He stated that 'In the year 2000, when they look back at this age, they will wonder why it was not until the year 1960 that anybody began seriously to move in this direction'. However, he did not specifically use the term 'nanotechnology'. The first use of the term 'nanotechnology' has been attributed to Norio Taniguchi[2] in a paper published in 1974 'On the Basic Concept of "NanoTechnology"'.

Since then several definitions[3] of nanotechnology have evolved. For example, the dictionary definition states that nanotechnology is 'the art of manipulating materials on an atomic or molecular scale especially to build microscopic devices'. Other definitions include the US government which state that 'Nanotechnology is research and technology development

at the atomic, molecular or macromolecular level in the length scale of approximately 1–100 nm range, to provide a fundamental understanding of phenomena and materials at the nanoscale and to create and use structures, devices and systems that have novel properties and functions because of their small and/or intermediate size'. The Japanese have come up with a more focused and succinct definition for 'True Nano' as nanotechnology which is expected to cause scientific or technological quantum jumps, or to provide great industrial applications by using phenomena and characteristics peculiar in nano-level.

Regardless of the definition that is used, it is evident that the properties of matter are controlled at a scale between 1 and 100 nm. For example, chemical properties take advantage of large surface to volume ratio for catalysis and interfacial and surface chemistry is important in many applications. Mechanical properties involve improved strength hardness in light-weight nanocomposites and nanomaterials, altered bending, compression properties, nanomechanics of molecular structures. Optical properties involve absorption and fluorescence of nanocrystals, single photon phenomena, photonic bandgap engineering. Fluidic properties give rise to enhanced flow using nanoparticles, and nanoscale adsorbed films are also important. Thermal properties give increased thermoelectric performance of nanoscale materials and interfacial thermal resistance is important.

## 1.2 APPROACHES TO NANOTECHNOLOGY

Numerous approaches have been utilized successfully in nanotechnology, and as the technology develops further approaches may emerge. The approaches employed thus far have generally been dictated by the technology available and the background experience of the researchers involved. Nanotechnology is a truly multidisciplinary field[4] involving chemistry, physics, biology, engineering, electronics, social sciences, etc., which need to be integrated together in order to generate the next level of development (Figure 1.1). Fuel cells, mechanically stronger materials, nanobiological devices, molecular electronics, quantum devices, carbon nanotubes, etc. have been made using nanotechnology. Even social scientists are debating ethical use of nanotechnology.

The two main approaches to explaining nanotechnology to the general public have been oversimplified and have become known as the 'top-down' approach and the 'bottom-up' approach. The top-down approach involves fabrication of device structures via monolithic processing on the nanoscale. This approach has been used with spectacular success in the semiconductor devices used in consumer electronics. The bottom-up approach involves the
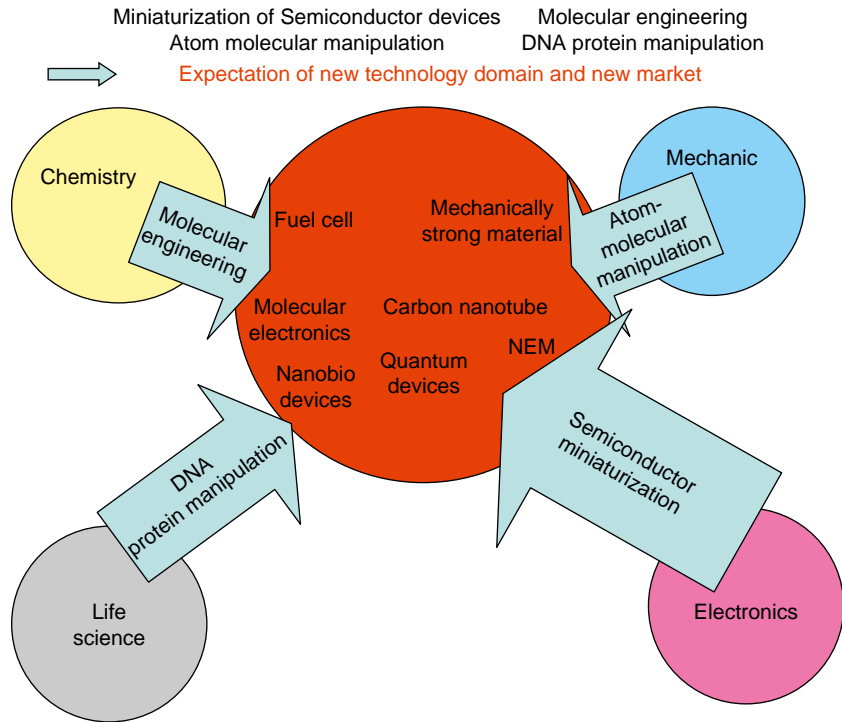
**FIGURE 1.1**  *Multidisciplinary nature of nanotechnology.*
*Source: Ref. [4].*

fabrication of device structures via systematic assembly of atoms, molecules or other basic units of matter. This is the approach nature uses to repair cells, tissues, organs of living and organ systems in living things, and indeed for life processes such as protein synthesis. Tools are evolving which will give scientists more control over the synthesis and characterization of novel nanostructures and yield a range of new products in the near future.

## 1.3  TRANSITION FROM NANOTECHNOLOGY TO NANOMANUFACTURING

Throughout the world a huge amount of research is being carried out, and governments and research organizations are spending large amounts of money and human resources into nanotechnology. This has generated interested scientific output and potential commercial applications, some of which have been translated into products produced on a large scale. However, in
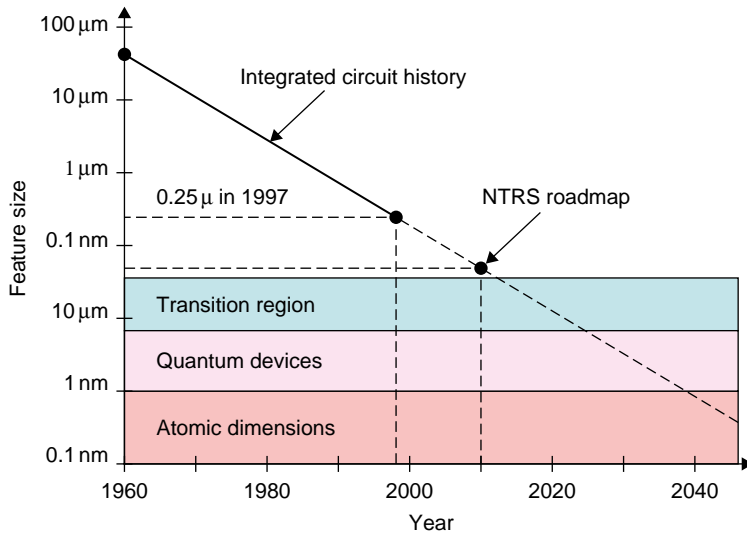
• History and future projections for minimum feature size in silicon chips.

**FIGURE 1.2**   *Features size evolution in silicon chips.*
*Source: Ref. [10].*

order to realize commercial benefits far more lab-scale applications need to be commercialized, and for that to happen nanotechnology needs to enter the realm of nanomanufacturing. This involves using the technologies available to produce products on a large scale which is economically viable. Regardless of whether a top-down or bottom-up approach is used, a nanomanufacturing/ nanofabrication technology should be:

- capable of producing components with nanometre precision;
- able to create systems from these components;
- able to produce many systems simultaneously;
- able to structure in three dimensions;
- cost-effective.

## 1.3.1  Top-down approach

The most successful industry utilizing the top-down approach is the electronics industry (Figure 1.2).

This industry is utilizing techniques involving a range of technologies such as chemical vapour deposition (CVD), physical vapour deposition (PVD),
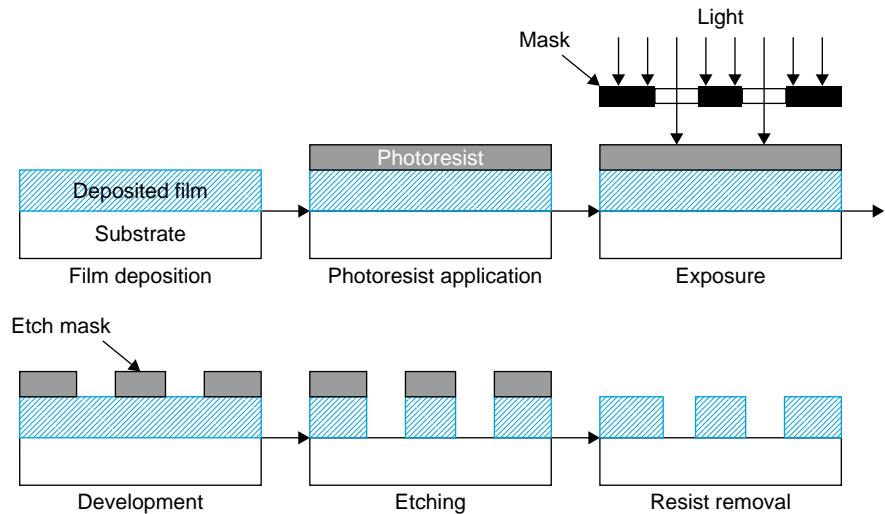
**FIGURE 1.3** *A typical process sequence employed in the electronics industry to generate functional devices at the micro- and nanoscale.*
*Source: Ref. [11].*

lithography (photolithography, electron beam and X-ray lithography), wet and plasma etching, etc. to generate functional structures at the micro- and nanoscale (Figure 1.3). Evolution and development of these technologies have allowed emergence of the numerous electronic products and devices that have enhanced the quality of life throughout the world. The feature sizes have been shrinking continuously from about 75 μm to below 100 nm. This has been achieved by improvements in deposition technology and more importantly due to the development of lithographic techniques and equipment such as X-ray lithography and electron beam lithography.

Techniques such as electron beam lithography, X-ray lithography and ion beam lithography, all have advantages in terms of resolution achieved; however, there are disadvantages associated with cost, optics and detrimental effects on the substrate. These methods are currently under investigation to improve upon current lithographic process used in the IC industry. With continuous developments in these technologies, it is highly likely that the transition from microtechnology to nanotechnology will generate a whole new generation of exciting products and features.

Let us take an example of a demonstration of how several techniques can be combined together to form a 'nano' wine glass (Figure 1.4). In this example, a focused ion beam and CVD have been employed to produce this striking nanostructure.
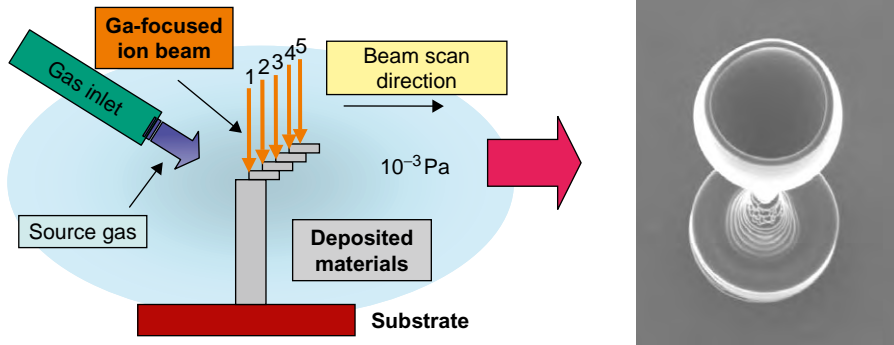
**FIGURE 1.4**  *Demonstration of three-dimensional nanostructure fabrication.*
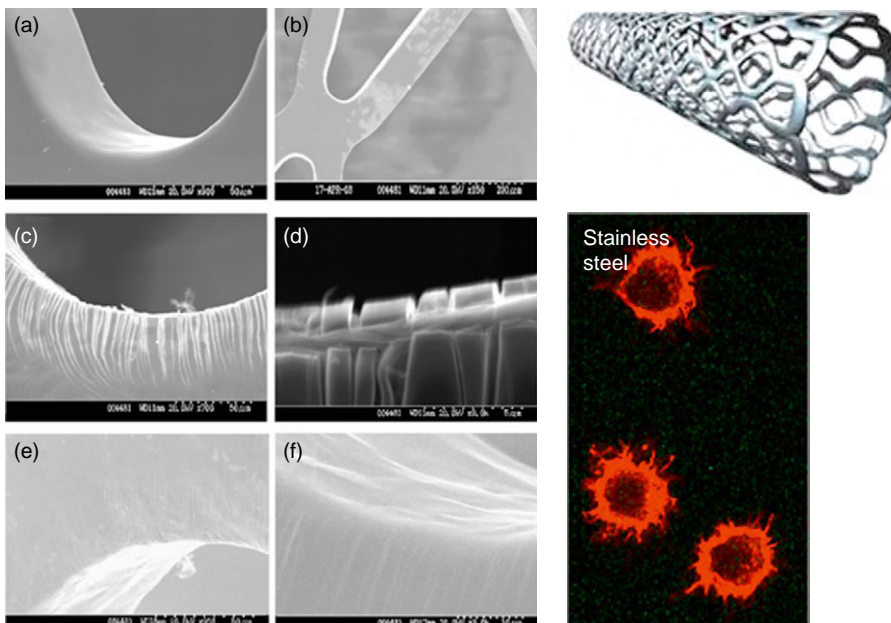*Source: Ref. [12].*



**FIGURE 1.5**  *Examples of stents coated with diamond-like carbon using plasma-enhanced CVD.*
*Source: Courtesy Okpalugo (2007).*

The top-down approach is being used to coat various coatings to give improved functionality. For example, vascular stents are being coated using CVD technology with ultra-thin diamond-like carbon coatings in order to improve biocompatibility and blood flow (Figure 1.5). Graded a-SixCy:H interfacial layers results in greatly reduced cracking and enhanced adhesion.

### 1.3.2 Bottom-up approach

The bottom-up approach involves making nanostructures and devices by arranging atom by atom. The scanning tunnelling microscope (STM) has been used to build nano-sized atomic features such as the letters IBM written using xenon atoms on nickel[5] (Figure 1.6). While this is beautiful and exciting, it remains that the experiment was carried out under carefully controlled conditions, that is liquid helium cooling and high vacuum, and it took approximately 24 hours to get the letters right. Also the atoms are not bonded to the surface just adsorbed and a small change in temperature or pressure will dislodge them. Since this demonstration significant advances have been made in nanomanufacturing.

The discovery of the STM's ability to image variations in the density distribution of surface-state electrons created in the artists a compulsion to have complete control of not only the atomic landscape, but also the electronic landscape[5]. Figure 1.7 shows 48 iron atoms positioned into a circular ring in order to 'corral' some surface-state electrons and force them into 'quantum' states of the circular structure. The ripples in the ring of atoms are the density distribution of a particular set of quantum states of the corral. The artists were delighted to discover that they could predict what goes on in the corral by solving the classic eigenvalue problem in quantum mechanics – a particle in a hard-wall box.

Probably, the most publicized material in recent years has been carbon nanotubes. Carbon nanotubes – long, thin cylinders of carbon – were
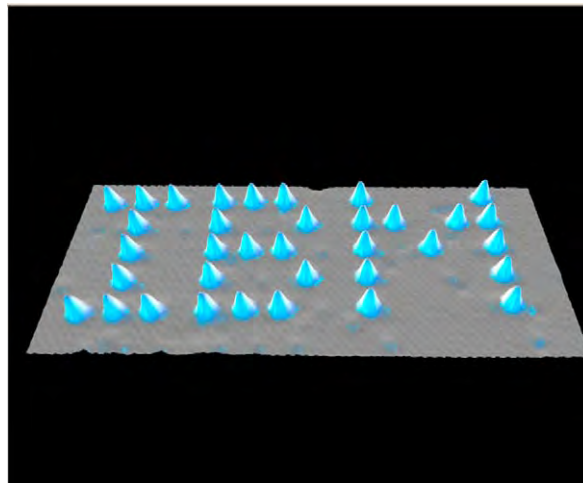


**FIGURE 1.6** *Positioning single atoms with an STM.*
*Source: Ref. [5].*

discovered in 1991 by S. Iijima[6]. These are large macromolecules that are unique for their size, shape and remarkable physical properties. They can be thought of as a sheet of graphite (a hexagonal lattice of carbon) rolled into a cylinder. These intriguing structures have sparked much excitement in the recent years and a large amount of research has been dedicated to their understanding. Currently, the physical properties are still being discovered and disputed. What makes it so difficult is that nanotubes have a very broad range of electronic, thermal and structural properties that change depending on the different kinds of nanotube (defined by its diameter, length and chirality, or twist). To make things more interesting, besides having a single cylindrical
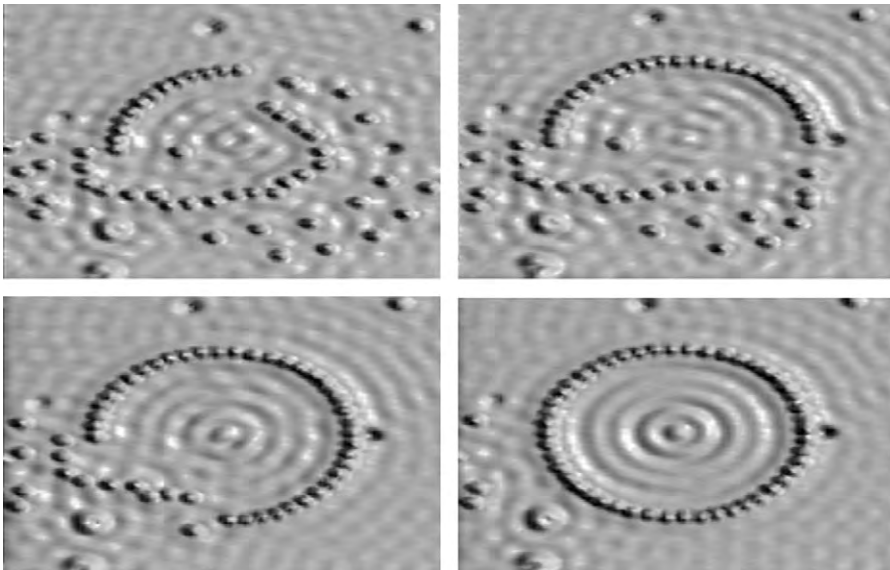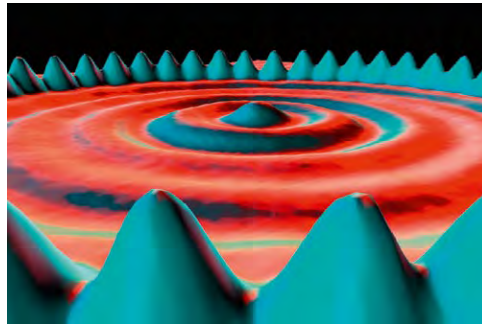


**FIGURE 1.7**   *Confinement of electrons to quantum corrals on a metal surface.*
*Source: Ref. [5].*

wall (SWNTs), nanotubes can have multiple walls (MWNTs) – cylinders inside the other cylinders (Figure 1.8).

Several researchers[7] have grown vertically aligned carbon nanotubes using a microwave plasma-enhanced CVD system using a thin-film cobalt catalyst at 825°C. The chamber pressure used was 20 Torr. The plasma was generated using hydrogen which was replaced completely with ammonia and acetylene at a total flow rate of 200 sccm.

Lithographic methods are important for micro- and nanofabrication. Lithography is the art of drawing or writing on a kind of yellow salty limestone so that impressions in ink can be taken; in the Oxford Dictionary the word 'lithos' comes from Greek for stone. In micro- and nanofabrication we mean pattern transfer. Owing to limitations in current (and future) photolithographic processes, there is a challenge to develop novel lithographic processes with better resolution for smaller features. One such development is that of *Dip-pen nanolithography* (DPN). Dip-pen technology[8], in which ink on a pointed object is transported to a surface via capillary forces, is approximately 4000 years old. The difference with DPN is that the pointed object has a tip which has been sharpened to a few atoms across in some cases.
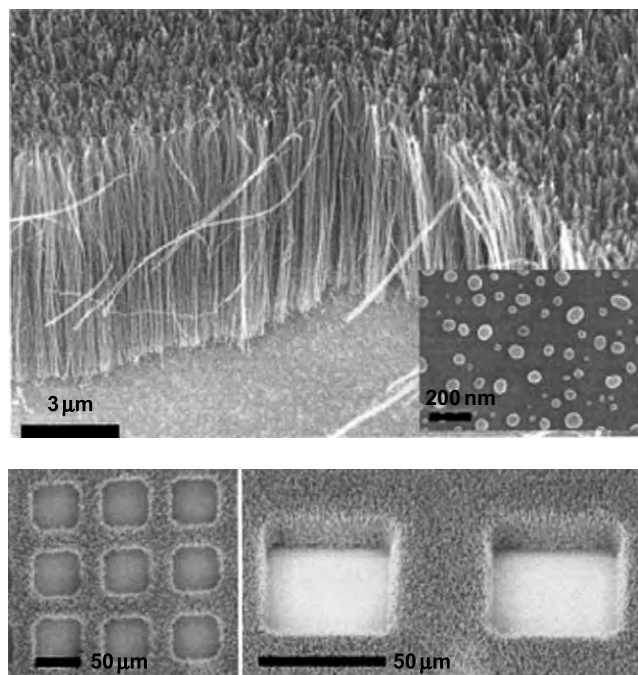


**FIGURE 1.8**  *Multiwall carbon nanotubes with a diameter of 30 nm and a length of 12 μm have been formed within 2 minutes.*

DPN is a scanning probe nanopatterning technique in which an atomic force microscope (AFM) tip is used to deliver molecules to a surface via a solvent meniscus, which naturally forms in the ambient atmosphere. It is a direct-write technique and is reported to give high-resolution patterning capabilities for a number of molecular and biomolecular 'inks' on a variety of substrates such as metals, semiconductors and monolayer functionalized surfaces.

DPN allows one to precisely pattern multiple patterns with good registration. It's both a fabrication and an imaging tool, as the patterned areas can be imaged with clean or ink-coated tips. The ability to achieve precise alignment of multiple patterns is an additional advantage earned by using an AFM tip to write as well as read nanoscopic features on a surface. These attributes make DPN a valuable tool for studying fundamental issues in colloid chemistry, surface science and nanotechnology. For instance, diffusion and capillarity on a surface at the nanometre level, organization and crystallization of particles onto chemical or biomolecular templates, monolayer etching resists for semiconductors and nanometre-sized tethered polymer structures can be investigated using this technique. In order to create stable nanostructures, it's beneficial to use molecules that can anchor themselves to the substrate via chemisorption or electrostatic interactions. When alkanethiols are patterned on a gold substrate, a monolayer is formed in which the thiol head groups form relatively strong bonds to the gold and the alkane chains extend roughly perpendicular to the surface (Figure 1.9). Creating nanostructures using DPN is a single step process that does not require the use of resists. Using a conventional AFM,
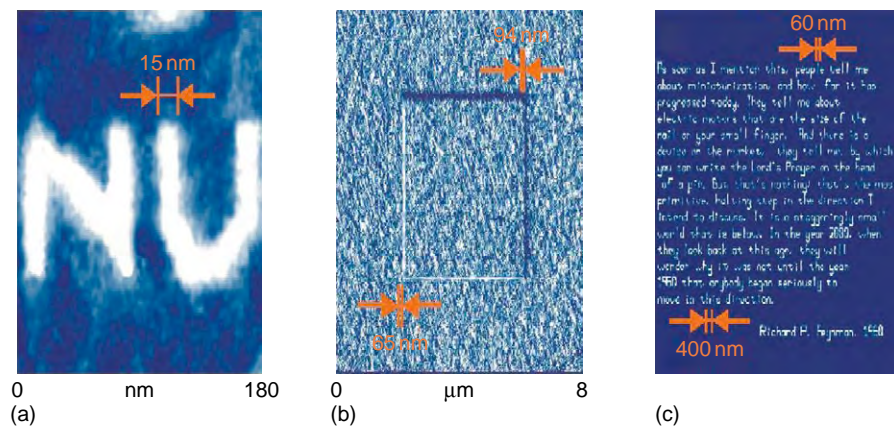


**FIGURE 1.9** *(a) Ultra-high resolution pattern of mercaptohexadecanoic acid on atomically flat gold surface. (b) DPN-generated multi-component nanostructure with two aligned alkanethiol patterns. (c) Richard Feynman's historic speech written using the DPN nanoplotter.*

**FIGURE 1.10**

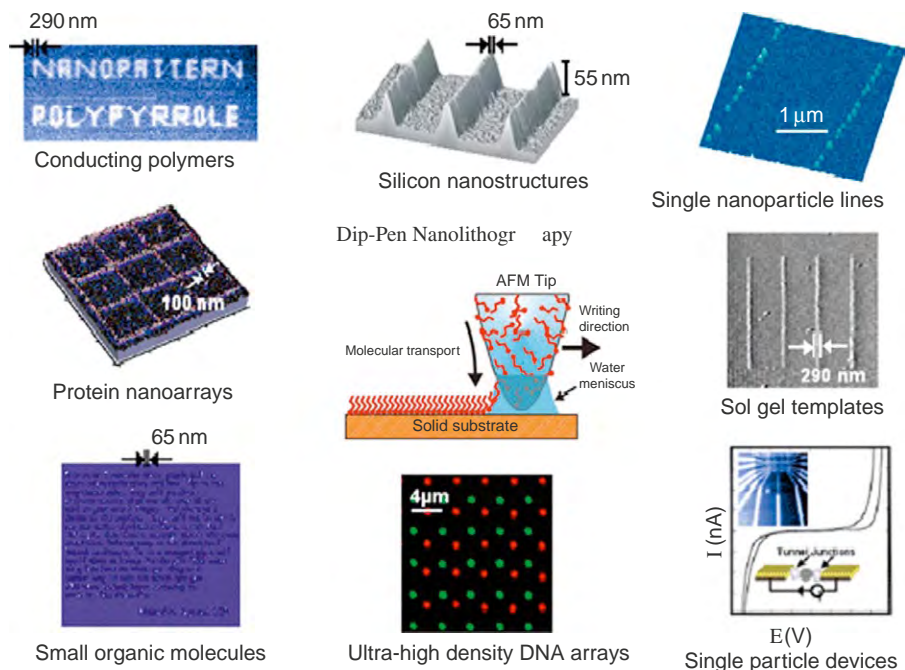*Some of the potential applications of DPN.*

290 nm

NANOPATTERN POLYPYRROLE

Conducting polymers

65 nm

55 nm

Silicon nanostructures

1 µm

Single nanoparticle lines

Dip-Pen Nanolithogr    apy

100 nm

Protein nanoarrays

AFM Tip

Writing direction

Molecular transport

Water meniscus

Solid substrate

290 nm

Sol gel templates

65 nm

Small organic molecules

4µm

Ultra-high density DNA arrays

I (nA)

Tunnel Junctions

E(V)

Single particle devices



**FIGURE 1.11**

*LFM images of nanolithography patterns, which were formed using an eight-pen nanoplotter capable of doing parallel DPN.*

180 nm

40 nm

2 µm
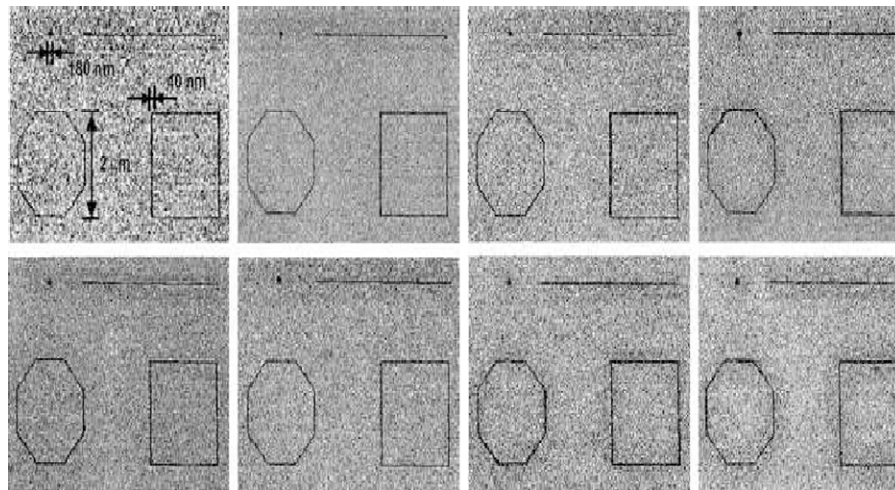
DPN has been reported to achieve ultra-high resolution features with line widths as small as 10–15 nm with ~5 nm spatial resolution (Figure 1.10). For nanotechnological applications, it is not only important to pattern molecules in high resolution, but also to functionalize surfaces with patterns of two or more components (Figure 1.11).
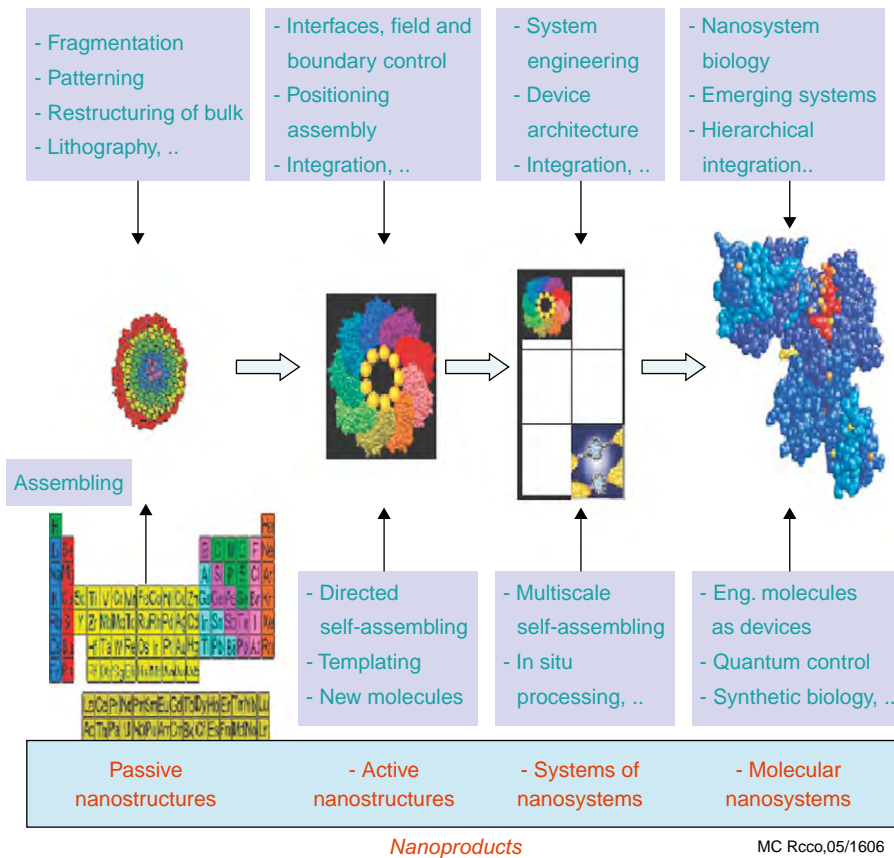
**FIGURE 1.12**

*Summary of Nanomanufacturing. Source: Ref. [9].*

Figure 1.12 shows the basic concept of nanomanufacturing[9]. Individual atoms, which are given in the periodic table, form the basis for nanomanufacturing. These can be assembled into molecules and various structures using various methods including directed self-assembly, templating, etc. and may be positioned appropriately depending on the final requirements. Further along the devices architecture, integration, in situ processing may be employed culminating in nanosystems, molecular devices, etc.

## 1.4 CONCLUSIONS

The transition from nanotechnology to nanomanufacturing is truly under way. Numerous products are now on the market and many new sophisticated and intelligent 'nano' products are being developed and will become widely

available. According to Roco, nanotechnology revolution can be conveniently divided into four generations:

i. The first generation of nanotechnology involved research and development into the synthesis and fabrication of passive structure. These included the following: nanostructures, for example nanostructured coatings, ultra-precision machining, dispersion of nanoparticles and surface nanopatterning.

ii. The second generation involved giving active functionality to active (evolving function) nanostructures, for example molecular machines, light-driven mechanical motors, laser-emitting devices and adaptive structures.

iii. The third generation involved developing systems of nanosystems, for example chemo-mechanical processing of molecular assemblies, artificial organs built from the nanoscale, modified viruses and bacteria.

iv. The fourth generation will involve research into integrated heterogeneous molecular nanosystems together with coordinated functionalities. This is approaching the way biological systems work, for example evolutionary cells and cell ageing therapies, human–machine interface.

## REFERENCES

[1] R.P. Feynman, There is plenty of room at the bottom, Eng. Sci. 23 (1960) 22–36.

[2] N. Taniguchi, On the basic concept of 'nano-technology' Proc. Int. Conf. Prod. Eng. Tokyo, Japan, Part II, Japan Society of Precision Engineering, 1974. pp. 5–10.

[3] R.W. Siegel, E. Hu, M.C. Roco (Eds.), Nanostructure Science and Technology, Springer, Dordrecht, Netherlands, 1999. (Also available at <www.wtec.org/loyola/nano/>)

[4] www.nseresearch.org (2005).

[5] M.F. Crommie, C.P. Lutz, D.M. Eigler, Confinement of electrons to quantum corrals on a metal surface, Science 262 (1993) 218–220.

[6] S. Iijima, Helical microtubules of graphite carbon, Nature 354 (1991) 56–58.

[7] K. Yoshihara, S. Honda, J.-G. Lee, H. Mori, K. Oura, M. Katayama, High-density growth of vertically aligned carbon nanotubes with high linearity by catalyst preheating in acetylene, Jpn. J. Appl. Phys. 47 (2008) 1941–1943.

[8] C.A. Mirkin, Dip pen nanolithography: automated fabrication of custom micro-components, sub-100 nanometer surface architectures, MRS Bull. 26 (2001) 535–538.

 [9]  O. Renn, M.C. Roco, Nanotechnology and the need for risk governance, J. Nanopart. Res. 8 (2) (2006) 1–41.

[10]  G. Moore, Lithography and the future of Moore's law, Proc. SPIE 2437 (May 1995).

[11]  J.D. Plummer, M.D. Deal, P.B. Griffin, Silicon VLSI Technology, Prentice Hall, New Jersey, 2000.

[12]  T. Fujii, J. Micromech. Microeng. 15 (2005) S286–S291.

# Gas Phase Nanofication: A Strategy to Impart Fast Response in Sensors

Abdul-Majeed Azad

*Department of Chemical Engineering, The University of Toledo, Toledo, OH, USA*

## CONTENTS

## ABSTRACT

Sensing mechanism is predominantly surface-dominated. Benign surface features in terms of small grain size, large surface area, high aspect ratio, and open and connected porosity are required to realize a successful sensor material. Such morphological artefacts could be incorporated in a number of promising semiconducting oxide-based gas sensors by employing a technique based on the thermodynamics of metal/metal oxide coexistence. By modulating the equilibrium oxygen partial pressure across the metal/metal oxide proximity line, renewed formulation and growth of an oxide surface on an atomic/submolecular level endowed with exotic morphology under oxygen 'deprivation' or 'enrichment' has been achieved in a number of potential ceramic sensor systems. In the case of oxides that are not amenable to such classical oxygen modulation, alternative techniques do exist. In such cases, a novel high temperature reductive etch process (HiTREP$^©$) could be exploited to re-create the smart nanofeatures imparting the desired response accentuation effect. The microscopic results of these strategies as applied to the oxides of molybdenum, tungsten and titanium made via low-cost, thick-film fabrication and their effect on the sensing characteristics are discussed.

## 2.1  INTRODUCTION

One aspect of current interest and great relevance to the fundamental understanding of the behaviour of materials is the role of dimensionality and size on their optical, chemical and mechanical properties for application in a wide range of devices. Owing to the nanoscale features, one-dimensional systems exhibit novel physical and chemical properties that can be exploited in optics, catalysis and data storage devices. Hence, such

systems are being synthesized and studied in great details. For instance, polymer nanofibres are used as selective gas separation membranes, filters, biomedical fillers, drug carriers and wound dressings, protective clothing, space mirrors, and precursor platforms or scaffolds for the nanotube/nanowire synthesis. Thus, they become model systems to study and correlate the theoretical explanations that are still in progress. Such behaviour is almost nonexistent in the bulk material where the particle size is in the micron level. There is growing interest in introducing such attributes in nanoscale inorganic materials as well. The most obvious advantage of doing so is the possibility of their application as quantum dots in a host of devices such as MEMs, lab-on-a-chip sensors/detectors, structural elements in artificial organs and arteries, reinforced composites, micro solar cell electrodes, micro fuel cells, photocatalysts (splitting of water and in the deactivation of chemical and biological weapons) and electrocatalysts, to name a few.

One area where nanofeatures in the materials are of immense relevance is the field of solid-state ceramic-based chemical sensors. Work on sensor development is carried out worldwide in industry, academia and government facilities. This is driven by the need for improved, fast, in situ and online detection and quantification of various gaseous pollutants in a host of industries including power generation, chemical, pharmaceutical, electronics, biomedical, health and environmental protection and preservation. The global market for advanced materials and sensors increased from $5.7 billion in 2006 to an estimated $6.8 billion by the end of 2007. It should reach $9.4 billion by 2012, a compound annual growth rate (CAGR) of 6.9%. The global market for automotive sensor technologies increased from $7.3 billion in 2006 to an estimated $8.0 billion by the end of 2007. It should reach $13.5 billion by 2012, a CAGR of 10.8%. The market for chemical process monitoring devices was $49.1 billion in 2005 and almost $50.9 billion in 2006. At a CAGR of 4%, the market will reach $61.8 billion by 2011. Demand for chemical sensors alone in the United States is forecast to be $4.1 billion in 2009, buoyed by continued strong demand for biosensor products in the medical and diagnostic industries, and increased spending on public safety and security in the face of a potential biological or chemical terrorist attack. Other markets such as environmental monitoring and industrial processing are also projected to experience healthy gains, though not as fast as medical and diagnostics[1].

Detection of chemical species and their quantification have become important in many industrial applications involving high temperatures and chemical contaminants. High selectivity, enhanced sensitivity and short response time are some of the key features sought in these devices.

Since the sensing mechanism and catalytic activity of ceramics are largely microstructure-dominated, benign surface features such as small grain size, large surface area, high aspect ratio and open/connected porosity are required to realize a successful sensor material[2–4].

Some routinely employed methods to achieve small grains and exotic morphologies in potential semiconducting sensor materials are sol–gel and other low temperature solution routes. However, in some of these cases, the benign microstructural features are compromised when the temperatures are elevated; grain growth and some phase transformations are unfortunately irreversible and hence undesirable. Hence, in the case of high temperature sensors with applications intended for harsh and unforgiving environment (corrosive, high velocity flux gas streams, etc.), what appears benign and promising under mild condition might not be sustained under real-life conditions at the application temperatures. On the other hand, microstructural features created under more severe conditions are not altered in application under milder experimental conditions.

Recently, a novel technique employed to impart benign attributes by modifying the microstructural artefacts in a number of ceramic-based sensor materials (such as $WO_3$ and $MoO_3$, $MoO_3$–$ZnMoO_4$ and $TiO_2$) has been reported. The effect of the variation in the ambient oxygen partial pressure across the metal/metal oxide boundary on the microstructure and gas sensing characteristics (viz., enhancement of sensitivity and shortening of response time) of potential oxides such as $WO_3$, $MoO_3$ and $TiO_2$ were also studied[5–9]. The methodology adopted to bring about the desired morphological variations is described briefly here.

## 2.2  PROPOSED RATIONALE

At a given temperature and standard pressure (ambient; 1 atm), the oxidation of a metal to its oxide or the reduction of an oxide to its suboxide or the corresponding metal occurs at a well-defined oxygen partial pressure ($p_{O_2}$). At a given temperature, on either side of this unique $p_{O_2}$, one of the two coexisting phases must disappear. This is illustrated in the following by considering a hypothetical metal oxidation reaction:

$$M(s) + \frac{x}{2}O_2(g) \rightarrow MO_x(s) \tag{2.1}$$
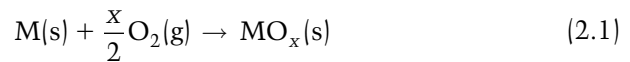
for which

$$K_1 = \frac{a_{MO_x}}{a_M \cdot p_{O_2}^{x/2}} \tag{2.2a}$$

and

$$\Delta G_{R(1)} = -RT \cdot \ln K_1 \qquad (2.2b)$$

where $K_1$ and $\Delta G_{R(1)}$ are the reaction equilibrium constant and the standard Gibbs' energy change, respectively, for reaction (2.1).

Equations (2.2a) and (2.2b) can be combined and simplified to give:

$$p_{O_2(M/MO_x)} = e^{(2 \cdot \Delta G_{R(1)} / xRT)} \qquad (2.2c)$$

Equation (2.2c) gives the thermodynamic equilibrium oxygen partial pressure for the coexistence of a metal with its adjacent oxide at a given temperature in terms of the standard Gibbs energy change for reaction (2.1); in the present case it is also equal to the standard Gibbs energy of formation of the oxide, $MO_x$. Consequently, a plot of $p_{O_2}$ or $\ln p_{O_2}$ versus temperature gives the contour of the path of the $M/MO_x$ coexistence. It can then be visualized that at a $p_{O_2}$ *lower* than the 'line of coexistence', the metal oxide would experience reduction either to its suboxide or to the corresponding metal. Similarly, at $p_{O_2}$ *above* the line, a metal (or its suboxide) would be oxidized to the corresponding stable oxide.

Ordinarily, an oxide can be reduced to a suboxide or the corresponding metal by $H_2$ or CO. Heating the reduced species in air (static or dynamic; $p_{O_2} = 0.21$ atm) leads to bulk oxidation, regenerating the parent phase whose morphological features may or may not be very different from the starting material. On the other hand, if the reduced surface is exposed to a well-defined $p_{O_2}$ that is only a few orders of magnitudes higher than the theoretical value for the $M/MO_x$ coexistence, interesting processes ensue. Under this condition, since the prevailing oxygen potential is only slightly *above* that established by virtue of thermodynamic equilibrium between M and $MO_x$ or between $MO_x$ and $MO_y$, it allows the formation and growth of new oxide surface on an atomic/molecular level, under conditions of well-defined 'oxygen enrichment' locally. Similarly, by exposing the oxide to a precisely controlled $p_{O_2}$ regime that is *below* the theoretical line of the metal oxide stability, one can modulate the extent of reduction of the said oxide either to a suboxide or ultimately to the metal under conditions of 'oxygen deprivation' locally. In any event, it can be envisaged that such a $p_{O_2}$ manipulation will deplete/enrich oxygen in a manner so as to cause atomic or submolecular level chemical variations. Hence, upon exposure to an environment that is only slightly rich in oxygen, new material build-up takes place layer by layer, thereby creating whole new morphological features that are alien to the starting bulk oxide.

## 2.3 METHODS OF ESTABLISHING THE DESIRED REDOX $p_{O_2}$

An oxygen potential in the vicinity of these equilibria could potentially be generated by manipulating the ratio of two gaseous species in a buffer mixture, such as $CO_2/CO$ or $H_2O/H_2$.

At high temperatures, CO and $CO_2$ can exist in equilibrium with traces of oxygen:

$$CO + \frac{1}{2}O_2 = CO_2 \tag{2.3}$$

for which

$$\Delta G^o = -RT \ln \left( \frac{p_{CO_2}}{p_{CO} \cdot p_{O_2}^{1/2}} \right) \tag{2.4a}$$

This gives

$$p_{O_2} = \left( \frac{p_{CO_2}}{p_{CO}} \right)^2 \cdot \frac{1}{e^{\frac{-2\Delta G^o}{RT}}} \tag{2.4b}$$

where

$$\Delta G^0 (J) = -282{,}400 + 86.81T \tag{2.4c}$$

Therefore, by controlling the ratio of the concentration of $CO_2$ and CO, it is possible to control the partial pressure of oxygen. Mixing $CO_2$ and CO in the ratio that ranges from $10^{-5}$ to $10^5$ provides good buffered systems. In this range, the theoretical $p_{O_2}$ varies between $10^{-35}$ and $10^{-15}$ atm at 600°C and between $10^{-29}$ and $10^{-9}$ at 800°C.

Similar $p_{O_2}$ can be generated by an equilibrium established in a mixture of $H_2/H_2O$. Such oxygen potentials could also be obtained with relative ease via establishment of the following equilibrium:

$$H_2 + \frac{1}{2}O_2 \rightarrow H_2O \tag{2.5}$$

for which

$$\Delta G^o = -RT \ln \left( \frac{p_{H_2O}}{p_{H_2} p_{O_2}^{1/2}} \right) \tag{2.6a}$$

This gives

$$p_{O_2} = \left(\frac{p_{H_2O}}{p_{H_2}}\right)^2 \cdot \frac{1}{e^{\frac{-2\Delta G^0}{RT}}} \tag{2.6b}$$

where

$$\Delta G^0 (J) = -239,500 + 8.14T \ln T - 9.25T \tag{2.6c}$$

Thus by varying the water vapour to hydrogen ratio in the range of $10^{-5}$ to $10^5$, the corresponding equilibrium oxygen partial pressure at 600°C can be conveniently varied between $10^{-34}$ and $10^{-14}$ atm. However, owing to the ease of mixing gaseous components and in order to eliminate the possibility of water condensation in the cooler section of the sensor set-up, a buffer mixture of $CO/CO_2$ is more preferred.

To put this in perspective, the equilibrium $p_{O_2}$ computed by using reliable Gibbs' energy data for the biphasic coexistence of several metal/metal oxide couples of relevance to gas sensing is shown in Table 2.1 at a few representative temperatures.

Using reliable Gibbs energy data[10,11], the loci of $\log_{10} p_{O_2}$ as a function of temperature in the range 400°C–800°C, for various metal/metal oxide couples are plotted in Figure 2.1a. Also shown (as open triangles) are the $p_{O_2}$ values obtained by varying the $CO_2/CO$ ratio in the range $10^{-5}$ to $10^5$ at 450°C, 600°C and 800°C. In the light of the above-mentioned rationale, it appears that thermodynamically it is impossible to cause reduction of $TiO_2$ to either TiO or Ti metal via the $CO_2/CO$ buffer gas technique; it is also true for the case of $H_2O/H_2$ mixture. This is due to the fact that the thermodynamic stability of titania is quite high and the corresponding dissociation oxygen

**Table 2.1**   Equilibrium $P_{O_2}$ Values for Some Representative Semiconducting Oxide Systems

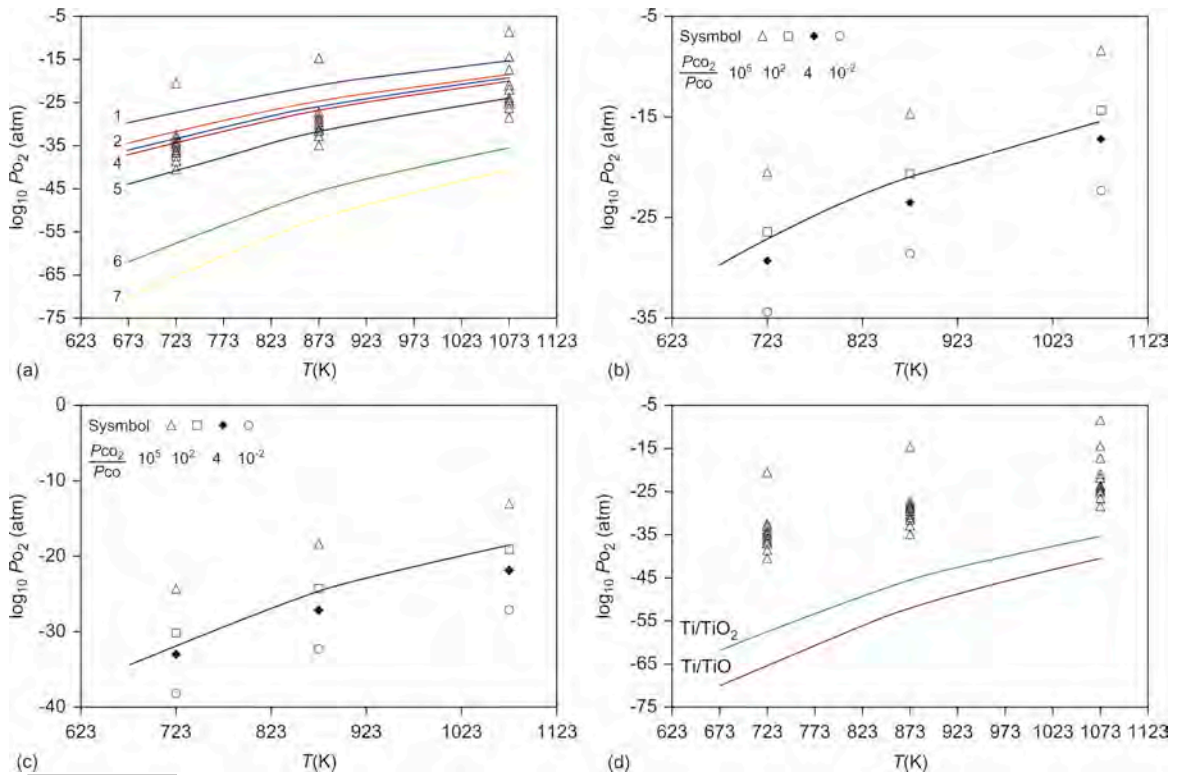| T(°C) | $P_{O_2}$ (atm) | | | | |
|---|---|---|---|---|---|
| | Mo/MoO$_3$ | W/WO$_3$ | Zn/ZnO | Ti/TiO$_2$ | Ti/TiO |
| 400 | $1.9 \times 10^{-30}$ | $3.4 \times 10^{-35}$ | $1.4 \times 10^{-44}$ | $1.5 \times 10^{-62}$ | $7.5 \times 10^{-71}$ |
| 600 | $1.2 \times 10^{-21}$ | $2.3 \times 10^{-25}$ | $2.1 \times 10^{-32}$ | $2.7 \times 10^{-46}$ | $1.2 \times 10^{-52}$ |
| 800 | $4.0 \times 10^{-16}$ | $3.1 \times 10^{-19}$ | $7.8 \times 10^{-25}$ | $4.3 \times 10^{-36}$ | $3.1 \times 10^{-41}$ |
| 1000 | | | | $4.2 \times 10^{-29}$ | $2.1 \times 10^{-33}$ |
| 1100 | | | | $2.3 \times 10^{-26}$ | $2.4 \times 10^{-30}$ |

**FIGURE 2.1** *(a) Temperature dependence of the equilibrium oxygen partial pressure in: 1, $Mo/MoO_3$; 2, $W/WO_3$; 3, $Mo/MoO_2$; 4, $W/WO_2$; 5, $Zn/ZnO$; 6, $Ti/TiO_2$ and 7, $Ti/TiO$; (b) $Mo/MoO_3$, (c) $W/WO_3$ and (d): $Ti/TiO_2$ and $Ti/TiO$ systems. The variation in $p_{O_2}$ by changing the $CO_2/CO$ ratio between $10^{-5}$ and $10^5$ at 450°C, 600°C and 800°C is also shown (open triangles).*

partial pressure in the $Ti/TiO_2$ system is rather low. No 'practical' mixture of CO and $CO_2$ (or even $H_2$ and $H_2O$) could cause reduction of $TiO_2$ to TiO or Ti. For example, the equilibrium oxygen partial pressure in the $Ti/TiO_2$ coexisting mixture ranges from $2.732 \times 10^{-46}$ atm at 873 K to $4.192 \times 10^{-29}$ atm at 1273 K. In the case of Ti/TiO, the equilibrium $p_{O_2}$ values range from $1.18 \times 10^{-52}$ atm at 873 K to $2.06 \times 10^{-33}$ atm at 1273 K. Calculations show that no 'practical' mixture of CO and $CO_2$ gases would be able to establish such low $p_{O_2}$ values. Hence, it is impossible to cause redox reaction of $TiO_2$ by this scheme. Thus, in this case alternative routes ought to be conceived to bring in the desired benign microstructural modifications. In such cases, significant morphological architect could be developed by using dilute $H_2/N_2$ mixtures; this aspect will be discussed subsequently in this chapter.

A plot of $\log p_{O_2}$ versus $T$ for the $Mo/MoO_3$ and $W/WO_3$ coexistence in the range 450°C–800°C is shown in Figure 2.1b and 2.1c, respectively, and that for Ti/TiO and $Ti/TiO_2$ in Figure 2.1d.

Utilizing the scheme outlined above, an oxygen partial pressure in the vicinity of Mo/MoO$_3$ and W/WO$_3$ proximity line could be generated by manipulating the ratio of two gaseous species in a buffer mixture, such as CO$_2$/CO or H$_2$O/H$_2$. From the point of experimental ease and in order to obviate the practical difficulty associated with water condensation, a buffer mixture of CO$_2$/CO in varying ratio is more amenable to create adequate oxygen partial pressure in these cases; this is represented by different symbols in Figure 2.1b and 2.1c. Values above the solid lines are those that could oxidize the respective metal; those below would reduce the oxides. In the following sections, the validation of the proposed technique as applied to bulk materials such as simple metals and oxides and its extension to double oxides and two-phase mixtures that are amenable to direct $P_{O_2}$ modulation via gas phase buffer mixtures are discussed. In those cases where such modulation using the CO$_2$/CO and/or H$_2$O/H$_2$ mixtures is not plausible, a high temperature reductive etching process (HiTREP$^©$) was established.

## 2.4  SAMPLE PREPARATION

### 2.4.1  Materials and processing

The materials investigated in this work included thin foils of Mo and W as well as the powders of MoO$_3$ and WO$_3$ (Alfa-Aesar, Ward Hill, MA; 99.8% or better). The vendor-specified average particle size of the oxides was between 20 and 45μm. The metal foils were used to demonstrate the authenticity of the proposed concept while the oxide powders were used to fabricate the sensor films whose sensing behaviour towards different levels of carbon monoxide or hydrogen in a 10% O$_2$-balance N$_2$ background was monitored before and after these films were subjected to the reduction–oxidation processes described above. A set of these films were also reduced in hydrogen and oxidized in air to differentiate the morphological attributes obtained in the proposed approach versus those resulting from classical redox method. Titania samples were subjected only to reduction in a H$_2$/N$_2$ mixture.

The stoichiometry of MoO$_3$ is known to be significantly dependent upon the method of preparation employed[12, 13]. To discern the effect of the synthesis methodology on the microstructural evolution, molybdenum trioxide was synthesized by two additional methods in addition to using the as-received powder from Alfa-Aesar. In the first case, commercial MoO$_3$ powder was used without further processing, except that it was thoroughly ground, ball-milled and sieved through 325 mesh screen prior to printing thick films. In the second case, the MoO$_3$ powder was obtained by oxidizing Mo metal foil in air at 600°C for 2h. In the third instance, MoO$_3$ was prepared

by a soft solution chemistry route using sodium molybdate dihydrate ($Na_2MoO_42H_2O$, AR grade from Alfa-Aesar) as the precursor. Then, 10.5g of sodium molybdate crystals were dissolved in 150 ml of de-ionized water with constant stirring and the solution was cooled in an ice-bath to 5°C. A measured quantity of 24ml of 1 M HCl acid were added to the cooled aqueous solution, stirred and the mixture was placed in the freezer overnight so as to maintain the temperature around 5°C. The frozen solution was thawed and heated slowly to 80°C with continuous stirring for 24h; a pale bluish precipitate of molybdic acid ($H_2MoO_4$) started to form after heating. The precipitate was washed several times with de-ionized water and centrifuged. In order to remove all the sodium ions, the conductivity of the filtrate was monitored after each wash until the conductivity was <0.05 mho. The solid thus obtained was dried, ground well and calcined for 1 h in air at 300°C. The formation of $MoO_3$ from the precipitated molybdic acid ($H_2MoO_4$) was confirmed by following the systematic phase evolution via X-ray diffraction (XRD) and scanning electron microscopy.

For titania-based systems, thick films were supplied by Henkel Corporation. The films were coated by an electrochemical process on 3-mm thick cp titanium plates and 18-SWG (1024-μm diameter) wires for 3min and are about $10 \pm 5$μm in thickness. In the case of plates, 12 mm × 12 mm coupons were cut out. In anticipation of their subsequent use as sensors after subjecting to HiTREP©, two tiny equispaced holes (1mm ID) were drilled close to one of the four edges. These holes would be used to connect lead wires to complete the circuit and measure the film resistance in sensing experiments. In the second case, the titania-coated wire was wound tight around a metal rod. Cylindrical sections of the coil, about 0.5-in. long were cut out. The samples were placed in an alumina boat which was kept in the uniform temperature zone of a horizontal PID-controlled tubular Lindberg Blue (NC) furnace and calcined in static air at 700°C and 900°C for 4h each, and at 1100°C for 2h. Coupons and coiled wire samples in sets of four were used for heat-treatment at each temperature. Two calcined samples from each batch were used for the reduction experiment in 5% $H_2$/Ar mixture (flow rate of 100 sccm) at 700°C for 6h. In one case, reduction was carried out for 8h as well.

## 2.4.2 Characterization

Structural and microstructural examination of the as-received foils, raw powders and the products after each of the redox reactions was conducted by XRD, scanning and transmission electron microscopy (SEM/TEM) to corroborate the observed enhancement in sensing characteristics of the thick-film sensors.

### 2.4.3  High temperature reductive etching process

In the case of powder samples, the thick-film sensors in chemiresistor mode were fabricated as follows. The powders were first ball-milled using 10 mm spherical zirconia milling media (Tosoh, NJ) in 2-propanol for 8 h, dried and sieved through a 325-mesh stainless steel screen. Each powder was mixed with V-006 (an organic-based resinous vehicle with dispersant, from Heraeus, PA) and α-terpineol (Alfa-Aesar) in an appropriate weight ratio (~70% solid loading) and stirred well so as to form a uniform slurry of adequate rheology. In order to improve the adhesion of the film to the substrate, 2 wt% of tetraethoxysilane (TEOS, Alfa-Aesar) was also added to the slurry and homogenized prior to printing. The film was screen-printed on high density α-alumina substrates (14 mm $\times$ 14 mm) pre-fabricated with interdigitated gold electrodes (12 mm $\times$ 12 mm) and contact pads. The films were first dried in an air oven at 150°C followed by firing in the range of 500°C–900°C, depending upon the physico-chemical properties of the oxides (stability, volatility, phase transformation, etc.) for 1–2 h in air. Gold lead wires (0.25 mm diameter, Alfa-Aesar) were attached to the contact pads via silver paste which was cured in three different stages between room temperature and 350°C so as to form good ohmic contacts.

The thick-film sensor made by a procedure described above, was subjected to reduction and oxidation at $p_{O_2}$ below and above the theoretical line of coexistence of the metal/metal oxide in the case of molybdenum and tungsten. Such oxygen partial pressures were created by mixing CO and $CO_2$ in appropriate concentration from compressed gas cylinders as per equation (2.4b) so that in one case it causes reduction of the oxide to metal and in the other case re-oxidation of metallic Mo and W to $MoO_3$ and $WO_3$, respectively, again. For example, at 600°C the oxygen partial pressure for the $Mo/MoO_3$ coexistence can be computed to be $1.2 \times 10^{-21}$ atm (using reliable thermodynamic data employed in the construction of Figure 2.1a). However, $MoO_2$ is also a stable phase in the Mo–O system under different oxygen partial pressure conditions ($1.2 \times 10^{-26}$ atm at 600°C). Thus, a $p_{O_2}$ nearly five orders of magnitude *lower* (~$10^{-30}$ atm) than the theoretical value for the $Mo/MoO_2$ was considered adequate to effectively and completely reduce $MoO_3$ to elemental Mo. This was generated by mixing CO and $CO_2$ in the ratio $CO_2:CO = 0.00231$ ($p_{O_2} = 1 \times 10^{-30}$ atm). This composition was used as the reducing mixture. Similarly, a $p_{O_2}$ nearly five orders of magnitude *higher* than the theoretical was generated by mixing CO and $CO_2$ in the ratio $CO_2:CO \approx 23,000$ ($p_{O_2} = 1 \times 10^{-16}$ atm). The actual mixing ratios used in this work turned out to be 0.2% $CO_2$ + 99.8% CO in the first case and 43 ppm CO + balance $CO_2$ in the second case. In order to generate the later mixture, a gas cylinder

containing 100 ppm CO + balance $CO_2$ was used as the CO source. A similar strategy was adopted in the case of oxygen partial pressure modulation in $WO_3$ in the light of the theoretical data illustrated in Figure 2.1c.

In the case of titania thick films electrodeposited on cp Ti plates and wires, the clacined samples were subjected to reduction experiment in 5% $H_2$/Ar mixture (flow rate of 100 sccm) at 700°C for 6 h. In one case, reduction was carried out for 8 h.

### 2.4.4 Gas sensing experiments

The sensor was placed on a flat platform in an all-quartz experimental set-up which was located in the uniform temperature zone of a compact horizontal Lindberg furnace (MiniMite) and the lead wires were taken out of the furnace through a twin-bore alumina tube. A type-K thermocouple was also placed just above the sensor to monitor the temperature and its variation (if any) during the test. The ends of the gold wires were connected to a high impedance Agilent 34220A digital multimeter, which in turn was connected to a desktop PC via HPIB interface card. Sensor resistance data was acquired and displayed in real time with the help of IntuiLink software.

A gas stream consisting of 10% $O_2$–90% $N_2$ (v/v) mixture was obtained by blending dry compressed air with high purity nitrogen to obtain the background (reference) gas. The sensor was first heated to a selected temperature in the background ambient and allowed to equilibrate at that temperature till a steady baseline resistance ($R_b$) was established. Given amount of CO from a CO/$N_2$ tank was then bled in and allowed to blend. Sensitivity of a given film was measured by recording change in film resistance with respect to $R_b$ upon introduction of a given amount of CO in the stream. The sensor behaviour was monitored both with increasing and decreasing levels of CO in the ambient to confirm the reversibility attribute of the sensor. The response time ($t_{90}$) was calculated by discerning from the recorded data, the time it took for the signal to attain 90% of the difference between the two steady states, viz., in the background ($R_b$) and that after CO was introduced ($R_g$).

## 2.5 RESULTS AND DISCUSSION

### 2.5.1 Mo- and MoO$_3$-based studies

#### 2.5.1.1 Microstructural evolution in MoO$_3$ derived from Mo foil oxidation

In order to first verify that modulation of oxygen potential in the vicinity of a metal or its oxide affects the morphological artefacts, small (25 mm × 12.5 mm) coupons cut from an Mo foil were subjected to several redox schemes and were characterized at the end of each treatment by XRD and SEM.

The comparative morphological features of the as-received Mo foil and that subjected to oxidation in air at 600°C for 2h are shown in Figure 2.2. The mechanical stress causing the disintegration of the foil upon oxidation is due to the phase and structural change from cubic Mo metal (ICDD 42-1120, unit cell volume 31.17Å$^3$) to orthorhombic $MoO_3$ (ICDD 05-0508, unit cell volume 202.99Å$^3$) which is attended by ~85% volume change or ~6.5-fold volume increase.

On the other hand, totally different microstructure results when the Mo foil is oxidized and reduced at 600°C for 24h in manipulative $p_{O_2}$ regimes (nearly five orders of magnitudes across the Mo/$MoO_3$ line in Figure 2.1b) generated by different ratios of CO/$CO_2$. This is shown in Figure 2.3a and 2.3b, respectively. The nanoscale features of the oxides subsequent to both oxidation and reduction treatments in CO/$CO_2$ mixture can be seen clearly. The lack of open porosity and presence of well-defined grain boundaries in both the cases is probably due to sintering via vapour phase transport (VPT) as a result of long soak duration (24h at 600°C).



(a)  (b)
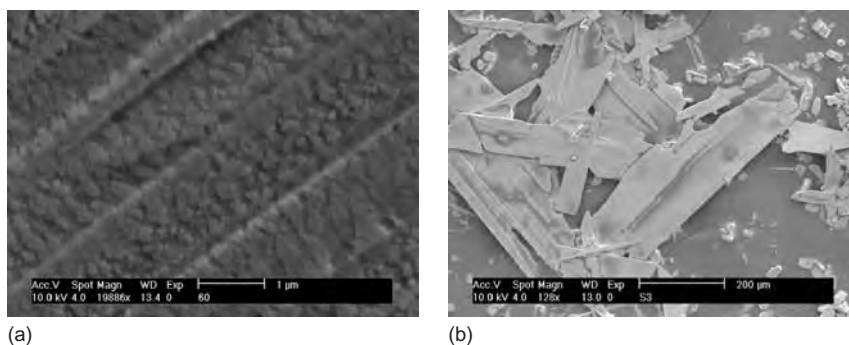
**FIGURE 2.2** *(a) Microstructural features of a pure Mo foil and (b) that heated in air at 600°C for 2h. Extreme fracture and deformation of the foil upon heating in air is due to the formation of MoO$_3$ from metallic Mo which is attended by ~6.5-fold increase in volume.*



(a)  (b)
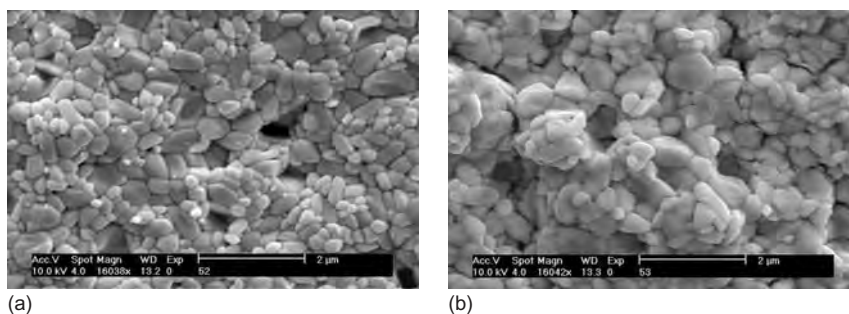
**FIGURE 2.3** *SEMs of Mo foil after (a) oxidation and (b) reduction by CO/CO$_2$ buffer mixtures at 600°C for 24h.*

Interestingly, when the foil oxidized and reduced in $CO/CO_2$ buffer mixture (Figure 2.3) is heated again in air at 600°C for 4h, thin, oriented platelets of $MoO_3$ of large aspect ratios and surface area result. The resulting morphology is quite similar to that seen in the commercial $MoO_3$ powders, albeit with much smaller and more uniform grain size and narrower particle size distribution. This is shown in Figure 2.4.

The microstructural features developed in films fabricated from the powder obtained after Mo foil oxidation in air at 600°C for 2h are compared with those in the films subjected to redox treatments in appropriate $P_{O_2}$ regimes at 600°C in Figure 2.5.

**FIGURE 2.4**

*SEM pictures of (a) Mo foil after redox treatment in CO/CO$_2$ buffer for 24h followed by air oxidation for 4h and (b) commercial MoO$_3$ powder.*



(a)
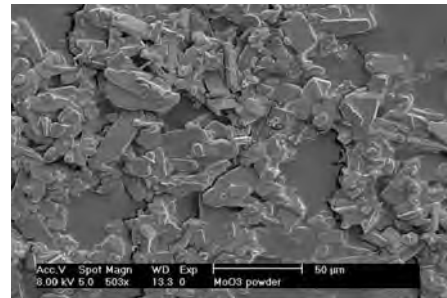
(b)

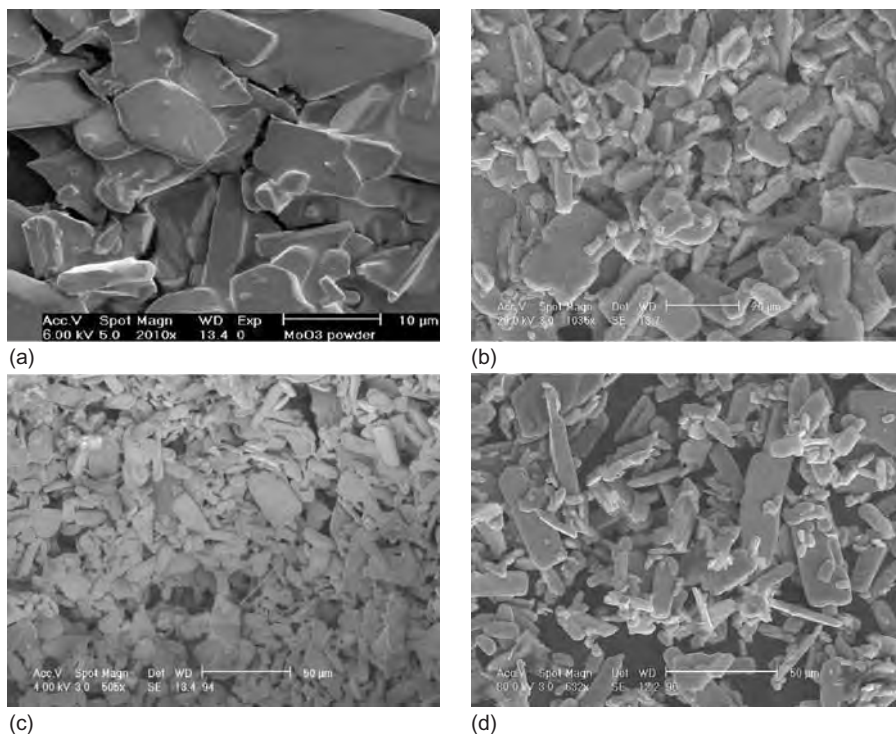**FIGURE 2.5**

*Microstructural evolution in the MoO$_3$ films fabricated from Mo foil oxidation. (a): Film calcined for 1h. (b): (a) reduced by CO/CO$_2$ for 12h. (c): (b) oxidized by CO/CO$_2$ for 12h. (d): (c) oxidized by air for 1h. Size bar = 5μm.*
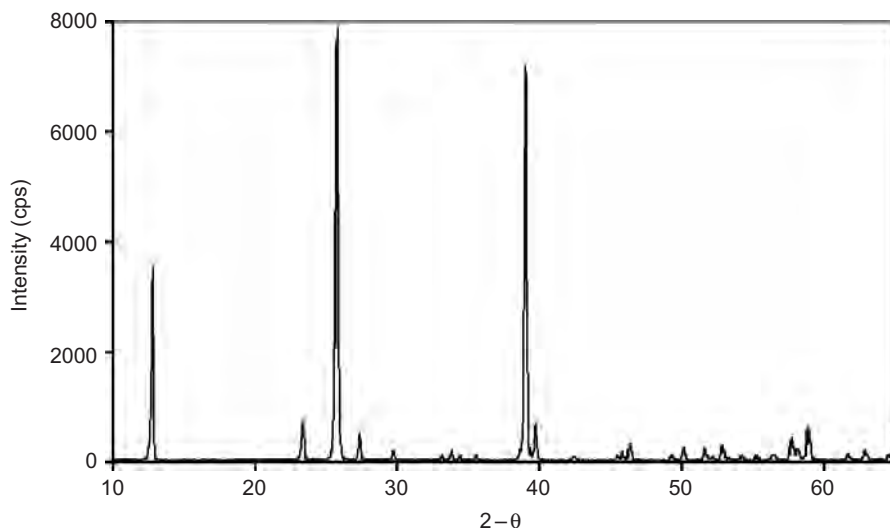


(a)
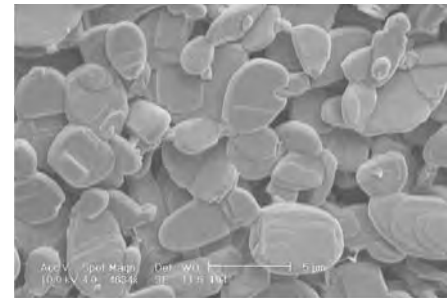
(b)
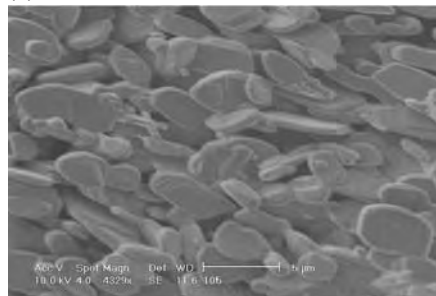
(c)
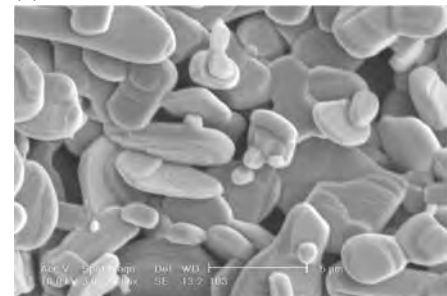
(d)

### 2.5.1.2 Microstructural evolution in MoO₃ thick films fabricated from the commercial powder

The morphological features in the $MoO_3$ thick films that were made by using the commercial oxide from Alfa-Aesar and subjected to different redox treatments at 600°C are shown in Figure 2.6.

It is apparent that while the grains maintain the unique platelet texture, so characteristic of $MoO_3$, the microstructure lacks the uniformity that was obtained as a consequence of identical treatment given to the $MoO_3$ powder derived from foil oxidation (nearly monosized small platelets with narrow plate size distribution; see Figure 2.5).

The nearly identical morphological features after subjecting molybdenum oxide films to different redox treatments under various oxygen partial pressure regimes suggest that the ultimate chemical state of the oxide were also restored. The XRD patterns collected at the end of each such treatment were identical (orthorhombic $MoO_3$)[14] except for some preferential texturing which corroborate and validate the stated assumption. One such pattern is shown in Figure 2.7.



**FIGURE 2.6**

*Microstructural evolution in the MoO₃ thick films fabricated from MoO₃ commercial powder. (a): Film calcined for 1h; (b): (a) reduced by CO/CO₂ for 12h; (c): (b) oxidized by CO/CO₂ for 12h and (d): (c) oxidized by air for 1h.*

**FIGURE 2.7**   *A typical XRD pattern of the MoO$_3$ thick films after various redox treatments with preferential texturing in the <060> direction[14].*

### 2.5.1.3 Microstructural evolution in MoO$_3$ films fabricated from sodium molybdate precursor

The morphological features of the molybdic acid (H$_2$MoO$_4$) precipitated from ammonium molybdate and of the MoO$_3$ powder obtained after the calcination of molybdic acid at 300°C for 1h are shown in Figure 2.8a and 2.8b, respectively. The triclinic habits of the molybdic acid crystals (ICDD 26-1449) are easily discernible as are the plate-like structure characteristic of MoO$_3$ in the fired sample.

The phase evolution in MoO$_3$ upon the molybdic acid dehydration appears to be textured along <020> direction rather than <021> direction as is the case with the bulk oxide[14]. This is shown in Figure 2.9.

The microstructural evolution in films made from this powder and subjected to different redox treatments is shown in Figure 2.10.

It is worth mentioning that while the films undergo drastic morphological variations as a result of exposure to the gas environment of varying oxygen potential, the XRD signatures collected on these samples reveal that the phase structures of **a**, **b** and **d** belong to those of MoO$_3$ (akin to that shown in Figure 2.7 with texturing along the directions of preferred growth) and that of **c** belongs to MoO$_2$[15]. It is also interesting to note that reduction–oxidation by the conventional H$_2$–air combination (Figure 2.10b) leads to a rather compact and dense microstructure albeit with large aspect
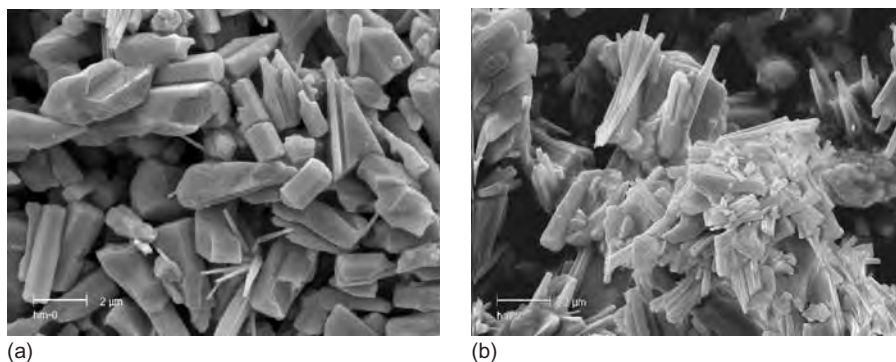
(a)                                              (b)

**FIGURE 2.8**   *Morphology of (a) $H_2MoO_4$ precipitate and (b) $H_2MoO_4$ precipitate fired at 300°C for 1h.*
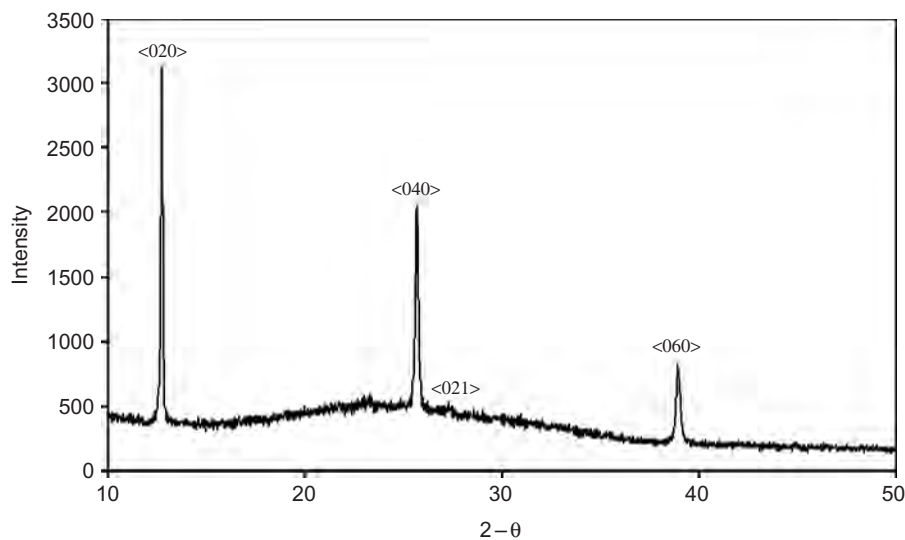


**FIGURE 2.9**   *XRD pattern of the oxide obtained from molybdic acid fired at 300°C for 1h. The pattern conforms to that of $MoO_3$ with preferred texturing along the <020> direction.*

ratio; in a clear contrast to this, the microstructure is rather open in Figure 2.10d when $CO/CO_2$ buffer is used as the redox medium. This is suggestive of layer-by-layer build-up of the parent oxide from the reduced intermediate phase in the case of redox treatment under conditions of restricted availability of oxygen. The XRD pattern (not shown here) obtained after reduction of the $MoO_3$ in the chosen $CO_2/CO$ buffer does contain peaks belonging to $MoO_2$, which later disappeared when subjected to oxidation in appropriate $CO_2/CO$ mixture. The phase change from $MoO_3$ to $MoO_2$ and

(a)

(b)

(c)

(d)
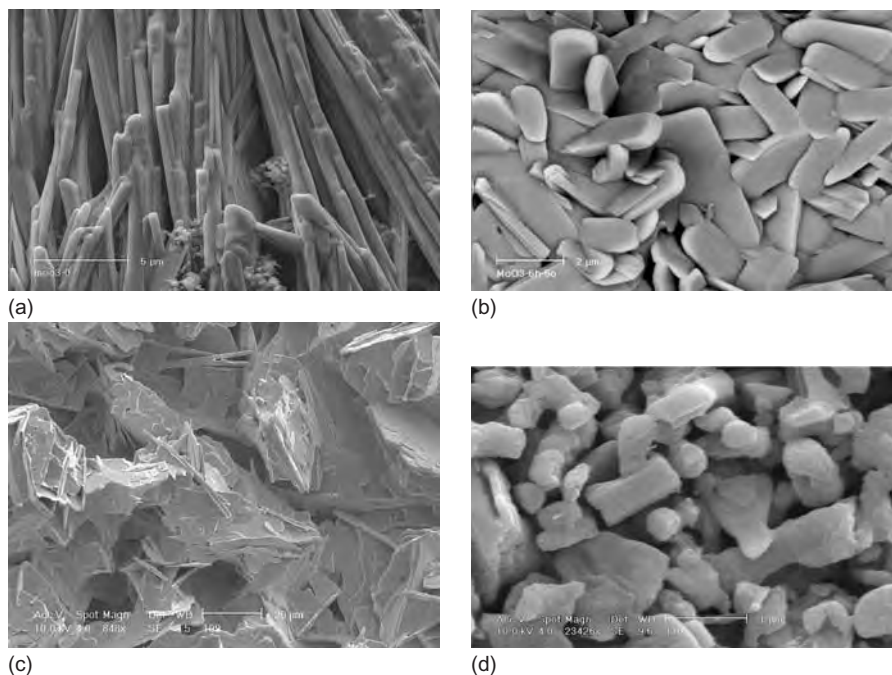
**FIGURE 2.10**  *Morphology in (a): film fabricated from $H_2MoO_4$-derived $MoO_3$ and calcined at 500°C for 2h; (b): (a) heated in 10% $H_2$–$N_2$ mixture at 500°C for 1h and oxidized in static air; (c): (a) reduced by CO/$CO_2$ and (d): (c) oxidized by CO/$CO_2$ (both at 600°C for 12h). Note the length of the scale bars.*

again to $MoO_3$ in the cyclic redox process is accompanied by concomitant volume changes, which lead to a porous structure. Similar observations have been made in the case of regeneration of the rejuvenated oxide phase in the $WO_3$ system as would be seen later in this chapter. This vividly illustrates that the oxygen potential prevalent in the vicinity of an oxide phase has profound effect on its morphological features, which could be tailored to accentuate the sensing behaviour of a potential semiconducting oxide.

### 2.5.1.4  Preparatory technique–microstructure–gas sensing property correlation in $MoO_3$ films

The sensitivity and response time of thick-film sensors fabricated from $MoO_3$, derived from three different preparatory techniques, to CO gas (14–100 ppm) at 450°C are compared in Figure 2.11 (**a**: as-prepared, **b**: sample **a** reduced and oxidized in CO/$CO_2$ mixtures and **c**: sample **a** reduced in CO/$CO_2$ mixture and oxidized in air). The response of the sensor towards CO is defined as the normalized variation of resistance of the n-type film,
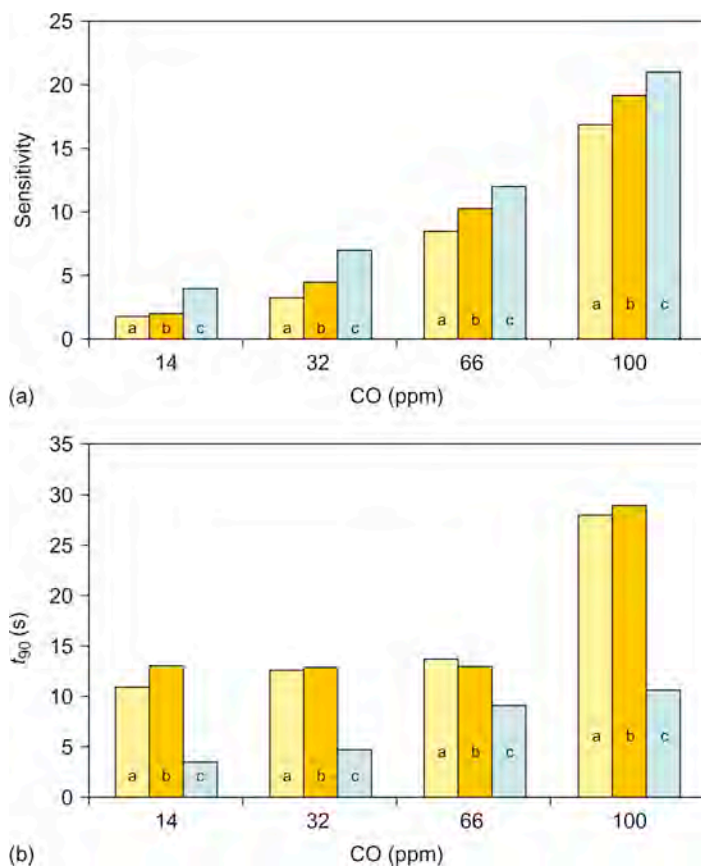
**FIGURE 2.11** *(a) Comparison of the sensitivity and (b) response time of the films derived from three different preparatory techniques (*$a$*: $MoO_3$ from vendor; *$b$*: $MoO_3$ from Mo oxidation and *$c$*: $MoO_3$ from sodium molybdate) and subjected to reduction by $CO/CO_2$ buffer followed by air oxidation. The sensor measurements were carried out at 450°C.*

namely, $(R_o - R_g)/R_o$, where $R_o$ is the steady-state resistance (identified as a time-independent plateau) in the background gas (in the present case, 10% $O_2$-balance $N_2$) and $R_g$ is the steady-state resistance of the sensor film (identified again as a time-independent plateau) when exposed to the gas of interest (i.e. CO). The response time $(t_{90})$ is calculated as the time taken to reach 90% of the difference $(R_o - R_g)/R_o$.

As can be seen, neither the sensitivity nor the response time changed significantly as a result of various redox treatments given to the films made from the commercial $MoO_3$ powder. The lack of improvement in either of the two characteristics is believed to be due to almost negligible variation in

the microstructural features of the films (see Figure 2.6). The film reduced and re-oxidized by $CO/CO_2$ (Figure 2.6b) showed somewhat marginally better sensitivity, while the film reduced by $CO/CO_2$ buffer and re-oxidized by air (Figure 2.6c) showed the quickest response ($\sim$27s).

Further, there was no improvement in the sensing behaviour in the case of films made from the powders obtained after oxidation of Mo foil either. This is understandable in the light of the negligible change in the microstructural features as a result of the three redox treatments (Figure 2.5).

On the other hand, the film prepared from $MoO_3$ powders, derived via precipitation technique, turned out to be the most promising in terms of sensitivity and response time. As can be seen from Figure 2.11, significant improvement in the sensitivity and the response time was observed in this case. The film subjected to redox treatment by $CO/CO_2$ showed improved sensitivity compared to the untreated sample. However, the film reduced by $CO/CO_2$ followed by air oxidation showed an increase of $\sim$40% in sensitivity and decrease of $\sim$300% in the response time at 100 ppm CO level. This is believed to be due to the unique microstructural artefacts developed in these films (Figure 2.10). Clearly, the third method resulted in sensor films with the most improved sensitivity to all levels of CO and particularly the lowest response time for 100 ppm CO.

### 2.5.1.5 Microstructural modulation in MoO₃-containing composite structures

Similar morphological changes have been observed in the case of sensors made with two-phase composite mixture, viz., $ZnMoO_4$–$MoO_3$ (MZM). It was found that the rod-like $MoO_3$ grains in the original mixture are regenerated as highly oriented thin platelets upon exposing the MZM film to a gas mixture containing 1% CO at 450°C for 1h followed by natural cooling in air. It was also observed that as a result of this bulk redox reaction, the morphological features of the major phase ($ZnMoO_4$) have undergone noticeable variation (from regular near-spherical grains to triclinic habits with well-defined sharp edges) without any chemical degradation, which was verified from the EDS spectra collected in different pockets of the composite after subjecting it to the above-mentioned redox treatment. These results are shown in the SEM pictures (Figure 2.12) and the EDS spectra (Figure 2.13). The morphology of regenerated $ZnMoO_4$ grains in Figure 2.12c is isostructural with that of the mineral microcline ($KAlSi_3O_8$) that belongs to the triclinic pinacoidal class of crystals;[16,17] see Figure 2.12e.
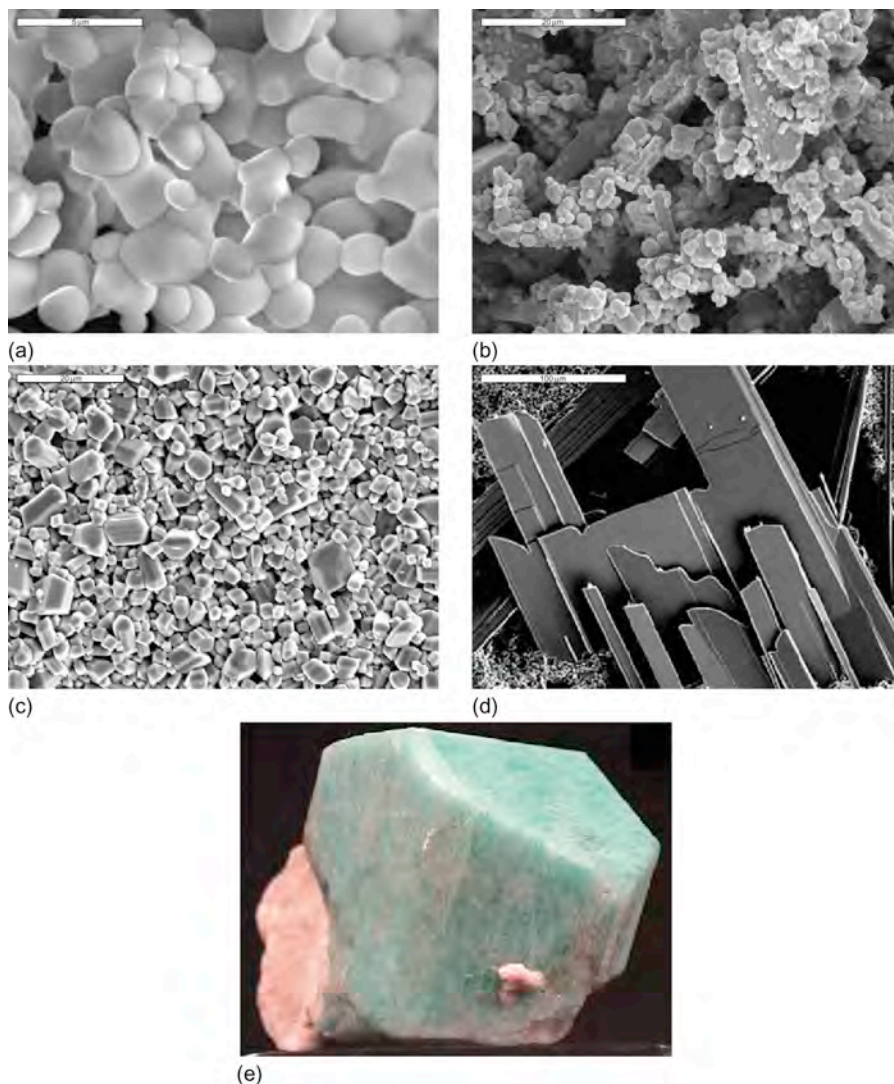
## 2.5.2  W- and WO$_3$-based studies

### 2.5.2.1  Microstructural evolution in WO$_3$ derived from W foil oxidation

Figure 2.14 compares the XRD signatures of the as-received W foil and the foil subjected to oxidation ($p_{O_2} \sim 10^{-15}$) and reduction ($p_{O_2} \sim 10^{-29}$) by CO/CO$_2$ buffers at 800°C for 24 h. Two obvious inferences can be drawn

*(a) EDS spectrum of ZnMoO$_4$ grains before and after the redox reaction in 1% CO at 450°C for 1h followed by natural cooling in air and (b) that of the regenerated platelets of MoO$_3$ shown in Figure 2.12d.*
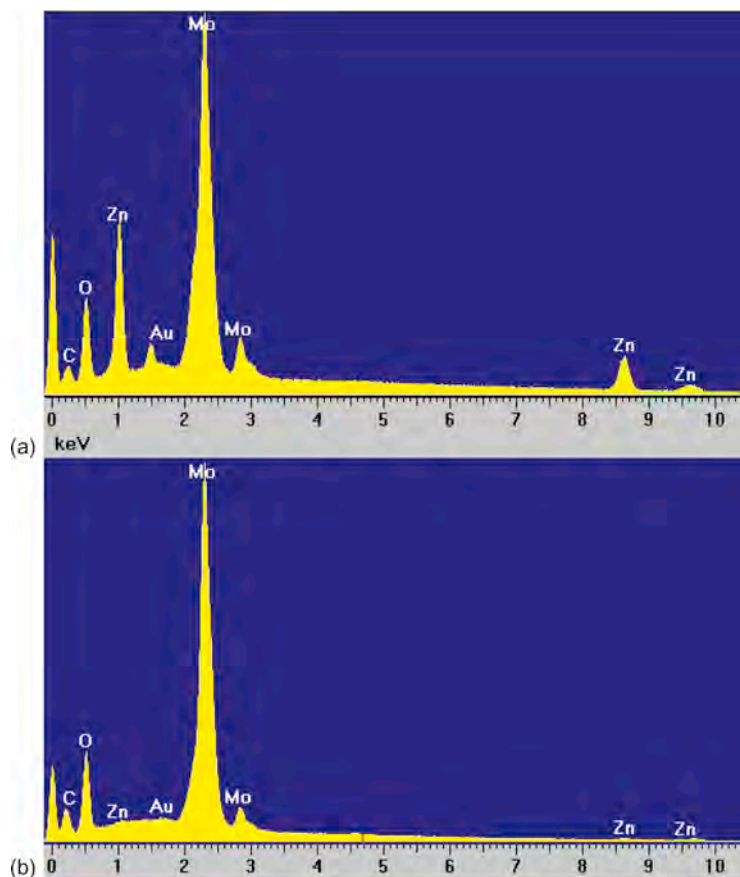
*XRD patterns of pure W foil and that subjected to redox reaction by the CO/CO$_2$ buffer.*
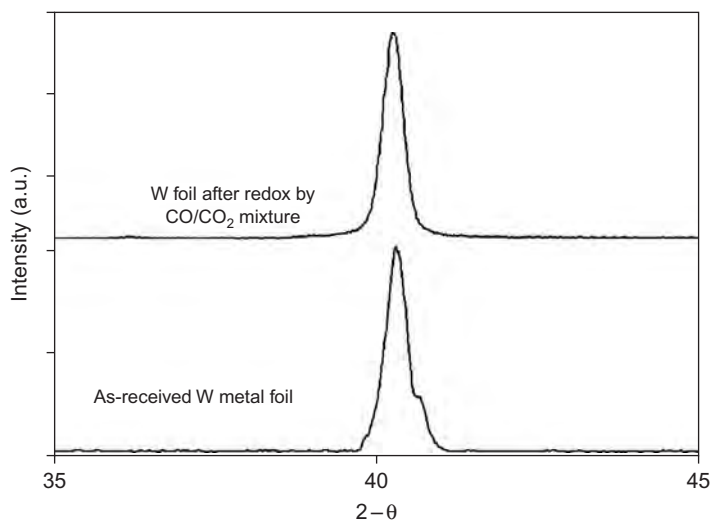
immediately: (i) elemental W is regenerated after oxidation and reduction in $CO/CO_2$ atmospheres and (ii) the regenerated metal has preferred orientation (higher intensity of the strongest <**110**> peak in the treated sample[18]). The comparative morphological features of these samples are shown in Figure 2.15.

The fractured morphology of the surface in Figure 2.15b clearly indicates that the material has undergone major phase and structural (metal (cubic) → oxide (triclinic)) changes prior to re-conversion to the metal again. This is corroborated by the EDS spectra collected after each event and is shown in Figure 2.16.

As shown in Figure 2.17, the XRD signature of a W foil directly oxidized in air at 800°C for 2h is identical with that of the foil subjected to an oxidation–reduction cycle in $CO/CO_2$ stream at 800°C for 36h, followed by oxidation in air. Phase analysis of the two patterns shows that in both cases, $WO_3$ is the dominant phase. This is understandable, since despite the intermediate heat-treatments in low $P_{O_2}$ regimes, the phase evolution is ultimately dictated by the final processing parameters and the ambient conditions which is the same in the two cases.

Accordingly, as shown in Figure 2.18 the microstructural features of the two samples are also similar albeit some grain growth and compaction are clearly visible in the second case, probably due to several heat-treatments leading to some sintering as well.

In contrast to this, the microstructural features seem to undergo drastic changes, when the W foil is oxidized in $CO/CO_2$ mixture in one case while in the other, it is oxidized, reduced and re-oxidized in manipulative $P_{O_2}$ regimes generated by different $CO/CO_2$ ratios. This is shown in Figure 2.19.
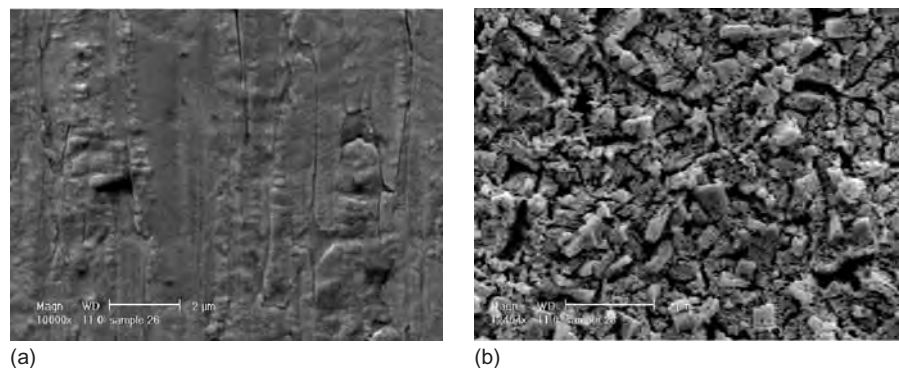


(a)  (b)

**FIGURE 2.15** *Electron micrographs of (a) pristine W foil and (b) the foil oxidized and reduced by a $CO/CO_2$ mixture at 800°C for 24h.*
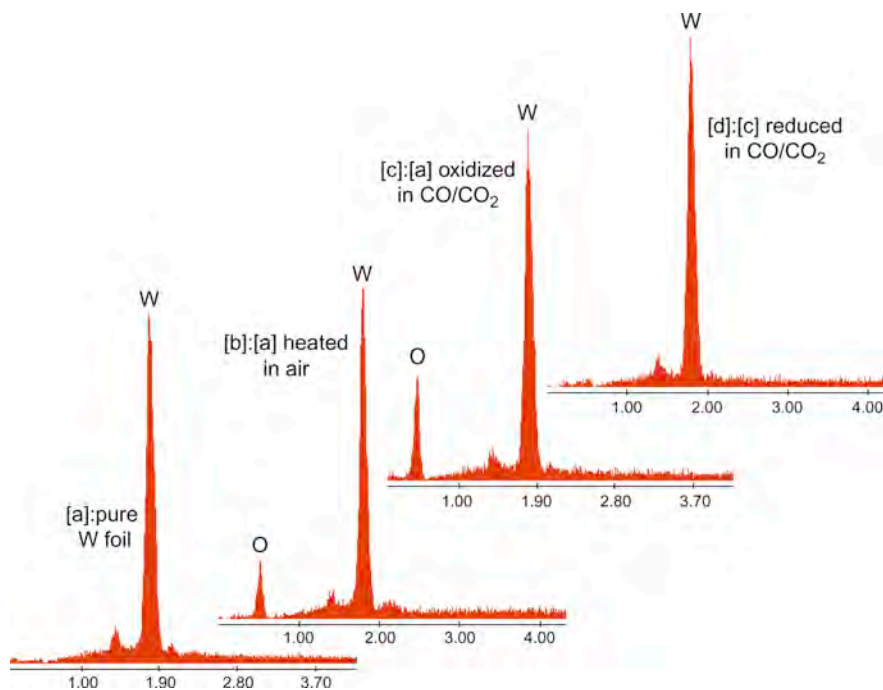
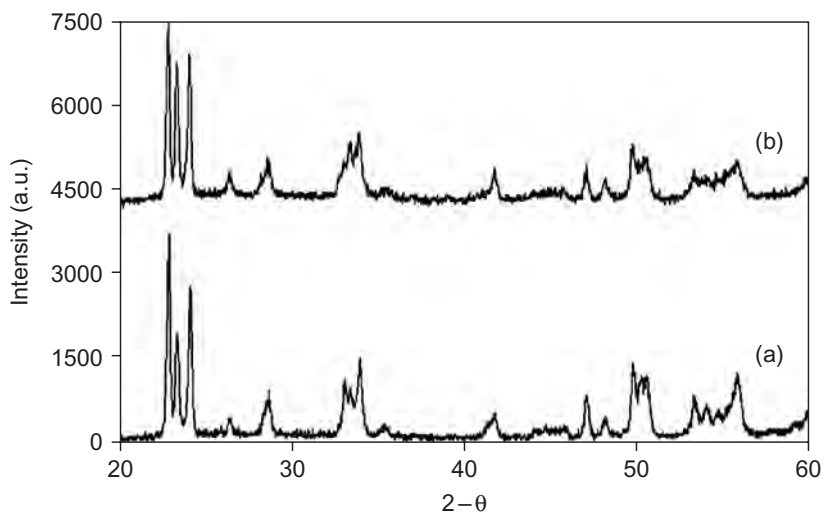**FIGURE 2.16** *EDS spectra of W foil subjected to various oxidation and reduction treatments.*



**FIGURE 2.17** *XRD pattern of (a) W foil after bulk oxidation in air at 800°C for 2h and (b) that oxidized and reduced in CO/CO$_2$ mixtures at 800°C for 36h followed by air oxidation at 800°C for 2h.*
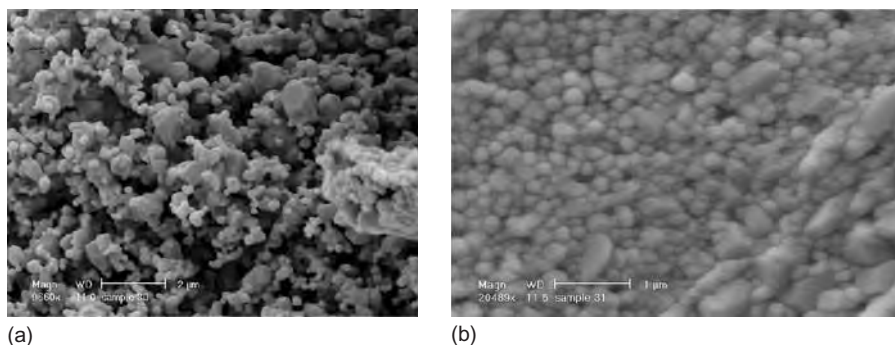
(a)

(b)

**FIGURE 2.18** *Microstructural features of W foil after (a) heating in air for 2h at 800°C and (b) oxidized and reduced for 36h in CO/CO$_2$ mixtures followed by air oxidation for 2h at 800°C.*

The microstructure shown in Figure 2.19a results when pure W foil (Figure 2.15a) is heated at 800°C for 24h in CO/CO$_2$ mixture in a $p_{O_2}$ range that is above the W/WO$_3$ line in Figure 2.1c, while the morphology shown in Figure 2.19b evolves when the foil in Figure 2.15b is subjected to an identical treatment.

A comparison of these features with those shown in Figure 2.18 lends credibility to the proposed notion that depending upon the location of the equilibrium oxygen potential across the M/MO line of coexistence, changes on microscopic levels are caused in the bulk oxides. This perhaps leads to atomic/submolecular level non-stoichiometry – that is nanoscale in nature and hence undetected by bulk techniques such as XRD. It is these defect sites that act as the nucleation and growth centres for the new oxide phase whose growth, due to the limited access to oxygen (defined by $p_{O_2}$ that is designed to be only slightly above the theoretical line of M/MO coexistence), is slow. Evidently, the reduced phase is subject to a concentration strain in terms of $p_{O_2}$. The need for 24h long dwell at 800°C for oxidation in the CO/CO$_2$ buffer compared to 2h for air oxidation supports the diffusion-like controlled build-up of the new oxide phase almost on atomic scale – one monolayer after another.

These observations are corroborated by the XRD patterns of the samples obtained under conditions leading to the microstructures in Figure 2.19a and 2.19b. These are shown in Figure 2.20a and 2.20b, respectively. Detailed analysis of the X-ray peaks reveals that such treatment yields a mixture of WO$_2$/WO$_3$, rather than either of the two oxides being the predominant phase. Thus, the role of controlled oxygen potential in the ambient and its effect on microstructural variation of a given phase are clearly brought out.

*Scanning electron micrographs of W foil after (a) single-stage oxidation and (b) cyclic oxidation–reduction–oxidation by $CO/CO_2$ buffer mixtures at 800°C for 24h.*
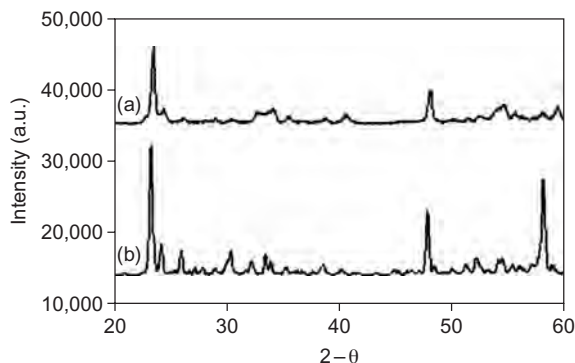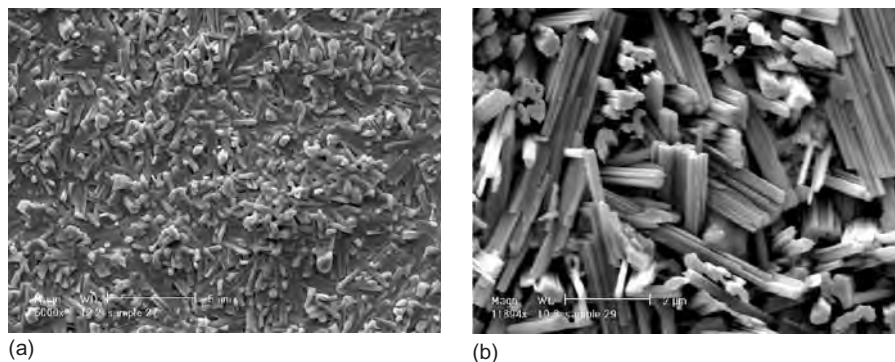


(a)



(b)



**FIGURE 2.20**  *XRD of W foil after (a) single-stage oxidation and (b) cyclic oxidation–reduction–oxidation by $CO/CO_2$ buffer mixtures at 800°C for 24h.*
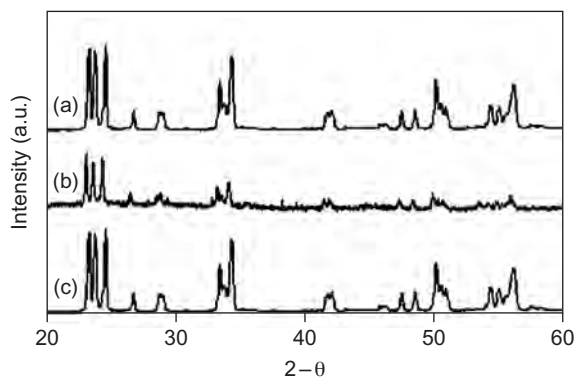


**FIGURE 2.21**  *Comparative XRD patterns of (a): $WO_3$ film calcined in air at 800°C for 2h; (b): (a) subjected to redox in $CO/CO_2$ mixtures at 800°C for 12h and (c): (b) heated in air at 800°C for 2h.*

Indeed, in many cases where bulk oxides were subjected to redox treatment by $CO/CO_2$ mixtures for shorter duration, it was rather difficult to discern quantitative phase changes based simply on the XRD signatures.

For example, when a $WO_3$ thick film is subjected to the reducing and oxidizing sequence in appropriate oxygen potential regimes created by $CO/CO_2$ buffers, and another film after the above-mentioned treatment is finally heated in air, no difference in their XRD signatures could be discerned, as shown in Figure 2.21. All the three patterns could be indexed as those belonging to triclinic $WO_3$[18].

On the contrary, the morphological features are significantly affected – both in terms of shape and size of the particles and in terms of the uniform porosity in the sample, as seen from the SEM pictures in Figure 2.22.

This vividly illustrates that the ambient oxygen potential in the vicinity of an oxide phase has profound effect on its morphological features, which could be tailored to accentuate the sensing behaviour of a potential semiconducting oxide.

The response characteristics (such as resistance, sensitivity and response time) of $WO_3$ thick-film sensors to CO gas (14–100 ppm) at 450°C are shown in Figure 2.23.
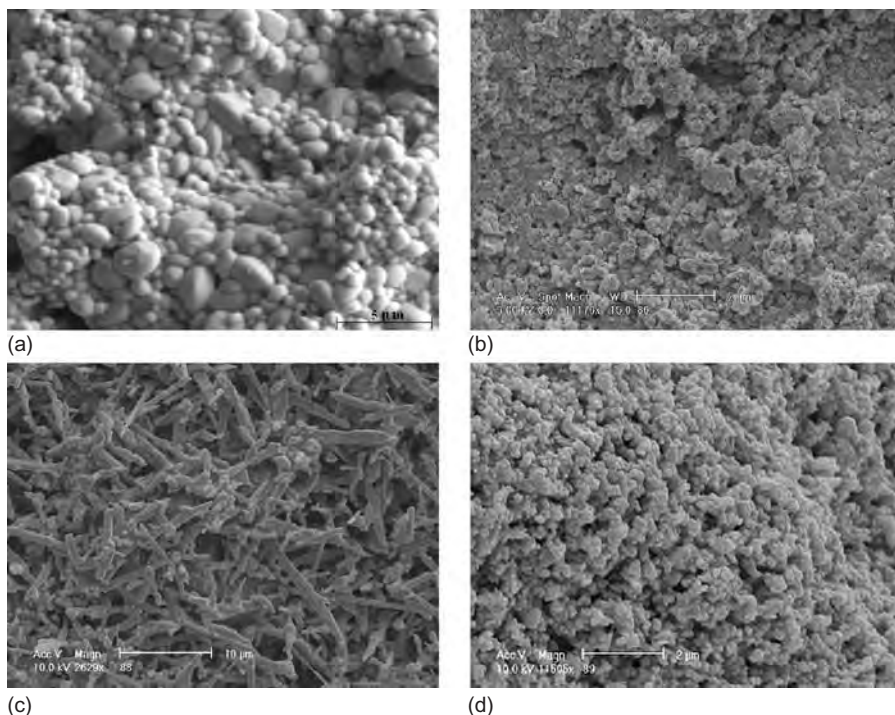
(a)

(b)

(c)

(d)

**FIGURE 2.22** *SEMs of WO$_3$ thick films (a): as-prepared; (b): (a) reduced in CO/CO$_2$; (c): (b) oxidized in CO/CO$_2$ and (d): (b) oxidized in air at 800°C for various periods of time.*

As can be seen from Figure 2.23, surface modification by the proposed scheme has certainly brought about marked changes in the behaviour of a WO$_3$-based CO sensor. The sensor could be operated in a cyclic fashion without compromising the signal, with a concomitant enhancement in sensitivity and significant shortening of the response time. In order to examine if such exotic microstructural features could be developed in bulk oxides, WO$_3$ thick films formed by heating the slurry at 600°C for 1h in air were subjected to reduction in a H$_2$/N$_2$ mixture at 600°C for 30 min, cooled to room temperature and again heated in air up to 500°C for 30 min. The evolved microstructures are shown in Figure 2.24.

In such cases also, the regeneration of the parent oxide with different morphological features can be explained in a way similar to that summarized above. The only notable difference is that in the latter case, the oxygen potential in the ambient is rather high (0.21 atm) – a parameter which could kinetically favour the process, leading to the faster attainment of thermodynamically most stable (M/O) stoichiometry upon regeneration.
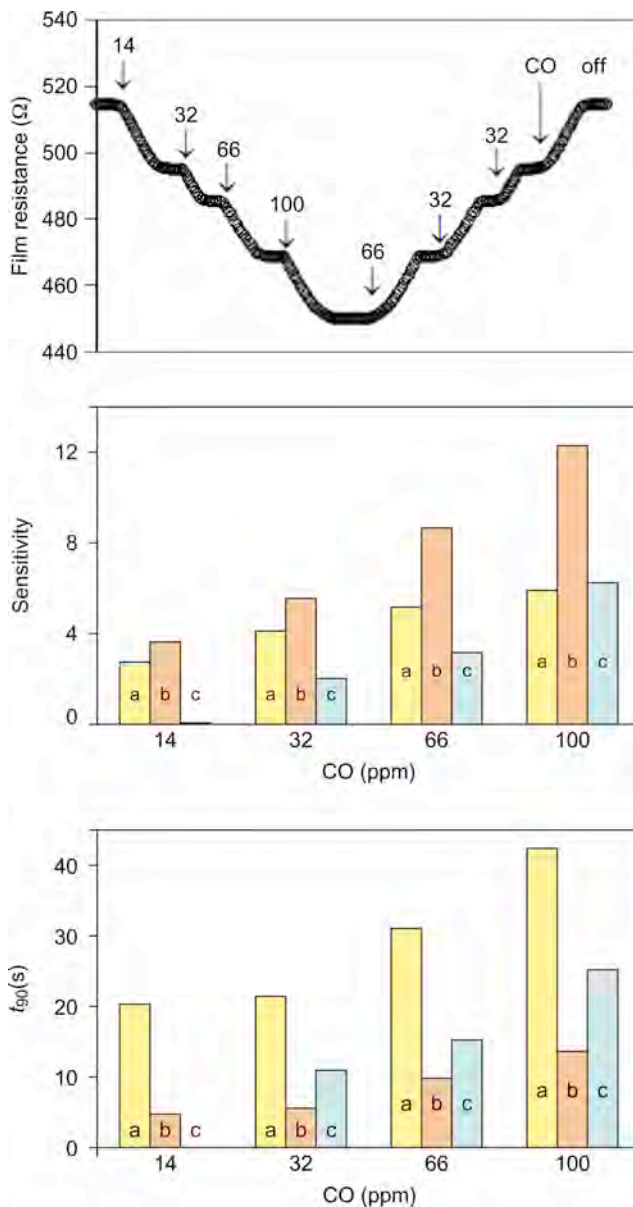
**FIGURE 2.23** *Response of a $WO_3$ thick-film sensor to CO at 450°C.* **a**: *as-prepared,* **b**: *sample* **a** *reduced and oxidized in $CO/CO_2$ mixtures, and* **c**: *sample* **a** *reduced in $CO/CO_2$ mixture and oxidized in air.*

### 2.5.3 TiO$_2$-based studies

#### 2.5.3.1 Microstructural evolution in thick films on titanium substrates

Figure 2.25 shows the SEM image of the titania thick film on a cp Ti substrate. Though the physical inspection with naked eye shows the film to
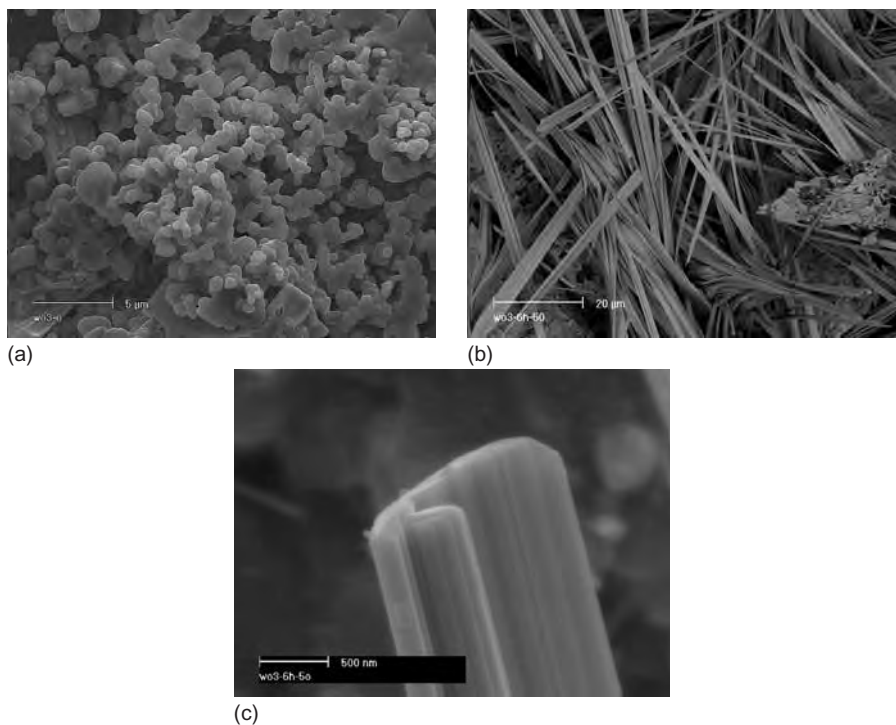
(a)


(b)


(c)

**FIGURE 2.24** *Evidence of microstructural modification in bulk oxides (a) via $H_2$ reduction-air oxidation (b); b at higher magnification is shown in c.*

be extremely uniform, high magnification micrograph shows the surface to be somewhat non-uniform and laced with almost evenly distributed pores. Scratch resistance of the film is also excellent, as it does not easily peel off when scratched with a sharp edge. XRD pattern collected on the film as-deposited on cp Ti plate revealed it to be a mixture of anatase (ICDD# 21-1272) and beta (ICDD# 35-0088) modifications of $TiO_2$. In addition, the diffraction pattern also includes some weaker peaks belonging to titanium metal, which are from the substrate on which the film is coated.

As evident from Figure 2.25, the as-fabricated titanium dioxide thick films did not possess any well-defined microstructural features and hence were not attractive for the anticipated gas sensing applications. In order to make use of these simple geometries as potential gas sensor devices, the films were subjected to a series of heat-treatments in a well-conceived temperature–time–environment profile. The samples were calcined in static air at 700°C or 900°C for 4 h each, or at 1100°C for 2 h. The calcined samples were then reduced in a 5% $H_2$/Ar mixture at 700°C for 6 h; in one case the reduction was carried out for 8 h.

Figure 2.26 shows representative SEM images of the samples fired in static air at 700°C and 900°C for 4 h each. Apparently, subsequent to the heat-treatment under these conditions, no noticeable morphological changes could be observed. However, dramatic morphological and micro-structural changes ensued when the titania films were heated in air at 1100°C for 2 h. Arrayed platelets were found to grow from the deposited film surface, as seen in the SEM images shown in Figure 2.27. As evident from the higher magnification SEM image, the platelets are clearly oriented along c-axis (out-of-the plane) and exhibit preferred texturing. Furthermore, the platelets appear to nucleate and grow individually, rather than by the traditional, global mechanism generally observed in ceramics; the plates are ~3–4 μm in width and ~500 nm in thickness.

In order to follow systematic phase evolution, the XRD signatures of variously heat-treated samples are compared in Figure 2.28, which shows several interesting features. First, the anatase modification (ICDD# 21-1272) is retained in samples heated up to 900°C for 4 h, albeit with decreasing intensity as it is known to undergo irreversible transformation into the more stable rutile phase (ICDD# 21-1276) which increases in intensity gradually; there are no traces of anatase titania in samples fired beyond 900°C. Second, the peaks belonging to cp Ti substrate that were present in the film fired at 700°C disappear in those heated at higher temperatures. This could be due to the grain growth, good adhesion and protective nature of the titania film – all of which limit the access of oxygen to underlying metallic surface and mitigate its exposure. The bright grey surface belonging to cp Ti metal could be seen by scratching the top oxide layer, which reinforces the belief that the heat-treatment
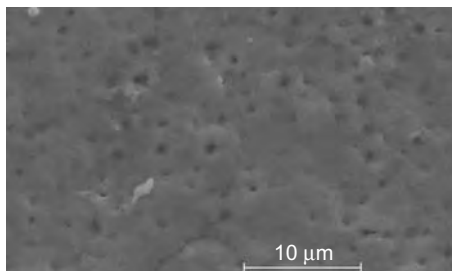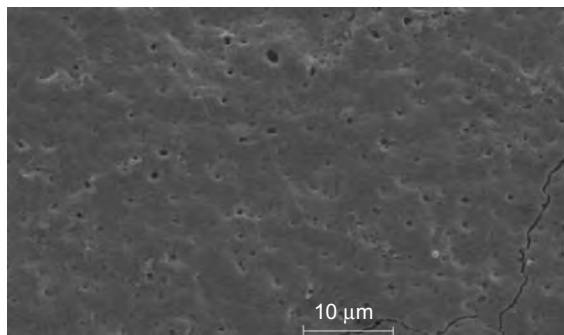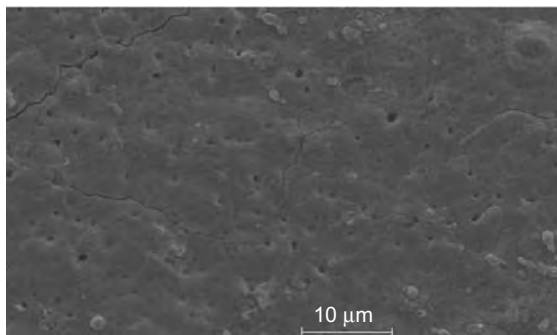


**FIGURE 2.25** *SEM of the as-fabricated titania film by Henkel Corporation.*



(a)

(b)

**FIGURE 2.26** *SEM images of Henkel TiO$_2$ thick films/cp Ti heated in air at (a) 700°C and (b) 900°C for 4 h.*

employed in this work did not cause bulk oxidation of the underlying metallic titanium substrate. The third and most surprising observation is the fact that the $\beta$-phase (ICDD# 35-0088) which was present in the as-fabricated thick-film sample itself is seen in those heated up to 1100°C for 2h. Thus, structurally, the platelets seen in the SEM images in Figure 2.27 are likely a mixture of titania in rutile and beta $(R + \beta)$ phases.
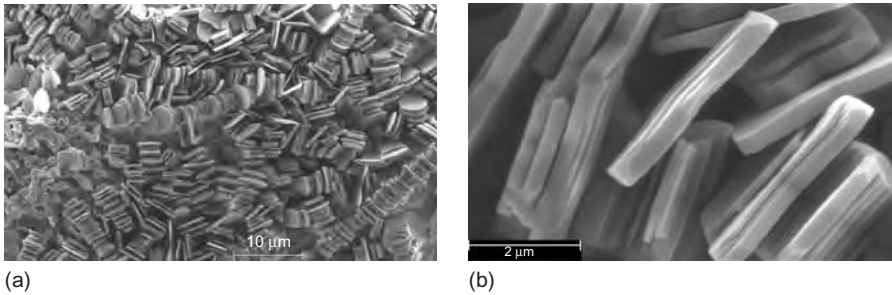


(a)                                    (b)

**FIGURE 2.27** *Microstructural evolution in the Henkel TiO$_2$ thick films/cp Ti heated in air at 1100°C for 2h that shows textured growth of plate-like structure.*
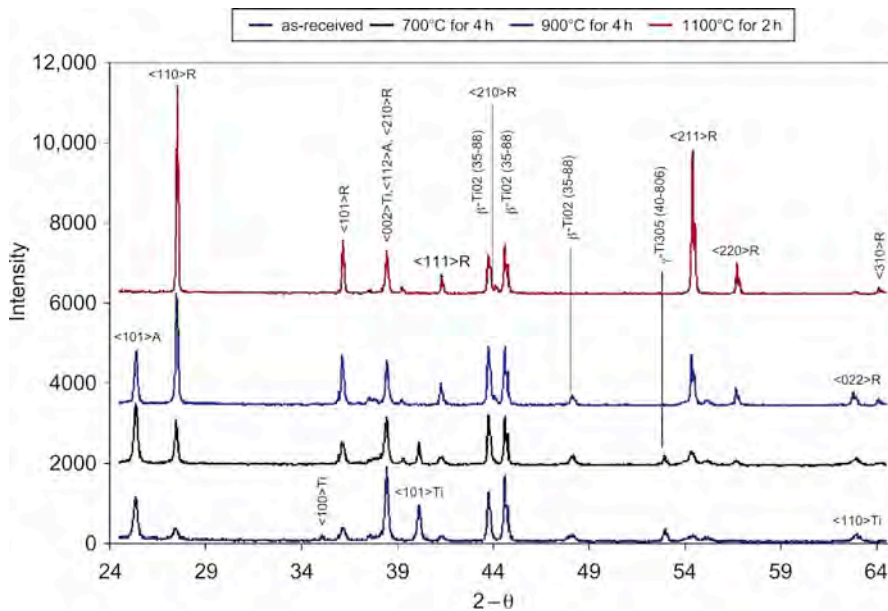


**FIGURE 2.28** *XRD patterns showing the systematic phase evolution in the Henkel TiO$_2$ thick films/cp Ti as a function of heat-treatment in the range of 700–1100°C.*

No noticeable morphological changes developed when the films fired at 700°C and 900°C for 4 h (Figure 2.26) were subjected to reduction in 5% $H_2$/Ar environment at 700°C for 6 h, as seen from the SEM images shown in Figure 2.29.

However, the morphological features underwent drastic change when films calcined at 1100°C for 2 h were soaked at 700°C for 6 h in a 5% $H_2$/Ar mixture flowing at a rate of 100sccm. The SEM images at different magnifications and locations of the same sample are shown in Figure 2.30. The surface etching attended by the nucleation and growth of nanofibrils at the tip of the platelets is quite evident.

At this juncture, it is worth pointing out the similarities between the present results and those reported on $TiO_2$ dense pellets and on $TiO_2$–$SnO_2$ thin films by Yoo et al.[19] and Carney et al.[20], respectively. For example, based on the thermogravimetric experiments conducted on dense polycrystalline titania in the range 680°C–780°C in $H_2$/$N_2$ mixture, Yoo et al.[21] speculated that the fibre formation was due to the anisotropic etching process. Furthermore, the results based on the mass spectrometry and inductively coupled plasma spectroscopy data indicated that oxygen, and not titanium, was removed from the specimen surface during the reaction with hydrogen. The appreciable depletion of oxygen from the reacting zone without an appreciable change in the Ti:O ratio at such surfaces was found to be consistent with the solid-state diffusion of titanium cations from the surface into the bulk of the specimen. The migration of $Ti^{4+}$ under the apparent concentration gradient created by the dynamic reductive etching leads to the creation of nanofibrillar structure along the path of migration. This mechanism is evident in the post-HiTREP© microstructure shown in Figure 2.31; the SEM image on the right shows continuously growing fibres 20–50nm in diameter and length up to several microns.
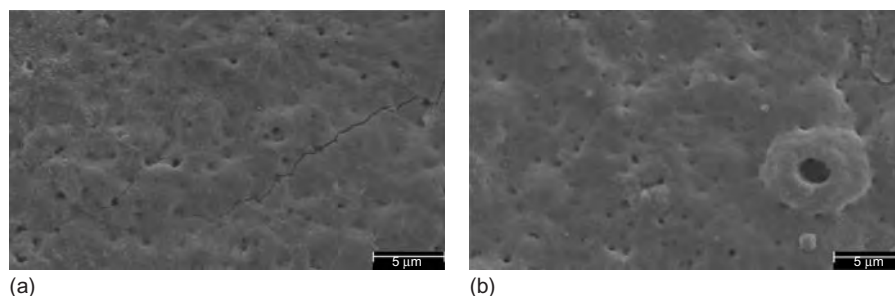


(a)  (b)

**FIGURE 2.29**  *Microstructural features in titania thick films subjected to (a) heating in air at 700°C for 4 h + reduction in 5% $H_2$/Ar at 700°C for 6 h and (b) heating in air at 900°C for 4 h + reduction in 5% $H_2$/Ar at 700°C for 6 h.*

Even though the physical makeup of the system in the present case (thick film on cp Ti substrate) is different from that employed by Yoo et al.[19, 21] (sintered pellet), identical processes appear to be operative in both the cases. Interestingly, in the present case as well, the gross composition of the thick-film surface remained intact, despite the dynamic nature of
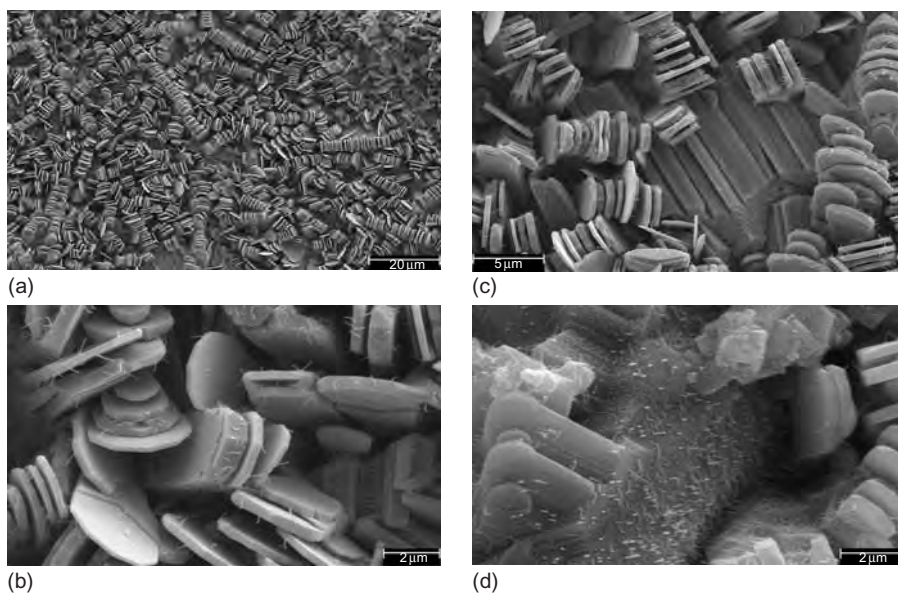


(a)

(c)

(b)

(d)

**FIGURE 2.30**   *SEM images of titania thick film on cp Ti calcined at 1100°C for 2h followed by reduction in 5% H$_2$/Ar at 700°C for 6h. Growth of nanofibrils at the tips of the platelets and in-between the ridges can be seen.*
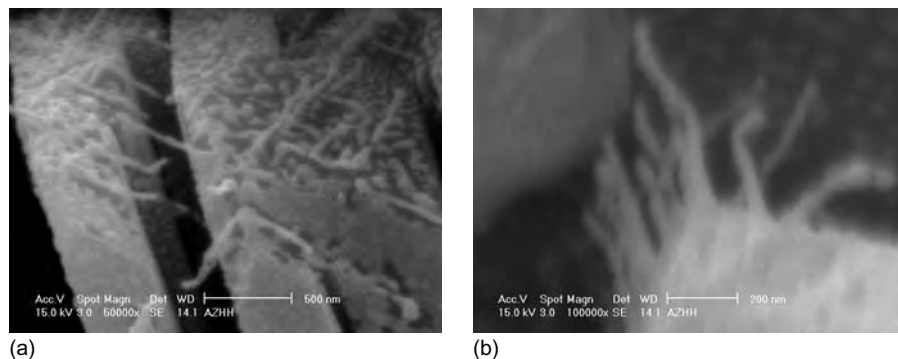


(a)

(b)

**FIGURE 2.31**   *SEM image depicting growth of nanofibres under HiTREP$^©$ employed in the present work; scale bar: (a) 500 nm and (b) 200 nm.*

the high temperature reductive etching process in dilute mixture of non-combustible gases ($H_2$:Ar = 5:95). This is strengthened by the fact that no new phase (i.e. titanium oxide with a different Ti:O ratio and hence a different crystal structure) was detected in the diffraction pattern of the film subsequent to high temperature etching. The XRD patterns collected on the films after calcination (1100°C for 2 h in static air) and HiTREP© (700°C for 6 h in 5% $H_2$/Ar stream) are compared in Figure 2.32.

As can be easily discerned, the two diffraction patterns are identical except for the intensity of some peaks; both could be indexed as rutile $TiO_2$ with some peaks still belonging to monoclinic β-$TiO_2$. Therefore, the reductive etching neither did cause variation in phase structure nor did it lead to the formation of any new chemical species. When soak time was increased from 6 to 8 h keeping all other parameters of reduction identical, no discernible morphological changes were recorded. However, the XRD pattern of the titania films subjected to 1100°C for 2 h (air calcination) + 700°C for 8 h (5% $H_2$/Ar reduction) showed preferential texturing along the <211> plane; in all the other samples, <110> is the most intense reflection. More importantly, β-$TiO_2$ phase eventually disappeared. This is shown in Figure 2.33.

Not much literature is available on β-phase and we speculate that its formation in our experiments is an artefact of the deposition technique.
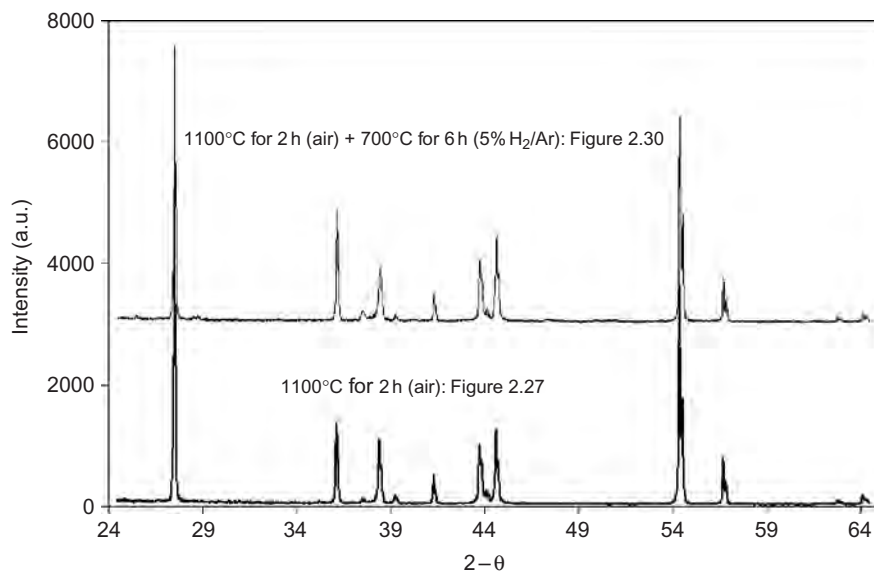


**FIGURE 2.32** *Comparative XRD patterns of Henkel $TiO_2$ thick films/cp Ti samples before and after HiTREP©; both the diffraction plots conform to the rutile phase of $TiO_2$.*

Moreover, there is no reported evidence of the gas sensing behaviour of $\beta$-$TiO_2$ in the published literature; therefore, evaluation of sensing characteristics of textured rutile phase obtained after reduction for 8 h at 700°C in 5% $H_2$/Ar stream appears to be a more adequate protocol, so that the uncertainty arising due to the role of the former can be ruled out.

Figure 2.34 shows the morphological features evolved in $TiO_2$ thick films coated on 18-SWG cp Ti wire when calcined in static air at 1100°C for 2 h.

The formation of unique 3-D prismatic solid structure in this case as opposed to the 2-D platelets in the case of films deposited on cp Ti plates under conditions of identical heat-treatment is likely an interplay of the structural stability of the film and the interfacial Gibbs' free energy per unit surface area. For example, in both cases, thermodynamically stable rutile titania is formed on cp Ti. Therefore, the macroscopic bulk Gibbs' free energy is identical in both the cases. Furthermore, the Pilling–Bedworth ratio for titania film (1.77) lies almost midway between those for magnesia (1.28) and silica (2.14) – two well-known stable oxides[22,23] – corroborating the visual and microstructural observation that stable titania films were formed on both the platforms. Therefore, the growth of the polycrystalline titania films in different morphological motifs could be explained as arising from the difference in the interfacial Gibbs' free energy in the two cases.
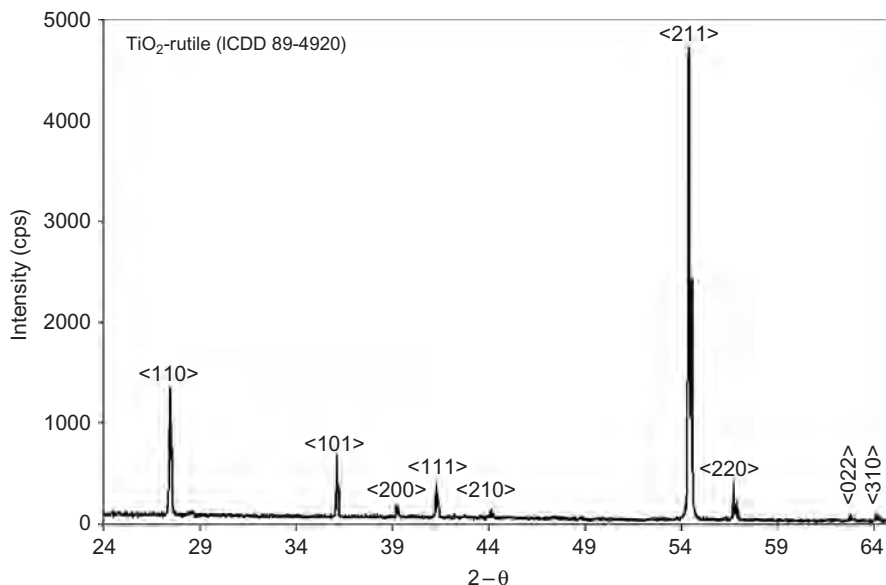


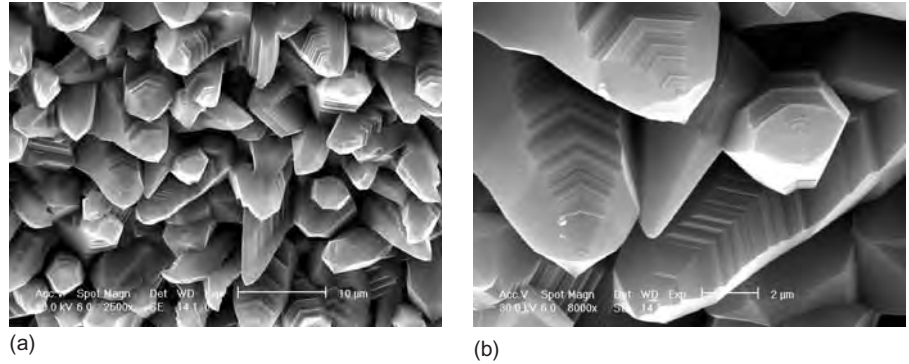**FIGURE 2.33**    *XRD of the titania thick film on cp Ti reduced at 700°C for 8 h in 5% $H_2$/Ar stream.*

(a)

(b)

**FIGURE 2.34** *Microstructural evolution in TiO$_2$ thick films coated on 18 SWG diameter cp Ti wire fired at in static air at 1100°C for 2h.*

If $\Gamma$ denotes the interfacial Gibbs' energy, then $\Gamma = \Delta G_f^o / area$ . In the present case

$$\Gamma_{\text{TiO}_2}(plate) = \frac{\Delta G_{f(\text{TiO}_2)}^o}{0.012 \times 0.012}\left(\frac{\text{kJ}}{\text{mol} \cdot \text{m}^2}\right)$$

for 12 mm ×12 mm coupons, and

$$\Gamma_{\text{TiO}_2}(wire) = \frac{\Delta G_{f(\text{TiO}_2)}^o}{\frac{\pi}{4}(0.001024)^2}\left(\frac{\text{kJ}}{\text{mol} \cdot \text{m}^2}\right)$$

for 18 SWG cylindrical wire. This gives

$$\Gamma_{\text{TiO}_2}(plate) = 6944.44 \times \Delta G_{f(\text{TiO}_2)}^o \left(\frac{\text{kJ}}{\text{mol} \cdot \text{m}^2}\right)$$

and

$$\Gamma_{\text{TiO}_2}(wire) = 1.21 \times 10^6 \Delta G_{f(\text{TiO}_2)}^o \left(\frac{\text{kJ}}{\text{mol} \cdot \text{m}^2}\right)$$

Therefore

$$\frac{\Gamma_{\text{TiO}_2}(wire)}{\Gamma_{\text{TiO}_2}(plate)} = 174.24$$

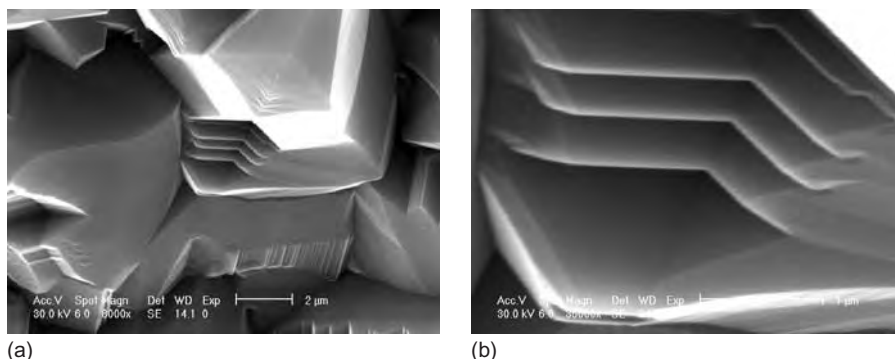(a)                                                                (b)

**FIGURE 2.35** *High magnification SEM images showing stacked layer structure (a) via ridge formation (b) in TiO$_2$ film grown on Ti wire on heating in static air at 1100°C for 2h.*

We believe that in order to accommodate about 174-fold difference in interfacial Gibbs' free energy, the titania–cp Ti interface on the wire platform undergoes a systematic self-reconstitution and reorganization on the microscopic level. This is manifested in the form of tightly packed growth consisting of stacked layers of consecutive triangular prismatic ridges, signifying the microstructural adjustment at each stage to satisfy the above-mentioned interfacial Gibbs' free energy criterion. The near-identical cone-shaped termination in sharp tips seen in Figure 2.34 typifies the end of growth process under this condition. These features can be seen more clearly in the SEM images presented in Figure 2.35.

In order to substantiate the mechanism proposed above, the heat-treatment schedule was slightly modified. In this case, the titania films on the cp Ti wire were soaked for 2h at 1100°C at ambient pressure (1 atm) in an environment of $p_{O_2} = 3.8 \times 10^{-21}$ atm. This was realized by using a CO/CO$_2$ gas buffer containing 100ppm of CO$_2$; at 1100°C, thermodynamic calculations as per equation (2.1), give an equilibrium $p_{O_2}$ value of $2.26 \times 10^{-26}$ atm for the Ti/TiO$_2$ couple (Table 2.1). Thus, a $p_{O_2}$ nearly five orders of magnitude higher than the theoretical value for the Ti/TiO$_2$ coexistence ensures that oxidizing conditions prevail and no reduction of the TiO$_2$ film either to TiO or Ti is likely. The microstructural features evolved under such acute lack of oxygen are shown in Figure 2.36. Three-dimensional prismatic growth via stacked layer ridge formation is quite evident.

Phase identification by XRD analysis (pattern not shown here to avoid redundancy) indicated the film structure to be rutile. The surface morphology showing the onset of nanofibre formation and growth as a result of reductive etching of these samples with 5% H$_2$/Ar is presented in Figure 2.37.
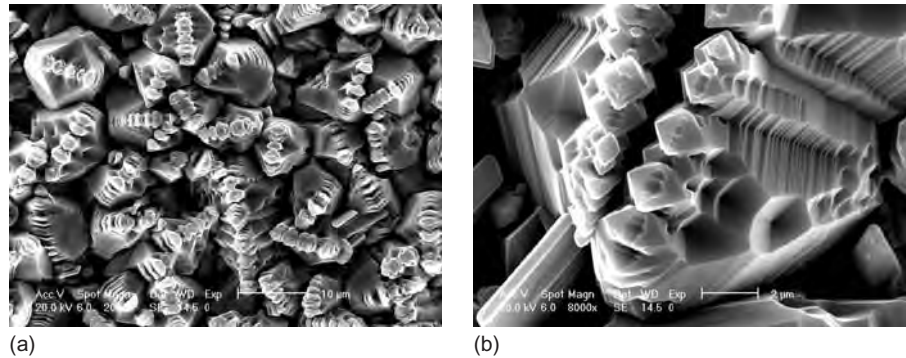
(a)                                    (b)

**FIGURE 2.36** *SEM images of TiO$_2$ films on cp Ti wire heated at 1100°C for 2h in a CO$_2$/CO ambient ($P_{O_2} = 3.8 \times 10^{-21}$ atm).*
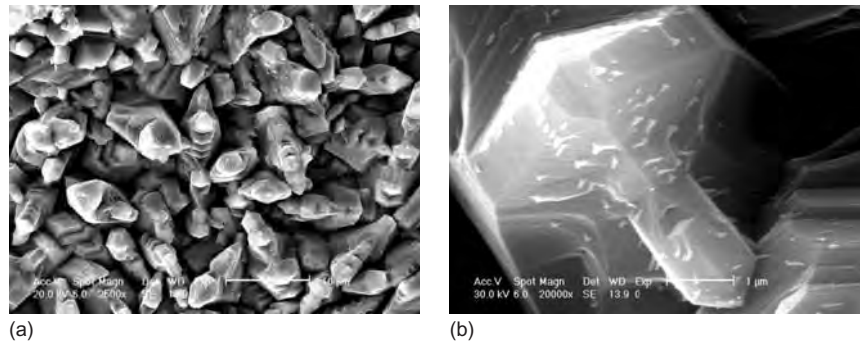


(a)                                    (b)

**FIGURE 2.37** *SEM images of TiO$_2$ films on cp Ti wire subjected to heat-treatment in CO$_2$/CO ($P_{O_2} = 3.8 \times 10^{-21}$ atm) at 1100°C for 2h followed by HiTREP© at 700°C for 6h.*

The sensing behaviour of a titania thick film on cp Ti plate subjected to HiTREP© for surface regeneration to 32 ppm CO at 450°C is shown in Figure 2.38. As can be seen, the nanofied surface registers a sensitivity value of ~25 in this case.

## 2.6 CONCLUSIONS

A new scheme for the microstructural modulation to endow the potential semiconducting oxide sensor materials has been outlined and elaborated in the case of a host of systems. Based on this formalism, the following conclusions can be drawn:

- Novel microstructural features could be incorporated in a given semiconducting oxide via precise oxygen potential modulation.
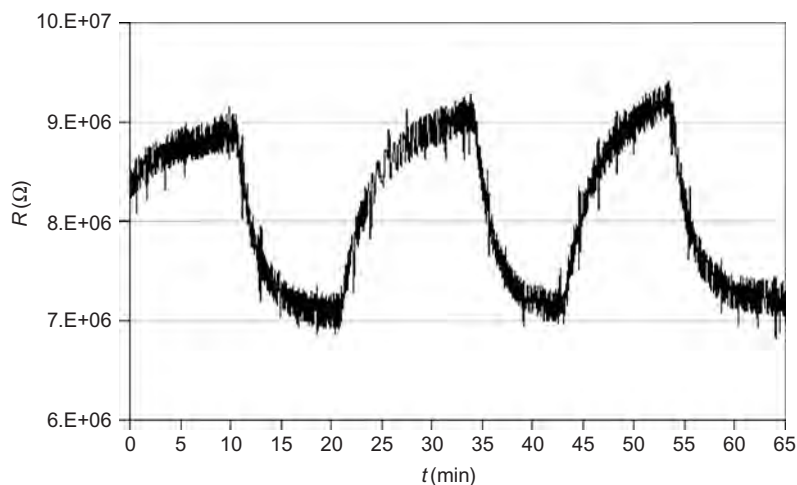
**FIGURE 2.38**  *Response of a TiO$_2$ film on cp Ti plate subjected to HiTREP$^©$ to 32ppm CO in 10% O$_2$-balance N$_2$ background at 450°C.*

- A buffer gas mixture (CO/CO$_2$ or H$_2$/H$_2$O) of appropriate ratio provides a convenient environment for the proposed redox scheme; from the point of view of experimental ease, CO/CO$_2$ is a better buffer mixture.

- The formation and growth of new oxide surface on an atomic or submolecular level, under conditions of oxygen enrichment/deprivation, appears to be the most likely pathway.

- Temperature–time–$P_{O_2}$ correlation is a benign microstructural determinant for oxide ceramics that are amenable to redox reactions; in other cases, a novel HiTREP$^©$ has been developed.

- The regenerated oxide phase with unusual microstructure possesses better gas sensing attributes.

- Applying the scheme to thin (1–10 μm) films is expected to enhance the sensor characteristics several fold; really thin films might suffer from spalling during the redox processes.

## REFERENCES

[1] BBC Research Instrumentation and Sensor Publication, 2007. <http://www.bccresearch.com/instrumentation-sensors/> .

[2] A.-M. Azad, 'Smart Sensors' – innovative R&D to tech transfer: Focus on environmental remediation, Eng. Horizons 114 (1998) 5–8.

[3] J.R. Stetter, W.R. Penrose, S. Yao, Sensors, chemical sensors, electrochemical sensors and ECS, J. Electrochem. Soc. 150 (2003) S11–S16.

[4] S.A. Akbar, P. Dutta, C. Lee, High-temperature ceramic gas sensors: a review, Int. J. Appl. Ceram. Technol. 3 (2006) 302–311.

[5] A.-M. Azad, S.A. Akbar, Ceramic materials and nano-structures for chemical sensing, Proceedings of the Optics East SPIE Conference on Sensors for Harsh Environments II, Boston, MA, October 23–26, 2005, vol. 5998 (2005) 599801–599815.

[6] A.-M. Azad, M. Hammoud, Thermodynamically-driven reconstitution of semiconducting ceramic oxides, in: Mark J. Jackson and Waqar Ahmed (Eds.), Proceedings of the fourth International Surface Engineering Congress and Exposition, August 1–3, 2005, St. Paul, MN, published by ASM International, Materials Park, OH, March 2006, pp. 231–240. ©2006. ISBN: 0-87170-835-31.

[7] A.-M. Azad, M. Hammoud, Fine-tuning of ceramic-based chemical sensors via novel microstructural modification. I: low level CO sensing by tungsten oxide, $WO_3$, Sens. Actuators, B 119 (2006) 384–391.

[8] A.-M. Azad, Fine-tuning of ceramic-based chemical sensors via novel microstructural modification. II: low level CO sensing by molybdenum oxide, $MoO_3$, Sens. Actuators, B 120 (2006) 25–34.

[9] A.-M. Azad, S.A. Akbar, Novel structural modulation in ceramic sensors via redox processing in gas buffers, Int. J. Appl. Ceram. Technol. 3 (2006) 177–192.

[10] O. Kubaschewski, C.B. Alcock Metallurgical Thermochemistry, fifth ed., Pergamon, New York, 1979 pp. 378–384.

[11] L.B. Pankratz, J.M. Stuve, N.A. Gockcen, Thermodynamic Data for Mineral Technology, US Department of Interior Bureau of Mines, Bulletin # 677 (Washington, D.C., 1984) pp. 261–295.

[12] M.B. Robin, P. Day H.J. Emelius, A.G. Sharpe (Eds.), Advantage in Inorganic and Radiochemistry, Academic Press, New York, 1967, pp. 335–344.

[13] A.-M. Azad, S.G. Mhaisalkar, L.D. Birkefeld, S.A. Akbar, K.S. Goto, Behavior of a new $ZrO_2$–$MoO_3$ sensor for carbon monoxide detection, J. Electrochem. Soc. 139 (1992) 2913–2920.

[14] ICDD reference card # 05-0408.

[15] ICDD reference card# 32-0671.

[16] S.C. Abrahams, Crystal structure of zinc molybdate $ZnMoO_4$, J. Chem. Phys. 46 (1966) 2052–2063.

[17] http://www.mineral.galleries.com/minerals/symmetry/triclini.htm.

[18] ICDD reference card # 32-1395.

[19] S. Yoo, S.A. Akbar, K.H. Sandhage, Nanocarving of bulk titania crystals into oriented arrays of single-crystal nanofibers via reaction with hydrogen-bearing gas, Adv. Mater. 16 (2004) 260–264.

[20] C. Carney, S. Yoo, S.A. Akbar, $TiO_2$-$SnO_2$ nanostructures and their $H_2$ sensing behavior, Sens. Actuators, B 108 (2005) 29–33.

[21] S. Yoo, S. Dregia, S.A. Akbar, H. Rick, K.H. Sandhage, Kinetic mechanism of $TiO_2$ nanocarving via reaction with hydrogen gas, J. Mater. Res. 21 (2006) 1822–1829.

[22] N.B. Pilling, R.E. Bedworth, The oxidation of metals at high temperatures, J. Inst. Metals 29 (1923) 529–582.

[23] K.H.J. Buschow (Ed.), Encyclopedia of Materials: Science and Technology, Elsevier, New York, 2001.

# Advanced Characterization Techniques for Nanostructures

D. Brabazon[1] and A. Raffer[2]

[1]Associate Dean for Research, Faculty of Engineering & Computing, Dublin City University, Glasnevin, Dublin 9, Ireland
[2]Centre for Research on Adaptive Nanostructures and Nanodevices, Trinity College Dublin, College Green, Dublin 2, Ireland

## CONTENTS

## ABSTRACT

This chapter presents many of the advanced techniques that can be used for visualizing and interacting with nanoscaled features. The techniques presented here fall into the three main categories of topology, internal structure and compositional investigation. Topological techniques presented here include field emission scanning electron microscopy (FESEM), scanning probe microscopy (SPM) and optical microscopy (confocal and NSOM). Internal structure techniques presented include transmission electron microscope (TEM), magnetic resonance force microscope (MRFM) and X-ray diffraction (XRD). Compositional techniques presented include X-ray photoelectron spectroscopy (XPS), energy dispersive X-ray spectroscopy (EDS), secondary ion mass spectroscopy (SIMS) and Auger electron spectroscopy (AES). In order to highlight the current capabilities and applications of these techniques, case studies from recent literature are presented.

## 3.1 MEASUREMENT OF THE TOPOLOGY OF NANOSTRUCTURES

### 3.1.1 Field emission scanning electron microscope

Scanning electron microscopes (SEMs) have been used by researchers since 1935 to examine micrometre scale structures and more often recently to examine nanoscale structures[1,2]. This is a versatile technique with which relatively large samples can be visualized, dimensional measurements can be taken and compositional analysis can be performed. The SEM works by initially firing primary electrons at the sample to be imaged. Electrons are dislodged from the atoms at the surface of the sample and are attracted to a positively charged detector grid. These electrons are known as secondary electrons. When a set pattern of primary electron beam scanning is used over the surface, recording of the secondary electrons allows the surface topology to be interpreted and displayed. Spatial resolution within a given SEM depends on the primary electron beam spot size and the volume of material with which the electrons interact. Under good conditions, such as high accelerating voltage (e.g. 30 kV), well-aligned apertures, well-corrected astigmatism, small spot size (small probe current) and no sample charging, resolutions of 3 nm can typically be achieved. Conventionally, tungsten and carbon elements were used in SEMs; to achieve longer gun lives, $LaB_6$ elements have been adopted more recently. Primary electrons that are bounced back off the surface are known as back scattered electrons (BSE). The energy of these electrons is directly related to the density of the atoms from

which they are repelled and therefore their recording allows the variation of surface composition to be visualized.

A field emission cathode in the electron gun of an SEM provides narrower probing beams resulting in both improved spatial resolution and less sample charging. Such systems are designated as field emission scanning electron microscopes (FESEMs). In order to achieve this increased electron focusing, a different gun design is required. In this design, electrons are expelled by applying a high electric field very close to the filament tip. The size and proximity of the electric field to the electron reservoir in the filament controls the degree to which electrons tunnel out of the reservoir. One type of field emission gun commonly used is known as the Schottky in-lens thermal FESEM electron gun. Cold gun alternatives are available for even finer FESEM resolution; however, these suffer rapid degradation and can therefore lead to expensive operation due to relatively frequent placement. The field emission guns have higher stability, can allow higher current and hence provide a smaller spot size. Under good operating conditions, a typical FESEM resolution of 1 nm is achievable. Elements that add to improved operation and FESEM resolution include designs with a beam booster to maintain high beam energy, an electromagnetic multihole beam aperture changer, a magnetic field lens and a beam path that has been designed to prevent electron beam crossover.

### FESEM case studies

Xie et al. were able to relate 3D nanoscale architectures of ZnO to intensive ultraviolet emission at 385 nm[3]. In this work a typical batch of ZnO was prepared by stirring 5 mL of $ZnCl_2$ (0.4 M), 5 mL of NaOH (5 M) and a solution of dodecylamine (DDA) in absolute ethanol (30 mL, 66.7 mM). The solution was then heated to 180°C for 12 h to form the ZnO. With the application of DDA aggregated assemblies of urchin-like architectures of hexagonal cross-sectional shape nanorods were formed. Without DDA stubbier nanorods of about 150 nm diameter were formed, see Figure 3.1. This FESEM image was taken at an accelerating voltage of 200 kV.

Copper phthalocyanine (CuPc) thin films deposited at room temperature (30°C) on quartz and post-annealed gold-coated quartz substrates were examined using FESEM[4]. Such structures can be used for the development of photoconductive or catalytic devices. FESEM images showed densely packed nanoparticles and nano-flower-like structures on the annealed gold-coated quartz
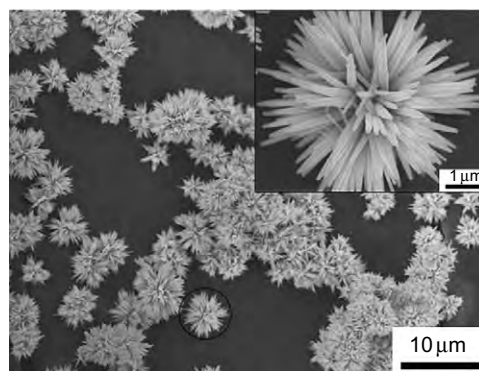


**FIGURE 3.1**   *FESEM of aggregated ZnO nanorod powder particles.*
*Source: Ref. [3].*

substrates. The further characterization by fractal dimension of the assembly of nanostructures in the films, estimated from FESEM images, agreed with optical measurements and indicated significant effect and potential control of the electronic and optical properties of these films.

Other workers have applied FESEM characterization for the implementation of cryo-SEM natural state colloidal solution capturing and studied the process of simultaneous deposition by immersion plating of palladium and silver seeds from 1 to 100 nm in size on porous silicon[5,6].

### 3.1.2  Scanning probe microscopy

Scanning probe microscopy (SPM) is a general term that covers a wide range of techniques within which a physical probe is passed over a surface via piezo-electric actuators in order to reproduce the surface features. The first of these, scanning tunnelling microscopy (STM) technique, was invented in 1981.

#### *3.1.2.1  Scanning tunnelling microscope*

In 1986 Binnig and Rohrer won the Nobel Prize in Physics for their work to develop the STM technique for imaging surfaces with atomic precision[7]. An STM consists of a tip [typically tungsten, platinum–iridium, gold or carbon nanotube (CNT)] sharpened to one atom width which is scanned over the surface to be measured. Piezoelectric actuators are used to control the scanning of the tip in the $x$, $y$ and $z$ (normal) directions with respect to the surface. This technique is used to image conductive or semiconductive materials surfaces and provides the highest resolution of many of the surface imaging techniques. Well-operated and constructed STMs can be used to provide for 0.1 nm lateral resolution and 0.01 nm depth resolution. In order to achieve these resolutions vibration control of the sample within the measurement system is crucial. Spring based and other vibration isolation systems are often used for this purpose. The sample can be measured in an air, liquid or alternate gas environment. However to avoid sample contamination, to achieve more stable operating conditions and to achieve higher resolutions, the sample is often measured under vacuum.

During operation of an STM the tip is brought close to the surface under coarse control and then to an equilibrium position between tip attraction and repulsion which is typically within a range from 4 to 7Å. When the conducting tip is brought so close to the surface, a bias between the two can allow electrons to tunnel between them. At low voltages, this current provides a record of the surface height. There are two modes of operation for the STM, the constant height and the constant current mode. In constant current mode, as the tip is scanned laterally over the surface the tip height

is moved in order to keep the current constant. The movement of the tip height is used to profile the surface. In constant height mode, the height and tip voltage are held constant. The change in current required to keep the voltage constant is related to local charge density to provide a record of the surface profile. Constant height mode is faster than constant current as piezoelectric movements in constant current require more time than the electronic control to keep voltage constant in constant height mode. This can provide a significant advantage as typical STM measurements for area profile recording can be very time consuming.

### STM case studies

In the work of Maffeis et al., thin films of tungsten trioxide ($WO_3$) were magnetron sputtered and sequences of ultra-high vacuum (UHV) anneals from 100°C to 900°C were performed[8]. $WO_3$ is a promising material for gas sensing devices due to its electrical conductivity and excellent sensitivity and selectivity. STM imaging showed that film surfaces which were annealed up to 600°C consisted of amorphous particles 35 nm in size while higher temperatures resulted in an increase in particle size, see Figure 3.2. Crystallization of the nanoparticles started to occur at temperatures of 600°C and above. The surface annealed at lower temperatures produced a larger surface area which would be expected to be more reactive and therefore better in sensing applications. The tunnelling current and sample voltage for STM imaging were 1 nA and 2.5 V, respectively. STM tips were fabricated by electrochemical etching of tungsten wire.

Appropriate sample handling and preparation procedures need to be developed for each material type to be examined[9]. Organic molecules can be imaged with STM when placed on a conducting substrate. It is important to minimize resolution loss due to unwanted mixing between molecular and substrate electronic levels. Better resolution can typically be achieved at UHV; however samples can provide difficulties with ultra-low vapour pressures or decomposition or can denature at elevated preparation temperatures. The benefits of using passivated substrates have been demonstrated for the capturing of organic molecules to allow examination with UHV STM.

Bowker and Fourre[10] recently examined the method of nanoparticulate formation of Pd catalysts on $TiO_2(1\ 1\ 0)$ using metal vapour deposition (MVD) to form particles in the size range 1–50 nm. These workers were able to use STM to image these particles and observe oxygen spill over from Pd particles to the titania support due to the fast adsorption of oxygen on Pd compared with titania. In another work, Pt was deposited from an electron beam evaporator and four distinctly different structures induced by platinum (Pt) adsorption on $Si(1\ 1\ 0)$ surface were found by STM[11].
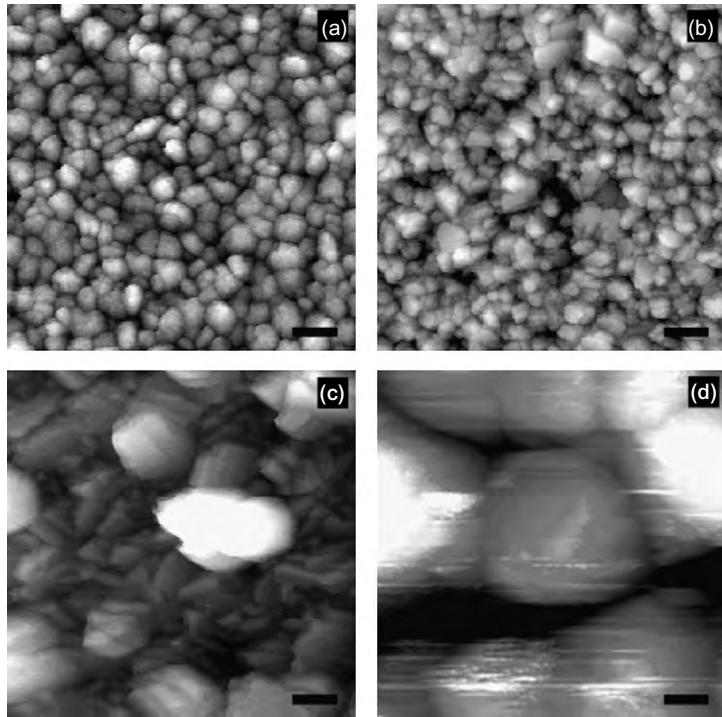
**FIGURE 3.2**  *Constant current STM images of the WO$_3$ film surfaces acquired after annealing at (a) 300°C, (b) 600°C, (c) 700°C and (d) 800°C; scale bar is 50 nm.*
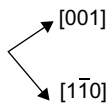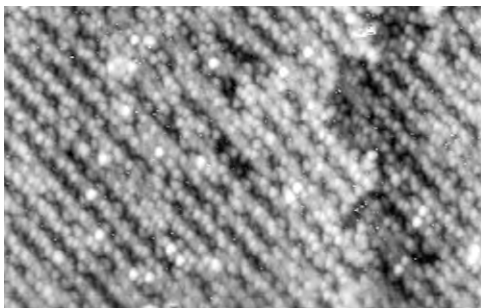*Source: Ref. [8].*



[001]

[1$\bar{1}$0]

**FIGURE 3.3**  *Si(1 1 0) surface after deposition of 0.35 monolayer of Pt on a hot substrate (~750°C, 50 nm × 31.5 nm).*
*Source: Ref. [11].*

Potential applications of such metal silicides include use as ohmic and Schottky junctions. Figure 3.3 shows the Si(1 1 0) atomic plane with platinum deposited. The tunnelling current and sample voltage for STM imaging were −2 V and 0.25 nA, respectively.

### 3.1.2.2 Atomic force microscope

The atomic force microscope (AFM), also called the scanning force microscopy (SFM), was developed in 1986, subsequent to the STM[12]. Similar in operation to the STM, the AFM involves scanning a sharp tip across a sample surface while monitoring the tip–sample interaction to allow the reconstruction of the 3D surface topography. A typical AFM has nanometre lateral and sub-angstrom vertical resolution and can image insulators as well as conductors. UHV AFM resolution

is comparable to that available from STM and transmission electron micro-scopy (TEM). An AFM consists of a sharp tip at the end of a flexible canti-lever which is moved across a sample surface by piezoelectric actuators. The cantilever is typically made from Si or $Si_3N_4$ with a tip curvature radius of a few nanometres. Displacement of the tip is recorded by a non-contact laser displacement measurement. A laser light directed onto the cantilever above the laser tip is recorded on a photodetector area which allows calculation of displacement via signal strength measurement or triangulation. A feedback loop maintains a constant tip–surface interaction force by vertically mov-ing the scanner to maintain a constant photodetector difference signal. The distance the scanner moves vertically is recorded and with each $x$, $y$ posi-tion which allows the surface information to be presented and analysed. A complicated set of forces can be present at the tip–sample interaction. For a surface under ambient conditions, when the tip touches the surface a repul-sive force is present, with the tip at a small distance from the surface attrac-tive forces can be present as well as van der Waals force and capillary force arising from condensation of water vapour in the contact area. Operating modes can be roughly classified as contact, non-contact and dynamic.

In contact mode, the scanning tip is dragged across the sample surface and the tip deflection is monitored. Using Hook's law, the force between the tip and the surface is automatically kept constant during scanning (typically between 0.1 and 100 nN). Lower stiffness cantilevers (spring con-stant, $k < 0.1$ N/m) are used in this mode to amplify the deflection signal. Contact mode may not be suitable for soft materials which can be easily deformed or damaged, such as for polymer or molecular imaging. When scanning is performed in the region where the tip is attracted to the sur-face, the scanning is termed non-contact mode. In this region, the cantilever bends towards the sample. If an oscillatory tip displacement is sufficiently large to pass through both regions, the probe experiences both attractive and repulsive forces. This mode is known as dynamic, intermittent or tapping mode. Tapping mode was developed for investigation of soft materials[13]. In this mode, the cantilever oscillates near its resonant frequency and lightly taps the surface during scanning. The tip rapidly moves in and out of the sample surface with an amplitude which is sufficiently high to overcome adhesion forces so that it stays in contact only for a short fraction of the oscillation period. Depending on the cantilever type, the frequency typically varies from 50 to 500 kHz and amplitudes up to 100 nm are used. The laser spot deflection is used to measure the amplitude of cantilever oscillation and a feedback loop maintains a constant oscillation amplitude by adjust-ments to the servo which adjusts the cantilever height. In addition to the favourable imaging conditions and high resolution, the AFM offers a variety

of new contrast mechanisms which can be used to provide information on differences in sample friction, adhesion, elasticity, hardness, electric fields, magnetic fields, carrier concentration, temperature distribution, spreading resistance and conductivity.

### AFM case studies

Jiménez et al. recently investigated a plasma-assisted physical vapour deposition technique to grow (TiAl)N films on H13 tool steel[14]. This tool steel is commonly used as a forming dye material at temperatures up to 600°C. Above this temperature the surface oxidizes and spalls quickly. In order to enable this tool material to be used at higher temperatures, a protective surface coating is needed. Thermal treatment of the H13 tool steel with and without (TiAl)N coatings were investigated with an AFM used in non-contact mode. Uncoated substrates showed appreciable increase in surface roughness due to oxidation at temperatures above 600°C whereas coated samples retained similar surface profiles after temperature treatments up to 1000°C (see Figure 3.4). X-ray diffraction (XRD) measurements were used to confirm and correlate these topographical measurements with the surface reactions. Extensions of the AFM, force modulation microscopy (FMM) and phase detection microscopy (PDM) were also used to image the surface. In FMM mode the tip is scanned in contact with the sample while a displacement sinusoid of a few kilohertz is applied to the tip or sample. The applied amplitude signal is modulated according to the elastic properties of

**FIGURE 3.4**

*H13 uncoated: (a) before heat treatment (b) after heat treatment; (TiAl)N-coated H1 samples: (c) before heat treatment and (d) after heat treatment. Source: Ref. [14].*
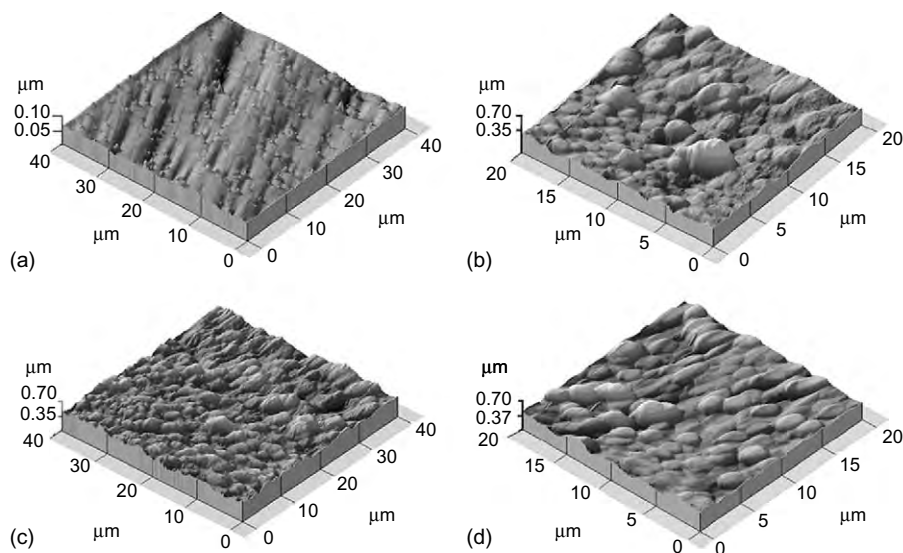
the sample. FMM can therefore be used to image hard and soft regions at the same time as topological information is recorded. PDM is used when the AFM is operated in intermittent contact mode. PDM refers to the monitoring of the phase lag between an applied signal driving cantilever oscillation and the cantilever oscillation output signal. Changes in the phase lag reflect changes in the mechanical properties of the sample surface.

Tanaka et al. investigated the effect of toner particle morphology on toner fluidity and adhesion strength using an AFM[15]. Particle fluidity and interactions are influenced by surface structure size and morphology as well as the particle size and morphology. A fractal dimension was used to quantify the particle surface shape, which was related to its flow properties, and particle adhesion forces, which were measured with an AFM. The fractal dimensions were directly scaled from the nanostructure on the toner particle surfaces. A toner particle of approximately 5.5 μm diameter was attached to the AFM tip (see Figure 3.5), which was then held close to compacted toner powder (with a pressure of 54.9 MPa). The force to move the tip/particle away from the surface was recorded. Toner particles were nanotextured to various degrees by mixing with fine $SiO_2$ particles (mean diameter of 20 nm) which adhered to the toner particles. As the fractal dimension increased, the shearing and adhesion force between particles was also seen to increase.

Matějka et al. examined the wear characteristics of SiC-reinforced iron-phenolic based brake disks using an AFM[16]. Abrasives, such as SiC, are added to brake disk composites in order to increase the friction coefficient and stabilize it at higher temperatures. At temperatures above 250°C an enhanced pull-out of SiC was noted from the AFM results. The AFM results also showed that these particles could help maintain the friction coefficient at higher temperature due to their abrasion of the disk surface. A potential drawback of quicker abrasion of the contact surface was also reported. An optimum of approximately 3.4% SiC addition was determined from this work.

### 3.1.3  Optical microscopes

#### *3.1.3.1  Confocal microscopy*

In confocal microscopy two focusing arrangements are used to focus on the point in a sample to be imaged[17]. One focuses laser light through an objective lens on the point of interest and the other focuses the reflected light on the imaging sensor. Light from the point to be imaged is passed through a pinhole such that all
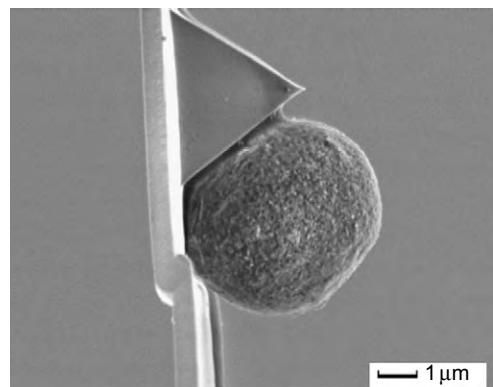


**FIGURE 3.5**   *Quadrangular pyramid-shaped AFM tip of 3 μm height with toner particle of approximately 5.5 μm diameter attached.*
*Source: Ref. [15].*

extraneous out of focus light is removed. This allows lateral resolutions approximately 1.4 times greater than in conventional microscopes to be achieved with confocal microscopy. The depth of the focal plane depends on the specimen optical properties and importantly on the squared value of the objective lens numerical aperture. Three-dimensional reconstructions of cells and surfaces can be achieved with this technique. To achieve this, the sample is scanned such that one 2D slice is recorded, the focal plane of the sample is then moved a prescribed amount where the next 2D slice is recorded and this sequence is repeated until the required volume is scanned. Image processing software is then used to process the collected data to reconstruct the 3D object. Confocal microscopes are most often used to image biological systems and semiconductor surfaces[18–20].

Three variations of scanning are available in confocal microscope systems. In the conventional confocal laser scanning microscope the sample is raster scanned which results in a scanning rate of about three frames per second. Such systems provide the highest spatial resolution; however for higher temporal resolution, the spinning disk (Nipkow) and the programmable array microscope (PAM) systems can provide rates of 30 frames per second[21]. In a Nipkow disk system, a thin disk with hundreds of spirally patterned pinholes is spun in the light path to the objective lens. The pinholes allow only perpendicularly oriented rays of light to penetrate which allows high scanning speeds independent of the laser scanning speed. PAM is a variation on this whereby an acousto- or electro-optical filter can be patterned to automatically produce the pinhole pattern required. Such a system can allow, for example, up to 1000 beams to simultaneously scan the entire field at millisecond scan speeds. High frequency scanning has the added advantage of reducing photon exposure to sensitive samples which may be damaged due to photobleaching or phototoxicity.

Fluorescent dyes are often added to a surface or fluorophores to cellular systems to enable enhanced imaging with confocal fluorescent microscopy. Various excitation laser wavelengths are available for these systems ranging from 442 to 647 nm depending on the fluorophore excitation and emission wavelengths used. Reflected and fluoresced light waves are emitted from the sample. A beam splitter can be selected to reflect only the fluoresced light to the detector which provides enhanced signal to noise ratio. As described above, the pinhole is also used in this set-up to eliminate the out of focus signal and record only the light from the region of interest.

## Confocal microscopy case studies

In a recent study Manara et al. examined an electrochemically assisted process for the deposition of hydroxyapatite/collagen coatings on titanium plate[22].

The produced coatings are biomimetic bone-like composites made of self-assembled collagen fibrils and carbonate hydroxyapatite nanocrystals. As well as studying these structures chemically, structurally and morphologically, these workers also evaluated their ability to bind fibronectin (FN) in order to test their bioactivity. FN (a high molecular weight glycoprotein) aids the development of the cytoskeleton by providing binding sites for cell surface receptors and other extracellular matrix (ECM) components. FN has been identified as a potential communication network directing bone growth and is also involved in wound healing. Manara et al. used laser scanning confocal microscopy to characterize the degree of FN adsorption on the various composite coatings which they produced. Confocal images showed collagen–FN fibre bundles more than 50 μm in size and 20 μm deep after 5 min of collagen deposition (Figure 3.6). It was seen from this work that when the apatite phase was inter-grown with collagen fibrils, higher FN adsorption was recorded. The authors pointed out that this can be accounted for as FN has at least three receptors for collagen located close to the amino terminus of the molecule. It was further noted that FN adsorption was irregular following somehow the specific topography of the sample.

Wang et al. presented work evaluating the mechanical properties and corrosion behaviours of oriented $Ca(PO_3)_2$ glass[23]. In order to produce these structures, polycrystalline $Al_2O_3$ plate was inserted into the $Ca(PO_3)_2$ glass melt. The crystallographic $c$-axis of most crystals were oriented in the direction perpendicular to the surface of $Al_2O_3$ plate. The plate was then cut to extract crystal samples oriented perpendicular and parallel to the plate. The influence of crystal alignment on corrosion behaviour in simulated body fluid (SBF) was investigated by measuring and comparing the changes of
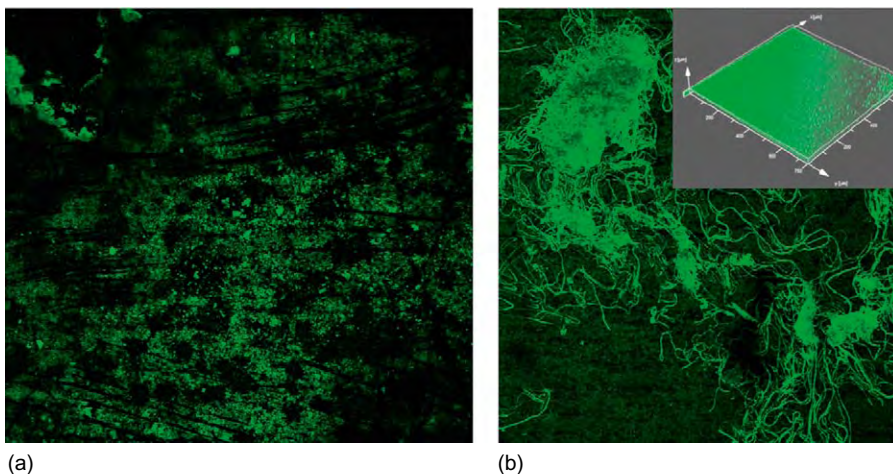


(a)  (b)

**FIGURE 3.6**

*(a) HA coating pre-adsorbed with fluorescein isothiocyanate tagged fibronectin (FITC–FN) and (b) collagen–FN network bundles after 5 min of collagen deposition with insert showing topographical view of bound FITC–FN. Source: Ref. [22].*

surface roughness from 3D surface topography which was measured using confocal laser scanning microscopy. By measuring surface area roughness from the topology measurements, it was found that crystals aligned parallel to the plate were attacked more strongly than those aligned perpendicular to the plate. This new information indicates that directionality of these coatings must be taken into account if these are to be used on implant surfaces. In another work the comparative mechanical and corrosion performances of electropolished superelastic 50.6%Ni–49.4%Ti alloy were evaluated[24]. Roughness measured with confocal laser microscopy was used to evaluate corrosion and surface structure development during testing. Samples examined included uncoated, coated with diamond-like carbon, nitrided and Ti coated. The specimens were strained at values up to 8% which may be experienced in stent implants, for example. Coated samples produced surface cracks at low strain values and could not withstand strain levels that developed during martensitic transformation in the superelastic NiTi alloy. In contrast the substrate material retained surface integrity and its unstrained level of corrosion resistance during testing.

### 3.1.3.2 Near field scanning optical microscopy

Near field scanning optical microscopy (NSOM) can be classified as an SPM technique as the scanning methodology places it in this category. However, due to the wave based principles behind its operation, it is placed under optical microscopy section here. When electromagnetic radiation is emitted, the near field is that part of the wave front that is within a couple of wavelengths from the surface of the emitter. An evanescent wave is a near field standing wave exhibiting exponential decay with distance. Evanescent waves are strongest within one-third wavelength ($\lambda$) from an electromagnetic emitter. NSOM (or SNOM) is a surface imaging technique with nanometre resolution. Synge, an Irish scientist, developed the idea for imaging by recording diffraction in the near field[25,26]. In 1928 he used light from an arc under pressure behind a thin opaque metal film with an orifice diameter of about 100 nm. The orifice was to remain within 100 nm of the surface, and information was to be collected by point-by-point scanning. It was not until the 1980s that the first papers were presented on near field scanning with visible light[27–29]. These works involved the use of a sub-wavelength metal-coated optical aperture at the tip of a sharp, pointed probe, and a feedback mechanism to maintain a constant distance of a few nanometres between the sample and the probe. Resolutions as low as 25 nm were achieved (about $\lambda_o/20$ where $\lambda_o$ is wavelength of light used in vacuum)[29].

As for an AFM the primary components of an NSOM are the scanning tip, the feedback mechanism and the piezoelectric actuation. An additional

element in the NSOM is the light source which is usually a laser focused into an optical fibre through a polarizer, a beam splitter and a coupler. The polarizer and the beam splitter would serve to remove stray light from the returning reflected light. The scanning tip is usually a sharpened optical fibre (pulled or etched) coated with metal except at the tip. Alternatively, a standard AFM cantilever with a hole in the centre of the pyramidal tip can be used. Feedback to maintain the probe at the correct working distance is performed by recording the normal force by measuring the tip displacement as described for the AFM. In another method, a tuning fork attached to the fibre tip is oscillated at resonant frequency which moves the tip laterally. Changes in amplitude are monitored to provide shear-force feedback. A number of operation modes can be selected for sample imaging, including: transmission, where the light travels through the probe and through the sample; reflection, where the light travels through the probe aperture and reflects from the surface which allows for opaque sample; collection, where the sample is illuminated from a large outside light source and the probe collects the reflected light; and illumination/collection, where the probe illuminates and collects the reflected light.

### NSOM case studies

Knutson et al. used NSOM to study the reactivity of nanoporous aluminium alloy 2024[30]. In particular they used a modified version for determining concurrent topography, fluorescence intensity and fluorescence spectroscopy on alloy surface. For microelectronic and micromagnetic applications, planar and homogeneous surfaces can be formed to provide lower reactivity and longer component working lives. Typically local reactivity varies due to heterogeneous polycrystalline and local impurities in surfaces. Susceptibility to corrosion also increases as the feature size decreases. By using these techniques concurrently, the authors were able to characterize the degree to which fluorescein dye could be used to detect corrosion of the nanoporous aluminium alloy. Second-phase particles, $4$–$5\,\mu m$ in diameter, were seen to contribute to the local corrosion (see Figure 3.7). An advantage
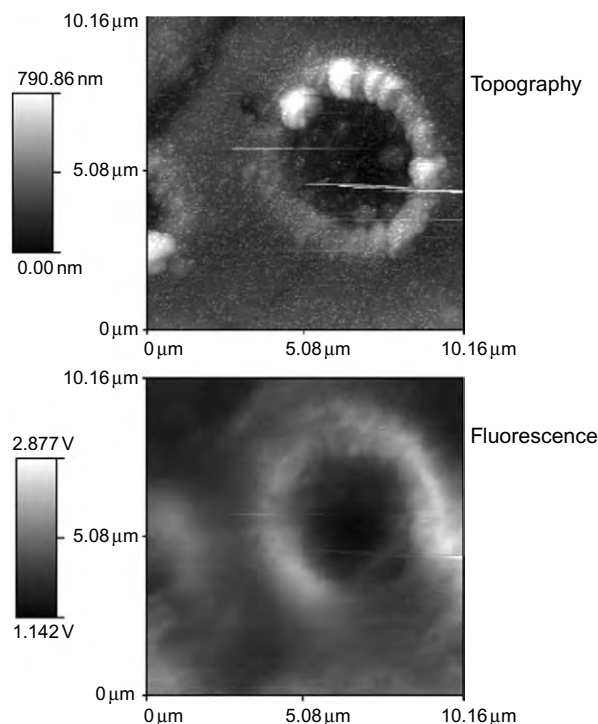


**FIGURE 3.7**   *Topographic and fluorescence NSOM image for aluminium sample exposed to aqueous solutions with fluorescein. Source: Ref. [30].*

of the developed technique is that topography and chemical concurrent mapping can be achieved to provide an understanding of the corrosion processes and evaluation of fluorescent dyes that can be used to evaluate them.

An investigation of new organic diarylethene films for data storage was conducted by Lee et al. using NSOM[31]. NSOM was used to characterize the nanoscale colour changes in these films in order to evaluate the applicability of this process for near field recording (NFR) which could provide a high density, rewritable recording media. Transparent, colourless and homogeneous thin diarylethene films were vacuum deposited onto substrates. Laser light with a wavelength of 514 nm was shown to produce distinct and quick marking of the film (30 ms per mark). These recordings were completely erased by exposure to UV light which produced a deep red colour in the film. This process was seen to be reversible.

The growth of PbS nanopyramidal particulate films for applications in quantum dot photovoltaics and nanoantennas was investigated with NSOM by Hawaldar et al.[32] In this work, a liquid–liquid interface reaction technique (LLIRT) was used to produce the novel pyramidal structures. Collage images of AFM topography maps and NSOM light intensity maps were produced to aid visualization of the nanopyramidal structures identified with TEM. Pyramidal structures were found to have an antenna effect whereby increased light intensity was emitted from the NSOM probe tip when it was over higher nanopyramidal structures.

## 3.2 MEASUREMENT OF INTERNAL GEOMETRIES OF NANOSTRUCTURES

### 3.2.1 Transmission electron microscope

TEM is an established characterization technique, which is capable of providing both image mode and diffraction mode information from a single sample[33]. It is regarded as one of the main techniques for nanomaterials characterization[34], largely due to its high lateral spatial resolution in the region of 0.08 nm. A feature of nanomaterials is that specific properties, for example colour, can be related to a particles size. Agglomeration of nanoparticles or failure to isolate individual nanostructures is likely to result in anomalous property characterization. Characterizing the elastic or mechanical properties of individual nanoparticle/nanotube/nanofibres is a challenge to many existing testing and measurement techniques. For example, it is difficult to pick up and clamp samples in order to test for tensile strength or creep[35].

## TEM case studies

TEM has shown itself to be capable of meeting such challenges. It is commonly used specifically for its ability to isolate and examine individual nanoparticles. This approach reduces the potential for agglomeration which can be a problem with wet based laser scattering techniques. Nanoparticles attached to CNTs have also been imaged, with remarkable clarity[36]. The select area electron diffraction (SAED) patterns revealed very clear diffraction rings owing to the polycrystalline nature of the iron oxide nanoparticles[36]. TEM's electron imaging and diffraction options allow property–structure relationships of nanostructures to be understood. It has the resolution to differentiate between nanotubes with subtle nanoscale structural patterns. Interlayer distances of about 0.34 nm have been measured and imaged with impressive clarity, consistent with the (002) plane lattice parameter of graphited carbon[37].

TEM is well renowned for its high resolution imaging capabilities. However, in recent years TEM has also gained acceptance as a viable means of measuring the elastic and mechanical properties of nanostructures[38]. Wang et al. demonstrated a technique to measure the mechanical strength of single CNTs using in situ TEM. This was done by using an externally applied voltage to induce a charge in the nanotube[35]. The electrostatic force resulted in a deflection of the nanotubes (see Figure 3.8).

Cyclical loading of the nanotube was achieved by subjecting the tube to positive and negative voltages. This approach was used to apply a load to an individual nanotube, thus allowing a direct measurement of its elastic limit[35]. Wang et al. also employed their in situ TEM set-up to measure the mass of particles as small as $22 \pm 6$ fg ($1$ f $= 10^{-15}$). This nanobalance worked by attaching the mass to be measured to the tip of a nanotube. The change in the resonance frequency of the altered nanotube enabled the calculation of the mass of the particle[35].
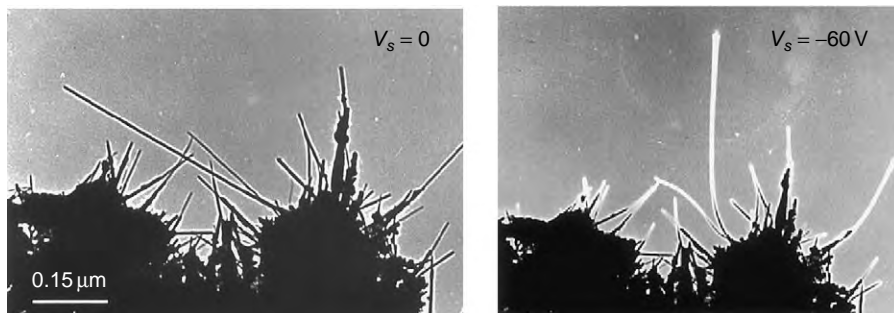


**FIGURE 3.8**

*Electrostatic deflection of a CNT induced by a constant field across the electrodes. Source: Ref. [35].*

The conductance of CNTs is of great interest, partly due to the possibility of using CNTs as interconnects for molecular devices without heat dissipation. AFM studies have shown that conductance effects are related to defects in the CNT which is in turn related to the production method used to make the CNTs. Wang et al. utilized their in situ TEM set-up to repeat this experiment by measuring the conductance of a CNT in contact with liquid mercury[35].

Nanotube alignment is important because in addition to mechanical properties, functional properties such as electrical, magnetic and optical properties of polymer/CNT nanocomposites are linked directly to the alignment of CNTs in the matrix. Jose et al.[39] successfully synthesized surface-modified multi-walled carbon nanotubes (MWNTs) via electrospinning, using a rotating mandrel. They used TEM to successfully verify high nanotube alignment.

### 3.2.2 Focused ion beam

Focused ion beams (FIBs) have become a popular tool for surface modification of materials and functional structure prototyping at the micro- and nanoscale. Modern FIBs have spot sizes of <5 nm and are produced by using electrostatic lenses to focus the image of a point source, often gallium liquid metal ion source, onto the substrate and to deflect it in a precise fashion. For a comprehensive review of recent developments in FIB implantation and sputtering, FIB gas-assisted etching and FIB-induced deposition, the reader is referred to[40].

#### FIB case studies

Hitachi pioneered the use of FIBs for integrated circuit cross-sectioning for failure analysis in 1985. FIB technology can quickly and selectively remove specific layers (dielectric or metal layers) for probing and material analysis of underlying surfaces[40]. FIB can locate, expose and analyse the fault area without destroying the surrounding areas or losing the information at the site of the fault. A growing application area is FIB 'microsurgery' for circuit modification, device modification and defect repair. FIB make-and-break microsurgery combines imaging, restructuring and verification in the same machine. Musil et al. demonstrated a rapid focused-ion-beam method for making connections between two conductors[41]. Combined with the ability of FIBs to also break connections, view the circuit and monitor voltage contrast, one has a useful debugging and diagnostics tool[41]. FIB offers ion milling and metal deposition for quick repair of partially functioning devices or even deposition of probing pads for single device characterization. Boit[42] and Schlangen et al.[43] have recently reported on the use of FIB in the context of failure analysis

and circuit edit. FIB is not restricted to failure analysis of microelectronic materials and structures. Moghadam et al. have recently reported on the use of FIB for analysis of pharmaceutical microspheres, which had been prepared by a double-emulsion, solvent-evaporation technique (Figure 3.9)[44].

Normally, cross-sectioning is required to examine such microspheres. However, in this case it was possible to remove the outer surfaces of the microspheres, layer by layer. Despite having non-porous surfaces, the microspheres were found to become increasingly porous towards the centre of the particle. FIB was also used to extract a sample from the centre of a microsphere, which was then used for TEM analysis. Figure 3.10 shows the initial stages of the FIB sample extraction.
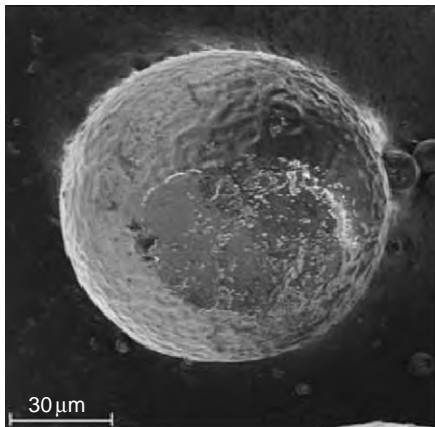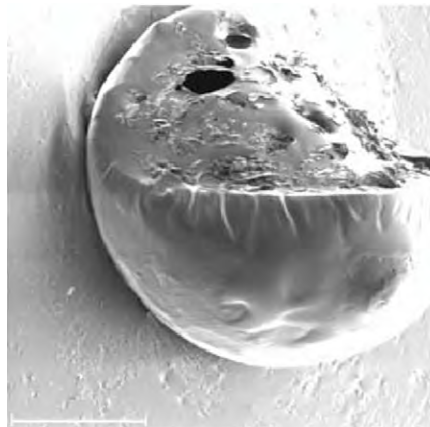


(a)  (b)

**FIGURE 3.9**

*Internal structure of a PLA (poly D,L-lactide) microsphere: (a) intact microsphere, scale bar is 30 μm and (b) after milling top half using FIB milling, scale bar is 10 μm. Source: Ref. [44].*
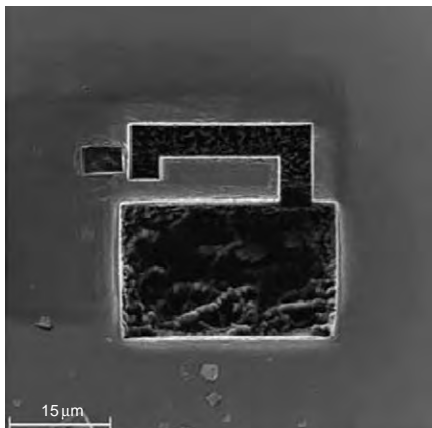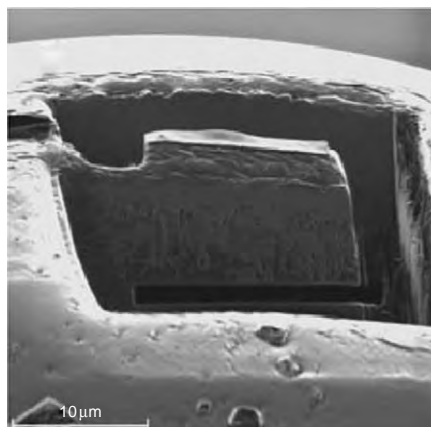


(a)  (b)

**FIGURE 3.10**

*Secondary ion images of a PLA microsphere at different stages of FIB sample preparation: (a) top view of ion-milled trenches, scale bar is 15 μm and (b) fully undercut sample, scale bar is 10 μm. Source: Ref. [44].*

### 3.2.3 X-ray diffraction

XRD is a powerful technique used to uniquely identify the crystalline phases present in materials and measure the structural properties (strain state, grain size, epitaxy, phase composition, preferred orientation and defect structure) of these phases. XRD is non-contact and non-destructive. XRD is most sensitive to high-Z elements; as a consequence, the sensitivity of XRD depends on the material of interest[45]. The regular array of atoms in a crystalline material forms a 3D diffraction grating for waves with a wavelength around that of the distance between the atoms. When waves enter a crystal, they are scattered in all directions by the atoms. In certain directions, these waves can interfere destructively. In other directions, constructive interference will occur resulting in peaks in X-ray intensity. The diffraction pattern that results is a map of the reciprocal lattice of the crystal and can be used to determine the structure of the crystal[46]. Bragg's law (equation 3.1) is the basis for crystal diffraction:

$$n\lambda = 2d\sin\theta \qquad (3.1)$$

where $n$ is an integer known as the order of diffraction, $\lambda$ is the X-ray wavelength, $d$ is the spacing between two consecutive scattering planes and $\theta$ is the angle between the atomic planes and the incident (and diffracted) X-ray beam[47].

### XRD case studies

Cengiz et al. used XRD to characterize nanoparticles of a novel calcium phosphate growth medium referred to as CaP–Tris[48]. This was prepared by mixing Tris $(CH_2OH)_3CNH_2$, HCL, $K_2HPO_4$ and $CaCl_2$ in deionized water. This new formulation was compared with a reference HA powder. Figure 3.11 shows the XRD patterns of reference HA and CaP–Tris. As can be seen, the XRD patterns are almost identical in terms of peak position and relative intensity. Thus, HA nanoparticles have been synthesized by a new precipitation method and CaP–Tris calcium phosphate growth medium.



**FIGURE 3.11** *XRD patterns of HA reference and CaP–Tris sythesized using CaP–Tris solution.*
*Source: Ref. [48].*

### 3.2.4 Mercury porosimetry

The mercury porosimeter is a device which is capable of generating suitably high pressures

and measuring simultaneously both the pressure and volume of mercury taken up by a porous material[49]. Mercury does not wet most substances and will only penetrate pores when forced to do so under high pressure. Entry of mercury into pores requires applying pressure in inverse proportion to pore size. In other words, large pores will fill first, with smaller pores filling at increasingly higher pressures. Equation (3.2), known as the Washburn equation, is the basis of the mercury porosimeter method for measuring pore size distribution:

$$D = \frac{-4\gamma\cos\theta}{P} \tag{3.2}$$

where $D$ is the pore diameter, $\gamma$ is the surface tension, $\theta$ is the contact angle and $P$ is the applied pressure. Mercury exhibits a high contact angle against most solids. Reported contact angles vary, with 130° being the most widely used value. Liquid mercury has a high surface tension;[50] usually its value is taken to be 485 dyne/cm. High pressure mercury porosimeters can normally attain maximum pressures of 30,000 psia or 60,000 psia. The measurable pore size ranges from a maximum of 360 μm to a minimum of 6 nm (for the 30,000 psia system) or 3 nm (for the 60,000 psia system)[50]. In principle it would be possible to explore in the pore range below 3 nm if a porosimeter with sufficiently high pressures could be made[49]. In practice, BET surface area is normally employed for micropore (<2 nm) analysis. In porosimetry, mercury filling apparatus is used to evacuate the sample and then to surround the sample with mercury. Evacuation is achieved by exposing the sample to a vacuum. The sample to be analysed is contained inside a penetrometer, which is a long glass capillary tube, the sample end being a bulb shape. Using the vacuum control on the filling apparatus, gases and vapours are removed from the sample. The vacuum valve is closed and the penetrometer titled so that the stem end is immersed in mercury. The vent control valve is then slowly opened such that air fills the mercury chamber. Mercury is forced up the capillary stem and into the bulb. The filled penetrometer is then removed and inserted in the high pressure porosimeter for pore analysis.

The construction of the glass penetrometer is key to pore measurement. A metal sheath fits over the capillary section. A metal seal is attached to the sample end of the penetrometer as a base electrode. The construction is thus mercury–glass–metal, or conductor–insulator–conductor. In this way a coaxial capacitor is created[50]. The capacitance changes as a result of the change in mercury level within the penetrometer. The mercury level will change as porous samples are filled with mercury under increasingly high pressure. In a similar way, a normal mercury thermometer will change mercury level,

indicating a temperature change. Some porosimetry systems operate on the basis of a wire dipped remotely into the mercury, with the change in electrical resistance of the wire being used as a means of measuring the volume of mercury taken up by the pores[49].

### Mercury porosimetry case studies

Controlled pore glass (CPG) has application as media for size exclusion and affinity chromatographic media, commonly used to separate proteins. Nominally, the pore diameter should be 10 times the protein diameter. Most proteins[51] have a diameter below 3 nm. CPGs are required to have sharp, unimodal pore distributions, that is a high volume of pores of similar size. Clearly, a means of investigating pore size, pore volume and pore distribution on the nanometre scale is required. Porcheron et al. have recently investigated mesoporous Vycor and CPG materials[52].

Porcheron et al. revealed different intrusion/extrusion characteristics and hysteresis behaviours between Vycor and CPG[52]. The intrusion/extrusion curves in Figure 3.12a reveal a type H1 hysteresis loop for the CPG sample and a type H2 hysteresis loop for the Vycor glass. Entrapment was also observed; that is mercury remains in the porous network after extrusion. Clearly the extrusion curve doesn't meet up with the intrusion curve at low pressures. A high pressure plateau observed for the CPG is not observed for the Vycor, since the Vycor material contains pores of sizes that are below the measurement limit of the instrument. During intrusion there are unfilled
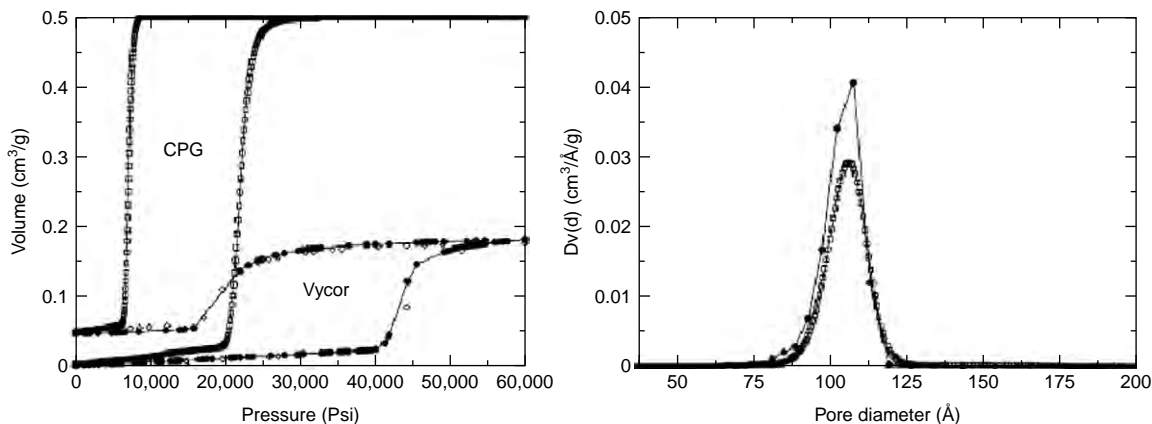


**FIGURE 3.12** *(a) Mercury intrusion/extrusion curves for Vycor and CPG 75, where the volume of mercury is a function of hydraulic pressure. (b) Pore size distribution from nitrogen adsorption and mercury porosimetry for CPG 75.*
*Source: Ref. [52].*

pores remaining and so the intrusion curve continues to rise slightly rather than coming to a plateau.

There is a scarcity of studies in the literature for pore size distributions in the range where mercury porosimetry and the BET Kelvin method overlap. However, the pore size distribution of CPG 75 in the 10 nanometre range as measured using porosimetry was in excellent agreement with that measured using BET surface area, as reported by Porcheron et al.[52] (see Figure 3.12b).

## 3.3  MEASUREMENT OF COMPOSITION OF NANOSTRUCTURES

### 3.3.1  Energy dispersive X-ray spectroscopy

Energy dispersive X-ray spectroscopy (EDS) is one of the most common spectroscopy techniques used as SEMs from the 1960s that have been commonly equipped with this chemical analytical device[53,54]. In this technique, electromagnetic radiation is bombarded into a material surface which in turn causes electrons from inner atomic shells to be ejected and subsequently filled with electrons from higher energy levels. Electromagnetic radiation used to excite the sample is usually a focused high energy stream of electrons, protons or X-rays. In a typical SEM, a stream of electrons is used. Electron transition from the higher energy shells to lower energy shells causes X-rays to be emitted. A detector of SiLi or more commonly now a silicon drift detector is used to collect and count the number of X-rays emitted at each energy level. The energy level characterizes the element from which the X-ray was emitted while the count of the number of X-rays with this energy level is used to characterize the amount of the element that is present. A typical spectrum presents the count of the X-rays versus the energy level of the X-rays. New EDS systems come pre-calibrated to allow automatic detection and quantification of the elements present within the sample.

Care must be taken when interpreting EDS results. Wrong elements, for example, can often be detected where energy levels emitted from different elements overlap. X-rays can be generated from K, L or M energy-level shells in a typical element. Therefore overlapping of energy levels detected can occur for example when Ti and Ba (Ti-$K_\alpha$ and Ba-L), or Mn and Fe (Mn-$K_\beta$ and Fe-$K_\alpha$), or Mn and Cr (Mn-$K_\alpha$ and Cr-$K_\beta$) are present. Some knowledge of the sample elemental chemistry or knowledge gained from other analytical techniques is often useful for element identification. Wavelength dispersive X-ray spectroscopy (WDS) is similar to EDS but analyses the diffraction patterns from the material–radiation interaction in order to identify one element at a time.

WDS provides greater spectral resolution. Often the use of EDS followed by WDS can provide further definition of sample elemental content. The interaction volume from which X-rays are emitted due to the primary electron bombardment is in the shape of a tear drop beneath the surface. The accelerating voltage used and the density of the material define the volume size. The depth from which X-rays are emitted to the detector[55] is usually from 1 to 5μm and can be calculated from the empirical expression $(0.1 \times E^{1.5})/\rho$. The width of the volume can be approximated from $(0.077 \times E^{1.5})/\rho$.

### EDS case studies

Titanium to stainless steel bonding is used for many industrial and aerospace applications. Direct Ti to Fe diffusion bonding is however largely not performed due to the formation of brittle intermetallics and differences in expansion which lead to bond cracking. In one study, the ability to use 500-μm thick aluminium as an interlayer, in the hot diffusion process, to aid the bonding of these materials was investigated[56]. EDS was used to evaluate the composition of the reaction products at the bond interfaces. Failure of the joint was found to occur at the steel–aluminium interface. EDS pointed to the formation of intermetallics as a cause of embrittlement at this interface. Line profiles of a joint formed at 450°C and 600°C are shown in Figure 3.13. The presence of these was supported by XRD detection of $FeAl_6$, $Fe_3Al$ and $FeAl_2$ in the diffusion zone.

An SEM equipped with EDS and ultra-thin window SiLi detector was used for X-ray measurement of electrodeposited hydroxyapatite coatings on $Ti_6Al_4V$ substrates[57]. X-ray spectra were acquired at a primary beam energy of 30 kV, a current of 5 nA and an acquisition time of 180 s. The stoichiometric molar ratio for pure hydroxyapatite is 1.67. X-ray spectra captured in this work showed CaP ratios of 1.51 corresponding to a Ca-deficient hydroxyapatite.

**FIGURE 3.13**

*Micrographs showing distribution of Fe and Al amounts across the diffusion boundary formed at: (a) 450°C and (b) 600°C.*
*Source: Ref. [56].*



(a)   (b)
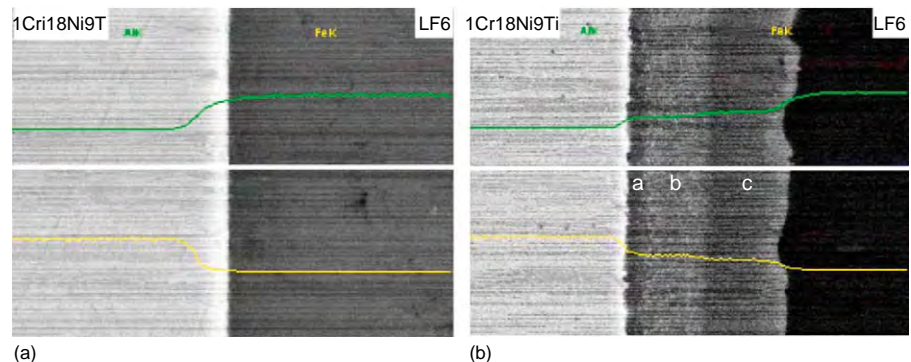
An Au-catalysed chemical vapour transport and condensation (CVTC) process was used to produce ZnO nanorods and nanowires on $SiO_2$ and Si substrates[58]. ZnO nanorods with a wide band gap (3.37 eV) are regarded as promising candidates for the fabrication of nanoelectronic devices. In this work EDX spectra of the tip and the body of ZnO nanorods were captured which indicates that Au–Zn alloyed droplets were present at the tips of the fabricated nanorods pointing to a nanorod growth via a vapor–liquid–solid (VLS) mechanism.

### 3.3.2 X-ray photoelectron spectroscopy

When excess electromagnetic energy is transferred to an electron that is in a further out shell, it is called an Auger electron. An analysis of these for chemical identification is known as Auger electron spectroscopy (AES). X-ray photoelectron spectroscopy (XPS) analyses electron emission of similar high energy[59,60]. XPS can be used to measure the chemical or electronic state of surface elements, detect chemical contamination or map chemical uniformity of biomedical implant surfaces.

For XPS the material to be examined is irradiated with aluminium or magnesium X-rays. Monochromatic aluminium $K_\alpha$ X-rays are normally produced by diffracting and focusing a beam of non-monochromatic X-rays off of a thin disk of crystalline quartz. Such X-rays have a wavelength of 8.3386 Å, a corresponding photon energy of 1486.7 eV and provide a typical energy resolution of 0.25 eV. Non-monochromatic magnesium X-rays have a wavelength of 9.89 Å, a corresponding photon energy of 1253 eV and a typical energy resolution of 0.90 eV. The kinetic energy of the emitted electrons is recorded. This kinetic energy of the ejected electrons is directly related to the element-specific atomic binding energy of the liberated. A plot of these energies against the corresponding number of electron counts provides the spectrum which indicates the qualitative and quantitative elemental composition. At these higher energies, XPS analyses only to a depth of 10 nm into the surface. Electrons emitted at greater depths are recaptured or trapped in various excited states within the material. Spectral profiles up to 1 μm deep can however be obtained by continuous spectral recording during ion etching or from consecutive ion etching and XPS measurement steps.

XPS is usually performed in UHV and typically provides resolutions down to 1000 ppm. With optimum settings and long recording times, resolutions down to 100 ppm can be achieved. Non-monochromatic X-ray sources can produce a significant amount of heat (up to 200°C) on the surface of the sample as the anode producing the X-rays is typically only a couple of centimetres from the sample. This level of heat when combined with high

energy Bremsstrahlung X-rays can degrade the surface. Organic chemicals are therefore not routinely analysed by non-monochromatic X-ray sources.

### XPS case studies

The preparation and characterization of vanadium oxide $(V_2O_5)$ modified tungsten oxide $(WO_3)$ films by pulse laser deposition were recently examined[61]. Tungsten oxide coatings are used in many electro-optical applications including catalysts, solar cell windows, electrochromic and gasochromic devices, optical memory and displays. The coatings in this work were prepared by pulsed laser vaporization from mixed pressed powders of $(WO_3)_{1-x}(V_2O_5)_x$, where $x = 0.09, 0.17, 0.23, 0.29$ and $0.33$ at $13.3\,Pa$ oxygen partial pressure and subsequent deposition onto glass substrates which were kept at 200°C. To excite the X-ray photoelectrons, an Al K$\alpha$ line at $1486.6\,eV$ was used and the energy scale was calibrated against carbon binding energy $(284.8\,eV)$. XPS showed the presence of $V^{5+}$, $V^{4+}$, $W^{6+}$ and $W^{5+}$ surface oxide states. From these results, the presence of $V_2O_5$ was seen to increase the $W^{5+}/W^{6+}$ ratio (see Figure 3.14). The XPS results showed that tungsten oxidation states were reduced in the presence of vanadium oxide. Reduced states have an important role in the light absorption of tungsten oxide surface layers. Lower light transmission, lower reflection, greater absorption, reduced porosity and lower band gap were noted for the $V_2O_5$ modified surface.

In other recent work by Tam et al., Cr–Ti–Al–N coatings on AISI M42 steel plates were examined for mechanical properties[62]. These coatings represent an alternative to conventional binary coatings for tooling. The coatings were deposited by closed-field unbalanced magnetron sputtering ion plating in a gas mixture of Ar and $N_2$. Chemical bonding states of the coatings were analysed with XPS scanning over an area of 1 $mm^2$ and with an Al K$\alpha$ X-ray source. XPS results indicated the compositional changes occurring during the coating process. Oxide phases such as $TiN_xO_y$, $Ti_2O_3$ and $TiO_2$ were detected. Samples were sputter cleaned with $Ar^+$ to remove the top contaminant layer prior to coating. After sputter etching, coating energies were shifted to energies at $454.8$ and $460.6\,eV$, respectively, corresponding to the titanium nitride bonds. No unbound Ti metallic bonds or sub-stoichiometric TiN



**FIGURE 3.14** *XPS spectra of WO$_3$ and samples WV1 to WV5 which contain progressively higher levels of V$_2$O$_5$.*
*Source: Ref. [61].*

bonds were observed in the coatings, indicating good chemical bonding status of the TiN phase. The lack of binding energy peaks at the surface for Cr metal (574.3 eV) and $Cr_2N$ (574.5 eV) pointed to the formation of CrN and $Cr_2O_3$.

### 3.3.3 Secondary ion mass spectroscopy

Secondary ion mass spectroscopy (SIMS) is a destructive analytical technique in which material is removed from a surface by ion beam sputtering and the resultant positive and negative ions are mass analysed in a mass spectrometer[63]. The technique is element specific and is capable of detecting all elements as well as isotopes and molecular species. Of all the beam techniques it is the most sensitive with detection limits for some elements in the range $10^{14}$ to $10^{15}$ $cm^{-3}$ if there is very little background interference signal. Lateral resolution is typically 100 μm but can be as small as 0.5 μm with a depth resolution of 5–10 nm[34].

SIMS works by removing material from a sample by sputtering using an ion beam. The mass/charge ratio of the removed ions is analysed, detected as a mass spectrum, as a count or displayed on a fluorescent screen[34]. *Static* SIMS employs very low primary ion density of around 1 nAcm$^{-2}$ and a low primary ion energy of 0.5–2 keV so that a nearly undisturbed monolayer of the surface can be analysed. *Dynamic* SIMS involves primary ion currents greater than 1 μAcm$^{-2}$ and usually more than one monolayer is removed during the analysis[46]. Dynamic SIMS can produce depth profiles, and quantitative depth profiling is unquestionably the major strength of SIMS. SIMS lends itself to investigations of grain boundary diffusion or diffusion across interfaces. It is a powerful tool for studying the transport processes in ceramics in the temperature range where diffusion distances are too small to be analysed by serial mechanical sectioning. Fielitz et al. used SIMS depth profiling to investigate oxygen grain boundary diffusion in mullite ceramics and its effect on sintering, grain growth and creep[64]. Kowalski investigated the diffusion of calcium in yttria-stabilized zirconia ceramics[65]. Haneda investigated bizmuth solubility and the grain boundary diffusion of oxygen ions in ZnO ceramics, which is important in terms of understanding electrical transport and the effects on varistor characteristics[66].

### SIMS case studies

Berezhinsky et al. used SIMS to measure the effects of thermal annealing on bulk and interface properties of ZERODUR glass ceramics[67]. ZERODUR is used as the mirror substrate for large-scale telescopes. Components of devices made of ZERODUR can be connected by diffusion welding using an aluminium film of 100 nm thickness. This film is then annealed. The
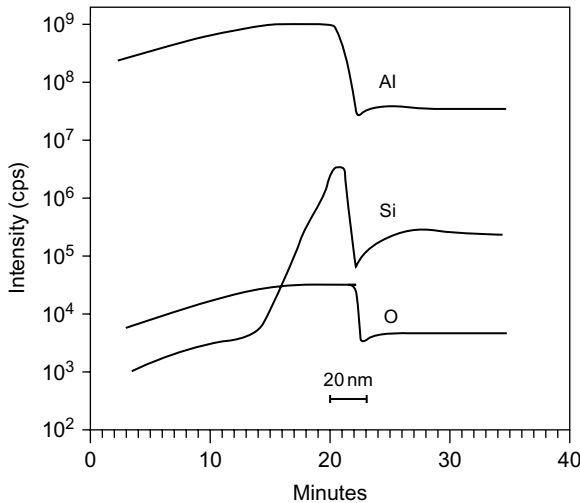
performance of the weld depends on chemical and physical phenomena occurring at the aluminium–ZERODUR interface. No peculiarities were observed for non-annealed samples; Si, Al and O were smoothly distributed under the sample surface. However, after annealing, this distribution changed dramatically. The Al and Si profiles overlapped (see Figure 3.15).

Annealing caused the Al overlayer to become enriched with Si. A combination of the chemical substitution reaction $4Al + 3SiO_2 = Al_2O_3 + 3Si$ at the interface and out-diffusion of Si into the metal was believed responsible. Local internal stresses in the ZERODUR were also detected, using a modulation–polarization technique.

## 3.3.4 Auger electron spectroscopy

When an electron or ion is incident on a semiconductor, it may transfer enough energy to an inner-shell electron to eject it from its parent atom. The atom is in an excited state, and, to lower its energy, an electron from a less tightly bound shell may fill the hole while simultaneously emitting a third electron from the atom. This ejected atom is known as an Auger electron[46]. Its energy is related specifically to the electron energy levels involved in the process and, therefore, is characteristic of the atom concerned. Since the Auger process is a three-electron process, neither hydrogen nor helium can be detected since both have less than three electrons. AES has two distinct advantages over EDX analysis.

1. It is a far more surface-sensitive technique. Escape depths range from less than a nanometre to a few nanometres. In EDX it can be difficult to analyse small particles on a substrate, because the electron beam passes through the particles and spreads out in the substrate below it[63].

2. There is the potential for chemical-state information in Auger spectroscopy; for example, the oxidation state of silicon at an Si–SiO$_2$ interface may be ascertained[46]. EDX lacks chemical-state information.

AES has found applications in measuring semiconductor composition, oxide film composition, silicides, metallization, particle analysis and the

effects of surface cleaning. AES measurements are made in a high vacuum environment $(10^{-12} - 10^{-10} \text{torr})$ to retard the formation of hydrocarbon contamination layers on the sample surface[34]. Scanning Auger microscopy (SAM) allows surfaces to be mapped for one selected element at a time. In this mode the electron beam is scanned over a selected area. The Auger intensity is measured at each point of the area[68]. SAM requires higher beam currents and is much slower than SEM/EDX[34].

### AES case studies

Pisarek et al.[69] used AES to investigate chemical and morphological changes to the surface of titanium following exposure to acidic or alkaline solutions. Control of these exposures may increase the effective surface area of Ti, and thus its biocompatibility. Auger electron microanalysis enabled subtle changes in the modified Ti surface layer to be examined in terms of local chemical composition. SEM images and AES spectra are shown in Figure 3.16 for as-received Ti (a) and after pre-treatment in NaOH (b).

Immersion in 5 M NaOH and subsequent heating up to 600°C results in a porous, 'honeycomb' morphology. In terms of the Auger spectra, the signals from Ti and O are well distinguishable, implying that the Ti is oxidized. The relative peak ratio of O KLL signal to Ti LMM signal is much higher for

the NaOH pre-treated sample than for the as-received sample, indicating a much higher degree of oxidation.

## 3.4 CONCLUSION

Nanotechnology has and will in the future have a large impact on technology development for a wide range of areas. Some of these include drug delivery systems, structural materials, data storage systems, biochemical and biomedical devices, adhesives, pigments, optical communication systems and catalytic systems. In recent years, with the advent of many new techniques to fabricate nanostructures and their potential applications, the tools to be able to characterize nanoscale systems are becoming more commonly used and increasingly required as standard research tools. In this chapter, methods to characterize to the nano- and angstrom-scale of topology and internal structure were discussed. Images captured for internal structure or surface topography mapping are often processed with software techniques to extract better resolution and further information from the captured data. Image processing and quantitative morphological measurements are therefore important areas for research to allow the most to be made of these often expensive and time-consuming characterization techniques. Recent applications and reviews of this software research by which nanoparticles can be characterized have been published[70–72].

Methods of chemical characterization of these structures down to 100 ppm were presented in this chapter. Two other spectroscopy techniques worth mentioning are Raman and Fourier transform infrared (FTIR) spectroscopy. Raman spectroscopy is commonly used to detect specific molecular bonds. For this technique, the sample to be analysed is generally illuminated laser light with frequency within the visible, infrared or ultraviolet ranges. Reflected light is focused through a monochromator filtering out wavelengths close to the laser wavelength to allow the detection of other scattered wavelengths. A very small percentage of scattered photons is scattered by excitation and has a frequency different from (usually lower) the frequency of the incident photons. As this frequency is specific to the chemical bond under investigation it allows identification of the species.

FTIR is similar to Raman spectroscopy in that it also uses molecular bond vibration for chemical species identification. In particular, though, in FTIR the resonant frequency of bond vibration after exposure to infrared radiation is detected as an identifier for the species under examination. Fourier transform techniques are based on measurement of the radiation temporal coherence. In the FTIR technique, this relates to the measurement of the frequencies of vibration of the molecular bonds. The resonant frequencies are determined by

the shape of the molecular potential energy surfaces, the masses of the atoms and associated vibronic coupling. Procedurally, a split beam of infrared light is typically sent though the sample dissolved in a liquid medium and at the same time through a sample of the solvent. Both beams are alternatively recorded in the detector. Differences between the signals are used to measure the frequencies of bond vibrations in the sample to be analysed. Typical applications of FTIR include forensic chemical analysis, measurement of polymer type, degree of polymerization, polymer degradation and semiconductor type. Most commercial instruments automatically suggest the type and quantity of species present by comparing the spectra to large databases of reference spectra.

It can be seen from a number of the case studies reported that additional information on the mechanism of fabrication or functionality of nanoscale features can be found by using a number of these techniques simultaneously or consecutively. Examples of these can be seen in the work presented above from Pap et al., Moghadam et al., and Pisarek et al.[6,44,69] Often one of these techniques is used to back up another. In the work of Clausell et al., FESEM was used to back up XRD measurements when measuring kaolinite crystal thickness[73]. In another work by Huiqian et al., BET, FESEM, TEM and X-ray scattering were used to characterize tungsten powders. Although BET and SEM could not characterize the particle size of nanometre powders, they provided a method to allow the exclusion of non-nanometre powders[74].

With so many advanced techniques for characterization of nanostructures available, it is important to understand these and their capabilities so that they can be selected and used correctly. Owing to the important technological advancements that can be envisaged from the control and understanding of nanostructures, the development of improved and new nano-characterization techniques is most likely to continue strongly for the foreseeable future.

## REFERENCES

[1] M. Knoll, Aufladepotentiel und Sekundäremission elektronenbestrahlter Körper, Z. Tech. Phys. 16 (1935) 467–475.

[2] M. Rieth, Nano-Engineering in Science and Technology: An Introduction to the World of Nano-Design, World Scientific publishing, Hackensack, New Jersey, USA, 2003 ISBN 9812380736.

[3] Q. Xie, Z. Dai, J. Liang, L. Xu, W. Yu, Y. Qi, Synthesis of ZnO three-dimensional architectures and their optical properties, Solid State Commun. 136 (2005) 304–307.

[4] S. Karan, D. Basak, B. Mallik, Copper phthalocyanine nanoparticles and nano-flowers, Chem. Phys. Lett. 434 (2007) 265–270.

[5] K. Krauel, L. Girvan, S. Hook, T. Rades, Characterisation of colloidal drug delivery systems from the naked eye to Cryo-FESEM, Micron 38 (2007) 796–803.

[6] A. Pap, K. Kordas, R. Peura, S. Leppavuori, Simultaneous chemical silver and palladium deposition on porous silicon; FESEM, TEM, EDX and XRD investigation, Appl. Surf. Sci. 201 (2002) 56–60.

[7] G. Binnig, H. Rohrer, Scanning tunneling microscopy, IBM J. Res. Dev. 30 (1986) 4. Reprinted 44,½ Jan/Mar (2000).

[8] T. Maffeis, D. Yung, L. LePennec, M. Penny, R.J. Cobley, E. Comini, G. Sberveglieri, S. Wilks, STM and XPS characterisation of vacuum annealed nanocrystalline $WO_3$ films, Surf. Sci. 601 (2007) 4953–4957.

[9] J. Boland, The best of both worlds – a novel approach to macromolecular STM studies, Surf. Sci. 602 (2008) 1–2.

[10] M. Bowker, E. Fourre, Direct interactions between metal nanoparticles and support: STM studies of Pd on $TiO_2$(1 1 0), Appl. Surf. Sci. 254 (2008) 4225–4229.

[11] A. Visikovskiy, M. Yoshimura, K. Ueda, Pt-induced structures on Si (1 1 0) studied by STM, Appl. Surf. Sci. (2008) Elsevier, online.

[12] G. Binning, C. Quate, Ch. Gerber, Atomic force microscope, Phys. Rev. Lett. 12 (1986) 930.

[13] Q. Zhong, D. Inniss, K. Kjoller, V. Elings, Surf. Sci. 290 (1993) 688.

[14] H. Jiménez, D.M. Devia, V. Benavides, A. Devia, Y.C. Arango, P.J. Arango, J.M. Velez, Thermal protection of H13 steel by growth of (TiAl)N films by PAPVD pulsed arc technique, Mater. Charact. 59 (2008) 1070–1077.

[15] M. Tanaka, M. Komagata, M. Tsukada, H. Kamiya, Fractal analysis of the influence of surface roughness of toner particles on their flow properties and adhesion behavior, Powder Technol. 186 (2008) 1–8.

[16] V. Matějka, Y. Lu, Y. Fan, G. Kratosova, J. Leskova, Effects of silicon carbide in semi-metallic brake materials on friction performance and friction layer formation, Wear 265 (2008) 1121–1128.

[17] Marvin Minsky, Patent US3013467 A, 19/12/1961.

[18] D.V. Patel, C.N. McGhee, Contemporary in vivo confocal microscopy of the living human cornea using white light and laser scanning techniques: A major review, Clin. Exp. Ophthalmol. 35 (1) (2007) 71–88.

[19] A. Hoffman, M. Goetz, M. Vieth, P.R. Galle, M.F. Neurath, R. Kiesslich, Confocal laser endomicroscopy: Technical status and current indications, Endoscopy 38 (12) (2006) 1275–1283.

[20] S. Astner, K. Swindells, S. Gonzalez, E. Stockfleth, J. Lademann, Confocal microscopy: Innovative diagnostic tools for monitoring of noninvasive therapy in cutaneous malignancies, Drug Discov. Today: Dis. Mech. (2008) 1-1, DOI: 10.1016/j.ddmec.2008.04.002.

[21] M. Fulwyler, Q. Hanley, C. Schnetter, I. Young, E. Jares-Erijman, D. Arndt-Jovin, T. Jovin, Selective photoreactions in a programmable array microscope (PAM): Photoinitiated polymerization, photodecaging, and photochromic conversion, Cytometry Part A 67A (2005) 68–75.

[22] S. Manara, F. Paolucci, B. Palazzo, M. Marcaccio, E. Foresti, G. Tosi, S. Sabbatini, P. Sabatino, G. Altankov, N. Roveri, Electrochemically-assisted deposition of biomimetic hydroxyapatite–collagen coatings on titanium plate, Inorganica Chimica Acta 361 (2008) 1634–1645.

[23] K. Wang, C. Russel, C. Liu, Preparation, mechanical properties and corrosion behaviors of oriented $Ca(PO_3)_2$ glass–ceramics, Mater. Chem. Phys. 111 (2008) 106–113.

[24] C. Heßing, J. Frenzel, M. Pohl, S. Shabalovskaya, Effect of martensitic transformation on the performance of coated NiTi surfaces, Mater. Sci. Eng. A 486 (2008) 461–469.

[25] E.H. Synge, A suggested method for extending the microscopic resolution into the ultramicroscopic region, Philos. Mag. 6 (1928) 356.

[26] E.H. Synge, An application of piezoelectricity to microscopy, Philos. Mag. 13 (1932) 297.

[27] D.W. Pohl, W. Denk, M. Lanz, APL, 44 (1984) 651–653. A. Lewis, M. Isaacson, A. Harootunian, A. Murray, Ultramicroscopy, 13 (1984) 227. Biophys. J. 41 (1983) 405a.

[28] D.W. Pohl, W. Denk, M. Lanz, Optical stethoscopy: image recording with resolution $\lambda/20$, Appl. Phys. Lett. (1984) 651.

[29] D.W. Pohl, Scanning near-field optical microscopy, in: C.J.R. Sheppard, T. Mulvey (Eds.), Advances in Optical and Electron Microscopy 12, Academic Press, London, 1990.

[30] T. Knutson, F. Guillaume, W.-J. Lee, M. Alhoshan, W. Smyrl, Reactivity of surfaces and imaging with functional NSOM, Electrochim. Acta 48 (2003) 3229–3237.

[31] H. Lee, Y. Kim, D. Jeon, E. Kim, J. Kim, K. Park, Rewritable organic films for near-field recording, Opt. Mater. 21 (2002) 289–293.

[32] R. Hawaldar, U. Mulik, K. Patil, R. Pasricha, S. Sathaye, A. Lewis, D. Amalnerkar, Growth of PbS nanopyramidal particulate films for potential applications in quantum-dot photovoltaics and nanoantennas, Mater. Res. Bull. 40 (2005) 1353–1360.

[33] C.R. Brundle, C.A Evans Jr., S. Wilson (Eds.), Transmission electron microscopy, in: Encyclopaedia of Materials Characterization, Surfaces, Interfaces, Thin Films, Butterworth-Heinemann, Oxford, UK, 1992.

[34] D.K. Schroder, Semiconductor Material and Device Characterization, third ed., IEEE Press, John Wiley & Sons, New Jersey, 2006.

[35] Z.L. Wang, P. Poncharal, W.A. de Heer, Measuring physical and mechanical properties of individual carbon nanotubes by in-situ TEM, J. Phys. Chem. Solids 61 (2000) 1025–1030.

[36] C. Huigan, Z. Meifang, L. Yaogang, Decoration of carbon nanotubes with iron oxide, J. Solid State Chem. 179 (2006) 1208–1213.

[37] C. He, N. Zhao, C. Shi, J. Li, H. Li, Magnetic properties and transmission electron microscopy studies of Ni nanoparticles encapsulated in carbon nanocages and carbon nanotubes, Mater. Res. Bull. 43 (2008) 2260–2265.

[38] J.P. Salvetat, J.M. Bonard, N.H. Thomson, A.J. Kulik, L. Forro, W. Benoit, L. Zuppiroli, Mechanical properties of carbon nanotubes, Appl. Phys. A 69 (1999) 255–260.

[39] M.V. Jose, B.W. Steinert, V. Thomas, D.R. Dean, M.A. Abdalla, G. Price, G.M. Janowski, Morphology and mechanical properties of Nylon 6/MWNT nanofibers, Polymer 48 (2007) 1096–1104.

[40] A.V. Stanishevsky, Focused ion beam nanofabrication, in: H.S. Nalwa (Ed.), Encyclopaedia of Nanoscience and Nanotechnology, vol. 3, American Scientific Publishers, Valencia, California, USA, 2004.

[41] C.R. Musil, J.L. Bartelt, J. Melngailis, Focused ion beam microsurgery for electronics, IEEE Electron Dev. Lett. EDL-,7,5 (1986) 285–287.

[42] C. Boit, New physical techniques for IC functional analysis of on-chip devices and interconnects, Appl. Surf. Sci. 252 (2005) 18–23.

[43] R. Schlangen, U. Jkerst, C. Boit, T. Malik, R. Jain, T. Lundquist, Non destructive 3D chip inspection with nano-scale potential by use of backside FIB and backscattered electron microscopy, Microelectron. Reliab. 47 (2007) 1523–1528.

[44] S.H. Moghadam, R. Dinarvand, L.H. Cartilier, The focused ion beam technique: a useful tool for pharmaceutical characterization, Int. J. Pharm. 321 (2006) 50–55.

[45] C.R. Brundle, C.A. Evans Jr., S. Wilson (Eds.), X-ray diffraction, in: Encyclopaedia of Materials Characterization, Surfaces, Interfaces, Thin Films, Butterworth-Heinemann, Butterworth-Heinemann, Oxford, UK, 1992.

[46] T.E. Jennings, Semiconductor Science; Growth and Characterisation Techniques, Prentice Hall International (UK) Ltd., Harlow, Essex, UK, 1995.

[47] W.R. Runyan, Semiconductor Measurements and Instrumentation, McGraw-Hill Book Company, Hightstown, New Jersey, USA, 1975.

[48] B. Cengiz, Y. Gokce, N. Yildiz, Z. Aktas, A. Calimli, Synthesis and characterisation of hydroxyapatite nanoparticles, Colloids Surf. A: Physicochem. Eng. Aspects 322 (2008) 29–33.

[49] S.J. Gregg, K.S.W. Sing, Adsorption, Surface Area and Porosity, Academic Press, New York, 1967.

[50] P.A. Webb, C. Orr, Analytical Methods in Fine Particle Technology, Micromeritics Instrument Corp., Norcross, Georgia, USA, 1997.

[51] A. Jungbauer, Chromatographic media for bioseparation, J. Chromatogr. A 1065 (2005) 3–12, Review Paper.

[52] F. Porcheron, M. Thommes, R. Ahmad, P.A. Monson, Mercury porosimetry in mesoporous glasses: a comparison of experiments with results from a molecular model, Langmuir 23 (2007) 3372–3380.

[53] J. Goldstein, D. Newbury, D. Joy, C. Lyman, P. Echlin, E. Lifshin, L. Sawyer, J. Michael, Scanning Electron Microscopy and X-ray Microanalysis, Kluwer Academic/Plenum, Southwalk, London, UK, 2003.

[54] E. Lifshin, X-ray Characterization of Materials, Wiley, Hoboken, New Jersey, USA, 1999 ISBN-10: 3527296573.

[55] P.J. Potts, A Handbook of Silicate Rock Analysis, Blackie, & Sons Ltd, Bishopbriggs, Glasgow, Scotland, 1987, p. 622.

[56] P. He, X. Yue, J.H. Zhang, Hot pressing diffusion bonding of a titanium alloy to a stainless steel with an aluminum alloy interlayer, Mater. Sci. Eng. A 486 (2008) 171–176.

[57] N. Dumelie, H. Benhayoune, D. Richard, D. Laurent-Maquin, G. Balossier, In vitro precipitation of electrodeposited calcium-deficient hydroxyapatite coatings on Ti6Al4V substrate, Mater. Character. 59 (2008) 129–133.

[58] S.R. Hejazi, H.R. Hosseini, M. Sasani Ghamsari, The role of reactants and droplet interfaces on nucleation and growth of ZnO nanorods synthesized by vapor–liquid–solid (VLS) mechanism, J. Alloys Compd. 455 (2008) 353–357.

[59] J.T. Grant, D. Briggs (Eds.), Surface Analysis by Auger and X-ray Photoelectron Spectroscopy, IM Publications, England, 2003.

[60] J.W. Robinson, Practical Handbook of Spectroscopy, CRC Press, Boca Raton, Florida, USA, 1991.

[61] M. Ranjbar, S.M. Mahdavi, A. Iraji zad, Pulsed laser deposition of W–V–O composite films: preparation, characterization and gasochromic studies, Solar Energy Mater. Solar Cells 92 (2008) 878–883.

[62] P.L. Tam, Z.F. Zhou, P.W. Shum, K.Y. Li, Structural, mechanical, and tribological studies of Cr–Ti–Al–N coating with different chemical compositions, Thin Solid Films 516 (2008) 5725–5731.

[63] A.C. Diebold (Ed.), Handbook of Silicon Semiconductor Metrology, Marcel Dekker Inc., Basel, Switzerland, 2001.

[64] P. Fielitz, G. Borchardt, M. Schmucker, H. Schneider, P. Willich, Measurement of oxygen grain boundary diffusion in mullite ceramics by SIMS depth profiling, Appl. Surf. Sci. 203–204 (2003) 639–643.

[65] K. Kowalski, A. Bernasik, A. Sadowski, Diffusion of calcium in yttria-stabilized zirconia ceramics, J. Eur. Ceram. Soc. 20 (2000) 2095–2100.

[66] H. Haneda, A study of defect structures in oxide materials by secondary ion mass spectrometry, Appl. Surf. Sci. 203–204 (2003) 625–629.

[67] L.I. Berezhinsky, V.P. Maslov, B.K. Serdega, V.V. Tetyorkin, V.A. Yukhymchuk, Study of chemical interaction at Al–ZERODUR interface, J. Eur. Ceram. Soc. 26 (2006) 3825–3830.

[68] J.C. Vickerman (Ed.), Surface Analysis. The Principal Techniques, John Wiley & Sons, Materials Chemistry and Physics, Elsevier, Amsterdam, The Netherlands, 1997.

[69] M. Pisarek, M. Lewandowska, A. Roguska, K.J. Kurzydlowski, M. Janik-Czachor, SEM, scanning Auger and XPS characterisation of chemically pre-treated Ti surfaces intended for biomedical applications, Mater. Chem. Phys. 104 (2007) 93–97.

[70] M.F. Costa, Application of image processing to the characterisation of nano-structures, Rev. Adv. Mater. Sci. 6 (2004) 12–20.

[71] P. Soille, Morphological Image Analysis, Springer-Verlag, Guildway Guildford, Surrey, UK, 1999.

[72] R.C. Gonzalez, R.E. Woods, S.L. Eddins, Digital Image Processing Using Matlab, Pearson Prentice Hall, Upper Saddle River, New Jersey, USA, 2004.

[73] J.V. Clausell, J. Bastida, F.J. Serrano, P. Pardo, F.J. Huertas, A new FESEM procedure for assessment of XRD microstructural data of kaolinites, Appl. Clay Sci. 37 (2007) 127–132.

[74] L. Huiqian, L. Tao, S. Huiping, W. Chengyi, G. Zhimeng, L. Ji, Characterization of nanometer tungsten powders, Rare Metals 27 (2) (2008) 197.

# Non-lithographic Techniques for Nanostructuring of Thin Films and Bulk Surfaces

**M. Ghanashyam Krishna and Prashant Kumar**

*School of Physics, University of Hyderabad, Hyderabad, India*

## CONTENTS

## ABSTRACT

The development of non-lithographic techniques for realizing nanostructured thin films and bulk surfaces for application in devices is a major area of current interest. In this chapter, the state-of-art in four different techniques, namely template assisted, electric field assisted, laser induced and vapour–liquid–solid techniques is reviewed. It is shown that these techniques have a lot of promise for the fabrication of nanoparticle arrays, nanowires and nanodots and other 'nano-forms'. The effects, in each case, can be localized by an intelligent choice of process parameters, making them very attractive for niche applications. Examples from a large variety of materials systems are presented demonstrating the universal nature of these approaches.

## 4.1 INTRODUCTION

Unusual nanostructures are currently being investigated for application in functional nanodevices. For example, conical and pin like structures are being used as local field emitters[1] and good light absorber[2]. Local field near the confined structure, if any, is different because grain boundary presents disruption in the continuity of electron density function. Nanowires, nanotubes and nanorods are material forms of interest to the scientific community due to their applications in photonic[3–6], electronic[7–13] and opto-electronic industries[14–17]. Apart from the above-mentioned applications, nanowires can be used for gas sensing[18–24], thermoelectric[25] and electrome-chanical switch[26] applications. There are a few review articles on nanowires demonstrating the progress so far[27–29]. Ever-shrinking size in industry for memory applications attracts electronic circuit components to be made in thin film form. Integrated circuits involving nanowire and nanodots are under study now, but the non-ohmic losses in the signal and noise pose the major deterrent to the development to such fields. Nanowires and nanodots can pave the way not only in fabrication of the components, but integration issues too will be solved to an extent. Nanostructured surfaces are also useful as a template for the growth of desired nanostructres[30].

Nanostructuring of thin films and bulk surfaces is an important theme in deriving functionality and therefore producing devices. The nanostructuring process can be realized by two main approaches which are the bottom–up approach and top–down approach. The top–down approach **for** producing nanostructures is an expensive route since it involves a large number of post-processing steps. Typically, these **involve** the use of various lithography-based tools such as electron beam, X-ray and focussed ion beam. The main advantages of such techniques are that they are very precise and reproducible and hence very easy to scale up. Consequently these are amenable, attractive and compatible to industrial applications. Several lithographic techniques have been developed in the past few years, among which lithography through controlled chemical etching, photolithography, electron beam lithography, ion beam lithography, SPM lithography and nanoimprint lithography are major technologies[31–39]. Such lithographic techniques are usually designed to achieve well-defined nanostructures starting from the continuous thin film or it is post-treatment design. Few non-conventional lithographic procedures are also developing [40–42] – angle resolved nanosphere lithography and X-ray lithography are among the few to mention.

The second approach is the bottom–up approach, which essentially relies on 'natural' conditions to achieve self-organized nanostructures. Organic and biological molecules as well as other soft-condensed matter are particularly

suitable for this approach and many interesting nanostructures, functional materials and devices have been demonstrated using this technique. These are mainly applied in sensors, optical devices and in some cases, electronic devices.

There has been recent interest in an intermediate approach that falls between the top–down and bottom–up approach and these are non-lithographic approaches to the nanostructuring of thin films and surfaces. Such techniques rely on providing favourable thermodynamic conditions during or after growth to realize nanostructures. Such techniques fall under the category of non-lithographic techniques for nanostructuring and are cost-effective solutions to achieve nanoparticle arrays, nanowires, nanopillars and other 'nano-forms' that will result in functionality and can be integrated into existing processing technologies without adding many steps. In many cases, these techniques can produce very local effects in the nanometre range, thus obviating the need for very tedious process steps as in the case of lithography-based technologies. These techniques form the focus of the current review. Among non-lithographic approaches, there are several other techniques of fabrication of nanowires, for example self-assembly[43], ion beam irradiation[44–48], electron beam irradiation, microwave-assisted nanostructuring[49], anodic oxidation assisted nanostructuring[50] and strain relief driven nanostructuring[51, 52], vapour phase evaporation[53–71], sol–gel method[72–85], laser ablation[86–89], arc discharge[90–93] and chemical processing[94, 95]. In this chapter, among non-lithographic techniques, we will concentrate primarily on four major techniques namely, template-assisted technique, electric field assisted technique, laser-assisted technique and vapour–liquid–solid technique. Detailed introduction to the techniques and the mechanisms involved and physics therein will be discussed in the following sections.

## 4.2  TEMPLATE-ASSISTED NANOSTRUCTURING

Self-assembly is the simplest method to attain nanostructured surfaces. Shi et al.[96] showed that Pd nanowires can be self-assembled via electroless deposition. The current authors have also achieved self-assembled Ni nanostructures on [311] silicon surface in a 50 nm thick film. Growth was found to follow the pattern; nanoparticulate to self-assembled nanostructures to discontinuous nanowires. In the absence of templates, the growth of nanowires through self-assembly route suffers mainly from three problems: (1) the periodicity of nanostructures, (2) the isolation of nanocomponents and (3) the ability to make electrical connections. The use of templates has been reported extensively in the past decade to fabricate site-specific nanostructures.

In brief, the role of the template is to guide the growth of nanofeatures. Porous templates and linear templates are usually used for fabricating vertical and planar assembly of nanowires and nanodots, single layer as well as multilayers of the concerned material. Template-assisted growth[97–104] ensures the fine placement of condensate to eventually yield periodic structures. Porous alumina templates are favoured due to the ease of preparation, ease in release of fabricated nanocomponents and high pore density ($10^{11}$ pores/cm$^2$). Under certain conditions, very good periodicity of the pore arrangement can be achieved, which is required in many technological applications. Apart from these qualities, porous alumina can withstand very high temperature without change in its pore periodicity and spacing (up to 800°C) as desired for the processing of the fabricated nanostructures (Figure 4.1).

When exposed to air or water, aluminium oxide is formed on the surface of aluminium, but the oxide thickness is in the nanometre range. However, anodization of aluminium can result in the formation of flat nanoporous aluminium oxide film, commonly called aluminium barrier type films. The electropolished aluminium is anodized in a strong acid (pH<4). The acid typically used is 15% sulphuric acid, 3% oxalic acid and 5% phosphoric acid.

The chemical reactions involved in the porous oxide growth are:
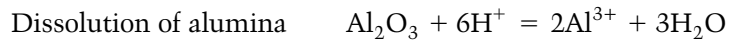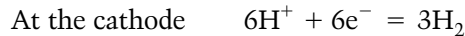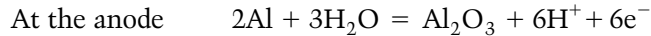
$$\text{At the anode} \qquad 2Al + 3H_2O = Al_2O_3 + 6H^+ + 6e^-$$

$$\text{At the cathode} \qquad 6H^+ + 6e^- = 3H_2$$

$$\text{Dissolution of alumina} \qquad Al_2O_3 + 6H^+ = 2Al^{3+} + 3H_2O$$
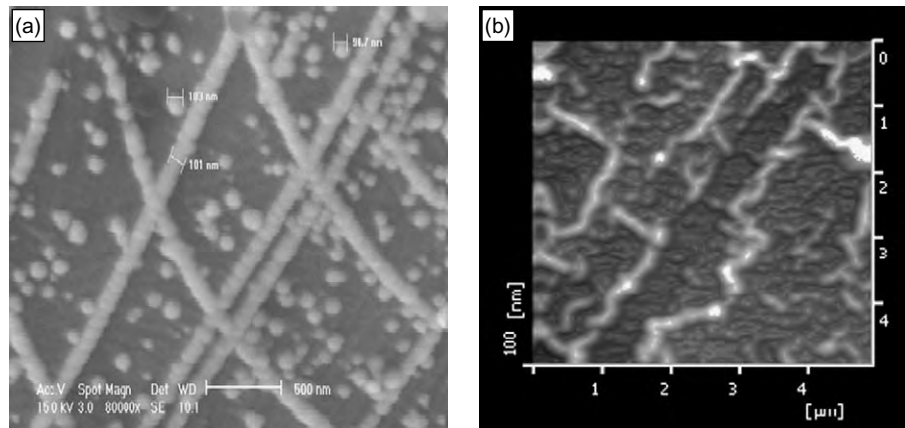
Al Mawlawi et al.[105] showed that the dependence of pore density $\rho$, (expressed in terms of pores/$\mathring{A}^2$) as a function of anodizing voltage is given by:

$$\rho = \alpha / (d + \beta V)^2$$

where $\alpha$ is a constant (1.15), $d$ is the pore diameter, $\beta$ is a constant also dependent on the acid and temperature. Pore diameter is in the range 8–100 nm. Increasing the soaking time of porous alumina in phosphoric acid is found[106] to increase pore diameter.

A detailed two-step procedure was adopted by Choi et al.[107] for achieving well-aligned array of nanopores in alumina. In this, a pure aluminium sheet (99.999% purity) was degreased in acetone and electropolished at a voltage of 20 V for 2 min. The electropolished aluminium sheet was anodized by immersing it in 0.3 M oxalic acid for 12 h under a constant voltage of 40 V. Then, it is etched in an aqueous mixture solution of phosphoric acid (6 wt%) and chromic acid (1.8 wt%) in order to remove the irregular porous oxide layer formed during the first anodization. The subsequent second anodization, with the same condition as the first anodization, but a different period of time, depending on the desired thickness of the oxide layer, yielded a highly ordered hexagonal nanopore array of anodic aluminium oxide (AAO) template. To separate an AAO membrane from the AAO template, a saturated $HgCl_2$ solution was applied. The separated AAO membrane was rinsed with de-ionized water several times. An additional pore-widening process was conducted in 5 wt% phosphoric acid at 30°C in order to obtain the desired pore diameter. The obtained AAO membrane was cleaned and annealed at 200°C in vacuum for 1 h.

Crouse et al.[108] devised a technique to achieve gold nanopillars using anodized porous alumina as the template on titanium-coated silicon substrate. It was then subjected to reactive ion etching to etch out titanium inside alumina pores that were refilled with gold by evaporation. A final reactive ion etching step gives free-standing gold nanopillars as shown in Figure 4.2.

Masuda et al.[109–113] developed a replication technique by which a nanohole array on alumina can be transferred on other metals. This way, it is possible to overcome some of the disadvantages presented by porous alumina (namely chemical and thermal instability and low mechanical strength). The schematic is as shown in Figure 4.3. In this method,
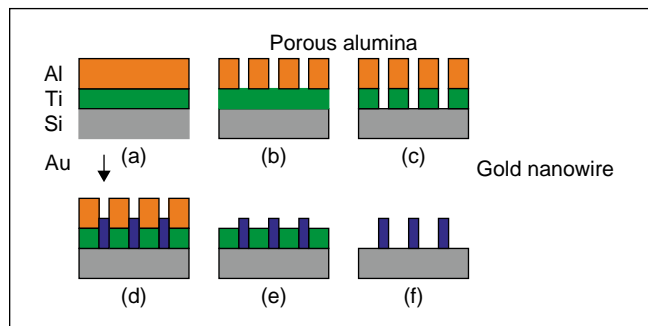


**FIGURE 4.2**   *Technique to grow metallic nanopillars.*
*Source: Adapted from Crouse et al. (2000).*
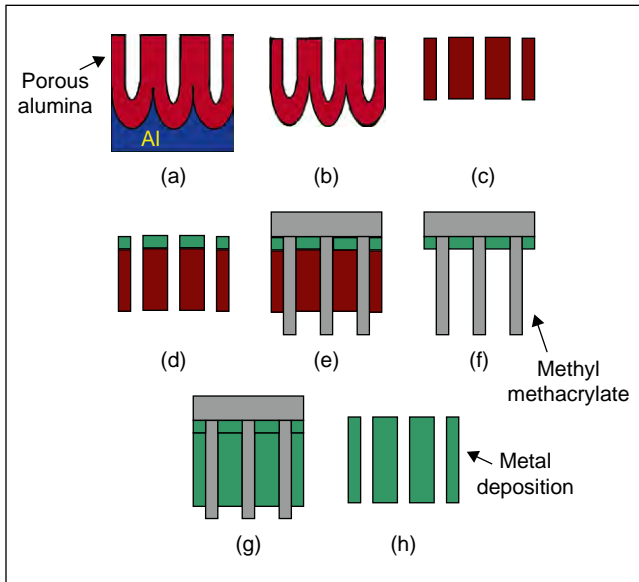
**FIGURE 4.3**   *Technique to replicate nanoporous pattern from alumina to metal.*

*Source: Adapted from Masuda et al.*

porous alumina is first detached from the bottom alumina by soaking in mercuric chloride solution followed by the removal of the barrier layer by soaking in 5% phosphoric acid. A thin layer of gold is then evaporated at the bottom. Methyl methacrylate monomer containing 5% benzoyl peroxide, which acts as an initiator for the polymerization, is injected into the holes under vacuum conditions and is polymerized by UV irradiation. After removal of alumina layer with 10% NaOH, a replicated negative type of PMMA with cylindrical structure is obtained. At the bottom of array of PMMA, a thin layer of metal is present. For the preparation of Pt nanohole array, electroless deposition of metal was carried out. PMMA may be removed by soaking it in acetone. A variety of nanostructures can be prepared by using the above replication technique.

Fan et al.[114] used gold mask as achieved by replication technique from AAO template and used it to realize gold dots on GaN/Si substrate to obtain patterned ZnO nanowire array. The detailed scheme is shown in Figure 4.4. Figure 4.5 shows the obtained gold tubes and ZnO nanowires.

Using a similar method, Deki et al.[115] fabricated nanopillars of oxide and ceramics using solution route as shown in Figure 4.6.

Magnetic nanostructures are useful for technological applications because information can be stored as magnetic bits. Magnetization reversal can be conveniently used as magnetic switch. Apart from the MRAM application of multilayer FM/NM/FM tunnel junction, FM/AFM superlattices are applicable as GMR sensors. Vertical magnetic nanowires have applications in Current perpendicular-to-plane (CPP) Giant Magnetoresistance (GMR). Small isolated magnetic islands themselves are magnetic domains. For such a system of magnetic dots, the condition $\Delta E = kT$ can be extended up to the superparamagnetic limit. An ordered perpendicular/longitudinal medium should exhibit much lower noise, as compared to the disordered medium. Thus, the signal to noise ratio for possible magnetic media for data storage applications is increased. Materials like Fe, Co and Ni electrodeposited into nanopores serve as a model system for the study of magnetic properties, interactions and thermal stability of nanometre
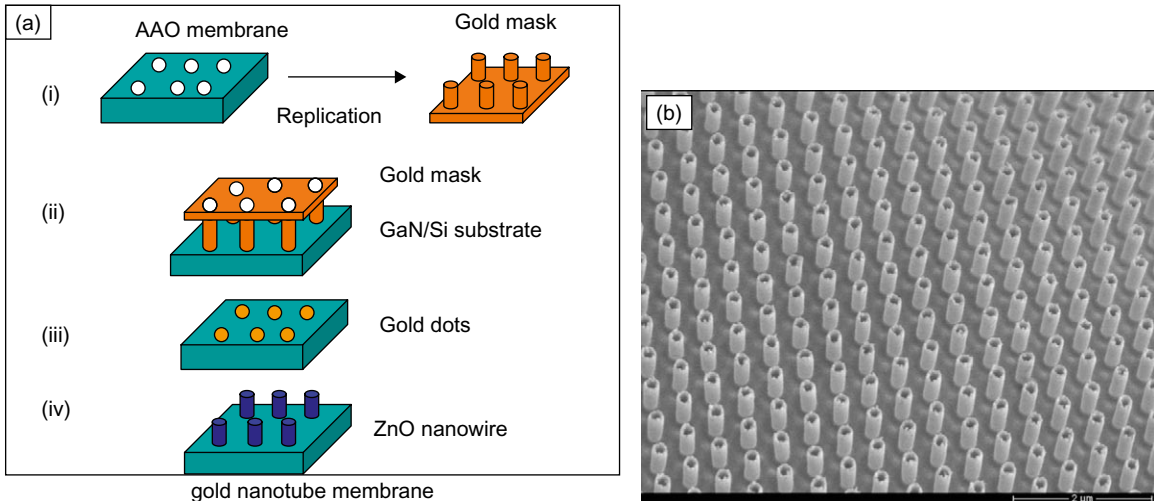
**FIGURE 4.4**   *Gold mask technique to fabricate metallic nanopillars. (a) Schematic and (b) image of As grown sample.*
*Source: (b) **Reprinted with permission from [Fan et al., 2005]. Copyright 2005, IOP publication.***
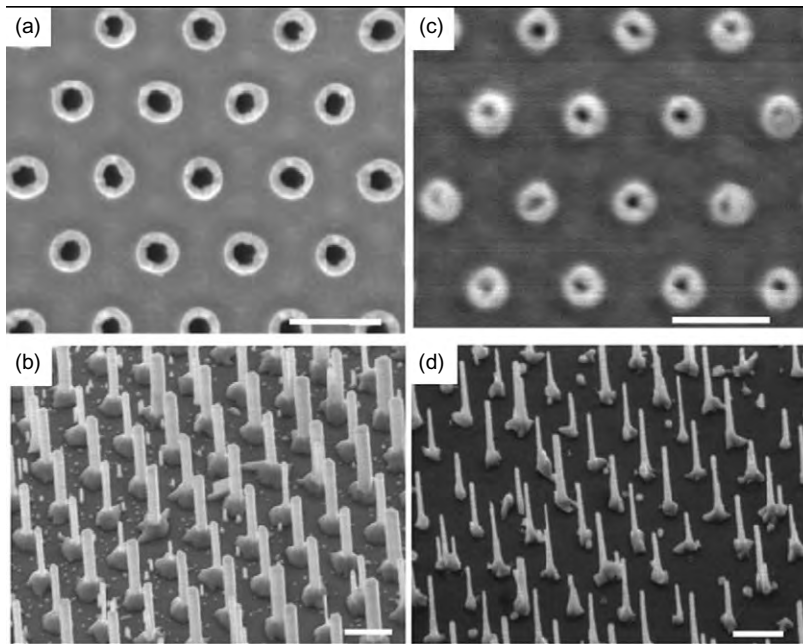


**FIGURE 4.5**   *(a) and (c) Gold nanotube membrane with inner diameter of 130 nm and 60 nm,*
*(b) and (d) ZnO nanopillars fabricated by technique as described in Figure 4.4.*
*Source: Reprinted with permission from [Fan et al., 2005]. Copyright 2005, IOP publication.*
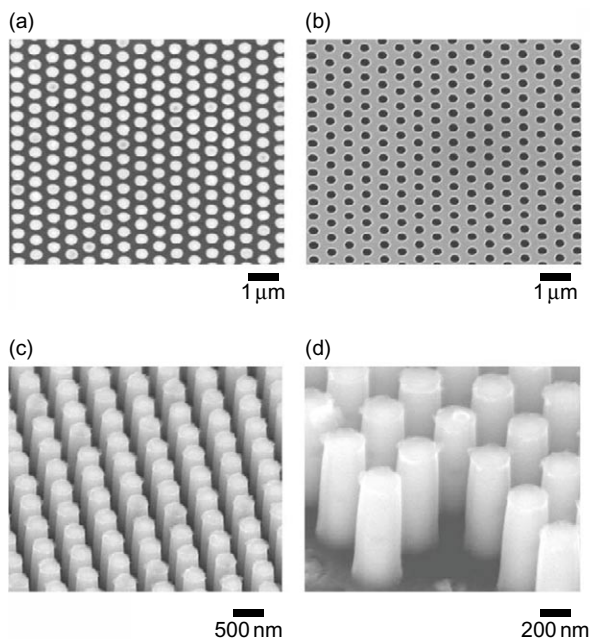
**FIGURE 4.6** *FE–SEM top view images of (a) graded oxide nanopillar arrays, (b) a template Si wafer with hole diameter of 270nm prior to deposition, (c) and (d) SEM images (tilted 45μ) of graded oxide arrays with a rod diameter of 270nm.*
*Source: **Reprinted with permission from [Deki et al., 2004].** Copyright 2004, Royal Society of Chemistry.*

sized magnetic dots. The magnetic wires thus formed are cylindrical in shape and are hcp, fcc and bcc for Co, Ni and Fe nanowires. Coercive field in the perpendicular directions is usually 5–7 times higher than that for the parallel orientation. The nanowires possess uniaxial anisotropy with easy axis perpendicular to the film plane. The large anisotropy arises mainly due to the shape anisotropy. The large perpendicular squareness and high remanence together with high coercive field can make these materials useful for magnetic recording media.

Coercive field is usually independent of the length, but is dependent on the diameter of nanowire (coercive field decreases with increase in diameter). Such increase in coercive field[116–118] can be attributed to the multidomain structures at higher diameter.

Li et al.[119] found that for a 11-nm diameter Fe nanowires, the activation volume is $1 \times 10^{-18}$ cm$^3$ and it is smaller than the actual particle volume suggesting that magnetization reversal is non-uniform. Peng et al.[120] used TEM and electron diffraction and suggested that each nanowire consists of a chain of dots, each dot being single crystalline. Zeng et al.[121] and Metzger et al.[122] worked on Co nanowire while Nielsch et al.[123] worked on Ni nanowires.

Electrodeposited magnetic nanowires in alumina nanopores as prospective candidates for data storage, suffer due to non-uniform length. However, according to Yin et al.[124], by fine-tuning electrodeposition parameters, one can obtain uniform magnetic nanowires. Using pulse reverse electrochemical deposition with a waveform consisting of square cathodic pulse and longer anodic pulse, one can give good uniformity[125, 126] in size of magnetic nanowires. Magnetic bimetallic alloy nanowires[127–129] containing a percentage of Fe/Co/Ni have been successfully synthesized in nanoporous alumina. CPP GMR for FM/NM multilayer films is usually higher than the CIP GMR, and therefore, fabrication of FM/NM is of scientific interest to the industry. Alumina membrane template assisted technique was extended to fabricate such multilayers[130] and study GMR.

Semiconducting nanowires, nanorods, nanodots, nanocones, nanopins, etc. are interesting due to their broad range of applications. Electrochemically, the most easily fabricated semiconductors are II–VI semiconductors, for example, CdS, CdSe. There are three approaches for electrodeposition of semiconductors. The first method[131] is deposition of metal in alumina nanopores, followed by etching of alumina surface by phosphoric/chromic acid to access metallic surface for sulphur or arsenic vapour to attain metal sulphide or arsenide nanostructures. The second method deals with electrolysis of sulphuric acid, causing the sulphide atoms to be deposited in pores. This is followed by AC electrodeposition of Cd in pores, allowing S to react with Cd. In the third method[132], a solution of dimethyl sulphoxide containing salt of M (50 mM) (M = Cd, Pb, Zn, etc.) and X (X = S, Se, Te, etc.) is used. CdS, CdSe, PbSe, ZnSe nanowires have been synthesized by this method and this method is found useful for the application of such nanowires for diode, transistor, photodetectors and light emitting diodes. An interesting effect, namely electronic bistability[133] of CdS nanowires, can be used for inexpensive ultradense non-volatile static random access memory. For the preparation of $Cd_{1-x}Mn_xSe$ nanowire[134], an electrolyte consisting of cadmium perchlorate and manganese perchlorate and selenium powder dissolved in dimethyl sulphoxide can be used. M/SC/M heterostructures (e.g. Fe/CdSe/Fe heterostructures) can be synthesized. These fabrication techniques can have the advantages[135, 136] of studying spin transistor and spin quantum computers. Lead[137], bismuth[138] and gold[139–142] nanowires also have been electrodeposited in alumina nanopores.

Template-synthesized polymers[143, 144] are expected to have applications in microelectronics, drug delivery, bioencapsulation, ultratrace chemical analysis and second-order templates for the growth of other nanoarrays. Carbon nanotube electronics are expected to provide a viable alternative to silicon. The development of an array of transistors using carbon nanotubes and the development of computer circuits using single-walled carbon nanotube was recently reported by IBM[145]. Carbon nanotubes also find use as cold cathode flat panel display[146]. Carbon nanotubes can also be used to encapsulate[147] other materials like Fe and Co. Well-ordered carbon nanotubes have been synthesized[148–150] in nanoporous alumina membrane template.

In some cases, nanowires can work like template. Goldberger et al.[151] showed that ZnO nanowire can work like template for the growth of GaN nanowire (Figure 4.7).

Self-assembled nanospheres (3D polystyrene spheres) can be conveniently used as a template to fabricate metallic nanobowl arrays[152] (Figure 4.8).

Physical vapour deposition (PVD) of metals on inert substrates such as highly oriented pyrolytic graphite (HOPG) can be used[153–161] to generate a

**FIGURE 4.8** (a) SEM micrograph of 3D colloidal template of 1mm polystyrene spheres, used as a template for the fabrication of nanobowl arrays. (b) SEM micrographs of nanobowl structure annealed at 500µC for 3h in $N_2$ atmosphere followed by toluene etching nanobowl array fabricated using polystyrene spheres as a template.
Source: *Reprinted with permission from [Srivastava et al., 2005]. Copyright 2005, Royal Society of Chemistry.*

large number of interesting and potentially useful structures with dimensions in the nanometre range (Figure 4.9). Control of the experimental parameters of substrate temperature and metal atom flux can be used to tailor the resulting nanostructure arrays. Penner's group[162, 163] have grown sub-monolayer quantities of gold via PVD on an HOPG substrate to achieve dendritic islands of gold (at Room Temperature (RT) deposition condition) and large arrays of gold 'beaded wires' (at 400°C substrate temperature).

Alumina is an interesting material; heating alumina at very high temperature (e.g. 1600°C–1800°C) for few hours, results in the development of ripple kind of structures. [1011] and [1012] planes are tilted usually at 32.4° and 17.6° with respect to the horizontal plane with a crest and trough pattern. As alumina is a good dielectric, at crests, the electric field value is very high due to the singularity present.
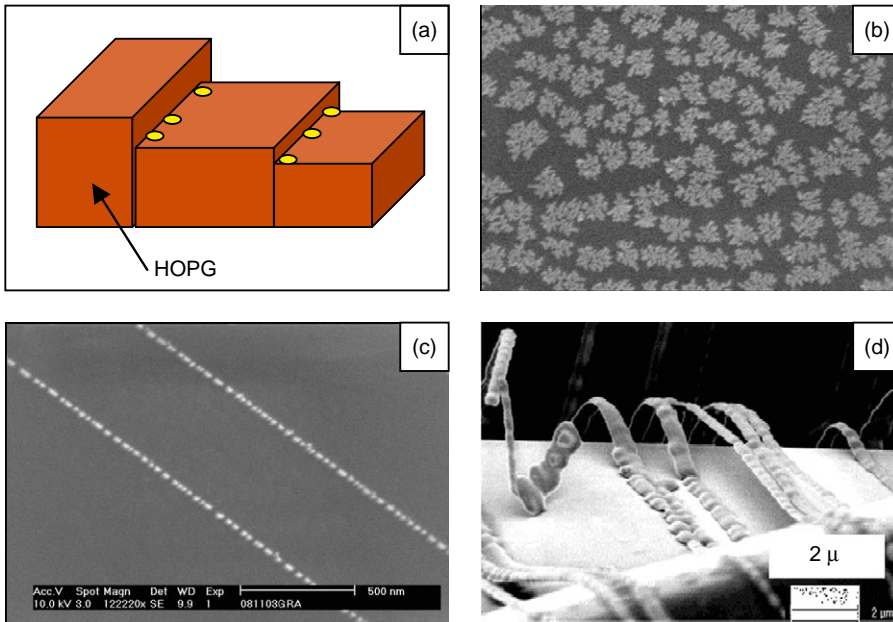
Near the crests,

$$E = K\rho^{-\beta}$$

where $\rho$ is the distance from the tip

Singularity in electric field $\qquad \beta = (\pi - \alpha)/(2\pi - \alpha) = 0.22$

Ravishankar et al.[164] have used such faceted alumina slanted surface to conveniently control the growth of nanoparticle on such crests. They have done a number of experiments to achieve good control over the dewetting process with the variation of substrate temperature and pressure. According to their belief, there are two basic models, what condensate can follow to assemble on the crests, one is the assembly of nanoparticle and the other is the formation of nanowires. For evaporation, 1800°C temperature and $10^{-4}$ torr was used. Well-aligned isolated beaded as well as continuous nanowires have been achieved using this novel technique as shown in Figure 4.10.

Carbon nanotube itself has been used[165] in longitudinal as well as vertical position to work as a template to grow metallic and semiconductor nanowires, nanotubes. Both DC and AC field can be conveniently utilized to give rise to electrically isolated beaded nanowires on carbon nanotube template as shown in Figure 4.11.
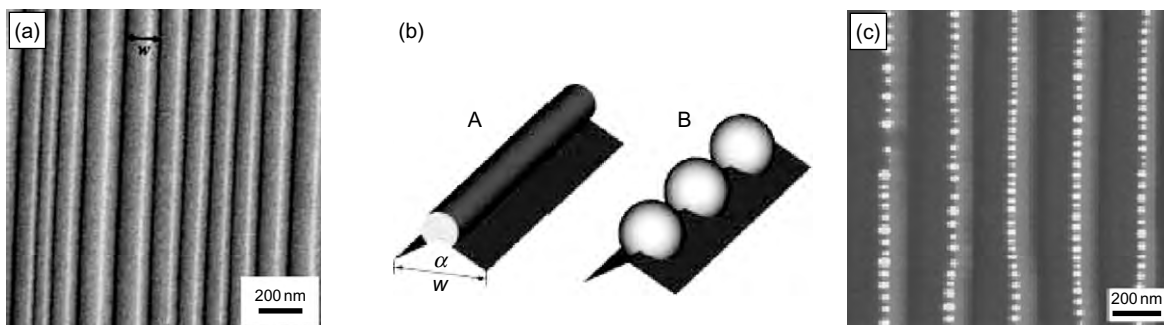
**FIGURE 4.10** *(a) Formation of crests and trough on m-plane alumina, (b) two basic models of condensate assembly, (c) electrically isolated beaded nanowires of platinum.*
*Source: Reprinted with permission from [Ravishankar et al., 2004]. Copyright 2004, Wiley-VCH.*

**FIGURE 4.11**

*Schematic of field-assisted self-assembly of nanoparticles using DC field.*
*Source: Adapted from*
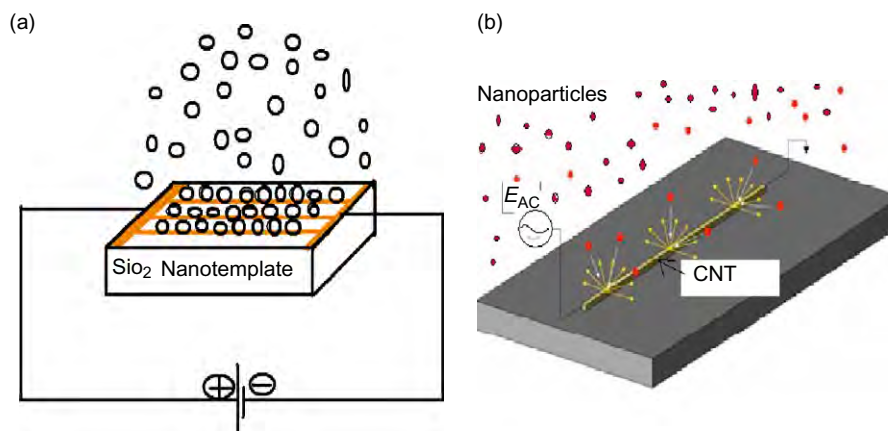


Partridge et al.[166] designed V-grooves on Si/SiO$_2$ by the selective etching process. Then into the V-groove, metal vapour was condensed using nanocluster deposition. Thereafter using argon ion etching, the rest of the material was cleaned, leaving only continuous nanowires. Such a growth of nanowires does not require any extra effort to give interconnections for electrical measurements, since it is already organized in a line (Figure 4.12).

Depending on the coverage, You et al.[167] have recently been successful in achieving nanodot arrays or nanowire array of Pt/ErSi$_2$ heterostructures. Reactive ion etching was used to clean the surface except in regions where well-patterned heterostructures were formed. The typical results are shown in Figures 4.13 and 4.14.

The work of Partridge et al.[166] and Ravishankar et al.[164] has yielded nanowire growth at the valley and at the vertex of hillocks itself. Both groups have worked with large slant angle (>30°). However, if the slant angle is
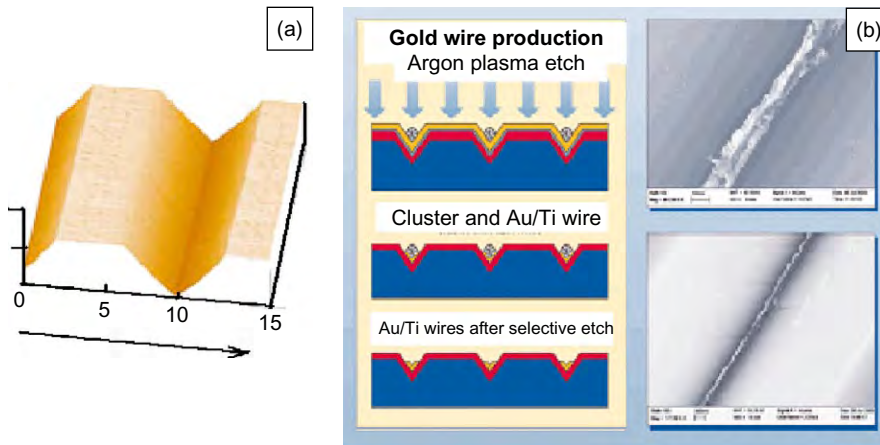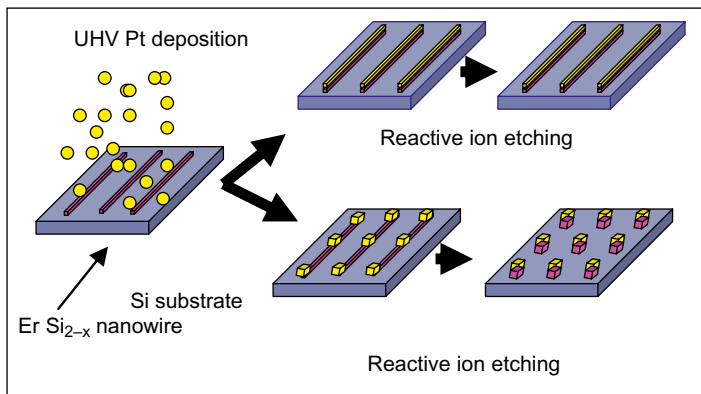
small enough, friction offered by the slant surface can be sufficient to hold nanoparticles and will not allow them to fall from the trench wall. We have demonstrated[168] nanowire growth inside V-trench during PVD of Ni inside the trench at ambient temperature. Apart from substrate surface smoothness, condensing vapour material, substrate temperature and rate of cooling of condensate determines the resulting curvature of the frozen structure. All metals have yielded nanowires of uniform diameter on BSG trench wall surface.

Trench diameter and film thickness was varied to study the effect of filtering of condensate vapour and the effect of material coverage on the formation of metallic nanowires. Lower trench diameter yielded no material inside the trench and higher trench diameter gave thin film growth inside the trench, but no nanowire assembly. With the coating thickness, diameter of nanowire can be controlled. Lower thickness gave beaded nanowires and higher thickness gave very thick nanowires. Therefore, there is a
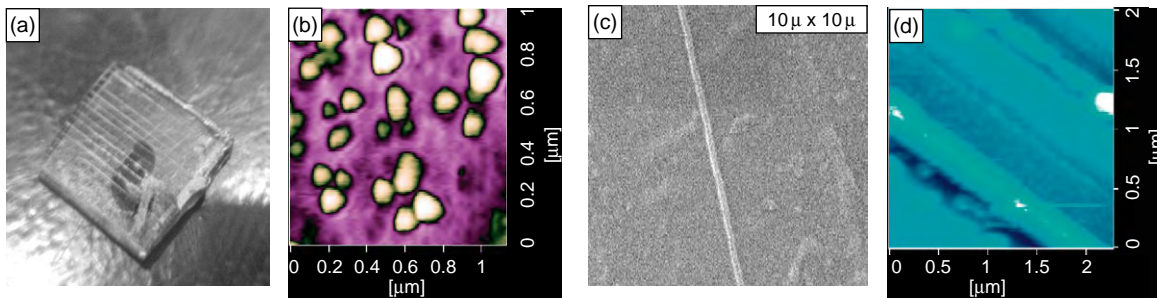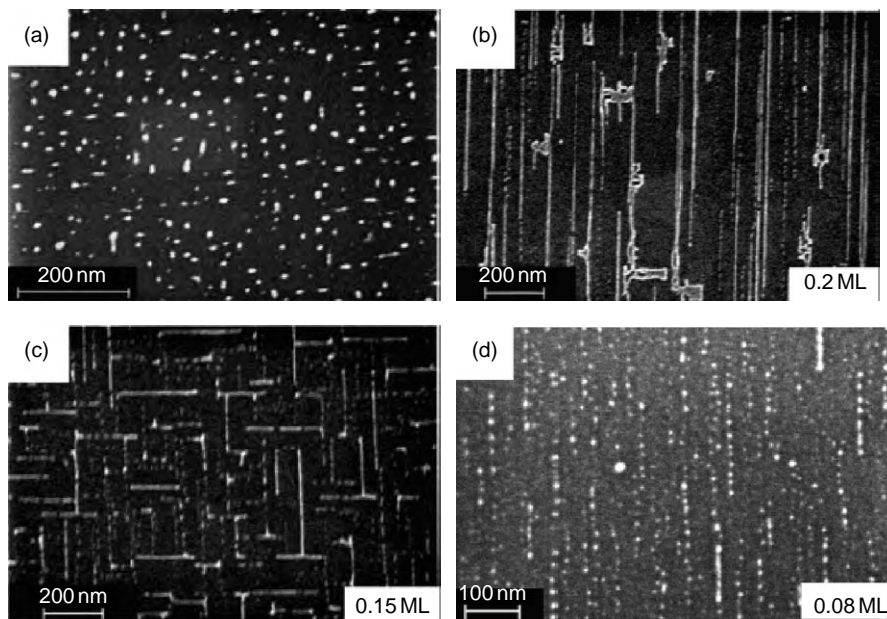
**FIGURE 4.15**   *(a) Photograph of scribed trench on BSG glass substrate (1 in. × 1 in.), (b) AFM image of thermally evaporated 50 nm Ni thin film as grown on non-templated BSG surface, (c) SEM image of Ni nanowire formed after evaporation inside the V-trench, (d) AFM image of evaporated Ni nanowire as grown inside the V-trench template.*
Source: *Courtesy of Prashant Kumar et al. (2008).*

window of trench depth/trench width (d/W ratio) where for a given metal of a particular thickness, nanowires will form. Formation of magnetic nickel nanowire using thermally evaporated physical vapour is shown in Figure 4.15. Figure 4.15c shows the diameter homogeneity of trench templated nanowires, while Figure 4.15d shows layer by layer growth of nanowires. Magnetoresistance behaviour with magnetic field was found to be different as compared to the thin film counterpart of the same thickness.
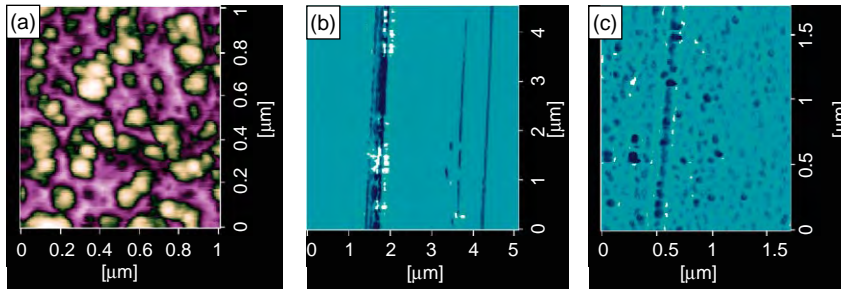
**FIGURE 4.16** *AFM images of (a) pulsed laser deposited 10 nm Ni ultrathin films on BSG substrate, (b) nanowire growth inside V-trench at low laser energy, (c) beaded nanowire grown at higher laser energy. Source: Reprinted with permission from [Prashant Kumar et al., 2008]. Copyright 2008, Inderscience.*
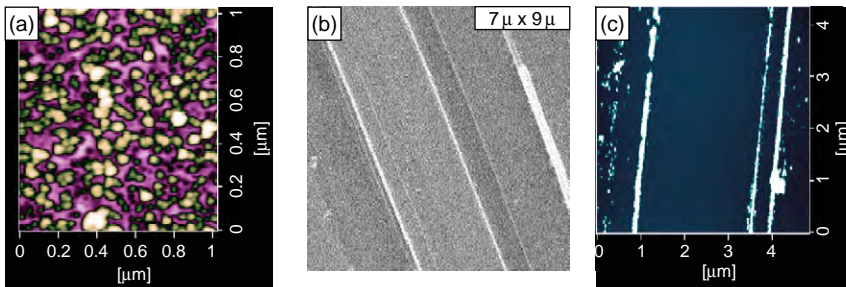


**FIGURE 4.17** *(a) AFM image of 40 nm DC sputtered Au thin films on BSG, (b) SEM image of gold nanowire growth inside the V-trench, (c) AFM image of gold nanowire growth inside the V-trench. Source: Reprinted with permission from [Prashant Kumar et al., 2008]. Copyright 2008, Inderscience.*

A further study was carried out on 10nm thin Ni film deposited by pulsed laser deposition (Figure 4.16) and 40nm Au films deposited by DC sputtering (Figure 4.17). It was found that depending on the excimer laser energy, nanowire is beaded or continuous. The V-trench template approach has yielded 40–200nm diameter of nanowire with diameter uniformity and of huge length depending on trench length. Nanostructures grown inside the trench were electrically isolated using malaeic acid before coating and after coating; lift-off was achieved by simply dipping the BSG substrate into water.

Template-assisted route has evolved as a good technique to achieve nanowires and nanodots and various nanostructures, but it has its own limitations. For a given material and given thickness range, there is a window for the ratio height (h)/diameter (W) of template size parameters where template helps condensate vapour to grow in an assembled manner, and outside the window, it does not yield assembled nanostructures. In this context, dose of material, velocity of condensate vapour and h/W ratio determines the extent of dewetting and size-selective filtering that are responsible for
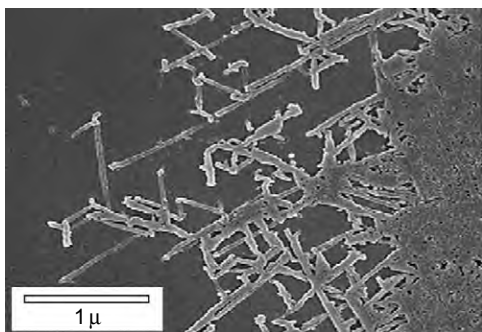
**FIGURE 4.18**   *Optical image of FILC of silicon.*
*Source: Reprinted with permission from [Wang et al., 2006]. Copyright 2006, Elsevier.*
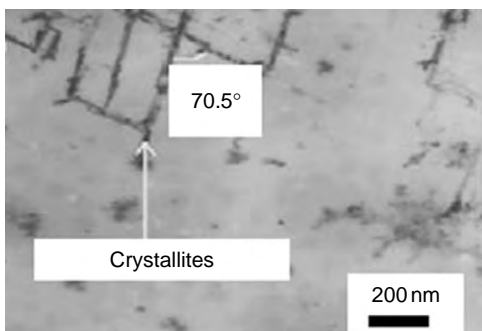


**FIGURE 4.19**   *SEM image of MIC of silicon.*
*Source: Reprinted with permission from [Jang et al., 1998]. Copyright 1998, Nature Publishing Group.*
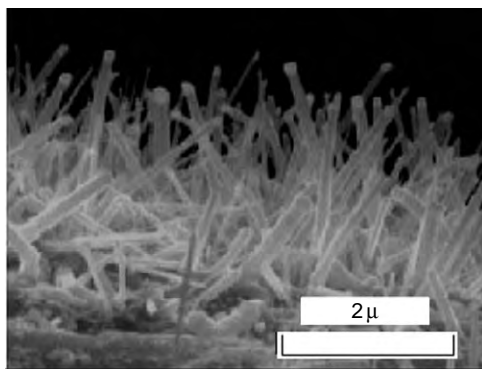


**FIGURE 4.20**   *SEM images of the $In_2O_3$ nanowires grown at 550°C at 2300V/cm.*
*Source: Reprinted with permission from [Li et al., 2008]. Copyright 2006, Elsevier.*

organized growth. There is a recent trend to use the template route in conjunction with other techniques to yield better control on growth process. Template-assisted routes, thus hold much promise as a powerful non-lithographic nanostructuring technique.

## 4.3 ELECTRIC FIELD INDUCED NANOSTRUCTURING

A technique that has been considered recently for nanostructuring of thin films is the electric field induced approach. The thermodynamics of grain growth in the presence of electric fields is quite well understood. It is known that due to a free energy minimization process, the grain growth is both accelerated and enhanced. Similarly, the nucleation rates for crystallization are expected to increase due to local Joule heating effects. It is also well known that the polarizability of metal nanoparticles is different from their bulk counterparts. However, there are very few reports, as will be discussed in the following, that exploit all three effects simultaneously. Some examples of morphological reconstruction and accelerated crystallization are presented.

Metal-induced lateral crystallization of amorphous Si has been investigated[169] under a wide range of electric fields. Wang et al.[170] investigated field-aided lateral crystallization of silicon. They found that branches add at 90°. They concluded that three effects are responsible for regrowth process namely, electromigration, chemical potential gradient and electric potential gradient (Figure 4.18).

Jang et al. demonstrated[171] that electric field enhances the rate of MIC (Figure 4.19). They showed that crystallization time at 500°C decreases from 25h to 10min on application of a modest electric field value 80Vcm$^{-1}$. Electric field alignment of vertical $In_2O_3$ nanowires has been reported (Figure 4.20)[172]. Under electric field, lateral growth of aligned multiwalled carbon nanotubes was achieved by Jang et al.[173] (Figure 4.21).

Zhang et al.[174] have reported field alignment effects on single-walled carbon nanotubes. According to them, large induced dipole moments lead to large aligning torques and forces on the nanotube, and prevent randomization of nanotube orientation by thermal fluctuations and gas flows (Figure 4.22).

Ichinokawa et al.[175] investigated the influence of electromigration and thermomigration. They found that with electron beam traversal, movement of metallic nanoislands can be controlled by the reversal of field direction. Saka et al.[176] applied electric field on material inside the trench in the presence of a thermal input, yielding metallic nanowires. They have explained the formation based on electromigration phenomena.

In studies carried out by the current authors, it has been demonstrated that there are three effects of the applied electric field on thin metal films. These are (1) grain growth, (2) alignment of grains along the direction of the applied field and (3) crystallization of the films. Each of these has a threshold energy above which the effects are evident. The process of grain growth has the lowest threshold followed by that for the alignment of these grains and the highest being the threshold for crystallization of the films. In our work, however, we have demonstrated[177] that thin metal films, under the influence of the electric field, crystallize without any external thermal input. Nanoparticle size has been found to increase 8–10 times.
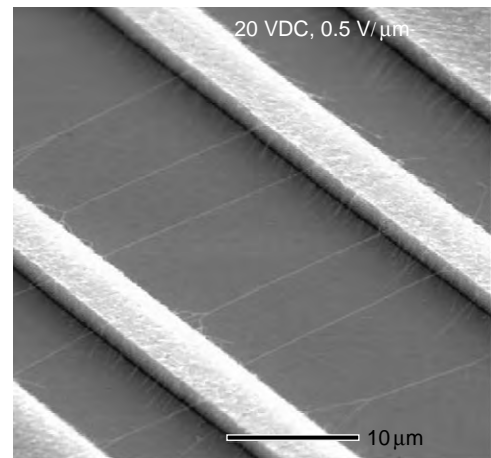


**FIGURE 4.22** SEM image of field alignment effect on single-walled carbon nanotube.
Source: Reprinted with permission from [Zhang et al., 2001]. Copyright 2001, American Institute of Physics.

The electric fields are of the order of $10^2$–$10^4$V/cm. Such high electric fields can generate very high temperature due to Joule heating causing thermal migration of particles and their agglomeration. Grain growth is usually stimulated in the presence of electric field.

In the presence of an external field[178], grain growth is governed by both the curvature and the distribution of energy density in different grains given by:

$$da/dt = -k' \left(1/a - 1/a^\star\right) - k(E - E^\star)$$

$$k = \varphi M/n$$

$$k' = M'$$

where $t$ = time, E and $E^\star$ are the energy densities in the absence and presence of applied field respectively, $a$ = grain diameter, $\phi$ = shape factor, $M$ and $M'$ = uniform mobilities of grains, $n$ = dimensionality of polycrystal and $\gamma$ is specific free energy.

Free energy optimization[179] can give critical nuclei size (number of molecules $N$ in 2D nuclei) under the action of field while nucleation is occurring.

$$N^\star = \{[\alpha\sigma]/[2kT \left(\ln S + pE^2\right)]\}$$

where $S$ is supersaturation ratio, $\alpha$ is a constant dependent on the shape of nuclei, $\sigma$ is interfacial tension, $k$ is Boltzmann's constant, $E$ is the energy density, that is electric field value, $T$ is temperature and,

$$p = -v/8\pi kT \left(1/\varepsilon_c - 1/\varepsilon_m\right)$$

where $-v$ is molecular volume, $\varepsilon_c$ and $\varepsilon_m$ are dielectric constants of crystalline and mother material respectively. Cecilia Noguez et al.[180] had given the origin of dielectric nature of metallic nanoparticles. It is also possible to define the critical electric field value as:

$$E^\star = [1/p \left(\Delta\mu^\star - \Delta\mu_0 \right)]^{1/2}$$

where $\Delta\mu^\star$ is the critical driving force in the absence of electric field.

Nickel thin films exhibited grain growth as well as organization when electric field was applied of the order of few kV/cm as shown in
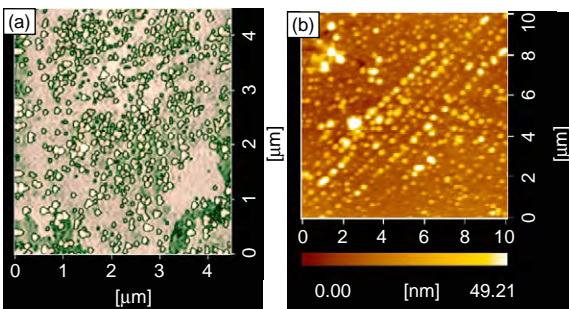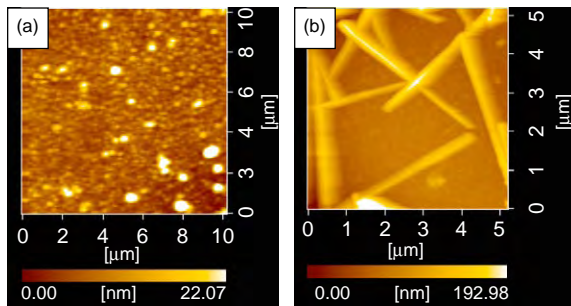


**FIGURE 4.23** *AFM image of electric field nanostructured Ni thin films. (a) As-deposited 50nm Ni thin film, (b) after the field treatment of 3.3kV/cm for 10s.*
*Source: Reprinted with permission from [Prashant Kumar et al., 2008]. Copyright 2008, World Scientific.*

Figure 4.23. Indium thin films, however, showed formation of nanowires as can be observed in Figure 4.24.

When DC sputtered gold ultrathin films are subjected to electric field treatment, a process of densification of the films can be observed (Figure 4.25). The As-deposited films show well-separated particles which at a field of 0.4 kV/cm exhibited a dense, well-ordered nanostructured morphology with an average diameter of 30–40 nm. At higher fields, 0.66 kV/cm, the film delaminates and is accompanied by field-induced emission in the form of arcing.

Similarly, silicon thin films are organized as nanoparticle arrays in the direction of the field as shown in Figure 4.26a. Interestingly, the formation of 1–2 μ trenches was also observed in the case of silver films as shown in Figure 4.26b. One can design wave guide or grating or else these silver films can, in principle, be used as a template to form nanowires inside them.



**FIGURE 4.24**  *AFM image of electric field nanostructured indium thin films. (a) As-deposited 15 nm thin film, (b) after the treatment of 3.33 kV/cm.*
*Source: Reprinted with permission from [Prashant Kumar et al., 2008]. Copyright 2008, World Scientific.*
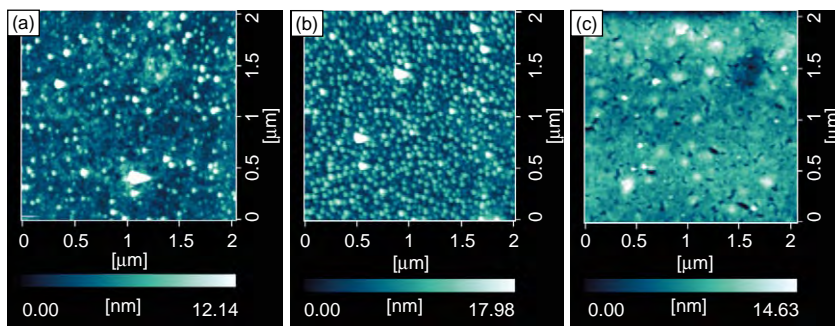


**FIGURE 4.25**  *AFM images of gold thin films, (a) As-deposited and subjected to electric fields of (b) 0.4 kV/cm, (c) 0.66 kV/cm.*
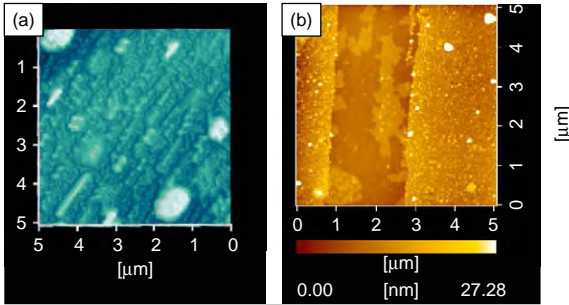
**FIGURE 4.26** *AFM images of electric field nanostructured thin films of (a) silicon, (b) silver.*

Nanostructuring by this technique, therefore, affords several control parameters crucial for nanowire formation that can be controlled accurately, viz. bias voltage, electrode tip diameter, voltage leads separation (which determines the field value), substrate material (should be robust to heat treatment), film material (lower melting points lead to agglomeration of material and require lower field for organization) and film thickness (which controls diameter and separation of nanoparticles).

## 4.4 LASER-INDUCED NANOSTRUCTURING

The unique combination of high pulse energy, high average power and deep ultraviolet (UV) wavelength make excimer laser capable of ablating a wide range of materials leading to several effects.

- Surface drilling.

- 'Non-thermal' energy delivery by a short wavelength radiation of the surface leading to modification.

- High temperature ablative plasma leading to catastrophic damage.

- Bulk heating and melting of these materials, accompanied by the following subsurface boiling in the melt pool and resulting in melt expulsion of the target.

- Nanopore and nanoparticle formation on the target surface due to ejection of neutral atoms or ion out of the target and backscattering of those ejected entities respectively.

- Material ejection from an illuminated surface.

- The deposition of a thin film on the surface of the specimen used as a target.

Apart from the change in optical properties, laser-induced surface features can also be used for further growth of nanostructures[181].

It has recently been shown that silicon becomes luminescent[182] in the visible range when they undergo size reduction to the nanometre dimensions. Creation of a thin layer on silicon surfaces using the intense conditions at the focus of a high intensity, excimer laser pulse can make silicon highly absorbing (bulk silicon has low absorption due to its indirect band gap) and an excellent

choice for photovoltaic applications[183]. Further, desired band gap of silicon can be accomplished in nanostructured form due to which it will find applications in antireflection coatings for microlens application[184]. Anisotropic growth features will give rise to gradient in refractive index and therefore can be used for polarization sensitive Si-based optical devices[185]. Nanostructured porous silicon can be used as a sensitive sensor to chemical species Si nanowires[186–193], as special forms of crystalline Si are expected to exhibit unusual quantum confinement effects as well as potentially useful applications. Recently, research is on for its high performance lithium battery anode application[194] and memory applications[195] apart from its unusual electrical, optical, mechanical and chemical properties because of their small dimensions, unique shapes and high surface-to-volume ratio. Apart from silicon surfaces, noble metal, $Al_2O_3$, GaAs and graphite surfaces have also been nanostructured for various applications. Thin film surfaces have been laser irradiated mainly for laser crystallization and partly for various assembled structures.

Kabashin et al.[196] used excimer laser to nanostructure Si and reported on the consequent PL spectra. They observed significant changes in the PL spectra due to laser irradiation (Figure 4.27).

Pedraza et al.[197] used various media and laser energy density to nanostructure silicon surface.

Henly et al.[198] nanostructured silicon thin film surface using KrF excimer laser in vacuum up to $10 J/cm^2$ fluence at 50 shots and at 10Hz repetition rate. They have shown that such nanostructured surfaces can be used for catalytic growth of vertical carbon nanotubes (Figure 4.28).
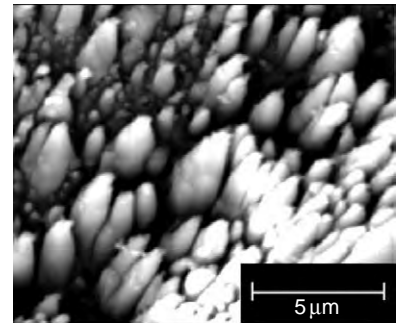


**FIGURE 4.27**  *SEM images of a silicon target after its irradiation by 200 pulses of the excimer laser near the plasma ignition threshold. Source: Reprinted with permission from [Kabashin et al., 2003]. Copyright 2003, Elsevier.*
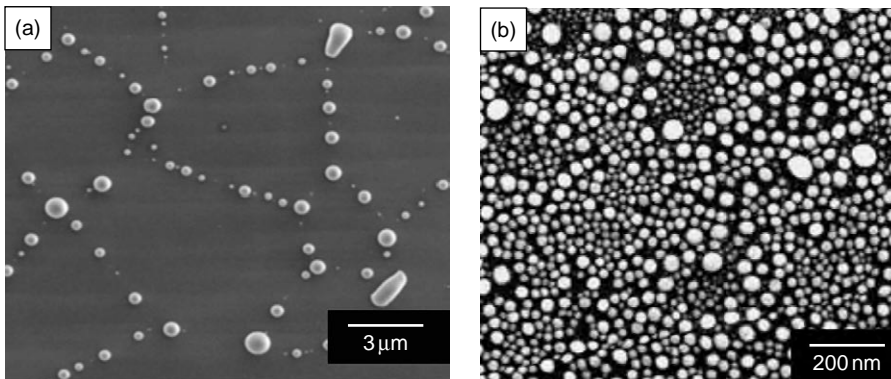


**FIGURE 4.28**  *SEM images of excimer laser nanostructured (a) 15nm Ni films, (b) 15nm Ag thin films by 400mJ/cm².*
*Source: Reprinted with permission from [Henly et al., 2007]. Copyright 2007, Elsevier.*

Loreti et al.[199] used excimer laser to anneal amorphous silicon seed layers deposited on a metallic Ti/Pd/Ag multilayer (Figure 4.29).

Cone formation by laser irradiation of silicon surface has been an interest in recent years for physicists. Resolidification starts at the edge of the molten zone and proceeds towards its centre. In contrast to the usual behaviour of materials with melting, the density of liquid Si, $\rho_l$(liquid Si) = 2.52 g/cm$^3$, is larger than the density of solid Si, $\rho_s$(Crystaline Si) = 2.32 g/cm$^3$. Thus, the volume of silicon increases during solidification. As a consequence, during cooling, the liquid silicon is squeezed radially to the centre and forms a protrusion. As a result, a solid cone surrounded by a ring-shaped trench is formed.

In our attempt to nanostructure silicon wafer, we shined KrF excimer laser in focussed and unfocussed conditions onto the neatly cleaned [311] $n$-type silicon wafer and did thorough systematic study of the nanostructures resulting due to the variation in laser energy density, number of shots, angle of incidence. We have also studied the effect of near edge on the laser-induced nanostructuring of surfaces. We extended our study to graphite, alumina and BSG bulk surfaces. Metallic thin films of thickness 10–50 nm have been laser irradiated to look into nanostructuring effects (Figures 4.30–4.32).

During focussed laser irradiation, silicon remains melted for a period of tens of nanoseconds and the gradient of surface tension is responsible for the formation of nanoripples. The modulated energy deposition during irradiation produces a temperature gradient, which in turn gives rise to the gradient in surface tension. Surface tension gradient drives the molten silicon from the hotter to the colder regions.



**FIGURE 4.29**   *ESEM cross-section micrographs of samples grown on the seed layer annealed at 853 K at repetition rate of 0.1 Hz.*
*Source: Reprinted with permission from [Loreti et al., 2004]. Copyright 2004, Elsevier.*

**FIGURE 4.30**

*AFM image for laser nanostructured silicon wafer in focussed condition (a) 20 shots at 2 J/cm$^2$, (b) 100 shots at 2 J/cm$^2$.*
*Source: Reprinted with permission from [Prashant Kumar et al., 2008]. Copyright 2008, American Scientific publisher.*
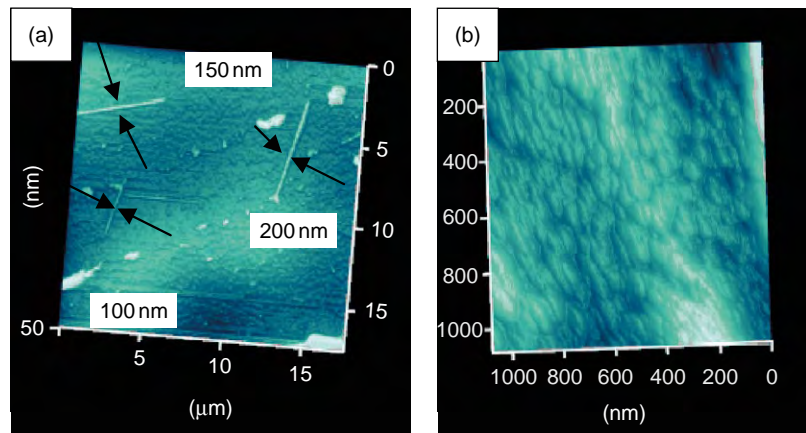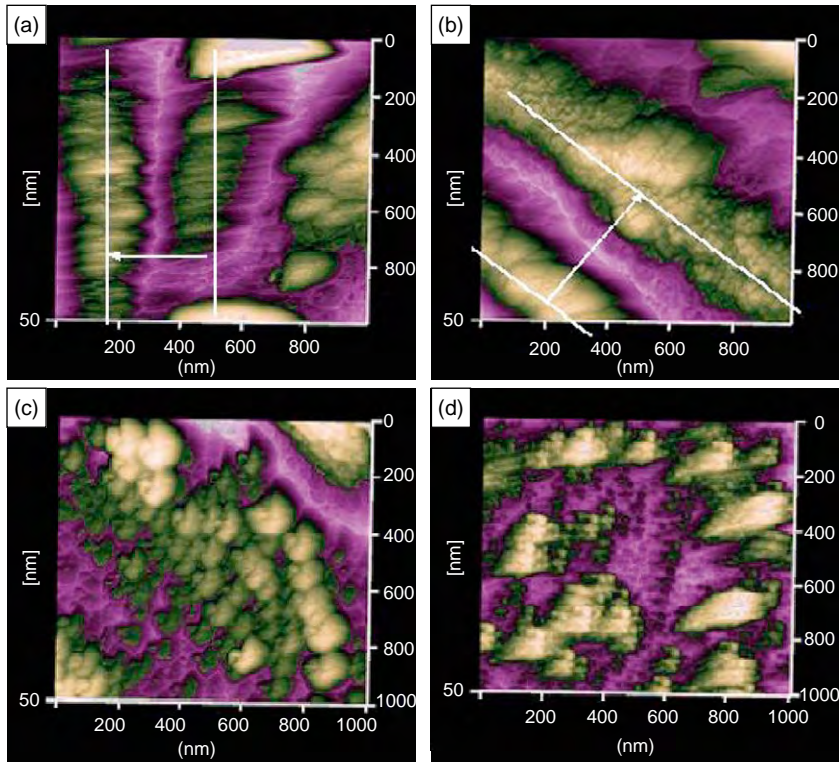
**FIGURE 4.31**   *AFM image in DFM mode for laser nanostructured silicon wafer in focussed condition at 5 J/cm$^2$ for 8 shots at different incident angles, (a) 10°, (b) 20°, (c) 30°, (d) 90°.*
*Source:* **Reprinted with permission from [Prashant Kumar et al., 2008]. Copyright 2008, American Scientific publisher.**
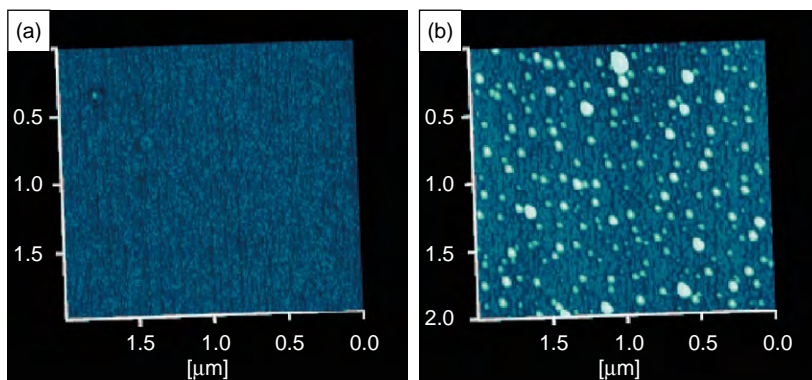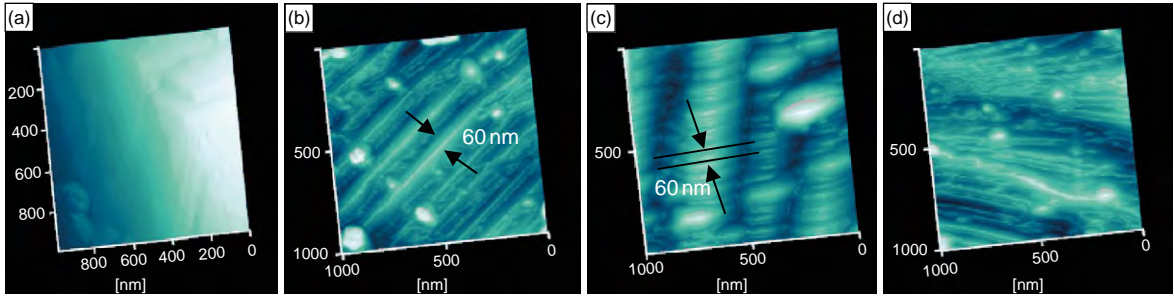


**FIGURE 4.32**   *AFM images for laser nanostructured silicon wafer in unfocussed excimer laser condition (a) without irradiation (b) 0.25 J/cm$^2$ for 1000 shots.*
*Source:* **Reprinted with permission from [Prashant Kumar et al., 2008]. Copyright 2008, American Scientific publisher.**

**FIGURE 4.33** *AFM images of laser nanostructured surface of alumina (a) untreated (b) at 0.075 J/cm$^2$, 1 Hz, 100 shots, (c) at 0 .075 J/cm$^2$, 1 Hz, 500 shots, (d) at 0.125 J/cm$^2$, 1 Hz, 100 shots.*
*Source: Courtesy of Prashant Kumar et al.*
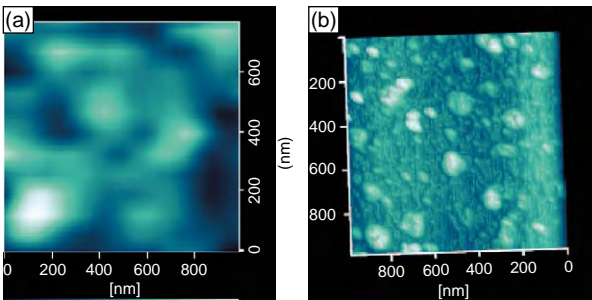


**FIGURE 4.34** *AFM images of laser nanostructured BSG surfaces for (a) untreated BSG, (b) at 0.092 J/cm$^2$, 1 Hz, 1000 shots.*
*Source: Courtesy of Prashant Kumar et al.*

Such ripples form only at higher fluences usually greater than $0.4$ J/cm$^2$, which are capable of melting the silicon surface globally and create such global capillary waves. We have observed such ripples for $2$–$5$ J/cm$^2$ fluence. However, in our experiment at low energy, $0.1$–$0.25$ J/cm$^2$, no such ripple formation is observed.

Nanoparticles form at fluences just higher than $0.15$ J/cm$^2$ for several hundred of laser shots in the presence of air backpressure. When the next pulse is incident on the surface, the spot is already hot and therefore less laser energy is required for melting it. However, for single pulse, the fluence requirement to melt the spot and hence to form nanoparticles of silicon will be manifold higher.

In our attempt to study the effect of excimer laser irradiation on alumina, it was observed that nanostructuring of alumina surface occurred at energy density as low as $0.075$ J/cm$^2$ for few hundred shots resulting in the formation of periodic array of nanolines, nanorings and nanosticks. At $2$ J/cm$^2$, however, the material on the surface reorganized giving rise to nanoparticles and nanoripples (Figure 4.33).

Borosilicate glass too shows a similar effect at very low energy density (Figure 4.34b), whereas graphite being a high melting point material was mostly unaffected at low energy. Visible effects could be seen in the case of graphite only above energy density of $2$ J/cm$^2$. For more than 30 shots only, nanostructural features started appearing (Figure 4.35b).
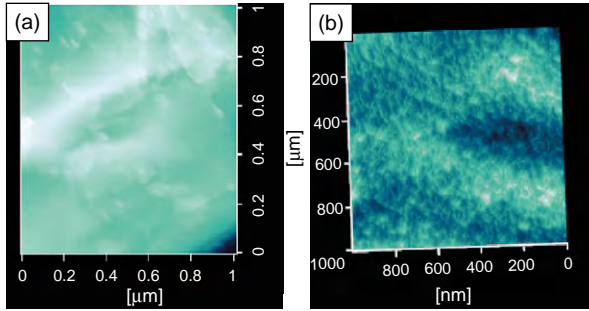
**FIGURE 4.35**   *AFM images of laser nanostructured graphite surfaces for (a) untreated graphite, (b) graphite at 2 J/cm², 1 Hz, 50 shots.*
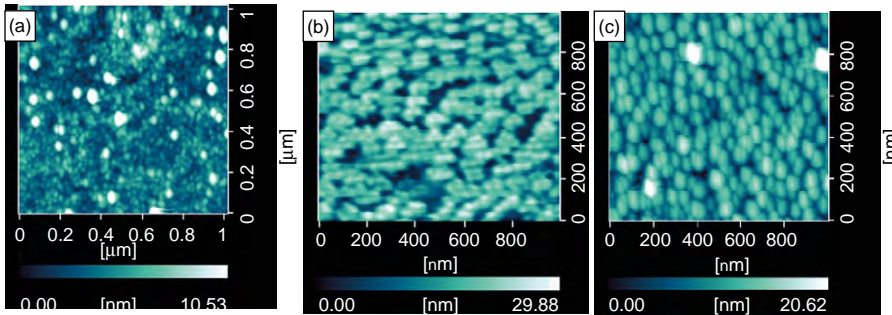*Source: Courtesy of Prashant Kumar et al.*



**FIGURE 4.36**

*Laser nanostructured surfaces of*
*(a) As-deposited Au,*
*(b) at 80 mJ, 2 shots,*
*(c) 80 mJ, 20 shots.*
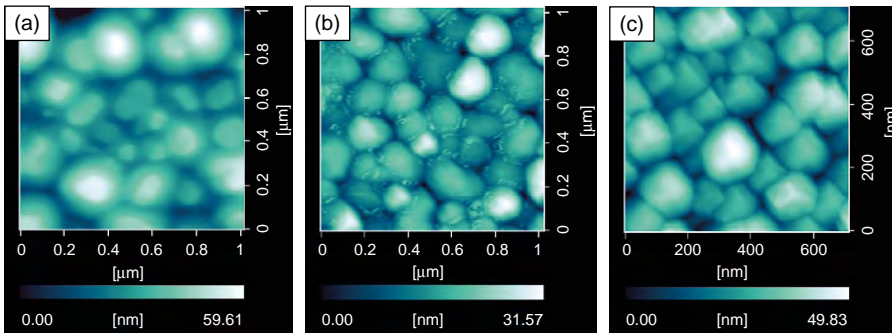*Source: Courtesy of Prashant Kumar et al.*



**FIGURE 4.37**

*Laser nanostructured surfaces of*
*(a) As-deposited In,*
*(b) 40 mJ, 10 shots,*
*(c) 100 mJ, 10 shots.*
*Source: Courtesy of Prashant Kumar et al.*

The current authors have also investigated the effect of excimer laser annealing on various metallic thin films. Examples of gold and indium ultrathin films are shown in Figures 4.36 and 4.37. Gold films exhibit a very disordered morphology in the As-deposited state (Figure 4.36a) which gets transformed into uniformly distributed grain morphology (Figure 4.36c). In the case of indium ultrathin films which had flat kind of morphological
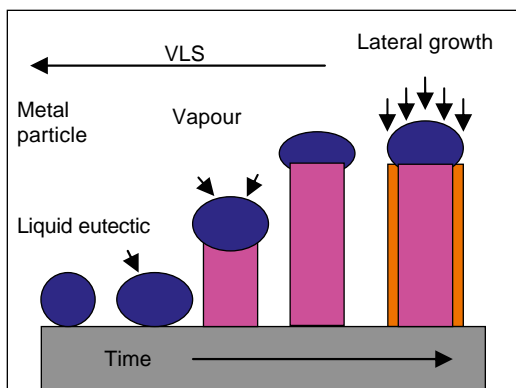
**FIGURE 4.38(a)**  *VLS growth mechanism.*
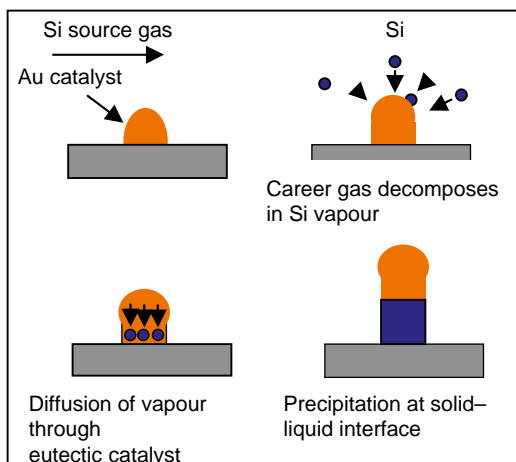


**FIGURE 4.38(b)**  *Detailed VLS phenomenon.*

features, the effect of laser annealing is to result in a well-ordered morphology of cubic-shaped grains (Fig. 4.37c).

## 4.5 VAPOUR–LIQUID–SOLID TECHNIQUE

In the vapour–liquid–solid process, as described in Figures 4.38a and b, a liquid alloy droplet composed of metal catalyst component (such as Au, Fe, etc.) and nanowire component (such as Si, III–V component, II–VI compound, oxide, etc.) is first formed under the reaction conditions. The metal catalyst can be rationally chosen from the phase diagram by identifying metals in which the nanowire component element is soluble in the liquid phase but do not form solid compound more stable than the desired nanowire phase. As described in Table 4.1, there exists a eutectic temperature for the combination of the nanowire component and the catalyst component. The essence is that ideal metal catalyst should be physically active but chemically stable. The best catalysts for various nanowires are Au (for ZnO NW), Fe (for $SiO_2$ NW), Co (for $SiO_2$ NW), Ni (for $Ga_2O_3$ NW).

The liquid droplet serves as a preferential site for absorption of gas phase reactant and when supersaturated, the nucleation site for crystallization. Nanowire growth begins after the liquid becomes supersaturated in the reactant materials and continues as long as the catalyst alloy remains in a liquid state and the reactant is available. During the growth, the catalyst droplet directs the nanowire's growth direction and defines the diameter of the nanowire. Ultimately, the growth terminates when the temperature is below the eutectic temperature of the catalyst alloy or the reactant is no more available. Therefore, nanowires as obtained from VLS process have diameters as that of the catalyst nanoparticle at the other end. Therefore, if the catalyst nanoparticle is still present, then it is inferred that nanowire growth was governed by VLS mechanism. The eutectic temperatures for the alloy formation of the nanowire component and the catalyst component are tabulated in Table 4.1.

| Table 4.1 | Table for Eutectic Temperatures for the Alloy Formation of the Nanowire Component and the Catalyst Component |
|---|---|

| Alloys | Eutectic Temperature (°C) |
|---|---|
| Au–Si | 360 |
| Au–GaAs | 630 |
| Au–Ge | 360 |
| Ag–Si | 837 |
| Fe–Si | >1200 |
| Al–Si | 577 |
| Al–Ge | 419 |

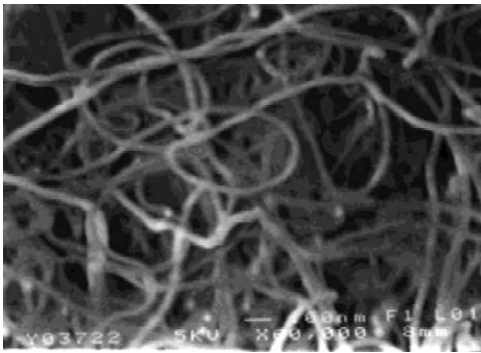*Source: Reprinted with permission from [Givargizov et al., 1975]. Copyright 1975, Elsevier.*



**FIGURE 4.39** *SiO$_2$ nanowire grown by VLS mechanism.*
*Source: **Reprinted with permission from [Liu et al., 2001]. Copyright 2001, Materials Research Society.***
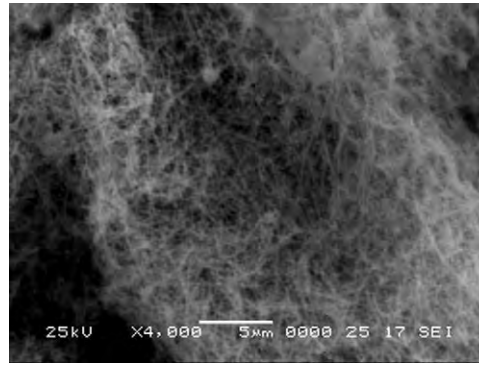


**FIGURE 4.40** *InO$_2$ nanowire grown by VLS technique.*
*Source: **Reprinted with permission from [Zhang et al., 2003]. Copyright 2003, Institute of Physics.***

Except for SiO$_2$, all other nanowires are well crystalline, mostly oriented along [111] direction. The VLS crystal growth mechanism was first proposed by Wagner et al.[200] for silicon whisker growth. Essentially, they reduced SiCl$_4$ using hydrogen in the presence of Au, Pt, Ag, Pd, Cu, Ni, etc. as catalyst. Westwater et al.[201] used pyrolysis of SiH$_4$ with Au as a catalyst to obtain silicon nanowires. To date, ZnO[202], SiO$_2$[203], Ga$_2$O$_3$[204], In$_2$O$_3$[205] nanowires have been grown successfully using VLS technique (Figures 4.39–4.40).

Sharma et al.[206] have successfully grown germanium nanowire on silicon [111] substrates using the VLS technique (Figure 4.41).

Because nanowires of binary and more complex stoichiometries can be created using the VLS mechanism, it is possible for one of these elements to serve

as the VLS catalyst. The major advantage of a self-catalytic process is that it avoids undesired contamination from foreign metal atoms typically used as VLS catalysts. Self-catalytic behaviour has been reported when the direct reaction of Ga with $NH_3$ or direct evaporation of GaN was used to produce GaN nanowires[207, 208].

The precise control of nanowire lengths and diameters using a self-catalytic VLS technique, as well as the universality of this approach, has yet to be demonstrated.

Lee et al.[209] successfully showed that gold can be used as a catalyst for ZnO nanowire growth by VLS route.

E. I. Givargizov[210] studied in detail the VLS crystal growth technique in 1975. His study shows that the equilibrium state is given by the equation in the case of silicon nanowire growth:

$$\Delta\mu_{NW} = \Delta\mu_{bulk} - 4(\alpha\Omega)/d$$
$$\Delta\mu_{bulk} = \mu_{bulk} - \mu_{vap}$$
$$\Delta\mu_{NW} = \mu_{NW} - \mu_{vap}$$

where, $\Delta\mu$ nanowire, bulk and vapour are the effective chemical potentials of silicon in the nanowire, in the bulk material and in the vapour phase respectively, $d$ is the diameter of the nanowire, $\Omega$ is the atomic volume of silicon and the specific surface free energy of the wire.

This relation shows that there is a critical diameter, $d_c$, at which the growth stops completely and given by the following expression:

$$\Delta\mu_{bulk}/kT = 4(\alpha\Omega)/kTd_c$$

where $k$ is Boltzmann's constant and $T$ is the temperature, $d_c$ is the critical diameter.

This can be explained by the fact that for very small nanodroplets, the effective chemical potential of silicon in the wire becomes higher than for the vapour phase.

## 4.6  SUMMARY AND OUTLOOK

In summary, the area of non-lithographic techniques for nanostructuring of thin films and surfaces has been reviewed. It has been shown that these techniques provide cost-effective solutions for the realization of nanostructures like nanowires, nanodots, nanocones, nanopores, nanopillars. Apart from nanostructure development, non-lithographic techniques are unique, since they cause mass re-crystallization of the materials.

There are essentially two major routes to such non-lithographic approaches – one is in situ and other being ex situ. Template-assisted approach has been proved to be a major success in achieving a variety of nanostructures. However, organization of nanoparticles is material specific and control of assembly process is subject to material–substrate adhesion, material melting point, its mobility in vapour form and surface tension. There exists a set of parameters, which affect the assembly process; for example, material dose, rate of deposition, template parameters (height/diameter ratio) and angle of deposition. Templates essentially work as size-selective filters and apart from the usual nanoporous alumina- and silica-based templates, V-grooves have been successfully used for growth at the apex and on slant surface. The issues that remain to be resolved before a range of applications can be considered are continuity, isolation and manipulation of the nanostructures, stability at higher temperatures and crystalline nature.

VLS is also an in situ growth technique that has developed as a major route to achieve all kinds of nanowires, but it is totally dependent on the catalyst material and its catalytic activity. The major drawback to such a method lies in the fact that it yields impure material depending on the stage of the catalytic reaction at the time of finish. These issues are being addressed by a number of groups.

Laser and electric field treatment to bulk surface or already deposited thin film are ex situ techniques for the development of nanostructures. Excimer and fs lasers have been used widely to achieve various nanostructures, majority of which are on semiconductor surfaces. A few of the nanostructures of interest that appear after laser treatment to surfaces are nanopores and nanocones. With a good control of laser energy density and number of shots, one can nanostructure surface and thin film for desired applications. The exact influence of each of these parameters on the nanostructuring process is, however, not very well understood and much remains

to be done in this area. Interestingly, both local and global effects can be achieved and therefore the technique has great promise for targeted nanostructuring. It has also emerged as a good technique for both amorphizing and crystallizing films and surfaces. Thus, in future, laser nanostructuring can be used to produce crystalline or amorphous nanostructures at specified locations.

Electric field induced nanostructuring is a nascent area of research and very few reports are available on this method of nanostructuring. Nanostructure development at local sites and directional growth are salient features of this technique. Electric field induced crystallization is very promising for the semiconductor industry, since there is a great need to achieve crystallization at ambient temperature. The alignment of nanoparticles and nanowires along the direction of electric field is of special significance for the electronics and optoelectronics industry. Detailed experiments have to be carried out on the effect of electrode diameter and separation, duration of the applied field as well as the nature of the film material.

In all the techniques discussed in this chapter, the theory is neither well developed nor is it well understood, so there is much scope for research along these lines.

In brief, the non-lithographic techniques developed so far are expected to have a broad industry-oriented thrust on one hand and on the other hand, they are expected to result in new physics leading to novel functional nanostructured materials.

## ACKNOWLEDGEMENTS

## REFERENCES

[1] T.-M. Chen, F.-M. Pan, J.-Y. Hung, L. Chang, S.-C. Wu, C.-F. Chen, J. Electrochem. Soc. 154 (2007) D215.

[2] H.J. Xu, X.J. Li, Opt. Express 16 (2008) 2933.

[3] Y. Nakayama, et al., Nature 447 (2007) 1098.

[4] F. Xu, V. Pruneri, V. Finazzi, G. Brambilla, Opt. Express 16 (2008) 1062.

[5] L. Chen, J.D. Leon, X. Jin, Chinese Opt. Lett. 5 (2007) 543.

[6] B. Liu, et al., Nanotechnology 15 (2004) 1745.

[7]   C. Li, D. Zhang, S. Han, X. Liu, T. Tang, B. Lei, Z. Liu, C. Zhou, Ann. N. Y. Acad. Sci. 1006 (2003) 104.

[8]   M.S. Islam, P.J. Kuekes, S.-Y. Wang, D.R. Stewart, S. Sharma, United States Patent 7307271.

[9]   Q. Li, et al., Nanotechnology 18 (2007) 235204.

[10]  V.M. Ayres, B.W. Jacobs, Q. Chen, L. Udpa, Y. Fan, N. Tram, A. Baczewski, S. Kumar, M. Crimp, J. Halpern, M. He, M.A. Tupta, R. Stallcup, A. Hartman, IEEE Trans. Electron. (2006) 1-4244-0078-3.

[11]  Y. Li, F. Qian, J. Xiang, C.M. Lieber, Mater. Today 9 (2006) 18.

[12]  S. Ju, A. Facchetti, Y. Xuan, J. Liu, F. Ishikawa, P. Ye, C. Zhou, T.J. Marks, D.B. Janes, Nature Nanotech. 2 (2007) 378.

[13]  E. Dattoli, Q. Wan, W. Lu, Mater. Res. Soc. Symp. Proc., 1018, EE11-06, 2007.

[14]  P. Yang, H. Kind, H. Yan, M. Law, B. Messer, Nanowire optoelectric switching device and method, in: United States Patent, 7239769, 2007.

[15]  B.Y. Geng, G.Z. Wang, Z. Jiang, T. Xie, S.H. Sun, G.W. Meng, L.D. Zhang, Appl. Phys. Lett. 82 (2003) 4791.

[16]  N.A. Sanford, L.H. Robins, M.H. Gray, Y.-S. Kang, J.E. Van Nostrand, C. Stutz, R. Cortez, A.V. Davydov, A. Shapiro, I. Levin, A. Roshko, Phys. Status Sol. 2 (2005) 2357.

[17]  X. Wang, J. Cole, A.M. Dabiran, H.O. Jacobs, Mater. Res. Soc. Symp. Proc., 1018, EE12-08, 2007.

[18]  Y.-J. Choi, I.-S. Hwang, J.-G. Park, K.J. Choi, J.-H. Park, J.-H. Lee, Y.-J. Choi, et al., Nanotechnology 19 (2008) 095508.

[19]  M.K. Hussain, S.C. Ghosh, Y. Boontongkong, C. Thanachayanont, J. Datta, J. Metastable Nanocryst. Mater. 23 (2005) 27.

[20]  Q. Wan, T.H. Wang, Chem. Commun. 14 (2005) 3841.

[21]  Y.-J. Choi, I.-S. Hwang, K.-J. Choi, J.-H. Park, J.-G. Park, Mater. Res. Soc. Symp. Proc., 951, E08-03, 2007.

[22]  K. Sawicka, M. Karadge, A. Prasad, P.I. Gouma, Microsc. Microanal. 10 (2004) 360.

[23]  T.-J. Hsueh, C.-L. Hsu, S.-J. Chang, I.-C. Chen, Sens. Actuators B: Chem. 126 (2007) 473.

[24]  M.K. Hossain, S.C. Ghosh, Y. Boontongkong, C. Thanachayanont, J. Datta, J.Metastable Nanocryst. Mater. 23 (2005) 27.

[25]  R.H. Scheffler, Q.L. Ye, M. McNeil, Mater. Res. Soc. Symp. Proc., 1018, EE10-22, 2007.

[26]  Q. Li, S.-M. Koo, M.D. Edelstein, J.S. Suehle, C.A. Richter, Mater. Res. Soc. Symp. Proc., 1018, EE09-07, 2007.

[27]  M. Law, J. Goldberger, P. Yang, Ann. Rev. Mater. Res. 34 (2004) 83.

[28]  W. Lu, et al., J. Phys. D: Appl. Phys. 39 (2006) R387.

[29]  D.R. Bowler, J. Phys.: Condens. Mater. 16 (2004) R721.

[30]  Y.F. Guan, A.V. Melechko, A.J. Pedraza1, M.L. Simpson, P.D. Rack, Nanotechnology 18 (2007) 335306.

[31] A. Rodriguez, D. Molinero, E. Valera, T. Trifonov, L.F. Marsal, J. Pallar`es, R. Alcubilla, Sens. Actuators B 109 (2005) 135.

[32] M. Abraham, Mater. Res. Soc. Symp. Proc., 820, R1.4.1, 2004.

[33] P.G. Shao, J.A. van Kan, K. Ansari, A.A. Bettiol, F. Watt, Nucl. Inst. Methods Phys. Res. B 260 (2007) 479.

[34] Z. Lu, A.N. Cartwright, Mater. Res. Soc. Symp. Proc., 961, 001-03, 2007.

[35] J.E.E. Baglin, A.J. Kellock, J.E. Frommer, Mater. Res. Soc. Symp. Proc., 1020, GG02-03, 2007.

[36] H. Loeschnera, E.J. Fantnera, R. Korntnera, E. Platzgummera, G. Stengla, M. Zeiningera, J.E.E. Baglinb, R. Bergerc, W.H. Brüngerd, A. Dietzelc, M.-I. Baratone, L. Merharif, Mater. Res. Soc. Symp. Proc., 739, H1.3.1, 2003.

[37] A.A. Tseng, A. Notargiacomo, T.P. Chen, J. Vac. Sci. Technol. B 23 (2005) 3.

[38] M. Fukuhara, H. Ono, T. Hirasawa, M. Otaguchi, N. Sakai, J. Mizuno, S. Shoji, J. Photopolym. Sci. Technol. 20 (2007) 499.

[39] L. Jay Guo, J. Phys. D: Appl. Phys. 37 (2004) R123.

[40] B.D. Gates, Q. Xu, J.C. Love, D.B. Wolfe, G.M. Whitesides, Annu. Rev. Mater. Res. 34 (2004) 339.

[41] C.L. Haynes, A.D. McFarland, M.T. Smith, J.C. Hulteen, R.P. Van Duyne, J. Phys. Chem. B, 106 (2002) 1898.

[42] K. Awazu, M. Fujimaki, X. Wang, A. Sai, Y. Ohki, Mat. Res. Soc. Symp. Proc., 820, R4.5.1, 2004.

[43] J.H.G. Owen, K. Miki, Mater. Res. Soc. Symp. Proc. 961, O15-07, 2007.

[44] U. Valbusal, C. Boragno, F.B. de Mongeot, J. Phys.: Condens. Mater. 14 (2002) 8153.

[45] N. Toyoda, I. Yamada, Mater. Res. Soc. Symp. Proc., 849, KK7.9.1, 2005.

[46] J. Munoz-Garcıa, L. Vazquez, R. Cuerno, J.A. Sanchez-Garcıa, M. Castro, R. Gago, Condense Matter Mater. Sci. 2625 (2007) 1–85.

[47] V. Abidzina, I. Tereshko, I. Elkin, V. Red'ko, S. Budak, C. Muntele, D. Walker, D. Ila, Mater. Res. Soc. Symp. Proc., 1020, GG07-17, 2007.

[48] A. Cuenat, M.J. Aziz, Mater. Res. Soc. Symp. Proc., 707, A3.8.1/N2.8.1, 2002.

[49] Q. Lu, F. Gao, D. Li, S. Komarneni, AZojomo 1 (2005) 1.

[50] S. Inoue, S.-Z. Chu, K. Wada, D. Li, H. Haneda, Sci. Technol. Adv. Mater. 4 (2003) 269.

[51] H. Brune, M. Giovannini, K. Bromann, K. Kern, Nature 394 (1998) 451.

[52] F.S. Flack, B. Yang, M. Huang, M. Marcus, J. Simmons, O.M. Castellini, M.A. Eriksson, F. Liu, M.G. Lagally, Mater. Res. Soc. Symp. Proc., 849, KK1., 3, 2005, 1.

[53] E. Stern, G. Cheng, J.F. Klemic, E. Broomfield, D. Turner-Evans, C. Li, C. Zhou, M.A. Reed, J. Vac. Sci. Technol. B 24 (2006) 231.

[54] M.H. Huang, S. Mao, H. Feick, H.Q. Yan, Y.Y. Wu, H. Kind, E. Weber, R. Russo, P.D. Yang, Science 292 (2001) 1897.

[55] W.H. Pan, Z.R. Dai, Z.L. Wang, Science 291 (2001) 1947.

[56] Z.R. Dai, W.H. Pan, Z.L. Wang, Solid State Commun. 118 (2001) 351.

[57] M.H. Huang, Y.Y. Wu, H. Feick, N. Tran, E. Weber, P.D. Yang, Adv. Mater. 13 (2001) 113.

[58] Y.C. Kong, D.P. Yu, B. Zhang, W. Fang, S.Q. Feng, Appl. Phys. Lett. 78 (2001) 407.

[59] C.H. Liang, G.W. Meng, Y. Lei, F. Phillip, L.D. Zhang, Adv. Mater. 13 (2001) 1330.

[60] Y.Q. Zhu, W.K. Hsu, M. Terrones, N. Grobert, H. Terrones, J.P. Hare, H.W. Kroto, D.R.M. Walton, J. Mater. Chem. 8 (1998) 1859.

[61] H. Takikawa, M. Yatsuki, T. Sakakibara, Japan J. Appl. Phys. 38 (1999) L401.

[62] C.H. Liang, L.D. Zhang, G.W. Meng, Y.W. Wang, Z.Q. Chu, J. Nanocryst. Solids 277 (2000) 63.

[63] X.C. Wu, W.H. Song, W.D. Huang, M.H. Pu, B. Zhao, Y.P. Sun, J.J. Du, Chem. Phys. Lett. 336 (2001) 53.

[64] Z.L. Wang, R.P. Gao, J.L. Gole, J.D. Staut, Adv. Mater. 12 (2000) 1938.

[65] X.C. Wu, W.H. Song, W.D. Huang, M.H. Pu, B. Zhao, Y.P. Sun, J.J. Du, Chem. Phys. Lett. 328 (2000) 5.

[66] H.Z. Zhang, Y.C. Kong, Y.Z. Wang, X. Du, Z.G. Bai, J.J. Wang, D.P. Yu, Y. Ding, Q.L. Hang, S.Q. Feng, Solid. State Commun. 109 (1999) 677.

[67] C.H. Liang, G.W. Meng, G.Z. Wang, Y.W. Wang, L.D. Zhang, S.Y. Zhang, Appl. Phys. Lett. 78 (2001) 3202.

[68] J.Y. Li, Z.Y. Quio, X.L. Chen, L. Chen, Y.G. Cao, M. He, H. Li, Z.M. Cao, Z. Zhang, J. Alloys Compound 306 (2000) 300.

[69] C.C. Tang, S.S. Fan, M.L. Chapelle, P. Li, Chem. Phys. Lett. 333 (2001) 12.

[70] Z.G. Bai, D.P. Yu, H.Z. Zhang, Y. Ding, Y.P. Wang, X.Z. Gai, Q.L. Hang, G.C. Xiong, S.Q. Feng, Chem. Phys. Lett. 303 (1999) 311.

[71] P.D. Yang, C.M. Lieber, Science 273 (1996) 1836.

[72] H. Nakamura, Y. Matsui, J. Am. Chem. Soc. 117 (1995) 2651.

[73] M. Zhang, Y. Bando, K. Wada, J. Mater. Res. 16 (2001) 1408.

[74] L.H. Wang, S. Tomura, F. Ohashi, M. Maeda, M. Suzuki, K. Inukai, J. Mater. Chem. 11 (2001) 1465.

[75] H.P. Lin, C.Y. Mou, Science 273 (1996) 765.

[76] M. Adachi, T. Harada, M. Harada, Langmuir 16 (2000) 2376.

[77] M. Harada, M. Adachi, Adv. Mater. 12 (2000) 839.

[78] Z.Y. Yuan, W.Z. Zhou, Chem. Phys. Lett. 333 (2001) 427.

[79] H.P. Lin, C.Y. Mou, S.B. Liu, Adv. Mater. 12 (2000) 103.

[80] M.E. Spahr, P. Bitterli, R. Nesper, M. Muller, F. Krumeich, H.U. Nissen, Angew. Chem. Int. Ed. England 37 (1998) 1263.

[81] K.S. Pillai, F. Krumeich, H.J. Muller, M. Niederberger, R. Nesper, Solid State Ion. 141 (2001) 185.

[82] H.J. Muhr, F. Krumeich, U.P. Schonholzer, F. Bieri, M. Niederberger, L.J. Gauckler, R. Nesper, Adv. Mater. 12 (2000) 231.

[83] M. Niederberger, H.J. Muhr, F. Krumeich, F. Bieri, D. Gunther, R. Nesper, Chem. Mater. 12 (2000) 1995.

[84] S. Kobayasi, K. Hanabusa, N. Hamasaki, M. Kimura, H. Shirai, Chem. Mater. 12 (2000) 1523.

[85] C. Hippe, M. Wark, E. Lork, G. Schulz-Ekloff, Microporous Mesoporous Mater. 31 (1999) 235.

[86] D.P. Yu, Q.L. Hang, Y. Ding, H.Z. Zhang, Z.G. Bai, J.J. Wang, Y.H. Zou, W. Qian, G.C. Xiong, S.Q. Feng, Appl. Phys. Lett. 73 (1998) 3076.

[87] A.M. Morales, C.M. Lieber, Science 279 (1998) 208.

[88] S.T. Lee, N. Wang, Y.F. Zhang, Y.H. Tang, Mater. Res. Soc. Bull. 24 (1999) 36.

[89] X.F. Duan, C.M. Lieber, Adv. Mater. 12 (2000) 298.

[90] G.S. Park, W.B. Choi, J.M. Kim, Y.C. Choi, Y.H. Lee, C.B. Lim, J. Cryst. Growth 220 (2000) 494.

[91] W.Q. Han, P. Kohler-Redlich, F. Ernst, M. Ruhle, Solid. State Commun. 115 (2000) 527.

[92] T.W. Ebessen, P.M. Ajayan, Nature 358 (1992) 220.

[93] S. Iijima, T. Ichihashi, Nature 363 (1993) 603.

[94] T. Kasuga, M. Hiramatsu, A. Hoson, T. Sekino, K. Niihara, Langmuir 14 (1998) 3160.

[95] T. Kasuga, M. Hiramatsu, A. Hoson, T. Sekino, K. Niihara, Adv. Mater. 11 (1999) 1307.

[96] Z. Shi, J.A. Szpunar, S. Wu, Microsc. Microanal. 11 (Suppl. 2) (2005) 1.

[97] J.S. Yin, Z.L. Wang, Adv. Mater. 11 (1999) 469.

[98] M. Li, R.B. Bhiladvala, T.J. Morrow, J.A. Sioss, K.-K. Lew, J.M. Redwing, C.D. Keating, T.S. Mayer, Nature Nanotechnol. 3 (2008) 88.

[99] P.B. Amama, B.A. Cola, T.D. Sands, X. Xu, T.S. Fisher, Nanotechnology 18 (2007) 385303.

[100] V.R. Caffarena, J.L. Capitaneo, R.A. Simao, A.P. Guimaraes, Mater. Res. 9 (2006) 205.

[101] W. Lee, M.-K. Jin, W.-C. Yoo, E.-S. Jang, J.-H. Choy, J.-H. Kim, K. Char, J.-K. Lee, Langmuir 20 (2004) 287.

[102] L. Zhaoa, M. Steinhart, M. Yosef, S.K. Lee, S. Schlecht, Sens. Actuators B 109 (2005) 86.

[103] K. Yamamoto, H. Kohno, S. Takeda, S. Ichikawa, Appl. Phys. Lett. 89 (2006) 083107.

[104] J. Goldberger, R. He, Y. Zhang, S. Lee, H. Yan, H.-J. Choi, P. Yang, Nature 422 (2003) 599.

[105] D. Al Mawlawi, N. Coombs, M. Moskovits, J. Appl. Phys. 70 (1991) 4421.

[106] L. Menon, M. Zheng, H. Zeng, S. Bandopadhyay, D.J. Sellmyer, J. Electron. Mater. 29 (2000) 510.

[107] Y.C. Choi, J. Kim, J.K. Han, S.D. Bu, J.B. Park, H. Lee, B.K. Ahn, J. Korean Phys. Soc. 49 (2006) S523.

[108] D. Crouse, Y.H. Lo, A.E. Miller, M. Crouse, Appl. Phys. Lett. 76 (2000) 49.

[109] H. Masuda, T. Mizuno, N. Baba, T. Ohmori, J. Electroanal. Chem. 368 (1994) 333.

[110] P. Hoyer, N. Baba, H. Masuda, Appl. Phys. Lett. 66 (1995) 2700.

[111] P. Hoyer, H. Masuda, J. Mater. Sci. Lett. 15 (1996) 1228.

[112] H. Masuda, H. Tanaka, N. Baba, Chem. Lett. 1990 (1990) 621.

[113] H. Masuda, K. Nishio, N. Baba, Japan J. Appl. Phys. 31 (1992) L1775.

[114] H.J. Fan, W. Lee, R. Scholz, A. Dadgar, A. Krost, K. Nielsch, M. Zacharias, Nanotechnology 16 (2005) 913.

[115] S. Deki, S. Iizuka, A. Horie, M. Mizuhata, A. Kajinami, J. Mater. Chem. 14 (2004) 3127.

[116] D. Al Mawlawi, N. Coombs, M. Moskovits, J. Appl. Phys. 70 (1991) 4421.

[117] L. Menon, M. Zheng, H. Zeng, S. Bandyopadhyay, D.J. Sellmyer, J. Electron. Mater. 29 (2000) 510.

[118] L.S. Jacobs, C.P. Bean, Phys. Rev. 100 (1955) 1060.

[119] F. Li, R.M. Metzger, J. Appl. Phys. 81 (1997) 3806.

[120] Y. Peng, H.L. Zhang, S.L. Pan, H.U. Li, J. Appl. Phys. 87 (2000) 7405.

[121] H. Zeng, M. Zhang, R. Skomski, D.L. Sellmyer, Y. Liu, L. Menon, J. Appl. Phys. 87 (2000) 4718.

[122] R.M. Metzger, V.V. Konovalov, M. Sun, T. Xu, G. Zangari, B. Xu, M. Benakli, W.D. Doyle, IEEE Trans. Magn. 36 (2000) 30.

[123] K. Nielsch, R.B. Wehrdpohn, J. Kirschner, U. Gosele, S.F. Fischer, H. Kronmuller, Appl. Phys. Lett. 79 (2001) 1360.

[124] A.J. Yin, J. Li, A.J. Bennet, J.M. Xu, Appl. Phys. Lett. 79 (2001) 1039.

[125] R.M. Metzger, M. Sun, G. Zangari, M. Shamsuzzoha, Mater. Res. Soc. Symp. Proc., 636, D9.33.1, 2001.

[126] M. Sun, G. Zangari, M. Shamsuzzoha, R.M. Metzger, Appl. Phys. Lett. 78 (2001) 2964.

[127] L. Menon, S. Bandopadhyay, Y. Liu, H. Zeng, D.J. Sellmyer, J. Nanosci. Nanotechnol. 1 (2001) 149.

[128] S. Kawai, R. Ueda, J. Electrochem. Soc. 122 (1975) 32.

[129] H. Daimon, O. Kitakami, O. Inagoya, A. Sakemoto, Japan J. Appl. Phys. 30 (1991) 282.

[130] P.R. Evans, G. Yi, W. Schwarzacher, Appl. Phys. Lett. 76 (2000) 481.

[131] M. Moskovits, International Patent, 5202290, 1993.

[132] D. Xu, X. Shi, G. Guo, L. Gui, Y. Tang, J. Phys. Chem. B 104 (2000) 5061.

[133] N. Kouklin, S. Bandopadhyay, S. Tereshin, A. Varfolomeev, D. Zaretsky, Appl. Phys. Lett. 76 (2000) 460.

[134] D. Routkevich, A.A. Tager, J. Haruyama, D. Almawlawi, M. Moskovits, J.M. Xu, IEEE Trans. Electron. Devices 43 (1996) 1646.

[135] D.J. Pena, B. Razavi, P.A. Smith, J.K. Mbindyo, M.J. Natan, T.S. Mayer, T.E. Mallouk, C.D. Keating, Mater. Res. Soc. Symp. Proc. 636, D4.6.1, 2001.

[136] N.A. Gershenfeld, L.A. Chuang, Science 275 (1997) 350.

[137]  G. Yi, W. Schwarzacher, Appl. Phys. Lett. 74 (1999) 1746.

[138]  X.F. Wang, L.D. Zhang, J. Zhang, H.Z. Shi, X.S. Peng, M.J. Zhang, J. Fang, J.L. Chen, B.J. Gao, J. Phys. D 34 (2001) 418.

[139]  G.L. Hornyak, C.J. Patrissi, C.R. Martin, J. Phys. Chem. B 101 (1997) 1548.

[140]  C.A. Foss Jr., G.L. Hornyak, J.A. Stockert, C.R. Martin, J. Phys. Chem. 98 (1994) 2963.

[141]  P. Forrer, F. Schlottig, H. Siegenthaler, J. Appl. Electrochem. 30 (2000) 533.

[142]  S.L. Pan, D.D. Zeng, H.L. Zhang, H.L. Li, Appl. Phys. A 70 (2000) 637.

[143]  H. Cao, C. Tie, Z. Xu, J. Hong, H. Sang, Appl. Phys. Lett. 78 (2001) 1592.

[144]  M.A. Rouhi, Chem. Eng. News 79 (2001) 29.

[145]  A. Hellemans, IEEE Spectrum 38 (2001) 6.

[146]  A.G. Rinzler, J.H. Hafner, P. Nikolaev, L. Luo, S.G. Kim, D. Tomanek, P. Nordlander, D.T. Colebert, R.E. Smalley, Science 269 (1995) 1550.

[147]  S. Liu, J. Xhu, Appl. Phys. A 70 (2000) 673.

[148]  J.S. Suh, J.S. Lee, Appl. Phys. Lett. 75 (1999) 2047.

[149]  Z.H. Yuan, H. Huang, H.Y. Dang, J.E. Cao, B.H. Hu, S.S. Fan, Appl. Phys. Lett. 78 (2001) 3127.

[150]  T. Iwasaki, T. Motoi, T. Den, Appl. Phys. Lett. 75 (1999) 2044.

[151]  J. Goldberger, R. He, Y. Zhang, S. Lee, H. Yan, H.-J. Choi, P. Yang, Nature 42 (2003) 599.

[152]  A.K. Srivastava, S. Madhavi, T.J. White, R.V. Ramanujan, J. Mater. Chem. 15 (2005) 4424.

[153]  L. Vazquez, et al., J. Phys. Chem. 96 (1992) 10454.

[154]  R.T. Potzschke, et al., Electrochim. Acta 40 (1995) 1469.

[155]  J.V. Zoval, et al., J. Phys. Chem. 100 (1996) 837.

[156]  H. Martín, et al., Langmuir 13 (1997) 100.

[157]  M.P. Zach, K.H. Ng, R.M. Penner, Science 290 (2000) 2120.

[158]  Y. Gimeno, et al., Chem. Mater. 13 (2001) 1857.

[159]  Y. Gimeno, et al., J. Phys. Chem. B 106 (2002) 4232.

[160]  F. Favier, et al., Science 293 (2001) 2227.

[161]  J.V. Zoval, et al., J. Phys. Chem. B 102 (1998) 1166.

[162]  M.P. Zach, J.T. Newberg, L. Sierra, J.C. Hemminger, R.M. Penner, J. Phys. Chem B 107 (2003) 5393.

[163]  M.P. Zach, K. Inazu, K.H. Ng, J.C. Hemminger, R.M. Penner, Chem. Mater. 14 (2002) 3206.

[164]  N. Ravishankar, V.B. Shenoy, C. Barry Carter, Adv. Mater. 16 (1) (2004) 76.

[165]  X. Xiong, P. Makaram, K. Bakhtari, S. Somu, A. Busnaina, J. Small, N. McGruer, J. Park, Mater. Res. Soc. Symp. Proc. Vol. 901E, 2006.

[166]  J.G. Partridge, S.A. Brown, C. Siegert, A.D.F. Dunbar, R. Nielson, M. Kaufmann, R.J. Blaikie, Microelectron. Eng. 73 (2004) 583.

[167]  J.P. You, J.H. Choi, S. Kim, X. Li, R. Stanley Williams, R. Ragan, Nano Letters 6 (2006) 1858.

[168] P. Kumar, M.G. Krishna, A.K. Bhatnagar, A.K. Bhattacharya, Int. J. Nanomanufacturing 2 (2008) 477.

[169] H. Kanno, A. Kenjo, T. Sadoh, M. Miyao, Mater. Res. Soc. Symp. Proc. 891, EE06-08.1, 2006.

[170] Y. Wang, L. Wang, B. Tang, D.-K. Choi, Thin Solid Films 515 (2006) 2507.

[171] J. Jang, J.Y. Oh, S.K. Kim, Y.J. Choi, S.Y. Yoon, C.O. Kim, Nature 395 (1998) 481.

[172] S.Q. Li, Y.X. Liang, T.L. Guo, Z.X. Lin, T.H. Wang, Mater. Lett. 60 (2006) 1492.

[173] Y.-T. Jang, J.-H. Ahn, B.-K. Ju, Y.-H. Lee, Solid State Commun. 126 (2003) 305.

[174] Y. Zhang, A. Chang, J. Cao, Q. Wang, W. Kim, Y. Li, N. Morris, E. Yenilmez, J. Kong, H. Dai, Appl. Phys. Lett. 79 (2001).

[175] T. Ichinokawa, H. Itoh, Y. Sakai, J. Anal. At. Spectrom. 14 (1999) 405.

[176] M. Saka, R. Ueda, J. Mater. Res. 20 (2005) 2712.

[177] P. Kumar, M.G. Krishna, A.K. Bhattacharya, Int. J. Nanoscience 7 (2008) 255.

[178] A.M. Deus, M.A. Fortes, P.J. Ferreira, J.B. Vander Sande, Acta Mater. 50 (2002) 3317.

[179] R. Dhanasekaran, P. Ramasamy, IL Nuovo Cimento 7 (1986) 506.

[180] C. Noguez, Opt. Mater. 27 (2005) 1204.

[181] Y.F. Guan, A.V. Melechko, A.J. Pedraza, M.L. Simpson, P.D. Rack, Nanotechnology 18 (2007) 335306.

[182] D. Riabinina, C. Durand, F. Rosei, M. Chaker, Phys. Status Solidi, A 204 (2007) 1623.

[183] G. Conibear, M. Green, R. Corkish, Y. Cho, E.-C. Cho, C.-W. Jang, T. Fangsuwannarak, E. Pink, Y. Huang, T. Puzzer, T. Trupke, B. Richards, A. Shalav, K.-L. Lin, Thin Solid Films 511 (2006) 654.

[184] T.D. James, J.S. Milne, A.J. Keting, G. Parish, C.A. Musca, J.M. Dell, L. Faraone, IEEE Trans. (2006) 431. 1-4244-453-3.

[185] J. Diener, N. Kunzner, E. Gross, D. Kovalev, M. Fujii, Phys. Status Solidi 202 (2005) 1432.

[186] A.M. Morales, C.M. Lieber, Science 279 (1998) 208.

[187] T. Ono, H. Saitoh, M. Esashi, Appl. Phys. Lett. 70 (1997) 1852.

[188] Y.F. Zhang, Y.H. Tang, N. Wang, D.P. Yu, C.S. Lee, I. Bello, S.T. Lee, Appl. Phys. Lett. 72 (1998) 1835.

[189] N. Wang, Y.H. Tang, Y.F. Zhang, C.S. Lee, S.T. Lee, Chem. Phys. Lett. 283 (1998) 368.

[190] Y.F. Zhang, Y.H. Tang, N. Wang, C.S. Lee, I. Bello, S.T. Lee, J. Cryst. Growth 197 (1999) 136.

[191] N. Wang, Y.F. Zhang, Y.H. Tang, C.S. Lee, S.T. Lee, Appl. Phys. Lett. 73 (1998) 3902.

[192] Y.H. Tang, Y.F. Zhang, C.S. Lee, N. Wang, D.P. Yu, I. Bello, S.T. Lee, Mater. Res. Soc. Symp. Proc. 526, 73, 1998.

[193] N. Wang, Y.H. Tang, Y.F. Zhang, C.S. Lee, S.T. Lee, Phys. Rev. B 58 (1998) R16024.

[194] C.K. Chan, H. Peng, G. Liu, K. McIlwrath, X.F. Zhang, R.A. Huggins, Y. Cui, Nature Nanotechnol. 3 (2008) 31.

[195] Q. Li, X. Zhu, H. Xiang, S.M. Koo, D.E. Ionnou, J. Kopanski, J.S. Suehlee, C.A. Richter, Nanotechnology 18 (2007) 235204.

[196] A.V. Kabashin, M. Meunier, Mater. Sci. Eng. B101 (2003) 60.

[197] A.J. Pedraza, J.D. Fowlkes, Y.F. Guan, Appl. Phys. A 77 (2003) 277.

[198] S.J. Henley, J.D. Carey, S.R.P. Silva, Appl. Surf. Sci. 253 (2007) 8080.

[199] S. Loreti, A. Santoni, J. Lancok, I. Menicucci, C. Minarini, D. Della Sala, Thin Solid Films 458 (2004) 1.

[200] R.S. Wagner, W.C. Ellis, Appl. Phys. Lett. 4 (1964) 89.

[201] J. Westwater, D.P. Gosain, S. Tomiya, S. Usui, H. Ruda, J. Vac. Sci. Technol. B 15 (1997) 554.

[202] H. Huang, S. Mao, H. Feick, H.Q. Yan, Y.Y. Wu, H. Kind, E. Weber, R. Russo, P.D. Yang, Science 292 (2001) 1897.

[203] Q. Liu, S.S. Xie, L.F. Sun, D.S. Tang, W.Y. Zhou, C.Y. Wang, W. Liu, Y.B. Li, X.P. Zhou, G. Wang, J. Mater. Res. 16 (2001) 683.

[204] C. Choi, W.S. Kim, Y.S. Park, S.M. Lee, D.J. Bae, Y.H. Lee, G.S. Park, W.B. Choi, N.S. Lee, J.M. Kim, Adv. Mater. 12 (2000) 746.

[205] J. Zhang, F. Jiang, Z. Dai, J. Phys. D: Appl. Phys. 36 (2003) 2046.

[206] V. Sharma, B.V. Kamenev, L. Tsybeskov, Mater. Res. Soc. Symp. Proc., 832, F7.20., 1, 2005.

[207] M. He, P. Zhou, S.N. Mohammad, G.L. Harris, J.B. Halpern, J. Cryst. Growth 231 (2001) 357.

[208] S.M. Zhou, Y.S. Feng, L.D. Zhang, Chem. Phys. Lett. 369 (2003) 610.

[209] C.Y. Lee, T.Y. Tseng1, S.Y. Li, P. Lin, Tamkang J. Sci. Eng. 6 (2003) 127.

[210] E.I. Givargizov, J. Cryst. Growth 31 (1975) 20.

# Engineering the Synthesis of Carbon Nanotubes to Fabricate Novel Nanostructures

M. Mann[1], B. Milne[1] and K. Teo[2]

[1]*Cambridge University Engineering Department, Cambridge, UK*
[2]*AIXTRON Ltd. Nanoinstruments, Swavesey, Cambridge, UK*

## CONTENTS

## 5.1  INTRODUCTION

Contrary to popular belief, carbon nanotubes (CNTs) were not discovered by Iijima[1] in 1991, but they were discovered by Radushkevich and Lukyanovich[2] in 1952, who published clear transmission electron micrographs of 50-nm diameter tubes made of carbon in the *Russian Journal of Physical Chemistry*. Unfortunately, because of the political tensions of that time, this work went largely unnoticed. With the discovery that CNTs were

responsible for the high strength of Damascus steel[3], it became clear that their favourable structural properties had been employed for some time, and that it was the inability to characterize material so small that prevented an even earlier discovery.

Iijima found CNTs in the insoluble material of arc-burned graphite rods and went onto produce extensive work on arc discharge grown CNTs. He is responsible for making the connection between CNTs and fullerenes, where the structure of the former was determined to be the latter split into two, conjoined by a graphene cylinder of varying length. Since this connection was made, there has been extensive research into the properties, synthesis and possible applications of CNTs.

CNTs are composed of $sp^2$ covalently bonded carbon in which graphene walls are rolled up cylindrically to form tubes. The ends can either be left open, which is an unstable configuration due to incomplete bonding, they can be bonded to a secondary surface, not necessarily of carbon, or they can be capped by a hemisphere of $sp^2$ carbon, with a fullerene-like structure[4]. In terms of electrical properties, single-walled CNTs can be either semiconducting or metallic and this depends upon the way in which they roll-up, as illustrated in Figure 5.1.

Multi-walled CNTs are non-semiconducting (i.e. semimetallic like graphite) in nature. Their diameters range from 2 to 500 nm and their lengths range from 50 nm to a few millimetres. Multi-walled CNTs contain several concentric, coaxial graphene cylinders with interlayer spacings of ~0.34 nm[6]. This is slightly larger than the single crystal graphite spacing which is 0.335 nm. Studies have recently shown that the inter-shell spacing can range from 0.34 to 0.39 nm, where the inter-shell spacing decreases with increasing CNT diameter with a pronounced effect in smaller diameter CNTs (such as those smaller than 15 nm) as a result of the high curvature in the graphene sheet[7, 8]. As each cylinder has a different radius, it is impossible to line the carbon atoms up within the sheets as they do in crystalline graphite. Therefore, multi-walled CNTs tend to exhibit properties of turbostratic graphite in which the layers are uncorrelated. For instance, in highly crystallized multi-walled CNTs, it has been shown that if contacted externally, electric current is conducted only through the outermost shells[9].

CNTs typically have a Young's modulus ~10 times that of steel[10] and an electrical conductivity many times that of copper[11]. Some important properties of CNTs are listed in Table 5.1.

CNTs can be applied to many devices and technologies. Semiconducting single-walled CNTs have been investigated as transistors or logic elements[13–16]. The electronic properties of a single CNT in these devices vary greatly with adsorbed chemical species, which means they can be used as
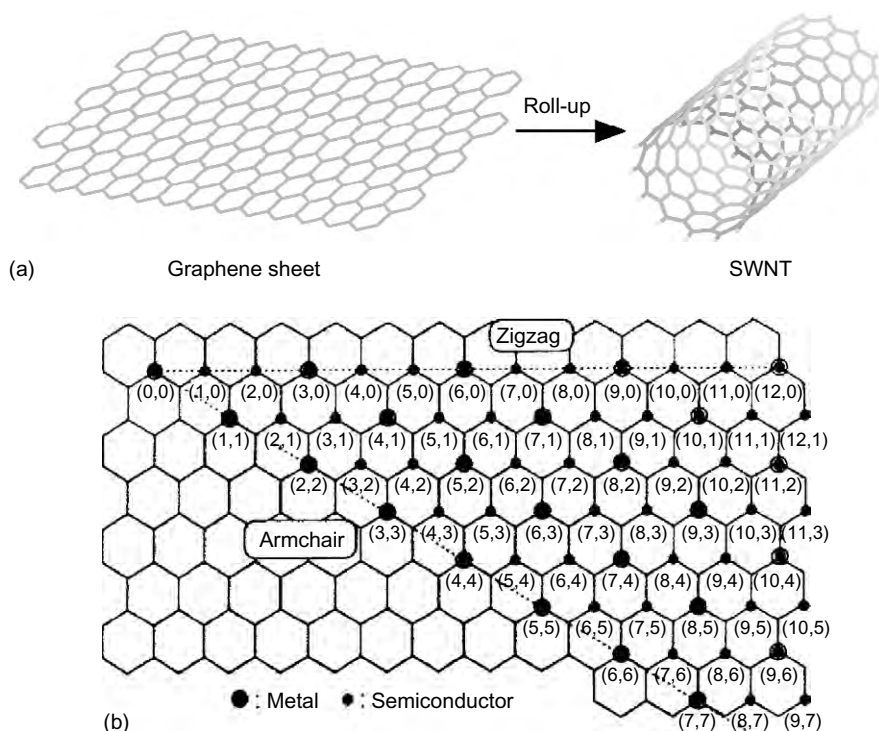
**FIGURE 5.1** *(a) A graphene sheet rolled up to obtain a single-walled CNT. (b) The map shows the different single-walled CNT configurations possible. Were the graphene sheet to roll-up in such a way that the atom at (0,0) would also be the atom at (6,6), then the CNT would be metallic. Likewise, if the CNT wrapped up so that the atom at (0,0) was also the atom at (6,5), the CNT would be semiconducting. The small circles denote semiconducting CNTs and the large circles denote non-semiconducting CNTs. Two-thirds of CNTs are semiconducting and one-third metallic.*
*Source: Ref. [5].*

sensors[17, 18]. In highly crystallized CNTs, the coherent nature of electron transport can be used in spin-electronic devices[19]. They can also be used as electromechanical sensors as their electrical characteristics change upon structural mechanical deformation[20].

CNTs can be used as electrodes in electrochemical supercapacitors[21] because their structure leads to large surface areas with higher charge storage capabilities. The high electrical conductivity and the relative inertness of CNTs also make them potential candidates as electrodes for use in electrochemical reactions[22]. There has been research into using CNTs to store hydrogen[23], though the amount stored is not as high as originally anticipated[24]. CNTs mechanically deflect upon electric stimulation which opens up the possibility of their application in cantilevers and actuators[21]. There has

| Table 5.1 | Properties of CNTs | |
|---|---|---|
| **Mechanical properties** | | |
| Young's modulus of multi-walled CNTs | $\sim$1–1.2 TPa | |
| Young's modulus of single-walled CNT ropes | $\sim$1 TPa | |
| Tensile strength of single-walled nanotube ropes | $\sim$60 GPa | |
| **Thermal properties at room temperature** | | |
| Thermal conductivity of single-walled CNTs | 1750–5800 WmK | |
| Thermal conductivity of multi-walled CNTs | >3000 WmK | |
| **Electrical properties** | | |
| Typical resistivity of single- and multi-walled CNTs | $10^{-6}\,\Omega$m | |
| Typical maximum current density | $10^7$–$10^9$ A cm$^2$ | |
| Quantized conductance, theoretical/measured | $(6.5\,k\Omega)^{-1}/(12.9\,k\Omega)^{-1}$ | |
| **Electronic properties** | | |
| Single-walled CNT band gap | | |
| Whose nanometre is divisible by 3 | 0 eV (metallic) | |
| Whose nanometre is non-divisible by 3 | 0.4–0.7 eV (semiconducting) | |
| Multi-walled CNT band gap | $\sim$0 eV (non-semiconducting) | |

*Source: Ref. [12].*

also been extensive work on their application in composites which utilize their physical strength and small size. Here single-walled CNTs are favoured as they are more flexible whilst still very strong[25].

In the near term, however, the CNT applications most likely to come to market first are their employment in various electron sources. Much research has been focused on the application of CNTs to field emission sources because they have several advantages over other field-emitting materials.

When compared with other commonly used emitters such as tungsten, the CNT's covalent bonds are much stronger than tungsten's metallic bonds. As a result, the activation energy for surface migration and diffusion of the emitter atoms is much larger than for a tungsten electron source, making it much more unlikely. Therefore, the tip can withstand the extremely strong fields (several volts per nanometre) needed for field emission. Related to this point, nanotubes can be high stable emitters, even at temperatures up to 2000K[26]. The combination of high temperature and electric field in metals causes the well-known mechanism of field-sharpening of tips by surface diffusion, which increases the local field, current and temperature further, creating a positive feedback mechanism resulting in unstable thermal runaway leading to emitter destruction for metal-based emitters. In contrast, the resistance

of a nanotube decreases with temperature which limits $I^2R$ heat generation. Consequently, its temperature varies sub-linearly with the current.

The best field emission tip should be whisker-like (such as a CNT), followed by the sharpened pyramid, hemispheroidal and pyramidal shapes[27]. When compared with other film field emitters such as diamond or amorphous carbon structures, CNTs have a high aspect ratio, a small radius of curvature of the cap and good conductance[28]. Because of the CNT's extremely large Young's modulus and maximal tensile strength, they are able to withstand the high fields around them and current densities coming from within. The graphene walls in them are parallel to the filament axis resulting in the nanotubes (whether metallic single-walled or multi-walled) exhibiting high electrical conductivity at room temperature. Finally, carbon has one of the lowest sputter coefficients[29], which is an advantage because an electron source is usually bombarded by positive ions.

Consequently, the application of CNTs to a wide array of field emission-based devices has been explored. However, to obtain a sufficiently high field at the tip of the CNT, the growth has to be tailored on a surface of the device.

The next section will describe the basics of various synthesis methods and will go on to detail how the growth of CNTs by these methods has been tailored to suit various device architectures.

## 5.2  SYNTHESIS METHODS

The synthesis of CNTs is of the utmost importance if they are to be seriously considered for device applications. It is possible to choose from a range of synthesis methods, but they each have their relative advantages and disadvantages. The lack of CNT-based products available in the marketplace indicates the level of difficulty engineers have to overcome in utilizing the various synthesis methods to produce stable and reliable CNT devices.

## 5.3  SYNTHESIS OF CNTS BY ARC DISCHARGE

CNTs were observed in 1991 by Iijima who employed a method to fabricate $C_{60}$ fullerenes[1]. The method used was the arc discharge method, which consisted of two carbon rods separated by approximately 1mm placed end-to-end in a chamber which is either held at low pressure or filled with inert gas[30]. A direct current of 50–100A driven by a potential difference of ~20V creates a high temperature discharge between the two electrodes. The discharge partly vaporizes one of the carbon electrodes and forms a small, rod-shaped deposit on the other electrode. On analysing the contents of the

(a)



(b)
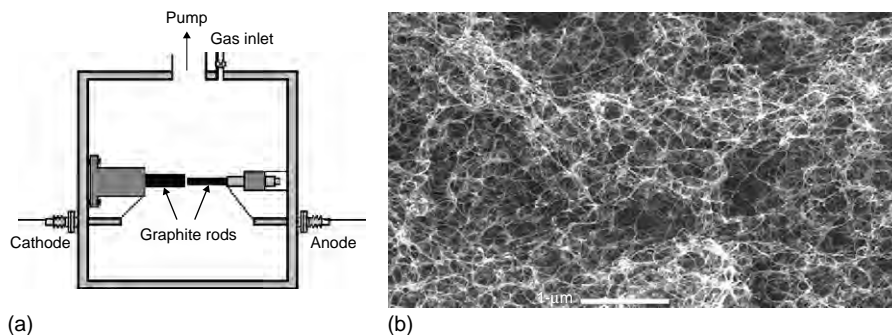
rods[31], there is a large amount of amorphous carbon – as much as 70%. To improve the yield, catalyst metals such as Ni, Fe or Co are added to the graphite rods[32] which results in catalyst particles being trapped inside the grown CNTs. Figure 5.2 illustrates both a schematic of a typical apparatus used and the resultant CNTs grown.

Arc discharge produces both single-walled and multi-walled CNTs of varying lengths. The CNTs are normally highly crystalline, have few defects and can be as long as 50μm, but during synthesis, they are covered by amorphous carbon detritus[33]. Consequently, CNTs grown by this method must be purified and separated before they can be put to significant use. A typical method[34] is to thermally anneal the CNTs in air at ~500°C, which burns away the carbonaceous detritus, followed by continual immersion and filtering in a strong acid, such as HCl, to remove the catalyst particles. To separate the CNTs, boiling CNTs in 30% nitric acid is a typical technique.

## 5.4 SYNTHESIS OF CNTs BY LASER ABLATION

Laser ablation works using similar principles to arc discharge, the difference being that with this method, a pulsed laser is focused onto a graphite target in a high temperature reactor. An inert gas is bled into the chamber and CNTs form on the cooler surfaces of the reactor when the vaporized carbon condenses. The process was developed by Smalley's group[35]. Smalley and co-workers modified an existing process used to create metal molecules; they substituted the metal target for graphite. The method was later refined when the graphite targets were changed to a graphite–catalyst composite; the best yield coming from a 50:50 mixture of cobalt and nickel within the graphite to synthesize single-walled CNTs[36]. Figure 5.3 illustrates both the schematic of the apparatus used and the resultant CNTs grown.

Even though this method produces only 30% detritus – the same purification and separation procedures must be observed – it is the most expensive[31]
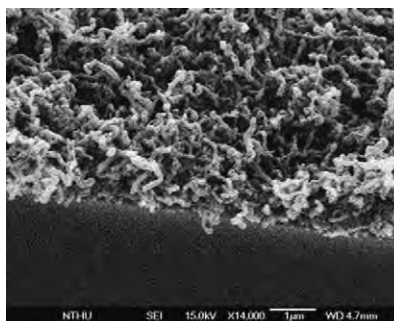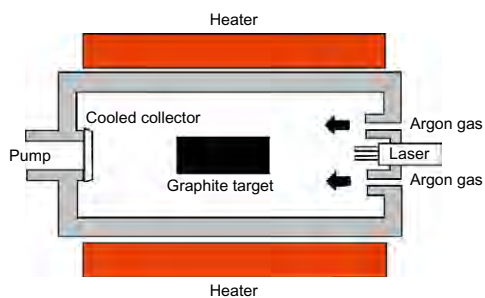
**FIGURE 5.3**

*(a) Schematic diagram of typical apparatus used to grow CNTs by laser ablation. (b) A typical result of CNTs grown by laser ablation. Note the lack of orientation in the grown CNTs. The scale bar is 1 μ.*

and widely used method. The diameter of the CNTs can be controlled by altering the reaction temperature which the arc discharge cannot control.

Both arc discharge and laser ablation are the principal methods for synthesizing small quantities of high-quality, low-defect CNTs. However, both methods involve sublimating the carbon source, so the process isn't realistically scalable to mass production. Also, both these methods produce tangled CNTs immersed in amorphous carbon detritus, so it is not practicable to make even small electrical devices with these CNTs due to the great difficulty in manipulating single CNTs on the nanoscale.

## 5.5  SYNTHESIS OF CNTs BY CHEMICAL VAPOUR DEPOSITION

The deposition of carbon from hydrocarbon vapour with the use of a catalyst was first reported in 1959[37], but CNTs were not synthesized by the chemical vapour deposition method, or CVD method until 1993[38]. The process is commonly enhanced by the addition of plasma (plasma-enhanced CVD, or PECVD) which can reduce the temperature required to initiate CNT growth and induces alignment of the grown CNTs because of the high local electric field.

The process involves two steps: (1) the preparation of the catalyst on a surface and (2) the growth by the decomposition of reactant gases. The catalyst metals commonly used for nanotube growth are Fe, Ni and Co[39].

There are several routes for the production of catalyst nanoparticles, the three main methods being (1) the wet catalyst method, (2) etching of a catalyst metal and (3) the coalescence of thin catalyst films. The wet catalyst method involves the deposition of a metal nitrate/bicarbonate solution onto a surface. On drying, the salt in this solution crystallizes to form small islands of the metal salt. The salt is reduced to a metal oxide by heating or calcinations and the oxide is then reduced by $H_2$ and/or thermal

decomposition resulting in the formation of metallic catalyst islands from which the CNTs grow[40, 41]. The etching technique involves depositing a layer (<100 nm) of the desired catalyst metal by either evaporation or by sputter coating. Catalyst islands are formed this time by bombarding the catalyst metal with ions or by plasma etching[42, 43].

The most commonly used form of catalyst preparation for devices is coalescence (shown in Figure 5.4).

A thin film (typically less than 10nm) of Fe, Co or Ni is deposited onto a substrate by evaporation or sputter coating. Upon heating, the thin film breaks up (known as dewetting), agglomerating to form nano-islands as a result of increased surface mobility and the strong cohesive forces between the metal atoms[44, 45]. CNT growth then nucleates from these nano-islands.

To initiate CNT growth, two gases are inlet into an evacuated reaction chamber, a process gas (ammonia, nitrogen or hydrogen, etc.) and a



**(a) Wet catalyst**

Catalyst metal salt solution (e.g. nitrate, bicarbonate)

Gas

Substrate

Inking, printing or spin coating

Catalyst metal oxide nano-particles

Substrate

Heat reduction or calcination to reduce metal salt to oxides

**(b) Etching**

Ions

Catalyst metal

Substrate

Thick catalyst layer or catalyst metal substrate

Catalyst metal surface islands

Substrate

Plasma etching or ion bombardment

**(c) Coalescence**

Metal thin film (nm)

Substrate

Thin catalyst film by evaporation/sputtering

Catalyst metal nanoclusters

Substrate

Heat to promote island formation

**FIGURE 5.4** *Methods of producing nanosized catalysts for nanotube growth.*

carbon-containing gas (acetylene, ethylene, methane, ethanol, etc.) at a temperature of 550°C–900°C. Growth occurs at the site of the metal catalyst. The carbon-containing gas is broken down at the surface of the catalyst particle and then diffuses around or through the particle (dependent on conditions) to the edge of the particle where the CNTs form. The mechanism of this process is still controversial.

Catalyst particles stay either at the tips of the CNTs during the growth process or they stay at the base of the CNTs depending on the adhesion between the catalyst particle and the support (as shown in Figure 5.5).

In CVD, the energy required to break down the reactant deposition gases into graphene comes solely from the heat supplied to the catalyst particle and its immediate environs. There is no alignment of CNTs from the CVD process. The grown CNTs are often randomly orientated and resemble spaghetti. However, under certain reaction conditions, even in the absence of a plasma, closely spaced nanotubes will maintain a vertical growth direction resulting in a dense array of tubes resembling a carpet or forest. In PECVD, the applied plasma creates a sheath above the substrate in which an electric field perpendicular to the substrate is induced. This field breaks down some of the deposition gases and vertically aligns the CNTs as they follow the induced field (as shown in Figure 5.6).

Both CVD and PECVD hold a number of advantages over other synthesis methods. For tip growth, nanotube length increases with deposition pressure, and linearly with deposition time up to certain lengths[46]. The diameter is controlled by the thickness of the catalyst deposited, and the position of the CNTs can be controlled by where the catalyst is positioned. For instance, lithographical techniques (described below) can be employed
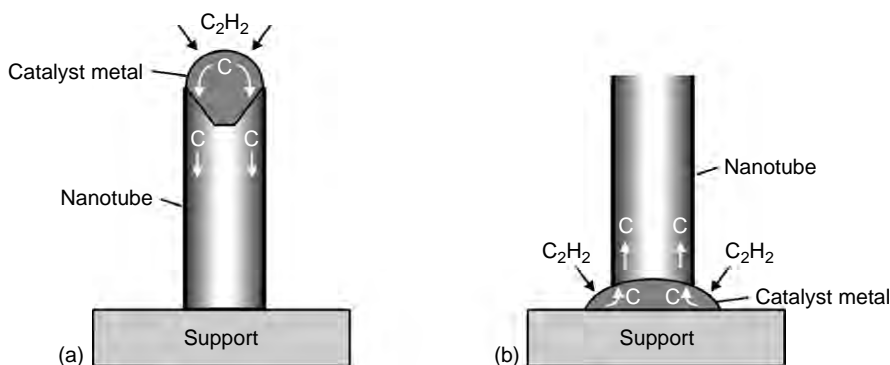


**FIGURE 5.5**   *There are two types of growth, tip or base growth, which results from differences in the catalyst–support interaction. (a) Weak catalyst–support interaction, (b) strong catalyst–support interaction. Source: Ref. [39].*
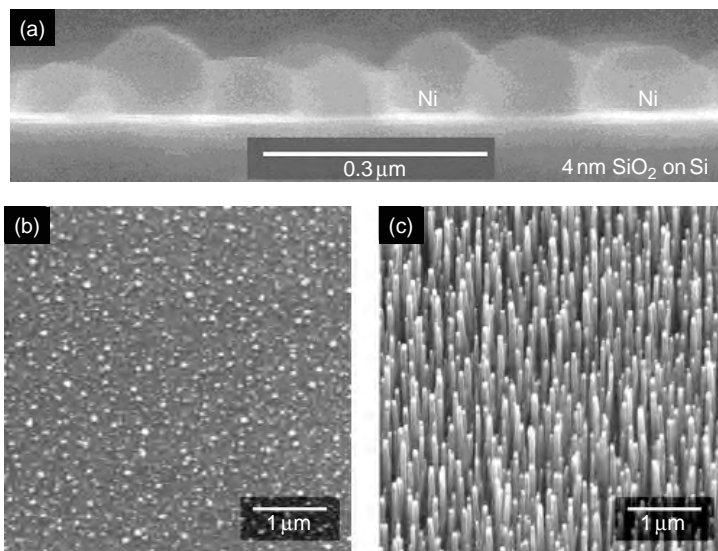
**FIGURE 5.6** *When Ni nanoclusters ((a) and (b)) are on a 4-nm layer of $SiO_2$ deposited onto a Si substrate, they exhibit weak interactions (c.f. 'hydrophobic') with their supports hence favouring tip growth (the Ni is the high contrast dot seen at the tip of the nanotube as in (c)).*

to deposit catalyst dots to control the position of grown CNTs which can be employed in field emission devices[47]. This results in much more control over the dimensions of the CNTs and removes the need to purify and separate CNTs which is needed when they are grown by other methods.

The quality of grown CNTs is subjective, since their quality depends on the structures required. Some applications require high purity and crystallinity, others require tight dimensional control, whilst others might require high packing densities and/or alignment.

## 5.6 FLUIDIZED BED CVD AND RESULTANT APPLICATIONS

For applications where the structure benefits from a tangled, spaghetti-like structure, such as supercapacitors, electrodes, hydrogen storage and composites, it is common for engineers to buy CNTs in bulk from suppliers and to fabricate devices post-growth, with CNTs grown by CVD but nucleating from catalysts in a fluidized bed. The nano-agglomerate fluidized bed method allows for the continuous production of CNTs, where catalyst metal compounds are loaded onto a support, reducing or dissociating the compounds to nanosized metal particles and growing CNTs on the catalyst

support by CVD. The process produces CNTs of high quality which are typically 100 nm in diameter and 0.5–1000 μm in length, inexpensively in large quantities. Therefore, when large numbers of CNTs are required, it makes sense to post-process CNTs rather than try to engineer their growth.

One particular application is the use of CNTs as network transistors, rather than individual transistors which have been demonstrated by many researchers[48], one of which is a group based at Cambridge University Engineering Department[49]. Single-walled CNT thin films were prepared by first dispersing high-purity tubes with a concentration of 0.1mg/L by surfactant-aided (1wt.% sodium dodecyl sulphate) sonication. This process is required because CNTs



**FIGURE 5.7**  *An electron micrograph showing the structure of a CNT network transistor.*

obtained from manufacturers tend to be bunched together. The CNTs were then separated from the solution by vacuum filtration through 220-nm diameter pores. The ester membrane containing the thin film of CNTs was then stamped onto a thermally oxidized $SiO_2$/Si (n-type) substrate with an oxide thickness of 200 nm, heated to 70°C on a hot plate and etched in acetone and isopropanol baths, leaving behind Single-Walled Nanotubes thin films. Pd contacts were then laid down on top of the network to test transistor characteristics (Figure 5.7). Transistors made in this way have been found to have on–off ratios of $10^3$ and mobilities of 0.14 cm$^2$/Vs, which clearly indicates that improvements need to be made with this process. However, this is a very cheap way of making devices and if characteristics are sufficiently improved, cheap logic circuits could be made, where size is not an issue. Incidentally, this process implemented using other nanowires, such as zinc oxide. Devices have been fabricated and have been shown to exhibit similar characteristics.

To make smaller devices, it is better to prepare the CNTs in situ. The next section will describe many ways in which the synthesis processes described above can be modified to grow CNTs with specific geometries to suit various applications.

## 5.7  LOWERING THE TEMPERATURE OF CVD

For CNTs to be compatible with current Complementary metal-oxide-semiconductor (CMOS) technology, the temperature at which they are grown needs to be either significantly reduced or the time taken to grow them needs to be sufficiently quick, so as not to damage already-fabricated devices. For growth times of more than 2 mins, the target temperature should be 400°C, significantly below the temperatures used for CNT growth, which typically begin at 550°C dependent on catalyst type.
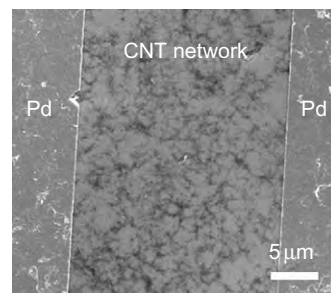
The temperature of the substrate can be reduced by cracking the gas feedstock remotely with a filament at a high temperature as shown in Figure 5.8a, and by heating the substrate separately at a lower temperature, the quality of already-fabricated devices is preserved.

Figure 5.8b shows multi-walled CNTs synthesized at a substrate temperature of 450°C. The growth temperature is slightly above that which CMOS can typically withstand, but because the growth time was short, the in-built devices suffer limited characteristic deformation as can be seen in Figure 5.9a and 5.9b. A mass spectrometer was positioned immediately below the substrate stage to determine the nature of species incident upon it with varying hot-filament power which is shown in Figure 5.9c. The mass spectrometer shows that when growth occurs, hydrocarbons of higher atomic mass are incident on the stage.
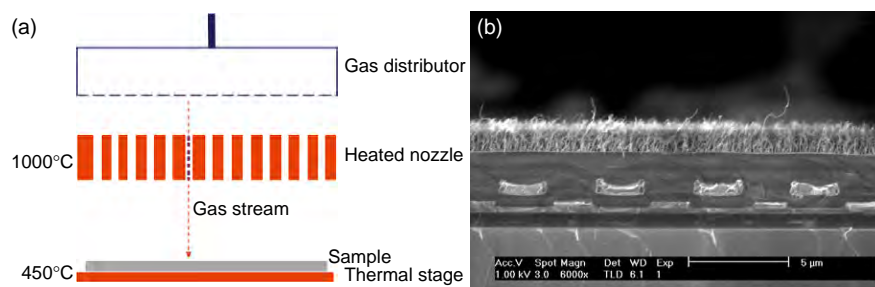


**FIGURE 5.8**   *(a) A schematic diagram of a setup used to grow CNTs at low temperatures. Gas is broken down by the heated nozzle at 1000°C instead of at the substrate surface enabling the substrate itself to be kept at a much lower temperature. (b) A cross section of the resultant growth of CNTs on CMOS. Four Al contacts can clearly be seen to be still intact.*
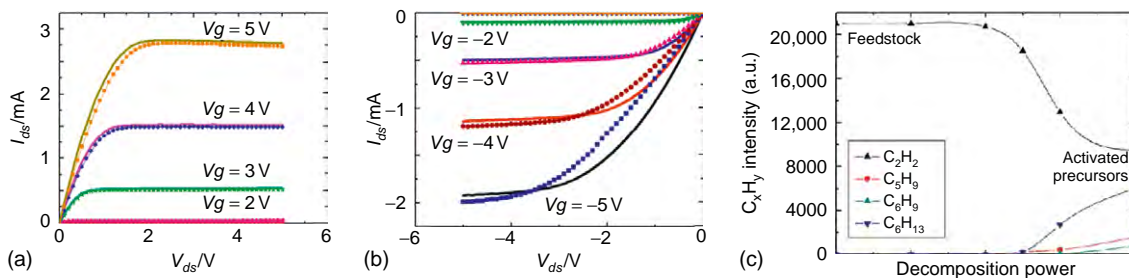


**FIGURE 5.9**   *(a) The transistor characteristic of a p-type MOSFET on CMOS before and after CNT growth with (b) showing the respective n-type device. In both cases, the smooth line shows the characteristic before deposition, with the dotted line showing the characteristic after deposition. The gaseous feedstock as a function of decomposition power is shown in (c). Longer chain hydrocarbons, rings and radical species are seen at higher power, indicating the breakdown of the acetylene feedstock.*

Single-walled CNTs have been grown using this method, also at a substrate temperature of 450°C (Figure 5.10a). A Raman spectrum of the grown CNTs was made to confirm the presence of single-walled tubes, which is shown in Figure 5.10b.

Modifying the growth in this way opens up the possibility of combining CNT devices with integrated circuits. Whilst there is currently no way to control CNT chirality during growth, and thus negating the possibility of single CNT transistors, it does enable the integration of devices such as sensors and may lead to the use of multi-walled CNTs as interconnects (provided that a reliable method can be found to contact the inner walls), or single-walled CNTs as interconnects (provided the growth density can be increased sufficiently). CNTs can also be used in CMOS as heat sinks because of their high surface area and high thermal conductivity, and they can also be utilized for the improvement of solder contacts.

## 5.8  LOCALIZED CNT GROWTH ON CHIPS

When CNTs are to be used for gas sensing applications, another way to protect already-fabricated devices on CMOS is to incorporate a micro-hot plate into the chip and to grow the CNTs on the heated area only. These micro-hot plates can also be used to subsequently raise the sensing CNTs to elevated temperatures to optimize their sensitivity and therefore isolate hot areas from destroying circuit devices. If the CNTs are not functionalized, they do not discriminate between gases. When gases adsorb onto the surface of CNTs, their conductivity changes. By measuring the change in
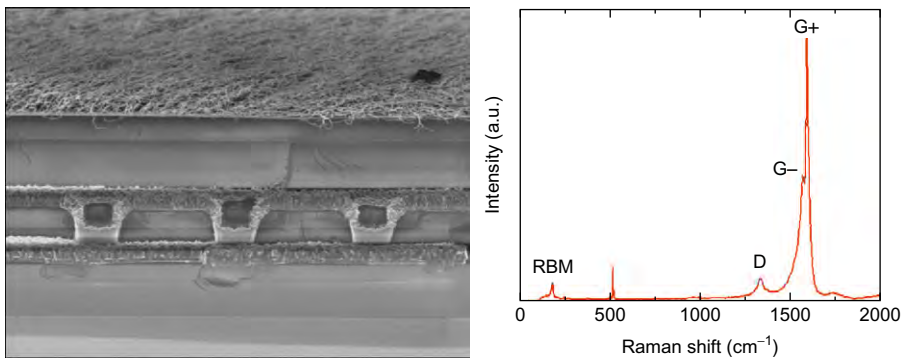


**FIGURE 5.10** *(a) A cross section showing a thin layer of single-walled CNTs grown on CMOS. Devices fabricated also survived. (b) The Raman spectrum of the grown CNTs. The G:D ratio is high, indicating low-defect single-walled CNTs. The radial breathing modes (RBM) indicate the CNTs to have radii around 1nm.*
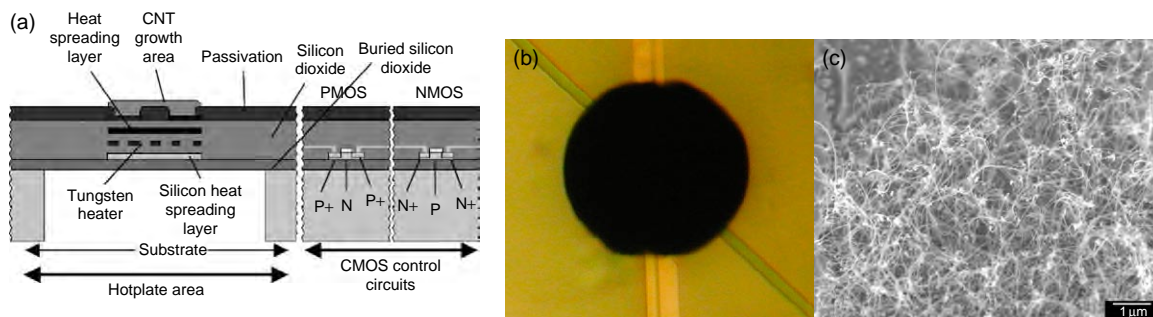
**FIGURE 5.11** *(a) Schematic cross section of the chip layout, (b) shows how the grown CNTs have turned the heater area black whilst (c) shows an electron micrograph of the grown CNTs. The scale bar is 1 μm.*
*Source: Ref. [50].*

conductivity, the amount of gas adsorbed can be found. Figure 5.11a shows a schematic diagram of such an integrated sensor[50]. The heater is made of tungsten embedded in an silcon-on-insulator (SOI) substrate. The CMOS control circuits are located in a different area of the chip.

CNTs were grown by CVD by heating the tungsten heater to 700°C. Gas feedstock was locally broken down above the heater with CNTs only growing in that area as seen in Figure 5.11b. Although the grown multi-walled CNTs (Figure 5.11c) were highly defective, which was confirmed by a Raman spectrum, this is actually an advantage for such a gas sensing device. The conductivity of the mat comes from the intertwining of the grown, spaghetti-like CNTs. The performance of the device would probably significantly improve by functionalization of the CNTs post-growth.

## 5.9 POSITIONAL CONTROL: LITHOGRAPHY

Lithography is by far the most commonly employed technique used to control the position of CNTs. In lithography there are three methods which are widely employed, optical lithography, electron beam lithography (e-beam) and focused ion beam (FIB) lithography.

The resultant pattern can be used in many ways. When growing CNTs, optical lithography is often used as a first step to produce alignment marks. Typically, small crosses are positioned in four corners of a substrate. Consequently, a metal with a high melting point such as molybdenum is then sputtered across the entire substrate. Metal is deposited on the resist, but also in the holes developed as a consequence of the lithography. If the substrate is then placed in acetone, this lifts off the resist and also the metal deposited on top of it, but leaves behind the molybdenum deposited
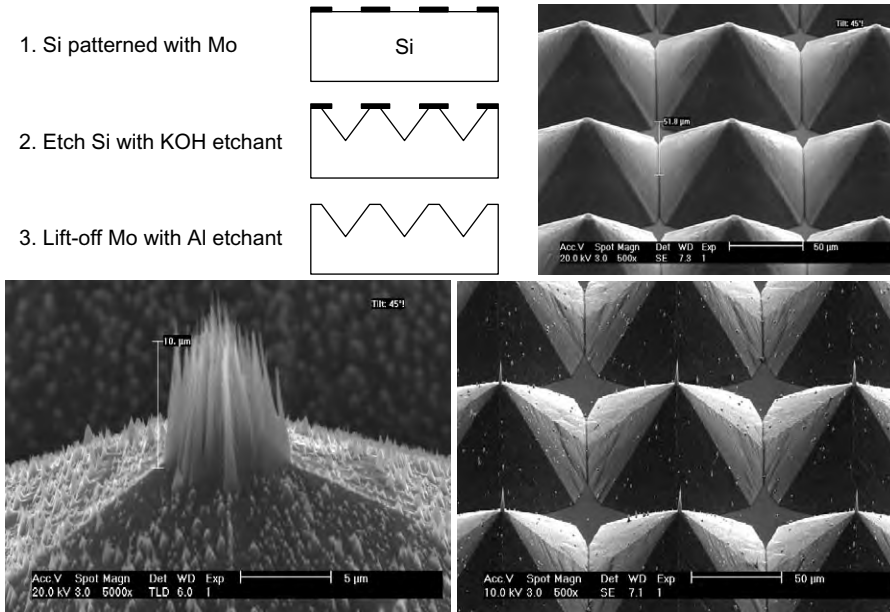
**FIGURE 5.12** *(a) Summary of the etching process of silicon, squares of molybdenum deposited by optical lithography act as a mask to produce an array of silicon pyramids shown in (b). By filling the etched gaps with PMMA leaving just the apex of the pyramid exposed, a group of CNTs can be grown at the top as in (c), but if e-beam lithography is employed, single CNTs can be grown at the apex of each pyramid as shown in (d).*

in the holes. The crosses can then be used to align an e-beam for higher resolution lithography, which will be described next. Optical lithography can also be used to deposit metal contacts or catalyst for CNTs on the micron scale. For instance, if patches of Fe 0.1nm in thickness are placed a few microns apart, single-walled CNTs grow between and have been used to fabricate and test single CNT transistors. They can also be used to grow localized, vertically aligned dense CNT forests, though this does not have any obvious application. For silicon of specific crystal orientations, a pattern can also be constructed so that a molybdenum patch can be used as a mask for silicon etching, which if done with squares as the mask will result in the formation of pyramids (see Figure 5.12).

The e-beam lithography can then be used to grow CNTs at the top of each silicon pyramid shown in Figure 5.12. By its nature, e-beam has a distinct advantage over optical lithography because of wave–particle duality and the much smaller wavelength of electrons. In practice, the minimum feature size is limited by the spot size which is of the order of a few tens of nanometres, but this process gives two orders of magnitude in resolution improvement
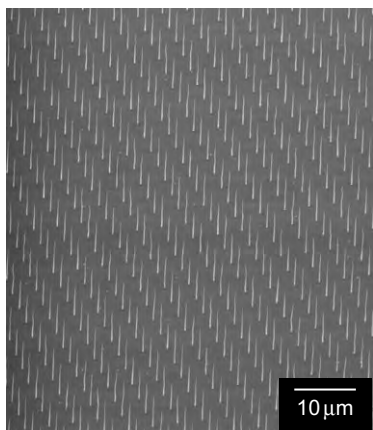
**FIGURE 5.13** *Highly uniform growth of individual nanotubes. Sample tilt 55°. The scale bar is 10μm.*

over optical lithography and can consequently be used to deposit an amount of catalyst equal to that required to grow a single CNT. This process, therefore, enables the placement of individual CNTs, which has uses in a variety of applications.

The simplest e-beam structures to make with individual CNTs are arrays. Arrays are made by exposing spin-coated resist to the e-beam to create a grid of spots approximately 100 nm across. The separation between spots can be varied. The resist is developed and catalyst sputtered to a thickness of 7–10 nm. After lift-off, array of 100-nm dots are left behind on the substrate surface. CNTs can then be grown by CVD, but if PECVD is used, the resultant CNTs will be aligned perpendicular to the surface. The key with this growth is to heat the substrate in such a way that the catalyst dewets to form only one particle. Higher growth temperatures approaching 1000°C tend to produce smaller CNTs as does a fast heating rate. Figure 5.13 shows such an array of CNTs grown by PECVD. The height is controlled by the growth time and is proportional for short growth times (of typically less than an hour).

One such application of arrays of CNTs is in the electron source in a microwave amplifier to replace the travelling wave tube (TWT). Microwave amplifiers are used extensively in satellites as transponders. The inefficient thermionic electron sources require heating and cannot be switched on instantaneously or directly modulated at the GHz frequencies required. An alternative method for microwave amplification reported recently[51] incorporates a microwave diode that instead uses a cold cathode (field-emitting) electron source consisting of 16 CNT arrays which operate at high frequency and at high current densities. The 16 arrays individually occupied an area of $0.5 \times 0.5 \, mm^2$ and consisted of 2500 uniform CNTs with an average diameter of 49 nm, height of 5.5 μm and a spacing of 10 μm (with a standard deviation in diameter of 4% and a standard height deviation of 6%)[52].

Cambridge University Engineering Department in collaboration with Thales, have successfully demonstrated a Class D (i.e. pulse mode/on–off) operation of a CNT array cathode at 1.5 GHz, with an average current density of 1.3 A/cm$^2$ and peak current density of 12 A/cm$^2$; these are compatible with TWT amplification requirements (>1 A/cm$^2$). Recently, they have also achieved 32 GHz direct modulation of a CNT array cathode under Class A (i.e. sine wave) operation, with over 90% modulation depth. This unique ability to directly modulate or generate RF/GHz electron beams from CNT emitters is especially important for microwave devices as it essentially replaces the hot cathode and its associated modulation stage. Because of their small size, and their ability to generate and modulate the beam
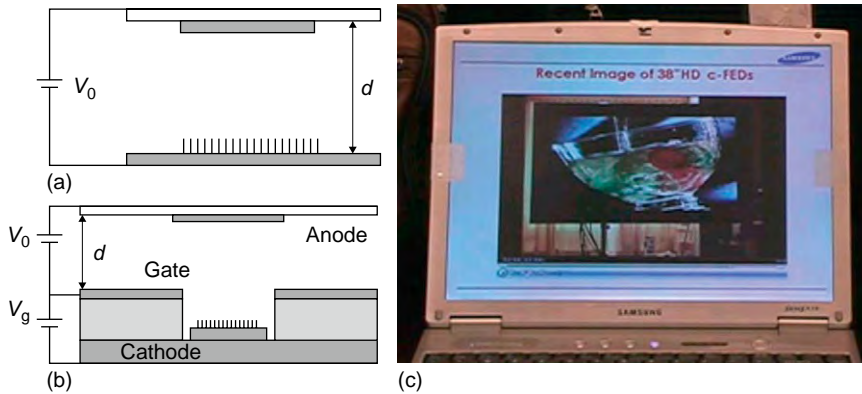
**FIGURE 5.14**   *Schematic of the working principle of a field emission display pixel. (a) Diode structure, (b) triode structure with ballast resistor in series with the emitters, (c) image of a prototype of a CNT field emission display with a gate structure, an active area of 38in. in diagonal, full colour and 100Hz.*

directly on demand without the need for high temperatures, CNT cathodes could be employed in a new generation of lightweight, efficient and compact microwave devices for telecommunications in satellites or spacecraft.

CNT electron sources have the largest potential market in their application to flat-panel field emission displays[53,54], where high-brightness displays can be fabricated for many applications. Figure 5.14 shows how the simplest forms of a display pixel could work with the patterning of CNTs, with the nanotubes deposited on a matrix of electrodes in a vacuum housing.

Theoretically, CNTs can be positioned in such a way as to maximize the field at their apex, whilst maintaining a high current density. However, such processing, though possible, would be very expensive over large areas. Industry has been researching ways in which to deposit already-grown CNTs.

Many companies, notably Samsung (SAIT)[55], have worked on the use of CNTs for TV applications. SAIT successfully produced demos of full colour 38in. diagonal TVs (Figure 5.14) and this technology was transferred to Samsung SDI for production in the mid-2000s. However, no displays based on this technology are yet on the market.

Similarly, CNT arrays can be used to create 'microlenses'[56]. After depositing CNTs with the same lithographical process, a liquid crystal deposited on top followed by a top gate will align itself with an induced electric field, alter the refractive index locally around a CNT and thus create a lens. The electric field required is typically lower than that at which field emission initiates. Additionally, by making the catalyst spot bigger, more than one CNT will grow which enhances the effect. A diagram showing this setup is shown in Figure 5.15.
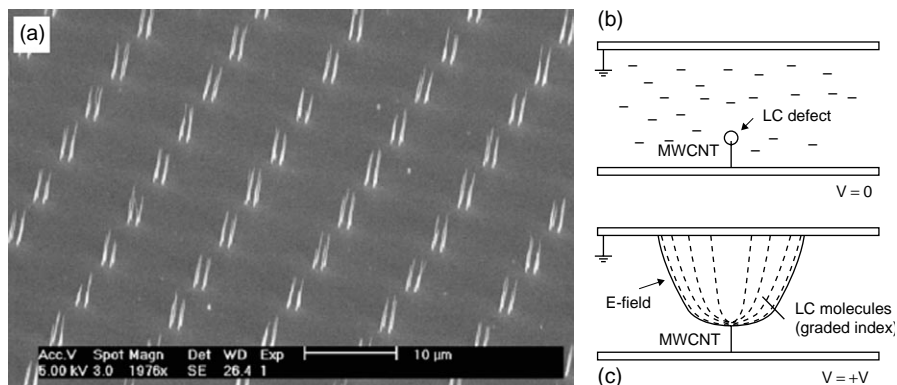
**FIGURE 5.15**    *(a) A pair of CNTs grown from single spots of catalyst separated by 10 μm. (b) Schematic diagram representing the multi-walled CNT (MWCNT) immersed in a liquid crystal (LC). (c) A voltage applied to the top gate causes the LC to align with the induced electric field which is distorted by the MWCNT.*

*Source: Copyright Wiley-VCH Verlag GmbH & Co. KGaA. Reproduced with permission.*

Such a device could have many potential applications such as in adaptive optical systems, wavefront sensors and optical diffusers.

Gated structures have many further possible applications. If the same principle used in field emission displays is applied to electron beam lithography, but with only one CNT as an electron source, then an array of parallel gates could be used to speed up parallel-write electron beam lithography. With several electron beams acting in parallel, this would vastly decrease the time it takes to write electron beam patterns onto silicon chips with lithography. Figure 5.16 shows what a typical array of electron sources would look like.

The fabrication process here is clearly more complicated than simple lithography. An etching step is required to create the cavity in which the CNT grows. The process is self-aligning, in that the CNT automatically grows in the centre of the gate and is aligned along the axis of the gate. The process developed for the CNT cathode, reported extensively by Gangloff et al.,[57] begins with the fabrication of a sandwich structure containing a gate electrode on top of an insulator which in turn is on top of an emitter electrode. An array of 300-nm diameter holes (20,000 in total), with a pitch of 5 μm, was patterned using e-beam lithography (as seen in Figure 5.17a showing a single resist hole) on top of the sandwich. Note that optical lithography has too poor a resolution to make such holes. A reactive ion etching step using $SF_6$ gas was used to isotropically etch the polysilicon gate to form an 800-nm aperture. The silicon dioxide insulator was then isotropically etched in buffered hydrofluoric acid (Figure 5.17b). Both the
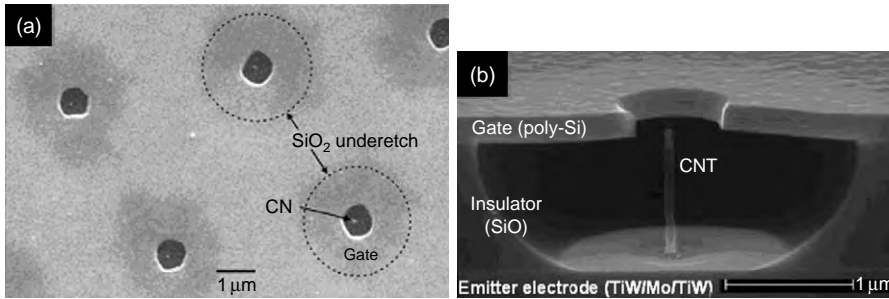
**FIGURE 5.16**   *(a) Top view of the integrated gate CNT cathode. The pitch of the gate apertures is 5 μm. The nanotube appears as a bright dot in each gate aperture. (b) Cross section SEM view of the integrated gate CNT cathode, showing the gate electrode, insulator, emitter electrode and vertically standing nanotube. Source: Ref. [57].*
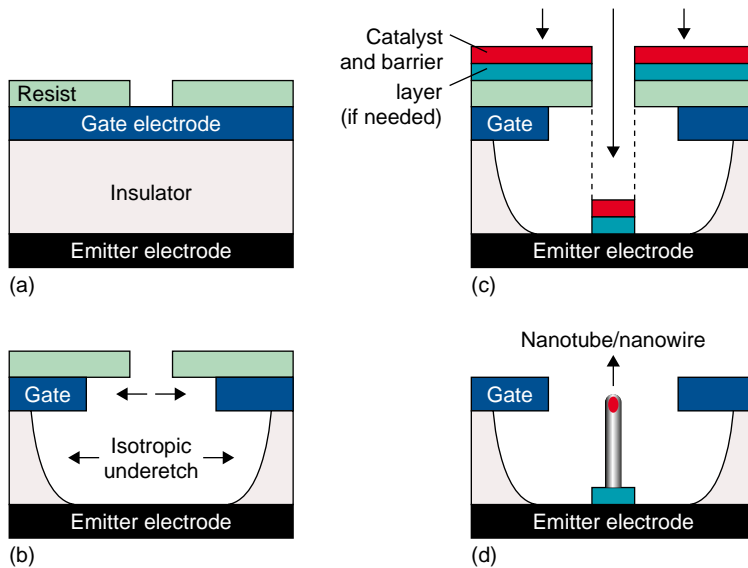


**FIGURE 5.17**   *The self-alignment process for fabricating an integrated gate with individual nanotube/ nanowire cathodes. (a) A resist hole is first patterned onto a gate electrode/insulator/emitter electrode sandwich. (b) The gate and insulator material are then isotropically etched. (c) A thin film of catalyst, and diffusion barrier (if required), are deposited on the structure. (d) A lift-off is then performed to remove the unwanted catalyst on top of the gate followed by the nanotube/nanowire growth inside the gate cavity.*

gate and insulator were over-etched to produce an undercut so as to prevent emitters from touching the gate and the silicon dioxide from being charged during field emission. A 15-nm thick conductive TiN layer (which prevents catalyst diffusion) was then deposited by sputtering, followed by 7 nm of Ni (Figure 5.17c). The resist hole defines the gate, insulator and

emitter position and this is why these features are said to be 'self-aligning'. The unwanted TiN and Ni over the gate are then removed by lifting off the e-beam resist. CNTs were then grown by PECVD using a mixture of $C_2H_2$ and $NH_3$ (54:200 sccm, respectively) at 5 mbar, 675°C, with a $-600$ V sample bias (Figure 5.17d). This process typically produces straight, vertically aligned CNTs (Figure 5.16b, deposition time 15 min).

The key advantages of this process are that no post-processing of the emitters is required and that the CNTs inside the gated cathode are essentially identical to those grown on a flat substrate. The nanotube-based gated nano-cathode array has a low field emission turn-on voltage of 25 V and a peak current of 5 μA at 46 V, with a gate current of 10 nA. These low operating voltage cathodes are also potentially useful as electron sources for field emission displays or miniaturizing electron-based instrumentation. CNTs are an ideal electron source for such a novel parallel e-beam lithography system, but currently, more work is still needed to increase the yield of functioning cathodes.

Of course, this is not the only way to create a gate-like structure, nor is the structure limited to the previously stated examples. FIB lithography can also be used to fabricate gate-like structures. Resists can be used in much the same way as before; indeed it has been reported that FIB has the potential to give higher resolution than e-beam[58].

FIB lithography resembles e-beam lithography, where the ion beam is substituted for the electron beam. However, the FIB technique can provide more lithographic regimes than e-beam: resist-based lithography, subtractive lithography (sputtering) or additive lithography (ion beam assisted deposition). FIB also allows simultaneous observation of the treated surface.

The ion source is a liquid metal source and is usually Ga. Its resolution is very similar to e-beam and is tens of nanometres. The main advantage of FIB is that it is not necessary to fabricate a mask in the case of sputtering and deposition. Catalyst could either be deposited at required positions (deposition), or the FIB can be used to mill through the substrate to layers beneath (sputtering).

Wu et al. reported the fabrication of gate-like structures by sputtering with an FIB. Metal-gated CNT field emitter arrays were fabricated using a multilayer structure with an embedded catalyst layer instead of depositing the catalyst into milled holes, as is common practice[59]. Fifteen nanometres of indium tin oxide (ITO) was deposited onto a silicon substrate which acted both as an adhesion layer and as a diffusion barrier followed by a 10-nm thin film of Ni, which served as the catalyst for CNT growth. A 1-μm thick layer of insulating $SiO_2$ was deposited onto the Ni catalyst by PECVD at 280°C. Following this, another 15-nm ITO adhesion layer was deposited on top of
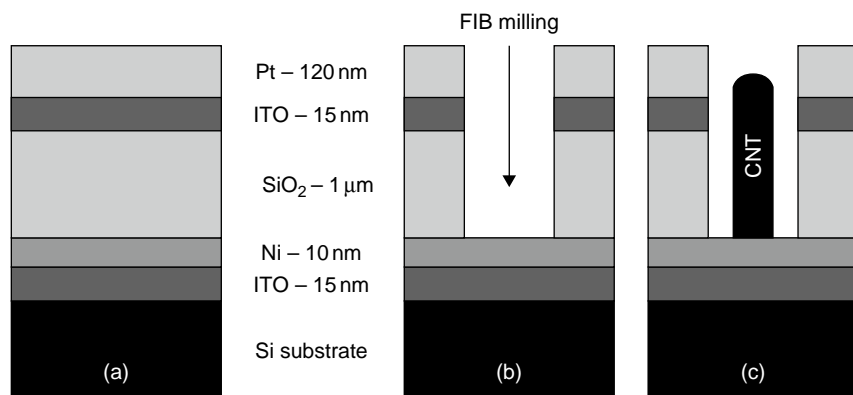
**FIGURE 5.18**  *(a) Array sample design including a Pt gate, a SiO$_2$ insulating layer, an embedded Ni catalyst and ITO adhesion layers, (b) shows the result of FIB milling and (c) the result of CNT synthesis.*

the SiO$_2$, followed further by a 120-nm thin film of Pt on top of the ITO. The function of the Pt layer was to serve as a gate electrode. A schematic diagram of the substrate design is shown in Figure 5.18a. An FEI Company dual-beam SEM/FIB was then used to mill arrays of holes (300 nm to 1 μm in diameter) to expose the Ni catalyst for CNT growth, as illustrated in Figure 5.18b.

This method has advantages over other reported methods, including the use of photolithography to etch arrays of holes into a silicon sample followed by the sputter coating of Fe into the holes to supply a catalyst[60] because the catalyst island deposition often yields additional undesired catalysed regions which require an additional procedure for removal. Using an FIB to expose the catalyst proves to be significantly easier than the deposition of a catalyst into pre-etched regions through sputtering, evaporation or electrochemical deposition. In this process, control over the milled depth and geometry as it approached such a thin film of catalyst is the greatest difficulty imposed by this process.

Once the gates had been fabricated and the catalyst exposed, vertically aligned CNTs were synthesized in each gated cavity using the PECVD process. During synthesis, the substrates were heated to 725°C and exposed to 50 sccm of C$_2$H$_2$ and 200 sccm of NH$_3$ gas for 30 min. This process transformed the Ni thin film into Ni nanoparticles which then served as the catalysts for CNT growth. The CNTs grown by PECVD were again vertically aligned due to the large electric field within the plasma sheath on the cathode. The results of this process are shown in Figure 5.19.

Combining this process with the remote hot-filament, CVD process could open the possibility of applying this process to vias, though the yield

(a)                                                 (b)
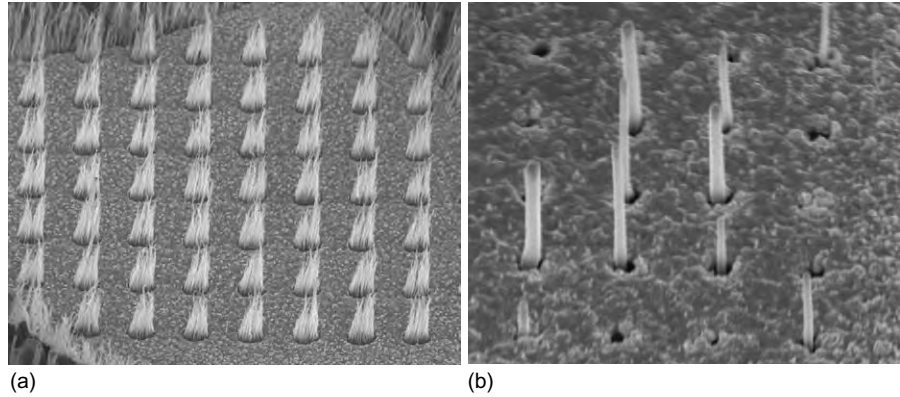
**FIGURE 5.19**   *(a) 1 μm wide holes with CNTs growing from within. (b) 300-nm holes with single CNTs growing from within the gate structure.*
*Source: Ref. [59].*

and growth density would have to significantly increase to carry sufficient current density.

## 5.10  GROWTH ON 3D SUBSTRATES

The processes detailed so far have all referred to growth on flat surfaces, which is particularly good when using lithography. When using a lift-off process, resists are typically spin-coated to produce the required uniformity in film thickness. However, if the surface isn't flat, uniformity goes down.

There is a trade-off. For example, Jang et al. have fabricated a nanoscale memory switch based on a nanoelectromechanical switched capacitor[61]. The e-beam lithography was used to position an individual CNT on top of three contacts as can be seen in Figure 5.20. Fortunately, the contact is quite flat on top, which means that spin coating of PMMA will produce a uniform thickness on each contact and hence fabricate reproducible functioning devices. When a potential is dropped between the contacts, the CNTs are electrostatically attracted to each other until contact is made, closing the switch. With the further addition of SiN and Cr to one of the CNTs, simple nanoelectromechanical memory devices have been demonstrated[63].

When the surface isn't flat, it becomes a challenge to use lithography. As mentioned earlier, Bell et al. got around this by filling the gap between the pyramids with PMMA, so that it just reached their apex (as can be seen in Figure 5.12). However, this is not an option when there are no adjacent pyramids to keep the PMMA in place; more on that later.
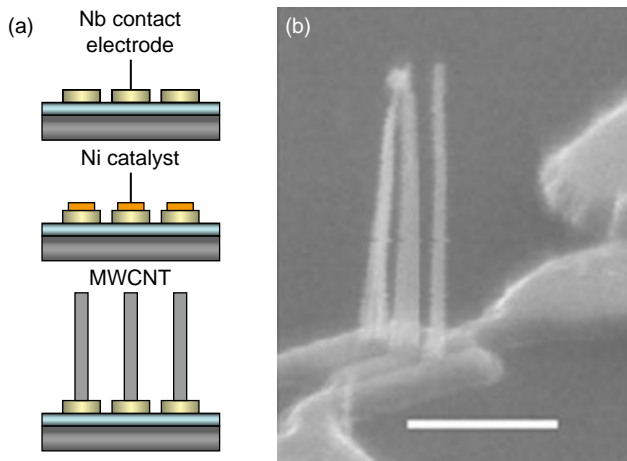
**FIGURE 5.20**   *(a) Schematic diagram showing the production process of the switch. Both contacts and catalyst were deposited with e-beam lithography. (b) An electron micrograph showing the grown CNTs acting as a switch.*
*Source: Ref. [62].*

It is often desirable to grow CNTs in a particular direction. This can be done by using thermal CVD along the 011 face of quartz or the R-face and A-face of sapphire[64]. If however, when growth from the surface is required, an alternative approach must be made. PECVD offers a potential route to controlling the growth direction, which can be achieved by controlling the field direction. The challenge lies in controlling the plasma around the substrate so that the field points in the direction the CNTs are required to grow in. Another process developed in Cambridge offers the opportunity of controlling CNT growth on 3D devices.

CNTs, as mentioned earlier, are particularly promising field emission sources. Consequently, it seems natural that they should be investigated as sources for electron microscopes. To test whether they can be applied, it is necessary to integrate them with existing electron source technology.

Electron microscopy demands a bright, stable, low-noise electron source with a low kinetic energy spread in order to maximize spatial resolution and contrast. Recent research found that the CNT can act as an improved electron source for this application when compared to the best electron sources available today[65]. Unfortunately, the method used to extract the data could not be applied to make a reproducible CNT source that could be marketed. To integrate the sources with existing microscopes, it was necessary to attach the CNT to an etched tungsten wire, which itself often acts as a source in electron microscopy. It is important that the bond between
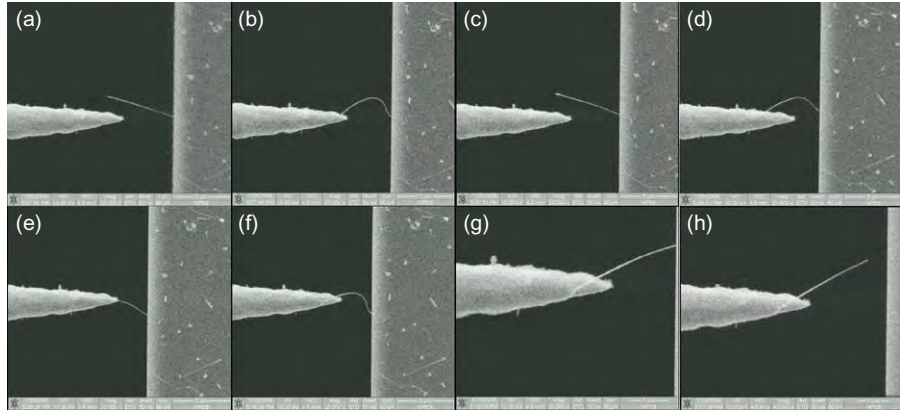
**FIGURE 5.21**   *Sequence of electron micrographs showing the attachment process of a CNT tip by Erwin Heeres at various magnifications. The tip apex radius is approximately 100nm. In (a), the CNT is brought close to the tip. In (b), a potential difference is applied between the CNT and the tip and the CNT attaches, but only partially, as the contact is lost at (c). In (d), the tip has been moved closer to the CNT and a potential applied again. The tip is moved in (e) showing a stronger bond this time. In (f), attempts are being made to snap the CNT; it breaks by (g). (h) shows the resultant tip attached at about 30° off-axis.*

the wire and CNT is strong and that the CNT is aligned with the optical axis to prevent astigmatism. The method used involved the attachment of a single CNT to the wire with carbon glue (which can be seen in Figure 5.21). It is not clear what the bond between the tungsten tip and the CNT is. Transportation across large distances is enough to cause the CNT to fall-off of the tip. This indicates that the bond between the CNT and the tip is weak and the lifetime of such a tip would suffer because of this weakness. Finally, the process of attaching a tip can be extremely time consuming and awkward. The process shown in Figure 5.21 took 20 min to complete and still produced a defective tip.

The most desirable option would be to grow an aligned CNT of reproducible dimensions directly onto the tungsten tip. One would presume that lithography offered an avenue for this, but this avenue fails because if one only wanted to deposit one CNT, there would be nowhere to focus the beam. There is also significant difficulty in depositing resist onto such a sharp object with reproducible thicknesses. Added to this, it is difficult to hit the tip exactly with the e-beam or by FIB precisely because the tip radius is so small.

Nevertheless, PECVD can be used to grow a single CNT directly onto a tungsten tip. When applying a potential difference between two parallel plates, approximately all of the voltage applied in the resultant plasma is dropped across the sheath. At the temperatures and pressures commonly used for PECVD (600–800°C, 2–5 mbar), the sheath in a plasma extends
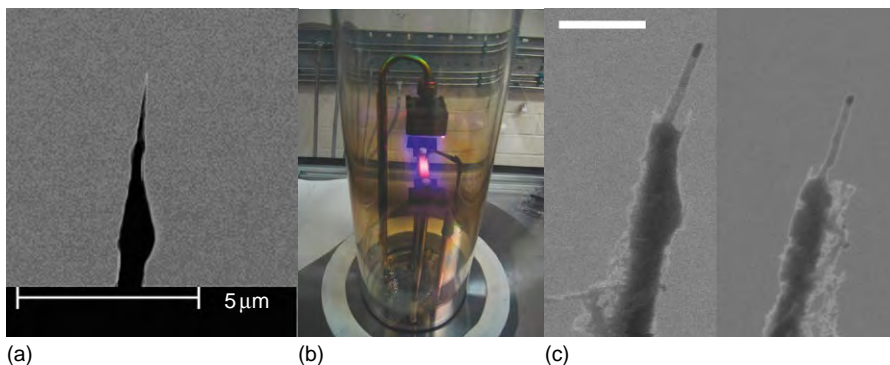
**FIGURE 5.22** *(a) An indication of the sharpness to which the tungsten wire is etched in order to grow a single CNT at the apex. (b) The wire submerged in a specially designed stage during growth. (c) The result of two single CNTs grown by PECVD; the Source of a single electron beam extracted by Fowler-Nordheim tunnelling.*

2–3 mm above the cathode surface. In order to obtain vertically aligned CNTs, the tip apex needs to sit within this sheath. Consequently, a special stage was constructed so that a tungsten wire could sit perpendicularly to a resistive heater and thus parallel to a field within a ceramic holder beneath the heater. The tip of the wire was positioned within the sheath. To grow a single CNT at the tip, the tungsten was etched to a sharp point (to less than 100 nm in diameter). The entire tungsten wire was coated in catalyst, but because of the sharpness of the tip, it was possible to grow only one CNT at the tip by carefully controlling the amount of catalyst deposited on it. Also, the grown CNTs align themselves with the plasma, whose direction can be controlled depending on the orientation of the wire within the ceramic holder. CNTs grown by this method are shown in Figure 5.22.

The single CNT yield is above 50% and continually improving. CNTs grown have been observed to be consistently aligned along the primary axis and form a robust bond with the tungsten wire. This method is a major advance in CNT growth and brings the prospect of CNT electron sources much closer to the market.

## 5.11 CONCLUSION

Processes are being continually developed to grow CNTs in new ways. The basic synthesis methods are identical, but different structures can be created by making even the smallest modifications. The examples given above are by no means exhaustive, but they indicate the way in which modifications can

be made. Research is ongoing into engineering CNT growth, but the first CNT devices are approaching the market because of the advances made.

The authors would like to acknowledge Laurent Gangloff and Erwin Heeres for their contributions to this chapter.

## REFERENCES

[1] S. Iijima, Nature 354 (1991) 56.

[2] L.V. Radushkevich, V.M. Lukyanovich, Russ. J. Phys. Chem. 26 (1952) 88–95.

[3] M. Reibold, et al., Nature 444 (2006) 286.

[4] N. de Jonge, J.-M. Bonard, Philos. Trans. R. Soc. Lond. A 362 (2004) 2239–2266.

[5] W.I. Milne, K.B.K. Teo, G.A.J. Amaratunga, P. Legagneux, L. Gangloff, J.-P. Schnell, V. Semet, V. Thien Binh, O. Groening, J. Mater. Chem. 14 (2004) 1–12.

[6] Y. Saito, T. Yoshikawa, S. Bandow, M. Tomita, T. Hayashi, Phys. Rev. B 48 (1993) 1907.

[7] M. Endo, K. Takeuchi, T. Hiraoka, T. Furuta, T. Kasai, X. Sun, C.H. Kiang, M.S. Dresselhaus, J. Phys. Chem. Solids 58 (1997) 1707.

[8] M. Endo, K. Takeuchi, T. Hiraoka, T. Furuta, T. Kasai, X. Sun, C.H. Kiang, M.S. Dresselhaus, J. Phys. Chem. Solids 58 (1997) 1707.

[9] A. Bachtold, C. Strunk, J.P. Salvelat, J.M. Bonard, L. Forro, T. Nussbaumer, C. Schonenberger, Nature 397 (1999) 673.

[10] H.J. Qi, K.B.K. Teo, K.K.S. Lau, M.C. Boyce, W.I. Milne, J. Robertson, K.K. Gleason, Determination of mechanical properties of carbon nanotubes and vertically aligned carbon nanotube forests using nanoindentation, J. Mech. Phys. Solids 51 (2003) 2213.

[11] J. Li, R. Stevens, L. Delzeit, H.T. Ng, A. Cassell, J. Han, M. Meyyappan, Electronic properties of multiwalled carbon nanotubes in an embedded vertical array, Appl. Phys. Lett. 81 (5) (2002) 910–912.

[12] K.B.K. Teo, C. Singh, M. Chhowalla and W.I. Milne, Encycl. Nanosci. Nanotechnol. 1 (2004) 665.

[13] A. Bachtold, P. Hadley, T. Nakamishi, C. Dekker, Science 294 (2001) 1317.

[14] S.J. Tans, A.R.M. Verschueren, C. Dekker, Nature 393 (1998) 49.

[15] R. Martel, T. Schmidt, H.R. Shea, T. Hertel, P. Avouris, Appl. Phys. Lett. 73 (1998) 2447.

[16] V. Derycke, R. Martel, J. Appenzeller, P. Avouris, Nano. Lett. 1 (2001) 453.

[17] J. Kong, N.R. Franklin, C.W. Zhou, M.G. Chapline, S. Peng, K.J. Cho, H.J. Dai, Science 287 (2000) 6212.

[18] P.G. Collins, K. Bradley, M. Ishigami, A. Zettl, Science 287 (2000) 1801.

[19] K. Tsukagoshi, B.W. Alphenaar, H. Ago, Nature 401 (1999) 572.

[20] T.W. Tombler, C.W. Zhou, L. Alexseyev, J. Kong, H.J. Dai, L. Lei, C.S. Jayanthi, M.J. Tang, S.Y. Wu, Nature 405 (2000) 769.

[21] R.H. Baughman, A.A. Zakhidov, W.A. de Heer, Science 280 (1998) 1744.

[22] J. Li, R. Stevens, L. Delzeit, H.T. Ng, A. Cassell, J. Han, M. Meyyappan, Appl. Phys. Lett. 81 (2002) 910.

[23] S. Musso, S. Porro, M. Rovere, A. Tagliaferro, E. Laurenti, M. Mann, K.B.K. Teo, W.I. Milne, Diamond Relat. Mater. 15 (2006) 1085–1089.

[24] M. Hirscher, M. Becher, M. Haluska, U. Dettlaff-Weglikowska, A. Quintel, G.S. Deusberg, Y.M. Choi, P. Downer, M. Hulman, S. Roth, I. Stepanek, P. Bernier, Appl. Phys. A 72 (2001) 129.

[25] P. Calvert, Nature 399 (1999) 210.

[26] S.T. Purcell, P. Vincent, C. Journet, V.T. Binh, Phys. Rev. Lett. 88 (2002) 105502.

[27] T. Utsumi, IEEE Trans. Electron Devices 38 (1991) 2276.

[28] A.G. Rinzler, J.H. Hafner, P. Nikolaev, L. Lou, S.G. Kim, D. Tomanek, P. Nordlander, D.T. Colbert, R.E. Smalley, Unraveling nanotubes: Field emission from an atomic wire, Science 269 (1995) 1550–1553.

[29] T. Paulmier, M. Balat-Pichelin, D. Le Queau, R. Berjoan, J.F. Robert, Physicochemical behavior of carbon materials under high temperature and ion radiation, Appl. Surf. Sci. 180 (2001) 227–245.

[30] T.W. Ebbesen, P.M. Ajayan, Nature 358 (1992) 220–222.

[31] P.G. Collins, P. Avouris, Nanotubes for electronics, Sci. Am. (December 2000) 67.

[32] T. Guo, Catalytic growth of single-walled nanotubes by laser vaporization, Chem. Phys. Lett. 243 (1995) 49–54.

[33] TW Ebbesen, PM Ajayan, Nature 358, 220–222 (16 July 1992).

[34] J.-M. Moon, K.H. An, Y.H. Lee, Y.S. Park, D.J. Bae, G.-S. Park, J. Phys. Chem. B 105 (2001) 5677–5681.

[35] Smalley, Guo, et al., J. Phys. Chem. 99 (1996) 10694–10697.

[36] Gue, et al., Chem. Phys. Lett. 243 (1997) 49–54.

[37] P.L., Walker Jr., et al., J. Phys. Chem. 63 (1959) 133.

[38] M. Jose-Yacaman, et al., Appl. Phys. Lett. 62 (1993) 657.

[39] R.T.K. Baker, Carbon 27 (1989) 315.

[40] R.T.K. Baker, J.R. Alonzo, J.A. Dumesic, D.J.C. Yates, J. Catal. 77 (1982) 74.

[41] J.I. Sohn, C.-J. Choi, T.-Y. Seong, S. Lee, Mater. Res. Symp. Proc. 706 (2002) Z3.8.1.

[42] Z.F. Ren, Z.P. Huang, J.W. Xu, J.H. Wang, P. Bush, M.P. Siegal, P.N. Provencio, Science 282 (1998) 1105.

[43] Z.P. Huang, J.W. Xu, Z.F. Ren, J.H. Wang, M.P. Siegal, P. Provencio, Appl. Phys. Lett. 73 (1998) 3845.

[44] O. Groening, O.M. Kuettel, Ch. Emmenegger, P. Groening, L. Schlapbach, J. Vac. Sci. Technol. B 18 (2000) 665.

[45] L. Nilsson, O. Groening, C. Emmenegger, O. Kuettel, E. Schaller, L. Schlapbach, H. Kind, J.M. Bonard, K. Kern, Appl. Phys. Lett. 76 (2000) 2071.

[46] M. Chhowalla, K.B.K. Teo, C. Ducati, N.L. Rupesinghe, G.A.J. Amaratunga, A.C. Ferrari, D. Roy, J. Robertson, W.I. Milne, J. App. Phys. 90(10) (2001) 5308–5317.

[47] K.B.K. Teo, M. Chhowalla, G.A.J. Amaratunga, W.I. Milne, D.G. Hasko, G. Pirio, P. Legagneux, F. Wyczisk, D. Pribat, Uniform patterned growth of carbon nanotubes without surface carbon, Appl. Phys. Lett. 79 (2001) 1534.

[48] Q. Cao, et al., Adv. Mater. 18 (2006) 304–309.

[49] Y. Zhang, et al. (submitted 2008).

[50] M.S. Haque, K.B.K. Teo, N.L. Rupesinghe, S.Z. Ali, I. Haneef, S. Maeng, J. Park, F. Udrea, W.I. Milne, On-chip deposition of carbon nanotubes using CMOS microhotplates, Nanotechnology 19 (2007) 025607.

[51] K.B.K. Teo, E. Minoux, L. Hudanski, F. Peauger, J.-P. Schnell, L. Gangloff, P. Legagneux, D. Dieumegard, G.A.J. Amaratunga, W.I. Milne, Nature 437 (2005) 968ff.

[52] K.B.K. Teo, S.-B. Lee, M. Chhowalla, V. Semet, V.T. Binh, O. Groening, M. Castignolles, A. Loiseau, G. Pirio, P. Legagneux, D. Pribat, D.G. Hasko, H. Ahmed, G.A.J. Amaratunga, W.I. Milne, Nanotechnology 14 (2003) 204ff.

[53] W.B. Choi, et al., Fully sealed, high-brightness carbon-nanotube field-emission display, Appl. Phys. Lett. 75 (1999) 3129–3131.

[54] Y. Saito, S. Uemura, Field emission from carbon nanotubes and its application to electron sources, Carbon 38 (2000) 169–182.

[55] Y.S. Choi, et al., Diamond Relat. Mater. 10 (2001) 1705–1708.

[56] T. Wilkinson, X. Wang, K.B.K. Teo, W.I. Milne, Sparse multiwall carbon nanotube electrode arrays for liquid crystal photonic devices, Adv. Mater. 20 (2), (2008) 363–366.

[57] L. Gangloff, E. Minoux, K.B.K. Teo, P. Vincent, V.T. Semet, V.T. Binh, M.H. Yang, I.Y.Y. Bu, R.G. Lacerda, G. Pirio, J.P. Schnell, D. Pribat, D.G. Hasko, G.A.J. Amaratunga, W.I. Milne, P. Legagneux, Nanoletters 4 (9) (2004) 1575–1579.

[58] K. Arshak, M. Mihov, A. Arshak, D. McDonagh, D. Sutton, D. Microelectronics, in: 24th International Conference 2 (16–19) (May 2004) 459–462.

[59] J. Wu, M. Eastman, T. Gutu, M. Wyse, J. Jiao, S.-M. Kim, M. Mann, Y. Zhang, K.B.K. Teo, Fabrication of carbon nanotube-based nanodevices using a combination technique of focused ion beam and plasma enhanced chemical vapour deposition, Appl. Phys. Lett. 91 (2007) 173122.

[60] G.S. Duesberg, A.P. Graham, M. Liebau, R. Seidel, E. Unger, F. Kreupl, W. Hoenlein, Nano Lett. 3 (2) (2003) 257.

[61] J.E. Jang, S.N. Cha, Y.J. Choi, D.J. Kang, T.P. Butler, D.G. Hasko, J.E. Jung, J.M. Kim, G.A.J. Amaratunga, Nanoscale memory cell based on a nanoelectromechanical switched capacitor, Nature Nanotechnol. 3 (2008) 26–30.

[62] J.E. Jang, S.N. Cha, Y. Choi, G.A.J. Amaratunga, D.J. Kang, D.G. Hasko, J.E. Jung, J.M. Kim, Nanoelectromechanical switches with vertically aligned carbon nanotubes, Appl. Phys. Lett. 87 (2005) 163114.

[63] J.E. Jang, S.N. Cha, Y.J. Choi, D.J. Kang, T.P. Butler, D.G. Hasko, J.E. Jung, J.M. Kim, G.A.J. Amaratunga, Nanoscale memory cell based on a nanoelectromechanical switched capacitor, Nature Nanotechnol. 3 (2008) 26–30.

[64] H. Ago, et al., Chem. Phys. Lett. 421 (4–6) (15 April 2006) 399–403.

[65] N. de Jonge, M. Allioux, M. Doytcheva, M. Kaiser, K.B.K. Teo, R.G. Lacerda, W.I. Milne, Characterization of the field emission properties of individual thin carbon nanotubes, Appl. Phys. Lett. 85 (2004) 1607.

# Upconverting Fluorescent Nanoparticles for Biological Applications

I. Amalraj Appavoo[1] and Y. Zhang[1,2]

[1]*Nanoscience and Nanotechnology Initiative, National University of Singapore, Singapore*
[2]*Division of Bioengineering, Faculty of Engineering, National University of Singapore, Singapore*

## CONTENTS

## ABSTRACT

Fluorescent labelling is widely used as an indispensable tool in biology for the study of complex molecular interactions. Conventional downconversion fluorescence labels with ultraviolet (UV) or short wavelength excitation suffer from the presence of autofluorescence, low signal-to-noise ratio and incident photodamage to living organisms. This chapter focuses on upconverting fluorescent nanoparticles with excitation in near-infrared region. This has several advantages including very low autofluorescence, absence of photodamage to living organisms, high detection sensitivity and high light penetration depth.

## 6.1 INTRODUCTION

Most biomolecules lack sensitive detectable fluorescent signal; hence there is a need for fluorescent labels to study their molecular interactions. Fluorescent probes emit fluorescence at certain wavelengths which can be detected using fluorescence microscope under in vitro and in vivo conditions. Exogenous labels for biological analysis were first introduced by American scientists Yalow and Berson in the form of radioimmunoassay (RIA). Apart from its high sensitivity ($10^{-9}$–$10^{-12}$) and wide application, it suffers from radioactivity and inherently short half-life. This has led to the introduction of various non-radioactive labelling techniques based on enzyme-catalysed reactions, bio/chemiluminescence and fluorescence. Of the three, fluorescent labelling is widely used in biology and medicine. Fluorescence is the luminescence phenomenon that occurs in fluorophores. It is a process by which a fluorophore absorbs particular wavelength of light and excites to higher energy state with emission of light. This emission energy corresponds to the energy difference between excited state and ground state. The optical properties of fluorophores such as fluorescence intensity, excitation spectrum, emission spectrum and fluorescence lifetime help to encode the happenings around the molecule that is monitored. For example, labels which are environmentally sensitive can be used as molecular reporters. Information on what is happening in their molecular environment can thus be derived from their fluorescence signals, and their exact locations can be monitored using fluorescence microscopy. Most of the conventional fluorescent labels follow the principle of Stokes law. They are excited under UV or short wavelength excitation. The main problems in using them are: autofluorescence (noise) from the analytes under UV and short wavelength excitation which decreases the signal-to-noise ratio, low light penetration depth and severe damage to living organisms[1–3]. Some conventional fluorescent labels used are organic dyes, fluorescent proteins, lanthanide chelates, semiconductor quantum dots (QDs), lanthanide doped inorganic nanoparticles and fluorophoretagged latex/silica nanobeads. However, the most commonly used are organic dyes and QDs.

Organic dyes, though popular owing to their low cost, availability and easy usage, also pose some challenges such as short Stokes shift, poor photo-chemical stability, susceptibility to photobleaching and decomposition under repeated excitation. However, recent research has overcome some of these problems. Some commonly used organic dyes are fluorescein, rhodamine, cyanine and Alexa dyes. QDs are semiconductor nanoparticles composed of atoms from groups II–VI or III–V of the periodic table. They are generally defined as particles having physical dimensions smaller than the exciton Bohr radius, typically 1–5 nm. This small size leads to a quantum

confinement effect, which endows nanoparticles with unique optical and electronic properties. Advantages of using QDs over other fluorescent labels include great assay sensitivity and stability and better emission selectivity. QDs with different sizes and compositions can be excited simultaneously with a single wavelength of light to produce emissions at different wavelengths useful in multiplex detection studies. Again QDs are not foolproof. Major problems involve presence of autofluorescence and toxicity. These obstacles in the application of conventional labels have paved the way to develop a new class of labelling materials.

Upconverting nanoparticles (UCN) with near-infrared (NIR) excitation are the best choice. The process in which the emission energies are found to exceed excitation energies by 10–100 times *KT* violating Stokes law in its basic statement is called upconversion (UC). Coupled lanthanide and uranide f ions and transition metal d ions, when embedded in solids, produce UC fluorescence under moderate to strong excitation density. UCN convert low energy exciting photons to visible emissions. They have various advantages such as absence of autofluorescence and of photodamage to living organisms as exciting NIR light does not excite the biological samples; deep tissue penetration as NIR light shows low scattering effect; high emission signals as the UC process occurring inside the host materials is not affected by external environment such as pH, temperature, etc.; multiplex imaging as under same excitation, the emission wavelengths of UCN can be varied by changing their doping ions[4, 5]. This chapter gives an overview of UCN and their bioapplications.

## 6.2 THE MECHANISM OF FLUORESCENT UC

A wide variety of mechanisms have been proposed for the occurrence of UC either alone or in combinations of absorption and non-radiative energy transfer steps. Absorption is in two basic forms, that is, the ground state absorption (GSA) – promotion of ions from its ground state to an excited state – and the excited state absorption (ESA) – promotion of ions from its excited state to a higher excited state – as shown in Figure 6.1a. Non-radiative energy transfer may take place between either like energy levels or unlike energy levels. Energy transfer among like levels of like ions is the common phenomenon of energy migration.

A similar process between unlike ions may lead to energy trapping or sensitization effect. Energy transfer between unlike levels may result in energy transfer upconversion (ETU) and cross relaxation (CR). ETU is a process in which a low lying neighbour donates its excitation energy to a neighbouring excited ion which is then promoted to a higher excited state. Figure 6.1b
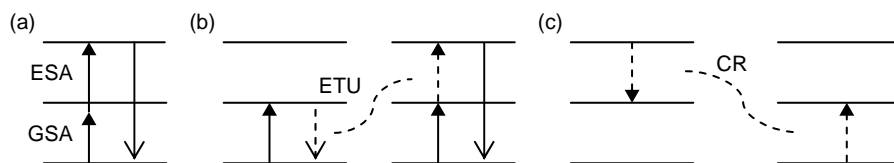
**FIGURE 6.1**   *Upconversion mechanism: (a) ground state absorption followed by excited state absorption (GSA/ESA); (b) ground state absorption followed by energy transfer upconversion (GSA/ETU); (c) Cross relaxation (CR).*

shows the mechanism of GSA followed by ETU. ETU is inherently a pairwise or multicentre effect which strongly depends upon concentration of ions. CR is the reverse of ETU. In CR, an ion (at higher excited levels) is partially deactivated through energy transfer to a ground state neighbour, with both ions at lower excited levels, as shown in Figure 6.1c.

## 6.3 UPCONVERTING NANOPARTICLES

UC occurs in various ion-doped solids such as crystals[6, 7] and glasses[8–11]. Usually lanthanide (4f), actinide (5f) and transition metal (3d, 4d, 5d) ions can produce UC fluorescent emission when embedded in solids or organic ligand. Of these, trivalent lanthanides based UC are predominantly used. This is because lanthanides have more than one metastable state (except $Yb^{3+}$) which makes them best suited for UC. This is due to the fact that the spectroscopically active 4f electrons are well shielded from their chemical environment by the outer-lying 5s and 5p electrons, resulting in particularly small electron–phonon coupling strength for various excited f–f states. As a consequence, luminescence processes are much more competitive with multiphonon relaxation in lanthanides compared to other ions, and their excited lifetime is typically in the range of $10^{-6}$–$10^{-2}$ s. Also, in lanthanide centred f–f transitions, there is only a small displacement between the ground state and the excited state. Lanthanide ions, $Pr^{3+}$, $Nd^{3+}$, $Dy^{3+}$, $Ho^{3+}$, $Er^{3+}$, $Yb^{3+}$, $Sm^{3+}$ and $Tm^{3+}$, have been used widely for synthesis of UC fluorescent materials[12–14]. Transition metal based UC is considerably less explored due to the much stronger electron–phonon coupling of d-electrons, which leads to dominant non-radiative relaxation based on multiphonon processes for most of the excited d–d states. Some examples are $Ti^{2+}$, $Ni^{2+}$, $Mo^{3+}$, $Re^{4+}$ and $Os^{4+}$ doped halides[15–20].

The principal strategies for obtaining new inorganic UC nanoparticles involve changing the host lattice and doping ions. Changing the host lattice may dramatically influence the radiative and non-radiative (multiphonon

| Table 6.1 | List of Examples of Upconverting Inorganic Nanoparticles | | | | |
|---|---|---|---|---|---|
| Host Material | Absorber Ion | Emitter Ion | Emission(s) | Wavelength (nm) | Reference |
| $YF_3$ | Yb | Er | Blue | 411 | [28] |
| $GdF_3$ | Yb | Er | Green, red | 520–550, 665 | [29] |
| $NaYF_4$ | Yb | Er, Tm | Green, red, blue | 518–545, 652–655, 475 | [30] |
| $LaF_3$ | Yb | Er, Tm, Ho | Green, blue, red | 545, 475.2, 657.8 | [31] |
| $Y_2O_2S$ | Yb | Er, Ho, Tm | Green, red | 520–580, 650–700 | [26] |
| | | | Green, red | 550, 640–680 | |
| | | | Blue, red | 460, 640–680 | |
| $Gd_2O_2S$ | Yb | Er | Green, red | 520–580, 650–700 | [32] |
| $Y_2O_3$ | Yb | Er | Red | 662 | [21] |
| $La_2(MoO_4)_3$ | Yb | Er | Green, red | 519–541, 653 | [33] |
| ZnO | | Er | Green | 520–550 | [34] |
| $Gd_2O_3$ | Yb | Er | Green, red | 520–580, 650–700 | [32] |
| $Y_3NbO_7$ | Er | | Green, red | 550, 665 | [35] |
| $Lu_2O_3$ | Yb | Ho | Green, red | 548, 667 | [36] |
| $Cs_2NaGdCl_6$ | Tm | Ho | Blue, green | 492, 543 | [37] |
| | | | Yellow, red | 588, 657 | |

relaxation as well as energy transfer) properties, leading to entirely different UC luminescence behaviour. For example, one can reduce the efficiency of multiphonon[21] relaxation processes by changing the lattice from high phonon energies (fluoride, oxide, etc.)[22–26] to low phonon energies (chlorides, bromides, iodides, etc.)[16, 18]. But most of these low phonon energy lattices are hygroscopic. Choosing a host with specific optical and/or magnetic properties may also influence the UC emission properties of a dopant ion through sensitization or perturbation by exchange interactions[27]. Similarly, a change in dopant ions has dramatic effect on UC emission. The most obvious effect is the change in emission wavelength. The choice of host lattice and co-dopant covers a very broad range of possibilities in the development of compounds with new and unprecedented UC properties, leaving much to the imagination and creativity of the researcher. Some upconverting nanocrystals are summarized in Table 6.1.

Usually lanthanide cations show very weak absorption that extensively decreases their emission. This drawback is overcome in coordination chemistry by the development of 'antenna effect'. This allows an increase in luminescence intensity through indirect excitation by tuning the absorption cross sections into regions unabsorbed by the nanoparticles. Some examples are: energy

transfer to lanthanide cations from anions present in bulk structure of phosphate and vanadate based nanoparticles; energy transfer from surface passivating shells in $SiO_2$ coated nanoparticles; capping chromogenic ligands[38–40].

## 6.4 CONJUGATION OF BIOMOLECULES TO UCN

For bioapplications, UCN should be hydrophilic, biocompatible and should possess functional groups to facilitate covalent bioconjugations[30]. Most of UCN are synthesized in organic solvents[5, 41, 42] or at high temperatures[30, 33]. Organic surfactants such as cetyl-trimethylammonium bromide (CTAB) or ethylenediamine tetra acetic acid (EDTA) are often used as ligands to control the particle growth and stabilization against aggregation resulting in a hydrophobic surface. Hence, surface modification is required for these UCN before employing them in biological studies[30, 43]. The surface modification is much dependent on surface chemistry of UCN; so, it is difficult to achieve all desired properties using one universal method.

The surface modification of UCN is made by coating a thin layer of either silica or polymer. Silica coating is an attractive method, as their surface chemistry is well documented[44–47]. The surface silica prevents nanoparticles from flocculation and provides room for decoration with functional groups such as thiol, amino and carboxyl groups, which allow greater control in conjugation protocols[48]. On the other hand, hydrophilic, biocompatible and bifunctional polymers are used as chelating and stabilizing agents for UCN. They render the surface of UCN hydrophilic and provide functional groups for bioconjugations. The polymers such as polyvinylpyrrolidone[49] chitosan[50–52], polyethylenimine (PEI)[49, 53], poly(acrylic acid)(sodium salt)(PAAcNa)[54] and polyethylene glycol (PEG)[55] are used for synthesis of UCN. The presence of polymer does not affect the fluorescence spectrum of polymer/UCN. Figure 6.2 shows the fluorescence spectrum of PEI/NaYF$_4$:Yb$^{3+}$, Ln3$^+$ (Ln: Er or Tm) nanoparticles. Also, further increase in functionality can be achieved by encapsulating polymer/UCN with a uniform layer of silica. The schematic representation of silica/PVP stabilized nanoparticles[49] is shown in Figure 6.3.

## 6.5 UCN FOR BIOLOGICAL APPLICATIONS

### 6.5.1 UCN in immunoassays

The immunoassay is used to measure the concentration of substance in biological liquid (serum or urine) using the bio-affinity between antibody and antigen. It has important applications in the diagnosis of infectious and genetic diseases. Labelling the antibody or antigen is commonly used
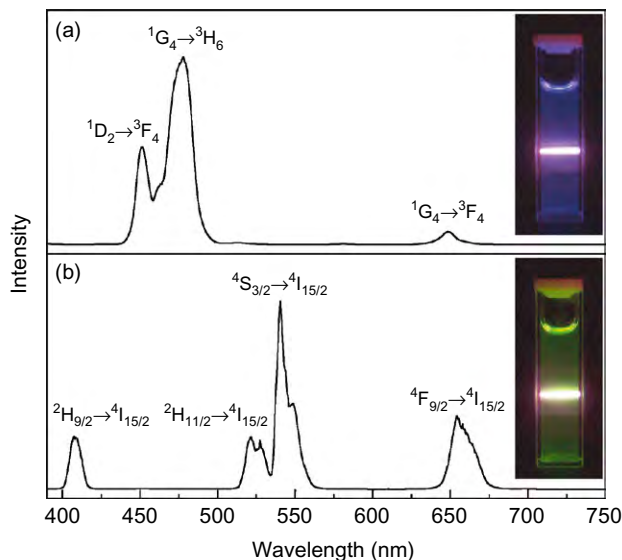
**FIGURE 6.2** *NIR-to-visible UC fluorescence spectra and photographs of the (a) PEI/NaYF$_4$:Yb$^{3+}$, Tm$^{3+}$ and (b) PEI/NaYF$_4$:Yb$^{3+}$, Er$^{3+}$ nanoparticles in aqueous solutions (1 mg mL$^{-1}$) excited at 980 nm using an NIR laser.*
*Source: Reproduced with permission from Ref. [53], IOP Publishing Ltd.*
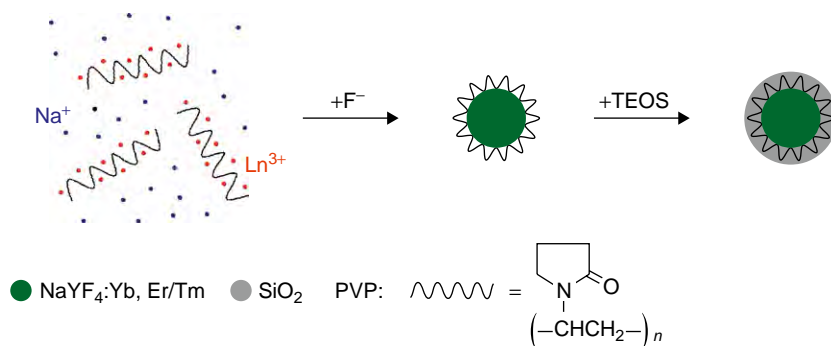


**FIGURE 6.3** *Synthesis of silica-coated PVP/NaYF$_4$ nanoparticles doped with lanthanide ions. TEOS = tetraethoxysilane.*
*Source: Reproduced with permission from Ref. [49]. Copyright Wiley-VCH Verlag GmbH & Co. KGaA.*

for detecting their quantity. Downconverting fluorescence labels suffer from photobleaching, toxicity, low luminescence intensity and decreasing fluorescence intensity in biological fluids[56–58]. The development of biological labels that are resistant to photobleaching, biocompatible, highly luminescent and ultrasensitive in both in vitro and in vivo bioassays remains a

challenging task. Lanthanide doped UCN with NIR excitation can be a good choice[59–61]. These nanoparticles are biocompatible, show high chemical stability and can be used for multiplex imaging. Most importantly, they show very low background signal as the interfering biomolecules in question do not get absorbed in the NIR region. The application of UCN as reporter in homogeneous immunoassays[60–62] and nucleic acid microarrays[63] provides 10–100 folds better detection limits than conventional fluorescence reporters.

Further enhancement in the detection sensitivity can be achieved by introducing UCN coupled with either lateral flow assay or fluorescence resonance energy transfer (FRET). The lateral flow assays are a simple device with a solid substrate, which is pre-treated with antibody or antigen, used for the detection of target analytes in the test sample. UCN based lateral flow assays lead to better detection sensitivity[64, 65]. FRET is one of the most important techniques used to monitor binding interactions based on the detection of proximity between a fluorescent energy donor and an acceptor species. The basic principle of FRET is described as non-radiative energy transfer from a donor to an acceptor species in close proximity with a distance smaller than critical radius known as Forster radius (typically <10 nm)[66]. FRET is a very simple and convenient method. This is used to measure changes in distance rather than the distance itself, thereby making them best suited for measuring protein conformational changes[67], monitoring protein interactions[68] and assaying of enzyme activity[69]. They are based on measurement of either donor quenching or sensitized emission from acceptor. An example for UCN–FRET system for the detection of trace amounts of avidin is shown in Figure 6.4. In this system, biotin conjugated UCN and 7 nm gold nanoparticles were used as energy donor and acceptor, respectively.
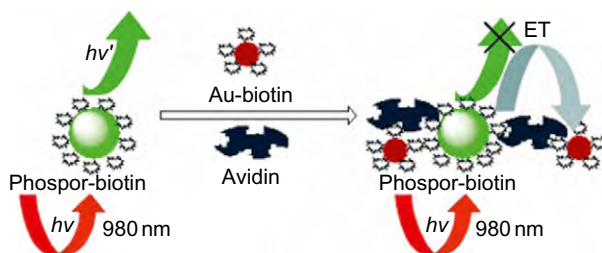


**FIGURE 6.4** *Scheme of the FRET system with phosphor-biotin nanoparticles as energy donors and Au-biotin nanoparticles as energy acceptors in the analysis of avidin. ET = energy transfer.*
*Source: Reproduced with permission from Ref. [43]. Copyright Wiley-VCH Verlag GmbH & Co. KGaA.*

Different concentrations of avidin were added to the mixture of these two nanoparticles and their fluorescent spectra were measured as a function of avidin concentration. It was observed that the luminescence was gradually quenched with increasing amount of avidin[43]. However, UCN–FRET has intrinsic limitations such as large size of UCN and instable conjugation of biomolecules on the surface of UCN. The reduction in size of UCN can increase its signal variation and decrease proximity based energy transfer efficiency. Most efficient energy transfer can be achieved with particles lesser than 40 nm in diameter, in which larger proportion of the emission ions can participate in non-radiative energy transfer due to short distances. The instable conjugation of biomolecules on the surface of UCN is due to the improper coating method that leads to dissociation of bioconjugates from the surface of nanoparticles and decreases their assay sensitivity. Further studies may pave the way to wider applications of these UCN in ultrasensitive multicolour detection of nucleic acids and proteins, and fluorescence immunoassays.

## 6.5.2 UCN in bioimaging

The morphological and optical properties of nanoparticles are key components for in vitro and in vivo imaging of living cells and animals, respectively. The nanoparticles ought to be compatible in size and chemical composition with the imaging systems. The chemical stability, non-photobleaching and biocompatibility of UCN over conventional labels make them best suitable for bioimaging. UCN of few hundred nanometres were used to image the digestive system of nematode *Caenorhabditis elegans* (*C. elegans*)[70]. Figure 6.5 shows the images of secretion of UCN in digestive system of *C. elegans* under 980 nm excitation. In our lab, PEI stabilized NaYF$_4$ nanoparticles of about 50 nm diameter and with amino functional groups were used for imaging of cells and deep tissues in animals[71]. Folic
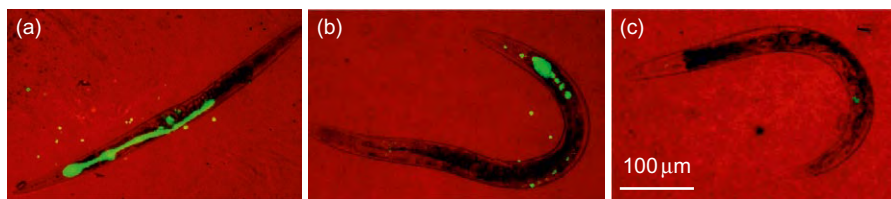


**FIGURE 6.5** *False colour two-photon images of C. elegans at 980 nm excitation. The worms were given food immediately after being fed with phosphors, showing decreasing amounts of phosphors at (a) 0 h, (b) 1 h and (c) 2 h.*
*Source: Reprinted with permission from Ref. [70]. Copyright 2008, American Chemical Society.*
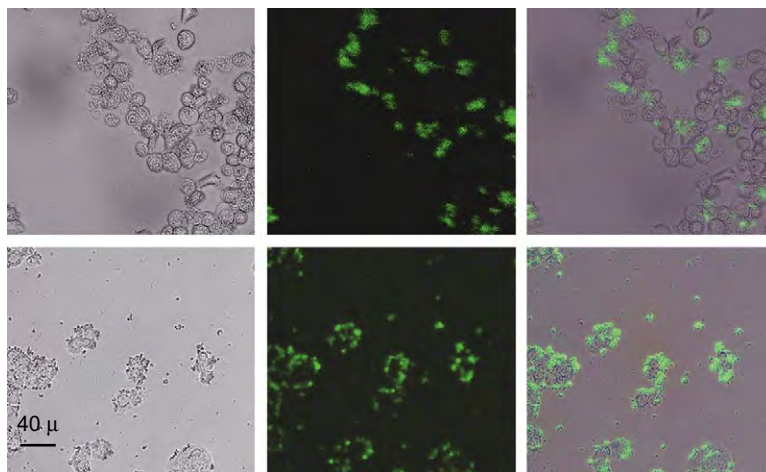
**FIGURE 6.6**   *Bright field, confocal and superimposed images of live human ovarian carcinoma cells (OVCAR3, top row) and human colonic adenocarcinoma cells (HT29, bottom row), with PEI/NaYF$_4$ nanoparticles attached. The nanoparticles were surface modified with folic acid.*
*Source: Reprinted with permission from Ref. [71]. Copyright 2008, Elsevier.*

acid coated PEI/NaYF$_4$ nanoparticles were used for imaging human HT29 adenocarcinoma cells and human OVCAR3 ovarian carcinoma cells. The demonstration of its live cellular imaging is shown in Figure 6.6.

The deep tissue imaging of Wistar rats is shown in Figure 6.7. Anaesthetized Wistar rats were injected subcutaneously at groin and upper leg regions with 100 mL of PEI/NaYF$_4$:Yb, Er. The nanoparticles injected show visible fluorescence from a depth of up to 10 mm. The muscles with skin removed show much stronger fluorescence from deep injection than intact skin at similar depths.

In general, the morphological and optical features of UCN make them best suited for continuous live imaging of tissues in small animal models, which can then be utilized in monitoring tumour and exploring pathologies without unnecessary sacrifice of animals. This is particularly important when temporal series of data are required.

### 6.5.3  UCN for photodynamic therapy

UCN can be administered in therapeutic applications such as photodynamic therapy (PDT). This involves destruction of pathological cells and tissues using toxic oxygen species generated from dynamic interaction of a photosensitizing agent with light and oxygen. This mechanism takes place in three different phases: first, absorption of light by photosensitizing agent
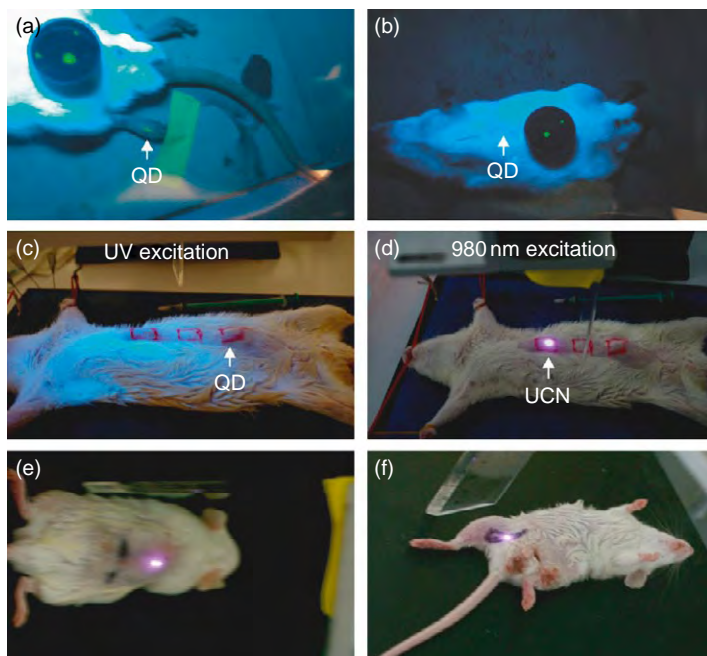
**FIGURE 6.7** *In vivo imaging of rat: quantum dots (QDs) injected into translucent skin of foot (a) show fluorescence, but not through thicker skin of back (b) or abdomen (c); PEI/NaYF₄:Yb, Er nanoparticles injected below abdominal skin (d), thigh muscles (e) or below skin of back (f) show luminescence. QDs on a black disk in (a) and (b) are used as the control.*
*Source: Reprinted with permission from Ref. [71]. Copyright 2008, Elsevier.*

to attain an excited state; second, release of energy to surrounding oxygen to convert them to oxygenated products or singlet oxygen and finally, induction of cell death by toxic products. There are some technical difficulties involved in PDT application which decrease their efficiency. They are: (1) most photosensitizers are hydrophobic – they aggregate easily under physical conditions and have low accumulation selectivity towards diseased tissue; (2) photosensitizer absorbs in visible spectral region below 700 nm which cannot penetrate deeply inside tissue. The use of UCN overcomes these drawbacks. UCN by themselves are unable to generate singlet oxygen species from dissolved oxygen and require the attachment of an appropriate photosensitizing agent with excitation band matching the emission of nanoparticles. In principle, incident NIR light is upconverted by UCN to visible light which is used by photosensitizer to produce singlet oxygen species from dissolved molecular oxygen environment. In addition, it helps to solubilize highly non-polar photosensitizer and target them to cancer cells. Accordingly, UCN acts as energy transducer for photosensitizer. UCN,

core-shell silica/$NaYF_4$:Yb, Er with merocyanine-540[72] and PEI/$NaYF_4$:Yb, Er with zinc pthalocyanine [73] are reported for PDT.

## 6.6  CONCLUSION

Conventional downconverting fluorescent labels suffer from autofluorescence, low light penetration and presence of severe photodamage to living organisms. UCN with NIR laser excitation is a good alternative. Advantages of UCN are strong anti-Stokes emission of discrete wavelengths, unmatched contrast in biological specimens due to the absence of autofluorescence upon excitation with NIR light and simultaneous detection of multiple target analytes. With these advantages, UCN find potential applications in immunoassay, bioimaging[22] and PDT[72, 74]. There is still room for improvement in characteristics of UCN which include its larger size, absence of functional groups for bioconjugations and its instability when dispersed in solutions. In addition, synthesis of bifunctional UCN with both fluorescence and paramagnetic properties has raised a significant interest in the field of bio-labelling[75, 76]. These bifunctional nanoparticles have potential application in fluorescence imaging[77], targeting[78], bioseparation, cancer diagnosis and treatment, DNA separation and magnetic resonance imaging (MRI)[79].

## ACKNOWLEDGMENTS

## REFERENCES

[1]  E. Beaurepaire, V. Buissette, M.P. Sauviat, D. Giaume, K. Lahlil, A. Mercuri, D. Casanova, A. Huignard, J.L. Martin, T. Gacoin, J.P. Boilot, A. Alexandrou, Functionalized fluorescent oxide nanoparticles: Artificial toxins for sodium channel targeting and imaging at the single-molecule level, Nano Lett. 4 (11) (2004) 2079.

[2]  K. Konig, Multiphoton microscopy in life sciences, J. Microsc.-Oxford 200 (2000) 83.

[3]  G.S. Yi, G.M. Chow, Colloidal LaF3:Yb,Er, LaF3:Yb,Ho and LaF3:Yb,Tm nanocrystals with multicolor upconversion fluorescence, J. Mater. Chem. 15 (41) (2005) 4460.

[4]  H. Zijlmans, J. Bonnet, J. Burton, K. Kardos, T. Vail, R.S. Niedbala, H.J. Tanke, Detection of cell and tissue surface antigens using up-converting phosphors: A new reporter technology, Anal. Biochem. 267 (1) (1999) 30.

[5] S. Heer, K. Kompe, H.U. Gudel, M. Haase, Highly efficient multicolour upconversion emission in transparent colloids of lanthanide-doped $NaYF_4$ nanocrystals, Adv. Mater. 16 (23–24) (2004) 2102.

[6] T. Tsuboi, H. Murayama, Energy-transfer upconversion of rare earth ions in ionic crystals: Case of $Tm^{3+}/Ho^{3+}$-codoped $LiYF_4$ crystals, J. Alloys Compd. 408–412 (2006) 680.

[7] H.W. Song, B.J. Sun, T. Wang, S.Z. Lu, L.M. Yang, B.J. Chen, X.J. Wang, X.G. Kong, Three-photon upconversion luminescence phenomenon for the green levels in $Er^{3+}/Yb^{3+}$ codoped cubic nanocrystalline yttria, Solid State Commun. 132 (6) (2004) 409.

[8] H. Lin, K. Liu, L. Lin, Y. Hou, D. Yang, T. Ma, E.Y.B. Pun, Q. An, J. Yu, S. Tanabe, Optical parameters and upconversion fluorescence in $Tm^{3+}/Yb^{3+}$-doped alkali–barium–bismuth–tellurite glasses, Spectrochim. Acta A 65 (3–4) (2006) 702.

[9] K. Kadono, H. Higuchi, M. Takahashi, Y. Kawamoto, H. Tanaka, Upconversion luminescence of $Ga_2S_3$-based sulfide glasses containing $Er^{3+}$ ions, J. Non-Cryst. Solids 184 (1995) 309.

[10] K. Kumar, S.B. Rai, UV/visible upconversion and energy transfer between $Nd^{3+}$ and $Pr^{3+}$ ions in co-doped tellurite glass, Solid State Commun. 142 (1–2) (2007) 58.

[11] M.A. Chamarro, R. Cases, Infrared to visible upconversion of $Er^{3+}$ ions in $Yb^{3+}$ doped fluorohafnate glasses, J. Lumin. 46 (1) (1990) 59.

[12] M. Liao, L. Wen, H. Zhao, Y. Fang, H. Sun, L. Hu, Mechanisms of $Yb^{3+}$ sensitization to $Tm^{3+}$ for blue upconversion luminescence in fluorophosphate glass, Mater. Lett. 61 (2) (2007) 470.

[13] P.V. dos Santos, M.V.D. Vermelho, E.A. Gouveia, M.T. de Araujo, A.S. Gouveia-Neto, F.C. Cassanjes, S.J.L. Ribeiro, Y. Messaddeq, Infrared-to-visible frequency upconversion in $Pr^{3+}/Yb^{3+}$- and $Er^{3+}/Yb^{3+}$-codoped tellurite glasses, J. Alloys Compd. 344 (1–2) (2002) 304.

[14] G. Hai, Y. Min, Z. Weiping, Upconversion of $Er^{3+}$ ions in LiKGdF5: $Er^{3+}$, $Dy^{3+}$ single crystal produced by infrared and green laser, J. Rare Earths 24 (6) (2006) 740.

[15] O.S. Wenger, M. Wermuth, H.U. Gudel, Chemical tuning of transition metal upconversion properties, J. Alloys Compd. 341 (1–2) (2002) 342.

[16] M. Wermuth, H.U. Gudel, Upconversion luminescence in a 5d transition-metal ion system: CsZrCl: Os, Chem. Phys. Lett. 281 (1–3) (1997) 81.

[17] S. Heer, M. Wermuth, K. Kramer, H.U. Gudel, Upconversion excitation of $Cr^{3+}$ 2E emission in $Y_3Ga_5O_{12}$ codoped with $Cr^{3+}$ and $Yb^{3+}$, Chem. Phys. Lett. 334 (4–6) (2001) 293.

[18] C. Reinhard, K. Kramer, D.A. Biner, H.U. Gudel, $V^{3+}$ sensitized upconversion in $Cs_2NaScC_{16}:Pr^{3+};V^{3+}$ and $K_2NaScF_6:Er^{3+};V^{3+}$, J. Alloys Compd. 374 (1–2) (2004) 133.

[19] J. Grimm, O.S. Wenger, H.U. Gudel, Broadband green upconversion luminescence of $Ni^{2+}$ in $KZnF_3$, J. Lumin. 102–103 (2003) 380.

[20] S. Heer, K. Petermann, H.U. Gudel, Upconversion excitation of $Cr^{3+}$ emission in $YAlO_3$ codoped with $Cr^{3+}$ and $Yb^{3+}$, J. Lumin. 102–103 (2003) 144.

[21] T. Hirai, T. Orikoshi, I. Komasawa, Preparation of $Y_2O_3$ : Yb, Er infrared-to-visible conversion phosphor fine particles using an emulsion liquid membrane system, Chem. Mater. 14 (8) (2002) 3576.

[22] Y. Wei, F.Q. Lu, X.R. Zhang, D.P. Chen, Synthesis and characterization of efficient near-infrared upconversion Yb and Tm codoped $NaYF_4$ nanocrystal reporter, J. Alloys Compd. 427 (1–2) (2007) 333.

[23] H. Guo, N. Dong, M. Yin, W. Zhang, L. Lou, S. Xia, Green and red upconversion luminescence in $Er^{3+}$-doped and $Er^{3+}/Yb^{3+}$-codoped $SrTiO_3$ ultrafine powders, J. Alloys Compd. 415 (1–2) (2006) 280.

[24] Y. Wei, F. Lu, X. Zhang, D. Chen, Synthesis and characterization of efficient near-infrared upconversion Yb and Tm codoped $NaYF_4$ nanocrystal reporter, J. Alloys Compd. 427 (1–2) (2007) 333.

[25] Y. Kuisheng, L. Yan, Y. Chaoyi, L. Liping, Y. Chanhua, Z. Xiyan, Upconversion luminescence properties of $Ho^{3+}$, $Tm^{3+}$, $Yb^{3+}$ co-doped nanocrystal $NaYF_4$ synthesized by hydrothermal method, J. Rare Earths 24 (6) (2006) 757.

[26] T. Hirai, T. Orikoshi, Preparation of yttrium oxysulfide phosphor nanoparticles with infrared-to-green and -blue upconversion emission using an emulsion liquid membrane system, J. Colloid Interface Sci. 273 (2) (2004) 470.

[27] H.U. Gudel, M. Pollnau, Near-infrared to visible photon upconversion processes in lanthanide doped chloride, bromide and iodide lattices, J. Alloys Compd. 303–304 (2000) 307.

[28] R.X. Yan, Y.D. Li, Down/up conversion in $Ln^{(3+)}$-doped $YF_3$ nanocrystals, Adv. Funct. Mater. 15 (5) (2005) 763.

[29] X.P. Fan, D.B. Pi, F. Wang, J.R. Qiu, M.Q. Wang, Hydrothermal synthesis and luminescence behavior of lanthanide-doped $GdF_3$ nanoparticles, IEEE Trans. Nanotechnol. 5 (2) (2006) 123.

[30] G.S. Yi, H.C. Lu, S.Y. Zhao, G. Yue, W.J. Yang, D.P. Chen, L.H. Guo, Synthesis, characterization, and biological application of size-controlled nanocrystalline $NaYF_4$ : Yb,Er infrared-to-visible up-conversion phosphors, Nano Lett. 4 (11) (2004) 2191.

[31] G.S. Yi, G.M. Chow, Colloidal $LaF_3$ : Yb,Er, $LaF_3$ : Yb,Ho and $LaF_3$ : Yb,Tm nanocrystals with multicolor upconversion fluorescence, J. Mater. Chem. 15 (41) (2005) 4460.

[32] T. Hirai, T. Orikoshi, Preparation of $Gd_2O_3$ : Yb,Er and Gd2O2S : Yb,Er infrared-to-visible conversion phosphor ultrafine particles using an emulsion liquid membrane system, J. Colloid Interface Sci. 269 (1) (2004) 103.

[33] G.S. Yi, B.Q. Sun, F.Z. Yang, D.P. Chen, Y.X. Zhou, J. Cheng, Synthesis and characterization of high-efficiency nanocrystal up-conversion phosphors: ytterbium and erbium codoped lanthanum molybdate, Chem. Mater. 14 (7) (2002) 2910.

[34] X. Wang, X.G. Kong, G.Y. Shan, Y. Yu, Y.J. Sun, L.Y. Feng, K.F. Chao, S.Z. Lu, Y.J. Li, Luminescence spectroscopy and visible upconversion properties of $Er^{3+}$ in ZnO nanocrystals, J. Phys. Chem. B 108 (48) (2004) 18408.

[35] A. Walasek, Z. Eugeniusz, J. Zhang, S.W. Wang, Synthesis, morphology and spectroscopy of cubicY(3)NbO(7): Er, J. Lumin. 127 (2) (2007) 523.

[36] L. An., J. Zhang, M. Lui, S. Wang, Preparation and upconversion properties of $Yb^{3+}$,$Ho^{3+}$:$Lu_2O_3$ nanocrystalline powders, J. Am. Ceram. Soc. 88 (4) (2005) 1010.

[37] D. Wang, Y. Guo, G. Sun, J. Li, L. Zhao, G. Xu, Blue, green, yellow and red upconversion fluorescence in $Tm^{3+}/Ho^{3+}:Cs_2NaGdCl_6$ crystals under 785 nm laser excitation, J. Alloys Compd. **451** (1–2) (2008) 122.

[38] D.S. Jacob, L. Bitton, J. Grinblat, I. Felner, Y. Koltypin, A. Gedanken, Are ionic liquids really a boon for the synthesis of inorganic materials? A general method for the fabrication of nanosized metal fluorides, Chem. Mater. 18 (13) (2006) 3162.

[39] K.L. Wong, G.L. Law, W.M. Kwok, W.T. Wong, and D.L. Phillips, **Simultaneous** observation of green multiphoton upconversion and red and blue NLO process from polymeric terbium(III)complexes, Angew. Chem. Int. Ed. 44 (2005) 3436.

[40] K.L. Wong, W.M. Kwok, W.T. Wong, D.L. Phillips, K.W. Cheah, Green and red three-photon upconversion from polymeric lanthanide complexes, Angew. Chem. Int. Ed. 43 (2004) 4659.

[41] J.H. Zeng, J. Su, Z.H. Li, R.X. Yan, Y.D. Li, Synthesis and upconversion luminescence of hexagonal-phase $NaYF_4 : Yb, Er^{3+}$, phosphors of controlled size and morphology, Adv. Mater. 17 (17) (2005) 2119.

[42] S. Heer, O. Lehmann, M. Haase, H.U. Gudel, Blue, green, and red upconversion emission from lanthanide-doped $LuPO_4$ and $YbPO_4$ nanocrystals in a transparent colloidal solution, Angew. Chem. Int. Ed. 42 (27) (2003) 3179.

[43] L.Y. Wang, R.X. Yan, Z.Y. Hao, L. Wang, J.H. Zeng, H. Bao, X. Wang, Q. Peng, Y.D. Li, Fluorescence resonant energy transfer biosensor based on upconversion-luminescent nanoparticles, Angew. Chem. Int. Ed. 44 (37) (2005) 6054.

[44] V. Sudarsan, S. Sivakumar, F. van Veggel, M. Raudsepp, General and convenient method for making highly luminescent sol–gel derived silica and alumina films by using $LaF_3$ nanoparticles doped with lanthanide ions ($Er^{3+}$, $Nd^{3+}$, and $Ho^{3+}$), Chem. Mater. 17 (18) (2005) 4736.

[45] J. Xue, C. Wang, Z. Ma, A facile method to prepare a series of $SiO_2$@Au core/shell structured nanoparticles, Mater. Chem. Phys. 105 (2–3) (2007) 419.

[46] G.Z.Y.M. Li, Z.L. Wang, J. Lin, R.S. Wang, J. Fang, Sol–gel fabrication and photoluminescence properties of $SiO_2$ @ $Gd_2O_3:Eu^{3+}$ core-shell particles, J. Nanosci. Nanotechnol. 6 (5) (2006) 1416.

[47] H.Y.M. Wang, C.K. Lin, J. Lin, Core-shell structured $SiO_2$@$YVO_4:Dy^{3+}/Sm^{3+}$ phosphor particles: Sol–gel preparation and characterization, J. Colloid. Interface Sci. 300 (1) (2006) 176.

[48] A. Wolcott, D. Gerion, M. Visconte, J. Sun, A. Schwartzberg, S.W. Chen, J.Z. Zhang, Silica-coated CdTe quantum dots functionalized with thiols for bioconjugation to IgG proteins, J. Phys. Chem. B 110 (11) (2006) 5779.

[49] Z.Q. Li, Y. Zhang, Monodisperse silica-coated polyvinylpyrrolidone/$NaYF_4$ nanocrystals with multicolor upconversion fluorescence emission, Angew. Chem. Int. Ed. 45 (46) (2006) 7732.

[50] M. Kumar, A review of chitin and chitosan applications, React. Funct. Polym. 46 (1) (2000) 1.

[51] S. Miyazaki, K. Ishii, T. Nadai, The use of chitin and chitosan as drug carriers, Chem. Pharm. Bull. 29 (10) (1981) 3067.

[52] W.B. Tan, Y. Zhang, Surface modification of gold and quantum dot nanoparticles with chitosan for bioapplications, J. Biomed. Mater. Res. A 75A (1) (2005) 56.

[53] F. Wang, D.K. Chatterjee, Z.Q. Li, Y. Zhang, X.P. Fan, M.Q. Wang, Synthesis of polyethylenimine/NaYF$_4$ nanoparticles with upconversion fluorescence, Nanotechnology 17 (23) (2006) 5786.

[54] T. Konishi, K. Shimizu, Y. Saito, K. Saga, Surface modification of upconversion nanophosphors with poly(acrylic acid), J. Photopolym. Sci. Technol. 20 (1) (2007) 11.

[55] T. Konishi, M. Yamada, K. Soga, D. Matsuura, Y. Nagasaki, PEG-based surface modification on upconversion nanophosphors for bio-imaging under IR excitation, J. Photopolym. Sci. Technol. 19 (2) (2006) 145.

[56] W.C.Y. Pham, R. Weissleder, C.H. Tung, Developing a peptide based near-infrared molecular probe for protease sensing, Bioconjugate Chem. 15 (2004) 1403.

[57] S.M.P.S. Messerli, Y. Tang, K. Shah, M.L. Cortes, V. Murthy, et al., A novel method for imaging apoptosis using a caspase-1 near-infrared fluorescent probe, Neoplasia 6 (2004) 95.

[58] C.R.M.C. Kagan, M. Nirmal, M.G. Bawendi, Electronic energy transfer in CdSe quantum dot solids, Phys. Rev. Lett. 76 (1996) 1517.

[59] C.G. Morgan, A.C. Mitchell, Prospects for applications of lanthanide-based upconverting surfaces to bioassay and detection, Biosens. Bioelectron. 22 (8) (2007) 1769.

[60] K. Kuningas, T. Rantanen, T. Ukonaho, T. Lovgren, T. Soukka, Homogeneous assay technology based on upconverting phosphors, Anal. Chem. 77 (22) (2005) 7348.

[61] K. Kuningas, T. Ukonaho, H. Pakkila, T. Rantanen, J. Rosenberg, T. Lovgren, T. Soukka, Upconversion fluorescence resonance energy transfer in a homogeneous immunoassay for estradiol, Anal. Chem. 78 (13) (2006) 4690.

[62] K. Kuningas, H. Pakkila, T. Ukonaho, T. Rantanen, T. Lovgren, T. Soukka, Upconversion fluorescence enables homogeneous immunoassay in whole blood, Clin. Chem. 53 (1) (2007) 145.

[63] F. van de Rijke, H. Zijlmans, S. Li, T. Vail, A.K. Raap, R.S. Niedbala, H.J. Tanke, Up-converting phosphor reporters for nucleic acid microarrays, Nat. Biotechnol. 19 (3) (2001) 273.

[64] P. Corstjens, M. Zuiderwijk, A. Brink, S. Li, H. Feindt, R.S. Neidbala, H. Tanke, Use of up-converting phosphor reporters in lateral-flow assays to detect specific nucleic acid sequences: A rapid, sensitive DNA test to identify human papillomavirus type 16 infection, Clin. Chem. 47 (10) (2001) 1885.

[65] P. Corstjens, M. Zuiderwijk, M. Nilsson, H. Feindt, R.S. Niedbala, H.J. Tanke, Lateral-flow and up-converting phosphor reporters to detect single-stranded nucleic acids in a sandwich-hybridization assay, Anal. Biochem. 312 (2) (2003) 191.

[66] J.N.T. Riegler, Application of luminescent nanocrystals as labels for biological molecules, Anal. Bioanal. Chem. 379 (2004) 913.

[67] T. Heyduk, Measuring protein conformational changes by FRET/LRET, Curr. Opin. Biotechnol. 13 (2002) 292.

[68] R.N.P.A. Day, F. Schaufele, Fluorescence resonance energy transfer microscopy of localized protein interactions in the living cell nucleus, Methods 25 (2001) 4.

[69] J.J.B.T. Li, A fluorescent analogue of UDP-N-acetylglucosamine:application for FRET assay of peptidoglycan translocase (MurG), Chem. Commun. 182 (2004).

[70] S.F. Lim, R. Riehn, W.S. Ryu, N. Khanarian, C.K. Tung, D. Tank, R.H. Austin, In vivo and scanning electron microscopy imaging of upconverting nanophosphors in *Caenorhabditis elegans*, Nano Lett. 6 (2) (2006) 169.

[71] D.K. Chatteriee, A.J. Rufalhah, Y. Zhang, Upconversion fluorescence imaging of cells and small animals using lanthanide doped nanocrystals, Biomaterials 29 (7) (2008) 937.

[72] P. Zhang, W. Steelant, M. Kumar, M. Scholfield, Versatile photosensitizers for photodynamic therapy at infrared excitation, J. Am. Chem. Soc. 129 (15) (2007) 4526.

[73] D.K. Chatterjee, Y. Zhang, Upconverting nanoparticles as nanotransducers for photodynamic therapy in cancer cells, Nanomedicine 3 (1) (2008) 73.

[74] X. Qin, T. Yokomori, Y.G. Ju, Flame synthesis and characterization of rare-earth ($Er^{3+}$, $Ho^{3+}$, and $Tm^{3+}$) doped upconversion nanophosphors, Appl. Phys. Lett. 90 (7) (2007).

[75] S.Y.Z.H. Yu, J.B. Yu, C. Wang, L.N. Sun, W.D. Shi, Bifunctional magnetic–optical nanocomposites: grafting lanthanide complex onto core-shell magnetic silica nanoarchitecture, Langmuir 23 (14) (2007) 7836.

[76] Z.Y. Liu, G.S. Yi, H.T. Zhang, J. Ding, Y.W. Zhang, J.M. Xue, Monodisperse silica nanoparticles encapsulating upconversion fluorescent and superparamagnetic nanocrystals, Chem. Commun. (6) (2008) 694.

[77] J. Wu, Z.Q. Ye, G.L. Wang, J.L. Yuan, Multifunctional nanoparticles possessing magnetic, long-lived fluorescence and bio-affinity properties for time-resolved fluorescence cell imaging, Talanta 72 (5) (2007) 1693.

[78] O. Veiseh, C. Sun, J. Gunn, N. Kohler, P. Gabikian, D. Lee, N. Bhattarai, R. Ellenbogen, R. Sze, A. Hallahan, J. Olson, M.Q. Zhang, Optical and MRI multifunctional nanoprobe for targeting gliomas, Nano Lett. 5 (6) (2005) 1003.

[79] W.B. Tan, Y. Zhang, Multi-functional chitosan nanoparticles encapsulating quantum dots and Gd-DTPA as imaging probes for bio-applications, J. Nanosci. Nanotechnol. 7 (7) (2007) 2389.

# Micro- and Nanomachining

**M.J. Jackson**

*Center for Advanced Manufacturing, MET, College of Technology, Purdue University,*
*West Lafayette, IN, USA*

## CONTENTS

## ABSTRACT

Advances in miniaturization have led to the understanding and development of small scale components that require advanced machining techniques in order to achieve the tolerances and feature sizes required at the micro and nanoscales. The chapter focuses on general machining effects, size effects, nanomachining processes, and a comparison between machining at the micro and nanoscales. An explanation of how size effects at the microscale affects the removal of material and its implications on shaping material at ever diminishing scales is provided.

## 7.1  INTRODUCTION

Recent advances in miniaturization have led to the development of microscale components, usually in silicon. However, components made from engineering materials require shaping processes other than those established for processing silicon. Therefore, traditional machining processes require further development in order to machine components that are fit for purpose at the micro- and nanoscales. This chapter provides a timely review of the current developments and recent advances in the area of micro- and nanomachining. There is a substantial increase in the specific energy required with a decrease in chip size during machining. It is believed that this is due to the fact that all metals contain defects such as grain boundaries, missing and impurity atoms, and when the size of the material removed decreases the probability of encountering a stress-reducing defect decreases. Since the shear stress and strain in metal cutting is unusually high, discontinuous microcracks usually form on the primary shear plane. If the material is very brittle, or the compressive stress on the shear plane is relatively low, microcracks will grow into larger cracks giving rise to discontinuous chip formation. When discontinuous microcracks form on the shear plane they will weld and reform as strain proceeds, thus joining the transport of dislocations in accounting for the total slip of the shear plane. In the presence of a contaminant, such as carbon tetrachloride vapour at a low cutting speed, the re-welding of microcracks will decrease, resulting in a decrease in the cutting force required for chip formation. A number of special experiments that support the transport of microcraks across the shear plane and the important role compressive stress plays on the shear plane are explained. An alternative explanation for the size effect in cutting is based on the belief that shear stresses increase with increasing strain rate. When an attempt is made to apply this to metal cutting, it is assumed in the analysis that the von Mises criterion applies to the shear plane. This is inconsistent with the experimental findings by

Merchant. Until this difficulty is resolved with the experimental verification of the strain rate approach, it should be assumed that the strain rate effect may be responsible for some portion of the size effect in metal cutting.

## 7.2  MACHINING EFFECTS AT THE MICROSCALE

It has been known for a long time that a size effect exists in metal cutting, where the specific energy increases with decrease in deformation size. Backer et al.[1] performed a series of experiments in which the shear energy per unit volume deformed $(u_S)$ was determined as a function of specimen size for a ductile metal (SAE 1112 steel). The deformation processes involved were as follows, listed from top to bottom with increasing size of specimen deformed:

- surface grinding;

- micromilling;

- turning;

- tensile test.

The surface grinding experiments were performed under relatively mild conditions involving plunge type experiments in which an 8-in. (20.3 cm) diameter wheel was directed radially downwards against a square specimen of length and width 0.5 in. (1.27 cm). The width of the wheel was sufficient to grind the entire surface of the work at different downfeed rates $(t)$. The vertical and horizontal forces were measured by a dynamometer supporting the workpiece. This enabled the specific energy $(u_S)$ and the shear stress on the shear plane $(\tau)$ to be obtained for different values of undeformed chip thickness $(t)$. The points corresponding to a constant specific energy below a value of downfeed of about 28 μin. (0.7 μm) are on a horizontal line due to a constant theoretical strength of the material being reached when the value of $t$ goes below approximately 28 μin. (0.7 μm). The reasoning in support of this conclusion is presented in Backer et al[1].

In the micromilling experiments, a carefully balanced 6-in. (152 cm) carbide-tipped milling cutter was used with all but one of the teeth relieved so that it operated as a fly milling cutter. Horizontal and vertical forces were measured for a number of depths of cut $(t)$ when machining the same sized surface as in grinding. The shear stress on the shear plane $(\tau)$ was estimated by a rather detailed method presented in Backer et al.[1] Turning experiments were performed on a 2.25-in. (5.72 cm) diameter SAE 1112 steel bar premachined in the form of a thin-walled tube having a wall thickness of 0.2 in. (5 mm). A zero degree rake angle carbide tool was operated in a steady-state
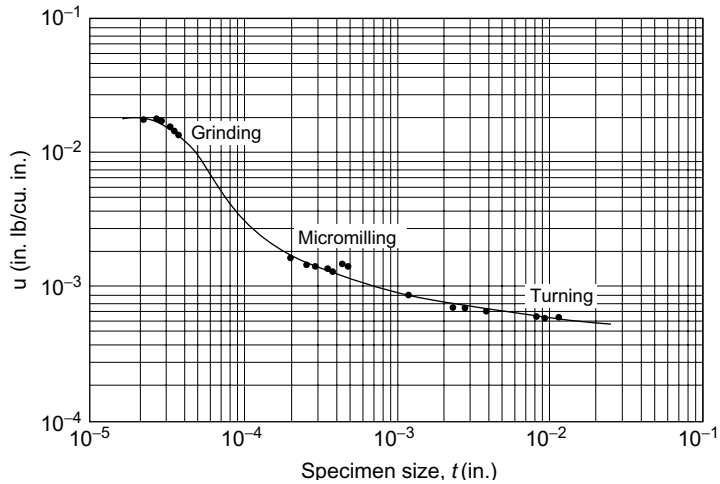
**FIGURE 7.1**   *Variation of shear stress on shear plane when cutting SAE 1112 steel.*
*Source: Ref. [1].*

2D orthogonal cutting mode as it machined the end of the tube. Values of shear stress on the shear plane $(\tau)$ versus undeformed chip thickness were determined for experiments at a constant cutting speed and different values of axial infeed rate and for variable cutting speeds and a constant axial infeed rate. The grinding, micromilling and turning results are shown in Figure 7.1.

A true stress–strain tensile test was performed on a 0.505-in. (1.28 cm) diameter by 2-in. (5.08 cm) length gauge specimen of SAE 1112 steel. The mean shear stress at fracture was 22,000 psi (151.7 MPa). This value is not shown in Figure 7.1 since it falls too far to the right. Taniguchi[2] discussed the size effect in cutting and forming and presented his version of Figure 7.1 in Figure 7.2. Shaw[3] discussed the origin of the size effect in metal cutting, which is believed to be primarily due to short-range inhomogeneities present in all engineering metals.

When the back of a metal cutting chip is examined at very high magnification by means of an electron microscope, individual slip lines are evident as shown in Figure 7.3. In deformation studies, Heidenreich and Shockley[4] found that slip does not occur on all atomic planes but only on certain discrete planes. In experiments on deformed aluminium single crystals, the minimum spacing of adjacent slip planes was found to be approximately 50 atomic spaces while the mean slip distance along the active slip planes was found to be about 500 atomic spaces. These experiments further support the observation that metals are not homogeneous and suggest that the planes along which slip occurs are associated with inhomogeneities in the metal. Strain is not
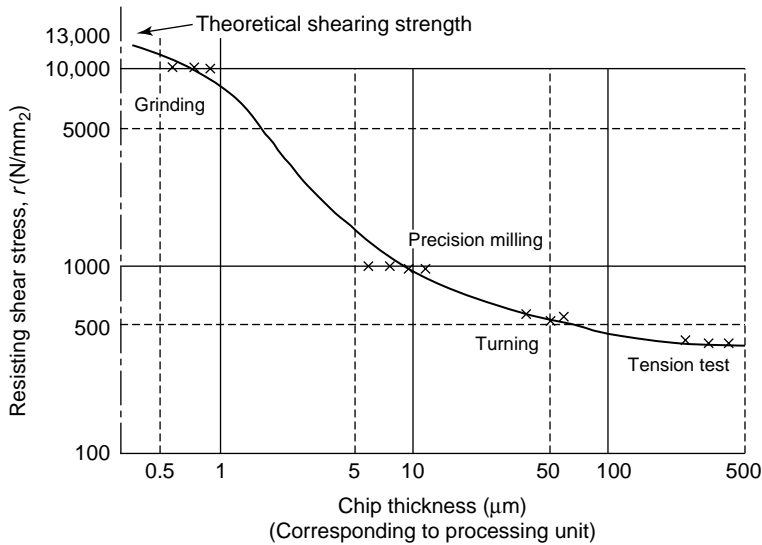
**FIGURE 7.2**   *Relationship between chip thickness and resisting shear stress for Figure 7.1 as modified by Taniguchi.*
*Source: Ref. [2].*

uniformly distributed in many cases. For example, the size effect in a tensile test is usually observed only for specimens less than 0.1 in. (2.5 mm) in diameter. On the other hand, a size effect in a torsion test occurs for considerably larger samples due to the greater stress gradient present in a torsion test than in a tensile test. This effect and several other related ones are discussed in detail by Shaw[3].

### 7.2.1  Shear angle prediction

There have been many notable attempts to derive an equation for the shear angle ($\rho$) shown in Figure 7.4 for steady-state orthogonal cutting. Ernst and Merchant[5] presented the first quantitative analysis. Figure 7.5 shows forces acting on a chip at the tool point. Here $R$ is the resultant force on the tool face, $R'$ is the resultant force in the shear plane, $N_C$ and $F_C$ are the components of $R$ normal to and parallel to the tool face, $N_S$ and $F_S$



**FIGURE 7.3**   *Back free surface of chip showing regions of discontinuous strain or microfracture.*

are the components of $R'$ normal to and parallel to the cutting direction, $F_Q$ and $F_P$ are the components of $R$ normal to and parallel to the cutting direction and $\beta = \tan^{-1} F_C/N_C$ is the friction angle.

Assuming the shear stress on the shear plane $(\tau)$ to be uniformly distributed, it is evident that:

$$\tau = \frac{F_S}{A_S} = \frac{R'\cos(\phi + \beta - \alpha)\sin\phi}{A} \tag{7.1}$$

where $A_S$ and $A$ are the areas of the shear plane and that corresponding to the width of cut $(b)$ times the depth of cut $(t)$. Ernst and Merchant[5] reasoned that $\tau$ should be an angle such that $\tau$ would be a maximum and obtained a relationship for $\rho$ by differentiating equation (7.1) with respect to $\rho$ and equating the resulting expression to zero:

$$\phi = 45 - \frac{\beta}{2} + \frac{\alpha}{2} \tag{7.2}$$

However, it is to be noted that in differentiating, both $R'$ and $\beta$ were considered independent of $\rho$.

Merchant[6] presented a different derivation that also led to equation (7.2). This time an expression for the total power consumed in the cutting process was first written as:

$$P = F_P V = (\tau A V)\frac{\cos(\beta - \alpha)}{\sin\phi\cos(\phi + \beta - \alpha)} \tag{7.3}$$

It was then reasoned that $\phi$ would be such that the total power would be a minimum. An expression identical to equation (7.2) was obtained when $P$ was differentiated with respect to $\phi$, this time
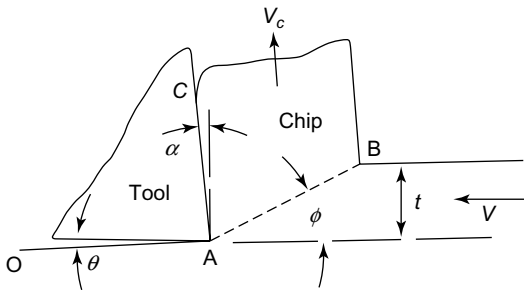


**FIGURE 7.4** *Nomenclature for 2D steady-state orthogonal cutting process.*
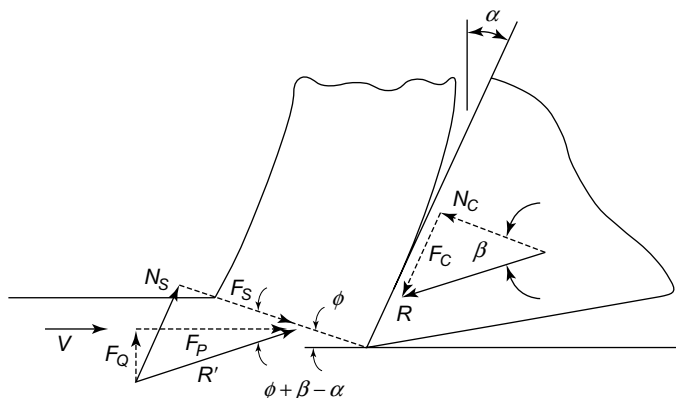


**FIGURE 7.5** *Cutting forces at the tool tip for the cutting operation shown in Figure 7.4.*

considering $\tau$ and $\beta$ to be independent of $\phi$. Piispanen[7] had done this previously in a graphical way. However, he immediately carried his line of reasoning one step further and assumed that the shear stress $\tau$ would be influenced directly by normal stress on the shear plane as follows:

$$\tau = \tau_0 + K_\sigma \tag{7.4}$$

where $K$ is a material constant. Piispanen then incorporated this into his graphical solution for the shear angle. Upon finding equation (7.2) to be in poor agreement with experimental data, Merchant also independently (without knowledge of Piispanen's work at the time) assumed the relationship given in equation (7.4), and proceeded to work this into his second analysis as follows. From Figure 7.5 it may be seen that:

$$\sigma = \tau \tan(\phi + \beta - \alpha) \tag{7.5}$$

or, from equation (7.4):

$$\tau_0 = \tau + K\tau \tan(\phi + \beta - \alpha) \tag{7.6}$$

Hence

$$\tau = \frac{\tau_0}{1 - K \tan(\phi + \beta - \alpha)} \tag{7.7}$$

When this is substituted into equation (7.3), we have:

$$P = \frac{\tau_0 AV \cos(\beta - \alpha)}{[1 - K \tan(\phi + \beta - \alpha)] \sin \phi \cos(\phi + \beta - \alpha)} \tag{7.8}$$

Now, when $P$ is differentiated with respect to $\rho$ and equated to zero (with $\tau_0$ and $p$ considered independent of $\rho$), we obtain:

$$\phi = \frac{\cot^{-1}(K)}{2} - \frac{\beta}{2} + \frac{\alpha}{2} = \frac{C - \beta + \alpha}{2} \tag{7.9}$$

Merchant called the quantity, $\cot^{-1} K$, the machining 'constant' $C$. The quantity $C$ is seen to be the angle the assumed line relating $\tau$ and $\phi$ makes with the $\tau$ axis[6–7, 9]. Merchant[8] has determined the values of $C$ given in Table 7.1 for materials of different chemistry and structure being turned under finishing conditions with different tool materials. From this table it is evident that $C$ is not a constant. Merchant's empirical machining 'constant' $C$ that gives rise to equation (7.9) with values of $\phi$ is in reasonably good agreement with experimentally measured values.

While it is well established that the rupture stress of both brittle and ductile materials is increased significantly by the presence of compressive stress (known as the Mohr effect), it is generally believed that a similar relationship for flow stress does not hold. However, an explanation for this paradox with considerable supporting experimental data is presented below. The fact that this discussion is limited to steady-state chip formation rules out the possibility of periodic gross cracks being involved. However, the role of microcracks is a possibility consistent with steady-state chip formation and the influence of compressive stress on the flow stress in shear. A discussion of the role microcracks can play in steady-state chip formation is presented in the next section. Hydrostatic stress plays no role in the plastic flow of metals if they have no porosity. Yielding then occurs when the von Mises criterion reaches a critical value. Merchant[9] has indicated that Barrett[10] found that for single crystal metals, $\tau_S$ is independent of the shear angle when plastics such as celluloid are cut. In general, if a small amount of compressibility is involved yielding will occur when the von Mises criterion reaches a certain value.

However, based on the results of Table 7.1 the role of compressive stress on shear stress on the shear plane in steady-state metal cutting is substantial. The fact that there is no outward sign of voids or porosity in steady-

| Table 7.1 | Values of $C$ in Equation (7.9) for a Variety of Work and Tool Materials in Finish Turning without a Cutting Fluid | |
|---|---|---|
| **Work Material** | **Tool Material** | **$C$ (degrees)** |
| SAE 1035 steel | HSS* | 70 |
| SAE 1035 steel | Carbide | 73 |
| SAE 1035 steel | Diamond | 86 |
| AISI 1022 (leaded) | HSS* | 77 |
| AISI 1022 (leaded) | Carbide | 75 |
| AISI 1113 (sul.) | HSS* | 76 |
| AISI 1113 (sul.) | Carbide | 75 |
| AISI 1019 (plain) | HSS* | 75 |
| AISI 1019 (plain) | Carbide | 79 |
| Aluminium | HSS* | 83 |
| Aluminium | Carbide | 84 |
| Aluminium | Diamond | 90 |
| Copper | HSS* | 49 |
| Copper | Carbide | 47 |
| Copper | Diamond | 64 |
| Brass | Diamond | 74 |

*HSS = High-speed steel.

state chip formation of a ductile metal during cutting and yet there is a substantial influence of normal stress on shear stress on the shear plane represents an interesting paradox. It is interesting to note that Piispanen[7] had assumed that shear stress on the shear plane would increase with normal stress and had incorporated this into his graphical treatment.

### 7.2.2  Plastic behaviour at large strains

There has been little work done in the region of large plastic strains. Bridgman[11] used hollow tubular notched specimens to perform experiments under combined axial compression and torsion. The specimen was loaded axially in compression as the centre section was rotated relative to the ends. Strain was concentrated in the reduced sections and it was possible to crudely estimate and plot shear stress versus shear strain with different amounts of compressive stress on the shear plane. From these experiments Bridgman concluded that the flow curve for a given material was the same for all values of compressive stress on the shear plane, a result consistent with other materials' experiments involving much lower plastic strains. However, the strain at gross fracture was found to be influenced by compressive stress. A number of related results are considered in the following subsections.

### 7.2.3  Langford and Cohen's model

Langford and Cohen[12] were interested in the behaviour of dislocations at very large plastic strains and whether there was saturation relative to the strain-hardening effect with strain, or whether strain hardening continued to occur with strain to the point of fracture. Their experimental approach was an interesting and fortunate one. They performed wire drawing on iron specimens using a large number of progressively smaller dies with remarkably low semi die angle (1.5°) and a relatively low (10%) reduction in area per die pass. After each die pass, a specimen was tested in uniaxial tension and a true stress–strain curve obtained. The drawing and tensile experiments were performed at room temperature and low speeds to avoid heating and specimens were stored in liquid nitrogen between experiments to avoid strain aging effects. All tensile results were then plotted in a single diagram, the strain used being that introduced in drawing (0.13 per die pass) plus the plastic strain in the tensile test. The general overlap of the tensile stress–strain curves gives an overall strain-hardening envelope, which indicates that the wire drawing and tensile deformations are approximately equivalent relative to strain hardening[13].

Blazynski and Cole[14] were interested in strain hardening in tube drawing and tube sinking. Drawn tubes were sectioned and tested in plane strain

compression. Up to a strain of about 1 the usual strain-hardening curve was obtained which is in good agreement with the generally accepted equation:

$$\sigma = \sigma_1 \varepsilon^n \tag{7.10}$$

However, beyond a strain of 1, the curve was linear corresponding to the equation:

$$\sigma = A + B\varepsilon \quad (\varepsilon < 1) \tag{7.11}$$

where $A$ and $B$ are constants. It may be shown that:

$$A = (1 - n)\,\sigma_1 \tag{7.12}$$

$$B = n\sigma_1 \tag{7.13}$$

From transmission electron micrographs of deformed specimens, Langford and Cohen found that cell walls representing concentrations of dislocations began to form at strains below 0.2 and became ribbon shaped with decreasing mean linear intercept cell size as the strain progressed. Dynamic recovery and cell wall migration resulted in only about 7% of the original cells remaining after a strain of 6. The flow stress of the cold-worked wires was found to vary linearly with the reciprocal of the mean transverse cell size[15].

## 7.2.4 Walker and Shaw's model

Acoustic studies were performed on specimens of the Bridgman type, but fortunately, lower levels of axial compressive stress than Bridgman had used were employed in order to more closely simulate the concentrated shear process of metal cutting. The apparatus used that was capable of measuring stresses and strains as well as acoustic signals arising from plastic flow is described in the dissertation of T.J. Walker[16]. Two important results were obtained:

1. A region of rather intense acoustical activity occurred at the yield point followed by a quieter region until a shear strain of about 1.5 was reached. At this point there was a rather abrupt increase in acoustical activity that continued to the strain at fracture which was appreciably greater than 1.5.

2. The shear stress appeared to reach a maximum at strain corresponding to the beginning of the second acoustic activity ($\gamma \approx 1.5$).

The presence of the notches in the Bridgman specimen made interpretation of stress–strain results somewhat uncertain. Therefore, a new specimen was designed which substitutes simple shear for torsion with normal stress on the shear plane. By empirically adjusting distance $\Delta x$ to a value

of 0.25 mm, it was possible to confine all the plastic shear strain to the reduced area, thus making it possible to readily determine the shear strain $(\gamma \approx \Delta y/\Delta x)$. When the width of minimum section was greater or lesser than 0.25 mm, the extent of plastic strain observed in a transverse micrograph at the minimum section either did not extend completely across the 0.25 mm dimension or extended beyond this width.

Similar results were obtained for non-resulphurized steels and other ductile metals. There is little difference in the curves for different values of normal stress on the shear plane $(\sigma)$ to a shear strain[17] of about 1.5. This is in agreement with Bridgman. However, beyond this strain the curves differ substantially with compressive stress on the shear plane. At large strains, $\tau$ was found to decrease with increase in $\gamma$, a result that does not agree with Bridgman[11].

It is seen that for a low value of normal stress on the shear plane of 40 MPa, strain hardening appears to be negative at a shear strain of about 1.5; that is, when the normal stress on the shear plane is about 10% of the maximum shear stress reached, negative strain hardening sets in at a shear strain of about 1.5. On the other hand, strain hardening remains positive to a normal strain of about 8 when the normal stress on the shear plane is about equal to the maximum shear stress.

### 7.2.5 Usui's model

In Usui et al.[18] an experiment designed to determine why $CCl_4$ is such an effective cutting fluid at low cutting speeds is described. Since this also has a bearing on the role of microcracks in large strain deformation, it is considered here. A piece of copper was prepared[18]. The piece that extends upward and appears to be a chip is not a chip but a piece of undeformed material left there when the specimen was prepared. A vertical flat tool was then placed precisely opposite to the free surface and fed horizontally. Horizontal $F_P$ and vertical $F_Q$ forces were recorded as the shear test proceeded. It was expected that the vertical piece would fall free from the lower material after the vertical region had been displaced a small percentage of its length. However, it went well beyond the original extent of the shear plane and was still firmly attached to the base. This represents a huge shear strain since the shear deformation was confined to a narrow band. When a single drop of $CCl_4$ was placed before the shear test was conducted, the protrusion could be moved only a fraction of the displacement in air before gross fracture occurred on the shear plane. Figure 7.6 shows photomicrographs of experiments without and with $CCl_4$. It is apparent that $CCl_4$ is much more effective than air in preventing microcracks from re-welding.

(a)

(b)
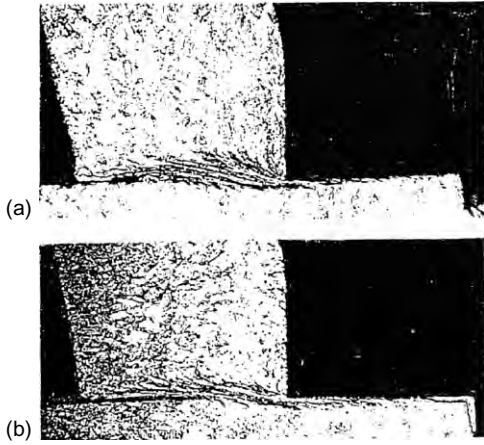
**FIGURE 7.6** *Photomicrographs of specimens that have been sheared a distance approximately equal to the shear plane length: (a) in air and (b) with a drop of CCl$_4$ applied.*

## 7.2.6 Saw tooth chip formation in hard turning

Saw tooth chip formation for hard steel discussed by Vyas and Shaw[19] is another example of the role microcracks play. In this case gross cracks periodically form at the free surface and run down along the shear plane until sufficient compressive stress is encountered to cause the gross crack to change to a collection of isolated microcracks.

## 7.2.7 Fluid-like flow in chip formation

An interesting paper was presented by Eugene[20]. Water was pumped into baffled chamber A that removed eddy currents and then caused flow under gravity past a simulated tool at B. Powdered bakelite was introduced at C to make the streamlines visible as the fluid flowed past the tool. The photographs taken by the camera at D were remarkably similar to quick stop photomicrographs of actual chips. It was thought by this author at the time that any similarity between fluid flow and plastic flow of a solid was not to be expected. That was long before it was clear that the only logical explanation for the results of Bridgman and Merchant involve microfracture[21]. A more recent paper was presented that again suggests that metal cutting might be modelled by a fluid[22–23]. However, this paper was concerned with ultra-precision machining (depths of cut $<4\,\mu m$) and potential flow analysis was employed instead of the experimental approach taken by Eugene.

It is interesting to note that chemists relate the flow of liquids to the migration of vacancies (voids) just as physicists relate ordinary plastic flow of solid metals to the migration of dislocations. Henry Eyring and co-workers[24–26] have studied the marked changes in volume, entropy and fluidity that occur when a solid melts. For example, a 12% increase in volume accompanies melting of Argon, suggesting the removal of every eighth molecule as a vacancy upon melting. This is consistent with X-ray diffraction of liquid argon that showed good short-range order but poor long-range order. The relative ease of diffusion of these vacancies accounts for the increased fluidity that accompanies melting. A random distribution of vacancies is also consistent with the increase in entropy observed on melting. Eyring's theory of fluid flow was initially termed the 'hole theory of fluid flow' but later 'The Significant Structure Theory' which is the title of the Eyring-Jhon book[25]. According to this theory, the vacancies in a liquid

move through a sea of molecules. Eyring's theory of liquid flow is mentioned here since it explains why the flow of a liquid approximates the flow of metal passed a tool in chip formation. In this case microcracks (voids) move through a sea of crystalline solid.

## 7.3 SIZE EFFECTS IN MICROMACHINING

It is appropriate at this point to mention that an alternative explanation for the increase in hardness that occurs when the indentation size is reduced in metals has recently been introduced[27–38]. This is based on the fact that there is an increase in the strain gradient with reduction in indentation size. This has been extended by Dinesh et al.[39] to explain the size effect in machining. In the Dinesh et al.[39] analysis the size effect in hardness is related to that in cutting by assuming the von Mises criterion is applicable. Based on the experiments of Merchant, it is evident that this is not applicable in steady-state chip formation.

In this strain gradient theory two types of dislocations are proposed: geometrically necessary dislocations ($\rho_g$) that are responsible for work hardening and statistically stored dislocations ($\rho_S$) that are affected by a strain gradient. When $\rho_g >> \rho_S$ conventional plasticity pertains (strain rate unimportant) but when $\rho_g << \rho_S$ a constitutive equation including strain rate should be included. The impression one obtains in reading Dinesh et al.[39] is that the strain gradient approach is uniquely responsible for the size effect in cutting. In their concluding remarks it is suggested that it should be possible to verify the validity of the strain rate formulation by experiments designed to test predictions of this approach. This has not yet been done and until it is done, it will not be possible to determine whether the influence of strain rate is significant in the chip formation application. In any case, it is believed that the explanation presented here is based on the influence of defects and normal stress on the shear plane is sufficiently well supported by the experiments described that it should not be considered insignificant.

## 7.4 NANOMACHINING

Nanomachining can be classified into four categories:

- Deterministic mechanical nanometric machining: This method utilizes fixed and controlled tools, which can specify the profiles of 3D components by a well-defined tool surface and path. The method can remove materials in amounts as small as tens of nanometres.

It includes typically diamond turning, micromilling and nano/microgrinding, etc.

- Loose abrasive nanometric machining: This method uses loose abrasive grits for removal of a small amount of materials. It consists of polishing, lapping and honing, etc.

- Non-mechanical nanometric machining: It comprises focused ion beam machining, micro-Electro Discharge Machining (EDM) and excimer laser machining.

- Lithographic method: It employs masks to specify the shape of the product. 2D shapes are the main outcome; severe limitations occur when 3D products are attempted. It mainly includes X-ray lithography, Lithographie Galvano Abformung (LIGA), electron beam lithography.

Mechanical nanometric machining has more advantages than other methods since it is capable of machining complex 3D components in a controllable way. The machining of complex surface geometry is just one of the future trends in nanometric machining, which is driven by the integration of multiple functions in one product. For instance, the method can be used to machine micromoulds and dies with complex geometric features and high dimensional and form accuracy, and even nanometric surface features. The method is indispensable to manufacturing complex micro and miniature structures, components and products in a variety of engineering materials. This chapter focuses on nanometric cutting theory, methods and its implementation and application perspectives[40–44].

## 7.4.1 Nanometric machining

Single-point diamond turning and ultra-precision grinding are two major nanometric machining approaches. They are both capable of producing extremely fine cuts. Single-point diamond turning has been widely used to machine non-ferrous metals such as aluminium and copper. An undeformed chip thickness of about 1nm is observed in diamond turning of electroplated copper[45]. Diamond grinding is an important process for the machining of brittle materials such as glasses and ceramics to achieve nanometre levels of tolerances and surface finish. A repeatable optical quality surface roughness (surface finish <10nm Ra) has been obtained in nanogrinding of hard steel by Stephenson et al. using 76μm grit cBN wheel on the ultra-precision grinding machine tool[46]. Recently, diamond fly-cutting and diamond milling have been developed for machining non-rotational, non-symmetric geometry, which has enlarged the product spectrum of

nanometric machining[47]. In addition the utilization of ultra-fine grain hard metal tools and diamond coated micro tools represents a promising alternative for microcutting of even hardened steel[48].

Early applications of nanometric machining are in the mass production of some high precision parts for microproducts, or microsystems. In fact, microproducts, or microsystems, will be the first path that enables nanoproducts to enter the marketplace since microproducts, or microsystems, have been dominating nanotechnology application markets worldwide[49]. It also anticipates that microproducts will have more and more requirements around the world. It is very interesting to see that the IT peripheral market is still the biggest market of microproducts. In 2005, the total turnover of microproducts had reached US $38 billion, which is two times that of the total turnover in 2000. Nanometric machining can be applied in bulk machining of silicon, aluminium substrates for computer memory disks, etc. In other areas such as biomedical, automotive, household and telecommunication the total turnovers of microproducts are still steadily growing. Nanometric machining is also very promising in the production of sensors, accelerometer, actuators, micro-mirror, fibre optics connectors, and micro-displays. In fact applications of nanoproducts will enhance the performance of microproducts in the form of sensitivity, selectivity and stability[50]. By 2006, IT lost this predominant position owing to new MEMS based applications in sectors such as biotechnology and communication (optical and radio frequency switching, for example, will become a major growth area)[51]. Nanometric machining still has priority in this application area. The microproducts are normally integrated products of some electronics, mechanical parts and optical parts while in miniature or micro dimensions. In fact only small number of microproducts solely relies on electronics. The mechanical and optical parts are of significant importance for microproducts. The indispensable advantage of nanometric machining is its applicability to manufacture 3D complex components/devices including micromoulds, dies and embossing tooling for cheap mass production of optical and mechanical parts. Therefore, it is undoubtedly one of the major enabling technologies for commercialization of nanotechnology in the future.

## 7.4.2 Theoretical basis of nanomachining

Scientific study of nanometric machining has been undertaken since the late 1990s. Much attention to the study has been paid especially with the advancement of nanotechnology[52]. The scientific study will result in the formation of the theoretical basis of nanometric machining, which enables the better understanding of nanometric machining physics and the development

of its controllable techniques to meet the advanced requirements for nanotechnology and nanoscience.

### 7.4.2.1 Cutting force and energy

In nanomanufacturing, the cutting force and cutting energy are important issues. They are important physical parameters for understanding cutting phenomena as they clearly reflect the chip removal process. From the aspect of atomic structures, cutting forces are the superposition of the interaction forces between workpiece atoms and cutting tool atoms. Specific energy is an intensive quantity that characterizes the cutting resistance offered by a material[53]. Ikawa et al. and Luo et al. have acquired the cutting forces and cutting energy by molecular dynamics (MD) simulations[52–55]. Moriwaki and Lucca have carried out experiments to measure the cutting forces in nanometric machining[52]. Figure 7.7 shows the simulation and experimental results in nanometric cutting. Figure 7.7a illustrates the linear relation that exists between the cutting forces per width and depth of uncut in both simulations and experiments. The cutting forces per width increase with the increment of the depth of cut.

The difference in the cutting force between the simulations and the experiments is caused by the different cutting edge radii applied in the simulations. In nanometric machining the cutting edge radius plays an important role since the depth of cut is similar in scale. Under the same depth of cut higher cutting forces are needed for a tool with a large cutting edge radius compared to a tool with a small cutting edge radius. The low cutting
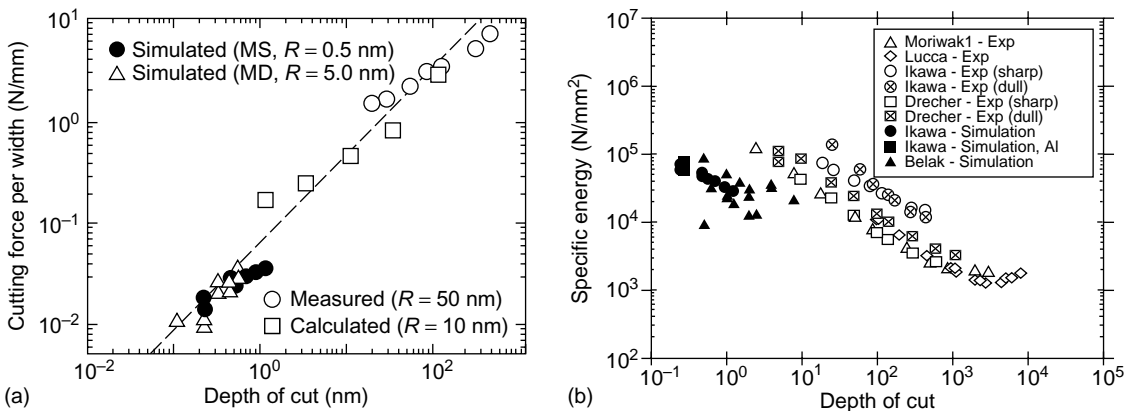


**FIGURE 7.7**   *Comparison of results between simulations and experiments: (a) cutting force per width against depth of cut; (b) specific energy against depth of cut.*

*Source: Ref. [52].*

force per width is obviously the result of fine cutting conditions, which will decrease the vibration of the cutting system and thus improve the machining stability and will also result in better surface roughness. A linear relationship between the specific energy and the depth of cut can also be observed in Figure 7.7b. The figure shows that the specific energy increases with a decrease in depth of cut, because the effective rake angle is different under different depths of cut. In small depths of cut the effective rake angle will increase with decreasing depth of cut. Large rake angle results with increasing specific energy. This phenomenon is often called the 'size effect', which can be clearly explained by material data listed in Table 7.2. According to Table 7.2, in nanometric machining only point defects exist in the machining zone in a crystal, so it will need more energy to initiate the atomic-crack or atomic-dislocation. The decrease in depth of cut will decrease the chance for the cutting tool to meet point defects and result in the increase of the specific cutting energy.

If the machining unit is reduced to 1nm, the workpiece material structure at the machining zone may approach atomic perfection; so more energy will be required to break the atomic bonds. On the other hand when the machining unit is higher than 0.1μm, the machining points will fall into the distribution distances of some defects such as dislocations, cracks and grain boundaries. The pre-existing defects will ease the deformation of workpiece material and result in a comparatively low specific cutting energy. Nanometric cutting is also characterized by the high ratio of the normal to the tangential component in the cutting force[53, 55], as the depth of cut is very small in nanometric cutting and the workpiece is mainly processed by the cutting edge. The compressive interactions will thus become dominant in the deformation of workpiece material, which will therefore result in the increase of friction force at the tool–chip interface and the

| **Table 7.2** | Material Properties under Different Machining Units | | |
|---|---|---|---|
| | 1nm − 0.1μm | 0.1 − 10μm | 10μm − 1mm |
| Defects/Impurities | Point defect | Dislocation/crack | Crack/grain boundary |
| Chip removal unit | Atomic cluster | Sub-crystal | Multi-crystals |
| Brittle fracture limit | $10^4 J/m^3 − 10^3 J/m^3$ | $10^3 J/m^3 − 10^2 J/m^3$ | $10^2 J/m^3 − 10^1 J/m^3$ |
| | Atomic crack | Microcrack | Brittle crack |
| Shear failure limit | $10^4 J/m^3 − 10^3 J/m^3$ | $10^3 J/m^3 − 10^2 J/m^3$ | $10^2 J/m^3 − 10^1 J/m^3$ |
| | Atomic dislocation | Dislocation slip | Shear deformation |

*Source: Ref. [56].*

relative high cutting ratio. Usually the cutting force in nanometric machining is very difficult to measure due to its small amplitude compared with the noise (mechanical or electronic)[52]. A piezoelectric dynamometer or load cell is used to measure the cutting forces because of their high sensitivity and natural frequency[57].

### 7.4.2.2 Cutting temperatures

In MD simulation, the cutting temperature can be calculated under the assumption that cutting energy totally transfers into cutting heat and results in the rising of cutting temperature and kinetic energy of the system. The lattice vibration is the major form of thermal motion of atoms. Each atom has three degrees of freedom. According to the theorem of equi-partition of energy, the average kinetic energy of the system can be expressed as:

$$\bar{E}_k = \frac{3}{2} N k_B T = \sum_i \frac{1}{2} m \left( V_i^2 \right) \qquad (7.14)$$

where $\bar{E}_k$ is the average kinetic energy in equilibrium state, $K_B$ is Boltzmann's constant, $T$ is temperature, $m_i$ and $V_i$ are the mass and velocity of an atom, respectively, and $N$ is the number of atoms. The cutting temperature can be deduced as:

$$T = \frac{2 \bar{E}_k}{3 N k_B} \qquad (7.15)$$

Figure 7.8 shows the variation of cutting temperature on the cutting tool in a MD simulation of nanometric cutting of single crystal aluminium. The highest temperature is observed at cutting edge although the temperature at the flank face is also higher than that at the rake face. The temperature distribution suggests that a major heat source exists in the interface between cutting edge and workpiece and the heat is conducted from there to the rest of the cutting zone in workpiece and cutting tool. The reason is that because most cutting actions take place at the cutting edge of the tool, the dislocation deformations of workpiece materials will transfer potential energy into the kinetic energy and result in a rise in temperature. The comparative high temperature at the tool flank face is obviously caused by the friction between tool flank face and workpiece. The released energy due to the elastic recovery of the machined surface also contributes to the increment of temperature at tool flank face. Although there is also friction between the tool rake face and the chip, the heat will be taken away from the tool rake face by the removal of the chip.
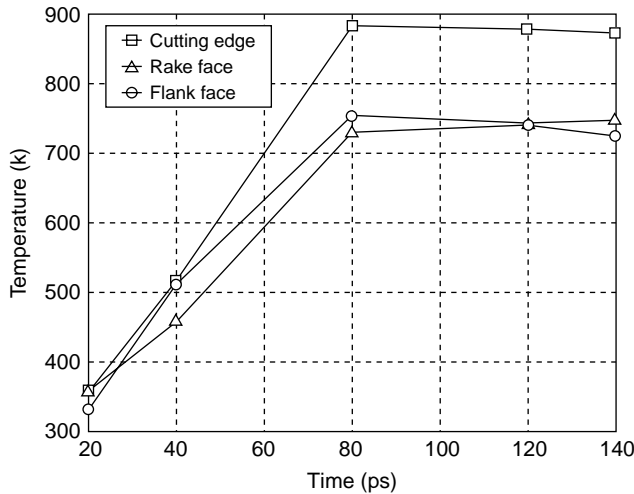
**FIGURE 7.8** *Cutting temperature distribution of cutting tool in nanometric cutting (cutting speed = 20 m/s, depth of cut = 1.5 nm, cutting edge radius = 1.57 nm).*
*Source: Ref. [58].*

Therefore, the temperature at tool rake face is lower than that at the tool cutting edge and tool flank face. The temperature value shows that the cutting temperature in diamond machining is quite low in comparison with that in conventional cutting, due to low cutting energy as well as the high thermal conductivity of diamond and the workpiece material. The cutting temperature is considered to govern the wear of a diamond tool in a MD simulation study by Cheng et al.[58] More in-depth experimental and theoretical studies are needed to find out the quantitative relationship between cutting temperature and tool wear, although there is considerable evidence of chemical damage on diamond in which temperature plays a significant role[52].

### 7.4.2.3 Chip formation

Chip formation and surface generation can be simulated by MD simulation. Figure 7.9 shows an MD simulation of a nanometric cutting process on single crystal aluminium. From Figure 7.9a it is shown that after the initial plow of the cutting edge, the workpiece atoms are compressed in the cutting zone near to the rake face and the cutting edge. The disturbed crystal lattices of the workpiece and even the initiation of dislocations can be observed in Figure 7.9b. Figure 7.9c shows the dislocations piled up to form a chip. The chip is removed with the unit of an atomic cluster as shown in Figure 7.9d. Lattice disturbed workpiece material is observed on the machined surface.
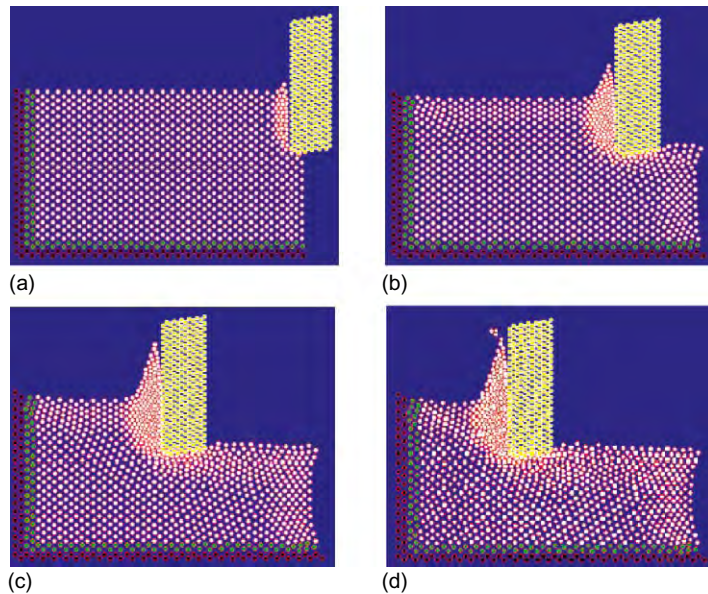
**FIGURE 7.9** *MD simulations of the nanometric machining process: (a) 3.4 ps; (b) 17.0 ps; (c) 30.6 ps and (d) 37.2 ps (cutting speed = 20 m/s, depth of cut = 1.4 nm, cutting edge radius = 0.35 nm). Source: Ref. [58].*

Based on the visualization of the nanometric machining process, the mechanism of chip formation and surface generation in nanometric cutting can be explained. Owing to the plowing of the cutting edge, the attractive force between the workpiece atoms and the diamond tool atoms becomes repulsive. Because the cohesion energy of diamond atoms is much larger than that of Al atoms, the lattice of the workpiece is compressed. When the strain energy stored in the compressed lattice exceeds a specific level, the atoms begin to rearrange so as to release the strain energy. When the energy is not sufficient to perform the rearrangement, some dislocation activity is generated. Repulsive forces between compressed atoms in the upper layer and the atoms in the lower layer are increasing, so the upper atoms move along the cutting edge, and at the same time the repulsive forces from the tool atoms cause the resistance for the upward chip flow to press the atoms under the cutting line. With the movement of the cutting edge, some dislocations move upwards and disappear from the free surface as they approach the surface.

This phenomenon corresponds to the process of the chip formation. As a result of the successive generation and disappearance of dislocations, the chip seems to be removed steadily. After the passing of the tool, the pressure at the flank face is released. The layers of atoms move upwards and

result in elastic recovery, so the machined surface is generated. The conclusion can therefore be drawn that the chip removal and machined surface generation are in nature the dislocation slip movement inside the workpiece material crystal grains. In conventional cutting the dislocations are initiated from the existing defects between the crystal grains, which will ease the movement of dislocation and result in smaller specific cutting forces compared with that in nanometric cutting.

The height of the atoms on the surface layer of the machined surface creates the surface roughness. For this, 2D MD simulation $R_a$ can be used to assess the machined surface roughness. The surface integrity parameters can also be calculated based on the simulation results. For example, the residual stress of the machined surface can be estimated by averaging the forces acting on the atoms in a unit area on the upper layer of the machined surface. MD simulation has been proved to be a useful tool for the theoretical study of nanometric machining[59]. At present the MD simulation studies on nanometric machining are limited by the computing memory size and speed of the computer. It is therefore difficult to enlarge the dimension of the current MD model on a personal computer. In fact, the machined surface topography is produced as a result of the copy of the tool profile on a workpiece surface that has a specific motion relative to the tool. The degree of the surface roughness is governed by both the controllability of machine tool motions (or relative motion between tool and workpiece) and the transfer characteristics (or the fidelity) of tool profile to workpiece[52]. A multi-scale analysis model, which can fully model the machine tool and cutting tool motion, environmental effects and the tool–workpiece interactions, is much needed to predict and control the nanometric machining process in a determinative manner.

### 7.4.2.4 *Minimum undeformed chip thickness*

Minimum undeformed chip thickness is an important issue in nanometric machining because it relates with the ultimate machining accuracy. In principle the minimum undeformed chip thickness will be determined by the minimum atomic distance within the workpiece. But in ultra-precision machining practices, it depends much on the sharpness of the diamond cutting tool, the capability of the ultra-precision machine tool and machining environment. The diamond turning experiments of non-ferrous work materials carried out at Lawrence Livermore National Laboratory (LLNL) show that the minimum undeformed chip thickness, down to 1nm, is attainable with a specially prepared fine diamond cutting tool on a highly reliable ultra-precision machine tool[45]. Based on the tool wear simulation, the minimum undeformed chip thickness is further studied in this chapter. Figure 7.10

illustrates chip formation of single crystal aluminium with the tool cutting edge radius of 1.57 nm. No chip formation is observed when the undeformed chip thickness is 0.25 nm. But the initial stage of chip formation is apparent when the undeformed chip thickness is at 0.26 nm. In nanometric cutting, as the depth of cut is very small, the chip formation is related to the force conditions on the cutting edge. Generally, chip formation is mainly a function of tangential cutting force.

The normal cutting force makes little contribution to the chip formation since it has the tendency to penetrate the atoms of the surface into the bulk of the workpiece. The chip is formed on condition that the tangential cutting force is larger than the normal cutting force in theory. The relationships between the minimum undeformed chip thickness, cutting edge radius and cutting forces are studied via MD simulations. The results are highlighted in Table 7.3. The data show that the minimum undeformed chip thickness is about 1/3 to 1/6 of the tool cutting edge radius. The chip formation will be initiated when the ratio of tangential cutting force to normal cutting force is larger than 0.92.

### 7.4.2.5 Critical cutting radius

It is widely accepted that the sharpness of the cutting edge of a diamond cutting tool directly affects the machined surface quality. Previous MD simulations show that the sharper the cutting edge is, the smoother the machined surface becomes. But this
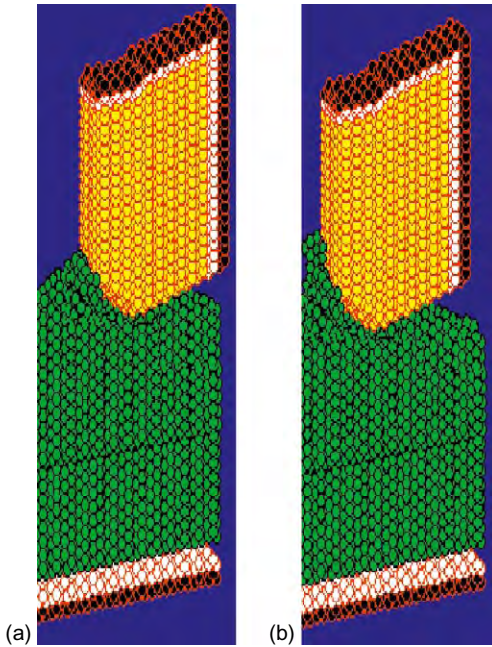


**FIGURE 7.10** *Study of minimum undeformed chip thickness by MD simulation: (a) undeformed chip thickness = 0.25 nm; (b) undeformed chip thickness = 0.26 nm.*
*Source: Ref. [58].*

| **Table 7.3** | Minimum Undeformed Chip Thickness against the Tool Cutting Edge Radius and Cutting Forces | | | | | |
|---|---|---|---|---|---|---|
| **Cutting edge radius (nm)** | **1.57** | **1.89** | **2.31** | **2.51** | **2.83** | **3.14** |
| Minimum undeformed chip thickness (nm) | 0.26 | 0.33 | 0.42 | 0.52 | 0.73 | 0.97 |
| Ratio of minimum undeformed chip thickness to tool cutting edge radius | 0.17 | 0.175 | 0.191 | 0.207 | 0.258 | 0.309 |
| Ratio of tangential cutting force to normal cutting force | 0.92 | 0.93 | 0.92 | 0.92 | 0.94 | 0.93 |

*Source: Ref. [58].*

conclusion is based on no tool wear. To study the real effects of cutting edge radius, the MD simulations on nanometric cutting of single crystal aluminium are carried out using a tool wear model[59].

In the simulations the cutting edge radius of the diamond cutting tool varies from 1.57 nm to 3.14 nm with a depth of cut of 1.5 nm, 2.2 nm and 3.1 nm. The cutting distance is fixed at 6 nm. The root mean square deviation of the machined surface and mean stress on the cutting edge are listed in Table 7.4. Figure 7.11 shows the visualization of the simulated data, which clearly indicates that surface roughness increases with the decreasing cutting edge radius

**Table 7.4** The Relationship between Cutting Edge Radius and Machined Surface Quality

|  | Cutting edge radius (nm) | 1.57 | 1.89 | 2.31 | 2.51 | 2.83 | 3.14 |
|---|---|---|---|---|---|---|---|
| Depth of cut: 1.5 nm | $S_q$ | 0.89 | 0.92 | 0.78 | 0.86 | 0.98 | 1.06 |
| Depth of cut: 2.2 nm | $S_q$ | 0.95 | 0.91 | 0.77 | 0.88 | 0.96 | 1.07 |
| Depth of cut: 3.1 nm | $S_q$ | 0.97 | 0.93 | 0.79 | 0.87 | 0.99 | 1.08 |
| Mean stress at cutting edge (GPa) |  | 0.91 | 0.92 | −0.24 | −0.31 | −0.38 | −0.44 |

*Source: Ref. [58].*
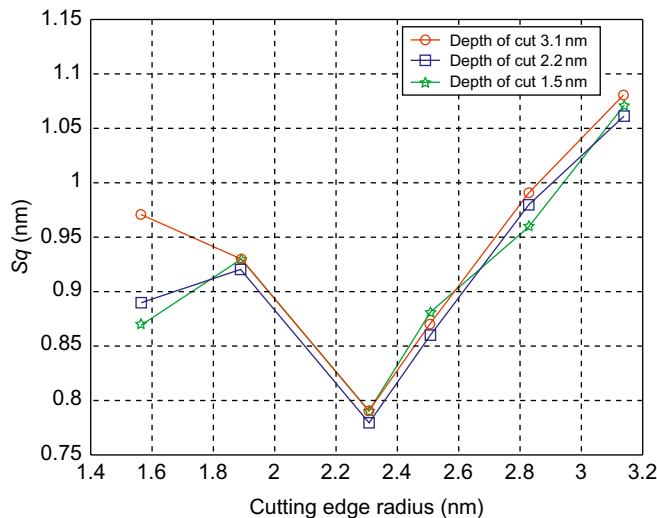


**FIGURE 7.11** *Cutting edge radius against machined surface quality.*
*Source: Ref. [58].*

when the cutting edge radius is smaller than 2.31nm. The tendency is obviously caused by the rapid tool wear when a cutting tool with small cutting edge radius is used. But when the cutting edge is larger than 2.31nm, the cutting edge is under compressive stress and no tool wear happens. Therefore, as in the previous MD simulations, the surface roughness increases with decreasing tool cutting edge radius.

The MD simulation results also illustrate that it is not true that the sharper the cutting edge, the better the machined surface quality. The cutting edge is destined to wear and results in the degradation of the machined surface quality if its radius is smaller than a critical value. But when the cutting edge radius is higher than the critical value, the compressive stress will take place at the tool edge and the tool condition is more stable. As a result a high quality machined surface can be achieved. Therefore, there is a critical cutting edge radius for stably achieving high quality machined surfaces. For cutting single crystal aluminium the critical cutting edge radius is at 2.31nm. The MD simulation approach is applicable for acquiring the critical cutting edge radius for nanometric cutting of other materials.

### 7.4.2.6 Workpiece materials

In nanometric machining the microstructure of the workpiece material will play an important role in affecting the machining accuracy and machined surface quality. For example, when machining polycrystalline materials, the difference in the elastic coefficients at the grain boundary and interior of the grain causes small steps formed on the cut surface since the respective elastic 'rebound' varies[60]. The study by Lee and Cheung shows that the shear angle varies with the crystallographic orientation of the materials being cut. This will produce a self-excited vibration between cutting tool and workpiece and result in a local variation of surface roughness of a diamond turned surface[61].

A material's destructive behaviour can also be affected by nanometric machining. In nanometric machining of brittle materials, it is possible to produce plastically deformed chips if the depth of cut is sufficiently small[62]. It has been shown that a 'brittle-to-ductile' transition exists when cutting brittle materials at low load and penetration levels. The transition from ductile to brittle fracture has been widely reported and is usually described as the 'critical depth of cut'[62], which is generally small up to 0.1–0.3μm. They will result in relatively slow material removal rates[62].

However, it is a cost-effective technique for producing high quality spherical and non-spherical optical surfaces, with or without the need for lapping and polishing[62]. The workpiece materials should also have a low affinity with the cutting tool material. If bits of the workpiece material are

| Table 7.5 | Current Diamond Turned Materials | |
|---|---|---|
| **Semiconductors** | **Metals** | **Plastics** |
| Cadmium telluride | Aluminium and alloys | Acrylic |
| Gallium arsenide | Copper and alloys | Fluoroplastics |
| Germanium | Electroless nickel | Nylon |
| Lithium niobate | Gold | Polycarbonate |
| Silicon | Magnesium | Polymethylmethacrylate |
| Zinc selenide | Silver | Propylene |
| Zinc sulphide | Zinc | Styrene |

*Source: Ref. [62].*

| Table 7.6 | Materials that can be Processed via Ductile Mode Diamond Grinding | |
|---|---|---|
| **Ceramics/intermetallics** | | **Glasses** |
| Aluminium oxide | Titanium aluminide | BK7 or equivalent |
| Nickel aluminide | Titanium carbide | SF10 or equivalent |
| Silicon carbide | Tungsten carbide | ULE or equivalent |
| Silicon nitride | Zirconia | Zerodur or equivalent |

*Source: Ref. [62].*

deposited onto the tool, this will cause tool wear and adversely affect the finished surface (surface finish and surface integrity). Therefore, workpiece materials chosen must process an acceptable machinability on which nanometric surface finish can thus be achieved. Diamond tools are widely used in nanometric machining because of their excellent characteristics. The materials currently turned with diamond tools are listed in Table 7.5. The materials that can be processed via ductile mode grinding with diamond wheels are listed in Table 7.6.

### 7.4.3  Comparison of nanometric machining and conventional machining

Table 7.7 summarizes the comparison of nanometric machining and conventional machining in all major aspects of cutting mechanics and physics.

The comparison highlighted in the table is by no means comprehensive, but rather provides a starting point for further study on the physics of nanometric machining.

**Table 7.7** The Comparison of Nanometric Machining with Conventional Machining

| | | Nanometric machining | Conventional machining |
|---|---|---|---|
| Fundamental cutting principles | | Discrete molecular mechanics/ micromechanics | Continuum elastic/plastic/ fracture mechanics |
| Workpiece material | | Heterogeneous (presence of microstructure) | Homogeneous (ideal element) |
| Cutting physics | | Atomic cluster or microelement model $\dot{q_i} = \dfrac{\partial H}{\partial p_i}$ $i = 1, 2, \dots N$ $p_i = -\dfrac{\partial H}{\partial q_i}$ | Shear plane model (continuous points in material) |
| | | First principal stress $\sigma = \dfrac{1}{S}\sum_{i=1}^{N_A}\sum_{j=1}^{N_B} f_{ij} - \dfrac{1}{S}\sum_{i=1}^{N_A}\sum_{j=1}^{N_B} f_{0ij}$ (crystal deformation included) | Cauchy stress principle $\tau_s = \dfrac{F_s}{A}$ (constant) |
| Cutting force and energy | Energy consideration | Interatomic potential functional $U(r^N) = \sum_i \sum_{<i} u(r_{ij})$ | Shear/friction power $P_s = F_s \cdot V_s$ $P_u = F_u \cdot V_c$ |
| | Specific energy | High | Low |
| | Cutting force | Interatomic forces $F_I = \sum_{j \ne i}^{N} F_{ij} = \sum_{j \ne i}^{N} -\dfrac{du(r_{ij})}{dr_{ij}}$ | Plastic deformation/friction $F_c = F(b, d_c, \tau_s, \beta_a, \rho_c, \alpha_r)$ |
| Chip formation | Chip initiation | Inner crystal deformation (point defects or dislocation) | Inter crystal deformation (grain boundary void) |
| | Deformation and stress | Discontinuous | Continuous |
| **Cutting tool** | Cutting edge radius | Significant | Ignored |
| | Tool wear | Clearance face and cutting edge | Rake face |

*Source: Ref. [55].*

## ACKNOWLEDGEMENTS

The author wishes to thank Springer for allowing the author to reprint the chapter.

## REFERENCES

[1]   W.R. Backer, E.R. Marshall, M.C. Shaw, Trans. ASME 74 (1952) 61.
[2]   N. Taniguchi, Precis. Eng. 16 (1994) 5–24.
[3]   M.C. Shaw, J. Franklin Inst. 254 (1952) 109.
[4]   R.O. Heidenreich, W. Shockley, Report on strength of solids, Phys. Soc. Lond. (1948) 57.
[5]   H.J. Ernst, M.E. Merchant, Trans. Am. Soc. Metals 29 (1941) 299.
[6]   M.E. Merchant, J. Appl. Phys. 16 (1945) 267–275.
[7]   V. Piispanen, Teknillinen Aikakaushehti (Finland) 27 (1937) 315.
[8]   M.E. Merchant, Machining theory and practice, Am. Soc. Metals (1950) 5–44.
[9]   M.E. Merchant, J. Appl. Phys. 16 (1945) 318–324.
[10]  C.S. Barrett, Structure of Metals, McGraw Hill Co., NY (1943) 295.
[11]  P.W. Bridgman, Studies in Large Plastic Flow and Fracture, McGraw Hill Co., NY, 1952.
[12]  G. Langford, M. Cohen, Trans. ASM 62 (1969) 623.
[13]  V. Piispanen, J. Appl. Phys. 19 (1948) 876.
[14]  T.Z. Blazynski, J.M. Cole, Proc. Inst. Mech. Eng. 1 (74) (1960) 757.
[15]  M.C. Shaw, J. Appl. Phys. 21 (1950) 599.
[16]  T.J. Walker, Ph.D. Dissertation. Carnegie-Mellon University, PA, 1967.
[17]  T.J. Walker, M.C. Shaw, Advances in Machine Tool Design and Research, Pergamon Press, Oxford, UK, 1969, pp. 241–252.
[18]  E. Usui, A. Gujral, M.C. Shaw, Int. J. Mach. Tools Res. 1 (1960) 187–197.
[19]  A. Vyas, M.C. Shaw, Trans. ASME, J. Mech. Sci. 21 (1) (1999) 63–72.
[20]  F. Eugene, Ann. CIRP 52 (11) (1952) 13–17.
[21]  M.C. Shaw, Int. J. Mech. Sci. 22 (1980) 673–686.
[22]  K.B. Kwon, D.W. Cho, S.J. Lee, C.N. Chu, Ann. CIRP 47 (1) (1999) 43–46.
[23]  H. Eyring, T. Ree, N. Harai, Proc. Natl Acad. Sci. 44 (1958) 683.
[24]  H. Eyring, T. Ree, Proc. Natl Acad. Sci. 47 (1961) 526–537.
[25]  H. Eyring, M.S. Jhon, Significant Theory of Liquids, John Wiley and Sons, NY, 1969.
[26]  D. Kececioglu, Trans. ASME 80 (1958) 149–168.
[27]  D. Kececioglu, Trans. ASME 80 (1958) 541–546.
[28]  D. Kececioglu, Trans. ASME, J. Eng. Ind. 82 (1960) 79–86.
[29]  T.L. Anderson, Fracture Mechanics, CRC Press, Florida, 1991.
[30]  B. Zhang, A. Bagchi, Trans. ASME, J. Eng. Ind. 116 (1994) 289.
[31]  A.S. Argon, J. Im, R. Safoglu, Metall. Trans. 6A (1975) 825.

[32] R. Komanduri, R.H. Brown, Metall. Mater. 95 (1967) 308.

[33] D.C. Drucker, J. Appl. Phys. 20 (1949) 1.

[34] N.A. Fleck, G.M. Muller, M.F. Ashby, J.M. Hutchinson, Acta Metall. Mater. 41 (10) (1994) 2855.

[35] N.A. Stelmashenko, M.G. Walls, L.M. Brown, Y.V. Milman, Acta Metall. Mater. 41 (10) (1993) 2855.

[36] Q. Ma, D.R. Clarke, J. Mater. Res. 46 (3) (1995) 477.

[37] W.D. Nix, H. Gao, J. Mech. Phys. Solids 1 (4) (1998) 853.

[38] H. Gao, Y. Huang, W.D. Nix, J.W. Hutchinson, J. Mech. Phys. Solids 47 (1999) 1239.

[39] D. Dinesh, S. Swaminathan, S. Chandrasekar, T.N. Farris, Proc. ASME-IMECE, NY (2001) 1–8.

[40] Committee on Technology National Science and Technology Council, National Nanotechnology initiative: Leading to the next industrial revolution. Washington D.C., 2000.

[41] K. Snowdon, C. McNeil, J. Lakey, Nanotechnology for MEMS components, MST News 3 (2001) 9–10.

[42] A. EI-Fatatry, A. Correial, Nanotechnology in microsystems: Potential influence for transmission systems and related applications, MST News 3 (2003) 25–26.

[43] M. Werner, T. Köhler, W. Grünwald, Nanotechnology for applications in microsystems, MST News 3 (2001) 4–7.

[44] H. El-Hofy, A. Khairy, T. Masuzawa, J. McGeough, Introduction, in: J. McGeough (Ed.), Micromachining of Engineering Materials, Marcel Dekker, New York, 2002.

[45] R. Donaldson, C. Syn, J. Taylor, N. Ikawa, S. Shimada, Minimum thickness of cut in diamond turning of electroplated copper. UCRL-97606-1987, 1987.

[46] D.J. Stephenson, D. Veselovac, S. Manley, J. Corbett, Ultra-precision grinding of hard steels, Precis. Eng. 15 (2001) 336–345.

[47] O. Rübenach, Micro technology: Applications and trends, Euspen online training lecture. <http://www.euspen.org/training/lectures/course2free2view/02MicroTechApps/demolecture.asp> (accessed July 2007).

[48] Diamond milling processes for the generation of complex optical mold inserts, <http://www.lfm.uni-bremen.de/html/res/res001/res108.html> (accessed July 2007).

[49] M. Weck, Ultraprecision machining of microcomponents, Mach. Tools (2000) 113–122.

[50] A. Schütze, L.-G. John, Nano sensors and micro integration, MST News 3 (2003) 43–45.

[51] A. EI-Fatatry, A. Correial, Nanotechnology in microsystems: Potential influence for transmission systems and related applications, MST News 3 (2003) 25.

[52] N. Ikawa, R. Donaldson, R. Komanduri, W. König, P.A. Mckeown, T. Moriwaki, I. Stowers, Ultraprecision metal cutting: The past, the present and the future, Ann. CIRP 40 (1991) 587–594.

[53]    M.C. Shaw, Principles of Abrasive Processing, Oxford University Press, New York, 1996.

[54]    R. Komanduri, H. Chandrasekaran, L. Raff, Effects of tool geometry in nanometric cutting: A molecular dynamics simulation approach, Wear 219 (1998) 84–97.

[55]    X. Luo, K. Cheng, X. Guo, R. Holt, An investigation on the mechanics of nanometric cutting and the development of its test-bed, Int. J. Prod. Res. 41 (2003) 1449–1465.

[56]    N. Taniguchi, Nanotechnology, Oxford University Press, New York, 1996.

[57]    T. Dow, E. Miller, K. Garrard, Tool force and deflection compensation for small milling tools, Precis. Eng. 28 (2004) 31–45.

[58]    K. Cheng, X. Luo, R. Ward, R. Holt, Modelling and simulation of the tool wear in nanometric cutting, Wear 255 (2003) 1427–1432.

[59]    S. Shimada, Molecular dynamics simulation of the atomic processes in microcutting, in: J. McGeough, (Ed.), Micromachining of Engineering Materials, Marcel Dekker, New York, 2002, pp. 63–84.

[60]    H. Nakazawa, Principles of Precision Engineering, Oxford University Press, New York, 1994.

[61]    W. Lee, C.A. Cheung, Dynamic surface topography model for the prediction of nano-surface generation in ultra-precision machining, Int. J. Mech. Sci. 43 (2001) 961–991.

[62]    J. Corbett, Diamond micromachining, in: J. McGeough (Ed.), Micromachining of Engineering Materials, Marcel Dekker, New York, 2002, pp. 125–146.

# Design of Experiments: A Key to Innovation in Nanotechnology

C. Yuangyai and H.B. Nembhard

*Harold and Inge Marcus Department of Industrial and Manufacturing Engineering,*
*The Pennsylvania State University, PA, USA*

## CONTENTS

## ABSTRACT

At the nanoscale, there are often very complex relationships among input design parameters and process or product outputs. It would be prohibitively time consuming to perform all of the combinatorially possible experiments in order to comprehend these relationships. However, statistical design of experiments (DoE) is a technique that can be used to efficiently explore the relationships and develop greater understanding. Consequently, DoE is becoming increasingly central to the advancement of nanotechnology and nanomanufacturing.

In this chapter, we begin with an introduction to DoE in Section 8.1. In Section 8.2, we discuss the One Factor At A Time approach which is generally used among scientists and engineers. In Section 8.3, we consider traditional methods implemented in nanotechnology experimentation in practice. Next, in Section 8.4, we propose modern DoE methods that are appropriate for nanotechnology and nanomanufacturing. Section 8.5 provides a table of suggested DoE methods that map to particular areas within nanotechnology as well as a table of all of the articles in nanotechnology that we reviewed for this chapter that use statistical experimentation. Finally, conclusions and final remarks are given in Section 8.6.

## 8.1 INTRODUCTION TO DoE

DoE has been used in agriculture trials for over 70 years. As noted by several authors[1–3], much of the early work was conducted The use of DoE then spread to other areas such as the pharmaceutical industry, continuous and discrete production processes, bioassay procedures, clinical trials, psychological experiments, laboratory analysis, as well as business and economics studies[2–4].

Notwithstanding the use of DoE is fairly uncommon in the field of nanotechnology. One impediment is the lack of similar terminologies. For example, 'parameter' refers to a controlled variable affecting the output of interest in nanotechnology, whereas this term is referred to as a 'factor' in

a DoE context. In order to establish a clear basis, we introduce some basic terminology generally used in DoE as follows:

- *Factor* is a controllable variable of interest. The factor can be either quantitative or qualitative. A quantitative factor can be measured on a numerical scale. Some examples of qualitative factors include the temperature of a furnace, amount of a chemical, ratio of a material portion, weight of a substrate, etc. A qualitative factor can be categorized into a group. Examples include type of material, suppliers, operators, etc.

- *Factor levels* are different values or types of factors in the range of interest.

- *A treatment or a treatment combination* is one of the possible combinations among all the factors level that apply to an experimental unit.

- *An experimental unit* is the smallest unit (it can be a physical unit or a subject) to which one treatment combination is applied independently.

- *A run or trial* is an implementation of a treatment combination to an experimental unit. Similar treatment combinations can be applied to several different experimental units.

- *Response* is a qualitative or quantitative characteristic of an experimental unit measured after we apply a treatment combination. Understanding the response is regularly an objective of the experiment.

In order to obtain an appropriate design and analysis, Fisher (1966)[5] suggests three principles in performing the experiment: randomization, local control (also called blocking) and replications. These can be explained as follows.

- *Randomization* is a process that collects all sources of variation affecting the treatment effects except those due to treatment itself. The randomization tends to reduce the confounding of uncontrolled factors and controlled factors. It is very important in experimental analysis because it is required to have a valid estimation of random error[2].

---

[2] Generally appears in ANOVA table which is a technique used to partition the total variation into the variation of each of the source of variation listed in a response model.

- *Local control or blocking* is a technique that is used to segregate an uncontrolled but known variation in an experiment not associated with the treatment effect. The blocking should be designed to have maximum variation among blocks (heterogeneous between blocks) but to have minimum variation with blocks (homogeneous within blocks).

- *Replication* refers to the replication of a treatment combination. It is needed for a specific degree of precision for measuring treatment effects. The reader should be aware that replications are not multiple readings. Replication requirements are stringent: to assure a proper replication, experimenters must reset every condition in the experiment. If the treatment combinations are not reset, the errors in the multiple readings are not independent. This, in turn, leads to the violation of the randomization principle.

## 8.2 OFAT: THE PREDOMINANT METHOD USED IN PRACTICE

The One Factor At A Time (OFAT) method is a basic approach that has been widely used in science and engineering experimentation. The OFAT method is performed by selecting a starting baseline by varying one factor level at a time while keeping other factor levels constant. Then, the experimenter determines which level provides the best result; that factor level is kept constant and the other factor levels are varied sequentially. While methodological, this method is not able to estimate interaction effects among the factors. Furthermore, there is no guarantee that the combination of the levels will provide optimal results[1–3, 6].

Ryan (2007)[1] provides a good example of an experiment where interaction among factors cannot be estimated. Suppose that in an engineering department, two engineers are asked to maximize process yield, where there are two factors of interest – temperature (*A*) and pressure (*B*). Assume that the first engineer uses the OFAT, whereas the second engineer decides to vary both the factors simultaneously.

Assume that the real process behaves as shown in Figure 8.1. If the first engineer studies the process by initially keeping temperature at the low level and varying the pressure from low to high, it would be suggested that the best condition is to set the pressure and temperature at the low level. However, if the experiment is started by setting this temperature at a high level and then varying the pressure, the opposite would be suggested: to keep the pressure at a low level when the temperature is high. The results could become rather confusing and possibly erroneous.
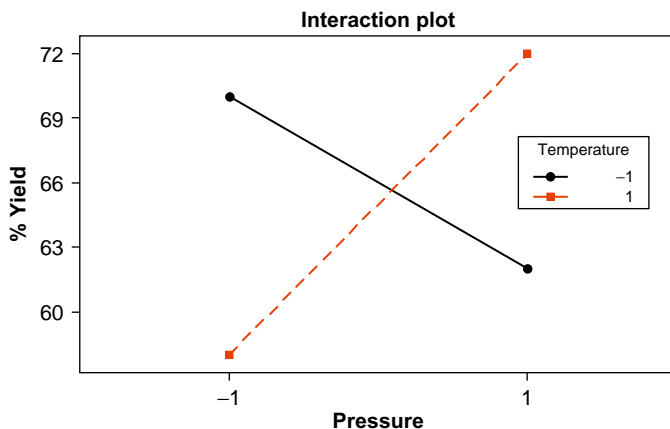
**FIGURE 8.1**   *Interaction plot of a process.*

On the other hand, the second engineer does the experiment by considering all treatment combinations. The results would lead the engineer to conclude that it is best to use high temperature and high pressure or low temperature and low pressure to increase the yield due to interaction phenomenon of the temperature and the pressure.

Anderson and Whitcomb (2006)[7] provide an additional example to illustrate that the OFAT method is not able to determine an optimal in some situations. Consider an experiment to study the effect of Factor $A$ and $B$ to Response $Y$ in Equation (8.1). The response surface plot for the equation is displayed in Figure 8.2.

$$Y = 77.57 + 8.80A + 8.19B - 6.95A^2 - 2.07B^2 - 7.59AB \qquad (8.1)$$

If the experimenter varies Factor $A$ from $-2$ to $+2$ and then plots a graph in Figure 8.2 (bottom left), it can be seen when Factor $A$ is set at 0.63, the response $Y$ is maximized. Following the OFAT method, the experimenter will keep Factor $A$ at 0.63 as a constant and then vary Factor $B$. The result indicates that now the response increases from 80 to 82 by adjusting Factor $B$ to 0.82 as shown in Figure 8.2 (bottom right). OFAT, if employed, would suggest keeping Factor $A$ at 0.63 and Factor $B$ at 0.82 in order to maximize the response. However, in the real process Figure 8.2 (top), it can be clearly seen that the Response $Y$ can be increased up to 94.

From these two brief illustrations, it is easy to see why OFAT approach is not recommended for experimentation. Nevertheless, the OFAT method is widely used. Anderson and Whitcomb (2007)[7] suggested that a possible reason for this unfortunate reality is because most basic coursework introduces and encourages the use of this method. As a demonstration, they
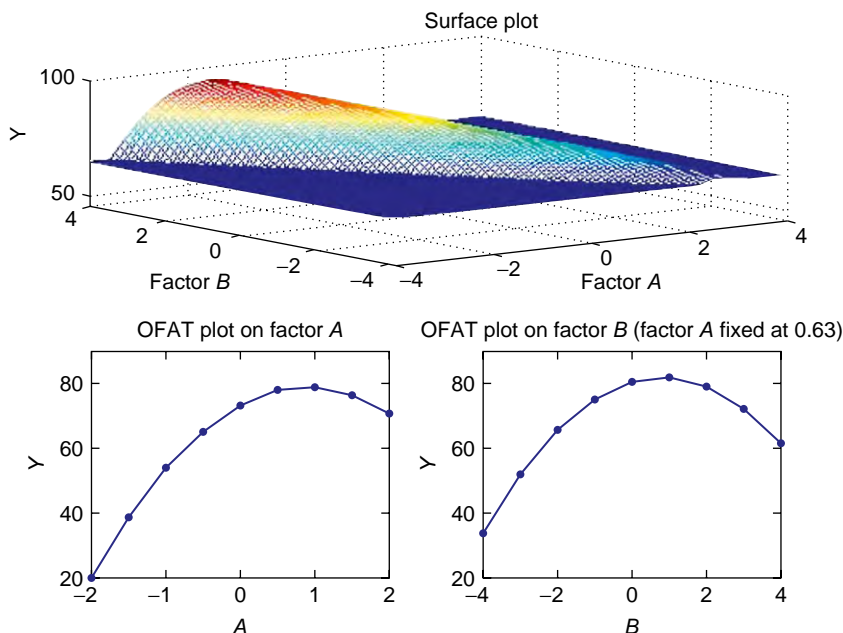
**FIGURE 8.2**  *OFAT experimentation.*

provided an example that a physical science text for ninth-graders in the United States suggests using the OFAT for a motion experiment. Since DoE coursework is not required across all science disciplines, OFAT is often carried into industrial, and even non-statistical academic settings.

We reviewed several articles that appeared in *Nanotechnology* and found that the OFAT method has been used in many published papers: Unalan and Chhowalla (2005)[8], Pan et al. (2005)[9], Buzea et al. (2005)[10], Zhang et al. (2005)[11], Xue et al. (2005)[12], Dimaki et al. (2005)[13], Chen et al. (2006)[14], Kim et al. (2006)[15], Chen et al. (2006)[16], Huang et al. (2006)[17], Li et al. (2006)[18], Lee and Liu (2007)[19], Mattila et al. (2007)[20] and Kim et al. (2007)[21].

In the next sections, we will discuss several DoE methodologies that can be used by experimenters in the nanotechnology field to gain a better understanding of a process.

## 8.3 TRADITIONAL METHODS USED IN RESEARCH AND DEVELOPMENT

In reviewing the literature that properly uses DoE in nanotechnology and nanomanufacturing, we found that four types of traditional designs

| **Table 8.1** | Traditional DoE Methods Used in Nanotechnology and Nanomanufacturing | |
|---|---|
| **Approach** | **Article References** |
| CRD | Panchapakesan et al. (2006)[22] |
| Two-level factorial design | Saravanan et al. (2001)[23], Barglik-Chory et al. (2004)[24], Gou et al. (2004)[25], Sun et al. (2005)[26], Roy et al. (2007)[27], Desai et al. (2008)[28] and Carrion et al. (2008)[29] |
| Fractional factorial design and RSM | Basumallick et al. (2003)[30], Yong et al. (2005)[31], Kubovecz et al. (2005)[32], Riddin et al. (2006)[33], Nourbakhsh et al. (2007)[34] and Rajaram et al. (2008)[35] |
| Taguchi's method | Chang et al. (2007)[37] and Hou et al. (2007)[36] |

are employed: completely randomized design (CRD), two-level factorial or fractional factorial design, response surface methodology (RSM) and Taguchi's method. The relevant articles are summarized in Table 8.1. Even though these methods are relevantly recently applied in nanotechnology, we refer to them as 'traditional' because of their long history in the applied statistics literature. In the following subsections, we discuss each of these four designs.

### 8.3.1  Completely randomized design

The term *completely randomized design* (CRD) means that we determine the total number of experimental units needed in the experimentation, and then select experimental units randomly to be executed first or last. Consider, for instance, that in lithographic nanofabrication experimentation, an engineer would like to study the output from using two levels of a chemical applied to three nanoparticle types and deposited on four sizes of mould. Therefore, a total of 24 runs must be executed. This, in turn, implies that the experimenter would have to make 24 slurry preparations and apply each to 24 moulds. If experimenters make only six slurry preparations and then divide the slurry to four portions and then deposit on the different moulds, this procedure is *not* a CRD. (To overcome this situation in practice, we suggest the use of a split plot design and its variants.)

The term *factorial design* which can also be called *combination design* or *crossed design*[1] means that all combinations of factor levels are executed. It is an efficient approach when two or more factors are considered because factor interactions can be estimated[3]. However, the factorial design can be quite burdensome because it requires the experimenter perform all possible

**Example: Factorial design in a tin–oxide nanostructure synthesis process**

Panchapakesan et al.[22] studied the effects of seven gas types, three levels of concentrations, six different types of seeded sensor ($SnO_2$) and six grain size diameters for the sensitivity of tin–oxide nanostructures on large area arrays of micro-hotplates. In this case, the authors used the full factorial design. There were $7 \times 3 \times 6 \times 6 = 756$ runs which they claimed to be randomized using sophisticated software program. They presented the results of the experiment using a graphical method.

An analysis of variance (ANOVA) would typically be conducted because we can estimate the interaction of all four factors and also use the two-level factorial designs with centre points to reduce the number of experimental runs.

combinations of all factor levels. For example, consider a process that has two factors and each factor has four and five levels, respectively. In this case, a total of 20 combinations must be randomized and tested.

### 8.3.2 Two-level factorial design

#### 8.3.2.1 Two-level full factorial design

Like the factorial design, the two-level factorial design requires all possible combinations to be executed. However, instead of using several levels of each factor, only two levels are selected. This design is helpful when used in the beginning of an experimental effort in order to select only the potential significant factors, especially if the experimenter has limited knowledge of the experiment.

#### 8.3.2.2 Two-level fractional factorial design

If there are $k$ factors of interest and the two-level factorial design is used, the number of treatment combinations increases rapidly as $k$ increases: the total number of treatment combinations is $2^k$. However, under the assumption that the higher order interactions have a smaller effect on the output compared to the main effects or the second-order effects, we can improve the cost and time of experimentation by reducing the number of experiments by a half or even a quarter or an eighth of the original design. With fewer experiments, there will be a loss of some information. A two-level fractional factorial design is generally expressed in the form of $2^{k-p}$, where $p$ is the fraction of the full $2^k$ factorial (i.e. $1/2^p$).

Once a few key factors are determined, the experimenter may want to improve the process by trying to optimize the process output. In this case, RSM will be employed. This approach allows the experimenters to estimate

**Example: Two-level full factorial design in a single-walled nanotubes synthesis process**

Gou et al. (2004)[25] provide a good example of using a two-level factorial design to study the effect concentration of suspension, sonication time and vacuum pressure to the average and standard deviation of rope and pore size of single-walled nanotubes (SWNTs). Then they estimate the relationships between the response and factor by using a regression method without the second-order effect. The authors could not optimize the process, so further experimentation is required. RSM would be helpful to optimize the processes.

**Example: Two-level fractional factorial design in a single-walled carbon nanotubes synthesis process**

Kukovecz et al. (2005)[32] reported the use of a $2^{7-4}$ design to study the effect of seven factors on the carbon percentage and the quality descriptor number (QDN). The factors are reaction temperature, reaction time, preheating time, catalyst mass, $C_2H_2$ volumetric flow rate, Ar volumetric flow rate and Fe:MgO molar ratio. The design is a resolution III design, which means the main effects are confounded with the second-order effects. They present their results in graphs that are difficult to interpret for the main effect and interaction effect.

As an alternative, the half normal probability plot[3] can be used to analyse the data. Figure 8.3 shows our half normal plot for the data in Kukovecz et al. (2005). In this analysis, we found that none of the factors is statistically significant at the 95% confidence level.

the second-order effect of factors that cannot be estimated from the two-level factorial designs.

### 8.3.3 RSM

The idea of RSM began in the early 1930s but was finally well established in 1951 by the work of Box and Wilson[38]. RSM is defined as a collection of statistical design and numerical optimization techniques for empirical model building and model exploitation used to optimize processes and product design[39, 40]. For example, a chemical engineer wishes to find the levels of temperature $(x_1)$ and pressure $(x_2)$ that maximize the yield $(Y)$ of

---

[3]A normal probability plot is a statistical tool to determine significant effects. If the effect value is far from the straight line, there is evidence to suggest that these effects are significant.
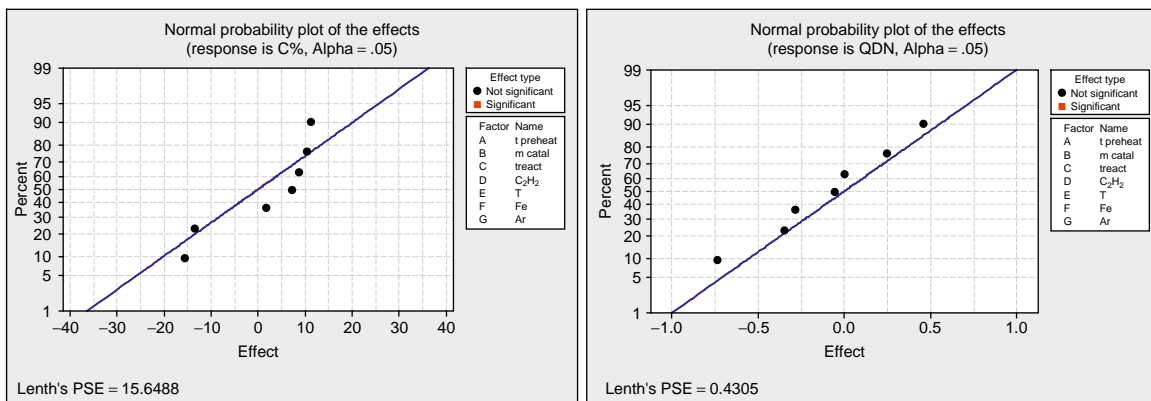
**FIGURE 8.3** *Normal probability plot for the data from Kukovecz et al. (2005).*

a process. The process yield is a function of the levels of temperature and pressure:

$$y = f(x_1, x_2) + \varepsilon$$

where $\varepsilon$ is the error observed in the response $y$. If the expected response is $E(y) = f(x_1, x_2) = \eta$, then the surface is represented by $\eta = f(x_1, x_2)$.

RSM is considered a sequential approach and consists of three steps: screening, region seeking and product/process characterization. Screening investigates which factors of interest are significant. Note that the method used in this stage can be a two-level (fractional) factorial design. The surface can be estimated by the following first-order model:

$$y = \beta_0 + \beta_1 x_1 + \beta_2 x_2 + \beta_k x_k + \varepsilon$$

The next step is to know whether the current response situation is in the optimal region. If not, we have to employ region seeking to find a path to an optimal region. Once the region is determined, the process phenomena can be estimated by a second-order model:

$$y = \beta_0 + \sum_{i=1}^{k} \beta_i x_i + \sum_{i=1}^{k} \beta_{ii} x_i^2 + \sum \sum_{i<j} \beta_{ij} x_i x_j + \varepsilon$$

Generally, the response surface is shown graphically as demonstrated in Figure 8.4. To help in interpretation, it is often useful to plot the contours of the response as well.
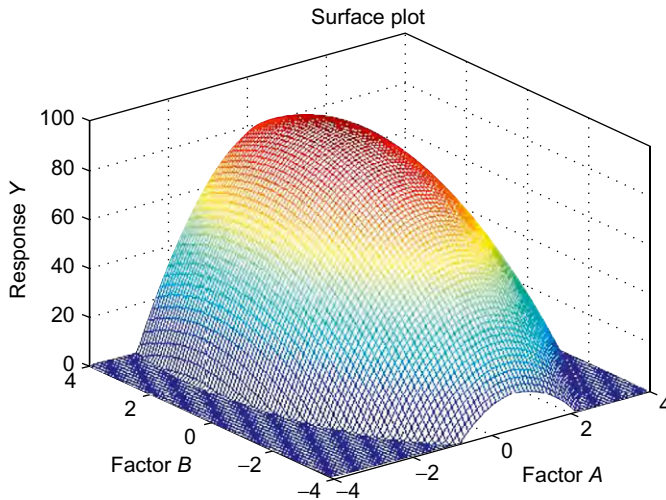
**FIGURE 8.4**   *A 3D response surface.*

For a more detailed discussion of RSM, the reader may refer to Box and Draper (2007)[40] and Myers and Montgomery (1995)[41].

### 8.3.4  Taguchi's method

Genichi Taguchi's methods have been widely known in industry for decades. The central idea of his methods is the quality loss function and robust parameter design[42, 43]. The quality loss function is used to estimate

---

**Example: RSM in a multi-walled carbon nanotubes synthesis process**

Nourbakhsh et al. (2007)[34] provide an example of using RSM. Their objective is to optimize the diameter and mean rectilinear length (MRL) of multi-walled carbon nanotubes under the effect of six factors, namely, synthesis time, catalyst mass, $H_2$ flow rate, synthesis temperature, reduction time and $C_2H_2$ flow rate. After using a $2^{6-3}$ design, they found that the $H_2$ flow rate, synthesis temperature and reduction time are significant factors. The authors then use Box-Behnken Design (BBD) to optimize the process.

In this type of application, it would be helpful to investigate the curvature effect by adding centre points and checking whether or not the optimal condition is in the range of interest. If not, path searching should be done before completely employing the BBD. The response surface graph demonstrates that the current solution is not yet within the optimal region.

costs when the product or process characteristics are shifted from the target value. This is represented by the following equation:

$$L(y) = k(y - T)^2$$

where $L(y)$ is a cost incurred when the characteristic $y$ is shifted from the target $T$ and $k$ is constant depending on the process. This concept is known as parameter design, which is a selection of a parameter level in order to make the process robust against environmental changes with minimum variation.

There have been some criticisms of Taguchi's approach in the applied statistics literature. For example, it sometimes fails to consider the interaction effect of factors much like fractional factorial design[44].

### 8.3.5 Opportunities for improvement in experimentation

In our reviewing of papers on DoE in nanotechnology, we found numerous occasions where the OFAT approach was speciously used. Where traditional designs were appropriately used, there were several gaps in the analysis. We summarize the key problem areas as follows:

- Improper randomization

- Lack of residual analysis

- Few implementations of blocking techniques

- Incorrect analysis and interpretation

- Poor focus on response variation reduction

Most papers did not directly discuss the randomization principle; the experiment may have been completely randomized or completely randomized in blocks, but the choice was not clearly stated. There may have been restriction on randomization, but it was unclear whether the experimenters knew this concept. Failure to obey the randomization principle

---

**Example: Taguchi's method in a nanoparticle wet milling process**

Hou et al. (2007)[36] applied the Taguchi method to study the effects of five factors: milling time, flow velocity of circulation system, rotation velocity of agitator shaft, solute-to-solvent weight ratio and filling ratio of grinding media. Each factor has three levels and the response lies in the mean and variance of grain size. The authors use an $L_{27}$ orthogonal array with 27 runs.

might lead to misinterpretation of the results. When randomization is not practical, a split plot design, which will be discussed in Sections 8.4.1 and 8.4.2, can often be used.

A few papers did not mention whether the output was tested for normality and independence. The issue here is that the variance will be underestimated if a positive correlation among responses exists. This could lead the experimenters to conclude that certain factors are significant when, in actuality, they are not. Repeated measures, which will be discussed in Section 8.4.3, can be used to address this situation.

The blocking technique was rarely used in the literature. This technique is beneficial for segregating the uncontrolled factors out of the model. It was unclear whether readings in some experiments were papers or replications or mere multiple readings.

RSM is quite popular in nanotechnology literature. However, in some cases, the results have been interpreted incorrectly. For example, if a two-level factorial design is used with centre points, it is this design that informs the experimenters as to whether there are second-order effects in the experimental region. It does not suggest *which* effect is contributing the second-order interaction. We also found that many papers fail to seek a path to reach the optimal experiment condition, which is one of the main reasons for employing RSM.

Some papers fall short in the proper use of parameter estimation. It is not always appropriate to keep all the parameter estimates in the model because some terms might not be significant and should be ignored. On the other hand, some insignificant terms may be maintained in order to adhere to the hierarchical principle. The point is to carefully consider both sides of the issue.

Much of this work focuses on mean response and ignores the response variability. In order to improve processes, we would like to have processes with both desirable results and a minimum variation. This topic can be addressed using the quality loss function concept suggested by Taguchi.

## 8.4  MODERN DoE METHODS APPROPRIATE FOR NANOTECHNOLOGY AND NANOMANUFACTURING

In practice, there are many restrictions on experimentation. These include the randomization restriction on the treatment combination, the dependence of the factor level, the restriction of treatment combination space and constraints in physical experiments. Therefore, there is a need for other kinds of design and analysis of experiments that overcome those

restrictions. We believe that the following designs can be effectively used in the area of nanotechnology and nanomanufacturing:

- Split plot design (and its variants)
- Multi-stage split plot (MSSP) design
- Repeated measures
- Supersaturated design
- Mixture design
- Computer deterministic experiments
- Computer-aided design (alphabetical optimal design)

### 8.4.1 Split plot design and its variants

The designs that we have previously discussed are based on the complete randomization principle. However, in many situations, it is impossible to randomize all treatment combinations. In such cases, the split plot design may be used. The name split plot comes from the agricultural experiment in which the whole plots are considered for a large plot of land and the sub-plots are used to represent a small plot of land within the large area.

The standard split plot design is a design which has a two-factor factorial arrangement. For example, Factor $A$ with $a$ level, is designed as a randomized complete design; the levels of Factor $A$ treatments are called a whole plot experimental unit. Each experimental unit is divided into $b$ split plot experimental units of Factor $B$.

The strip block[4] design is another type of design which is a bit different from the split plot design. This design has two factors, Factor $A$ with $a$ level and Factor $B$ with $b$ level. The levels of Factor $A$ are randomly assigned to the whole plot experimental unit. Then the $B$ experimental units are formed perpendicular to the $A$ experimental units, and the $b$ levels of Factor B are randomly allocated to the second set of $b$ whole plot units in each of the complete blocks.

Box and Jones (2000–2001)[45] discussed the CRD, split plot design and split block design using a cake-mixing experiment which consists of two processes: mixing and baking. There are five factors with two levels each; three factors in the mixing process and two factors in the baking process. If the CRD is used, 32 preparations for mixing and baking are required.

---

[4]The strip block also known as split block design, strip plot design, two-way whole plot design and criss-cross design[47].

On the other hand, the split plot design requires fewer experimental resources based on three cases. First, if the mixing factors are whole plot factors, eight cake-mixing preparations are required. However, if the baking factors are whole plot factors, four settings of a baking oven are prepared. Note that the subplot factor setting in both cases requires 32 preparations. In the split block arrangement, only eight mixes and four bakes are required. Table 8.2 shows four possible arrangements for the different designs.

This split plot structure is a foundation of the multi-stage process DoE. Further studies are provided by Kowalski and Potcner (2003)[46] and Federer and King (2007)[47].

**Table 8.2**  Four Possible Arrangements for the Cake Mix Experiment

| Type of Design | Number of Settings In | |
| --- | --- | --- |
| | **Mixes** | **Bakes** |
| Fully randomized | 32 | 32 |
| Split plot: Bakes are the subplot | 8 | 32 |
| Split plot: Recipes are the subplot | 32 | 4 |
| Split block | 8 | 4 |

*Source: Ref. [45].*

### Example: Split plot design and split block design in a gel-casting lithography process

Yuangyai and Nembhard (2007)[48] discussed different arrangements of the split plot and split block design based on the process of making ceramics parts using gel-casting and lithography method developed by Antolino et al. (2006)[49]. The process is composed of six sub-processes: particle preparation, mould fabrication, monomer addition, colloid deposition, sintering and final dressing. We will use this process to demonstrate the different arrangements of CRD, split plot design and split block design.

Let us consider only two sub-processes – monomer addition and sintering – and assume that there are two factors of interest: amount of ethylene glycol ($d$) and amount of monomer ($e$), with two levels in the preparation process and two furnace conditions ($x$) in the sintering process. If a CRD is used, eight samples are prepared at different times, then each sample must be placed into a furnace at different times (see Figure 8.5a).

If the split plot design is used, there are only four sample preparations required and each sample is split into two sub-samples, then each sub-sample is placed into the furnace at a different time. Therefore, there are four sample preparations and eight sintering settings (see Figure 8.5b).

Even in the split block design, only four samples are prepared and then each is split into two sub-samples (similar to those in split plot design). However, these sub-samples are then regrouped and placed into the furnace at the low level or the high level *together*. This reduces the sintering settings from eight to only two (Figure 8.5c).
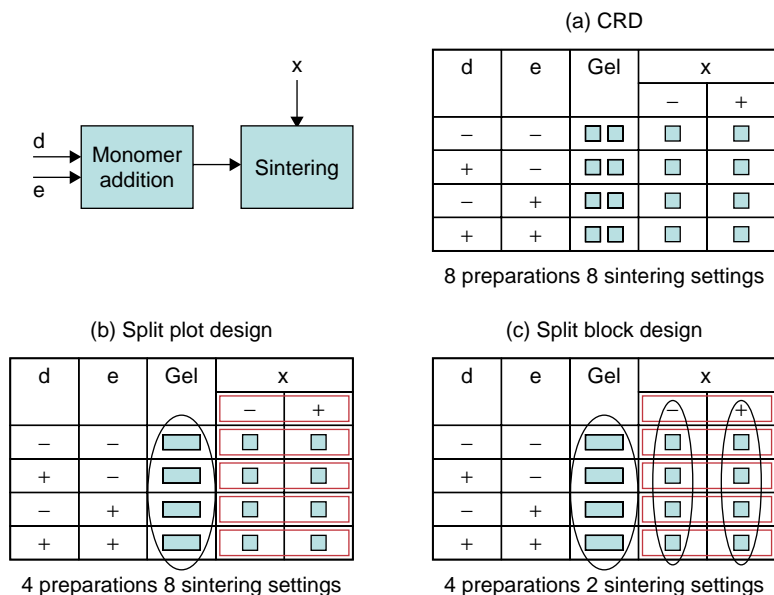
**FIGURE 8.5** *CRD, split plot and split block designs arrangements.*

## 8.4.2 MSSP design

The MSSP design is an extension of the split plot design and can be thought of as having a single whole plot and a subsequent series of sub-plots[50]. The structure of the series of sub-plots can be split plot structure or strip plot structure based on the nature of experimentation.

Bisgaard and Vivacqua (2004)[51], Acharya and Nembhard (2008)[50] as well as Yuangyai and Nembhard (2007)[48] suggest applying the split plot,

---

**Example: MSSP design in a gel-casting lithography process**

Acharya and Nembhard (2008)[52] used an MSSP design in scaling up a three-step surface initiated polymerization process – preparation of self-assembled monolayer (SAM), anchoring catalyst on the SAM and synthesis of polymer brush. However, past literature indicates that the operative levels of the stage one factors – amount of gold evaporated, thickness of silicon wafer, amount of Cr, temperature and time – are pre-determined. Therefore, these factors are ignored in the experimentation. Accordingly, the authors considered only the last two stages. There are four factors in stage one: amount of catalyst, type of rinsing solvent, drying time and reaction time. There are three factors in stage two: reaction temperature, type of Ar flow and reaction time. The authors propose catalogues of fractional factorial split plot design for three and four stages according to optimal criteria: robustness and maximum number of mixed three-way interaction.

strip plot and combination of split plot and strip plot structures to the multiple stage experiment. The MSSP design will considerably decrease the number of settings in experimentations.

### 8.4.3  Repeated measures

The problem of designing a statistical experiment with repeated measures has been extensively studied in the DoE literature. Repeated measures implies that experimental units or subject will be used more than once (i.e. at two or more periods of time)[2]. Consequently, any potential model for the response variable in terms of the factors considered in the experiment will need to contain parameters for unit or subject effects, period or time effects and possible carryover effects. Many studies of repeated measures involve observations over time (or space) and the evolution of response is often of special importance[53]. Because the same unit is producing several successive responses, those that are closer together will tend to be more closely related; in other words, a previous result is playing a role on the ensemble of the response variable realization. Therefore, in such cases, these relationships must also be included in the model.

### 8.4.4  Saturated and supersaturated design

In many nanotechnology and nanomanufacturing processes, the execution of many runs is impractical due to limited resources. The idea behind the saturated and supersaturated designs is similar to fractional factorial design where the goal is not to estimate all possible effects simultaneously but rather to screen several factors. Unlike fractional factorial designs, the total number of runs in the supersaturated design is less than or equal to the

---

**Example: Repeated measures in a nanoparticle wet milling process**

Kumar et al. (2005)[54] presented an experimental design to explore the significant factors to efficiently mill alumina by a chemically aided attrition milling (CAAM) process in nanophase alumina powder. Three factors – powder addition rate, media size and agitator shaft speed – were studied. Each factor was tested at two levels with three centre points. These milling responses were recorded as average agglomeration number (ANN) for 1 h, 2 h, 3 h or 4 h of milling. The authors analysed this experiment by treating each response at different hour independently. However, these data behaved dependently as the ANN at previous hour affects to the following hour. The repeated measures analysis is more appropriate for this application.

number of factors. When the number of runs is equal to the number of factors, it is called a saturated design. When the number of runs is less than the number of factors, it is called a supersaturated design[55].

In order to obtain unbiased estimator of effects, the number of runs must be equal to the number of factor effects to be estimated plus one. However, in a situation, that the insignificant factors are not of interest, estimating all main effects may not be useful if it is only the detection of a few important factors that is important. If the number of active factors is small compared to the number of runs, the careful use of biased estimates will still make it possible to identify significant factors.

### 8.4.5 Mixture design

The mixture design is a class of experimentation that is different from the previous designs we have discussed, wherein the assumption is that all factor levels are independent. In the case of the mixture design, there is an assumed relationship among factors. Suppose that in a chemical mixing experiment of two chemicals, the experimenter would like to test how the quantity of each chemical affects the properties of mixed chemical. In this case, we use the previous design. However, if the experimenter would like to study the effect of chemical ratio of two substances such as 1:1 or 2:3, a mixture design is used under a constraint that summation of the ratio must be equal to $1$[57].

The main distinction between mixture experiments and independent variable experiments is that with the former, the input variables or components are non-negative proportionate amounts of the mixture. Also, if expressed as a fraction of the mixture, they must sum to 1. If for some reason, the sum of the component proportions is less than one, the variable proportions can be rewritten as scaled fractions so that the scaled fractions sum to 1.

When the mixture components are subject to the constraint that they must sum to one, there are standard mixture designs for fitting standard models, such as *Simplex-Lattice* designs and *Simplex-Centroid* designs. When mixture components are subject to additional constraints, such as

**Example: Supersaturated design in nanorod fabrication**

Acharya and Lin (2008)[56] presented the use of supersaturated designs to study the growth of ZnO nanorods with consistent measurement of surface roughness in the process of ZnO fabrication process involving nine factors with two levels each: substrate, carrier gas, process temperature, carrier gas flow rate, synthesis time, catalyst, distance between powder and substrate, optical density and time for deposition. There were only six runs required to study those nine factors.

a maximum and/or minimum value for each component, designs other than the standard mixture designs, such as constrained mixture designs or *Extreme-Vertices* design, are appropriate.

### 8.4.6  Computer deterministic experiments

Some investigations in nanotechnology research use computer simulation to explain physical phenomena. Much of this simulation requires running complex and computationally expensive analysis and codes. Despite continuing increases in computer processor speed and capabilities, the time and computational costs of running complex algorithms are high.

A way to overcome this problem is to generate an approximation of complex analysis code that describes the process accurately, but at a much lower cost. Metamodels offer an approximation in that they provide a 'model of the model'. Clarke et al. (2005)[58] suggested metamodelling techniques, namely response surface methodology (RSM), radial basis function (RBF), kriging model and multivariate adaptive regression splines (MARS) as potentially useful approaches. Computer deterministic experiments have been addressed by Charles et al. (1996)[59], Simpson et al. (1998)[60], Cappelleri et al. (2002)[61] and Aguire et al. (2007)[62].

### 8.4.7  Computer-generated design: Alphabetical optimal design

In some experimental situations, it is not possible to experiment over all factor regions and the experimenter cannot use any standard design[63]. In these cases, computer-generated (optimal) designs are alternatives to be considered. These designs are optimized based on some user-selected criterion and a prescribed experimental process. The concept of this approach is to generate all possible design sets and then use search methods to determine which set of designs provide the best result.

In general, there are four types of optimal designs. Their names are based on the alphabet and so these designs are called alphabetical optimal design[64].

- The D-optimal design seeks to maximize the determinant of the information matrix of the design. This criterion results in minimizing the generalized variance of the parameter estimates based on a pre-specified model.

- The A-optimal design seeks to minimize the trace of the inverse of the information matrix. This criterion results in minimizing the average variance of the parameter estimates based on a pre-specified model.

- The G-optimal design seeks to minimize the maximum prediction variance over a specified model.

- The V-optimal design seeks to minimize the average prediction variance over a specified set of design points.

Since the optimality criterion of most computer-aided designs is based on some function of the information matrix that the experimenter must specify a model for the design and the final number of design points desired before the optimal design can be generated. The design generated by the computer algorithm is optimal only for that model. Alphabetical optimal designs are used by Charles et al. (1996)[59], Hooker et al. (2003)[65] and Chuang et al. (2004)[66].

## 8.5 SUMMARY OF NANOTECHNOLOGY ARTICLES THAT USE STATISTICAL EXPERIMENTATION

It is quite evident from the above discourse that modern DoE techniques have a potential to be used in nanotechnology and nanomanufacturing. Table 8.3 gives a brief summary of the DoE methods we have considered in this chapter along with the nanotechnology areas in which they may be potentially useful.

Table 8.4 summarizes the 40 articles we examined for this chapter. They are listed in order of experimental method used and then by year of publication.

## 8.6 FINAL REMARKS

Nanotechnology is becoming a key driver in economic growth around the globe[68]. It is also highly multi-disciplinary and integrates many areas of science and engineering. The impact of nanotechnology extends to advanced materials science, manufacturing, energy and environment preservation, medicine and others.

Corresponding with the rapid growth of nanotechnology, there has been growing concern over how these technologies will be properly employed. If employed incorrectly, this will eventually lead to a negative impact to humanity and the environment. Several organizations have announced intentions or preparations for product certification and standards for nanotechnology[68]. In particular, the International Organization for Standardization (ISO) is focused on developing and promoting standards for using nanotechnology.

| Table 8.3 DoE Method and Nanotechnology Mapping | | |
|---|---|---|
| **Method** | **Summary** | **Potential Nanotechnology Applications** |
| Split plot design and multi-stage split plot design | This design is suitable for the randomization restrictions that frequently occur in experimentation. The key concept of this design is that there is more than one error structure that the experimenter must analyse. The MSSP design can be extended to more than two processes. | Lithography |
| | | Process, coating process, plasma arcing process, nanoelement assembly process, laser-based synthesis process, etc. |
| Repeated measure | When the experimental unit is measured more than once and the response is dependent on the previous value, it is recommended to use this design. The importance of this design is to model an appropriate error structure. | Nanoparticle ball milling process, sol-gels process, self-assembly process, chemical vapour deposition method, electrodeposition method, etc. |
| Saturated and supersaturated design | This design is useful when there is a practical limitation on experimental resources or the number of runs, whereas there are a large number of factors of interest. | Lithography |
| | | Process, coating process, plasma arcing process, etc. |
| Mixture design | This design is used in chemical mixing contexts where the total amount of each chemical is fixed. | Nanopowder and nanomaterial preparation, sol-gels process, etc. |
| Deterministic experiment | If physical experiments cannot be done, this design can be used to seek the optimal conditions. | Simulation modelling of nanostructure, biological computing, etc. |
| Alphabetic optimal design | This design can be used in a situation wherein the experimenters cannot perform all possible experimental regions of the factors. | All the above |

| Item | Authors | Year | Technique | Title |
|---|---|---|---|---|
| **Table 8.4** | Summary of Articles in Nanotechnology | | | |
| 1 | Unalan and Chhowalla[8] | 2005 | OFAT | Investigation of single-walled carbon nanotube growth parameters using alcohol catalytic chemical vapour deposition |
| 2 | Pan et al.[9] | 2005 | OFAT | Surface crystallization effects on the optical and electric properties of CdS nanorods |
| 3 | Buzea et al.[10] | 2005 | OFAT | Control of power law scaling in the growth of silicon nanocolumn pseudo-regular arrays deposited by glancing angle deposition |
| 4 | Zhang et al.[11] | 2005 | OFAT | Microstructure and magnetic properties of ordered $La_{0.62}$, $Pb_{0.38}$, $MnO_3$ Nanowire arrays |
| 5 | Xue et al.[12] | 2005 | OFAT | In situ fabrication and characterization of tungsten nanodots on $SiO_2$/Si via field-induced nanocontact with a scanning tunnelling microscope |
| 6 | Dimaki et al.[13] | 2005 | OFAT | Frequency dependence of the structure and electrical behaviour of carbon nanotube networks assembled by dielectrophoresis |
| 7 | Chen et al.[14] | 2006 | OFAT | The influence of oxygen content in the sputtering gas on the self-synthesis of tungsten oxide nanowires on sputter-deposited tungsten films |
| 8 | Kim et al.[15] | 2006 | OFAT | The effect of metal cluster coatings on carbon nanotubes |
| 9 | Chen et al.[16] | 2006 | OFAT | The influence of seeding conditions and shielding gas atmosphere on the synthesis of silver nanowires through the polyol process |
| 10 | Huang et al.[17] | 2006 | OFAT | Effects of plasma treatment on the growth of $SnO_2$ nanorods from $SnO_2$ thin films |
| 11 | Li et al.[18] | 2006 | OFAT | Influence of Triton X-100 on the characteristics of carbon nanotube field-effect transistors |
| 12 | Lee and Liu[19] | 2007 | OFAT | The effect of annealing temperature on the microstructure of nanoidented Au/Cr/Si |
| 13 | Mattila et al.[20] | 2007 | OFAT | Effect of substrate orientation on the catalyst-free growth of InP nanowires |
| 14 | Kim et al.[21] | 2007 | OFAT | Statistical analysis of electronic properties of alkanethiols in metal–molecule–metal junction |
| 15 | Panchapakesan et al.[22] | 2006 | CRD | Sensitivity, selectivity and stability of tin oxide nanostructures on large area arrays of micro-hotplates |
| 16 | Saravanan et al.[23] | 2001 | Two-level factorial design (FD) | Experimental design and performance analysis of alumina coatings deposited by a detonation spray process |
| 17 | Barglik-Chory et al.[24] | 2004 | Two-level FD | Adjustment of the band gap energies of biostabilized CdS nanoparticles by application of statistical DoE |

| Table 8.4 | Continued | | | |
| --- | --- | --- | --- | --- |
| Item | Authors | Year | Technique | Title |
| 18 | Gou et al.[25] | 2004 | Two-level FD | Experimental design and optimization of dispersion process for single-walled carbon nanotube buckypaper |
| 19 | Sun et al.[26] | 2005 | Two-level FD | Y. Sun, Z. Zhang, C. P. Wong, Study on mono-dispersed nanosize silica by surface modification for underfill applications |
| 20 | Roy et al.[27] | 2007 | Two-level FD | Optimization of process parameters for the synthesis of silica Gel–WC nanocomposite by DoE |
| 21 | Desai et al.[28] | 2008 | Two-level FD | Understanding conductivity of single-walled nanotubes (SWNTs) in a composite resin using DoE |
| 22 | Carrion et al.[29] | 2008 | Two-level FD | Characterization of the SilSpin etch-back (breakthrough) process for nanolithography with $CHF_3$ and $O_2$ chemistry |
| 23 | Basumallick et al.[30] | 2005 | FD with RSM | DoE for synthesizing in situ $Ni–SiO_2$ and $Co–SiO_2$ nanocomposites by non-isothermal reduction treatment |
| 24 | Yong et al.[31] | 2005 | FD with RSM | Dispersant optimization using DoE for SiC/vinyl ester nanocomposites |
| 25 | Kubovecz et al. [32] | 2005 | FD with RSM | Optimization of CCVD synthesis conditions for single-walled carbon nanotubes by statistical DoE |
| 26 | Riddin et al.[33] | 2006 | FD with RSM | Analysis of the intercellular and extracellular formation of platinum nanoparticles by *Fusarium oxysporum* f. sp. *lycopersici* using response surface methodology |
| 27 | Nourbakhsh et al.[34] | 2007 | FD with RSM | Morphology optimization of CCVD-synthesized multi-walled carbon nanotubes, using statistical DoE |
| 28 | Rajaram et al.[35] | 2008 | FD with RSM | RSM-based optimization for the processing of nanoparticulate SOFC anode material |
| 29 | Hou et al.[36] | 2007 | Taguchi's method | Parameter optimization of a nanoparticle wet milling process using the Taguchi method, response surface method and genetic algorithm |
| 30 | Chang et al.[37] | 2007 | Taguchi's method | A study of process optimization using the combined submerged arc nanoparticle synthesis system for preparing $TiO_2$ |
| 31 | Acharya and Nembhard[50] | 2008 | Split plot design | Statistical design and analysis for a three-step surface-initiated polymerization process |
| 32 | Yuangyai and Nembhard[48] | 2008 | MSSP | A multi-stage experiment design in a nano-enabled medical instrument production process |
| 33 | Kumar et al.[54] | 2005 | Repeated measures | Optimized de-aggregation and dispersion of high concentration slurry of nanophase alumina by chemically aided attrition milling |
| 34 | Acharya and Lin[56] | 2008 | Super-saturated design | Understanding a ZnO nanorods fabrication process |

(*Continued*)

| Table 8.4 | Continued | | | |
|---|---|---|---|---|
| **Item** | **Authors** | **Year** | **Technique** | **Title** |
| 35 | Charles et al.[59] | 1996 | Deterministic experiment, computer-generated design | Photolithography equipment control through D-optimal design |
| 36 | Simpson et al.[67] | 1998 | Deterministic experiment | Comparison of response surface and kriging models for multi-disciplinary design optimization |
| 37 | Cappelleri et al.[61] | 2002 | Deterministic experiment | Design of a PZT bimorph actuator using a metamodel-based approach |
| 38 | Aguire et al.[62] | 2007 | Deterministic experiment | A framework for DoE and deterministic simulation in nano-enabled surgical instrument design |
| 39 | Hooker et al.[65] | 2003 | Computer-generated design | An evaluation of population D-optimal designs via pharmacokinetic simulation |
| 40 | Chuang et al.[66] | 2004 | Computer-generated design | Optimal designs for microarray experiments |

Within ISO, three working groups are considering proper terminology and nomenclature, measurement and characterization, as well as health, safety and environmental aspects of nanotechnologies[69].

The nanotechnology research and development community will be compelled to make adjustments to adhere to these standards as well as ensure customer satisfaction. DoE is an important tool that can help to fulfil both customer and industry needs effectively and efficiently.

## REFERENCES

[1] T.P. Ryan, Modern Experimental Design, John Wiley and Sons, New Jersey, 2007.

[2] F.G. Giesbrecht, M.L. Gumpertz, Planning, Construction, and Statistical Analysis of Comparative Experiments, John Wiley and Sons, New Jersey, 2004.

[3] D.C. Montgomery, Design and Analysis of Experiments, Fifth ed., John Wiley and Sons, 2004.

[4] J. Neter, M.H. Kutner, C.J. Nachtsheim W. Wasserman, Applied Linear Statistical Models, 1990.

[5] R.A. Fisher, The Design of Experiments, Eighth ed., Oliver and Boyd, Edinburgh, 1966.

[6] G.E.P. Box, Improving Almost Anything: Ideas and Essays, John Wiley and Sons, 2006.

[7]   M.J. Anderson, P.J. Whitcomb, RSM Simplified: Optimizing Process Using Response Surface Methods for Design of Experiments, Productivity Press, New York, 2005.

[8]   H.E. Unalan, M. Chhowalla, Investigation of single-walled carbon nanotube growth parameters using alcohol catalytic chemical vapour deposition, Nanotechnology 16 (2005) 2153–2163.

[9]   A. Pan, X. Lin, R. Liu, C. Li, X. He, H. Gao, B. Zou, Surface crystallization effects on the optical and electric properties of CdS nanorods, Nanotechnology 16 (2005) 2402–2404.

[10]  C. Buzea, G. Beydaghyan, C. Elliott, K. Robbie, Control of power law scaling in the growth of silicon nanocolumn pseudo-regular arrays deposited by glancing angle deposition, Nanotechnology 16 (2005) 1986–1992.

[11]  T. Zhang, C. Jin, J. Zhang, X. Lu, T. Qian, X. Li, Microstructure and magnetic properties of ordered $La_{0.62}Pb_{0.38}MnO_3$ nanowire arrays, Nanotechnology 16 (2005).

[12]  K. Xue, J.B. Xu, L. Xi, J. An, J. Chen, *In Situ* fabrication and characterization of tungsten nanodots on $SiO_2/Si$ via field induced nanocontact with a scanning tunnelling microscope, Nanotechnology 16 (2005) 2993–3000.

[13]  M. Dimaki, P. Boggild, Frequency dependence of the structure and electrical behaviour of carbon nanotube networks assembled by dielectrophoresis, Nanotechnology 16 (2005) 759–763.

[14]  C.-H. Chen, R.-M. Wang, S.-J. Ko, Y.-C. Kuo, K.-M. Uang, T.-M. Chen, B.-W. Liou, H.-Y. Tsai, The influence of oxygen content in the sputtering gas on the self-synthesis of tungsten oxide nanowires on sputter-deposited tungsten films, Nanotechnology 17 (2006) 217–223.

[15]  B. Kim, N. Park, P.S. Na, H.-M. So, J.-J. Kim, H. Kim, K.-J. Kong, H. Chang, B.-H. Ryu, Y. Choi, J.-O. Lee, The effect of metal cluster coatings on carbon nanotubes, Nanotechnology 17 (2006) 496–500.

[16]  C. Chen, L. Wang, G. Jiang, Q. Yang, J. Wang, H. Yu, T. Chen, C. Wang, X. Chen, The influence of seeding conditions and shielding gas atmosphere on the synthesis of silver nanowires through the polyol process, Nanotechnology 17 (2006) 466–474.

[17]  H. Huang, O.K. Tan, Y.C. Lee, M.S. Tse, J. Guo, T. White, Effects of plasma treatment on the growth of $SnO_2$ nanorods from $SnO_2$ thin films, Nanotechnology 17 (2006) 743–746.

[18]  J. Li, Q. Zhang, H. Li, M.B. Chan-Park, Influence of Triton X-100 on the characteristics of carbon nanotube field-effect transistors, Nanotechnology 17 (2006) 668–673.

[19]  W. Lee, T.-Y. Liu, The effect of annealing temperature on the microstructure of nanoidented Au/Cr/Si, Nanotechnology 18 (2007) 1–10.

[20]  M. Mattila, T. Hakkarainen, H. Jiang, E.I. Kauppinen, H. Lipsanen, Effect of substrate orientation on the catalyst-free growth of InP nanowires, Nanotechnology 18 (2007).

[21]  T.-W. Kim, G. Wang, H. Lee, T. Lee, Statistical analysis of electronic properties of alkanethiols in metal–molecule–metal junction, Nanotechnology 18 (2007) 1–8.

[22] B. Panchapakesan, R. Cavicchi, S. Semancik, D.L. DeVoe, Sensitivity, selectivity and stability of tin oxide nanostructures on large area arrays of microhotplates, Nanotechnology 17 (2006) 415–425.

[23] P. Saravanan, V. Selvarajan, S.V. Joshi, G. Sundrararajan, Experimental design and performance analysis of alumina coatings deposited by a detonation spray process, J. Phys. D: Appl. Phys. 34 (2001) 131–140.

[24] C. Barglik-Chory, C. Remenyi, H. Strohm, G. Miller, Adjustment of the band gap energies of biostabilized CdS nanoparticles by application of statistical design of experiments, J. Phys Chem. B 108 (2004) 7637–7640.

[25] J. Gou, Z. Liang, B. Wang, Experimental design and optimization of dispersion process for single-walled carbon nanotube Buckypaper, Int. J. Nanosci. 3 (2004) 293–307.

[26] Y. Sun, Z. Zhang, C.P. Wong, Study on mono-dispersed nano-size silica by surface modification for underfill applications, J. Colloid Interface Sci. 292 (2005) 436–444.

[27] S.K. Roy, R. Dey, A. Mitra, S. Mukherjee, M.K. Mitra, G.C. Das, Optimization of process parameters for the synthesis of silica gel–WC nanocomposite by design of experiment, Mater. Sci. Eng. 27 (2007) 725–728.

[28] S. Desai, R. Mohan, J. Sankar, T. Tiano, Understanding conductivity of single wall nanotubes (SWNTs) in a composite resin using design of experiments, Int. J. Nanomanufact. (2008).

[29] H. Carrion, M. Rogosky, H.B. Nembhard, S. Joshi, Characterization of the SilSpin etch-back (breakthrough) process for nanolithography with $CHF_3$ and $O_2$ chemistry, Int. J. Nanomanufact. (2008) to appear.

[30] A. Basumallick, G.C. Das, S. Mukherjee, Design of experiments for synthesizing *in situ* Ni–$SiO_2$ and Co–$SiO_2$ nanocomposites by non-isothermal reduction treatment, Nanotechnology 4 (2003) 903–906.

[31] V. Yong, H.T. Hahn, Dispersant optimization using design of experiments for SiC/vinyl ester nanocomposites, Nanotechnology 16 (2005) 354–360.

[32] A. Kubovecz, D. Mehn, E. Nemes-Nagy, R. Szabo, I. Kiricsi, Optimization of CCVD synthesis conditions for single-wall carbon nanotubes by statistical design of experiments (DoE), Carbon (2005) 2842–2849.

[33] T.L. Riddin, M. Gericke, C.G. Whiteley, Analysis of the inter- and extracellular formation of platinum nanoparticles by *Fusarium oxysporum* f. sp. *lycopersici* using response surface methodology, Nanotechnology 17 (2006) 3482–3489.

[34] A. Nourbakhsh, B. Ganjipour, M. Zahedifar, E. Arzi, Morphology optimization of CCVD-synthesized multiwall carbon nanotubes, using statistical design of experiments, Nanotechnology 18 (2007) 1–7.

[35] G. Rajaram, S. Desai, Z. Xu, D.M. Pai, J. Sankar, RSM-based optimization for the processing of nanoparticulate SOFC anode material, Int. J. Nanomanufact. (2008).

[36] T.-H. Hou, C.-H. Su, W.-L. Liu, Parameter optimization of a nano-particle wet milling process using the Taguchi method, response surface method and genetic algorithm, Powder Technol. (2007) 153–162.

[37] H. Chang, C.S. Jwo, C.H. Lo, S.H. Pai, A study of process optimization using the combined submerged arc nanoparticle synthesis system for preparing $TiO_2$, J. Alloys Compd. (2007) 668–671.

[38] R. Mead, D.J. Pike, A review of response surface methodology from a biometric viewpoint, Biometrics (1975) 803–851.

[39] R.H. Myers, D.C. Montgomery, G.G. Vining, C.M. Borror, S.M. Kowalski, Response surface methodology: A retrospective and literature survey, J. Qual. Technol. 36 (2004).

[40] G.E.P. Box, N.R. Draper, Response Surfaces, Mixtures, and Ridge Analyses, Second ed., Wiley-Interscience, 2007.

[41] R.H. Myers, D.C. Montgomery, Response Surface Methodology, Second ed., Wiley, New York, 1995.

[42] G. Taguchi, S. Chowdhury, S. Taguchi, Robust Engineering, McGraw-Hill, 1999.

[43] G. Taguchi, S. Chowdhury, Y. Wu, Taguchi's Quality Engineering Handbook, John Wiley and Sons, New Jersey, 2005.

[44] D.C. Montgomery, Introduction to Statistical Quality Control, Fifth ed., John Wiley and Sons, 1996.

[45] G. Box, S. Jones, Split plots for robust product and process experimentation, Qual. Eng. 13 (2000–2001) 127–134.

[46] S.M. Kowalski, K.J. Potcner, How to recognize a split plot experiment, Qual. Prog. (2003).

[47] W.T. Federer, F. King, Variations on Split Plot and Split Block Experiment Designs, John Wiley and Sons, 2007.

[48] C. Yuangyai, H.B. Nembhard, A multi-stage experiment design in a nano-enabled medical instrument production process, Working paper, 2008.

[49] N. Antolino, G. Hayes, M. Frecker, Ceramic nanocolloids for medical applications: Meso-scale surgical instrument fabrication, drug delivery and bio-imaging, Presented at International Conference on the Characterization and Control of Interfaces, Kurashiki, Japan, 2006.

[50] N. Acharya, H.B. Nembhard, Statistical design and analysis for a three-step surface initiated polymerization process, Int. J. Nanomanufact. (2008) to appear.

[51] S. Bisgaard, C. Vivacqua, Strip-block experiments for process improvement and robustness, Qual. Eng. 16 (2004).

[52] N. Acharya, H.B. Nembhard, Statistical design and analysis for a three-step surface initiated polymerization process, Int. J. Nanomanufact. (2008).

[53] J.K. Lindsey, Models for Repeated Measurements, Second ed., Oxford University Press, New York, 1999.

[54] R. Kumar, N. Antolino, J.E. Wichard, K.J. Sutovich, D.M. Chapman, T.G. Roberie, J.H. Adair, Optimized de-aggregation and dispersion of high concentration slurry of nanophase alumina by chemically aided attrition milling, Working paper, 2005.

[55] D.K. Lin, Industrial experimentation for screening, in: R. Khattree, C.R. Rao (Eds.), Handbook of Statistic, 2003.

[56] N. Acharya, D. Lin, Understanding a ZnO nanorods fabrication process, Int. J. Nanomanufact. (2008).

[57] H.B. Nembhard, N. Acharya, M. Artan, S. Kim, Design issues and analysis of experiments in nanomanufacturing, in: Handbook of Industrial and Systems Engineering, 2006.

[58] S.M. Clarke, J.H. Griebsch, T.W. Simpson, Analysis of support vector regression for approximation of complex engineering analyses, J. Mech. Des. 127 (2005) 1077–1087.

[59] A. Charles, Y. Chandon, F. Bergeret, L. Garcia, Photolithography equipment control through D-optimal design, Proceedings of SPIE: The International Society of Optical Engineering (1996).

[60] T.W. Simpson, T.M. Mauery, J.J. Korte, F. Mistree, Comparison of response surface and kriging models for multidisciplinary design optimization, AIAA J. (1998) 1–11.

[61] D.J. Cappelleri, M.I. Frecker, T.W. Simpson, A. Snyder, Design of a PZT bimorph actuator using a metamodel-based approach, Trans. ASME 124 (2002) 354–357.

[62] M. Aguirre, M. Frecker, H.B. Nembhard, A framework for DOE and deterministic simulation in nano-enabled surgical instrument design, Int. J. Nanomanufact. (2008) to appear.

[63] NIST/SEMATECH e-Handbook of Statistical Methods, vol. 2007, 2006.

[64] C. Berding, W. Kleider, R. Gossl, DoPE: D-optimal planning & experimentation, the tool for experimental design in research and development, Stat. Software Newsletter (1996).

[65] A.C. Hooker, M. Foracchia, M.G. Dodds, P. Vicini, An evaluation of population D-optimal designs via pharmacokinetic simulation, Ann. Biomed. Eng. 31 (2003) 98–111.

[66] H.-Y. Chuang, H.-K. Tsai, C.-Y. Kao, Optimal designs for microarray experiments, Presented at Proceeding of the 7th International Symposium on Parallel Architectures, Algorithms and Networks (ISPAN'04), 2004.

[67] T.W. Simpson, T.M. Mauery, J.J. Korte, F. Mistree, Comparison of response surface and kriging models for multidisciplinary design optimization, AIAA J. (1998).

[68] H.B. Nembhard, Nanotechnology: A big little frontier for quality, Qual. Prog. (2007).

[69] Business Plan of TC229, vol. 2007: International Organization for Standardization, 2007. http://isotc.iso.org/livelink/livelink/6356960/TC_229_BP_2007-2008.pdf?func=doc.Fetch&nodeid=6356960.

# Environmental and Occupational Health Issues with Nanoparticles

**R. Handy, M. Whitt, M. Rodriguez and M.J. Jackson**

*Center for Advanced Manufacturing, MET, College of Technology, Purdue University, West Lafayette, IN 47907, USA*

## CONTENTS

## ABSTRACT

There are various environmental as well as worker health and safety issues involved with manufacturing or fabrication efforts that result in the creation of particles in the nanoparticle size range. While the research in this area is in the relatively early stages, several studies have been conducted over the last decade or so that focus on the environmental and human exposure issues surrounding the anthropogenic generation of airborne ultrafine or nanometre-range particles. The purpose of this chapter is to elucidate the current state of the literature regarding nanoparticles in the workplace and environment as well as to provide the latest characterization techniques used to conduct airborne nanoscale particle measurement.

## 9.1 INTRODUCTION

Various nanotechnologies used in fabrication and manufacturing have been around for several years now and there is currently very little disagreement about the potential benefits that could be realized by their increasing

implementation in industry. However, one major area of concern in the application of nanotechnologies in manufacturing is the subsequent potential compromise of worker health and safety due to airborne nanoparticles produced during their application.

Studies have indicated that exposures to low solubility nanoscale particles are more toxic to internal and external tissues and organs than larger particles on a mass for mass basis[1–4]. Thus, effective strategies for accurately sampling nanoscale particles are necessary due to the number of workers potentially being exposed in industries employing nanotechnologies such as surface coating, optoelectronics, electronics, medical imaging and drug delivery.

The current best practice in measuring employee exposures to airborne particulate concentrations is to use a personal sampling device to collect a representative volume of potentially contaminated air, typically conducted over an 8-h workshift. The metric most often used to determine a relative exposure to microscale particles is the time-weighted mass concentration of each particular aerosol. However, due to the inherent nature of the nanoscale particle, it is a widely accepted premise that the measurement of mass is not a sufficient worker health exposure metric[5]. In contrast to traditional theories about the health effects from microscale particle exposures, the detriments from nanoparticles are likely to be dependent on the specific particle, its morphology, surface, composition and size. Thus, ideally, a measurement of particle number or particle surface area would provide a more preferred means of biological relevance. Unfortunately, the technology to provide one or both of these parameters is currently only in the developmental stage.

The purpose of this chapter is to present an overview of the current state of the literature regarding nanoparticles in the workplace and environment and their associated health effects as well as to provide the latest characterization techniques used to conduct airborne nanoscale particle measurement. In doing so, the advantages and disadvantages to the use of each of these characterization techniques are elucidated, while efforts are made to restrict the discussion to only those potential applications in industries utilizing nanotechnologies in their processes.

## 9.2 POTENTIAL HEALTH EFFECTS

Particles at the nanoscale size range can enter the body through the lungs, gastrointestinal tract and skin. The chances and degree of penetration from all of these transport mechanisms depend on the size and surface properties of the particles and also on the point of contact on the particular tissue or organ. The surface characteristics and morphology of the particle play a crucial role in determining the destiny or main target organ once the particle is inside the body.

The potential for human and ecological toxicology associated with airborne ultrafine particles generated in nanotechnology is a growing area of concern. However, at the time of writing, very few definitive studies of human health detriments caused from exposures to nanoparticles have been published. Of the studies published, several raise safety concerns related to significant exposures in industries applying nanotechnologies in manufacturing and fabrication. As a matter of fact, this concern has given raise to a whole new area of toxicology known as *nanotoxicology*[6].

When evaluating ultrafine particles in the environment or workplace, issues also raise in differentiating between naturally occurring particles in this size range and those produced by the specific nanotechnology or nanomaterial being used. Another difficulty exists in categorizing health effects due to the inherent nature of the nanoparticle with respect to material type, since each will elicit its own unique ecological or biological response. Thus, it would only make sense to characterize separately the different material-types of particles in the ultrafine range as well as by differences in routes of exposure (i.e., inhalation, dermal, ingestion and injection).

A critical problem in conducting investigations in this area is the requirement for the researchers to follow specific (and sometimes unique) measures for every newly produced nanoparticle[7]. In essence, there is no ubiquitous ultrafine particle to use as a model to fit all cases and studies, and each nanotechnology and associated potential airborne nanomaterial produced should be treated independently with respect to human health risk potential.

An assessment of the conclusions from the different approaches and methods used to date in order to characterize the potential human health effects from exposures to ultrafine particles of varying material compositions has led to widely variable results. It could be argued that these inconsistencies indicate the need for standardized tests and occupational limits for comparing results in evaluating nanotechnologies and associate airborne nanoparticles with potential adverse impact on human health and the environment. It will take a combined effort from legislators, manufacturers and risk assessors (such as nanotoxicologists) to devise and test a series of methods, proven both economical and effective, to characterize the ultrafine particle or nanoparticle in settings where nanotechnologies and nanomaterials are being employed.

The following section provides a few of the most recent efforts by researchers in the area of environmental issues related to the increasing use of nanotechnologies in industry. It is not meant to be an exclusive list of the most important studies being conducted to date but instead, to the contrary, it is an attempt to provide the reader with a cross-section of the various efforts being currently undertaken by researchers in this critical field of investigation.

## 9.3 CURRENT STATE OF THE LITERATURE

The objective of this section is to elucidate some of the current literature findings of environmental and health/safety issues with airborne nanoparticles. The literature review of the most recent articles in this area includes topics related to the multiple components of the risk assessment framework. This includes such important aspects as particle characteristics effecting toxicity, their fate and transport throughout the environment, the routes of exposure and the metrics by which exposure ought to be measured and the mechanisms of translocation to different parts of the body. In addition, recent studies are presented that involve the characterization of nanoparticles in the workplace during different operations and conditions.

Boccuni et al. [researchers at the National Institute for Occupational Safety and Prevention (ISPESL) and Department of Occupational Medicine in Rome, Italy] used data from the Health and Safety Executive (HSE) report published in 2004, which outlined a method for assessing workers exposed to nanoparticles in the United Kingdom, and applied it to a group of Italian workers. This paper involved a technical analysis on industrial applications of nanomaterials, and a comprehensive risk assessment was conducted to develop a model applied to the Italian working population to define the magnitude and impact on workers potentially exposed to manufactured nanoparticles. Using an exposure-assessment approach based on the HSE report, they found a significant number of workers were potentially exposed to ultrafine particles from various existing manufacturing and powder handling processes. According to the National Nanotechnology Initiative, different work processes may bring about substantially different exposures to nanomaterials. This was a preliminary step for developing methods for assessing the risk of occupational exposure to nanomaterials in Italy. These researchers recognized the importance of carefully analysing the scenario in which workers are exposed, the duration of exposure and the concentrations of nanoparticles present in the workplace, and the importance of developing accurate environmental monitoring methods[8].

Schulte et al. (researchers at the National Institute for Occupational Safety and Health, Centers for Disease Control and Prevention in Cincinnati, Ohio, USA) conducted a comprehensive review using a conceptual framework for nanomaterial risk management programme, which incorporated key elements intended to minimize worker exposure to engineered nanoparticles. Since the number of workers involved in nanotechnology is increasing, the authors recognized the critical importance of using this framework and a hazard-based approach and its hierarchy of controls such as elimination or substitution, engineering controls, administrative controls and use of

personal protective equipment in order to establish control strategies to prevent occupational exposure to nanoparticles. According to this hierarchy, engineering controls are recommended before the use of work practices or personal protective equipment, such as respirators, to prevent worker exposure to hazardous substances. They may include containment of the process, isolation of the worker, local exhaust ventilation to remove the hazardous substance and process changes. In addition, the authors added that associated administrative controls contribute to the overall effectiveness of a workplace safety and health programme. Additional components to a workplace safety and health programme include worker training programmes, exposure monitoring and medical screening and surveillance. They concluded that since inhalation and skin exposures to nanoparticles are considered the main potential routes of exposure, the physicochemical properties of nanoparticles, including size, surface area, surface coating, shape, solubility, charge and attached functional groups, may influence biological activity and potential toxicity of nanomaterials. This premise is supported by earlier studies regarding the toxicity of nanoparticles based on two characteristics: (1) surface activity is an important factor in toxicity and mass for mass; the smaller the particles, the greater the surface; (2) particles tens of nanometres in size can readily cross cell membranes. An important consideration in this study was the assumption that nanoparticles that become airborne will follow the established laws of aerosol physics and classic fluid dynamics. Airborne nanoparticles have little or no inertia and thus are highly mobile and will diffuse and remain in air for a long time if not contained. The review concluded with a control banding approach or performance-based occupational exposure limits developed in late 1980s by H&S in the pharmaceutical industry, describing four main control bands for exposure to chemical by inhalation: Band 1 – use good industrial hygiene practice and general ventilation; Band 2 – use engineering control, typically local exhaust ventilation; Band 3 – enclose the process and Band 4 – seek expert advice[9].

Aitken et al. (researchers at the Institute of Occupational Medicine in Edinburgh, Scotland) conducted a detailed review that contained four main elements: a conventional scientific review, a Web-based review, discussion with key individuals involved in the research, and development of nanoparticles and the associated health effects and the experience and interpretation of the project team. While they did not review the toxicity of nanoparticles, they examined the routes, sources, level of exposure, control measures and numbers exposed. The study concluded that all processes give raise to exposure (by inhalation, dermal and ingestion) during recovery, powder handling and product processing. Other conclusions included the idea that control strategies and methods for exposure from inhalation are available

and should be effective in nanoparticles processes; however, for dermal and ingestion exposure, controls methods based on personal protective equipment may not be as effective. The authors indicated the need to fulfil the gap of information regarding exposure to nanoparticles during the various processes such as powder handling where exposures may be significant. The report concludes with a synopsis of the knowledge gaps in terms of nomenclature, methods by which particles surface area is assessed in the workplace and information to judge whether exposure to various forms of nanoparticles is occurring at significant levels in production processes. The report suggests that there is little evidence to support that the exposure of workers arising from the production of nanoparticles is adequately assessed and that there is a need to develop control strategies and an associated database for other researchers to use[10].

Balbus et al. performed a comprehensive review of the existing toxicological literature on nanomaterials, outlined and analysed the current regulatory framework by two of the main regulatory bodies (the US Environmental Protection Agency and the US Occupational Safety and Health Administration) and provided recommendations for safe nanotechnology development. However, they noted that the novel properties that make nanotechnologies so interesting have also raised many unanswered questions and concerns related to the impacts nanotechnology may have on society and the environment from the point of sustainability. Some of the questions that the authors ask in the study are: Will some nanoparticles persist in the environment and accumulate within living organisms? Do the novel physicochemical and structural properties of nanomaterials cause unanticipated toxicological behaviour at the cellular or organism levels? Can the potentially harmful properties of nanomaterials be efficiently identified during the development process and engineered out of final products or otherwise effectively managed? The authors brought out that the similarity of combustion-related fine and ultrafine particles in other studies provide some basis for concerns about environmental and health risks from products of nanotechnology. The importance of understanding the toxicity of nanoparticles and its relationship to the surface area to mass ratio is stressed in the study. They found that the higher the surface area to mass ratio the higher will be the particle surface energy, which may translate into higher reactivity according to other previous studies. They also stated that for worker safety it is critical to assure the stability of surface properties throughout the lifespan of manufactured nanoparticles as well as the need to improve the database of toxicity studies on nanomaterials. The authors argued that there were three main challenges to the current occupational and environmental regulatory frameworks: standards are based on mass

and mass concentration, structure–activity models are used to extrapolate to new materials and nanomaterials are being developed by very small companies with few products. They concluded with the premise that the pace of the regulatory process lags far behind the speed with which nanomaterials are being brought to market.

The authors present the fact that the US Occupational Safety and Health Administration (OSHA) had not published any standards, guidance or position papers on nanotechnology. However, it is noted that OSHA has developed several useful draft guidance documents regarding occupational safety and health practices for the nanotechnology industry. These documents address health and safety concerns, exposure monitoring, engineering controls and workplace practices for nanotechnology manufacturing facilities. The Occupational Safety and Health Act (OSHAct) contains four types of standards relevant for protecting workers from overexposure to nanomaterials: substance-specific standards, general respiratory protection standards, the hazard communication standard and the 'general duty clause'. In the absence of specific standards, inhalable nanoparticles will only be addressed by the 5mg/m$^3$ standard that applies to particulates not otherwise regulated, sometimes called 'nuisance dust' (29 CFR section 1910.1000 Table Z-1). It is elucidated that these mass-based standards may not be appropriate to protect workers from adverse effects of chronic nanoparticle exposures.

The authors continue by discussing that, according to the US OSHA respiratory protection standard (29 CFR section 1910.134), employers must provide workers with respirators or other protective devices when engineering controls are not adequate to protect health and must establish relevant workplace respiratory protection programmes. The authors stressed the importance of improving the knowledge on validated means to measure and characterize the form and size of nanoparticles in the air, as well as uncertainties regarding respirator performance, which may complicate the accomplishment of this standard. OSHA's hazard communication standard (CFR section 1910.1200) stipulates that it is mandatory for employers to develop material safety data sheets (MSDSs), which contain information on hazardous ingredients in products, so that workers get educated on safe handling practices.

Finally, Balbus et al. concluded their paper by stressing that the US Environmental Protection Agency conducts both regulatory and research activities relevant to protecting the general public and the environment from potential risks of nanotechnology. As evidence, they present the agency's efforts in part by introducing a draft Nanotechnology White Paper released in December 2005, which summarized hazard- and exposure-related and environmental concerns; this paper concluded with recommendations for

integrating nanotechnology into its pollution prevention programmes, a research programme on environmental applications and environmental and health implications of nanotechnology, a cross-agency coordinating work-group, case studies on risk assessment and training needs[11].

Lee et al. (researchers from various research centres interested in nano-particles and occupational health issues) performed a study to evaluate the influence of two ventilation systems on resultant welding aerosol size distributions and characteristics at the different locations in the booths where welding operations were in progress. For this study, two different booths were used, each equipped with a different type of ventilation system. The first was an existing welding booth with the ventilation duct located over-head at the top in the ceiling and with a flow rate of 11 cubic metres per minute. The second booth was a modified system where the welding table had an integrated vent that draws flow through a set of grates away from the weld region and operating at a flow rate of 11 cubic metres per minute. An additional overhead duct was in place. The sampling time total weld-ing operation ran for about 5 min while using two real-time aerosol instru-ments: an electrostatic classifier and a condensation particle counter. The modified booth was effective at removing the particles in the nanometre size ranges, resulting in a significant decrease in the measured total number con-centration. The authors realized that by changing the ventilation system in the booth, the particle concentrations became considerably lower, which also resulted in a faster clearance of the generated particles. The study provided evidence that effective ventilation systems are important in order to effec-tively reduce nanoparticle concentrations and reduce human exposure[12].

Brouwer et al. (researchers at the Department of Food and Chemical Risk Analysis, The Netherlands) reported the results of two small-scale studies, a workplace and a laboratory study, to evaluate a proposed sam-pling strategy to assess personal exposure to ultrafine particles in the work-place. The authors agreed that the current toxicological and epidemiological research had not revealed agreement on the most relevant dose-metric(s) to express human exposure to ultrafine nanoparticles. The current methods of sampling and tools to assess the workers' exposure, such as mass and par-ticles concentration and surface area, are mainly applicable only for static sampling and most of these don't afford full-shift measurements.

A detailed explanation of the available instruments and techniques for the characterization of ultrafine aerosols was provided in a table for the metrics of mass, number, surface area and identification. The results from this study bring attention to the importance of comparison studies involv-ing the results of static sampling and personal sampling of particles and fibres in workplaces and the premise that personal exposure is greater than

environmental concentrations; however, this is mostly applicable in manufacturing processes where dust generation is operator dependent. The size-selective sampling used was conducted with two techniques: static samplers and condensation particle counting (CPC). Both the workplace study (in the MIG welding scenarios) and the experimental study showed that there were spatial variations in both particle number concentration and size distribution. The authors concluded that the placement of static samplers at fixed locations slowed down the interpretation of the results for personal exposure of ambulatory workers and, subsequently, stated the need for further research to enable accurate quantification of personal exposure of workers as well as to identify determinants of exposure[13].

Arumugam et al. (researchers at the Material and Manufacturing Research Lab (MRL), Department of Mechanical Engineering, University of Arkansas) were interested in the fact that dry machining generates particles instead of mist and conducted research involving dry machining with Al–Si alloy (A390) with 18% silicon as the workpiece material. The study investigated the effect of tool morphology, chip morphology and current production machining parameters on aerosol generation. A unique feature of this study was the quantification of the health hazards by defining a factor, a green factor, that determines the human hazard associated with the aerosol generation as a function of machining input parameters. Hypereutectic Al–Si alloy (A390) (hollow cylinders – 107 mm O.D. × 80 mm I.D. × 270 mm long) was chosen because of its wide range of applications in the automotive industries. Chemical vapour deposited (CVD) diamond-coated tools were used for the tests with polycrystalline diamond (PCD) as a reference. The test was performed on a CNC lather, and an aerodynamic particle sizer was used and located inside the machine enclosure. The location was chosen to obtain an average count in the enclosure along the lines and it was directed normal to the workpiece at mid-length between the workpiece and at a distance of 0.5 m away from it. The tests were carried out using the PCD inserts for 5 min and the CVD inserts for 3.5 min of machining. In terms of aerosol mass concentration for PCD inserts, feed, depth of cut, and the interaction between speed and feed are significant. The mass concentration increased by increasing the feed or depth of cut. Similarly, the concentration increased at low speed (480 m/min) and high feed (0.4 mm/rev). For CVD, the concentration decreased by increasing the speed to 690 m/min. In terms of aerosol number concentration, for PCD inserts, depth of cut is a significant main effect. The number concentration increased by increasing the speed or depth of cut. For CVD, feed was the only critical parameter having a significant effect. The green factor is defined as: GF = MRR/MC where MRR is the material removal rate and MC is the mass concentration of aerosol. Thus, the

higher the green factor, the safer the process. The highest GF was obtained for a combination of high speed, high feed and high depth of cut runs. It was evident that the GF is consistently higher for PCD than for CVD[14].

Japuntich et al. (researchers at the Institute of Technology, University of Minnesota, USA) performed a comparison between two different filter test methodologies in the nano-sized particle range of 10–400 nm, evaluation of the test procedure development and the factors affecting variability and characteristics of the different systems. One method involved the use of a monodisperse aerosol obtained through a differential mobility analyser. A commercially available automated filter tester was used in this study as well as another method of filter penetration testing for nano-sized particles. The second method produced a stable, small particle aerosol with a wide size distribution, which is electrostatically neutralized and used as a direct filter challenge. In this case a scanning mobility particle sizer (SMPS) was used to sample the particle size distributions downstream and upstream of an air filter to obtain a continuous filter penetration versus particle size curve. The authors followed the testing standards and protocols for filter penetration by the American Society of Heating Refrigeration and Air-Conditioning Engineers (ASHRAE) Standard 52.2 (1999), which outlines specific requirements for the evaluation of penetration through filter media, and the American Society for Testing and Materials (ASTM) standards F778-88 (2001) and F2519-05 (2005).

The authors' experimental design included the use of four medium-efficiency fibreglass filter papers of very low variability in order to effectively evaluate filter penetration versus particle diameter. A detailed description of the filters was tabulated and the homogeneity of these samples was demonstrated by the low coefficients of variation shown for both pressure drop and Q127 DOP penetration tests. It was apparent that the key to getting reliable results was based on the proper calibration of the automated filter tester to ensure consistent results, as well as continual maintenance cleaning of the aerosol transport lines. For both of these nano-sized particle air filtration tests, the penetration versus particle size curves for the filter media studied follow the trends of the theoretical Brownian capture model of decreasing penetration with decreasing particle diameter below 100 nm. There was no evidence of 'particle bounce'. The authors suggested the need to collect personal exposure samples to determine how these nano-sized particles should be correctly measured and assessed[15].

Hsu and Chein (researchers at the Energy and Environment Research Laboratories and the Industry Technology Research Institute, Taiwan) were interested in improving the knowledge related to the potential emission of

particles from nanomaterials that employ or apply nanopowder coating. Anatase polycrystalline single crystal $TiO_2$ nanoparticles are being used increasingly in photocatalytic surface coatings. Particle emission evaluation is critical to answer the question of whether such coatings will release nanoparticles during their use. The authors evaluated nanoparticle emissions from $TiO_2$ nanopowder coating materials in a simulated utilization stage of three different substrates (wood plate, polymer film and tile plate). UV light/fluorescent lamps, a fan and a rubber knife were used to simulate the sunlight, wind and human contact with the materials in a closed box. The particle emissions from the substrate and $TiO_2$ coating materials were monitored at different operation conditions. An SMPS was used to measure the particle size distribution and number concentration during tests. A comparison of the three selected substrates (wood, polymer and tile) revealed that the tile coated with $TiO_2$ nanopowder was found to have the highest particle emission (22 particles/cm$^3$ at 55 nm). In addition, UV light was shown to increase the release of particles below 200 nm from $TiO_2$ coating products. The study elucidated the clear need to investigate nanopowder coatings for their potential adverse human exposure impact[16].

Conclusively, this section brings out the importance to the overall experimental design and study of having effective and portable means for characterizing nanoparticles in the field. The following section provides a more detailed explanation of some of these techniques and/or associated instrumentation used by the authors and other investigators in this emerging area.

## 9.4 CHARACTERIZATION OF AIRBORNE NANOPARTICLES

Much like the means for determining the health impact and risks associated with exposure to nanoparticles, the research into the characterization of nanoscale particles is in its infancy. In addition, it is recognized that monitoring instrumentation used in the field requires improvement in both portability and measurement sensitivity. Table 9.1 provides a summary of nanoparticle measurement techniques that are either currently in the developmental stages or have already been implemented in the nanotechnology industry. The table includes the method, the metric measured and the major capabilities and limitations of each.

The first method discussed is a personal sampling device that discriminates based on size. Currently, most analytical methods for particulate matter are based on the collection on a pre-weighed (typically on a laboratory balance) filter of any additional mass sampled at a known

| Table 9.1 | Particle Measurement and Characterization Techniques | |
|---|---|---|
| **Method or Instrument** | **Measurement Metric** | **Major Capabilities and Limitations** |
| Personal sampler with accessories (e.g., cyclone, impactor) | Mass | Acceptable for exposure compliance; no size fraction cut-off in nanometre size; 0.02 mg/m$^3$ sensitivity |
| Laser particle counter and other optics counters | Number concentration | Portable and easy to operate; mainly for microscale use; 300 nm sensitivity; segregated size ranges |
| Condensation particle counter | Number concentration | Portable and easy to operate; not size selective; 10 nm sensitivity |
| Scanning mobility particle sizer | Number concentration | Excellent sensitivity; not portable or user friendly and cost; 3 nm sensitivity |
| Nanometer aerosol size analyser | Number concentration | Excellent sensitivity; not portable and in development stage; 3 nm sensitivity |
| MiPac particulate classifier | Number concentration | Ease of use; no detection under 10 nm; 10 nm sensitivity |
| Electrical low-pressure impactor | Number concentration | Successful use studies; cost and not very portable; 7 nm sensitivity |
| Epiphaniometer | Surface area | Successful use studies; bulky, complex and costly; measurement based on surface area |
| Gas adsorption | Surface area | Well understood technology; large samples sizes needed for validity; measurement based on surface area |
| Scanning electron microscopy | Number, morphology and size | Excellent sensitivity and resolution; sophisticated instrumentation; 5 nm sensitivity |
| Transmission electron microscopy | Number, morphology and size | Excellent sensitivity and resolution; complicated sampling routine; 1 nm sensitivity |
| Laser induced plasma system | Composition | Outstanding for composition studies; composition information only; 3 nm sensitivity |

flow rate. The full production shift (i.e., 8 h) detection limit is approximately 0.02 mg/m$^3$. Obviously, this would present a problem in analysing by mass an air sample comprising of mainly nanoscale particles which weighs considerably less. However, developing personal samplers that would discriminate out particulate matter exceeding 100 nm has been proposed[5]. With this achievement, there would be statistical accuracy for measuring coating aerosols above 50 nm.

The second through seventh methods provided in Table 9.1 are particle count based. These methods, with several in the developmental stages, include laser optical particle counters, condensation nuclei counters, SMPS

and electrical low pressure impactors (ELPIs). These are primarily real-time counters and range in relative portability and, thus, applicable to workplace exposure assessments.

Owing to its portability, versatility and lower detection size limit, laser particle counters have been traditionally used to measure particles down in the low microscale range. However, particles that are less than 300 nm will not be detected by this method[17]. This limits the applicability in some nanotechnology industries, where particles are quite frequently found an order of magnitude smaller. The more sensitive optical samplers that currently exist are not easily portable, thereby greatly reducing their industrial applications for workplace exposures assessments.

The most commonly used instrument to measure ultrafine particles employs CPC technology. The CPC condenses vapour onto the sampled particles in order to 'grow' them to a detectable size range. This type of instrument is relatively portable and user friendly. The primary disadvantage of this instrument is its inability to discriminate particulate sizes above the detection limit, which ranges from 3 to 100 nm on commercially available units, giving a total particle count[18]. Figure 9.1 shows an example of a typical CPC used to characterize ultrafine particles.

The current measurement methods that provide both size-selective information and number concentration are complicated, cumbersome and ill suited for field exposure assessments. In addition, their higher costs typically eliminate applicability altogether in the workplace. Examples of these methods are the ELPI and the SMPS, shown in Figures 9.2 and 9.3, respectively. Both of these instruments can provide size-selective concentration data of particles to less than 10 nm in diameter[18, 19].

Since the majority of nanoparticles generated agglomerate to some extent, it has been argued that the best way to characterize nanoscale particles is the measurement of its surface area. The primary instrument that is currently employed to measure surface area is called an epiphaniometer[20, 21], which uses radioactive tagging to determine the particle's surface area. Again, this instrument is very complicated and lacks versatility for field use. Gas adsorption techniques that require rather large sample sizes have also been used infrequently as a bulk method of ascertaining particle surface areas.

Scanning electron microscopy (SEM) and transmission electron microscopy (TEM) also provide the means of determining ultrafine particle characteristics. While these instruments provide the morphology of the particles and excellent resolutions



**FIGURE 9.1** *Condensation particle counter.*
*Source: With permission from TSI, Inc.*



**FIGURE 9.2** *Electrical low pressure impactor.*
*Source: With permission from Dekati Ltd.*

**FIGURE 9.3** *Scanning mobility particle sizer.*
*Source: With permission from TSI, Inc.*

(i.e., TEM = 1 nm; SEM = 5 nm), they are both complicated and costly. However, recent studies point to the merit of this technique to characterize exposures in the workplace[22].

Nanoparticle composition measurement is normally an essential component for nanoscale particle studies. Unlike many of the number, size-selective and surface area techniques discussed previously, nanoparticle composition techniques are mainly in the developmental stages. The laser induced plasma system and the high temperature nanoparticle measurement systems[23] can detect the composition of nanoscale particles as small as 3 nm.

Given that each of the methods discussed has its own merits and limitations, a combination technique may provide the best solution. While the more sophisticated instruments have excellent resolution and, many times, both concentration and size-selectability, they are primarily limited to research settings due to their complexity, size and cost.

The concerted use of portable techniques such as laser counting and CPC could minimize some of the major drawbacks of their individual usage for nanoscale aerosol characterization. For instance, a technique employing both a laser counter, with size-selective information down to 300 nm, and several condensation nuclei counters, with differing resolutions below 300 nm, could greatly reduce exposure-assessment costs. The number of CPCs needed by a user would be as few as one, depending on how much information is already known about the size of the particles or their specific aggregate. Figure 9.4 provides an example of a pilot run involving the use of a CPC with a sensitivity of 20 nm coupled with a size-selective laser detection device with a sensitivity of 300 nm. It is worth noting that this methodology is portable, economical and well suited for field aerosol exposure studies.

Further research is required to prove that this technique has statistical merit. Additional pilot studies should be conducted and a mathematical algorithm that relates the output from the instruments with each other as well as workplace exposures to nanoparticles should be produced. The studies should be conducted initially under tightly controlled laboratory conditions, and subsequently field tested. Ideally, the studies should begin with the use of a laser particle counter and one condensation particle counter, and then CPCs should be added as the study becomes more involved. In addition, it is proposed that electron microscopy (or other proven technologies) can be used as a means of measurement quality assurance/control.



**FIGURE 9.4**  *Pilot set-up involving both CPC and laser particle counter.*

## 9.5  CONCLUSIONS

In conclusion, an overview of the literature involving issues surrounding the creation of airborne nanoparticles in industries employing nanotechnologies was provided. In addition, the currently available methods for segregating and measuring concentrations of airborne nanoscale particles in the field were elucidated. A few of these techniques could be somewhat beneficial to the user in determining the worker exposure profiles but, implemented alone, additionally have several limitations. Future efforts to characterize the environmental exposures will likely include the combination of more than one method of monitoring and measurement of airborne nanoparticles.

## REFERENCES

[1]  The Royal Society and The Royal Academy of Engineering <http://www.nanotec.org.uk/finalreport.htm>, July 19, 2007.

[2]  M. Jamriska, et al., Control strategies for sub-micrometer particles indoors: model study of air filtration and ventilation, Indoor Air 2003 13 (1) (2003) 96–105.

[3]  National Institute of Occupational Safety and Health (NIOSH), <http://www.cdc.gov/niosh/topics/nanotech/>, 2 July 2005.

[4]  J.A. Sarnat, et al., Measurement of fine, coarse and ultrafine particles, Ann. 1st Super Sanita 39 (3) (2003) 351–355.

[5]  Institute of Occupational Medicine for Health & Safety Executive (2004) Research Report 274, <http://www.hse.gov.uk/research/rrpdf/rr274.pdf>.

[6] G. Oberdoster, et al., Principles for characterizing the human health effects from exposure to nanoparticles: elements of a screening strategy, Part. Fibre Toxicol. 2 (8) (2005) 8–43.

[7] P. Hoet, et al., Nanoparticles: known and unknown health effects, J. Nanobiotechnol. 2 (1) (2004) 12.

[8] F. Boccuni, B. Rondinone, C. Petyx, S. Iavicoli, Potential occupational exposure to manufactured nanoparticles in Italy, J. Clean. Prod. 16 (8) (2008) 949–956.

[9] P. Schulte, C. Geraci, R. Zumwalde, M. Hoover, E. Kuempel, Occupational risk management of engineered nanoparticles, J. Occup. Environ. Hyg. 5 (4) (2008) 239–249.

[10] R.J. Aitken, K.S. Creely, C.L. Tran, Research report 274 – nanoparticles: an occupational hygiene review, Institute Occupational Medicine, Edinburgh, Scotland, 2004 http://www.hse.gov.uk/research/rrpdf/rr274.pdf.

[11] J. Balbus, K. Florini, R. Denison, S. Walsh, Protecting workers and the environment: an environmental NGO's perspective on nanotechnology, J. Nanopart. Res. 9 (1) (2007) 11–22.

[12] M. Lee, W. McClellan, J. Candela, D. Andrews, P. Biswas, Reduction of nanoparticle exposure to welding aerosols by modification of the ventilation system in a workplace, J. Nanopart. Res. 9 (1) (2007) 127–136.

[13] D. Brouwer, J. Gijsbers, M. Lurvink, Personal exposure to ultrafine particles in the workplace: exploring sampling techniques and strategies, Ann. Occup. Hyg. 48 (5) (2004) 439–453.

[14] P. Arumugam, A. Malshe, S. Batzer, D. Bhat, Study of airborne dust emission and process performance during dry machining of aluminum–silicon alloy with PCD and CVD diamond-coated tools, J. Manuf. Processes 5 (2) (2003) 163–169.

[15] D. Japuntich, L. Franklin, D. Pui, S. Kuehn, A. Viner, A comparison of two nano-sized particle air filtration tests in the diameter range of 10 to 400 nanometers, J. Nanopart. Res. 9 (1) (2007) 11–22.

[16] L. Hsu, H. Chein, Evaluation of nanoparticle emission for $TiO_2$ nanopowder coating materials, J. Nanopart. Res. 9 (1) (2007) 57–163.

[17] HACH Ultra Analytics, <http://www.hachultra.com>.

[18] TSI Incorporated, <http://www.tsi.com>.

[19] Dekati Ltd., <http://www.dekati.com>.

[20] H.W. Gaggeler, et al., The epiphaniometer, a new device for continuous aerosol monitoring, J. Aerosol Sci. 20 (6) (1989) 557–564.

[21] D.B. Kittleson, Engines and nanoparticles: a review, J. Aerosol Sci. 29 (6) (1998) 575–588.

[22] A.D. Maynard, et al., Examining elemental surface enrichment in ultrafine aerosol particles using analytical scanning transmission electron microscopy, Aerosol Sci. Technol. 38 (4) (2004) 365–381.

[23] Washington University-St. Louis, Dr. Da Ren Chen's faculty Web page, <http://www.me.wustl.edu/faculty/dc/index.html>.

# Commercialization of Nanotechnologies: Technology Transfer from University Research Laboratories

M.J. Jackson[1], M.D. Whitt[1], R.G. Handy[1], G.M. Robinson[2] and M.D. Whitfield[2]

[1]*Purdue University, MET, College of Technology, West Lafayette, IN, USA*
[2]*Micro Machinists, L.L.C., Purdue Research Park, West Lafayette, IN, USA*

## CONTENTS

## ABSTRACT

The commercialization of nanotechnology from university spin-out companies is viewed as critical for the sustainable development of tertiary-level technologies. This chapter outlines the roles of venture capitalists, Government, academic institutions, and entrepreneurs in providing society with nanotechnology companies that turn science into money. The chapter also explains how the technology is transferred in the marketplace through patents, trade secrets, and copyrights, and allows the academic entrepreneur to understand the role of consumers and markets.

## 10.1 INTRODUCTION

Technology transfer from universities is dependent on the support from Government agencies, private investors and private companies. Investment decisions are a major force in how nanotechnology develops, and this is dependent on the support from Government, academia, private investors and companies. Nanoscale science and engineering activities are growing in the United States at an ever-increasing rate. The National Nanotechnology Initiative (NNI) is a long-term research and development (R&D) programme that began in 2001, and co-ordinates 25 departments and independent agencies, including the National Science Foundation (NSF), the Department of Defense, the Department of Energy, the National Institutes of Health, the National Institute of Standards and Technology and the National Aeronautical and Space Administration. The total R&D investment in 2001–2005 was over $4 billion, increasing from the annual budget of $270 million in 2000 to $1.2 billion including congressionally directed projects in 2005. An important outcome of the NNI is the formation of an interdisciplinary nanotechnology community with about 50,000 contributors. An R&D infrastructure with over 60 large centres, networks and user facilities has been established since 2000. This expanding industry consists of more than 1500 companies with nanotechnology products with a value exceeding $40 billion at an annual rate of growth at about 25%. With such growth and complexity, participation of a coalition of academic organizations, industry, businesses, civil organizations and Government in nanotechnology development becomes essential. The role of Government continues in basic research but its emphasis is changing especially in workforce education and individual enterprise, while the private sector becomes increasingly dominant in funding nanotechnology applications. The promise of nanotechnology will not be realized by simply supporting research. A specific governing approach is necessary for emerging nanotechnologies and their implementation.

This chapter explains the roles of each player and their impact on the technology transfer process in commercialization of nanotechnologies.

## 10.2  VENTURE CAPITALISTS

Investment in nanotechnology can gain much from venture capitalists (VCs). Venture capital is the money that is invested in unproven companies with the potential to grow into multi-billion dollar industries of the future. VCs are sources of financial and business resources that seek to control part of the business. VCs expect to capture 50%–70% of return on their investments in a 4–7 year time period, which is the time it takes to get the start-up company to reach liquidity in terms of acquisition, merger or initial public offering. Nanotechnology start-ups are not particularly attractive to VCs at the present time because the commercialization horizon is far too long. Start-up companies are particularly attractive to VCs because the company has:

1. a particularly innovative product that is disruptive and has a sustainable business advantage;
2. a large and growing market that is worth $1 billion and grows at a rate of 50%–70% per year;
3. products with a very short time-to-market horizon (less than 2 years);
4. a successful management structure with experienced executives;
5. an established customer base with strategic partners that will provide a strong revenue stream.

Nanotechnology is not a single market, but a series of enabling technologies that provide groundbreaking solutions to high value problems in every industry. Product innovations are characterized by the application of nanoscale materials, or with process technology conducted at the nanoscale that changes the functionality of the product.

## 10.3  START-UP COMPANIES IN NANOTECHNOLOGY

Start-up companies in nanotechnology should be measured by the same metrics as other start-up companies in terms of income generating business dynamics and cost controlling business issues such as sales strategy, management structure, allocation of capital, marketing, business models and product introduction. The key difference of nanotechnology start-ups is that they possess a technology platform that is composed of intellectual property (IP) generated by a team of scientists who are interdisciplinary in nature with no business strategy, focus or management structure. The team

is composed of highly respected academic scientists who can lever sources of funding through research contracts. In their initial stages, these companies team up with established companies to help them validate products, provide a channel for marketing and selling products and provide expertise in manufacturing. At this stage, nanotechnology start-ups are characterized in the following primary categories: materials, biotechnology, software, electronics, instrumentation and photonics. The greatest growth is in the area of materials even though most of the funding has gone to developing nanophotonics and nanoelectronics products.

## 10.4 ROLE OF GOVERNMENT IN COMMERCIALIZATION

The role of Government in nanotechnology is to support research and development relevant to national priorities, support the development of a skilled workforce and support infrastructure such as Government laboratories and research centres to advance nanotechnology. In 2000, the US Government announced the NNI, which was signed into law in 2003 by President George W. Bush, that creates a mission enabling the Government to establish goals, priorities and metrics for the evaluation of federal spending on nanotechnology. The law also provides for investment in nanotechnology through strategic programmes and provides inter-agency co-operation between Government departments. The Government also supports the development of workforce education by allowing interested parties to promote the development of curricula via funds channelled through the NSF. NSF funds in workforce development are focused on universities to establish the fundamental education in nanoscience and technology, and on community colleges who provide training in nanotechnology activities such as manufacturing process operations and materials production. Articulation agreements also provide pathways so that community college graduates can proceed to universities involved in nanoscience and technology in the form of two-plus-two degree programmes. Recently, the US Department of Labor has started to fund workforce innovation programmes directed at intentionally contributing to regional economic development. One such scheme is directed at promoting the use of nanostructured coatings for increasing productivity in the north central Indiana region. This programme also provides for workforce development by allowing professors from Purdue University to attend local companies in order to educate the workforce in the area of nanotechnology. Government also provides funds to allow the National laboratories to conduct fundamental research in nanotechnology. The provision of instrumentation is essential especially to major corporations and small-to-medium enterprises that normally cannot afford to purchase such instrumentation. In the United States, job creation is down to major

corporations and especially SMEs, and it is considered essential that job creators gain unfettered access to these facilities. Nanotechnology education and outreach has impacted over 10,000 graduate students and teachers since 2005. Changes are in preparation for education by the introduction of nanoscience at an early age. Nanotechnology education has been expanded systematically to earlier education, including undergraduate (The NSF's Nanotechnology Undergraduate Education programme has awarded over 80 awards since 2002) and high schools (since 2003), as well as informal education, science museums and public dissemination. All major science and engineering colleges in the United States have introduced courses related to nanoscale science and engineering in the last 5 years. NSF has established recently three other networks with national outreach addressing education and societal dimensions: (1) The Nanoscale Center for Learning and Teaching aims to reach 1 million students in all 50 states in the next 5 years; (b) The Nanoscale Informal Science Education Network will develop, among others, about 100 nanoscale science and technology museum sites in the next 5 years; (c) The Network on Nanotechnology in Society was established in September 2005 with four nodes at the Arizona State University, University of California at Santa Barbara, University of South Carolina and Harvard University. The Network will address both short-term and long-term societal implications of nanotechnology as well as public engagement. All 15 Nanoscale Science and Engineering Centers (NSECs) sponsored by NSF have strong education and outreach activities.

## 10.5  ROLE OF ACADEMIC RESEARCH IN COMMERCIALIZING NANOTECHNOLOGY PRODUCTS

Under the NNI, the NSF plays the largest role in funding nanotechnology research in the United States. Additional funding is provided by the Department of Defense, Department of Energy, National Institute of Health, NASA, Environmental Protection Agency and the Department of Agriculture. The NSF has created a tier of funding where 1 year exploratory research is funded in addition to 5–10 year centre awards. Each tier creates a different level of maturity of nanotechnological development that is cross-disciplinary. NSECs are awarded for 5 years initially, and are used as focal points for developing infrastructure and to provide a basis for further funding from other sources of funding. NNI has been recognized for *creating an interdisciplinary nanotechnology community in the United States.* Two significant and enduring results have emerged from this investment: the creation of a nanoscale science and engineering community and the fostering of a strong culture of interdisciplinary research. The following centres have

been created under the auspices of the NNI: Columbia University – Center for Electron Transport in Molecular Nanostructures; Cornell University – Center for Nanoscale Systems; Rensselaer Polytechnic Institute – Center for Directed Assembly of Nanostructures; Harvard University – Science for Nanoscale Systems and their Device Applications; Northwestern University – Institute for Nanotechnology; Rice University – Center for Biological and Environmental Nanotechnology; University of California, Los Angeles – Center for Scalable and Integrated Nanomanufacturing; University of Illinois at Urbana-Champaign – Center for Nanoscale Chemical, Electrical, Mechanical, and Manufacturing Systems; University of California at Berkeley – Center for Integrated Nanomechanical Systems; Northeastern University – Center for High Rate Nanomanufacturing; Ohio State University – Center for Affordable Nanoengineering; University of Pennsylvania – Center for Molecular Function at the Nanoscale; Stanford University – Center for Probing the Nanoscale; University of Wisconsin – Center for Templated Synthesis and Assembly at the Nanoscale; Arizona State University, University of California, Santa Barbara, University of Southern California, Harvard University – Nanotechnology in Society Network Centers from the Nanoscale Science and Engineering Education Solicitation; Northwestern University – Nanotechnology Center for Learning and Teaching; and NSF Networks and Centers that complement the NSECs include: Cornell University and 12 other nodes creating the National Nanotechnology Infrastructure Network; Purdue University and 6 other nodes creating the Network for Computational Nanotechnology; Oklahoma University, Oklahoma State University and the Oklahoma Nano Net; and Cornell University, STC: The Nanobiotechnology Center.

With about 25% of global government investments in nanotechnology, the United States accounts for about 50% of highly cited papers, ~60% of USPTO patents and about 70% of start-up companies in nanotechnology worldwide. Industry investment in the United States has exceeded the NNI in R&D, and almost all major companies in the traditional and emerging fields have nanotechnology groups at least to survey the competition. Small Times magazine reported 1455 US nanotechnology companies in March 2005, with roughly half being small businesses and 23,000 new jobs were created in small start-up 'nano' companies. The NNI SBIR investment was about $80 million in 2005. More than 200 small businesses, with a total budget of approximately $60 million, have received support from NSF alone since 2001. Many of these are among the 600 nanotechnology companies formed in the United States since 2001. All Fortune 500 companies in emerging materials, electronics and pharmaceutical markets have nanotechnology related activities since 2003. In 2000, only a handful of

companies had corporate interest in nanotechnology (under 1% of the companies). A survey performed by the National Center for Manufacturing Sciences at the end of 2005 showed that 18% of surveyed companies are already marketing nanoproducts. Over 80% of the companies are expected to have nanoproducts by 2010 and 98% in the longer term. Therefore, the role of academic research will play a significant part in this growth.

## 10.6 TECHNOLOGY TRANSFER

Technology transfer is conducted at research-intensive universities for a number of reasons. The first is that there is a *federal mandate* that makes universities allow discoveries to be available for commercialization, and that this is an important way of attracting talented *faculty* into positions within a university who would not otherwise be attracted to a teaching environment. The other reasons include providing equity to faculty members and providing goodwill that will encourage faculty, alumni and alumnae to become donors to the university and get engaged with the process of commercialization at the university.

Technology is usually transferred when the professor responsible for the invention allows the university to file a provisional patent, thereby allowing the university to provide a licence to the professor to commercialize the technology. The commercialization is dependent upon the knowledge created by the professor and this in turn allows the professor to be rewarded with a 25%–50% share of the royalties generated by the patent, which is very generous compared to the private sector. The office of technology transfer at the university is a key gateway to commercializing such a patent. However, the office of technology transfer has responsibilities such as protecting the professor's IP, the ability to find a market for the invention and the ability to formulate contracts between professor, university and the private investor. Thus, the success of commercializing the invention depends on the abilities of both the technology transfer office and the professor. There are cultural issues that need to be addressed at universities which are keen on transferring technology to the market. The ability to share the knowledge with the public must be restricted, and this is usually at odds with the 'publish or perish' attitude at most academic institutions. However, the type of business relationship will dictate what can and can't be revealed. In various forms, the relationship can be based on providing licences to commercialize, faculty consultancy, strategic partnerships with university spin-off companies, special funding schemes for faculty research and research partnerships with major corporations.

### 10.6.1 IP: impact and ownership

During the growth of nanotechnology in the 1990s, the number of papers containing the word nano increased fourfold according to the ISI Science Citation Index. By 2004 it had risen to over 20,000 articles. The US Patent Office has issued over 15,000 patents containing the word nano up to the year 2006. Many companies are now placing a greater emphasis on IP. Strong IP portfolios decide whether a nanotechnology company can survive or not.

### 10.6.2 Patents

Utility patents offer protection for inventions that can be classified as a novel process or method, or a piece of apparatus that is useful and non-trivial. The exchange of the idea for protection seems obvious, but may also alert the world of the idea. However, under US law the patent is protected for 20 years and prevents others from making and selling the invention contained within the patent. Once granted, it is essential that the patent is protected so that maximum returns can be made from the patent. A strong patent with a solid portfolio can be the foundation of creating wealth from a nanotechnology patent. Protecting nanotechnology-based patents may be difficult because not all of the knowledge is known to protect it from being exploited by other nanotechnology players. Because nanotechnology is interdisciplinary, it is more difficult to create a novel patent because it may be on a different scale. Therefore, partial protection can only be guaranteed. Therefore, the decision to protect the idea using patents must be considered very carefully.

### 10.6.3 Trade secrets

A nanotechnology company can also use trade secrets to protect their IP through the use of trademarks. As of 2005, approximately 1800 trademarks containing the word 'nano' have been registered and are pending. Trade secrets can be indefinite unless publicly disclosed. Trade secrets can be revealed if the product is reverse engineered. However, because of the scale involved it may be difficult to reverse engineer a nanotechnology product. Hence, trade secrets may work if employees maintain confidentiality even when they leave the employment with a particular company. The employment of non-disclosure agreements may also be useful especially when employees move from their original employment with the company.

### 10.6.4 Copyright

Copyrights protect the idea, which is not the case for patents. Copyright protects the idea for up to 100 years for work that is made for hire. This is

the case for nanotechnology industries. The case for patenting appears to be self-defeating compared to trade secrets and copyright protection. However, filing a 'provisional patent' as opposed to a 'utility patent' does indeed show to potential investors that the patent is pending and also shows whom the inventor is. This last statement is interesting in that in the United States, the patent system is based on a 'first to invent' standard rather than 'first to file' standard. This is unique to the United States and does not exist in other countries. The process of filing a provisional patent is simple, low cost and announces the origin of the invention. A provisional filing also preserves the right to foreign filings.

The restrictions on innovation may stem from patent filings. This may be due to the narrow scope of the inventor's claims in the patent, or may be due to the way that the research was initially funded. If the patent is borne out of Government funding, then the Government can issue a royalty-free licence to the inventor of the patent. This provision was made under the 1980 Bayh–Dole Act and it gives universities and small business entities freedom to commercialize the invention at no cost. However, innovations that stem from the invention are still governed by the original licence, which may cause problems if the business is sold to a third party after the patent and licence have been issued. The issue of developing an IP policy and its impact can take many different forms depending on the short-, medium-, and long-term goals of a nanotechnology business. However, combinations of using patents, trade secrets, copyrights and trademarks can ensure that businesses create revenue streams over differing timescales.

## 10.7 ROLE OF THE ENTREPRENEUR, MAJOR CORPORATIONS AND NATIONAL LABORATORIES IN COMMERCIALIZATION

It should be noted that entrepreneurs are individuals who commercialize products with the aim of making money. This does not appear to match that of the requirements of a professor or research team employed in a university or a national laboratory. The entrepreneurial activity is characterized by the building of a team dedicated to commercialize nanotechnology products and this is discussed elsewhere in this book. The major corporations play a very important role in commercializing nanotechnology. They are particularly interested in using nanotechnology to enhance and functionalize existing products at all length scales. The corporations are heavily involved in developing their own technology, but do maintain an active interest how Government is funding nanotechnology programmes and actively looking

at the spin-offs that emerge from nanotechnology-funded programmes. The national laboratories are not charged with commercializing nanotechnology products, but they do provide access to very expensive equipment that can be used to develop nanotechnology products. This is particularly so with large equipments such as synchrotron radiation sources that are used in LiGA applications.

## 10.8 CONCLUSIONS

The NNI has done much to fund the research and development needed in US universities to commercialize nanotechnology products. However, the commercialization of nanotechnologies for US universities is dependent upon research teams and their relationship with offices of technology transfer at their home institutions. Although funding is well supported by many US Government departments, commercialization is left in the hands of the business relationships made between research group, offices of technology transfer at universities and the private sector. Further strengthening of the commercialization route may be necessary in the future if nanotechnology products are to become more widespread in our society. Governments need to address this problem owing to the amount of resources that need to be provided by them to fund research and developments in nanotechnology.

## WEB SOURCES

[1]  http://www.osha.gov
[2]  http://www.cdc.gov/niosh/
[3]  http://www.epa.gov
[4]  http://www.niehs.nih.gov
[5]  http://www.fda.gov
[6]  http://www.nano.gov/NNI_Strategic_Plan_2004.pdf
[7]  http://www.nnin.org
[8]  http://ncn.purdue.edu/
[9]  http://www.cpsc.gov
[10] http://www.nanomanufacturing.eu
[11] http://www.doleta.gov/wired

# Fabrication of Hydrogel Micropatterns by Soft Photolithography

K. Subramani

*Institute for Nanoscale Science and Technology (INSAT), University of Newcastle upon Tyne, Newcastle upon Tyne, UK*

## CONTENTS

## ABSTRACT

Microfabrication techniques have been employed to fabricate integrated circuits (ICs), semiconductors, microelectromechanical systems (MEMS), nano-electromechanical systems (NEMS), BioMEMS, microfluidic, electromechanical, mechanical, chemical, optical, photonic and multifunctional devices. Nano-technology has borrowed microfabrication techniques for miniaturization science. Some of these techniques have very old origins, not connected to manufacturing, like lithography or etching. Biomedical research, over the past decade, has exploited these microfabrication techniques to fabricate biomaterials in order to study the cell–biomaterial interaction at the micro/nanoscale environment. These approaches can be used to provide model surfaces that would allow scientists to explore the relationship between cells: biomaterial substrate morphology. Biomaterials with controlled morphology can be effectively utilized to induce favourable cell response. In this chapter, a simple, cost-effective technique of 'soft photolithography', a combination of photolithography and soft lithography is described. Such a technique has been used to fabricate hydrogel micropatterns of sub-cellular dimensions as fine as $10\,\mu m$. These sub-cellular biomaterial micropatterns can be effectively employed to study cell–biomaterial interactions and for their applications in tissue engineering.

## 11.1 INTRODUCTION

Nanotechnology is the multidisciplinary science which aims at creation of materials, devices and systems at the nanoscale level (one-billionth of a metre). It refers to the manipulation, precise placement, measurement, modelling or manufacture of sub-100 nm scale matter[1]. In other words, it has been described as the ability to work at atomic, molecular and supra-molecular levels (on a scale of $\sim$1–100 nm) to understand, create and use material structures, devices and systems with fundamentally new properties and functions resulting from their small structure[2]. The technology has been approached in two ways: from 'top–down' and 'bottom–up' approaches. The 'top–down' approach is nothing but the utilization of miniaturization techniques to construct micro/nanoscale structures from a macroscopic material or a group of materials by utilizing machining or etching techniques. The best example of a 'top–down' approach is the photolithography technique used in the semiconductor industry to fabricate components of an integrated circuit (IC) by etching micro/nanoscale patterns on a silicon wafer[3]. The 'bottom–up' approach refers to the construction of macromolecular

structures from atoms or molecules that have the ability to self-organize or self-assemble to form a macroscopic structure[4,5]. In other words, the 'bottom–up' approach has been referred to as 'molecular nanotechnology'[6]. Nanotechnology has much more to offer than just simple miniaturization and building the molecular structures from the atomic scale. By investigating and understanding the functionality of materials at the micro/nanoscale level, the scientific community is working towards finding new techniques to achieve maximum functional output from these materials with minimum energy and resource input. In short, microfabrication techniques along with nanotechnology have offered us the ability to design materials with totally new desirable characteristics. These micro/nanomaterials fabricated by 'top–down' or 'bottom–up' approach have been effectively applied in many areas of science and engineering: physics, chemistry, material science, computer science, ultra-precision engineering, fabrication processes and equipment designing[7]. Microfabrication techniques are also utilized in inter-disciplinary research bridging physics–chemistry–material science with bio-medical science, for example, in the fabrication of microelectromechanical systems (MEMS) for biosensor applications (diagnostics, sensing and detec-tion) and in the field of pharmacotherapeutics and medical health care towards novel drug delivery techniques, gene therapy, hybrid devices and 3-D artificial organs, to mention a few[8].

## 11.2 MICROFABRICATION

'Microfabrication' or 'micro manufacturing' are the terms used to describe techniques to fabricate miniature structures of microscale level and smaller. In other words, it is the 'top–down' approach. Historically, the earliest microfabrication was used in IC fabrication for semiconductor devices. Microfabrication technologies originate from the microelectronics indus-try and the devices were usually made on silicon wafers, even though glass, plastics and many other substrates are currently in use [7, 8]. Micromachining, semiconductor processing, microelectronic fabrication, semiconductor fab-rication, MEMS fabrication and IC technology are the terms used instead of microfabrication, but microfabrication is the broad general term. Some of them have very old origins, not connected to manufacturing, like lithog-raphy or etching. Polishing was borrowed from optics manufacturing, and many of the vacuum techniques come from nineteenth-century physics research. Electroplating is also a nineteenth-century technique adapted to produce micrometre scale structures, as are various stamping and embossing techniques[9].

### 11.2.1 Microfabrication techniques

Microfabrication techniques can be classified as follows: (1) property modification, (2) patterning, (3) subtractive processes, (4) additive processes and packaging[10].

#### 11.2.1.1 Property modification

Property modification techniques include alteration of the substrate by (i) *doping* (the process of intentionally introducing impurities into an extremely pure semiconductor substrate like silicon in order to change its electrical properties), (ii) *ion implantation* (a technique by which ions of a material are implanted into another solid substrate, thereby changing the physical properties of the solid)[10].

#### 11.2.1.2 Microfabrication by patterning

Microfabrication by patterning is based on lithography techniques (or micro printing). It involves (i) photolithography and (ii) soft lithography. (i) *Photolithography* (also known as optical lithography) is a process used to selectively remove parts of a thin film (or bulk of a substrate). It uses light to transfer a geometric pattern from a photomask to a light-sensitive chemical (photoresist) on the substrate. A series of chemical treatments then engraves the exposure pattern into the material underneath the photoresist. (ii) *Soft lithography* refers to a group of techniques for fabricating or replicating structures using elastomeric stamps, moulds and photo masks[11].

#### 11.2.1.3 Additive microfabrication

Additive microfabrication techniques involve microfabrication by deposition or growth of specific layers on a substrate[10]. A few examples of this technique are (i) *Thermal oxidation*, to produce a thin layer of oxide (usually silicon dioxide) on the surface of a wafer (for semiconductor applications), (ii) *chemical vapour deposition* (*CVD*), a chemical process employed to produce high-purity, high-performance solid materials. The process is often used in semiconductor industry to produce thin films. In a typical CVD process, the wafer (substrate) is exposed to one or more volatile precursors, which react and/or decompose on the substrate surface to produce the desired deposit. Frequently, volatile by-products are also produced which are removed by gas flow through the reaction chamber. (iii) *Physical vapour deposition* (*PVD*) is an additive microfabrication technique used to describe any of a variety of methods to deposit thin films by condensation of vaporized form of the materials onto various surfaces (e.g., onto semiconductor wafers). The coating method involves purely physical processes

such as high-temperature vacuum evaporation or plasma sputter bombardment rather than involving a chemical reaction at the surface to be coated as in CVD. (iv) *Epitaxy*, an additive microfabrication method of depositing a monocrystalline film on a monocrystalline substrate. Epitaxial films may be grown from gaseous or liquid precursors[10].

### 11.2.1.4 Subtractive microfabrication

Subtractive microfabrication techniques employ removal or etching of a portion of substrate to fabricate microstructures/patterns. Dry etching and wet etching are two types of subtractive microfabrication techniques. (i) *Dry etching* refers to the removal of material, typically a masked pattern of semiconductor material by exposing the material to a bombardment of ions (usually plasma of reactive gases such as fluorocarbons, oxygen, chlorine, boron trichloride; sometimes with addition of nitrogen, argon, helium and other gases) that dislodge portions of the material from the exposed surface. (ii) *Wet etching* is chemical etching performed with a liquid chemical (etchant) instead of plasma[10].

## 11.3 LITHOGRAPHY

Lithography (in Greek: 'líthos' means stone; 'graphein' means to write) is a planographic printing technique using a plate or stone with a smooth surface. This technique was invented by Bavarian author Alois Senefelder in 1976[12]. Lithography uses oil or fat and gum arabic to divide the smooth surface into hydrophobic regions that take up the ink, and hydrophilic regions that do not and thus become the background. Most books, indeed all types of high-volume text, are now printed using offset lithography, the most common form of printing production. Semiconductor industry has borrowed this principle to fabricate ICs and MEMS by photolithography. Biomedical researchers employ soft lithography, a technique using elastomeric stamps to fabricate biomaterial micropatterns to study cell–biomaterial interaction. The following sections will discuss in detail about 'soft photolithography', a combination of photolithography and soft lithography techniques to fabricate hydrogel micropatterns on a silicon substrate.

## 11.4 HYDROGEL AS A BIOMATERIAL

Hydrogel is a network of polymer chains that swell in aqueous solution. Hydrogel is composed of long polymer chains connected by cross links. The cross links may be degradable or non-degradable and are ionic interactions

between polyelectrolyte chains. Cross linking of polymer molecules or polymerization can be achieved by photopolymerization, changes in temperature, radiation, self-assembly or by cross linking enzymes. Hydrogels undergo responsive swelling by absorbing solvent when placed in an aqueous solution (solvation). Swollen hydrogels can absorb many times their own weight in water and can switch between swollen and collapsed forms. The key properties of hydrogels for biomedical applications are better biocompatibility, biodegradability, ability to incorporate biomolecular cues (due to high-permeability for oxygen, nutrients and water-soluble metabolites). These key characteristics along with the ease of in-situ fabrication have made hydrogels as a biomaterial of choice in in-vitro studies for analysing cell–biomaterial interactions and in biomedical applications[13]. Hydrogels are extensively used in cosmetic and reconstructive surgery[14], as a matrix for the fabrication of artificial organs in tissue engineering[15] and as 'intelligent' stimuli-sensitive drug delivery systems[16]. Hydrogels have also been extensively used to fabricate contact lenses[17], breast implants[18], tissue engineering scaffolds[19], delivery vehicles for bioactive drug molecules[20], coatings for biosensors[21], dressings for wound healing and burn injuries[22] and as carrier scaffolds for guided bone regeneration (GBR) using osteogenic growth factors[23]. Although many polymer hydrogels have been studied, poly (ethylene glycol) hydrogel (PEG) is one of the most widely investigated systems. PEG hydrogel can be fabricated into 3-D microstructures to study the response of cells for their applications in tissue engineering. PEG hydrogel offers the simplicity and advantage of incorporating bioactive molecules into the hydrogel matrix passively or by covalent linking with the PEG monomer. Time-dependent release of these biomolecular cues from the PEG hydrogel micropatterns serves as an excellent platform for studying cell response in tissue culture. PEG hydrogel micropatterns have been fabricated by photopolymerization through a micro-patterned photomask (photolithography)[24]. Soft lithography, as mentioned earlier, is a technique by which micropatterns can be fabricated on a substrate using a poly (dimethyl siloxane) (PDMS) stamp[11].

## 11.5 SOFT PHOTOLITHOGRAPHY OF HYDROGEL MICROPATTERNS

Soft-photolithography, a combination of photolithography and soft lithography using a PDMS stamp is described in the following sections. Ultraviolet (UV) embossing has been used to fabricate poly (ethylene glycol) hydrogel–diacrylate (PEG–DA) micropatterns varying from 50 to 500 μm[25]. The spatial organization of cells and their response to minute hydrogel patterns of

sub-cellular dimensions less than 40μm could serve as a crucial element in understanding cell behaviour in tissue culture experiments and in their biomedical applications ranging from tissue engineering, BioMEMS and biosensors. Using the soft photolithography technique, PEG hydrogel micropatterns were fabricated on a silicon substrate of varying dimensions from 40μm to as fine as 10μm within the same substrate. The microfabrication steps employed for the fabrication of the PEG micropatterns using soft photolithography are described in the following sections.

## 11.5.1 Fabrication of PDMS stamp

### 11.5.1.1 Design of the photomask

The design for the photomask to be used for the PDMS stamp fabrication was designed using the 'Clewin' software (PhoeniX Technologies, Netherlands). Different patterns including squares, circles, lines and diamonds were designed of varying dimensions from 10 to 40μm. These patterns were repeated in quartets throughout the mask design. From this mask design, a $5 \times 5$ in. chrome/sodalime photomask was manufactured by Deltamask Co (Netherlands). The micropatterns on the fabricated photomask as visualized under a light microscope (Olympus BX37, London, UK) is represented in Figure 11.1.

### 11.5.1.2 Fabrication of 'master' or negative mould

The 'master' or negative mould was produced on a silicon wafer using the conventional photolithography technique (Figure 11.2). The silicon wafer was silanized with hexamethyldisilazane (HMDS) in YES oven (Sanjose, CA, USA) at 150°C and the photoresist was spin coated at 3500 rpm for 60 s in an EVG101 resist spincoater (Schaerding, Germany). The photoresist was soft baked for 5 min at 95°C in a precision hotplate (Electronic Microsystems, Boerne, TX, USA) and was exposed to UV light at 365 nm, $10 \, mW/cm^2$ for 15 s through a chrome/sodalime photomask in an EVG620 mask aligner (Schaerding, Germany). The exposed photoresist was developed in an EVG103 developer with Shipley MF–26A (Marlborough, MA, USA) developer solution for 2 min. The pattern of the photoresist on the negative mould was visualized under a light microscope (Figure 11.3).

### 11.5.1.3 Fabrication of PDMS

The Sylgard 184 base silicone elastomer and Sylgard 184 curing agent for the fabrication of the PDMS stamp was purchased from Dow Corning GmbH (Wiesbaden, Germany). Ten percent of Sylgard 184 curing agent
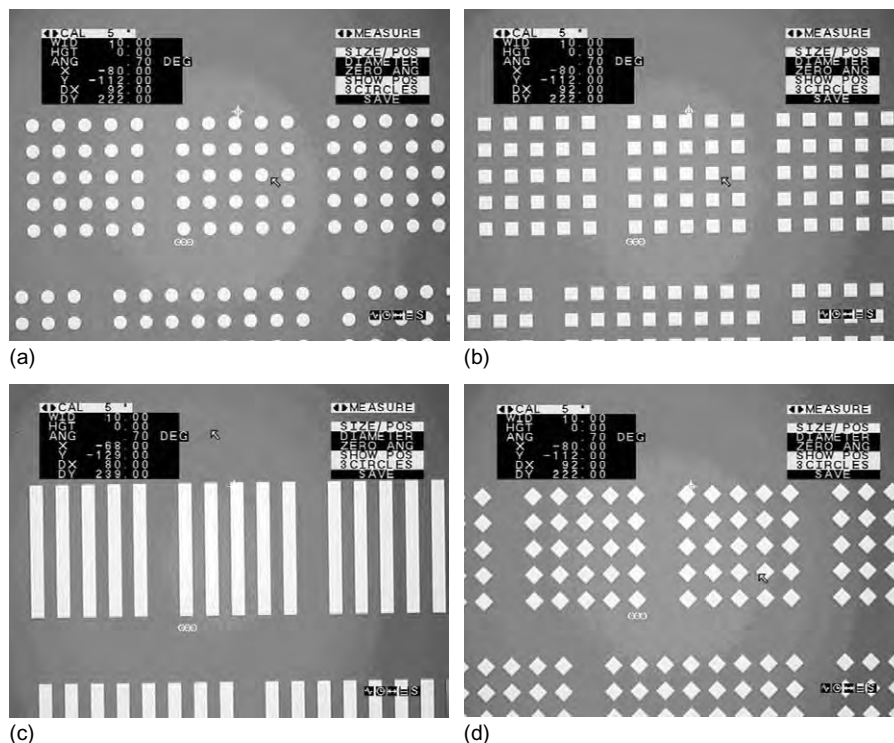
**FIGURE 11.1**  *Reflected light microscopy images of micropatterns on the photomask. All the micropatterns are 10 μm in width. The lighter areas are chrome coated and opaque and do not transmit light. The darker areas are transparent and allows light to pass through. (a) circles, (b) squares, (c) lines and (d) diamonds.*

was mixed with 90% of Sylgard 184 base silicone elastomer and was mixed thoroughly. The air bubbles entrapped in the mixture were removed under vacuum. The PDMS solution was poured over the 'master' and left to cure overnight (Figure 11.2). The cured PDMS stamp was removed from the 'master' and used in the subsequent steps.

## 11.5.2  Surface functionalization of silicon substrates by silanization

Silanization is the process of functionalizing the silicon or borosilicate substrates with a silane solution resulting in the formation of a silane monolayer which acts as a coupling agent between the PEG hydrogel and silicon substrate thereby improving the adherence of PEG hydrogel to the silicon substrate[26]. The silane solution used was 3-(trichlorosilyl) propyl
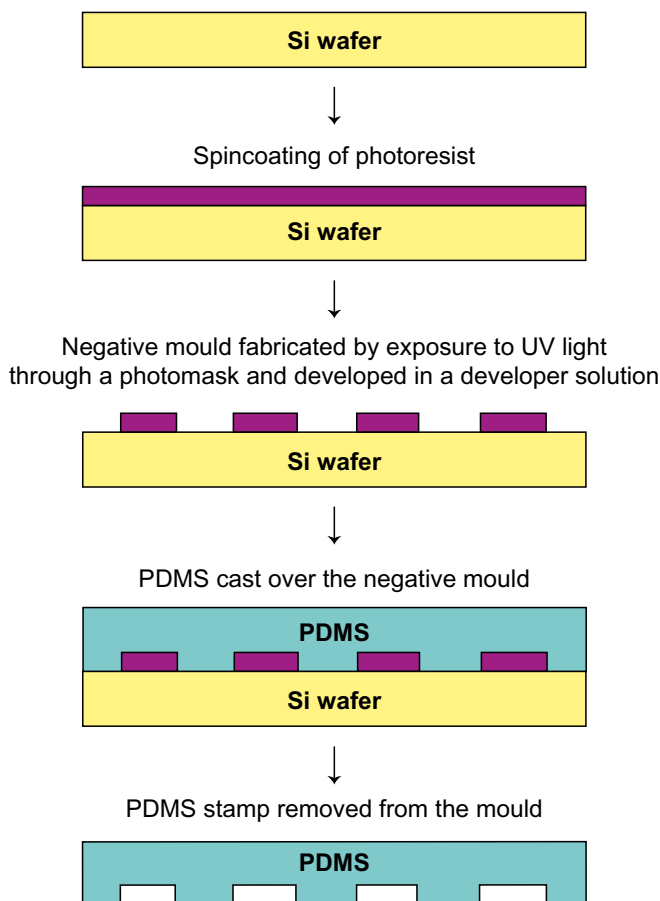
**FIGURE 11.2**   *Schematic illustration of PDMS stamp* ***fabrication.***

methacrylate (TPM). It was purchased from Sigma-Aldrich Chemical Co (Germany). 1,1,1-Trichloroethane was purchased from BDH Chemical Ltd (Poole, UK). Sulphuric acid and hydrogen peroxide were purchased from Rockwood Electronic Materials (Derbyshire, UK). The silanization procedure was performed according to the protocol described in published literatures[26, 27]. The glass coverslips were heated in 'piranha' solution which is a mixture of aqueous solutions of 50% (v/v) sulphuric acid (3 parts) and 30% (w/v) hydrogen peroxide (1 part) for 10 min in a ventilated acid hood. The piranha solution was handled with extreme care as it reacts violently with organic materials. Rubber gloves and personal protective safety clothing were used while handling the piranha solution. After 10 min, the silicon
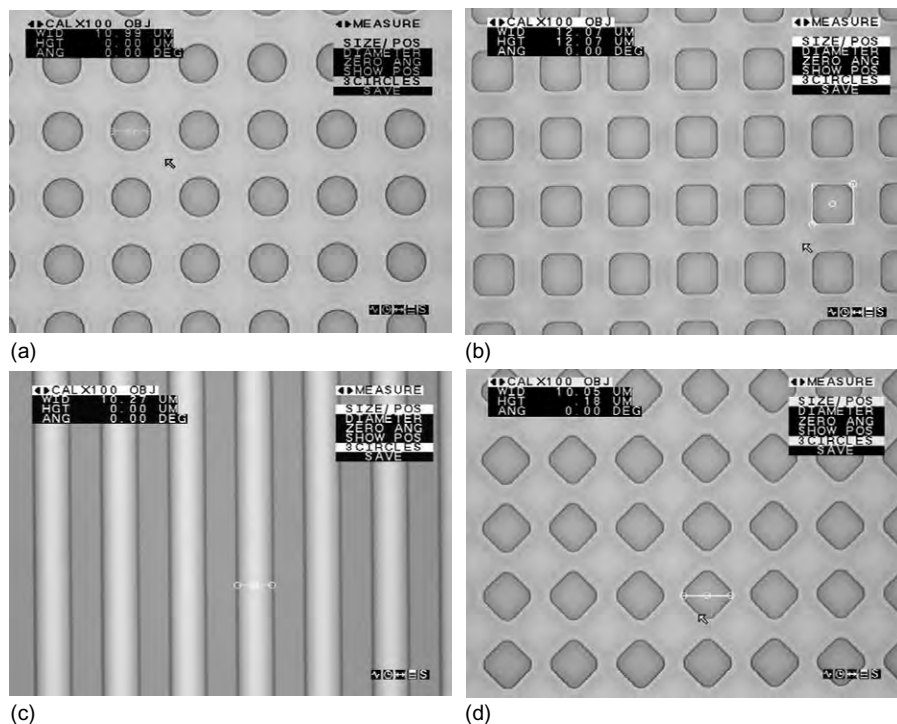
**FIGURE 11.3** *Reflected light microscopy images of micropatterns of photoresist on silicon wafer ('Master' or negative mould). All the micropatterns are 10 μm in width. The lighter areas are the silicon surfaces and the darker areas are the photoresist micropatterns. (a) circles, (b) squares, (c) lines and (d) diamonds.*

substrates were removed from the piranha solution and thoroughly rinsed with deionized (DI) water and dried under nitrogen. Surface functionalization of the borosilicate glass and silicon substrates with the silane solution was done by immersing them overnight in 20% (v/v) of TPM and 80% (v/v) of 1,1,1-trichloroethane solution (Figure 11.4). The silanized silicon substrates were removed from the silane solution and rinsed thoroughly with 1,1,1-trichloroethane solution to remove the excess silane molecules from the silicon substrates and thus ensuring the presence of a silane monolayer. The silicon substrates were then dried under nitrogen.

## 11.5.3 Soft photolithography

PEG–DA precursor solution (MW 575) was prepared by adding 10 mg of 2,2′-dimethoxy-2-phenylacetophenone (DMPA) (photoinitiator) to 10 mL of each PEG monomers (1% w/v). DMPA serves as the photoinitiator which
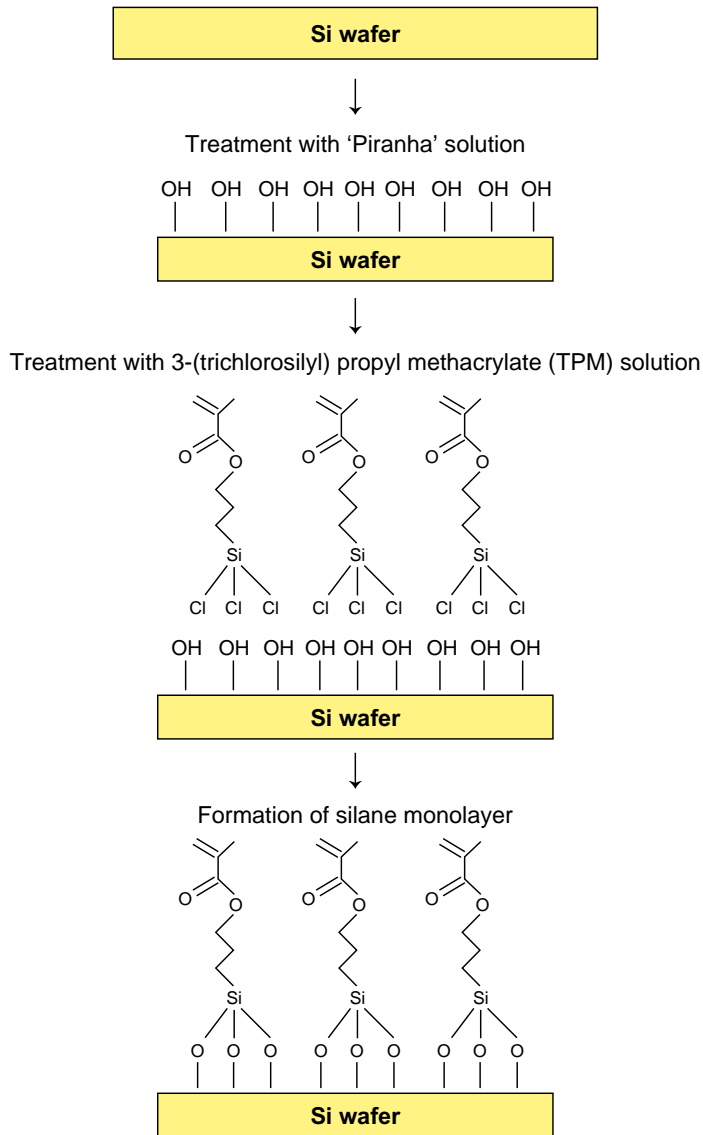
**FIGURE 11.4** *Silanization of silicon substrate.*

initiates photopolymerization of the PEG–DA molecules on exposure to UV light. This solution was spin coated onto the silanized silicon substrate at 1000 rpm for 6 s using an EVG101 resist spin coater (Schaerding, Germany). The spin-coated uniform layer of the PEG–DA solution was exposed through the PDMS stamp to UV light (365 nm, 10 mW/cm$^2$) for
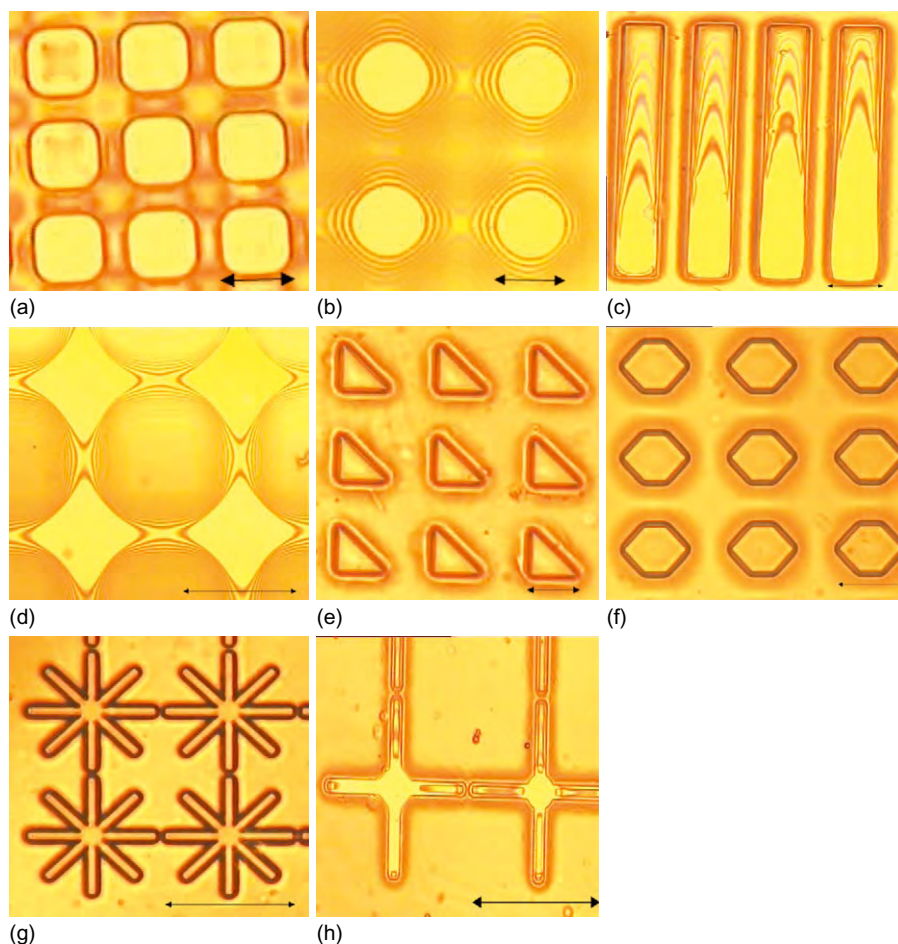
**FIGURE 11.5** *Reflected light microscopy images of PEG micropatterns fabricated by soft photolithography technique. (a) microsquares, (b) microcircles, (c) microgrooves and (d) diamond-like micropatterns. In addition, (e) triangle, (f) hexagon, (g) star and (h) cross-shaped micropatterns were also fabricated. Scale bars in Figures (a)–(f): 10μm and Figures (g) and (h): 40μm.*

10 s. After exposure to UV light, the PDMS stamp was removed. PEG–DA hydrogel micropatterns on the silicon substrate were developed by immersing the silicon substrates in DI water after 5 min. The micropatterns were visualized under a light microscope and the dimensions of the fabricated hydrogel micropatterns varied from 10 to 40μm (Figure 11.5). Surface profilometry measurements showed that the depth of the micropatterns ranged between 4 and 10μm (~7μm) as shown in Figure 11.6. The cross linking and photopolymerization of PEG–DA molecules (Figure 11.7) is
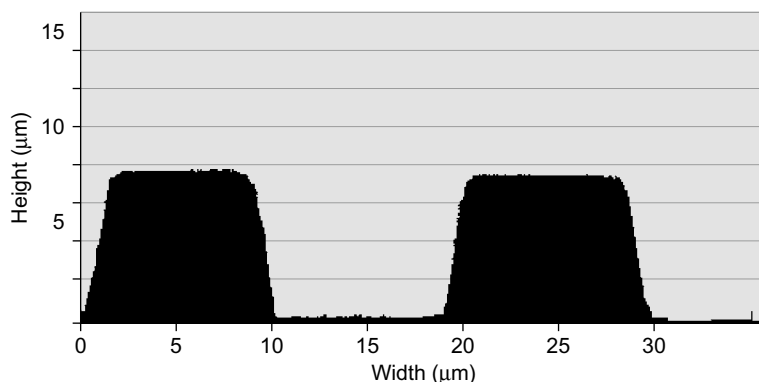
**FIGURE 11.6** *Surface profilometry showing the height of the PEG hydrogel micropatterns. Surface profilometry across two walls of the PEG patterns showing height of ~ 7μm and width of 10μm.*

initiated by the reactive methyl radical from DMPA, the photoinitiator. This methyl radical attacks the double bond of PEG–DA molecules and initiates the cross linking resulting in the formation of PEG hydrogel as depicted in Figure 11.8[28]. Silanization was performed to functionalize the surface of silicon substrates with a chemical substance that can function as a coupling agent between the PEG hydrogel and the silicon substrate. The treatment with 'piranha' solution resulted in a hydrophilic surface due to increase in hydroxyl groups over the silicon substrate. Further treatment with TPM resulted in silanization of the silicon substrate. As described in Figure 11.4, silanization of the silicon substrates resulted in the formation of a silane monolayer which acted as a coupling agent of PEG hydrogel with the substrate. The height of the PEG hydrogel micropatterns was measured with a Dektak surface profiler (Veeco instruments). The height of these hydrogel patterns varied from 5 to 10μm (Figure 11.6). The width of these micropatterns was 10μm in the microsquares, microcircles, microgrooves and diamond-like patterns. A variety of other shapes like microtriangles and microhexagons of 10μm in width and microstars and cross-shaped micropatterns of 40μm in width were fabricated as depicted in Figure 11.5.



**FIGURE 11.7** *Chemical structure of poly (ethylene glycol) diacrylate (PEG–DA).*

The use of PDMS was based on pressure-moulding technique of the spin-coated PEG hydrogel on a silicon substrate. The use of PDMS stamp was effective in producing PEG hydrogel micropatterns of features lesser than 50–10μm. Photopolymerization through the PDMS stamp resulted in the fabrication of PEG hydrogel micropatterns of sub-cellular dimensions
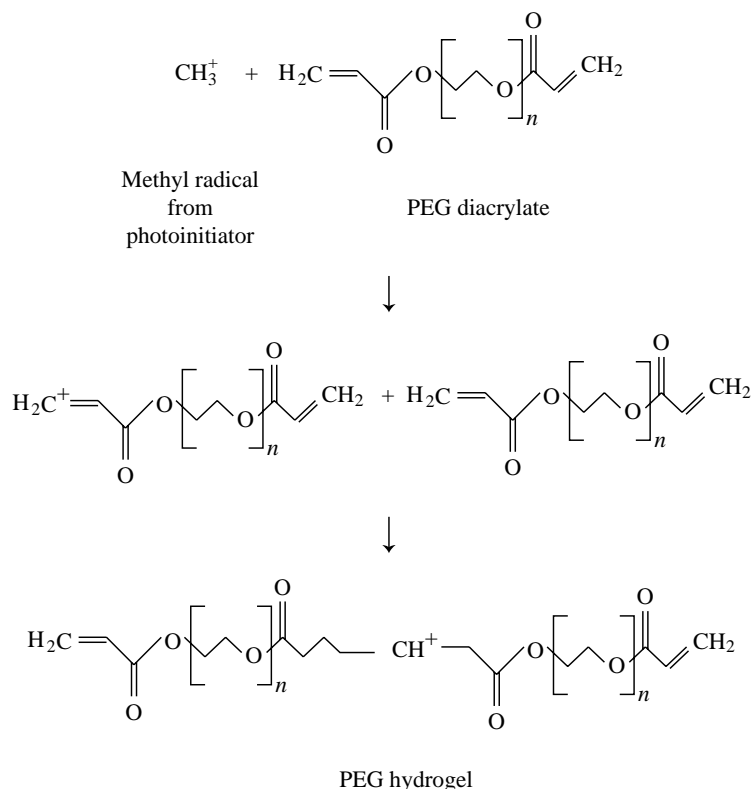
**FIGURE 11.8**  *Photopolymerization reaction of PEG–DA molecules initiated by the methyl radical from photoinitiator (DMPA) resulting in the formation of the PEG hydrogel.*

(10–40 μm) and sharper resolutions. In addition, (e) triangle, (f) hexagon, (g) star and (h) cross-shaped micropatterns were also fabricated (Figure 11.5).

## 11.6 CONCLUSION

Soft-photolithography technique has several advantages over photolithography technique as it is relatively inexpensive, simple and PEG micropatterns of sub-cellular dimensions with better resolution were fabricated. The use of PDMS-based elastomeric stamp to produce microstructures of sub-cellular dimensions (10–40 μm) can be modified by the use of lower molecular weight PEG monomer and alternative techniques like capillary force lithography[29] where a moulding process by capillary force has been utilized for fabrication of PEG hydrogel microstructures. Along with

the use of PDMS for the fabrication of the PEG hydrogel micropatterns, it can also be used as a stamp for patterning extracellular matrix proteins like fibronectin or collagen onto the silicon substrate during capillary force lithography technique resulting in PEG hydrogel microstructures imprinted with extracellular protein patterns. This will provide a unique environment for the cells to migrate and proliferate under the influence of the hydrogel microstructures with the protein patterns. Such sub-cellular micropatterns can be effectively utilized to study cell–biomaterial interactions and for their applications in tissue engineering.

## REFERENCES

[1] N. Taniguchi, On the basic concept of nano-technology, in: Proceedings of International Conference of Production Engineering London: Part II, British Society of Precision Engineering, 1974.

[2] M.C. Roco, R.S. Williams, P. Alivisatos, Nanotechnology Research Directions, Kluwer Academic Publications, Boston, 2000 (Chapter 8).

[3] R.W. Siegel, E. Hu, M.C. Roco, Nanostructure Science and Technology, Kluwer Academic Publications, Boston, 2000.

[4] M.D. McGehee, S.M. Gruner, N. Yao, C.M. Chun, A. Navrotsky, I.A. Aksay, Synthesis of mesoscopic structure by co-assembly, in: Proceedings of 52nd Microscopy Society of America Conference, San Francisco, San Francisco Press, 1994, pp. 448–449.

[5] S.I. Stupp, B.V. Lebonheur, K. Walker, Supramolecular materials: Self-organized nanostructures, Science 276 (1997) 384.

[6] K. Subramani, A. Khraisat, A. George, Self-assembly of proteins and peptides and their applications in bionanotechnology, Curr. Nanosci. 4 (2008) 201.

[7] N.P. Mahalik, Micromanufacturing and Nanotechnology, Springer, New York, 2006.

[8] R. Bashir, BioMEMS: State-of-the-art in detection, opportunities and prospects, Adv. Drug Delivery Rev. 56 (11) (2004) 1565.

[9] A. Hierlemann, O. Brand, C. Hagleitner, H. Baltes, Microfabrication techniques for chemical/biosensors, in: Proceedings of the IEEE 91 (6) (2003) 839.

[10] M. Madou, Fundamentals of Microfabrication: The Science of Miniaturization, second ed., CRC Press, Boca Raton, FL, 2002.

[11] Y. Xia, G.M. Whitesides, Soft Lithography, Annu. Rev. Mater. Sci. 28 (1998) 153.

[12] P.B. Meggs, A History of Graphic Design, John Wiley and Sons, New York (1998) 146–148.

[13] A.S. Hoffman, Hydrogels for biomedical applications, Ann. N.Y. Acad. Sci. 944 (2001) 62.

[14] S. Srouji, A. Rachmiel, I. Blumenfeld, E. Livne, A simple soft lithographic route to fabrication of poly (ethylene glycol) microstructures for protein and cell patterning, J. Craniomaxillofac. Surg. 33 (2) (2005) 79.

[15] R. Landers, U. Hübner, R. Schmelzeisen, R. Mülhaupt, Rapid prototyping of scaffolds derived from thermoreversible hydrogels and tailored for applications in tissue engineering, Biomaterials 23 (23) (2002) 4437.

[16] K.S. Anseth, A.T. Metters, S.J. Bryant, P.J. Martens, J.H. Elisseeff, C.N. Bowman, In situ forming degradable networks and their application in tissue engineering and drug delivery, J. Controlled Release 78 (1–3) (2002) 199.

[17] M.G. Harris, M.D. Sarver, K.A. Polse, Patient response to thin hydrogel contact lenses: A comparative study, J. Am. Optom. Assoc. 48 (3) (1977) 295.

[18] G.F. Maillard, Carboxy-methyl cellulose hydrogels used to fill breast implants: A 15-year experience, Eur. J. Plast. Surg. 24 (4) (2001) 177.

[19] J.L. Drury, D.J. Mooney, Hydrogels for tissue engineering: Scaffold design variables and applications, Biomaterials 24 (24) (2003) 4337.

[20] Y. An, J.A. Hubbell, Intraarterial protein delivery via intimally-adherent bilayer hydrogels, J. Control Release 64 (1–3) (2000) 205.

[21] C.P. Quinn, C.P. Pathak, A. Heller, J.A. Hubbell, Photo-crosslinked copolymers of 2-hydroxyethyl methacrylate, poly(ethylene glycol) tetra-acrylate and ethylene dimethacrylate for improving biocompatibility of biosensors, Biomaterials 16 (5) (1995) 389.

[22] D. Eisenbud, H. Hunter, L. Kessler, K. Zulkowski, Hydrogel wound dressings: Where do we stand in 2003?, Ostomy Wound Manage. 49 (10) (2003) 52.

[23] L. Hong, Y. Tabata, M. Yamamoto, S. Miyamoto, K. Yamada, N. Hashimoto, Y. Ikada, Comparison of bone regeneration in a rabbit skull defect by recombinant human BMP-2 incorporated in biodegradable hydrogel and in solution, J. Biomater. Sci. Polym. Ed. 9 (9) (1998) 1001.

[24] V.A. Liu, S.N. Bhatia, Three-dimensional photopatterning of hydrogels containing living cells, Biomed. Microdevices 4 (2002) 257.

[25] A.P. Zhu, M.B. Chan-Park, J.Z. Gao, Foldable micropatterned hydrogel film made from biocompatible PCL-b-PEG-b-PCL diacrylate by UV embossing, J. Biomed. Mater. Res. B Appl. Biomater. 76 (1) (2006) 76.

[26] A. Revzin, R.J. Russell, V.K. Yadavalli, W.G. Koh, C. Deister, D. Hile, M.B. Mellott, M.V. Pishko, Fabrication of poly(ethylene glycol) hydrogel microstructures using photolithography, Langmuir 17 (2001) 5440.

[27] A. Revzin, R.G. Tompkins, M. Toner, Surface engineering with poly(ethylene glycol) photolithography to create high-density cell arrays on glass, Langmuir 19 (2003) 9855.

[28] M.B. Mellott, K. Searcy, M.V. Pishko, Release of protein from highly cross-linked hydrogels of poly(ethylene glycol) diacrylate fabricated by UV polymerization, Biomaterials 22 (9) (2001) 929.

[29] K.Y. Suh, J. Seong, A. Khademhosseini, P.E. Laibinis, R. Langer, A simple soft lithographic route to fabrication of poly (ethylene glycol) microstructures for protein and cell patterning, Biomaterials 25 (2004) 557.

# Nanocrystalline Diamond for RF-MEMS Applications

S. Balachandran[1], T. Weller[1], A. Kumar[2], S. Jeedigunta[1], H. Gomez[2], J. Kusterer[3] and E. Kohn[3]

[1]*Department of Electrical Engineering, University of South Florida, Tampa, FL, USA*
[2]*Department of Mechanical Engineering, University of South Florida, Tampa, FL, USA*
[3]*Institute of Electron Devices and Circuits, University of Ulm, Ulm, Germany*

## CONTENTS

## ABSTRACT

This article presents thermally actuated nanocrystalline diamond bridges for microwave and high power RF applications. The growth process along with the seeding technique for generating the diamond films has been discussed. RF applications which include mechanical resonators and

electrostatically actuated switches demonstrated by other researchers is presented. The diamond bridges are integrated in CPW and microstrip topologies to operate as a switch and tunable inductor. In addition to small signal measurements, high power measurements in the range of 24-47 dBm are performed for the switches integrated in the microstrip topology.

## 12.1 INTRODUCTION

Micro-electro–mechanical system (MEMS) attract large attention in many fields of application that include the wireless[1], automotive[2] and biomedical industries[3]. Reliable radio frequency microelectromechanical system (RF-MEMS) devices have been fabricated utilizing electrostatic[4], thermal[5] and piezoelectric[6] actuation schemes. Most of the RF-MEMS devices designed and fabricated till date are fabricated on silicon, glass, quartz substrates[4–6] and are monolithically integrated. RF switches are one of the most researched and fabricated devices in the MEMS technology. These devices outscore their counterparts in terms of loss at high frequencies, linearity and power consumption. Although very popular, RF-MEMS switches lose to the active devices on the basis of reliability, switching speed, packaging and power handling capabilities. Table 12.1[7] presents a comparison of MEMS switches with PIN diodes and field-effect transistors (FETs).

Although they are small in size and exhibit low parasitic losses, the monolithic configuration confines the device to a substrate common to the entire system. Furthermore, the power handling[8] capabilities of RF-MEMS devices have been limited due to the use of all metal structures in the devices. Diamond has long been used in active devices such as FETs for high power electronics[9]. Also its stability under high temperature (1000°C) makes it a

| **Table 12.1** | Performance Comparison Between FETs, PIN Diodes and RF-MEMS Switches | | |
|---|---|---|---|
| **Parameters** | **RF-MEMS** | **PIN** | **FET** |
| Actuation voltage (V) | 20−80 | +/−3−5 | 3−5 |
| Power consumption (mW) | 0.05−0.1 | 5−100 | 0.05−0.1 |
| Switching time | 1−300μs | 5−100ns | 1−100ns |
| Isolation (1−10 GHz) | Very high | High | Medium |
| Isolation (10−40 GHz) | Very high | Medium | Low |
| Loss (1−40 GHz) (dB) | 0.05−0.2 | 0.3−1.2 | 0.4−2.5 |
| Power handling (W) | <1 | <10 | <10 |

very good candidate for realizing reliable, high power and temperature stable RF-MEMS and microwave devices.

## 12.2  DIAMOND CRYSTAL STRUCTURE AND PROPERTIES

The crystal structure of a material plays a key role in determining the properties of a material. A face centred cubic (FCC) crystal lattice of diamond consists of a unique arrangement of carbon atoms with eight corner atoms, six face centred atoms and four other atoms from adjacent interpenetrating lattices offset by one-quarter of the body diagonal as shown in the ball and stick model of Figure 12.1[10]. Each of the carbon atoms is covalently bonded to four nearest neighbouring atoms by $\sigma$ bonds resulting in a strong sp$^3$ character. The (111) planes of the diamond are along the bond direction with a lattice constant ($a_0$) of 3.567Å and a bond length of 1.54Å. Due to this unique chemical bonding, and atomic density of $1.76 \times 10^{23}$/cm$^3$, diamonds possess several extraordinary material properties.



**FIGURE 12.1**   *Crystal structure of diamond lattice.*

Diamond has several outstanding material properties making it a unique candidate for multifunctional applications. Diamond-coated tools are used in grinding, polishing, cutting and dicing. It has the highest Young's modulus, hardness and thermal conductivity and it is transparent from the UV to far IR region. Furthermore, it has superlative electronic properties and hence can be useful in high power electronics, heat sinks and radiation detectors[11]. Diamond is chemically inert and is suitable for operation in harsh environments (except oxygen ambience)[12]. Many of the above-mentioned properties have attracted diamond as an ideal material for microelectronic and microelectromechanical systems and devices. As silicon microfabrication technology is well matured, most of the current day electronic devices are fabricated using silicon. Unlike integrated circuits (ICs), MEMS devices involve moving components and therefore limit the wide range application of silicon due to its poor mechanical and tribological properties[13]. Some of these limitations have put forth other materials such as SiC, GaN and diamond under investigation. Table 12.2 compares the mechanical properties of nanocrystalline diamond (NCD) films over other materials used in microsystems technology. These properties of NCD films can be used for high temperature and high power RF-MEMS devices. Furthermore, NCD films also possess low loss when used as a thin film at microwave frequencies.

| Table 12.2 | Mechanical Properties of NCD Thin Films in Comparison to Materials Used in Microsystems Technology | | | | |
|---|---|---|---|---|---|
| | **Si** | **(3c)SiC** | **(6c)SiC** | **(h)GaN** | **Diamond** |
| Bandgap (eV) | 1.12 | 2.2 | 2.9 | 3.45 | 5.45 |
| Break down field ($10^6$ V/cm) | 0.5 | 4–6 | 3 | 3–6 | 10 |
| Young's modulus (Gpa) | 170 | 450 | – | 390 | 1050 |
| Fracture strength (Gpa) | 1.37 | – | – | ~2.5 | 10.3 |
| Thermal conductivity (W/cm K) | 1.47 | 4.9 | 4.9 | 1.3 | 22 |
| Thermal stability (°C) | 500 | 900 | 1300 | 650 | 1500 |

## 12.3 CHEMICAL VAPOUR DEPOSITION OF DIAMOND FILMS

Chemical vapour deposition (CVD) involves the dissociation of chemical species in a vapour phase to form a coating or a thin film. CVD was widely investigated for growing synthetic diamonds. As diamond consists of purely carbon, the growth could be initiated by adding one carbon atom at a time to an initial template, so that a tetrahedral bonded carbon network is formed. Typically, CVD diamond consists of the following process steps[14]:

- A gas phase must be activated either by high temperature (e.g. hot-filament CVD) or by plasma excitation (e.g. microwave CVD).

- The gas phase must contain carbon-containing species such as hydrocarbon, carbon dioxide or carbon monoxide.

- A sufficiently high concentration of atomic hydrogen to etch graphite and suppress gaseous graphite precursors must be provided.

- The substrate must be seeded to initiate the nucleation and growth of diamond from the vapour phase.

- A driving force must exist to transport the carbon-containing species from the gas phase to the surface of the substrate. In most CVD methods, the temperature gradient acts as a driving force for the motion of diamond-producing species via diffusion.

Microwave plasma enhanced CVD (MPECVD), hot-filament CVD (HFCVD), radio frequency plasma assisted CVD (RFPACVD) are the most widely used CVD methods. Based on the grain size, CVD diamond films are classified into different types – microcrystalline diamond (MCD), nanocrystalline diamond (NCD) and ultra-nanocrystalline diamond

(UNCD). Typically, MCD films are deposited in $CH_4$ (1%)/$H_2$ (99%), NCD films are deposited in $CH_4$ (1%)/Ar (98%)/$H_2$ (1%) and UNCD films in $CH_4$ (1%)/Ar (99%) gas chemistry respectively. MCD films consist of large grains (grain size: $\sim$ 5–10 $\mu$m) and rough surfaces (mean surface roughness: $\sim$ 300–700 nm) and thereby limit its application to cutting tools, abrasive coatings and heat sinks[15–17]. The limited applications of MCD films have been surpassed by synthesizing a new class of material known as 'nano-crystalline diamond' films. The NCD films can be grown by altering the CVD process[18]. Unlike MCD, NCD films consist of small grains on the order of 20–50 nm and a low surface roughness of $\sim$20 nm. Recently, 'ultra-nanocrystalline diamond' (UNCD) films having smaller grain size (3–5 nm) than NCD have been developed[19]. The growth of NCD/UNCD films opened wide a window of applications ranging from tribology, MEMS, optics, RF applications and field emission devices[20–22]. The intrinsic diamond films are electrically insulating with resistivity on the order of $10^{13}$–$10^{16} \Omega$ cm. Electrical conductivity can be achieved by doping the films during the deposition. The diffusion of dopants into the diamond films is not a practical method of doping as the surface is not diffusive to most of the impurities. Though there are few reports on the ion-implantation of diamond films[23], it is an expensive technique and can damage the surface. Therefore, dopants such as boron (*p*-type), nitrogen, phosphorous and sulphur (*n*-type) are incorporated in the gas chemistry during the growth[24]. The most widely used dopants are boron (*p*-type) and nitrogen (*n*-type), as these are readily soluble with diamond. It was observed that the quality of the films improve with the incorporation of trace amounts of boron by reducing the point defects. On the other hand, excess concentration of boron promotes graphitization due to the incorporation of boron interstitial sites. In case of single crystal or microcrystalline diamond, *p*-type conductivity can be easily achieved. But, it is difficult to obtain *n*-type conductivity at room temperature in these films as nitrogen forms a deep donor ($\sim$1.7 eV). On the other hand, nitrogen forms a shallow donor level ($\sim$ 0.4 eV)[25] in NCD/UNCD films and results in high *n*-type conductivity ($\sim$143/$\Omega$/cm).

## 12.4  GROWTH MECHANISM OF NCD FILMS

Thin-film NCD films are grown through a CVD process wherein the growth occurs by the decomposition of carbon-containing precursor molecules (typically methane) in either a pure hydrogen, or hydrogen and argon environment. NCD growth is done through a thermal (hot filament)[26], plasma (microwave or RF)[27] activation or use of a combustion flame (oxyacetylene). Of the three, hot filament and microwave plasma methodologies are the most

popular techniques used for thin film diamond growth. Prior to diamond growth, the wafer needs to go through a seeding step which aids in the growth of the thin film. Seeding is popularly done through three different techniques:

1. *Mechanical polishing of the wafer*: In this technique, nanometre sized diamond powder is sprinkled on the silicon wafer and the wafer is mechanically scratched. By this, the diamond powder is spread uniformly throughout the wafer and this acts as a seeding layer in the CVD system. Seeding[28] through this method results in a nucleation density of $10^7/cm^2$.

2. *Ultrasonication*: Silicon wafer is suspended in slurry of nanometre sized powder with acetone or methanol for 20–30 min. Through this process, the surface of the paper is 'damaged' and seeded with the diamond powder for the subsequent growth process. Nucleation density of $10^6$–$10^{10}/cm^2$ is achieved through this method[29].

3. *Bias enhanced nucleation* (BEN): Although the first two processes are popular and result in good diamond films, the nucleation density is best in the BEN process[30]. In the MPECVD process, prior to growth in the BEN stage, the substrate is negatively biased at around 250 V resulting in starting current value of 10 mA. The current increases and saturates at 100 mA (Figure 12.2) in a half-hour seeding procedure, beyond which the current tends to decrease with time. Nucleation density achieved through this procedure is highest at around $10^{15}/cm^2$.

The drastic reduction in the grain size of the diamond films from several microns to few nanometres by changing the gas chemistry suggests that the
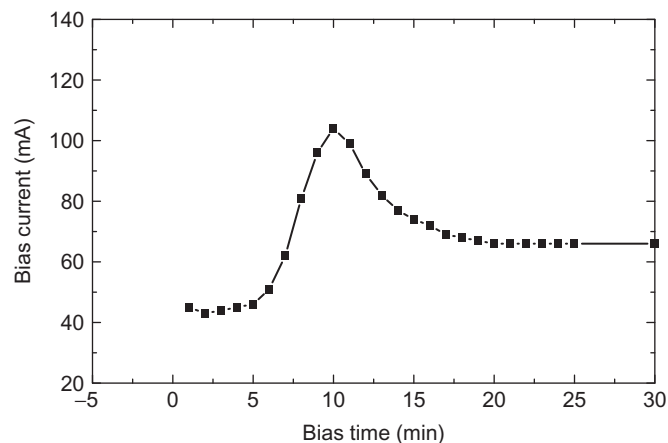


**FIGURE 12.2**   *Varying current value (mA) in time during the BEN seeding process.*

growth mechanism of NCD films is different from conventional CVD diamond films. Methyl radicals ($CH_3$) and acetylene molecules ($C_2H_2$) are the dominant species in the growth of conventional CVD films using $CH_4$ and $H_2$ gas chemistries[31]. NCD films are typically grown in 1% $CH_4$, with or without 1% $H_2$ and 98% or 99% Ar. Reduction in the hydrogen concentration from 99% to 1% reduces the grain size of the diamond from several microns to few nanometres. The phase-pure nanodiamond films were grown from a gaseous mixture of $C_{60}$/Ar in microwave plasma CVD with a total argon pressure of 98 torr, $C_{60}$ partial pressure of 0.01 torr, a total flow of 100 sccm and at a microwave power of 800 W. A $C_2$ dimer-based growth mechanism that would result in nanocrystalline structure was proposed[32]. In the films deposited using 5% $CH_4$ and 95% Ar, the $C_2$ dimers resulted in the inclusion of an amorphous carbon or graphitic carbon[33]. Such non-diamond form of carbon was due to the homogenous nucleation that resulted from high ratio of hydrocarbon to carbon dimers. But on the other hand, during the deposition of nanodiamond films, heterogeneous nucleation rate ($>10^{10}$ cm$^2$/s) increases due to highly reactive $C_2$ species, resulting in the smaller grain size of the diamond films[32]. Figure 12.3 shows the schematic of the growth mechanism of NCD[19]. According to this model, the feed gases methane and argon disassociate and favour the formation of $(C_2H_2)^+$ at a low ionization potential. The positively charged acetylene radical attracts an electron to form a highly reactive carbon dimer and hydrogen. Hydrogen is then desorbed away while the carbon dimers nucleate at the reconstructed surface. As the reaction continues, the number of carbon dimers in the plasma increase and they join the previously hybridized carbon atoms. In this way, a closely hybridized sp$^3$ network of carbon atoms forms a continuous film of NCD.

## 12.5  TECHNIQUES FOR THE CHARACTERIZATION OF NCD FILMS

Unlike the MCD films, NCD films deposited in hydrogen-poor gas chemistry have a complex grain boundary structure with grain size on the order of few nanometres. These differences in the grain structure result in different mechanical and electrical properties of NCD films. The structural, mechanical and electrical properties of these films have been studied by several analytical and metrology techniques.

Scanning electron microscopy (SEM) has been a very useful technique in the characterization of diamond thin films. The microstructure of diamond films changes dramatically with the continued addition of Ar to reacting gas mixtures during CVD process[19]. The transition from microcrystallinity to nanocrystallinity by systematically adding argon to hydrogen-rich plasma has
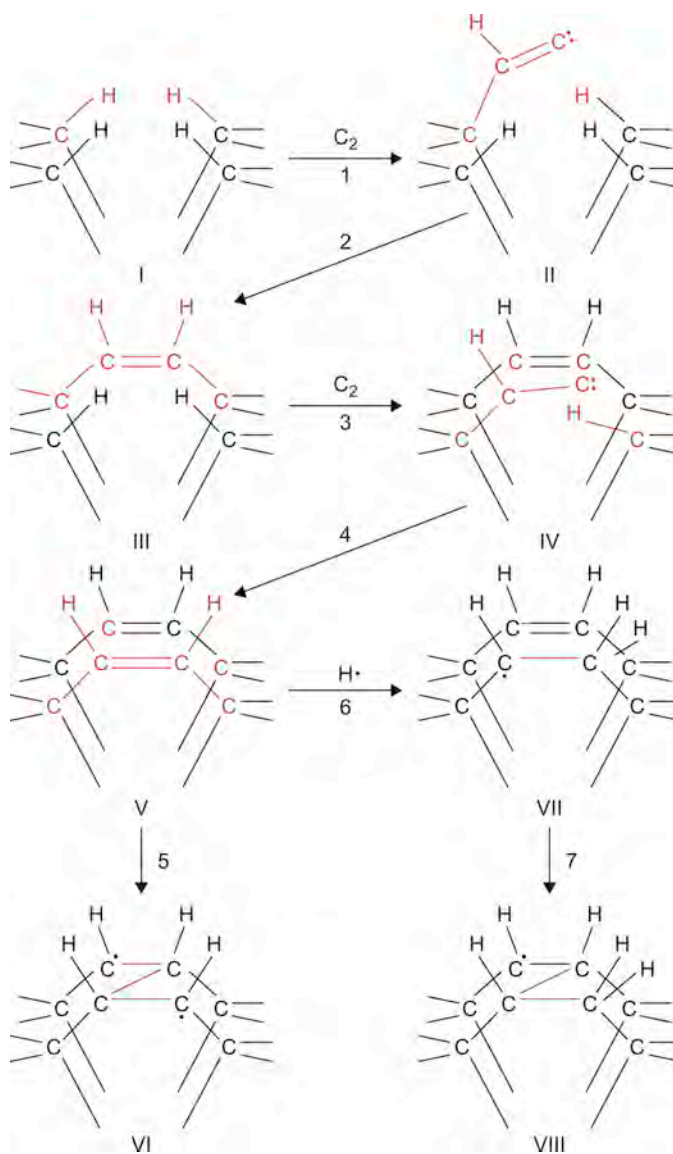
**FIGURE 12.3** *Growth mechanism of NCD.*

been characterized by SEM micrographs as a function of argon content shown in Figure 12.4. Different combinations of gas mixtures have been used.

Raman spectroscopy is a powerful technique to determine the chemical and structural properties of liquid or solid materials by a simple non-destructive and non-contact method of measurement. In the case of Raman
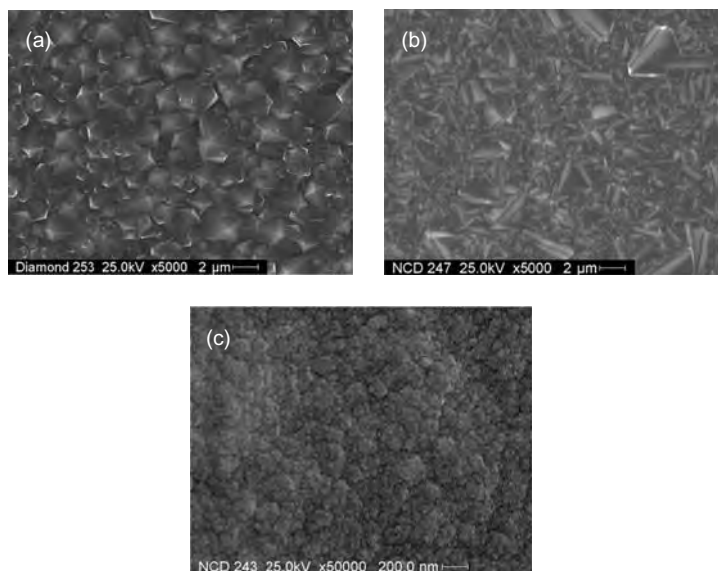
**FIGURE 12.4**  *SEM images of diamond films grown with different Ar: (a) 0%, (b) 50% and (c) 98%.*

spectroscopy of carbon-based materials, the Raman scattering is about 50 times more sensitive to $\pi$-bonded amorphous carbon and graphite than to the phonon band of diamond. Hence, Raman spectroscopy could be used to establish the crystalline quality of diamond thin films by estimating the amount of $sp^2$-bonded carbon in the films. Lin et al.[34] performed the Raman analysis of diamond films grown with $Ar/CH_4/H_2$ plasmas with different gas mixtures. For films grown without Ar, a sharp diamond characteristic peak is observed at 1332/cm. No Raman scattering can be found in the range from 1400 to 1600/cm suggesting that the diamond film contains very little $sp^2$-bonded carbon. With the addition of argon to the reactant gas up to 92%, a sharp diamond peak still exists indicating the presence of MCD grains. The typical Raman spectrum of a single crystal diamond, highly ordered pyrolytic graphite (HOPG), MCD and NCD are shown in Figure 12.5a–d respectively.

In addition to Raman spectroscopy, a technique that can distinguish between $sp^2$-bonded carbon (graphite) and $sp^3$-bonded carbon (diamond) would be very useful for characterizing the NCD films. X-ray core-level reflectance and absorption spectra is site and symmetry selective and the magnitudes and energy positions of spectral features contain bonding information of the films. Particularly, the near-edge region of the core-level photo absorption has been used to estimate the relative quantity of $sp^2$ or $sp^3$ bonding in BN powders and thin films[35]. Its sensitivity to the local bond order in a material arises from the dipole-like electronic transitions
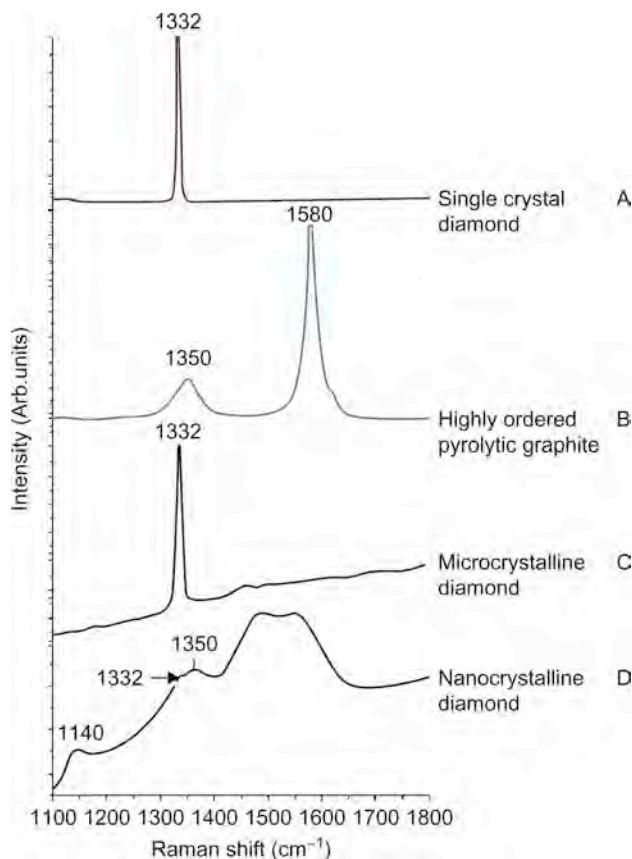
**FIGURE 12.5**   *Raman spectra of carbon-based materials.*

from core states, which have well-defined orbital angular moment, into empty electronic (e.g. antibonding) states[36]. Therefore, the symmetry of the final state can be determined and the difference between $sp^2$ and $sp^3$ can be distinguished. Besides, NEXAFS with a photon beam the size of a millimetre has the ability to investigate the film over a large area.

The NEXAFS spectra of carbon-based materials are dominated by $\pi$ and $\sigma$ resonances[37]. The measurements are made in two modes: (1) total electron yield (TEY) and (2) photon yield (PY). For nitrogen incorporated NCD films three features, corresponding to $\pi^\star$, $\sigma^\star$ and the second-order band gap of diamond, can be observed at $\sim284.7\,\mathrm{eV}$, $\sim289\,\mathrm{eV}$ and $\sim302\,\mathrm{eV}$, respectively. The $\pi^\star$ and $\sigma^\star$ features correspond to the $sp^2$- and $sp^3$-bonded carbons, respectively. From the NEXAFS spectra of intrinsic films shown in Figure 12.6, a sharp and well-defined peak corresponding to $\sigma^\star$ bonding can be observed. The $\pi^\star$ peak is weak and the full width at half maximum (FWHM) of second-order band gap of diamond is narrow. With the

addition of 20% nitrogen in the gas chemistry, the area under the $\pi^\star$ peak increased, $\sigma^\star$ peak is not as distinct as intrinsic diamond film and FWHM of the second-order band gap increased. These changes in the NEXAFS spectra suggest that the sp$^2$ content increases with the addition of nitrogen.

X-ray diffraction (XRD) is sensitive to the presence of crystalline carbons such as diamond or graphite instead of amorphous carbon. Hence, it is frequently used to characterize CVD diamond films. NCD films exhibit a similar pattern compared to conventionally synthesized MCD films[38]. Three peaks, related to (111), (220) and (311) crystalline diamond peaks are observed. Compared to the MCD films, the diffraction peaks of NCD are significantly broadened due to the very small diamond grain sizes.



**FIGURE 12.6**   *NEXAFS spectra of NCD films grown using 0% and 20% nitrogen in the gas chemistry.*

Since MCD has grain size as large as several microns, SEM micrograph can successfully show the structure of the film. However, NCD has very small crystals compared to MCD and it is necessary to use transmission electron microscopy (TEM) to analyse these nanosized crystals. Figure 12.7 shows a bright-field TEM image revealing the plan-view morphology of the NCD thin film. The grain boundary width estimated from the TEM micrograph is 0.2–0.5 nm. The insert image shows a selected area (over 10 μm in diameter) electron diffraction pattern. Sharp Bragg reflections are located in concentric circles, indicating the random orientation of NCD grains. Addition of argon to the microwave plasma results in smaller nanocrystalline grain sizes.



**FIGURE 12.7**   *A plan-view TEM image of the diamond film. Film was prepared from an Ar/CH$_4$ plasma at 100 torr. It shows that the diamond film consists of nanocrystalline grains ranging from 3 to 20 nm. The inset image shows a SAED pattern image.*

## 12.6  MECHANICAL RESONATORS

Mechanical resonators are commonly used in many RF and microwave circuits today. In spite of operating at GHz frequencies, the popular mechanical resonators are limited due to the motional resistance caused by the acoustic velocity of the material. Thin film diamond, which has one of the highest acoustic velocities, is used in realizing resonators with better performance. Pacheco et al.[39] has successfully implemented an

**FIGURE 12.8**   *Cross section of the UNCD MEMS resonator.*
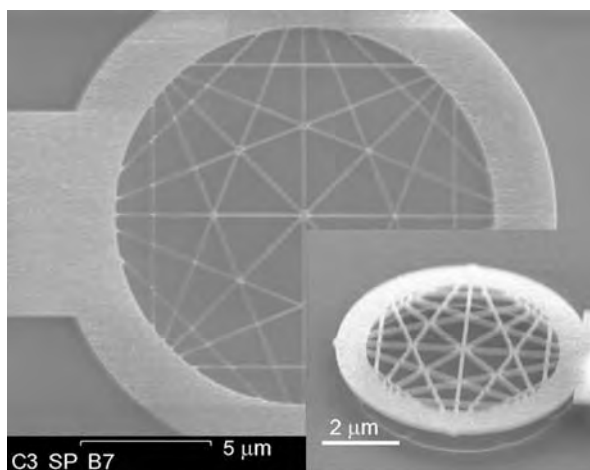


**FIGURE 12.9**   *SEM image of the NEMS diamond resonator.*

NCD-based MEMS resonator and achieved the highest reported acoustic velocity which is the fundamental limitation of other materials used in acoustic sensors. The device comprises of a UNCD thin film deposited under low temperature conditions making it CMOS compatible. The measured Young's modulus and acoustic velocity of the UNCD resonator (Figure 12.8) are 710 GPa and 14,243 m/s respectively. The 10-MHz resonator was tested between 15 and 25 V yielding a tunability of 15% in the resonance frequency.

Apart from MEMS resonators, there has been significant development in the area of NCD-based nanoelectromechanical systems (NEMS) resonant structures. L. Sekaric et al.[40] developed a ring oscillator fabricated out of a 30-nm NCD film with a gold electrode on top. Figure 12.9 shows the

SEM image of the nano resonator. The radius of the resonator used for testing was between 2 and $8\,\mu m$ and the measured resonance frequency was between 8 and 30 MHz with a $Q$ of 3000.

## 12.7 ELECTROSTATIC AND THERMAL SWITCHES

Electrostatically actuated NCD switches have been designed and implemented in a coplanar waveguide (CPW) topology by Adamschik et al. Although suffering from high and low actuation voltages, these switches prove to be good replacement to an all-metal switch in terms of reliability and power han-



**FIGURE 12.10**   *SEM image of the NCD-based electrostatic RF-MEMS switch.*

dling capabilities. Furthermore, diamond-based switches can be operated at high temperatures and have been tested mechanically up to 850°C. Figure 12.10[41] shows the SEM image of the diamond-based CPW switch. The device was fabricated using sacrificial technology and later integrated into a CPW structure. The switch was tested in both atmospheric and vacuum conditions in which, due to air damping, the switching speed is doubled to those tested in vacuum conditions. Small signal measurements were done on the switches yielding an $S_{11}$ and $S_{21}$ of around 35 dB and 2 dB at 10 GHz respectively.

## 12.8 DESIGN OF THE THERMALLY ACTUATED NCD ACTUATOR

NCD film is deposited onto a low resistive silicon substrate by HFCVD. The diamond bridge is 1200-$\mu m$ long and 300-$\mu m$ wide. The bridges are thermally actuated using a bi-metal actuation scheme[42]. Compared to electrostatic actuation, thermal actuation has the advantage of having a lower actuation voltage and a higher contact force. The main drawback of the thermal actuation scheme is the static power consumption which can be avoided by using a bi-stable layout. The basic device consists of a bridge made of doped diamond. A second metal layer (copper) is deposited on top of the diamond bridge. The difference in coefficient of thermal expansion between the two materials, $0.8 \times 10^{-6}$/K for diamond and $13 \times 10^{-6}$/K for copper, causes the bending moment, and resistive heating of the doped areas forces a bending of the beam and hence switching into the actuated state. The pull-in voltage (and current) to switch the bridge depends on the geometry of the diamond heating elements. The design of the diamond actuator is shown in Figure 12.11. In the first iteration of the design, nickel
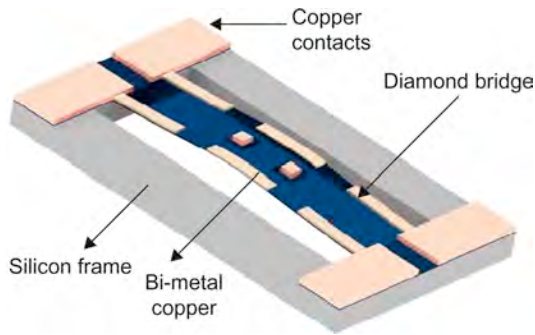
**FIGURE 12.11** *Design of the thermally actuated diamond microbridge.*
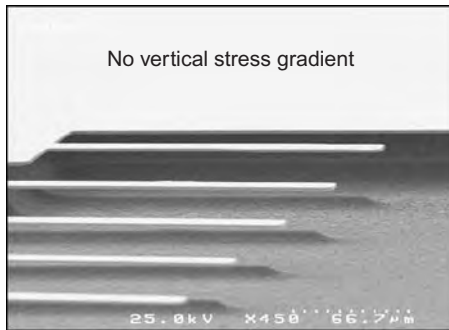


**FIGURE 12.12** *Micromachined diamond cantilevers without vertical stress gradient.*

was chosen to the bi-metal. Apart from the higher coefficient of thermal expansion, the number of processing steps can be reduced if copper was used. Gold wirings are included in the design to provide a DC electrical path to the contact pad at the centre of the diamond bridge. The contact pads are $100\,\mu m \times 100\,\mu m$ in dimension.

Stress engineering during the growth phase of NCD is very important. Diamond growth, in its normal state, has vertical stress associated with it. In this application, growth recipes were optimized in order to achieve diamond bridges and cantilevers with no vertical stress. Figure 12.12 shows a SEM image of free-standing diamond cantilevers without any vertical stress gradient.

## 12.9 FABRICATION AND INTEGRATION

The diamond bridges are fabricated on a 500-$\mu$m thick low resistive silicon wafer. The fabrication steps (Figure 12.13) are as follows:

- The silicon wafer is nucleated by BEN and an intrinsic diamond layer of 1500 Å thickness is grown through a microwave plasma assisted CVD process. Boron doped diamond ($p$-type) is later grown with HFCVD to a thickness of 8500 Å. This boron doped diamond is the heart of the micromachined actuator.

- Intrinsic diamond is selectively grown using a $SiO_2$ mask. The 4000-Å thick diamond layer is used for electrical isolation of the contact areas while actuating the bridges.

- A Cr/Au seed layer of 700 Å is deposited using an ion beam reactor following which a 1-$\mu$m thick copper film is deposited by electroplating, which serves as the bi-metal for thermal actuation.

- Copper pads which are used to integrate the diamond switches onto the host substrate are electroplated to a thickness of 12 $\mu$m. The RF contact areas are also formed by electroplating in this step.

- The previously deposited seed layer is patterned to provide electrical continuity to actuate the bridges.

- 400 Å of platinum is patterned over the copper contact area using lift-off technique.

(a)

Intrinsic diamond is selectively grown on top of boron doped diamond. Resistivity of boron is around 1 mΩ.cm.

(b)

Copper bi-metal pads electroplated. A seed layer of Cr+Au is deposited using a thermal evaporator prior to the plating process.

(c)

Copper pads for integration are electroplated. After this, seed layer is patterned to provide electrical continuity for the diamond bridge to be thermally actuated.

(d) Finally, the diamond bridges are released through a DRIE process. Prior to this a thin layer of platinum is deposited on top of the copper contact through lift-off process.

- Diamond bridges are then etched in an RIE system using titanium as the hard mask.

- Finally, using patterned silicon dioxide as a backside hard mask, diamond structures are released from the silicon wafer through a DRIE process resulting in a free-standing diamond bridge that is embedded in a silicon frame.

Prior to this design, the diamond actuator was fabricated in which the bridge was composed of intrinsic diamond with areas of selectively grown doped diamond. The doped diamond bridge was chosen, so that resistance of the heaters can be lower without actually making the bridge thicker and

stiffer. Figure 12.14a and 12.14b shows the front view and the back view of the fabricated diamond actuator. The overall size of the entire chip is 1600-μm long and 900-μm wide.

Being monolithic in design, this diamond actuator is substrate independent and can be integrated to any microwave substrate depending on the application. For the first set of results, these actuators were flip-chip bonded to an alumina substrate using a Cu/Sn solid liquid interdiffusion (SOLID) process[43]. Figure 12.15 shows the integration process of the diamond actuator to the host substrate.

In addition to the copper pads in the actuator frame, copper pads along with tin should be included in the host substrate for integration. Solid–liquid interdiffusion occurs between the two phases, resulting in a phase transformation of the liquid component to a higher melting point material, which is strong enough to serve as a bond and withstand elevated temperatures. Copper–tin has been considered a SOLID couple where tin acts as a melting phase and copper as a solid phase. While integrating, the copper pads on the actuator are kept on top of the copper–tin stack and heated till 250°C (melting

*Microphotograph of the fabricated diamond actuator (a) front view (b) back view with the silicon frame.*
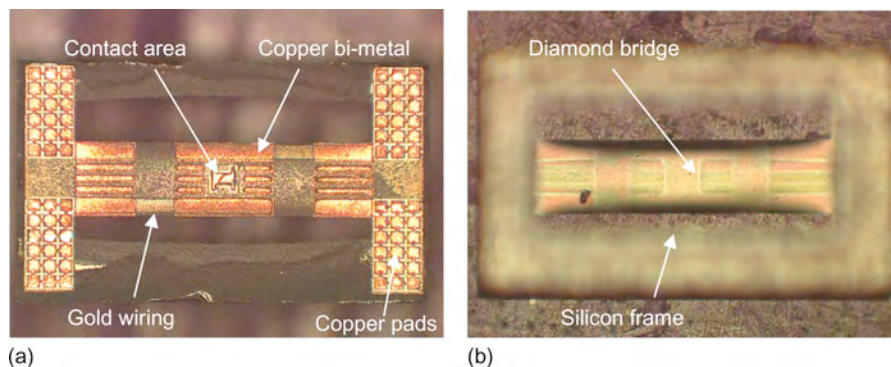
*Diamond actuator integrated onto the host alumina substrate using the SOLID process.*
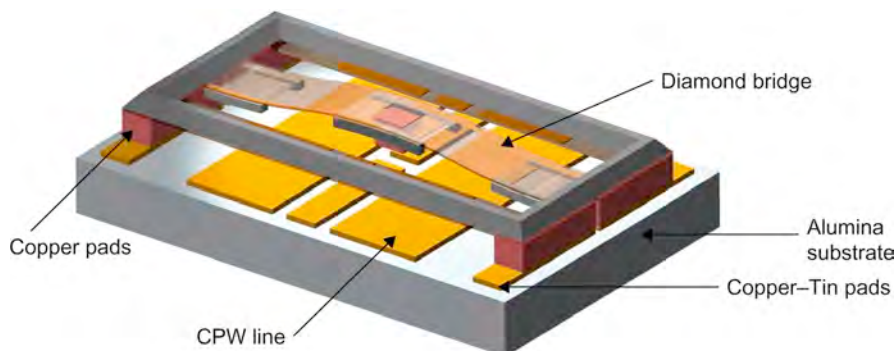
point of tin). During the diffusion process, one of the intermetallic compounds forms the bond between the two structures and is stable till 600°C.

## 12.10  MEASUREMENT AND ANALYSIS

The diamond actuators are used to realize RF-MEMS DC contact type switches in CPW and microstrip topologies. The CPW transmission lines are designed on a 650-μm thick alumina substrate ($\varepsilon_r$ = 9.9, tan $\delta$ = 0.0002). The transmission lines are 3000-μm long with a centre conductor width ($W$) of 100 μm and slot width ($G$) of 50 μm. The centre conductor of these lines is purposefully interrupted in the middle resulting in two transmission lines which are 1475-μm long. During actuation, the contact pad in the diamond bridge closes this gap resulting in regular transmission line. Small signal measurements are done in the frequency span of 1–30 GHz using an Anritsu lightning vector network analyzer (VNA). A bias tee was used to protect the VNA test ports from DC current. Before measuring the structures, a probe-tip short-open-line-thru (SOLT) calibration is performed on a commercial GGB CS-9 calibration. The diamond bridges are thermally actuated at 2 V wherein the platinum-coated copper pad makes contact with the CPW line. Figure 12.16 shows the $S_{11}$ and $S_{21}$ of the transmission line in the non-actuated and actuated state.

The return loss and insertion loss in the actuated state are 20 dB and 0.2 dB at 20 GHz. It is evident from S-parameters that in the actuated state,
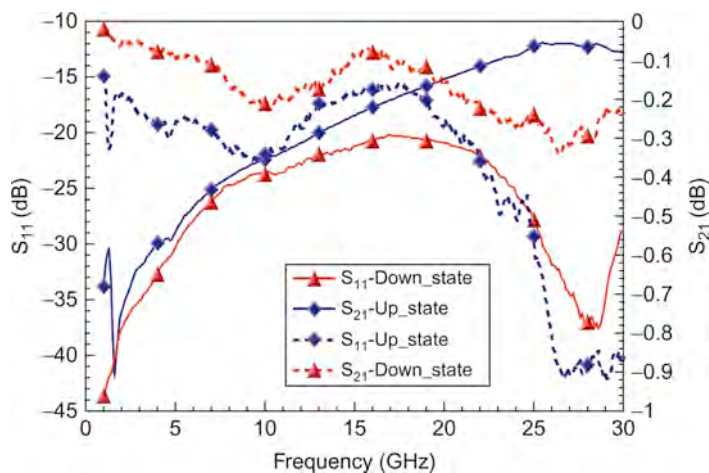


**FIGURE 12.16**    *Measured $S_{11}$ and $S_{21}$ of the CPW switch in the non-actuated and actuated state of the diamond bridge.*
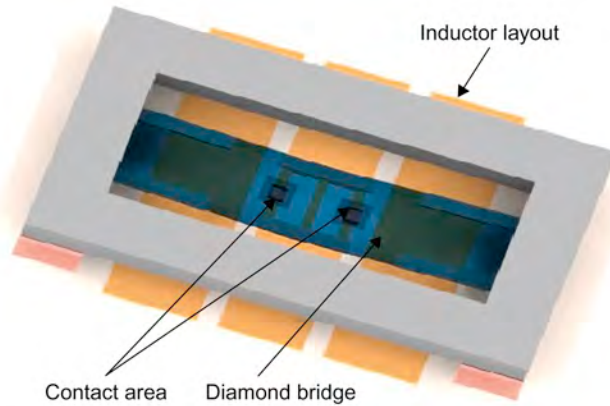
**FIGURE 12.17** *Design of the integrated CPW inductor and diamond actuator.*

the diamond bridge makes a very good contact with the transmission line with little contact resistance. Similar to the CPW circuits, diamond bridges were also integrated onto alumina substrate with microstrip transmission lines. In addition to implementing the devices as a simple RF switch, tunable inductors were also realized wherein the non-actuated and the actuated state of the bridges yield different net inductance values[44]. The inductor circuits fabricated on the alumina substrate are 400-μm long. Figure 12.17 shows the inductor layout along with the integrated diamond bridge.

The difference in inductance is due to the change in impedance of the device due to the varying widths of *W* and *G*. The design of the tunable inductors is based on the equivalence of a distributed transmission line. For a short electrical length ($<\pi/4$), a high impedance *t*-line section emulates a series inductor as given in Equation 12.1[44]. Tunable operation is achieved by changing the effective width of the slot and/or the centre conductor by using the diamond actuator.

$$L_d = \frac{Z_h\theta_1}{\omega}, L_u = \frac{Z_1\theta_2}{\omega} \qquad (12.1)$$

In the non-actuated state of the actuator, the inductor represents a high impedance state which translates into a high inductance value. When the bridges are actuated, the contact pads make a DC short with the transmission lines, leading to low impedance and in turn a low inductance state. The inductors were measured in the frequency range of 1–30 GHz in the same setup as that of the RF switches. Figure 12.18 shows the insertion loss and the return loss of the tunable inductor in the non-actuated and the actuated state of the diamond bridge.
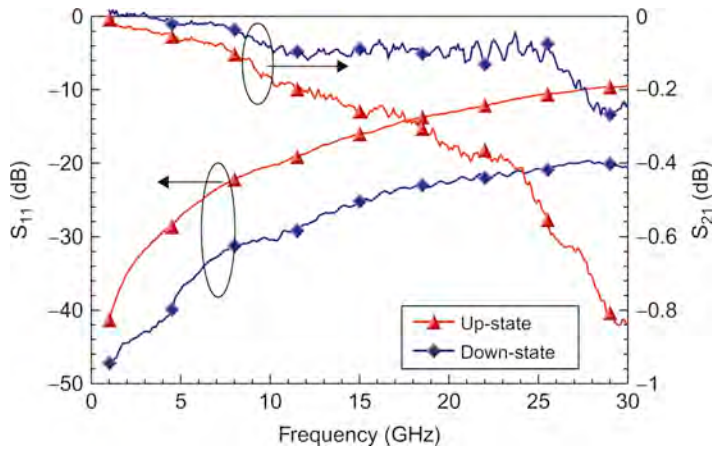
**FIGURE 12.18**   *Measured $S_{11}$ and $S_{21}$ of the tunable inductor in the non-actuated and actuated state.*
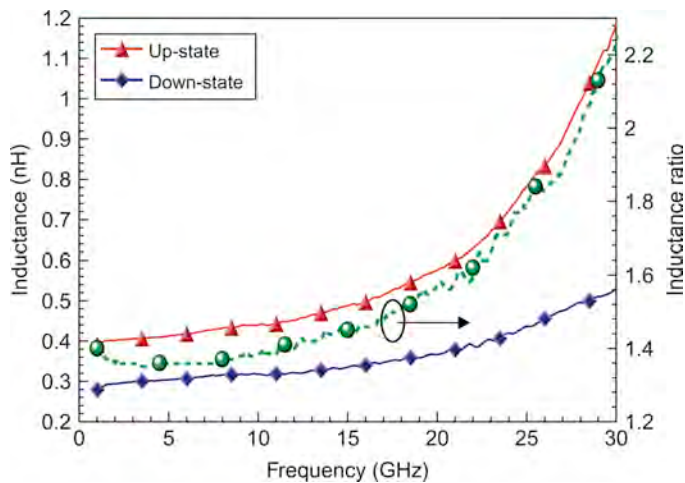


**FIGURE 12.19**   *Measured inductance in the two states and the inductance ratio ($L_{ratio}$).*

The effective inductance ($L_{eff}$) of the circuit is extracted by numerically shorting port 2 of the inductor and is related to the input impedance ($Z_{in}$) by Equation 12.2.

$$L_{eff} = \frac{\text{Imaginary term of the input impedance } \{\text{Imag}(Z_{in})\}}{2 \times \pi \times \text{freq}} \quad (12.2)$$

The measured inductance in the two states and the inductance ratio ($L_{ratio}$) are shown in Figure 12.19. An inductance ratio of 2.2 was achieved at 30 GHz with 1.2 being the maximum inductance value.
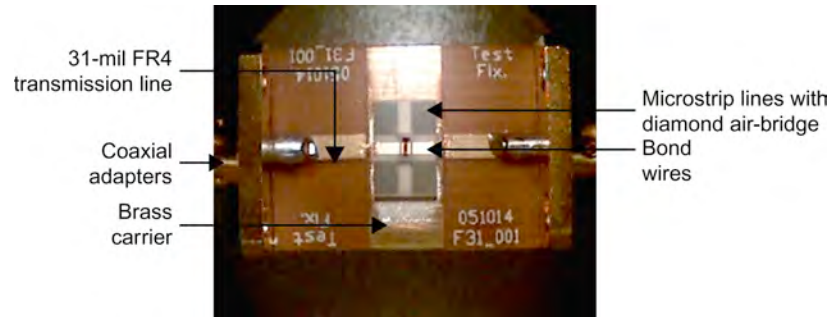
**FIGURE 12.20**  *Microstrip line with diamond air-bridge fixture for high power measurement.*
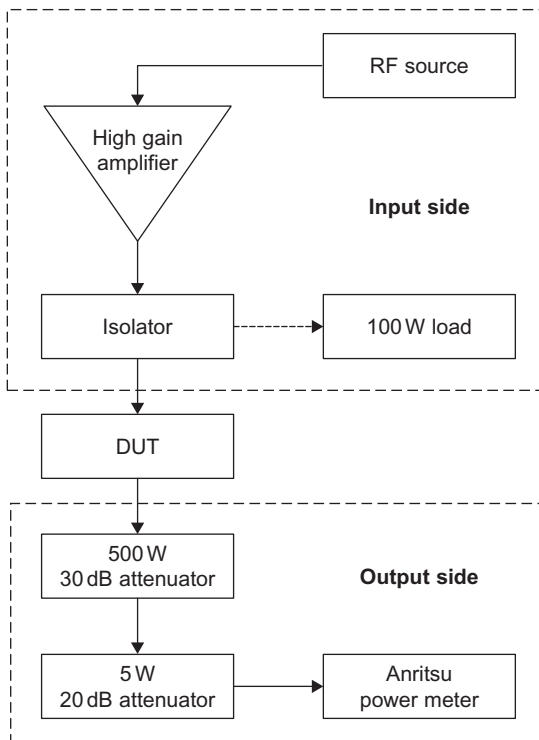


**FIGURE 12.21**  *High power measurement setup for testing the diamond switches.*

Power handling capabilities of RF-MEMS devices have been previously investigated for series[45] and shunt capacitive switches[46] at X-band frequencies up to an input power of 7 W. In this work, the micromachined diamond air-bridge integrated in the microstrip topology is tested at 2.1 GHz until 45 W. Prior to testing, the microstrip substrate with the diamond bridge is modified for the measurement setup. The alumina wafer is solder attached to a brass carrier. Two 250-mil long, 50-$\Omega$ microstrip lines are fabricated on a 31-mil FR4 substrate and solder mounted on either side of the alumina wafer. This is done to connect the SMA coaxial adaptors on either side of the carrier for testing. Bond wires which are 3-mil in diameter are used to connect the 50-$\Omega$ lines with the microstrip line on the alumina substrate. Figure 12.20 shows the details of the coaxial test fixture used for high power measurement.

The setup for high power measurement is shown in Figure 12.21. Maury microwave ATS 400 software was used to extract the data. An Anritsu 68169B signal generator is used as the RF source where there is 2.1 GHz, 15 dBm input signal. In the next stage, the input signal is passed through a commercially available 100-W amplifier with a gain of 50 dB. A three-port circulator is used as an isolator with the third port terminated by a 100-W load. This is done to isolate the signal source and the amplifier from any high power reflected signal. The isolator and the brass carrier are mounted on a heat sink to avoid thermal issues. The signal source, amplifier and the isolator
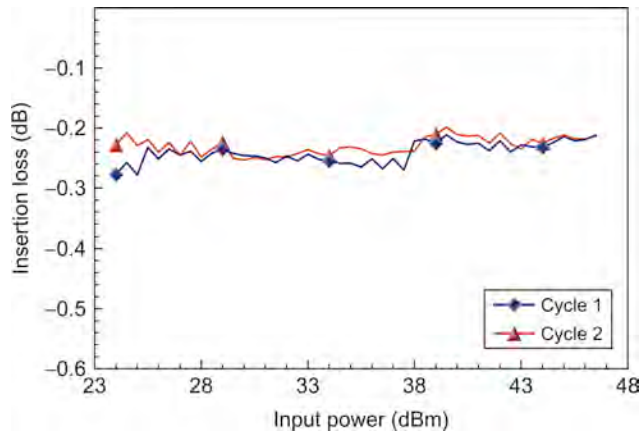
**FIGURE 12.22** *Measured insertion loss of the diamond bridge in the microstrip topology with varying power level.*

constituted the input side of the high power setup. The output signal from the diamond actuator device under test (DUT) is passed through stages of high power commercially available attenuators before measuring the power level in an Anritsu power meter.

Prior to measurement, a two-port thru calibration is performed wherein the references planes were shifted to the inner edges of the 31-mil FR4 transmission line. Measurements are performed in the power range of 24–47 dBm at 2.1 GHz with the diamond bridges mechanically actuated in addition to the applied DC voltage.

In the initial high power tests, some variation in the device performance was noticed and complete contact was not obtained using electrical actuation; this can be attributed to the height differences in the flip-chip mounted structures. Therefore, the devices used in the high power testing were found to require such mechanical actuation, which was achieved using a needle probe attached to a micropositioner. The insertion loss is recorded with varying input power level up to 47 dBm. As shown in Figure 12.22, the insertion loss is around 0.2–0.3 dB throughout the entire power spectrum. Measurements were made for more than one instance for repeatability and there was no significant difference in the insertion loss. The diamond bridge was stable at such power with little or no damage due to heating of the structure. Diamond which also is an excellent conductor of heat acts as a good heat sink during measurement. As an improvement to this device, dual actuation scheme-based NCD bridges are being developed. In this scheme, the advantages of electrostatic and thermal actuation are used together to develop more reliable NCD actuators.

In addition to these, there has been considerable amount of research demonstrating the use of NCD thin film in packaging and thermal applications[47]. Active devices, like transistors, have been mounted on diamond carriers thereby improving their performance due to better thermal management. The high thermal conductivity exhibited by thin film diamond has been a positive impact in packaging approaches in the MEMS devices, as well. Furthermore, NCD has been used for many optical applications to fabricate resonators[48], two-dimensional photonic crystals[49], UV transparent electrodes on $SiC$[50] and in some sensor applications[51].

## ACKNOWLEDGEMENTS

## REFERENCES

[1] M. Suster, et al., An optically powered wireless telemetry module for high-temperature MEMS sensing and communication, J. Microelectromech. Syst. June (2004).

[2] D.S. Eddy, et al., Application of MEMS technology in automotive sensors and actuators, Proc. IEEE August (1998).

[3] D.L. Polla, et al., MEMS technology for biomedical applications, in: 6th International Conference on Solid-State and Integrated-Circuits Technology, October 2001.

[4] V. Milanovic, et al., Batch transfer integration of RF microrelays, IEEE Microwave and Wireless Components Lett. August (2000).

[5] P. Blondy, et al., Packaged mm-wave thermal MEMS switches, in: 31st European Microwave Conference, September 2001.

[6] H.C. Lee, et al., Piezoelectrically actuated RF MEMS DC contact switches with low voltage operation, IEEE Microwave and Guided Wave Lett. April (2005).

[7] G.M. Rebeiz, RF MEMS-Theory, Design and Technology, John Wiley and Sons Publication, 2003.

[8] D. Peroulis, et al., RF MEMS switches with enhanced power handling capabilities, IEEE Trans. Microwave Theory Tech. January (2004).

[9] A. Aleksov, et al., First diamond FET RF power measurement on diamond quasi-substrate, in: 60th Device Research Conference, June 2002.

[10] Electronic reference: http://newton.ex.ac.uk/research/qsystems/people/sque/diamond/structure/

[11] P. Bergonzo, et al., Improving diamond detectors – A device case, Diamond Relat. Mater. April–July (2007).

[12] W.P. Kang, et al., Nanodiamond lateral VFEM technology for harsh environments, IEEE Trans. Nucl. Sci. August (2007).

[13] K.J. Gabriel, et al., In situ friction and wear measurements in integrated poly-silicon mechanisms, Sens. Actuators, A, February (1990).

[14] I. Ahmed "Deposition of textured diamond growth using hot-filament assisted chemical vapor deposition method" MS Thesis, University of South Alabama (1998).

[15] M. Belmonte, et al., Wear resistant CVD diamond tools for turning of sintered hardmetals, Diamond Relat. Mater. March–July (2003).

[16] S. Turchetta, et al., CVD diamond insert in stone cutting, Diamond Relat. Mater. March–July (2005).

[17] A. Glaser, et al., Deposition of uniform and well adhesive diamond layers on planar tungsten copper substrates for heat spreading applications, Mater. Sci. Eng. B, February (2006).

[18] D.M. Gruen, et al., Deposition and characterization of nanocrystalline diamond films, J. Vac. Sci. Technol. A (1994).

[19] D. Zhou, et al., Control of diamond film microstructure by Ar additions to $CH_4/H_2$ microwave plasmas, J. Appl. Phys. (1998).

[20] O. Auciello, et al., Materials science and fabrication processes for a new MEMS technology based on ultrananocrystalline diamond thin films, J. Phys.: Condens. Matter (2004).

[21] M. Kubovic, et al., Surface channel MESFETs on nanocrystalline diamond, Diamond Relat. Mater. (2005).

[22] N.S. Xu, et al., Study of field electron emission from nanocrystalline diamond thin films grown from a $N_2/CH_4$ microwave plasma, J. Phys. D: Appl. Phys. (2000).

[23] U.A. Palnitkar, et al., Adhesion properties of nitrogen ion implanted ultra-nanocrystalline diamond films on silicon substrate, Diamond Relat. Mater. (2008).

[24] R. Haubner, et al., Comparison of sulfur, boron, nitrogen and phosphorus additions during low-pressure diamond deposition, Diamond Relat. Mater. (2001).

[25] S. Bhattacharyya, et al., Synthesis and characterization of highly-conducting nitrogen-doped ultrananocrystalline diamond films, Appl. Phys. Lett. (2001).

[26] M. Amaral, et al., Growth rate improvements in the hot-filament CVD deposition of nanocrystalline diamond, Diamond Relat. Mater. November (2006).

[27] M. Miyake, et al., Characteristics of nano-crystalline diamond films prepared in $Ar/H_2/CH_4$ microwave plasma, Diamond Relat. Mater. March (2007).

[28] X. Zheng, et al., Investigation on the etching of thick diamond film and etching as a pretreatment for mechanical polishing, Diamond Relat. Mater. December (2006).

[29] Y.K. Liu, et al., Comparative study of nucleation processes for the growth of nanocrystalline diamond, Diamond Relat. Mater. February (2006).

[30] J.C. Arnault, et al., Comparison of classical and BEN nucleation studied on thinned Si (1 1 1) samples: A HRTEM study, Appl. Surf. Sci. May (2003).

[31] S.J. Harris, et al., Growth on the reconstructed diamond (100) surface, J. Phys. Chem. (1993).

[32] D.M. Gruen, Nanocrystalline diamond films, Annu. Rev. Mater. Sci. (1999).

[33] W. Zhu, et al., Effects of noble gases on diamond deposition from methane–hydrogen microwave plasmas, J. Appl. Phys. (1990).

[34] T. Lin, et al., Compositional mapping of the argon–methane–hydrogen system for polycrystalline to nanocrystalline diamond film growth in a hot-filament chemical vapor deposition system, Appl. Phys. Lett. (2000).

[35] A. Chaiken, et al., Electronic and atomic structure of metastable phases of boron nitride using core-level photoabsorption, Appl. Phys. Lett. (1993).

[36] D.M. Gruen, et al., Characterization of nanocrystalline diamond films by core-level photoabsorption, Appl. Phys. Lett. (1996).

[37] J. Stöhr, NEXAFS Spectroscopy, Springer Series in Surface Sciences, New York, 2003.

[38] R.W. Siegel, et al., Mechanical properties of nanophase metals, Nanostruct. Mater. (1995).

[39] S.P. Pacheco, et al., Characterization of low-temperature ultrananocrystalline diamond RF MEMS resonators, in: 35th European Microwave Conference, October 2005.

[40] L. Sekaric, et al., Nanomechanical resonant structures in nanocrystalline diamond, Appl. Phys. Lett. (2002).

[41] M. Adamschik, et al., Diamond microwave micro relay, Diamond Relat. Mater. November (2002).

[42] P. Schmid, et al., Diamond switch using new thermal actuation scheme, Diamond Relat. Mater. March–July (2003).

[43] P. Benkart, et al., 3D chip stack technology using through-chip interconnects, IEEE Des. Test Comput. November–December (2005).

[44] S. Balachandran, et al., MEMS tunable planar inductors using DC contact switches, in: 34th European Microwave Conference, October 2004.

[45] J.B. Muldavin, Design and analysis of series and shunt MEMS switches, Ph.D. dissertation, Department of Electrical Engineering and Computer Science, The University of Michigan at Ann Arbor, Ann Arbor, MI, 2001.

[46] D. Peroulis, et al., RF MEMS switches with enhanced power handling capabilities, IEEE Trans. Microwave Theory Tech. January (2004).

[47] C. Schaffauser, et al., Optimized thermal and microwave packaging for wide-band gap transistors: Diamond and flip chip, in: European Microwave Conference, October 2005.

[48] C.F. Wang, et al., Observation of whispering gallery modes in nanocrystalline diamond microdisks, Appl. Phys. Lett. (2007).

[49] C.F. Wang, et al., Fabrication and characterization of two-dimensional photonic crystal microcavities in nanocrystalline diamond, Appl. Phys. Lett. (2007).

[50] M.J. Tadjer, et al., Nanocrystalline diamond films as UV-semitransparent Schottky contacts to 4H–SiC, Appl. Phys. Lett. (2007).

[51] Z. Xu, et al., A study of polyaniline deposited nanocrystalline diamond films for glucose detection, J. Nanosci. Nanotechnol. (2007).

# Analysis of the Effects of Micromachining using Nanostructured Cutting Tools

M.J. Jackson[1], M.D. Whitfield[1], G.M. Robinson[1], and W. Ahmed[2]

[1]MET, College of Technology, Purdue University, 401 North Grant Street, West Lafayette, IN 47907-2021, USA

[2]School of Computing, Engineering and Physical Sciences, Faculty of Science and Technology, University of Central Lancashire, Preston PR1 8ST, UK

## CONTENTS

## ABSTRACT

This chapter describes the analysis of the high-speed mechanical micro-milling process. The chapter not only compares computational approaches to the solution of shear plane and tool face temperatures, but also explains why there is a difference in calculating temperatures generated during the micromachining process. The analysis shows that the computed temperature of the shear plane never exceeds 35°C during micromilling at spindle speeds approximately 310,000 revolutions per minute. Machining AISI 1040 steel at significantly high speeds presents significant challenges to

prevent the accelerated wear of the cutting tool that is caused by the frictional interactions between chip and tool and the nature of the intermittent contact. The analysis also shows the effect of coating on reducing the interface temperatures between chip and tool and concludes that each coating has very little effect on reducing temperature at the tool face and at the primary shear zone.

## 13.1 INTRODUCTION

The validity of single shear plane metal cutting theories is being questioned as a result of recent advances in computational mechanics. Astakhov and co-workers[1–3] are justly critical of single shear plane theories developed in the 1940s that describe the mechanics of metal cutting at the macroscale. In response to Astakhov's[1] comments that the previous theories do not apply to certain machining operations, the authors of this chapter have conducted a series of finite element analyses of machining AISI 1040 steel in order to understand if one particular method[4] can be applied to calculate shear plane and tool face temperatures by comparing with finite element models. The following analysis allows one to understand if the initial stages of rapid chip formation when machining AISI 1040 steel contribute to the applicability of using Loewen and Shaw's methods to calculate various machining variables during high-speed micromachining.

## 13.2 COMPUTATIONAL ANALYSES

### 13.2.1 Computational analysis of temperature in micromachining

There are several analytical approaches well described in the literature that are used to determine the cutting temperature, for example, Loewen and Shaw[4], Wright and Trent[5]. These methods are suitable for the analysis of relatively soft materials, in particular low carbon hypoeutectoid steels containing a high percentage of ferrite. Stephenson[6] found that the most accurate model used to determine temperature at the chip–tool contact zone was Loewen and Shaw's model because it accounted for the change in thermal properties of the tool and workpiece with increasing temperature. Therefore, Loewen and Shaw's approach will be used as outlined by Shaw[7]. However, since there is no suitable dynamometer available to measure cutting forces at this scale, the horizontal force can be closely approximated by the formula proposed by Isakov[8]. Once this quantity has been determined, Loewen and Shaw's approach can be used. Isakov's formula to find the

tangential force or the force in the horizontal orientation, $F_{HO}$, of a milling cutter is given by:

$$F_{HO} = \sigma_{UTS} A n_c C_m C_w \qquad (13.1)$$

where, $\sigma_{UTS}$, is ultimate tensile strength (UTS) of the workpiece (for AISI 1040 steel, $\sigma = 4.2 \times 10^{10}$ MPa), $A$ is the uncut chip cross sectional area, $n_c$ is the number of teeth engaged in the workpiece, $C_m$ is a machinability adjustment factor and $C_w$ is a tool wear adjustment factor. The feed per tooth, $f_t$, must be calculated. To do this the following quantities must be known: the feed, $f = 0.025$ m/min $= 0.0042$ m/s, the spindle speed, $N = 310,000$ rpm, the angular velocity, $\omega = 31,415.93$ rad/s and the number of cutting teeth, $n = 6$. The feed per tooth can now be calculated using the following equation.

$$f_t = \frac{f}{Nn} \qquad (13.2)$$

$$f_t = \frac{0.025\,(\text{m/min})}{310,000\,(\text{rpm}) \times 6} \qquad (13.3)$$

$$f_t = 1.39 \times 10^{-8}\,(\text{m})$$

The feed per tooth correction factor, $f_{tc}$, is given by:

$$f_{tc} = \frac{f_t}{\cos \alpha} \qquad (13.4)$$

$$f_{tc} = \frac{1.39 \times 10^{-8}\,(\text{m})}{\cos 5°} \qquad (13.5)$$

$$f_{tc} = 1.40 \times 10^{-8}\,(\text{m})$$

However, the edge radius of the cutting tooth is approximately 3 μm. Therefore, the tool is not sharp enough to form a chip owing to the degree of curvature at the tool edge. This has been reported previously by Kim et al.[9], who showed that chips are only formed when the uncut chip thickness is much larger than the edge radius of the tool; unfortunately, no exact ratio has been determined during micromachining. Therefore, it is assumed that a chip will form when the uncut chip thickness reaches 5 μm. This means that the tool rotates 360 times before the chip is formed. Thus, the feed per tooth is replaced by the thickness required to form a chip. The rake angle is measured to be $\alpha = 5°$, and the width of cut, $b$, is replaced by the axial

depth of cut for a milling operation, which in this case is $100 \times 10^{-6}$ m. The uncut chip cross sectional $A$ is given by:

$$A = f_{tc}b \tag{13.6}$$

$$A = (5.02 \times 10^{-6} \, (\text{m}))(100 \times 10^{-6} \, (\text{m})) \tag{13.7}$$

$$A = 5.02 \times 10^{-10} \, (\text{m}^2) $$

The tool diameter $d = 900 \times 10^{-6}$ m and the width of cut $W = 450 \times 10^{-6}$ m. The number of teeth engaged in the cut, $n_c$, can now be calculated by:

$$n_c = \frac{n\{90 + \sin^{-1}[(2W - d)/d]\}}{360} \tag{13.8}$$

$$n_c = \frac{6\{90 + \sin^{-1}[(2(450 \times 10^{-6} \, (\text{m})) - (900 \times 10^{-6} \, (\text{m})))/(900 \times 10^{-6} \, (\text{m}))]\}}{360}$$

$$\tag{13.9}$$

$$n_c = 1.5$$

The machinability adjustment factor is taken from Isakov[8] and is unity; the tool wear adjustment factor is taken as 1.1, also from Isakov[8]. Therefore, $F_{HO}$ can be calculated as:

$$F_{HO} = \sigma A n_c C_m C_w \tag{13.10}$$

$$F_{HO} = (4.2 \times 10^8 \, (\text{Pa}))(5.02 \times 10^{-10} \, (\text{m}^2)) \times 1.5 \times 1 \times 1.1 \tag{13.11}$$

$$F_{HO} = 0.35 \text{N}$$

The chip thickness, $t_c$, was measured to be $5 \times 10^{-6}$ m; thus, the chip thickness ratio $r$ can be calculated from:

$$r = \frac{t_0}{t_c} \tag{13.12}$$

$$r = \frac{5 \times 10^{-6} \, (\text{m})}{5 \times 10^{-6} \, (\text{m})} \tag{13.13}$$

$$r = 1$$

This allows the shear plane angle, $\Phi$, to be calculated from:

$$\Phi = \tan^{-1}\left(\frac{r\cos\alpha}{1 - r\sin\alpha}\right) \tag{13.14}$$

$$\Phi = \tan^{-1}\left(\frac{1 \times \cos 5°}{1 - 1 \times \sin 5°}\right) \tag{13.15}$$

$$\Phi = 47.5°$$

Based on the works of Bowden and Tabor[10] the coefficient of friction between dry tungsten carbide and low carbon steel (in this case, AISI 1040 steel) is $\mu = 0.78$. This allows the calculation of the force in the vertical orientation, $F_{VO}$, which is given by:

$$F_{VO} = \frac{\mu F_{HO} - F_{HO}\tan\alpha}{1 + \mu\tan\alpha} \tag{13.16}$$

$$F_{VO} = \frac{(0.78 \times 0.35(\text{N})) - (0.35(\text{N})\tan 5°)}{1 + 0.78(\tan 5°)} \tag{13.17}$$

$$F_{VO} = 0.23(\text{N}) $$

The force along the tool face, $F_{AT}$, is given by:

$$F_{AT} = F_{HO}\sin\alpha + F_{VO}\cos\alpha \tag{13.18}$$

$$F_{AT} = (0.35(\text{N})\sin 5°) + (0.23(\text{N})\cos 5°) \tag{13.19}$$

$$F_{AT} = 0.26(\text{N}) $$

The force normal to the tool face, $F_{NT}$, can be calculated by:

$$F_{NT} = F_{HO}\cos\alpha - F_{VO}\sin\alpha \tag{13.20}$$

$$F_{NT} = (0.35(\text{N})\cos 5°) - (0.23(\text{N})\sin 5°) \tag{13.21}$$

$$F_{NT} = 0.33(\text{N}) $$

The force along the shear plane, $F_{AS}$, is given by:

$$F_{AS} = F_{HO} \cos\Phi - F_{VO} \sin\Phi \qquad (13.22)$$

$$F_{AS} = (0.35(N))(\cos 47.5°) - (1.35(N))(\sin 47.5°) \qquad (13.23)$$

$$F_{AS} = 0.069(N)$$

The force normal to the shear plane, $F_{NS}$, is given by:

$$F_{NS} = F_{VO} \cos\Phi + F_{HO} \sin\Phi \qquad (13.24)$$

$$F_{NS} = (0.23(N))(\cos 47.5°) + (0.35(N))(\sin 47.5°) \qquad (13.25)$$

$$F_{NS} = 0.41(N)$$

Since the milling process is being approximated by an orthogonal cutting operation, the milling depth of cut is equal to the width of the chip, $b$. The area of the shear plane, $A_S$, is given by:

$$A_S = \frac{bt_0}{\sin\Phi} \qquad (13.26)$$

$$A_S = \frac{(100 \times 10^{-6} (m))(5 \times 10^{-6} (m))}{\sin 47.5°} \qquad (13.27)$$

$$A_S = 6.78 \times 10^{-10} (m^2)$$

The shear stress, $\tau$, is given by:

$$\tau = \frac{F_{AS}}{A_S} \qquad (13.28)$$

$$\tau = 0.069(N)/6.78 \times 10^{-10} (m^2) \qquad (13.29)$$

$$\tau = 101.36 \times 10^6 (N/m^2) \quad \text{or} \quad 101.36 \times 10^6 (Pa)$$

Similarly the normal stress, $\sigma$, is given by:

$$\sigma = \frac{F_{NS}}{A_S} \qquad (13.30)$$

$$\sigma = 0.41 (\text{N})/6.78 \times 10^{-10} (\text{m}^2) \tag{13.31}$$

$$\sigma = 602.76 \times 10^6 (\text{N/m}^2) \quad \text{or} \quad 602.76 \times 10^6 (\text{Pa})$$

The shear strain, $\gamma$, is given by:

$$\gamma = \frac{\cos \alpha}{\sin \Phi \cos (\Phi - \alpha)} \tag{13.32}$$

$$\gamma = \frac{\cos 5°}{(\sin 47.5°)(\cos (47.5° - 5°))} \tag{13.33}$$

$$\gamma = 1.83$$

The cutting velocity, $V$, at the tool tip is given by:

$$V = r_t \omega \tag{13.34}$$

where $r_t$ is the tool radius and $\omega$ is measured in radians per second:

$$V = (450 \times 10^{-6} (\text{m})) \left( \frac{2\pi}{60 (\text{s})} \times 300{,}000 (\text{rpm}) \right) \tag{13.35}$$

$$V = 14.14 (\text{m/s})$$

The chip velocity, $V_C$, is given by:

$$V_C = \frac{V \sin \Phi}{\cos (\Phi - \alpha)} \tag{13.36}$$

$$V_C = \frac{(14.14 (\text{m/s})) \sin 47.5°}{\cos (47.5° - 5°)} \tag{13.37}$$

$$V_C = 14.14 (\text{m/s})$$

Similarly the shear velocity, $V_S$, is given by:

$$V_S = \frac{V \cos \alpha}{\cos (\phi - \alpha)} \tag{13.38}$$

$$V_S = \frac{(14.14 (\text{m/s})) \cos 5°}{\cos (4.5° - 5°)} \tag{13.39}$$

$$V_S = 19.11 (m/s)$$

In order to determine the strain rate, $\dot{\gamma}$, the shear plane spacing, $\Delta y$, must be determined from chip images – in this case, $\Delta y$ is approximately $1 \, \mu m$.

$$\dot{\gamma} = \frac{V \cos \alpha}{\Delta y \cos(\Phi - \alpha)} \tag{13.40}$$

$$\dot{\gamma} = \frac{(14.14 (m/s)) \cos 5°}{(1 \times 10^{-6} (m)) \cos(47.5° - 5°)} \tag{13.41}$$

$$\dot{\gamma} = 19.11 \times 10^{-6}/s$$

The theoretical scallop height, $h$, which reflects the surface roughness of the side of the cut surface in an end milling operation is given by:

$$h = \frac{f_t^2}{4d} \tag{13.42}$$

$$h = \frac{(5 \times 10^{-6} (m))^2}{4(900 \times 10^{-6} (m))} \tag{13.43}$$

$$h = 6.94 \times 10^{-9} (m)$$

The energy per unit time, $U$, is given by:

$$U = F_{HO} V \tag{13.44}$$

$$U = (0.35 (N)) \times (14.14 (m/s)) \tag{13.45}$$

$$U = 4.92 (Nm/s) \quad \text{or} \quad 4.92 (J/s)$$

The energy per unit volume, $u$, is given by:

$$u = \frac{F_{HO}}{b t_0} \tag{13.46}$$

$$u = \frac{0.35 (N)}{(100 \times 10^{-6} (m))(5 \times 10^{-6} (m))} \tag{13.47}$$

$$u = 695.65 \times 10^6 (Nm/m^3)$$

The shear energy per unit volume, $u_S$, is given by:

$$u_S = \tau\gamma \tag{13.48}$$

$$u_S = (101.36 \times 10^6\,(\text{N/m}^2)) \times 1.83 \tag{13.49}$$

$$u_S = 185.76 \times 10^6\,(\text{Nm/m}^3) \quad \text{or} \quad 185.76 \times 10^{-6}\,(\text{J/m}^3)$$

The friction energy per unit volume, $u_f$, is given by:

$$u_f = \frac{F_{AT}\,r}{b t_0} \tag{13.50}$$

$$u_f = \frac{(0.26\,(\text{N})) \times 1}{(100 \times 10^{-6}\,(\text{m}))(5 \times 10^{-6}\,(\text{m}))} \tag{13.51}$$

$$u_f = 509.88 \times 10^6\,(\text{Nm/m}^3) \quad \text{or} \quad 509.88 \times 10^{-6}\,(\text{J/m}^3)$$

To determine the shear plane temperature, we must utilize the method outlined by Shaw and Loewen taken from Shaw[7]. The process involves several iterations, and for brevity, the final iteration is shown. The initial step is to estimate the shear plane temperature, $\theta_S = 58°C$, and the ambient temperature is $\theta_o = 25°C$. Calculate the average of these two temperatures:

$$\theta_{AV} = \frac{\theta_s + \theta_o}{2} \tag{13.52}$$

$$\theta_{AV} = \frac{58°C + 25°C}{2} \tag{13.53}$$

$$\theta_{AV} = 41.5°C$$

The thermal properties of the workpiece, in this case a low carbon steel, must be determined; Shaw[7] states that these properties are shown in figure 12.25 of his book using nomographs developed for orthogonal machining operations. At 41.5°C, the thermal diffusivity, $K_1 = 1.57 \times 10^{-5}\,\text{m}^2/\text{s}$ and the volume specific heat $\rho_1 C_1 = 3{,}000{,}000\,\text{J/m}^3{°}\text{C}$. Calculate the quantity $R_1$ from:

$$R_1 = \frac{1}{1 + 1.328\left(\dfrac{K_1\gamma}{V t_0}\right)^{1/2}} \tag{13.54}$$

$$R_1 = \frac{1}{1 + 1.328\left[\dfrac{(1.57 \times 10^{-5}\,(\text{m}^2/\text{s})) \times 1.83}{(12.5\,(\text{m/s}))(5 \times 10^{-6}\,(\text{m}))}\right]^{1/2}} \tag{13.55}$$

$$R_1 = 0.54$$

Calculate the quantity $\theta_s - \theta_o$ from:

$$\theta_s - \theta_o = \frac{R_1 u_s}{J \rho_1 C_1} \tag{13.56}$$

where $J$ is the mechanical equivalent of heat, the value of which is quoted from Shaw[7] to be 9340 lbin/BTUs$^2$ for low carbon steel, or 0.99310 Nm/Js$^2$ can be used.

$$\theta_s - \theta_o = \frac{0.54(185.76 \times 10^6\,(\text{J/m}^3))}{(0.99\,(\text{Nm/Js}^2))(3 \times 10^6\,(\text{J/m}^3\,{}^\circ\text{C}))} \tag{13.57}$$

$$\theta_s - \theta_o = 33.53^\circ\text{C}$$

Therefore

$$\theta_s - \theta_o = 58.53^\circ\text{C}$$

Shaw[7] states the process should be repeated until initial estimate produces a shear plane temperature within 3.88°C of the initial estimate. Therefore, in this case the accepted shear plane temperature is 58.53°C. In order to calculate the tool face temperature, it is necessary to estimate the tool face temperature. The initial estimate is 142°C. It is important to determine the thermal properties of the workpiece at this temperature – in this case, a low carbon steel; they are taken from Shaw's[7] figure 12.25. At 142°C, $K_1 = 1.44 \times 10^{-5}$ m$^2$/s, $\rho_1 C_1 = 3{,}862{,}619.8$ J/m$^3$°C. For the macroscale case the chip contact length, $l$, was calculated. However, the cutting velocity, $V$, is used to derive the formula and since it has been established, a chip is not formed at each revolution of the tool. Therefore, applying a formula to find $l$, that is dependent upon $V$, is incorrect. Based on geometrical relationships the chip contact length, $a$, is estimated to be $3.35 \times 10^{-5}$ m. Hence:

$$\frac{m}{l} = \frac{b}{2a} \tag{13.58}$$

$$\frac{m}{l} = \frac{100 \times 10^{-6} \, (\text{m})}{2(3.35 \times 10^{-5} \, (\text{m}))} \tag{13.59}$$

$$\frac{m}{l} = 1.49$$

Using Shaw's[7] figure 12.17, $\overline{A} = 1.2$. Next, the thermal conductivity of the workpiece, $k_S$, at the previously calculated shear plane temperature of 58.53°C must be determined; in this case, $k_T = 6.12 \times 10^{-3} \, \text{J/ms°C}$. This allows $C'$ to be calculated from:

$$C' = \frac{u_f V t_0 \overline{A}}{J k_T} \tag{13.60}$$

$$C' = \frac{(509.88 \times 10^6 \, (\text{J/m}^3))(14.14 \, (\text{m/s}))(5 \times 10^{-6} \, (\text{m})) \times 1.2}{(0.99 \, (\text{Nm/Js}^2))(6.12 \times 10^{-3} \, (\text{J/ms°C}))} \tag{13.61}$$

$$C' = 7.07 \times 10^6$$

Calculate $B'$ from:

$$B' = \left(\frac{0.754 u_f}{J \rho_S C_S}\right)\left(\frac{V t^2}{a r K_S}\right)^{1/2} \tag{13.62}$$

where the subscript $S$ denotes the properties at the previously calculated shear plane temperature of 58.53°C, $\rho_S C_S = 3.86 \times 10^6 \, \text{J/m}^3\text{°C}$ and $K_S = 1.44 \times 10^{-5} \, \text{m/s}^2$.

$$B' = \left(\frac{0.754(509.88 \times 10^6 \, (\text{J/m}^3))}{(0.99 \, (\text{Nm/Js}^2))(3.86 \times 10^6 \, (\text{J/m}^3\text{°C}))}\right)$$
$$\left(\frac{(14.14 \, (\text{m/s}))(5 \times 10^{-6} \, (\text{m}))^2}{(3.35 \times 10^{-5} \, (\text{m})) \times 1 \times (1.44 \times 10^{-5} \, (\text{m}^2/\text{s}))}\right)^{1/2} \tag{13.63}$$

$$B' = 85.38$$

Calculate the quantity $R_2$ from:

$$R_2 = \frac{C' - \theta_S + \theta_o}{C' + B'} \tag{13.64}$$

$$R_2 = \frac{(7.07 \times 10^6) - 58.53(°\text{C}) + 25(°\text{C})}{(7.07 \times 10^6\,(°\text{C})) + 85.38} \tag{13.65}$$

$$R_2 = 0.99$$

Calculate the temperature rise in the chip surface due to friction $\Delta\theta_F$ from:

$$\Delta\theta_F = R_2 B' \tag{13.66}$$

$$\Delta\theta_F = 0.99 \times 58.38 \tag{13.67}$$

$$\Delta\theta_F = 85.38°\text{C}$$

Finally the tool face temperature, $\theta_T$, can be calculated from:

$$\theta_T = \theta_S + \Delta\theta_F \tag{13.68}$$

$$\theta_T = 58.53(°\text{C}) + 85.38(°\text{C}) \tag{13.69}$$

$$\theta_T = 143.91°\text{C}$$

Compared to the initial estimate temperature of 142°C, the error is 1.91°C. Shaw states that the error should be zero. However, since the thermal properties are being determined by graphical means, the error of 1.91°C is considered close enough to a final solution given the inaccuracies in determining values from interpreting various line diagrams.

Shaw and Loewen's method has been used to predict the cutting temperatures. The microscale shear plane temperature is predicted to be 58.53°C and the tool face temperature is predicted to be 143.91°C. These temperatures are not high enough to cause any coating on the tool to oxidize, or to trigger atomic diffusion of the coating elements to migrate into the chips. In addition the theoretical sidewall scallop height for microscale milling is $6.94 \times 10^{-9}$ m.

## 13.2.2 Finite element analysis

Another method available to determine the cutting temperature is to conduct a computational analysis using finite elements. AdvantEdge™ was used to conduct the computational analysis and is specifically designed for metal cutting computations. Third Wave AdvantEdge™ allows improvement

and optimization of machining processes and with it, it is possible to determine optimum machining parameters and tool configurations allowing lower cutting and feed forces and temperature, without spending time and money with experimental processes. To model the thermal-viscoplastic behaviour of the workpiece materials, the software uses a constitutive equation, the Johnson–Cook strain hardening law, which can be represented by the following formula.

$$\sigma_{eq} = (A + B\varepsilon^n)\left[1 + C\ln\left(\frac{\dot{\varepsilon}}{\dot{\varepsilon}_0}\right)\right]\left[1 - \left(\frac{T - T_{room}}{T_m - T_{room}}\right)^m\right] \qquad (13.70)$$

where, $\varepsilon$ is the plastic strain, $\dot{\varepsilon}$ is the plastic strain rate $(s^{-1})$, $\dot{\varepsilon}_0$ is the reference plastic strain rate $(s^{-1})$, $T$ is the temperature of the workpiece material $(°C)$, $T_m$ is the melting temperature of the workpiece material $(°C)$ and $T_{room}$ is the room temperature $(°C)$. Coefficient $A$ is the yield strength (MPa), $B$ is the hardening modulus (MPa) and $C$ is the strain rate sensitivity coefficient; $n$ is the hardening coefficient and $m$ is the thermal softening coefficient. The flow stress curve of the workpiece material is represented by the software values for the low carbon steel used in the present study (the data of the Johnson–Cook law parameters were automatically given by the software). The friction coefficient was obtained using the Coulomb model and was calculated with the following formula.

$$u = \frac{F_f + F_c \times \tan\gamma}{F_c - F_f \times \tan\gamma} \qquad (13.71)$$

where $F_f$ represents the feed force, $F_c$ is the cutting force and $\gamma$ is the rake angle. Both cutting forces were obtained experimentally. There are many different computational options but the pertinent ones include 2D orthogonal cutting, 2D up- or down-milling and 3D up- or down-milling. There is also a micromachining option available for 2D orthogonal cutting that uses a smaller mesh size to account for the reduction in scale if micro- or nanoscale machining is being studied. The workpiece material used in the experiments, that is, AISI 1040 steel, is in the software's material database; similarly the coating database contains TiN and TiAlN coatings. If the material properties of other workpiece materials or coatings are known, they can be added to the database and AdvantEdge™ can compute their effects. However, some of these properties are extremely difficult to measure and are currently unknown. The composition of the TiAlN coating in AdvantEdge™'s database is 50%wtTi:50%wtAl. Table 13.1

| Table 13.1 | Two-Dimensional Computational Parameters Used in Micromachining | | | | |
|---|---|---|---|---|---|
| **Parameter** | **Units** | **2D 3 μm** | **2D 6 μm** | **2D 15 μm** | **2D TiN** | **2D TiAlN** |
| Workpiece height | mm | 0.5 | 0.5 | 0.5 | 0.5 | 0.5 |
| Workpiece length | mm | 5 | 5 | 5 | 5 | 5 |
| Workpiece material | | AISI 1040 | AISI 1040 | AISI 1040 | AISI 1040 | AISI 1040 |
| Cutting edge radius | μm | 3 | 6 | 15 | 3 | 3 |
| Rake angle | degrees | 5 | 5 | 5 | 5 | 5 |
| Relief angle | degrees | 10 | 10 | 10 | 10 | 10 |
| Tool material (carbide type) | | General carbide | General carbide | General carbide | General carbide | General carbide |
| Feed | mm/rev | 0.005 | 0.005 | 0.005 | 0.005 | 0.005 |
| Depth of cut | mm | 1 | 1 | 1 | 1 | 1 |
| Length of cut | mm | 3 | 3 | 3 | 3 | 3 |
| Cutting speed | m/min | 6 | 6 | 6 | 6 | 6 |
| Initial temperature | °C | 20 | 20 | 20 | 20 | 20 |
| Coating | | Uncoated | Uncoated | Uncoated | TiN | TiAlN |
| Coefficient of friction | | 0.78 | 0.78 | 0.78 | 0.4 | 0.3 |

shows the microscale 2D computational parameters. The edge radius for the microscale end milling cutter is $3 \times 10^{-3}$ mm and the feed per tooth is $1.1 \times 10^{-5}$ mm; for milling this is the uncut chip thickness for a single tooth. In this case it is not large enough to form a chip. It is estimated that an uncut chip thickness of $5 \times 10^{-3}$ mm is large enough to cause a chip to be formed. Therefore, a chip is formed approximately every 500 rotations of the tool. Thus, the uncut chip thickness used in the microscale computational simulations is $5 \times 10^{-3}$ mm or 5 μm.

## 13.3 COMPUTATIONAL RESULTS

A unique problem in computing ultra high-speed micromilling effects is that the ratio of the tool edge radius to depth of cut becomes problematic. If the depth of cut is too small a chip cannot form. The ultra high spindle speed means that the feed per tooth, or depth of cut when translated from the 3D machining case to orthogonal cutting, is much less than the tool edge radius. Essentially, simulations using the exact machining parameters can show that no cutting takes place, or if chips are formed, the large tool radius acts as an extreme negative rake angle cutter (Figure 13.1).

In practice, each rotation of the tooth does not form a chip with a negative rake angle. Practically, this leads to numerous rotations of the tool
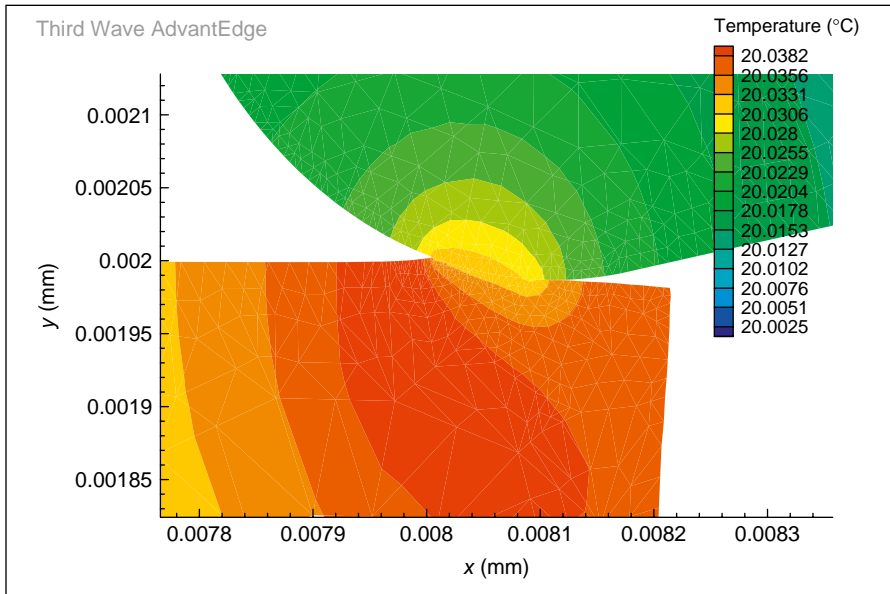
without chip formation, the resulting effect being bending of the tool. During each rotation of the tool, the workpiece advances by a distance equal to the feed per tooth. Eventually, the cumulative movement of the workpiece reaches a critical distance and a chip can form. It has been estimated that a new micro tool with an edge radius of 3 μm has a minimum uncut chip thickness of approximately 5 μm.

## 13.3.1  Uncoated micro tools

The following computations were completed with the macroscale option; the micro-machining option was not selected. Because the micro-machining option is designed for nanometre edge radius tools, the mesh size is much smaller and this drastically increases the computational time. This computation is for a single tooth of the end milling cutter; the computational option chosen is 2D macro up-milling. The edge radius of the end milling cutter used in the macroscale experiments was found to be 3 μm. Figure 13.2 shows the temperature distribution, the output plots of the peak tool temperature and forces produced in the *x* and *y* orientations computed using the edge radius of 3 μm for an uncoated tool. This computation is essentially the control for a new microscale uncoated tool. To account for a worn tool, the edge radius of the tool was increased from 3 μm to 10 μm; all other computational parameters were identical. The results can be seen in Figure 13.3.

*Microscale 2D computation of an uncoated tool, 3 μm edge radius. The solid model temperature distribution and output plots of x- and y-forces and peak tool temperature are evident.*
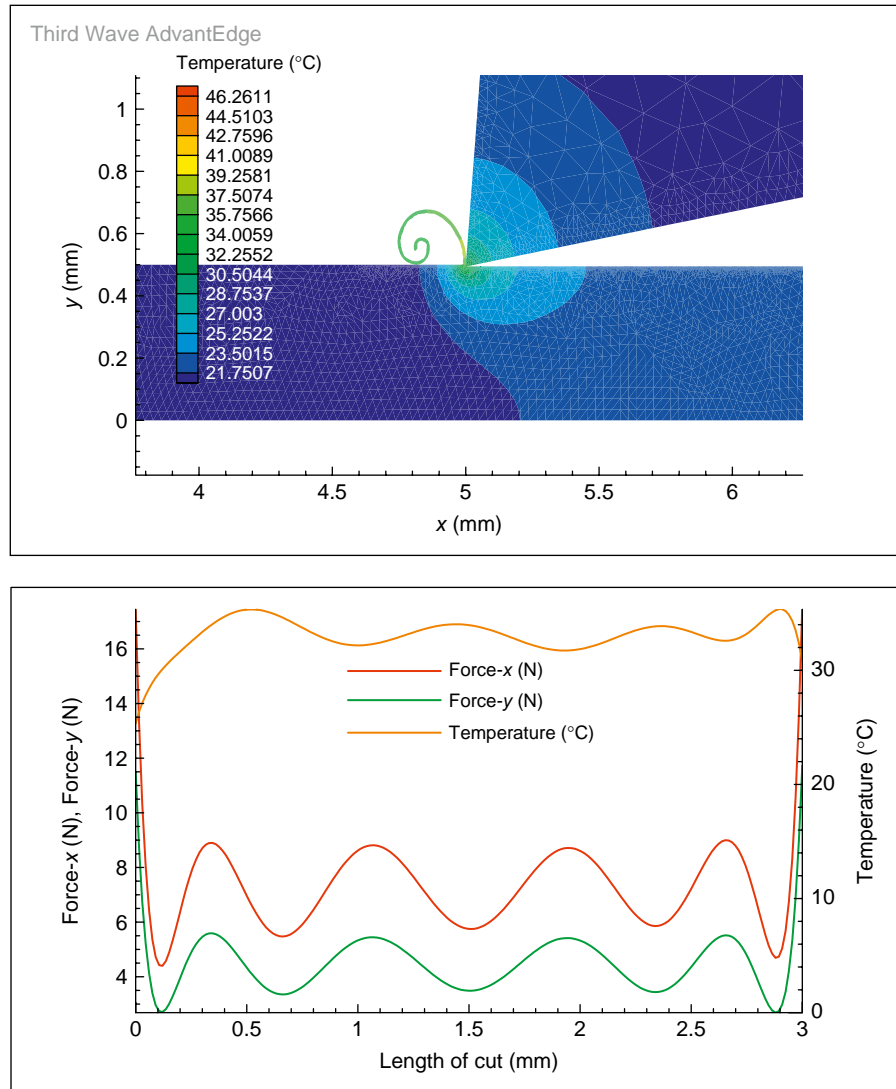


The edge radius of the tool was increased from 3 μm to 20 μm; all other computational parameters were identical. The results can be seen in Figure 13.4.

Initial studies using a thermal camera machining pure metals and 1040 steel indicate that the interface temperature shows an average value of 24.9°C, which shows that finite element generated results are remarkably accurate. The experimental thermal characteristics of machining at such high speeds will be reported in another paper. However, Figure 13.5 shows

*Microscale 2D computation of an uncoated tool 10 $\mu$m edge radius. Output plots of x- and y-forces and peak tool temperature are evident.*

typical output trace from the thermal camera showing the low interface temperatures generated using extremely high machining spindles.

### 13.3.2  Coated cutting tools

To account for a coated tool, the tool was coated with a 4-$\mu$m thick TiN coating and TiAlN coating; all other computational parameters were identical. The results can be seen in Figures 13.6 and 13.7, respectively.
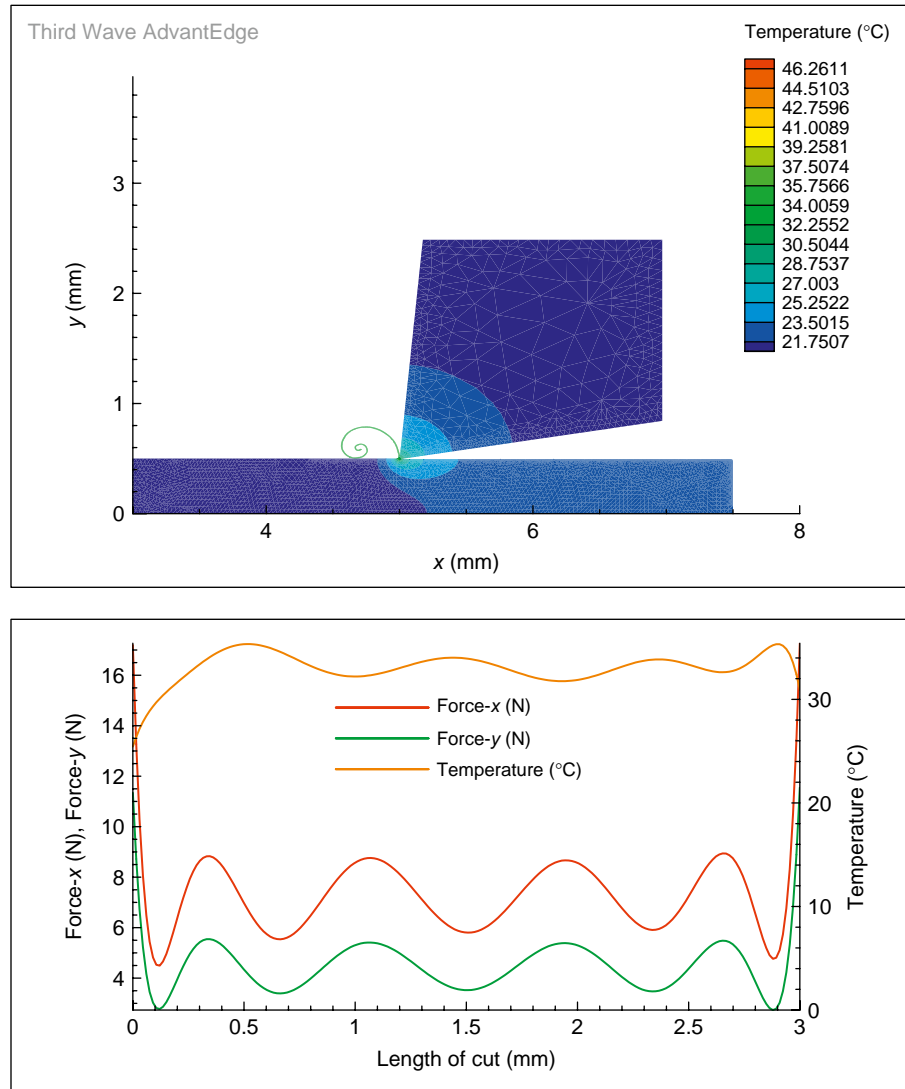
AdvantEdge™ used Tecplot™ to display the computational results shown in Figures 13.2–13.7 and Table 13.2. It can be seen that there is very little variation in the forces or temperatures for any of the computational conditions. Changing the edge radius had virtually no effect on the results. However, the TiN and TiAlN coating did affect the results, but only slightly. The coatings reduced the peak x-force by approximately 4 N but increased the mean force by 1 N to 1.5 N. The peak y-force was about the same for all
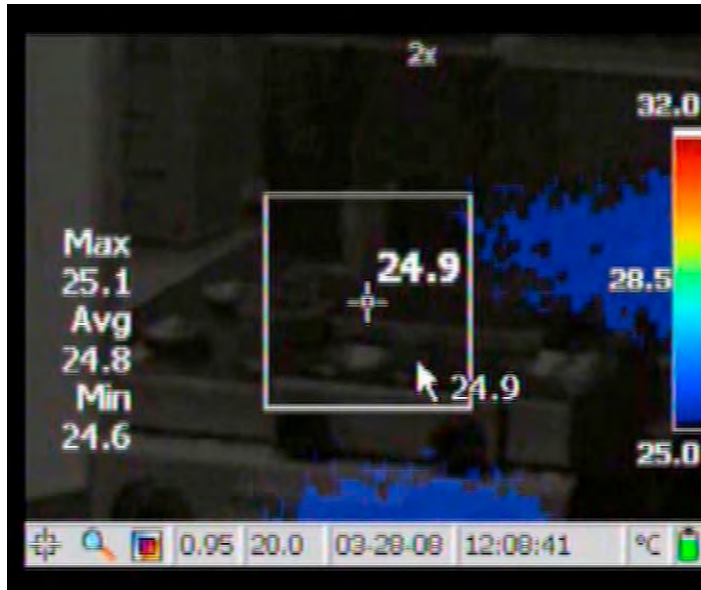
computations, around 4.5 N, but the TiN coating increased the mean *y*-force by 3.6 N and the TiAlN coating by 4 N. The coatings reduced the peak temperature of approximately 35.35°C by 1°C. However, the TiN coating caused the mean temperature of 32.94°C to increase by approximately 0.6°C. There is little variation between the computational results. Therefore, it appears that coatings at the microscale have very little effect.

## 13.4  DISCUSSION

For all computations at the microscale the maximum temperature was 35.35°C, which is well below the oxidation or diffusion temperature for the coating. Since validation of the computations is somewhat difficult at the microscale, pure metals with exact melting points were machined to indicate confidence in using computational results for the cutting temperature. It should be noted that the detailed results of machining pure metals will be reported in a subsequent paper. Initial studies of micromilling pure metals show that the lowest melting point pure metal machined was potassium with a melting temperature of 64°C and there was no evidence of melting. Therefore, it is highly likely that the simulations are accurate. Initial temperature measurements indicated that the maximum temperature at the chip–tool interface is approximately 24.9°C when machining pure metals and 1040 steel with an uncoated tool. Small deposits of each element were

*Microscale 2D computation of a TiN coated tool with a 3 μm edge radius. Output plots of x- and y-forces and peak tool temperature are evident.*
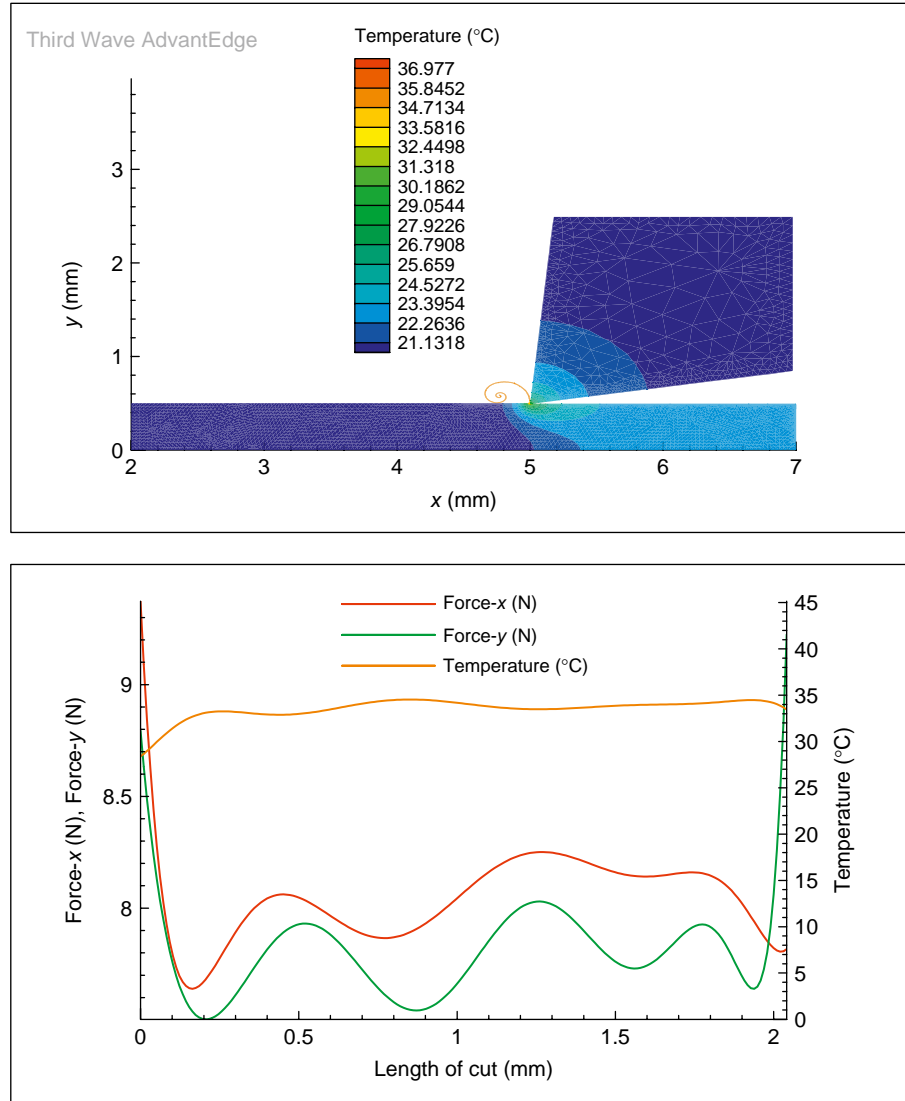


detected on the tool edge, but the adhesion was not very strong and did not block the flutes of the tool to prevent chip evacuation. It is acknowledged that the cutting temperature is dependent on the material being machined, but the machining of pure metals is one more piece of evidence along with the observation of a lack of change in chip colour and the computational analysis in that the cutting temperature in the ultra high-speed machining regime is very low compared to the macroscale. This allows materials
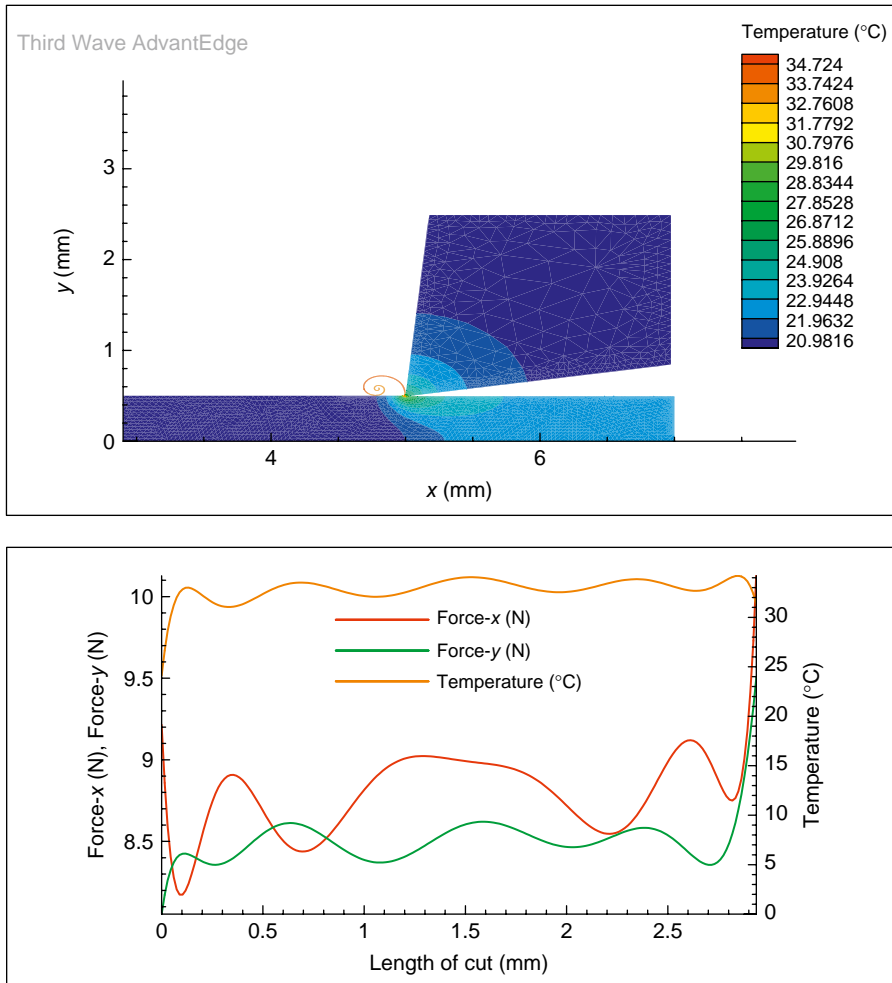
*Microscale 2D computation of a TiAlN coated tool with a 3 μm edge radius. Output plots of x- and y-forces and peak tool temperature are evident.*

to be machined with no heat transferred into the part. This is particularly important for the creation of microscale features where local differences in material properties induced by heat cause the micro part to malfunction, especially due to low fatigue strength. This is a particular problem when micro-machining with pulsed and continuous wave lasers.

An additional consideration when coating micro tools is the increase in the cutting edge radius. When the coating is deposited onto the cutting edge of the tool it reduces the sharpness, and the concern from a coating point of view is that a chip cannot be formed. It has been discussed here and shown by others that in the ultra high-speed machining regime, the feed per tooth is so small that a chip cannot be formed even with a very sharp uncoated

**Table 13.2** Summary of Microscale Computations

| Output | Computation | | | | |
| --- | --- | --- | --- | --- | --- |
| | Uncoated 3 μm | Uncoated 10 μm | Uncoated 20 μm | TiN 3 μm | TiAlN 3 μm |
| Maximum Force-$x$ (N) | 13.41 | 13.41 | 13.27 | 9.37 | 9.21 |
| Mean Force-$x$ (N) | 7.23 | 7.23 | 7.23 | 8.05 | 8.77 |
| Maximum Force-$y$ (N) | 8.81 | 8.81 | 8.72 | 8.79 | 8.62 |
| Mean Force-$y$ (N) | 4.45 | 4.48 | 4.48 | 7.08 | 8.49 |
| Max temperature (°C) | 35.35 | 35.35 | 35.34 | 34.53 | 34.06 |
| Mean temperature (°C) | 32.94 | 32.94 | 32.94 | 33.53 | 32.62 |

tool; this leads to tool bending. Increasing the tool edge radius with the coating exacerbates this effect but does not cause it. Therefore, the problem appears to be concerned with the initial sharpness of the micro tool.

The microscale cutting temperatures calculated by the Loewen and Shaw's[4] method are 58.33°C for the shear plane temperature and 142°C for the tool temperature. Although these temperatures seem realistic compared to the computational analysis and the experimental results, their validity is questionable. One issue with the validity of Isakov's formula is that it has never been proven in the ultra high-speed microscale regime. Another problem is that Ernst and Merchant's[11] and Merchant's[12] approaches were used to determine the cutting forces needed to calculate the temperatures, and that the microscale provides special problems in applying these methods. Ernst and Merchant assume that the workpiece material is perfectly plastic; this cannot be the case at the microscale since the tool is so small that it no longer encounters bulk material properties but the individual properties of the grains, which is known as the size effect. This leads to another violation of Ernst and Merchant's assumption that the tool is infinitely sharp. At the macroscale the tool is relatively sharp and the assumption is valid. However, at the microscale the tool is blunt and the assumption is incorrect. Ernst and Merchant's method is based upon geometrical considerations and should be independent of scale. However, when the microscale shear plane area is calculated, it turns out to be very small; this drastically affects the values of the normal and shear stress. As the shear plane area becomes infinitely small, the shear and normal stress become infinitely high. Therefore, at some point the concept of the shear plane area becomes impractical and the method breaks down. That point is probably not reached in this study but would become problematic if the scale of the cutting tool was reduced further.

As mentioned previously, the approximation that the slip plane spacing is replaced with the shear plane spacing may not be true for milling. The approximation is questioned further since its validation in the ultra high-speed regime is unknown. Nevertheless, the chip thickness and shear plane spacing must be measured. These are both challenging measurements to make at the microscale. The authors believe that the measurements made are correct, but they are taken at the limit of the optical microscope used; further investigation of the chip thickness and shear plane spacing measurements using an SEM would increase the accuracy of the calculations.

Another difficulty in applying Ernst and Merchant's approach is that the uncut chip thickness must be known. Usually, this is calculated from parameters set on the machine tool. However, the very small feed per tooth leads to bending of the tool as discussed by Kim et al.[9] The feed per tooth must accumulate to a sufficient critical value so that a chip can form; this critical value means that the uncut chip thickness is variable. The uncut chip thickness, therefore, was estimated based on geometrical considerations and is one of the main limitations in accurately applying the Ernst and Merchant method. Finally, Loewen and Shaw's method to calculate the cutting temperature requires the determination of the tool–chip contact length. When inspecting images of the chips, there is no evidence to suggest what this length might be, thus making an accurate estimation impossible. Therefore, there are many limitations in applying these calculations at the microscale.

## 13.5 CONCLUSIONS

1. The ratio of the tool edge radius to the uncut chip thickness required to form a chip is unknown.

2. Loewen and Shaw's method of calculating shear plane and tool face temperature appears to be applicable at the first stages of intimate contact between chip and tool.

3. Loewen and Shaw's method of calculating shear plane and tool face temperature does not appear to be applicable under steady-state conditions when the secondary shear zone is firmly established. This is confirmed by the finite element generated calculations.

4. The finite element generated ultra high-speed micromachining cutting temperature when machining AISI 1040 steel is approximately 35°C.

5. There is a need to determine the tool face and shear plane temperatures using experimental methods at very high cutting

speeds. Initial studies show that interface temperatures between tool and chip are approximately 25°C when machining 1040 steel at 310,000 revolutions per minute spindle speed.

## REFERENCES

[1] V.P. Astakhov, On the inadequacy of the single-shear plane model of chip formation, Int. J. Mech. Sci. 47 (2005) 1649–1672.

[2] V.P. Astakhov, S.V. Shvets, M.O.M. Osman, Chip structure classification based on mechanisms of its formation, J. Mater. Process. Technol. 71 (1997) 247–257.

[3] V.P. Astakhov, The assessment of cutting tool wear, Int. J. Mach. Tools Manuf. 44 (2004) 637–647.

[4] E.G. Loewen, M.C. Shaw, On the analysis of cutting tool temperatures, Trans. Am. Soc. Mech. Eng. 76 (1954) 217–231.

[5] P.K. Wright, E.M. Trent, Metallographic methods of determining temperature gradients in cutting tools, J. Iron Steel Inst. 211 (5) (1973) 364–368.

[6] D.A. Stephenson, Assessment of steady-state metal cutting temperature models based on simultaneous infrared and thermocouple data, J. Eng. Ind. 113 (2) (1991) 121–128.

[7] M.C. Shaw, Metal Cutting Principles, second ed., Oxford University Press, Oxford, UK, 2005.

[8] E. Isakov, Engineering Formulas for Metalcutting, Industrial Press, New York, 2004.

[9] C.J. Kim, M. Bono, J. Ni, Experimental analysis of chip formation in micro milling, Technical Paper – Society of Manufacturing Engineers, MR, MR02-159, 2002, pp. 247–254.

[10] F.P. Bowden, D. Tabor, The Friction and Lubrication of Solids, Clarendon Press, Oxford, UK, 1954.

[11] H. Ernst, M.E. Merchant, Chip formation, friction, and high quality machined surfaces, in: Surf. Treat. Met., The Society, Cleveland, 1941, pp. 299–378.

[12] E.M. Merchant, Mechanics of the metal cutting process 1. Orthogonal cutting and a type 2 chip, J. Appl. Phys. 16 (5) (1945) 267–275.

# Metal Oxide Nanopowder

**Taimur Athar**

*Indian Institute of Chemical Technology, Hyderabad (AP), India*

*Nature uses only the longest threads to weave her patterns, so each small piece of her fabric reveals the organization of the entire tapestry.*

Richard Feynman

*I want to build a billion tiny factories, models of each other, which are manufacturing simultaneously…The principles of physics, as far as I can see, do not speak against the possibility of manoeuvring things atom by atom. It is not an attempt to violate any laws; it is something, in principle, that can be done; but in practice, it has not been done because we are too big.*

Richard Feynman

## CONTENTS

## ABSTRACT

Research into soft chemical techniques has gained an importance for the synthesis of high quality advanced nanosized materials with desired properties at the low crystallization temperature. The closer interaction between the material chemists and alkoxide chemists has led to the molecular design of more suitable precursors, for fabrication of functional material has resulted in synergetic developments in both the fields. Metal alkoxide is a versatile

precursor and is used for the synthesis of functional gradient nanomaterials and characterization of materials was carried out in term of composition, microstructure and specific surface area. The write-up provides simple and convenient routes to many building blocks for assembling the structure with novel properties and its functional use in nanotechnology.

## 14.1 INTRODUCTION

During the Stone Age, the material research was limited to the mechanical treatment of natural products. When Dalton discovered atomicity and Mendeleev revealed the periodic table, the research trends drastically changed in the intervening period and research was focussed on fundamental principles of basic molecular structure and simple chemical reactions. During the late twentieth century and the early twenty-first century, an exciting revolution in chemistry has taken place, with multidisciplinary approaches in nanoscience and nanotechnology to the creation of molecules with pre-specified complex structures to perform novel functions. In the present century, research is focussed on control of crystal structures, nanostructures and microstructures with distinct mechanical, electrical, optical and magnetic properties[1–5].

Metal oxides are found in rocks and minerals, where atoms or ions are packed together in a regular fashion. Nature combines hard and soft materials in hierarchical architecture to get a combination of properties with proven and complex functionalities. Since then, man and material science have developed a symbiotic relationship. Metal oxides have emerged as a promising class of new materials whose compositional and structural diversity leads to an array of unique chemical and physical properties[6–14]. Metal oxide materials have attracted significant attention due to their potential applications.

The study of nanomaterials has an interdisciplinary approach with chemistry, physics, material science and engineering science.
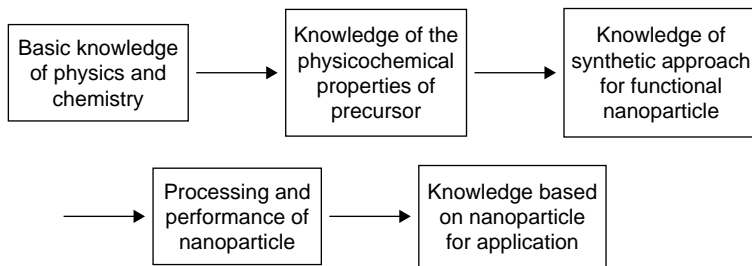


*Knowledge spectrum using combined knowledge of chemistry and physics helps to functionally synthesize nanopowder with favourable particle properties.*
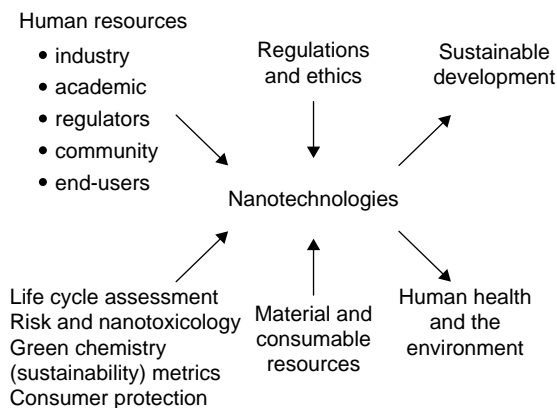
**FIGURE 14.1** *The impact of nanotechnology towards the safety of human health and to the environments.*

The change in the following properties (thermal, mechanical, electronic, magnetic, optical, surface and interfacial) takes place with the particle size and shape. Nanoparticles are very reactive species. Its reactivity is based on particle size and shape and surface-to-volume ratio[15–20]. Nanoparticles are not compatible to human beings and to the environment due to their non-biodegradable nature.

The size-dependent properties of metal oxide nanopowder have generated diverse scientific interest. Their high surface area, shape, surface chemistry and intrinsic properties lead to their use in nanotechnology.

Figure 14.1 gives the impact of nanotechnology towards the safety of human health and environments.

Natural materials can be synthesized at bench level with refined properties for use in modern society. Figure 14.2 outlines the time framework of chemical age. The importance of nanoscience was recognized from the year 2000 onwards.

Metal oxide nanopowder with large surface areas and small particle size has tremendous effects in chemical and mechanical properties due to the presence of electrostatic and electromechanical forces. The quantum-confinement effects have distinct technological use based on size-dependent properties for electronic and optical applications. The cost-effective synthesis of technological-grade nanoparticles needs strict control of the chemical composition, crystalline properties in particle size and shape; while a controlled state of agglomeration and monodispersity is still a long-standing challenge[20–34].
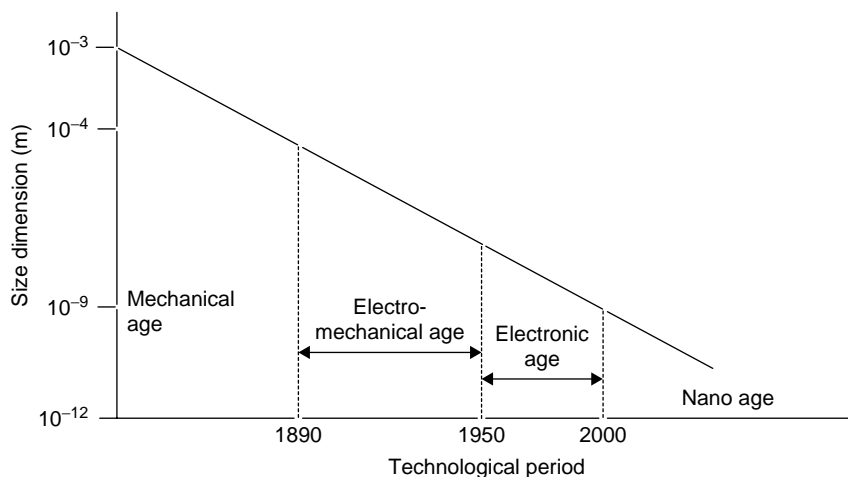
**FIGURE 14.2**  *The time framework of nano.*

The integrated approach of nanomaterials depends on the computational analysis based on the law of quantum physics for synthesis and processing for their successful utility in nanotechnology as illustrated in Figure 14.3.

The design of metal oxide nanomaterials with refined functional, physical or structural properties depends on the conductivity behaviour of metal ion for catalytic and photonic applications as shown in Figure 14.4.

Surface chemistries depend on the electrostatic and intermolecular forces present on the surface of the particle which help them to retain the particle size and shape under control as shown in Table 14.1.

The fabrications of nanodevices with broad spectrum of applications depend on the use of ultra fine powder with favourable properties as shown in Figure 14.5.

The future nanomaterials-based programme has been highlighted as shown in Figure 14.6.

Properties of nanomaterials depend on the ionization potential and electronegativity of the metal ion, which has a characteristic influence on the electronic and surface properties by retaining the stoichiometry,
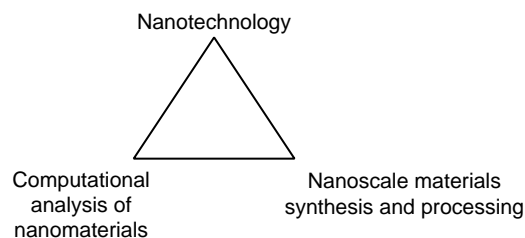


**FIGURE 14.3**  *The integrated approach of nanomaterials.*
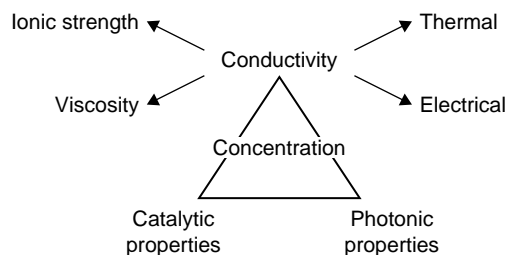


**FIGURE 14.4**  *New science with the help of nanopowder.*

| Table 14.1 | Morphology Control in Parameters and Their Resultant Effects for Their Application |
| --- | --- |

| Parameter to Control Aggregate Size | Application Effects |
| --- | --- |
| Residence time | |
| Pressure | |
| Loading | Rheology |
| Nature of precursor | Optical effects |
| Thermal treatment | Reinforcement |
| Densification | Scratch resistance |
| Surface chemistry | |
| Structure modification | |
| Dispersing energy | |
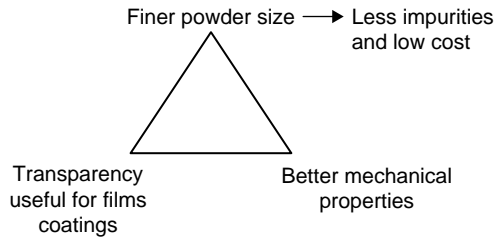


**FIGURE 14.5** *Application of nanopowder.*

**FIGURE 14.6**

*Use of nanotechnology.*
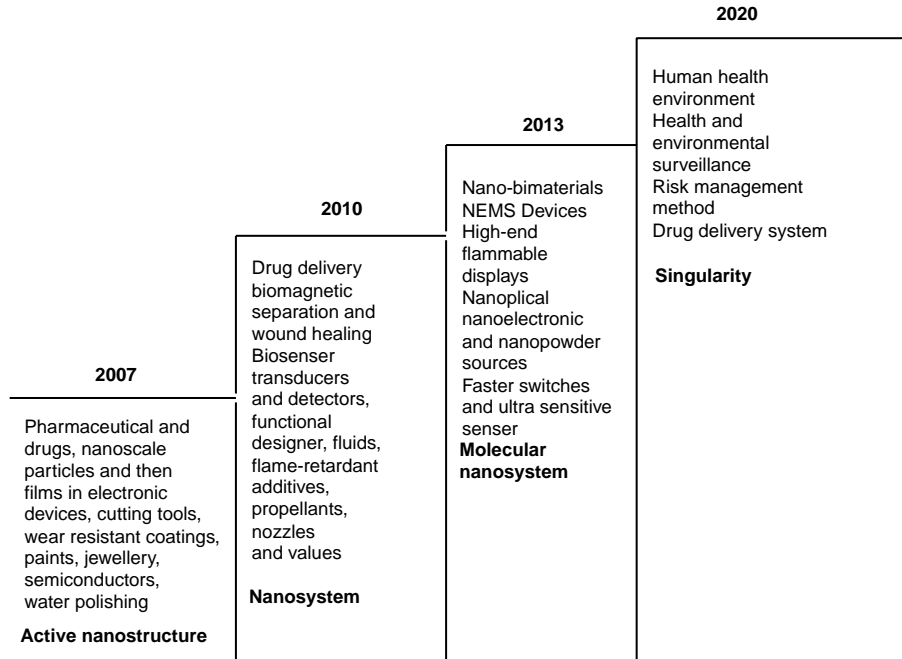
homogeneity and other physico-chemical properties under control as illustrated in Tables 14.2 and 14.3[34–37].

Figure 14.7 gives the importance of green chemistry for the synthesis and its utility for nanotechnology.

| **Table 14.2** | Basic Properties of Metal Oxide Materials |
|---|---|
| 1. Physical properties | → Density and melting point |
| 2. Mechanical properties | → Strength, stiffness, hardness, ductility, toughness and wear resistance |
| 3. Electrical properties | → Resistivity, conductivity and resistance to electrical break down |
| 4. Thermal properties | → Expansivity, heat capacity, thermal conductivity melting point |
| 5. Optical properties | → Refractive index and transmissivity |
| 6. Chemical properties | → Corrosion and solvent resistance |
| 7. Magnetic properties | → Inductor |

| **Table 14.3** | Properties Effected by Decrease in Particle Size |
|---|---|

- The catalytic activity increases
- The mechanical reinforcement increases
- The electrical conductivity of ceramics increases
- The electrical conductivity of metals decreases
- Increase the decrease in magnetic coercivity, finally it is superparamagnetic
- Increase in hardness and strength
- Increases ductility, hardness and formability of ceramics; decreases the sintering and superplastic forming temperature of ceramics
- Increase in blue-shift of optical spectra of nanoparticles
- Increase in luminescence of semiconductors

*Source: Refs [5–9].*
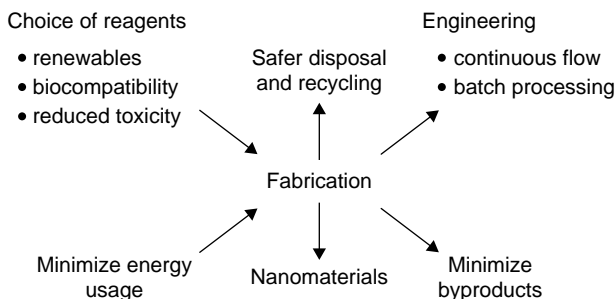


**FIGURE 14.7**   *The importance of green chemistry for the synthesis and its utility for nanotechnology.*

The main objective of metal oxide powder based on high purities, small crystalline size, well-defined particle morphologies and small particle size distribution are as follows:

1. Synthesis of metal oxide with appropriate functionality.

2. Assembly of building blocks into hierarchically organized superstructures.

3. Fabricate particles into nanodevices.

## 14.2 USE OF NANOPOWDERS SINCE THE YEAR 2000

- *Sunscreens and cosmetics*: Titanium and zinc oxide nanopowders are widely used in sunscreens, creams and lotions.

- *Textiles*: Teflon and other polymer nanoscale fibres are used in some stain- and wrinkle-resistant clothing.

- *Coatings*: Custom-made nanocomposites and titanium dioxide nanopowders are used in anti-scratch coatings for lenses and to treat glass surfaces to give them self-cleaning properties. New stretching coatings for walls contain nanoparticles.

- *Explosives, propellants and pyrotechnics*: Aluminium nanopowders are being used to further enhance the burning characteristics of these materials.

- *Catalysts*: The performance is based on surface area – the greater the surface area, the more effective a catalyst will be for the reactions to take place.

- *Electronic storage media*: Hard-disks based on nanostructured magnetic multilayers currently dominate the market.

- *Filtration*: Filters made of nanofibres are used to trap materials such as viruses, bacteria, animal cells, endotoxins and macromolecules such as DNA. They are also used for removing trace toxic metals from water.

- *Disinfectants*: Nanoemulsions and nanoparticles of a lanthanum-based compound are being used in surface disinfectants and to prevent the growth of algae in pools and aquariums.

- *Medical uses*: Silver nanoparticles are used as an antibacterial agent for bandages and in the coatings on hearing aids.

- *Alloys and metals*: Alloys and metals are being produced with nanocrystalline structures to increase their strength.

- *Non-metallic components*: Nanoparticles of diamond are being added as reinforcing agents to rubbers, plastics and resins.

- *Abrasives*: Abrasive waste made from diamond nanopowders are being used for high precision polishing of lenses and mirrors in optical instruments.

- *Lubricants*: The lubricating properties of oils are being improved by the addition of diamond nanopowders.

- *Batteries*: Prototype batteries based on nanoparticles have been developed that offer 10 times the charge rate of conventional rechargeable batteries.

- *Fuel cells*: Nanostructured catalysts are being used as a critical component in making fuel cells. The other impact nanotechnology will have is on the way fuel is stored in the fuel cells.

- *Electronic storage media*: Nanopowder has a promising new type of RAM for computers that would be non-volatile (i.e. the information stored in the RAM would not be lost when the power is turned off) and could have enough capacity to make disc storage unnecessary for applications such as personal computers.

- *Display technologies*: Nanopowder is used in the wall television screen.

- *Bioanalysis and biodetectors*: Nanoparticles, small enough to behave as quantum dots, can be made to emit light at varying frequencies. Efforts to exploit this property for bioanalysis are being pursued by a number of companies. For example, by getting nanoparticles to attach to different molecules and emit different frequencies, it would be possible to spectroscopically determine the presence of many substances in one sample. Nanostructured materials, coupled with liquid crystals and chemical receptors, offer the cheap, portable biodetectors that might be worn as a badge.

- *Drug delivery systems*: Drug delivery is an area that is already showing significant impact of nanotechnology.

| Table 14.4 | Scientific Use and Properties of Metal Oxide Nanopowder | |
|---|---|---|
| **Applications** | **Materials** | **Properties** |
| Packaging/IC substrate | $Al_2O_3$, BeO | High insulation, high thermal conductivity, low permittivity. |
| Capacitors | $BaTiO_3$, Rare earth oxide | High permittivity, low dielectric loss, controllable coefficients of thermal expansion, high breakdown voltages |
| Piezoelectric transducers and surface acoustic wave devices | $PbZrO_3$, $PbTiO_3$, $BaTiO_3$, $LiNbO_3$ | High piezoelectric coefficients, high coupling coefficients |
| Thermistors | $BaTiO_3$ | Change of resistance with temperature |
| Varistors | ZnO | Change of resistivity with applied field |
| Pyroelectric detector | $PbZrO_3$, $PbTiO_3$ | Change of polarization with temperature |
| Electro-optic components | $PbZrO_3$, $PbTiO_3$, $LiNbO_3$ | Change of birefringence with electric field |
| Gas sensors | $ZrO_2$, $SnO_2$ | Ionic conductivity, surface controlled conductivity |
| Display devices | $WO_3$, Pb(LaTi)O, ITO | High contrast images relatively good fatigue characteristics |
| Transparent electrodes | $SnO_2$ | Good transparency, high conductivity. |
| Electromagnetic signature control | $Na_4Zr_2Si_3O_{12}$, $Y_3Fe_5O_{12}$ | Low coefficients of thermal expansion, high temperature stability, high electro-magnetic damping characteristics |
| Solar battery electrodes insulating glass coating | $Cd_2SnO_4$, $SnO_2$, f-doped $SnO_2$ | High current density, good infrared, reflectivity hard |



*Different types of metal oxide nanopowder synthesized at the bench level.*

■ *Use metal oxide nanopowder as a new organ*: The ability to produce stronger structures with required surface properties that are capable to encourage or discourage cell growth or increase biocompatibility in transplantations (Table 14.4).

The nanoparticles are very reactive and the issues related to toxicity are summarized in Figure 14.8.
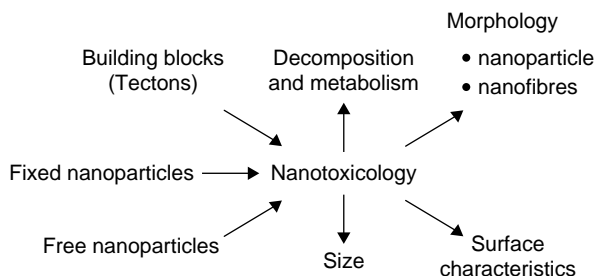
**FIGURE 14.8**   *Issues related to nanoparticle toxicity.*

## 14.3 THE CHEMISTRY OF METAL OXIDE NANOPOWDER
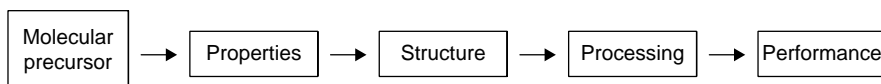


*The five components of the discipline of chemistry and material science and their inter-relationship help to control their properties for their successful use.*

Nanochemistry is a typical bridge between molecular chemistry and physics. A symbiotic relationship exists between the molecular chemistry and new materials.

Molecular chemistry plays an important role in nanoscience for understanding the transformation steps from well-defined precursor to metal oxide. To design molecular precursor with right stoichiometry and physico-chemical properties depends on the use of metal ion. The correct selection of phase purity needs the role of physical science (chemistry and physics). The transition from microparticles to nanoparticles leads to a number of changes in their physical properties such as (1) increase in the ratio of surface area to volume and (2) the size of the particle moving into the realm where quantum effects predominate[36–40]. The change of metal oxide chemistry depends on the synthesis of molecular precursor with favourable structures and with novel properties such as change in dehydration enthalpy, temperature and coordination number[41–43]. The key step to synthesize the ultra pure and highly dispersed powder depends on the physico-chemical properties of molecular precursor with their favourable structural chemistry. A single source precursor may be defined as a molecular compound which on activation changed to a material by retaining all the constituents intact with the help of energy transfer or by reaction with the solvent molecules. Metal alkoxide has pre-existent metal–oxygen bonds that help to synthesize clean nanomaterials with desired properties at low temperature. The intramolecular rearrangement of precursor

leads to the formation of M–O–M novel nanoarchitectural framework. The physico-chemical properties of molecular precursor depend on intermolecular forces such as Van der Waals interactions, $\pi$-stacking or hydrogen bonding[30–40]. Metal alkoxide used in chimie douce process has competitive $\pi$-bonding at the metal centre which can induce $\pi$ donor ligands to adopt a bridging role[41–46]. The properties of metal alkoxides are as follows:

1. The change in electronegativity controls hydrolysis, condensation and other nucleophilic reactions.

2. The greater reactivity of precursor requires strict controls in processing conditions.

3. With the help of alkoxy groups, intramolecular bonding increases which leads to the change of coordination numbers.

4. The metal ion has control in the kinetic properties within coordination sphere.

5. Chemical reactivity is influenced by the degree of aggregation.

6. The nature of oxygen–metal bond affects structural properties.

7. Stability and solubility in organic solvent with limited sensitivity towards moisture.

Metal alkoxide guarantees **homogeneous dispersion of metal source at** the molecular level and thus provides uniform reaction sites for their conversion into the metal oxide materials at nanoscale. Lewis acidity of the central metal ion plays a central role in moderating properties in nanomaterials[41–45].

Geometric, chemical and electronic information is necessary for establishing the relationship between the precursor and nanomaterials, and their useful utility in a wider sense and to better understand their functional properties as shown in Figure 14.9[46–50]. The nanomaterial requires flexible routes for their technological use based on the bottom–up approach. The growth in nucleation plays a very important role on the synthesis of nanomaterials with required properties. Nucleation process can be classified as (1) primary and (2) secondary growth which is induced by crystal seed.
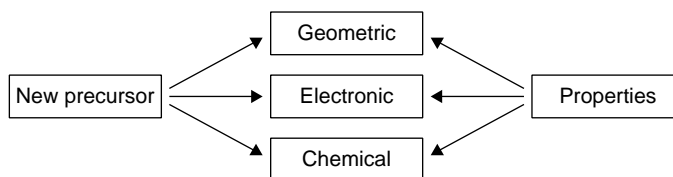


**FIGURE 14.9**

Homogeneity depends on the matching stoichiometry at a molecular level between the precursor and resulting material[41–45]. The single source molecular precursor helps to generate activation energy for the synthesis of nanomaterials with refined properties[30–31]. Particles encounter with other particles in the growing process due to their active surface energies leading to the formation of agglomerated particles with heterogeneous phase properties with poor solubility. The exact mechanism for the formation of nanomaterials from synthons is not fully understood. The increase in particle size leads to change in morphology and crystalline structure via Ostwald ripening process. Depending on the application of the nanoparticle, dispersant chemistry plays an important role at a particular pH for processing highly stable, concentrated aqueous dispersion of technological-grade nanopowder to retain the electrostatic charge and with surface reactivity under control[51–53].

### 14.3.1 Important behaviour of metal oxide nanopowder

1. As grain size decreases, the physico-chemical properties of nanomaterials changes, along with an increase in total surface area and the increase in total grain volume relative to unit structure.

2. Having discrete electronic levels (quantum behaviour) changes the electrical and optical properties of nanomaterials as the grain size approaches at the molecular scale.

### 14.3.2 Criteria for the synthesis of metal oxide

Better understanding and manipulating the properties of particles for their technological use is an active area of research in nanoscience. The size-dependent properties of nanoparticles have generated diverse scientific interest as illustrated in Figure 14.10. The synthesis, structure, properties and performance of molecular precursors have their interlinked approach in
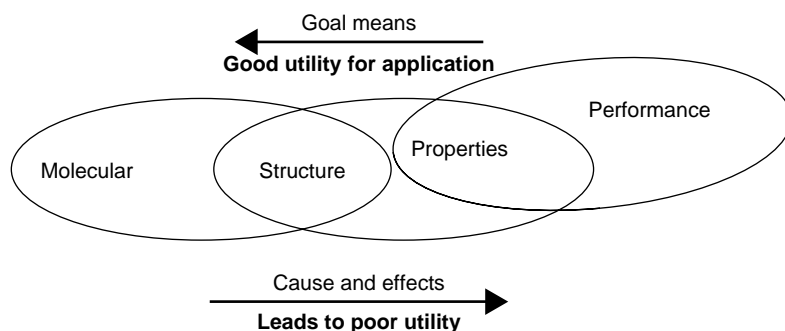


**FIGURE 14.10** *Synthesis of molecular precursor, structure, properties and performance.*

nanotechnology. Defect in any of these links causes its non-utility due to heterogeneous phase related properties. It is concluded that the morphology of the powder and the properties of the final materials strongly depend on the chemical composition and the experimental conditions used in the synthesis.

The following properties have to be controlled for the synthesis of nanopowder:

- Based on the properties of precursor to design functional particle size with morphology and crystallinity.

- Control of degree of crystallization with functional utility.

- To retain the chemical composition from its use of precursor at molecular level to nanomaterials at the nanoscale.

- Surface reactivity depends on the homogeneity of powder at the nanometre scale and the reaction time.

The objective for the synthesis of nanopowder depends on its use in nano-technosphere. Therefore, the synthesis of new nanopowder based on 'bottom–up' approach is a new methodology for synthesizing and characterizing chemical structures within the size range of about 1–100 nm in one, two or three dimensions by retaining the well-defined stoichiometries. Dimensionality is a crucial factor in determining the properties of nanomaterials which itself depends on the control over particle size and shape for their functional use. The self-assembly of functional components takes place into well-defined crystalline materials based on structure–properties relationship. Figure 14.11 illustrates the use of two types of precursor used for the synthesis of nanopowder by different methodology.



**Liquid precursor**

Coprecipation, Alkoxide, Emulsion
Combustion, Microemulsion and
solvothermal method

Hydrothermal
Sol–gel method

Oxalate method
Citrate method

**Solid precursor**
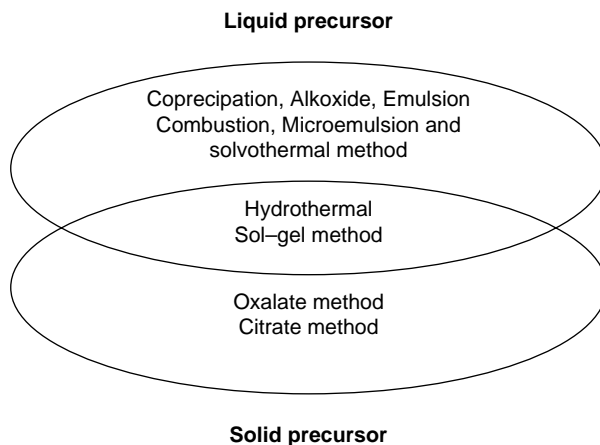
**FIGURE 14.11**   *Synthetic route for the preparation metal oxide nanopowder.*

To establish the formation of metal oxide nanopowder with controlled properties, we have to follow the steps shown below.
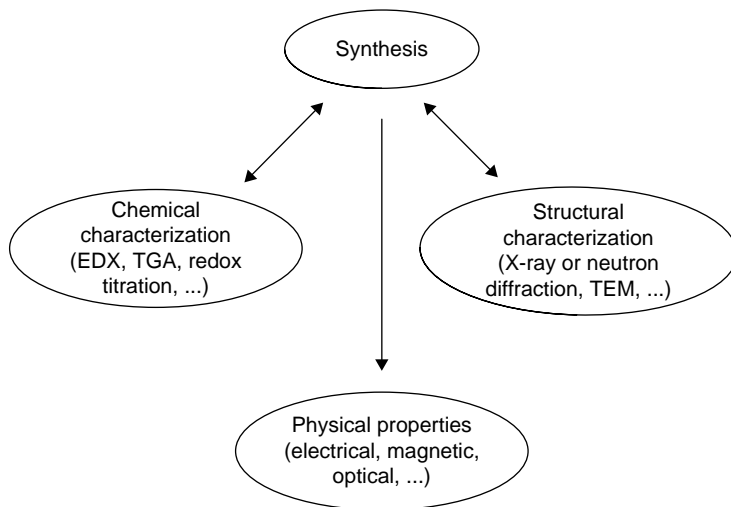


1. Selection criteria for the nano system
   - interest for industry;
   - availability to synthesize the nanosized powders, that is from the raw materials group or directly from the processing group;
   - nature of the matrix and the dispersed phase, that is oxide–oxide or oxide–non-oxide, particle–particle or fibre–particle;
   - interaction between matrix and dispersed phase, that is chemical interaction or physical interaction (thermal and elastic).

2. Materials to be selected on the basis of the following criteria:
   - interest for industry, easy synthetic methodology;
   - availability of precursors and without toxicity;
   - high yield with high purity for synthetic routes;
   - interest and expertise of the partners in handling and processing.

The main aspects to be considered for the improvement of processing techniques are:

■ *Conditioning of nanopowders surface* to avoid particle agglomeration.

■ *Development of powder treatment methods* for the dispersion of the second phase and for the introduction of sintering aids.

- *Development of forming techniques* to produce green shapes, aiming at the possibility to produce complex-shaped components as required by industrial applications.

- *Development and improvement of densification techniques* using processing parameters (temperature, atmosphere, pressure) which allow the attainment of the desired shape.

### 14.3.3 Requirements for the synthesis of nanoparticles

The requirements for the synthesis of nanoparticles are as follows:

- Single step leads to monodispersity with non-agglomerated grain properties.

- Environmentally benign approach for the large-scale production with time saving.

- Cost-effective and reproducible process with refined properties and high yield.

- Chemical reactivity of particle size leads to agglomeration due to high surface energy.

The **homogeneous solution leads to monodispersity. The formation** of **homogeneous particles takes place when all nuclei and growth occurs** simultaneously during reaction time.

The heterogeneous property leads to polydispersity. The formation of heterogeneous particle takes place when all nuclei and growth takes place at different time during reaction.

### 14.3.4 Controlling factors for the growth of nanopowder

1. Molecular precursor with correct physico-chemical properties.

2. Kinetics of nucleation and growth in synthetic process.

3. Concentration of the stabilizing agent.

4. Structure of the stabilizing agent.

5. The pH and temperature of the reaction medium.

The synthesis of nanopowder takes place in the following two synthetic routes as shown in Table 14.5.

Table 14.6 illustrates the bottom–up approach based on molecular precursors.

| Table 14.5 | The Composition, Size and Shape Along with Surface Properties of the Nanoparticles Determine the Synthetic Methodology |
|---|---|
| **Top-Down** | **Bottom-Up (Molecular Nanotechnology)** |
| Mechanical attrition lithography etching | Powder/aerosol compaction chemical synthesis sculpt from bulk assemble |

| Table 14.6 | Bottom-Up Approach Synthetic for Nanopowder |
|---|---|
| **Low Temperature (Wet Synthesis) (<250°C)** | **High Temperature (Dry Synthesis) (>250°C)** |
| Mechanical attrition | Gas condensation |
| Replication method | Wire explosion |
| Chemical precipitation | Liquid aerosol thermolysis |
| (a) Hydrothermal synthesis | |
| (b) Inverse micelle method | |
| (c) Sol–gel synthesis | |
|     (1) Hydrolytic sol–gel | |
|     (2) Non-hydrolytic sol–gel | |

Synthesis of nanomaterials is not simple due to their thermodynamic and kinetic tendency of particle to agglomerate into bulk particles due to high surface energies. For the synthesis of nanomaterial, it is necessary to know the mechanism for the change of molecular precursor to their final materials. The soft chemical approach in nanoscience leads to the synthesis of fairly monodispersed nanoparticle and the non-aggregated nanoparticle is no longer a constraint for bulk production in material science.

The synthesis of advanced materials requires a strict control in stoichiometries with controlled particle size and shape to their design novel nanoarchitecture with functional gradient properties in nanomaterials. To tailor the properties in precursor, by soft chemical approach for the synthesis of technological-grade nanoparticles with favourable properties, is a challenge to material scientist. The structural–functional relationship plays an important factor in designing the cost-effective synthesis with the ability to retain well-defined stoichiometries and properties in nano-devices, from the molecular precursor at molecular scale to nanomaterials at nanoscale[1–7, 54–64]. So, it is necessary to synthesize a new protocol synthon for single source that is capable of retaining all the elements for controlling the desired properties in the solid state material framework at the atomic level.
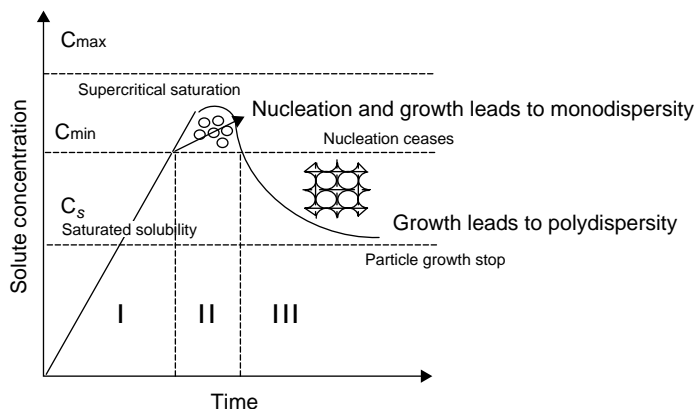
**FIGURE 14.12** *Once the nucleus is formed the growth starts.*

Figure 14.12 highlights how to control the particle size and shape with nucleation in relation to the concentration of solute with time.

## 14.4 DIFFERENT METHODS USED FOR THE SYNTHESIS OF METAL OXIDE NANOPOWDER

### 14.4.1 High temperature synthesis

(a) In wire explosion method
The metal wire is melted or vaporized explosively by the application of pulsed current.

The liquid *aerosol thermolysis* involves the decomposition of aerosolized solution in high temperature.

(b) Gas condensation
It is one of the first techniques used to synthesize nanocrystalline materials. In this technique, the precursor is vaporized by using thermal evaporation source in the presence of gas atmosphere with pressure ranging from 1 to 50 mbar. In gas evaporation process, a presence of high residual gas pressure helps in the formation of ultra fine particle by collision. This method is extremely slow due to source–precursor incompatibility, and dissimilar evaporation rates with respect to temperature pressure are some of the drawbacks.

(c) Vacuum deposition process
In this process, the precursor is vaporized and deposited in a vacuum chamber. The synthesis was carried out at pressure of 1 mtorr retaining the

vacuum level at $10-0.1$ MPa with temperature ranging from room temperature to 500°C. Vapour phase nucleation takes place in dense cloud vapour by collision. The atoms are passed through a gas to provide necessary collision and cooling for the nucleation. It is economical and the deposition rate is high. In this process, the decomposition of the precursor is sometimes difficult. The nanoparticles obtained from a supersaturated vapour are usually longer than the cluster.

(d) Chemical vapour deposition

A substrate is deposited on a heated surface via a chemical decomposition from the vapour or gas phase used as a molecular precursor at reduced pressure.

With the downsizing method, the synthesis of nanomaterials helps to control the size, morphology and compositional distribution at the nanometre level. The application of nanomaterials depends on the ability to disperse the particle in a fluid with compatible phase properties.

### 14.4.2  Low temperature synthesis

Table 14.7 illustrates soft-chemistry approach for the synthesis of metal oxide nanopowder with advantages and disadvantages.

### 14.4.3  Replication method

The synthesis was carried out in the microspores and mesopores with crystalline or amorphous materials.

### 14.4.4  Mechanical attrition

During the preparation of the nanoparticles, high energy is used for the reduction of the particle size from coarse-grained materials. The powder obtained has both the nanocrystalline particles and coarser particles. During the mechanical process, it is impossible to get defect-pure nanocrystal free from contamination. The contamination takes place from the reactor. The process is simple and both energy and time efficient.

### 14.4.5  Hydrothermal synthesis

This process involves the reaction between heterogeneous phases below supercritical temperature of water. Hydrothermal synthesis depends on the solubility of minerals in hot water in a high pressure autoclave. This process gives good quality of nanopowder with correct chemical composition thereby providing the best mechanism to understand the interaction

| Table 14.7 | Methods Used for the Synthesis of Nanopowder Based on Wet Chemistry Along with Advantages and Disadvantages | |
| --- | --- | --- |
| **Methods** | **Advantages** | **Disadvantages** |
| Sol–gel | (a) Large scale up area<br>(b) Precise control on composition<br>(c) Low temperature is required<br>(d) High homogeneity is obtained<br>(e) Required product obtained<br>(f) Simple process treatment | (a) Sensitive towards atmospheric condition<br>(b) Raw material expensive<br>(c) Sometimes toxic solvents are used<br>(d) Limited to bench level |
| Hydrothermal synthesis | (a) No heat treatment is required<br>(b) Less energy consumption<br>(c) No milling process less impurity<br>(d) Complex chemical composition is obtained<br>(e) Controlled particle size and shape<br>(f) Cheap raw material<br>(g) Environmental benign<br>(h) Large scale industrial production | (a) Aggregation rate is high<br>(b) Chemical contamination due to corrosion<br>(c) High cost equipment<br>(d) Stringent safety precautions |
| Solvothermal synthesis | (a) Narrow size distribution<br>(b) Monolayer ligand coating required<br>(c) Absence of aggregation in polymer matrix<br>(d) Crystallization rate is high | (a) Difficult for mass production<br>(b) High cost<br>(c) Complicated processing treatment |
| Plasma process | (a) High temperature controls high activity, rapid chemical reactions and less processing time<br>(b) Rapid quenching<br>(c) Controlled atmosphere maintained | (a) Bulk processing is limited |
| Mechanical attrition | (a) Simple and energy efficient | (a) Contamination from equipment<br>(b) Particle size and shape difficult to control |

between the solid–fluid phase at high reaction temperature for controlling the phase properties at high pressure. The material was dissolved and then cooled which helped in growth of the particle at high pressure and temperature.

Hydrothermal synthesis is of two different types: (1) microwave hydrothermal and (2) microwave solvothermal.

## 14.4.6 Inverse micelle method

The synthesis of particle takes place in a microheterogeneous environment in the presence of oil and surfactant. The dispersed nanodrop formed acts

as a stable phase in a microreactor and then dispersed in a second phase known as continuous phase which is used for the preparation of nanomaterials with phase selection.

### 14.4.7  Sol–gel process

It is a versatile approach which helps to develop a novel methodology for the synthesis of high purity nanopowder with controlled microstructure and surface properties. The sol–gel process is the best method for synthesizing high purity advanced materials with control in the microstructure and surface properties. Later on, these materials can be processed into monoliths, fibres, thin film and porous gel. The gel is sensitive to their physico-chemical environments. The conventional sol–gel process is based on liquid-phase hydrolysis and condensation reactions of molecular precursors. Metal alkoxides requires low processing temperature for fabrication of nanomaterials with required phase selection with correct stoichiometric ratio. The nanopowder has multiple applications for technological use due to its high flexibility and tolerance to the processing chemistry. These nanomaterials can be deposited in a wide range of substrates[53–64]. The sol–gel process takes place in two conditions:

1. *Aqueous sol–gel process*: It is an economical and ecological process. Agglomeration is a major drawback.

2. *Non-aqueous sol–gel process*: It is expensive with limited ecological and agglomeration properties.

*The efficient use of sol–gel process for the synthesis of self-assembled structure and the degree of ordering patterns depends on the following parameters.*

■ The nature of metal alkoxide

■ pH of the solution

■ The ratio of water/alkoxide in solute

■ Reaction temperature

■ Nature and polarity of the solvent and stabilizers

■ The rate of solvent evaporation

■ Ageing time with solvent and pH conditions

■ Concentration of the nanocrystals

Uniform mixing at the molecular level leads to the formation of sol with the help of metal alkoxide or with their allied derivatives. The sols are
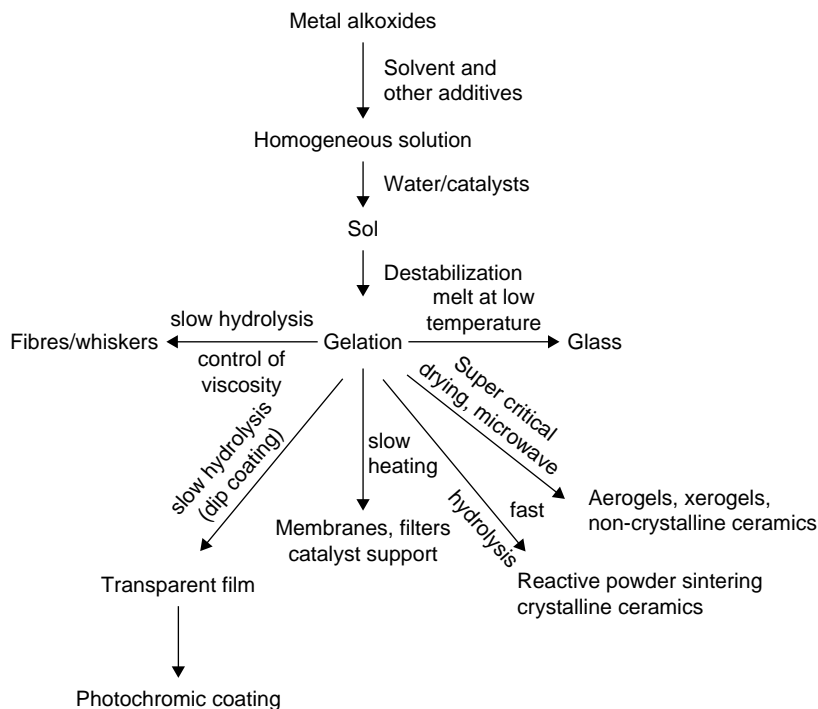
**FIGURE 14.13**  *The stages of the sol–gel process.*

extremely sensitive to pH, ionic strength, temperature and concentration and this leads to aggregation. The self-assembly takes place with the help of coulomb interactions between the colloidal structures and surfactant chemistries[58–64]. The harsh conditions are required for nanoparticle preparation with the functionalizing of nanoparticle surface which involves stripping off non-functional ligands and then redispersing the particles with functionalized ligands. In general the sol–gel process takes place in three stages: (1) formation of particles with polymerization of precursor (2) growth of particles with the help of chain network and (3) formation of gel.

The graph shown in Figure 14.13 illustrates the various steps involved in the synthesis of nanopowder via sol–gel process.

Figure 14.14 shows the modification in the sol–gel process to improve the properties of nanopowder.

### 14.4.8 General mechanism for sol–gel process

The reaction takes place in the following steps to synthesize nanomaterials with high compositional homogeneity. Sometimes, on heating, every
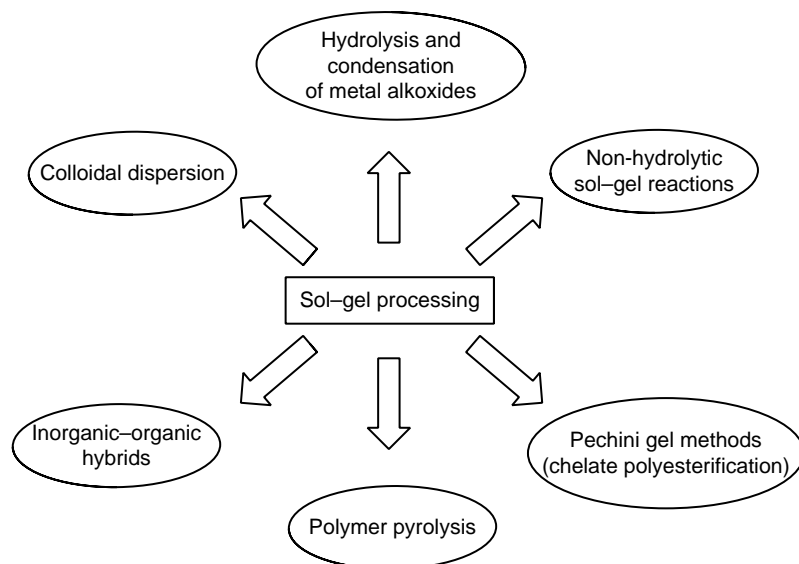
alkoxide molecule is subjected to hydrolysis leading to the formation of partially hydrolysed alkoxide molecule or to the formation of a large amount of unhydrolysed alkoxide groups with polarized species due to their ionic nature of the solvents medium[53–58].

(a) Hydrolysis (forward reaction), esterification (reverse reactions)

$$MOR + H_2O \rightleftharpoons MOH + ROH \qquad \textit{Hydroxylation}$$
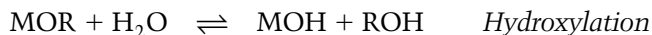
(b) Alcohol condensation (forward reaction) alcoholysis (reverse reactions)

$$MOR + HOM \rightleftharpoons MOH + ROH \qquad \textit{Oxolation}$$

(c) Water condensation (forward reaction) hydrolysis (reverse reactions)

$$MOH + HOM \rightleftharpoons MOM + H_2O \qquad \textit{Olation}$$

## 14.4.9  Acid-catalysed mechanism

The alkoxy group is protonated with electron density from metal atom making it more electrophilic and more susceptible to attack from water leads to the formation of transition state with SN-2 type reaction.
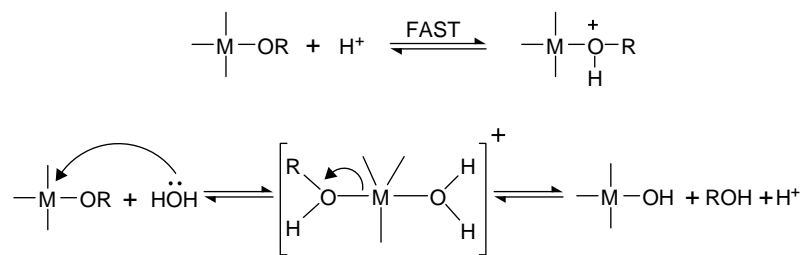
**Acid-catalysed hydrolysis**

**Base-catalysed mechanism:**

$$H_2O \rightleftharpoons H^+ + \ddot{O}H$$
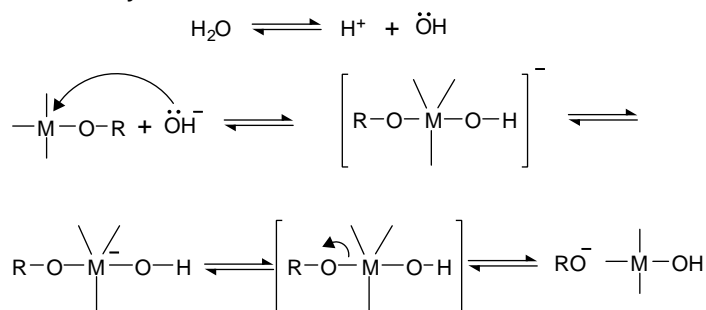


**Base-catalysed hydrolysis**

Base-catalysed hydrolysis reaction of an alkoxide proceeds much slower than acid-catalysed hydrolysis. Once hydrolysis has taken place, the reaction proceeds gradually. It is also nucleophilic SN-2 type of reaction.

Figure 14.15 illustrates visible properties of silver nanoparticles with different grain size at different pH.

Figures 14.16 and 14.17 highlight the flow chart for the synthesis of nanopowder.
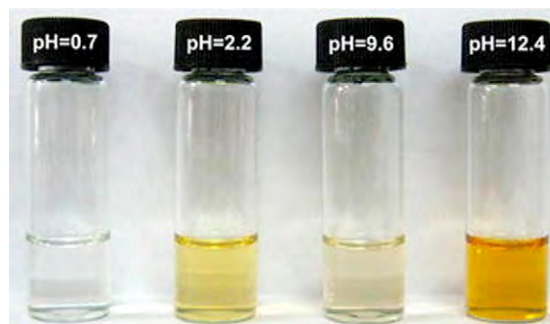


**FIGURE 14.15**  *Silver nanoparticles prepared from sol–gel process.*

Figure 14.18 shows the application of technological-grade nanopowder prepared by sol–gel process.

The quantum size effects relates to dimensionality of the system in the nanometre range.

Figure 14.19 highlights the phase selection properties along with their applications.

Tables 14.8–14.10 depict the illustrative use of metal oxide nanopowder prepared by sol–gel process.

The non-hydrolytic sol–gel process involves the reaction of a metal halide or metal alkoxide with organic ether acting as oxygen donor under non-aqueous conditions to form an inorganic oxide framework with refined properties
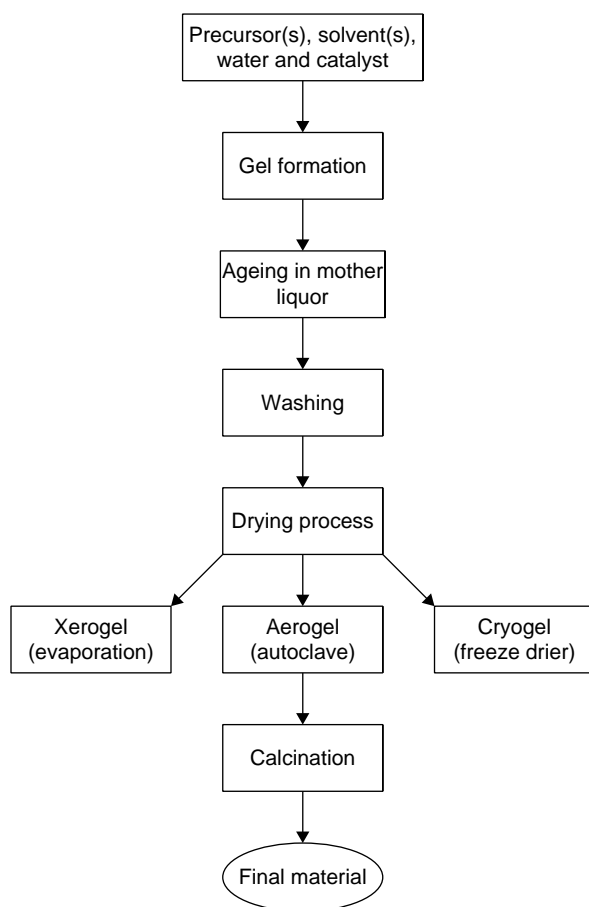


**FIGURE 14.16**   *Sol–gel and drying flow chart. The aging and washing steps are optional.*
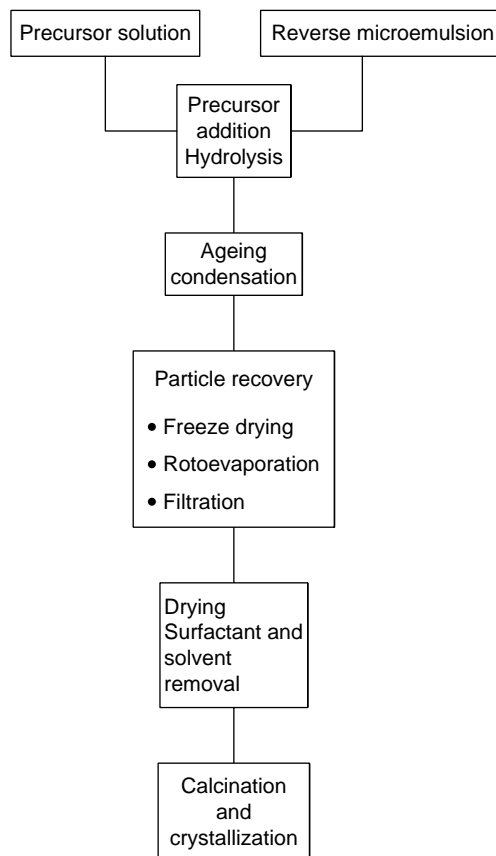


**FIGURE 14.17**   *Reverse microemulsion – sol–gel processing.*
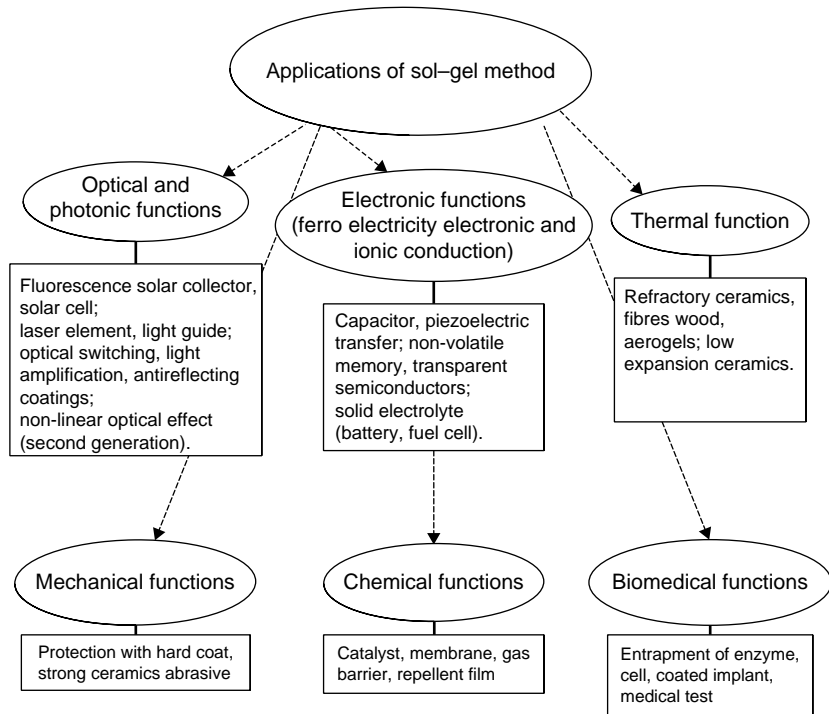
**FIGURE 14.18** *Application of the technological-grade nanopowder prepared by the sol–gel process.*



**FIGURE 14.19** *Properties and applications by sol–gel process.*

**Table 14.8** Electronic Materials prepared by Sol–Gel Processing

| Type of Material | Applications | Example |
|---|---|---|
| High-Tc-superconductors Dielectrics | Thin film/bulk devices capacitors, sensors, phase shifters, dynamic RAMs | $YBa_2Cu_3O_7$, $BaTiO_3$ |
| Piezoelectrics | Acoustic transducers, wave guides, nonlinear optics, micro-actuators | $PbZrO_3$, $PbTiO_3$, $LiNbO_3$ |
| Pyroelectrics | Pyrodetectors | $PbTiO_3$ |
| Ferroelectrics | Non-volatile memories | $PbZrO_3$, $PbTiO_3$ |

**Table 14.9** Optical Applications of Electronic Materials via Sol–Gel Process

| Optical Effects | Applications | Compositions |
|---|---|---|
| Light transmission | Optical wave guide | $PbO–SiO_2$, $SiO_2–TiO_2$, $Na_2O–B_2O_3–SiO_2$, $SiO_2$ |
| Optical absorption | UV shielding optical absorption colouration of glass | $TiO_2–SiO_2$, $Fe_2O_3$, $CoO$, $NiO$ $SiO_2$ + transition metal oxide, $CeO_2–TiO_2$, $GeO_2–V_2O_5$ |
| Interference | Colouration | $TiO_2$ |
| Reflection | Radiation shield reflecting solar energy | $In_2O_3–SnO_2$, $VO_2–SiO_2$, $PbO–TiO_2$, $Bi_2O_3–TiO_2$ |
| Anti-reflection | Increase of damage threshold of fusion laser glass, clear vision | $Na_2O–B_2O_3–SiO_2$, $SiO_2–TiO_2–SiO_2$ |
| Fluorescence | Optical shutter switch optical IC luminescent solar concentrator laser displays | $SiO_2$, $LiNbO_3$ $SiO_2$ doped with organics $Al_2O_3$ with organic dyes |
| Electrochromism | Displays transparent electrode for ion passing | $WO_3$ $CeO_2–TiO_2$ |
| Patterning | Optical RAM disk | $B_2O_3$, $TiO_2$, $ZrO_2–SiO_2$ |

**Table 14.10** A Classification of Heterogeneously Catalysed Reactions

| Class of Materials | Types of Reactions | Examples | Types of Catalyst |
|---|---|---|---|
| Semiconducting oxides | Oxidation | $CH_4 \rightarrow C_2H_4$ $C_6H_6 \rightarrow CH_2=CH–CHO$ $nC_4H_{10} \rightarrow C_4H_6$ $SO_2 \rightarrow SO_3$ | $MgO$, $CuO$, $NiO$, $MnO_2$  Fe–Mo oxide $Na_2O$, $V_2O_5$ |
| | Redox | $NO + NH_3 \rightarrow N_2 + H_2O$ $CO_2 + H_2 \rightleftarrows CO + H_2$ | V–Mo–Ti oxide $Fe_3O_4–Cr_2O_3$ |
| | Reduction | $C_2H_4 + H_2 \rightarrow C_2H_6$ $CH_3COOH \rightarrow C_2H_5OH$ | $ZnO$, $Cr_2O_3$ $CuCr_2O_4/$, $ZnCr_2O_4$ |
| Sulphides | Hydrodesulphurization | $\langle\!\!\!\langle\,\rangle\!\!\!\rangle$ S | Co–Mo/$Al_2O_3$ |
| Insulater | Polymerization | $C_3H_6 \rightarrow (C_3H_6)_n$ | $SiO_2–Al_2O_3$ |
| | Dehydrogenation | $C_2H_5OH \rightarrow (C_2H_5)_2O + C_2H_4$ | $Al_2O_3$ |
| | Isomerization | $nC_4H_{10} \rightarrow Iso\text{-}C_4H_{10}$ | $SiO_2–Al_2O_3$ |

with the liberation of volatile alkyl halide as side product. The synthesis of nanomaterials takes place at moderate temperature and pressure via chimie douce leads to high crystallinity and well-defined particle phase selection and surface morphologies. The importance of oxygen donor is very critical to define the particle size, shape and surface properties. It is expensive and with limited ecological and aggregation properties. The reaction mechanism involves the coordination of the oxygen donor to the central metal atom of the halide followed by cleavage of the carbon–oxygen bonds[65, 66].

$$MCl_n + M(OR)_n \rightarrow 2MO_{n/2} + nRCl \text{ alkoxide route}$$

$$MCl_n + (n/_2)ROR \rightarrow MO_{n/2} + nRCl \text{ ether route}$$
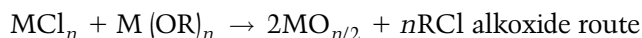
The formation of the M–O–R framework occurs from the condensation between M–Cl and M–OR functions, which is as follows:

$$\equiv M-Cl + \equiv M-O-R \rightarrow \equiv M-O-M$$
$$\equiv + R-Cl \text{ condensation}$$
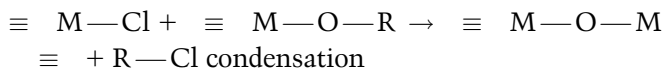
By ether route, the alkoxide is formed in situ along with alkyl halide:

$$\equiv M-Cl + R-OR \rightarrow \equiv M-OR + R-Cl \text{ alkoxylation}$$

The speed for ligand exchange process is slow at room temperature and increases with increase in temperature and use of catalyst.

$$M-Cl + \equiv M-OR \rightarrow \equiv M-OR$$
$$\equiv + \equiv M-Cl \text{ redistribution}$$
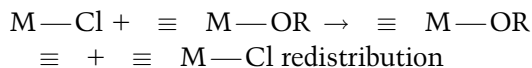
### 14.4.10 Pechini method

This method is based on citric acid and ethylene glycol using water in the presence of metal chloride or nitrates as a metal source. Citric acid chelates to the metal cations on heating forming polyesterification reaction. By adjusting the ratio of citric acid/ethylene helps to maintain the viscosity of the solution under control.
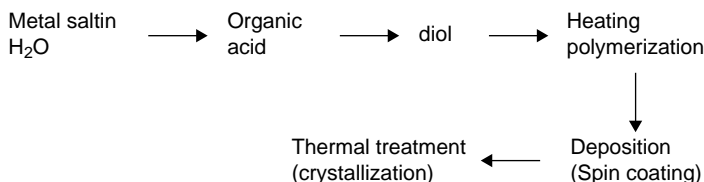


*Steps in thin film with the Pechini method.*

## 14.5 CHARACTERIZATION OF METAL OXIDE NANOPOWDER

The characterization of metal oxide nanopowder can be done with the help of the following techniques:

1. Infrared spectroscopy
2. Ultraviolet spectroscopy
3. Thermal analysis
4. Raman spectroscopy
5. Surface plasmon resonance
6. Atomic force microscopy (AFM)
7. X-ray diffraction (XRD)
8. Scanning electron microscope (SEM)
9. Transmission electron microscope (TEM)
10. Brunauer–Emmett–Teller method

### 14.5.1 Infrared spectroscopy

The IR spectra based on electromagnetic radiation is divided into three regions: These division are not strict nor based on electromagnetic properties.

1. The near region − 14,000 − 4000/cm – is used to excite harmonic vibrations.

2. The mid region − 4000 − 400/cm – is used to study the fundamental vibrations and its associated vibrations for rotational spectroscopy (used for chemical analysis).

3. The far infra red − 400 − 10/cm – lying adjacent to the microwave region has low energy used for rotational spectroscopy.

Each molecule has specific frequencies at which they rotate or vibrate at their matching energy levels. The resonant frequencies are determined by the shape of the molecular potential surface energies, the mass of the atom and vibronic coupling. The infrared spectrum is obtained by passing the infrared light through the sample. Each molecule absorbs some energy and then transmits light. Analysis of absorption reveals the characteristic details about the molecular structure of the sample[67–69]. IR spectra was obtained by using nujol mulls and KBr pellets.

### 14.5.2  Ultraviolet spectroscopy

The absorbance of a solution increases as the beam of monochromatic light increases. Absorbance is directly proportional to the path length and to the concentration. Different molecules absorb radiation of different wavelengths corresponding to structural groups within the molecule. The absorption of UV radiation corresponds to the excitation of outer electrons. With decrease in particle size, the band gap energy increases resulting in the shifting of the absorption band in the following fashion[69, 70]:

1. Transitions involving $\pi$, $\sigma$ and $n$ electrons.

2. Transitions involving charge-transfer electrons.

3. Transitions involving d and f electrons.

### 14.5.3  Thermal analysis

Thermal analysis consists of a group of techniques in which a physical property of a substance is measured as a function of temperature, when the substance was subjected to heating in a controlled temperature programme. Differential thermal analysis (DTA) may be defined as a technique used for recording the difference in temperature between a substance and a reference material with respect to time or temperature. When the sample is subjected to heating in an identical environmental condition, the difference of temperature was observed. With heating, the change in the sample leads to the absorption or evolution of heat that can be detected relative to the inert reference. Thermal gravimetric analysis (TGA) is a simple technique in which the weight loss or weight gain of a material takes place as a function of temperature. When no significant weight lost was observed with temperature, it was attributed to crystallization[71, 72].

### 14.5.4  Raman spectroscopy

Raman effect takes place when light enters in a molecule and interacts with the electron density of the chemical bond causing electromagnetic field in the molecule leading to vibrational and deformation of frequency shift. The incident photon excites the electron into a virtual state. The spontaneous Raman effect takes place when the molecules are excited from the ground state to a virtual state and relax into a vibrational excited state forming Stokes Raman scattering. If the molecules are already in the excited vibration state, the phenomenon is known as anti-Stokes Raman scattering. In nanotechnology, a Raman spectroscopy is used to better understand the composition of the structures, crystallographic orientation of the sample

and the change in vibrational frequency for chemical bond. In general, infrared spectroscopy and Raman spectroscopy are complementary techniques but the selection rule is different[68, 69].

Surface plasmon resonance is a phenomenon taking place at the metal surface when *p*-polarized light strikes the surface at a particular angle through a prism. In such conditions, photon–plasmon surface electromagnetic waves were created at the metal/dielectric interface depending on the thickness of the molecular layer. Surface plasmon resonance results in a reduction in intensity of the reflected light. It is used to analyse the functional properties of biomolecules by observing the change in refractive index of ultra thin film at the metal surfaces[73].

Formation of surface plasmon resonance bands depends on (1) the size for metal ion with its nature, (2) dielectric constant and refractive index of the medium surface, (3) nature and properties of the capping agent and (4) finally, the average distance between the neighbouring particles.

### 14.5.5 Atomic force microscopy

By using AFM, the image of a surface can be obtained in atomic resolution with force of interaction at nano-Newton scale. Specific surface area is one of the characteristic features for nanopowder. However, the functionalization of nanoparticle is one of the main challenges to provide top-end functional applications[47].

It is based on measuring attractive or repulsive forces between a tip and the sample. It is based on (1) sensitive detection (2) flexible cantilever (3) sharp tip (4) high resolution tip-sample positioning and (5) force feedback.
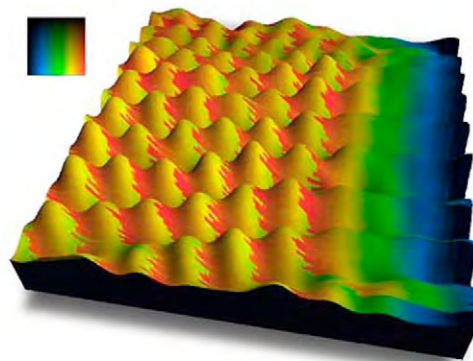


*Topographic imaging uses the up and down deflection of the cantilever, friction imaging uses torsional deflection.*

### 14.5.6 X-ray diffraction studies

It is an important technique used to identify the phase selection and crystalline state of nanoparticle with reference to temperature. The intensity of the diffraction peaks increases as the calcination temperature is increased. The broad diffraction peaks support the absence of long-range order due to small particle size of the nanopowder. The diffraction peaks represent the interparticle distance with narrow size distribution. X-rays are short-wavelength electromagnetic radiation produced by the deceleration of high energy electrons or by electronic transition involving the inner orbital of atom. X-rays are produced in three different ways from $10^{-4}$ to $10\,nm$ which are as follows: (1) use of high energy electron for the

bombardment of a metal target, (2) to expose a substance with a primary beam in order to give a secondary beam of X-ray fluorescence and finally (3) using the radioactive source for the X-ray emission and for the decay process. X-ray tube is basically used for the measurement of scattering and diffraction of X-rays. This technique is more sensitive to electron densities. The diffraction patterns were recorded by using external reference standard using powdered silicon mesh. X-ray is also used for qualitative and quantitative chemical identification and to determine residual stress and crystal size[74, 75]. The XRD patterns show that the compounds are amorphous and the peaks became sharper on heating supporting high homogeneity at the near-atomic level supporting the crystalline phase. Further thermal treatment does not lead to any appreciable change in the diffraction pattern. The particle size was calculated by using Scherer equation, $D = 0.9\,\lambda/\beta\cos\theta$, where $\lambda$, $\beta$ and $\theta$ are the X-ray wavelength (1.5405 Å for Cu–K$\alpha$).

### 14.5.7 Wide angle X-ray scattering

This technique is used to study the crystal structures in polycrystalline materials. Monochromatic beam was passed in powder with randomly arranged crystal in every possible orientation with lattice planes. According to Bragg's laws, some crystal is oriented at the Bragg's angle $\theta$. Some diffraction was noticed with crystal and planes according to Bragg's laws. X-ray intensities were detected at various positions by using a Geiger counter or scintillation counter connected with a diffractometer.

### 14.5.8 Small angle X-ray scattering

As suggested by Bragg's law, when the wavelength of the X-ray is constant, smaller angles lead to a large d-spacing in the nanomaterial with less than 5°. This technique has two advantages: (1) simple structure information can be evaluated at low running cost and (2) the efficiency of particle characterization increases due to its high intensity.
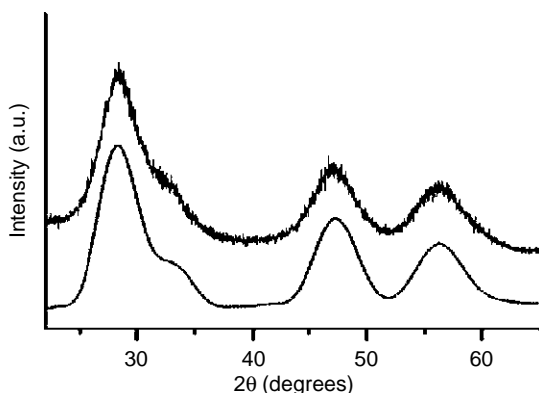


### 14.5.9 Electron microscopy

Electron microscopy plays an important role in providing the structural information of a wide range of resolution from 10 μm to 2 Å. Electron microscopy operates either on transmission or reflection mode for topographical map studies[76, 77].

## 14.5.10 Transmission electron microscopy

A ray of electrons is given by the pin-shaped cathode when it is heated. The electrons are then vacuumed by a high voltage at the anode between 50 and 150 KV. If voltage is high, the electron waves are shortened with an increase in power of resolution. A beam of electron passes through a drill-hole at the bottom of the anode. The lens is covered with an electronic coil for generating the electromagnetic field. The beam is first focussed by a condenser and then passed through the object, where it is partially deflected based on the electron density of the object. After passing, the object-scattered electron is then collected by an objective lens. The image formed by the lens is made visible on the fluorescent screen. With low contrast, it is difficult to obtain better images of separated nanoparticles. The morphology of nanomaterials depends on experimental conditions such as polarity of the solvent, the rate of solvent evaporation and the concentration of the nanocrystal. Presence of well-defined lattice fringes indicates the presence of crystallinity. Energy-dispersive X rays (EDX) analysis helps to determine the composition of nanoparticle along with $Cu^{2+}$ ion peak.

## 14.5.11 Scanning electron microscopy

The surface was scanned with the electron beam point and then reflected beams of electrons were collected and displayed at the same scanning rate on a cathode ray tube thus releasing the secondary electron. The intensity of secondary radiation is dependent on the angle of inclination. The secondary electron is collected by a detector that sits at the side above the object. The image of the specimen gives the information of the surface featured and then enhanced electronically and magnified. Accessory equipment permits the qualitative and semi-qualitative analysis of electronic composition of the localized surface area. The particles have been compared with respect to crystallization temperature, crystallite size and compositional purity. Therefore, it is concluded that the morphological changes take place in the microstructure particles which strongly depends on the nature, synthesis and routes of the nature of the molecular precursor.
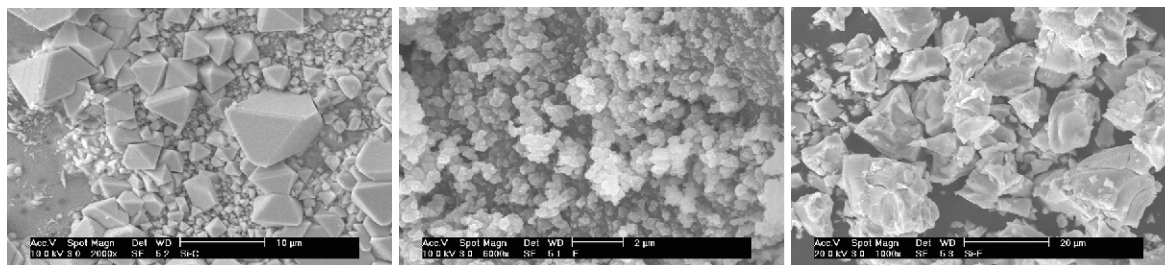
### 14.5.12 Characterization of porosity

The pore size and specific surface area are the most relevant properties for the porous materials. The porosity was measured by the gas adsorption isotherm by using Horvath–Kawazoe method. The relative pressure is expressed by $p/po$.

$p$ is the pressure of the vapour and $po$ is the saturation vapour of the adsorptive. The isotherm of one substance can be utilized to determine its pore size quantitatively. The specific area is determined by the following equation: $A = a/m$.

$A$ = specific surface area $(m^2/g)$.

$a$ = total area of the specimen $(m^2)$.

$m$ = mass of the specimen.

Generally BET is used to evaluate the specific surface area by fitting the absorption data to the BET model and the equation[46].

Utility of nanomaterials depends on the physical properties for the solubility of ultra pure particles in aqueous phase or organic phase retaining the correct stoichiometric ratio. Aqueous phase soluble nanomaterials are used for biological applications as a biosensor and the particle soluble in organic phase is used for electronic applications as shown in Figure 14.20. The efficiency of nanoparticles depends on the functionalization, which depends on the microstructural properties with phase selections. The successful application of particles depends on the compatible interaction within the particles or between the particle and the substrates for their self-assembly structures with pre-defined geometry at the nanoscale.
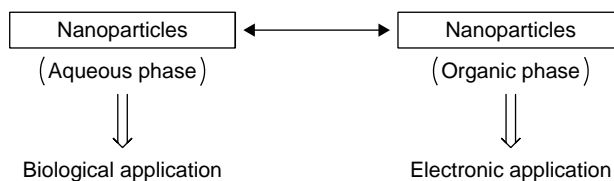


**FIGURE 14.20**

## 14.6 APPLICATION BASED ON PHASE TRANSFER

### 14.6.1 The synthesis of monometal-based nanopowder

Pure metal alkoxide was taken in an oven-dried glassware. It was heated and magnetically stirred at 260°C–270°C for 48 h under a flow of nitrogen

until gelation took place and then cooled to room temperature by removing the heat source. Absence of $^1$H NMR for molecular precursor was observed indicating a high purity of gel on NMR timescale. The gel was calcined at 350°C–450°C in inert atmosphere to identify the various phase transitions taking place with the removal of organic residues. The key step involved for making the process a success is to heat the alkoxide at constant temperature, so that the nucleation and growth of nuclei takes place simultaneously in a controlled manner. The gels are amorphous at room temperature and form crystalline materials at high temperature. On calcination, the monodispersible powder was obtained in quantitative yield with required phase selection. The physico-chemical properties of powder show that the synthesis has a high potential for the preparation of other high-tech metal oxide nanomaterials. After 72 h, the powder was obtained with crystallinity at room temperature on self-hydrolysis of the gel.

The exact mechanism for particle nucleation and its growth mechanism are not clear so far. It is assumed that the nucleation occurs and growth takes place by an intramolecular rearrangement within primary particles system (see Athar, unpublished).

$$
M(OBu)_4 \xrightarrow{\text{Thermal}} \begin{array}{c} RO \\ RO \end{array}\!\!>\!\!M = O \ + \ 2ROR \uparrow
$$

$$
\begin{array}{c} RO \\ RO \end{array}\!\!>\!\!Zr = O \xrightarrow[\text{in } N_2]{\text{Calcination}} ZrO_2 \ + \ 2ROR \uparrow
$$
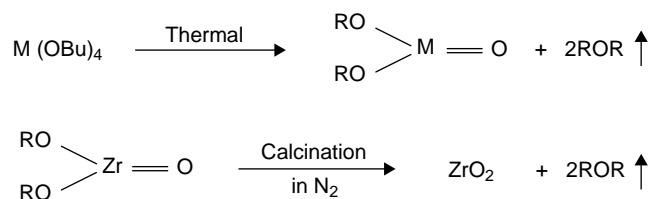
Pure metal alkoxide was heated in a microwave reactor (CEM discover) at a 60 Hz/150 W up to 300°C in an inert atmosphere. Appearance of white fumes and change in viscosity with an increase in temperature supports the formation of gel. $^1$H NMR supports purity of the gel with correct integration ratio. The gel changed to powder on self-hydrolysis at room temperature. On pyrolysis at 350°C–450°C for 1 h in the presence of argon atmosphere gives monodispersible powder with good crystallinity.

$$
M(OBu)_4 \xrightarrow[\text{Irradiation}]{\text{Microwave}} \begin{array}{c} RO \\ RO \end{array}\!\!>\!\!M = O \ + \ 2ROR \uparrow
$$

$$
\begin{array}{c} RO \\ RO \end{array}\!\!>\!\!M = O \xrightarrow[\text{in } N_2]{\text{Calcination}} ZrO_2 \ + \ 2ROR \uparrow
$$

M = Ti and Zr
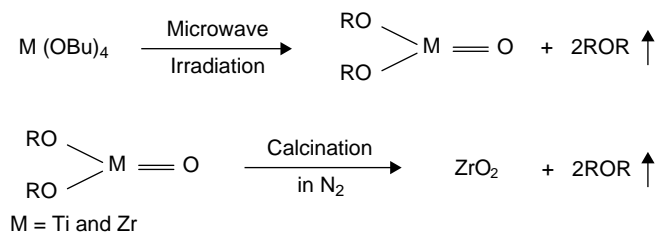
Different characteristic patterns for zirconia obtained by thermal and microwave processes are given below:

Thermal  Microwave
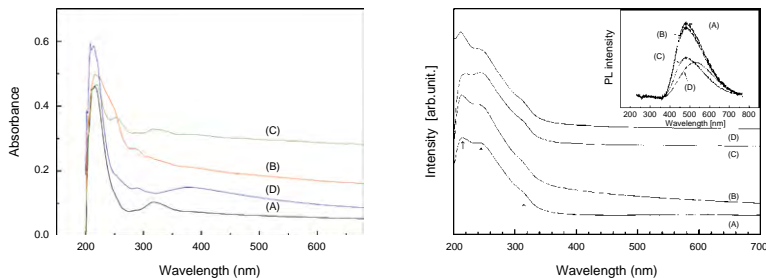


UV–Vis absorption spectra of zirconia powder:
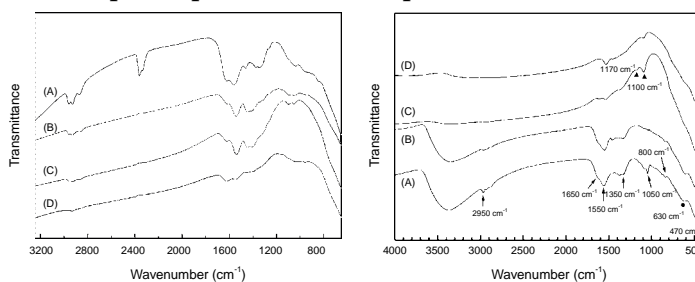


Fourier transform infrared spectroscopy (FTIR) spectra of zirconia powder:
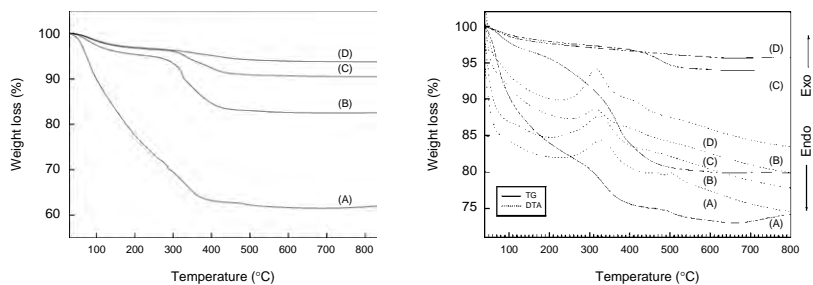


TG data shows that the weight loss was expressed as a function of temperature.
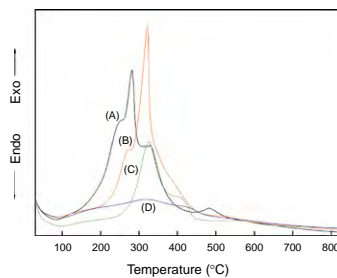
DTA data shows that the exothermic peaks correspond to crystalline phase as a function of temperature.
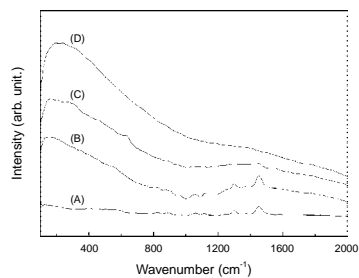


Raman spectra of the zirconia samples.
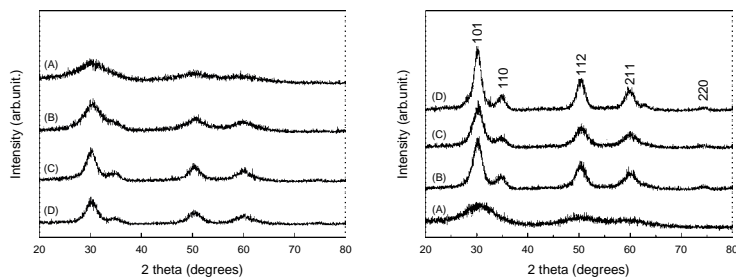


XRD data for zirconia samples show its nature of increase in crystallinity with increase in temperature.

Thermal



Air dried



350°C



400°C



450°C
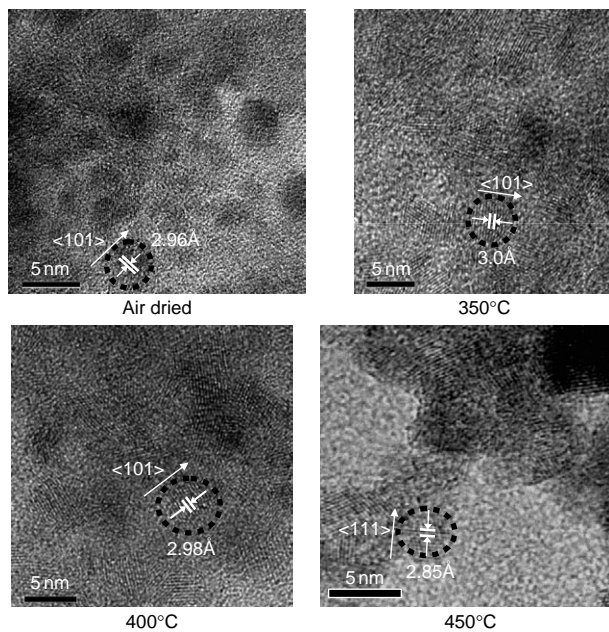
Microwave
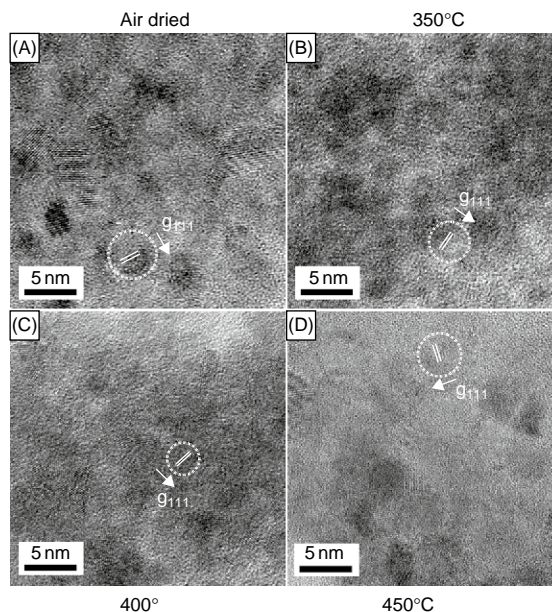


HRTEM images for isolated tetragonal zirconia samples. The average particle size is 5 nm with limited size distribution. Regions of brighter contrast show the larger crystallites with high purity.

These studies show that the properties of zirconia depend on the synthetic methodologies.

The titania is prepared by using oleic acid and octanol at pH 4–6 via sol–gel process. The colour of the particles depends on the particle size and shape at a particular pH (see Athar, unpublished).

FTIR studies for two samples of titania prepared in similar reaction conditions at a constant pH.

Oleic Acid Octanol
Crystallization temperature
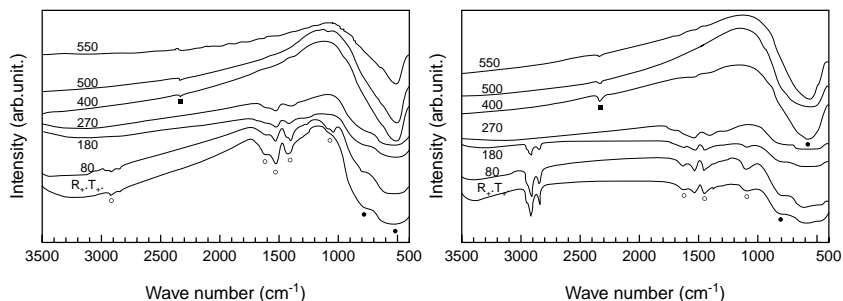
UV–Visible
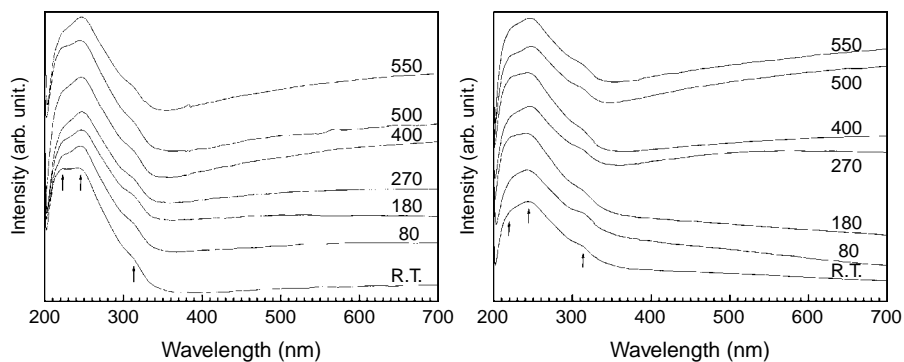


TG and DTA data
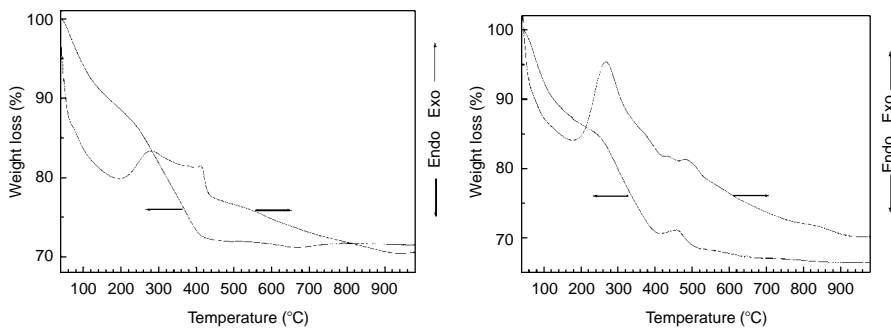


XRD
(a) Low angle (1~10)
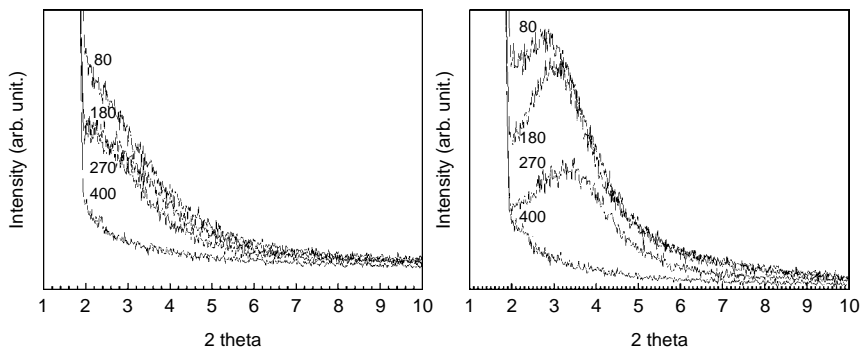
(b) High angle (10~60)
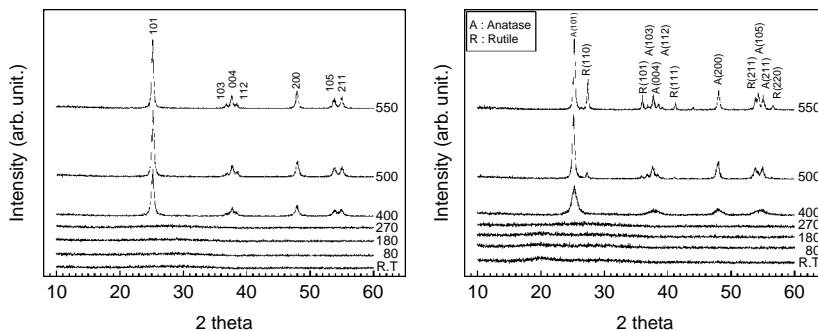


TEM data (a) room temperature (b) 400
Oleic acid Octanol
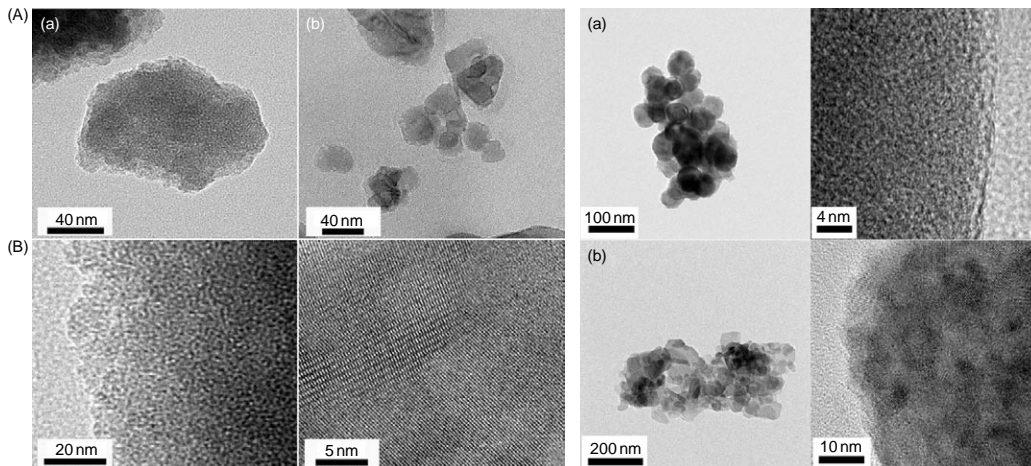


Oleic acid Octanol

*HRTEM images show that the synthetic procedure has important role to play for defining the properties of titania under similar reaction conditions.*
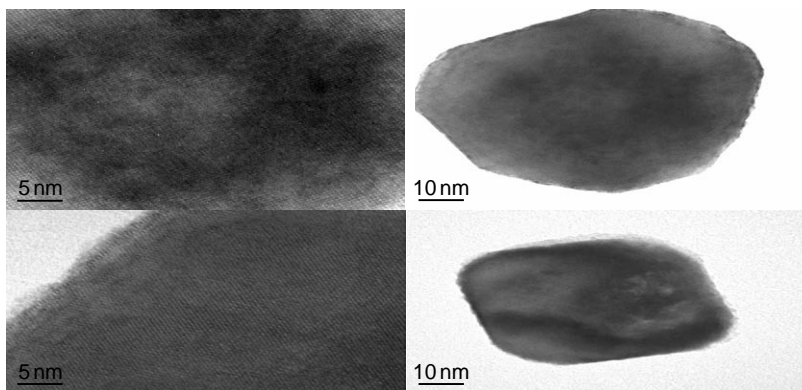
Similarly many allied nanomaterials have been reported in the literature[78–92].

It was observed that due to high surface energy, the ageing properties play an important role to define functional properties of the particle for its applications. The particles are more reactive due to an increase in surface energy with respect to decrease in size of the particles. The smallest particle is most reactive and kinetically unstable and changes into a big particle due to interparticle interaction as a function of time leads to the formation of heterogeneous phase with stability as shown in $Er_2O_3$ nanoparticles.



*Some of the SEM figures of metal oxide synthesized by using the sol–gel process.*
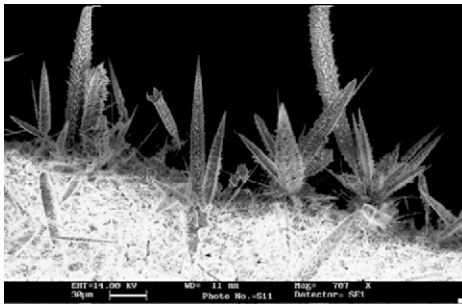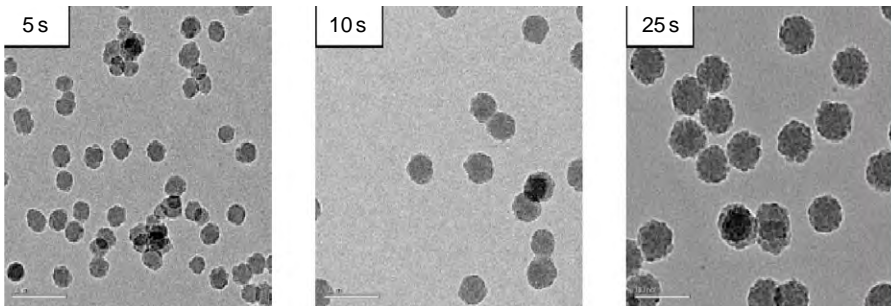
Cactus-like formations ⟷ $GeO_2$  Needle-like structures
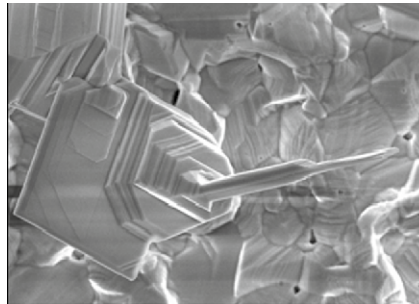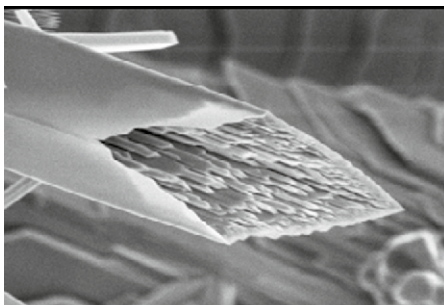
$SnO_2$ tube with nanoneedles            Wire of $In_2O_3$
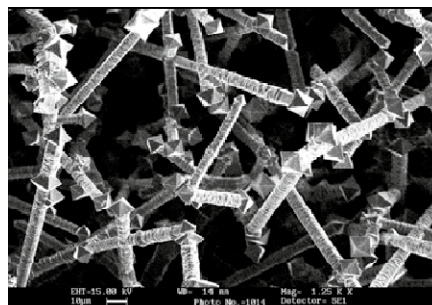
### 14.6.2 Use of titania film in car



These figures show the use of titania film in a car during the winter season: rear-view mirror (a) covered with snow without titania film and (b) the snow does not deposit on the titania film.



A rear window with titania coating increases visibility.

## 14.7 SYNTHESIS OF BIMETALLIC ALKOXIDE FOR THE PREPARATION OF BIMETALLIC OXIDE NANOPOWDER

Metal alkoxides and its organic derivatives have pre-existent metal–oxygen bonds that help to synthesize nanomaterial with desired functional gradient properties for its use in technology. The intramolecular rearrangement of molecular precursor leads to the formation of M–O–M architectural framework with novel properties. The electronic effects help for a good

understanding of the reactivity. The reactivities of metal alkoxide can also be controlled with the help of chelating ligands. Basic principles and properties for the synthesis of bimetallic alkoxide are as follows:

1. *Lewis acid*: base interaction based on electronegativity. In which, the metal centre acts as a stronger acceptor for the electron density and ligands acting as a better donor.

2. Formation of metal–oxygen–metal bond depends on donor–acceptor relationship.

3. Isomorphous substitution provides a homogenization at the molecular level.

The synthesis of new and novel bimetallic alkoxide was carried out by applying a molecular structure design concept based on the choice of a proper metal–oxygen core and its completion with ligands to provide the necessary number of donor atoms and sterical protection around the core simultaneously. The freshly prepared alkoxide is highly soluble in mother alcohol, but the solubility decreases on ageing due to the loss of solvating molecules and air hydrolysis which leads to the formation of hydrated oxides[92–97].

The alkoxide is prepared in the following procedure.

$$K + ROH \rightarrow KOR + H_2 \uparrow$$
$$MCl_x + x + 1KOR \rightarrow [KM(OR)_{x+1}] + XKCl \downarrow$$
$$MCl_{x'} + [X'KM(OR)_{x+1}] \rightarrow \{[M'M(OR)_{x+1}]_{x'}\} + X'KCl \downarrow$$
$$M = M' = Al, Ga, Sn, P, Ti, Zr, Er, Yb, Eu$$
$$R = C_3H_7, C_4H_9$$
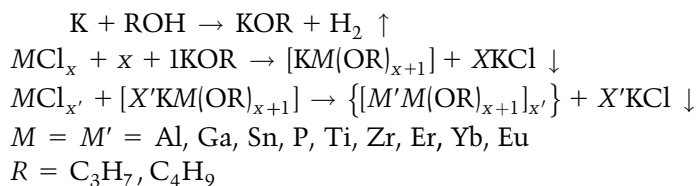
In general, the properties in bimetallic alkoxides show the down field shift when compared to simple alkoxide or their synthons.

## 14.7.1  Physico-chemical properties of bimetallic alkoxides[94–96]

Significant absorption peaks were observed by FTIR for characterization of the compounds by observing for $\nu_{M–O}$ (asymm), $\nu_{Er–O}$ (asymm), $\nu_{M–O}$ (symm) and the stretching for M–O bonds. In down field, frequency shift was observed in metal alkoxide when compared with their parent synthon as well as simple alkoxides.

UV–visible spectra of the alkoxides can be attributed to the charge-transfer band of unshared electron pairs on the oxygen atoms to the empty

metal orbital. Metal ion is suitable for studying subtle changes in the coordination number and oxygen donor ligands. The visible emission is believed to stem from defect levels associated with oxygen vacancies. The broadness of the emission frequencies indicates a presence of broad particle size distribution or low crystallinity.

The fine structural peak is virtually unchanged in solvent supporting the very weak interaction. In solution state, the metal alkoxides do not show any ageing effect for many days in dry atmosphere.
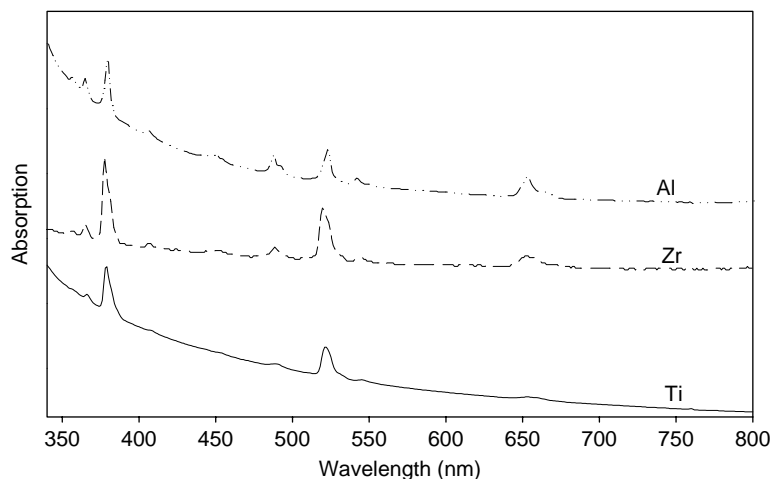


The NMR has proved to be a very useful technique to achieve a better understanding of the hydrolysis and condensation process and to elucidate their molecular structures at room temperature. The resonance peaks indicate that the molecules are slightly fluxional and remain mononuclear in solution. The up field chemical shift was observed for nuclei due to their coordination with metal ion through $\pi$ bonding.

The thermal behaviour of bimetallic alkoxides was investigated by thermogravimetry (TG) and DTA. The thermal decomposition of metal alkoxides may be described as a smooth stepwise process. The first weight loss occurs below 200°C and is attributed to the removal of solvent trapped in molecular system. The second significant weight loss was observed between 250°C and 850°C, which corresponds to the pyrolysis of inorganic residues as indicated by one or more prominent exothermic peak in the DTA curves. No significant weight loss was observed beyond 900°C in the TGA pattern thus indicating the formation of well-organized crystalline oxides with definite chemical composition.
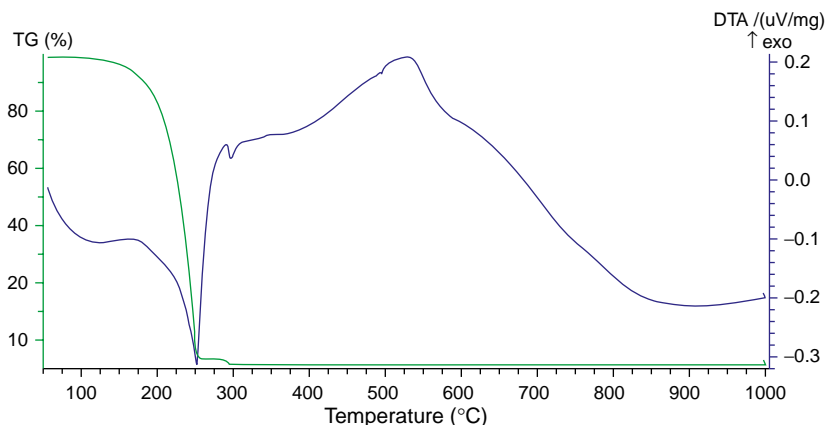
The mass spectra do not give any conclusive evidence in the gas phase probably due to the breakdown of the heterometallic alkoxides into simple metal alkoxides, and finally decomposes into simple metal oxides under the high vacuum pressure used in mass spectrometer.

The purity of metal alkoxide was established with the help of quantitative yield of compound and with microelemental analysis.

The XRD pattern shows an enhanced homogeneity in metal alkoxide. The pattern of diffraction peaks is the same for all metal alkoxide and corresponds to the related peaks. On calcinations the broadness of diffraction peaks reduces, thereby supporting the formation of crystalline nanopowder of bimetallic oxide with correct phase, and with favourable microstructural properties.
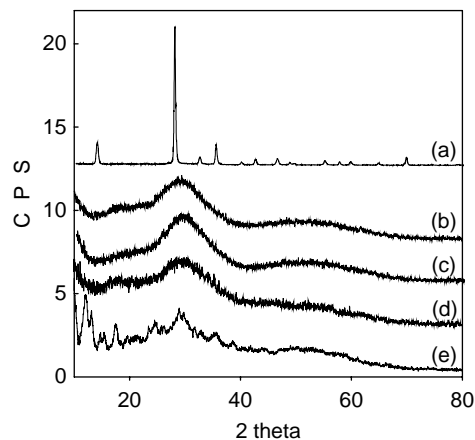


(a) 450°C (b) 400°C (c) 3500°C (d) 300°C (e) Air dried

The SEM micrograph shows a comparative study with respect to crystallization, morphology, temperature, crystallite size and compositional purity

of metal alkoxide, which depends on the nature of the molecular reactants and the synthetic methodology.
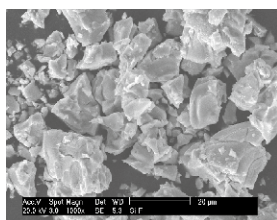


[Er{Si(OR)$_5$}$_3$]
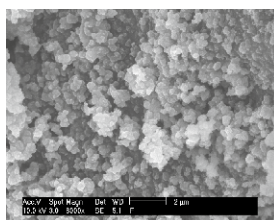


[Er{As(OR)$_4$}$_3$]
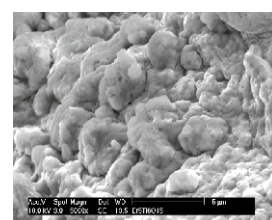


[Er{Sn(OR)$_5$}$_3$]
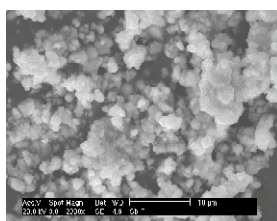


[Er{Sb(OR)$_4$}$_3$]
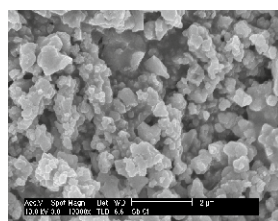


[Er{Sb(OR´)}$_4$}$_3$]
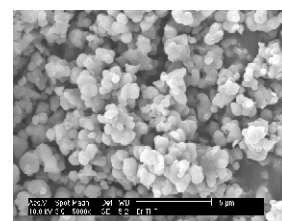


[Er{Ti(OR)$_5$}$_3$]
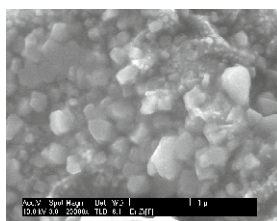


[Er{Zr(OR)$_5$}$_3$]
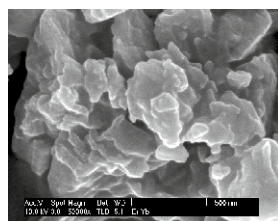


[Er{Yb(OR´)$_4$}$_3$]
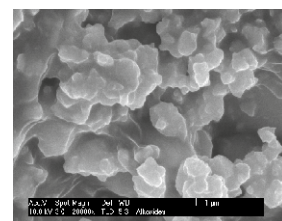


[Er(OR´)$_4$P{Yb(OR´)$_4$}$_2$]

Based on the physico-chemical properties, the following structure can be elucidated for bimetallic oxide:



$\left[ \{MM´(OR)_4\}_3 \right]$

M = M´=3$^+$

$\left[ M\{M´(OR)_5\}_3 \right]$

M = 3$^+$, M´ = +4



$\left[ M\{M´(OR)_5\}_3 \right]$

M´ = 4$^+$, M = 3$^+$
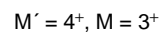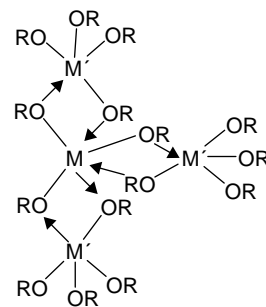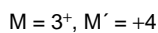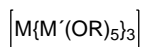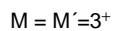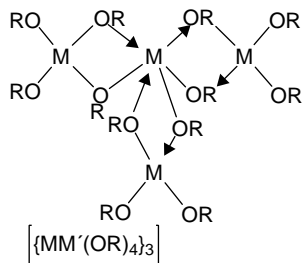
### 14.7.2 Preparation of bimetallic oxide nanopowder via sol–gel process

Heterometallic alkoxide is used for the preparation of high purity multicomponents oxide in good yield. Stoichiometric ratio of anhydrous metal chloride and bimetallic alkoxide was taken in anhydrous dichloromethane. The reaction mixture was refluxed with catalytic amounts of ferric chloride (anhydrous). After completion of reaction, a heterogeneous solution was washed with anhydrous dichloromethane and dry benzene, the insoluble powder was obtained in quantitative yield and then dried in an inert atmosphere under vacuum[94–97].

$$4MCl_3 + \{M[M'(OPr^i)_4]_3\} \rightarrow [M_5M'_3O_{12}] + 12Pr^iCl \downarrow$$
$$M = M'Al,As,Sb,Er,Yb,Eu$$
$$R = C_3H_7,C_4H_9$$
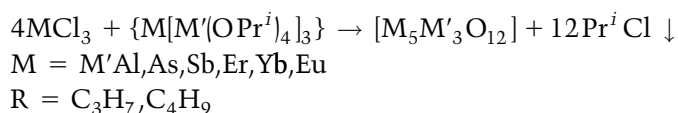
In principle, the same types of information can be obtained for bimetallic oxide from IR, UV, thermal analysis and TEM which matches well to simple metal oxide.

### 14.7.3 Some SEM data of bimetallic oxide
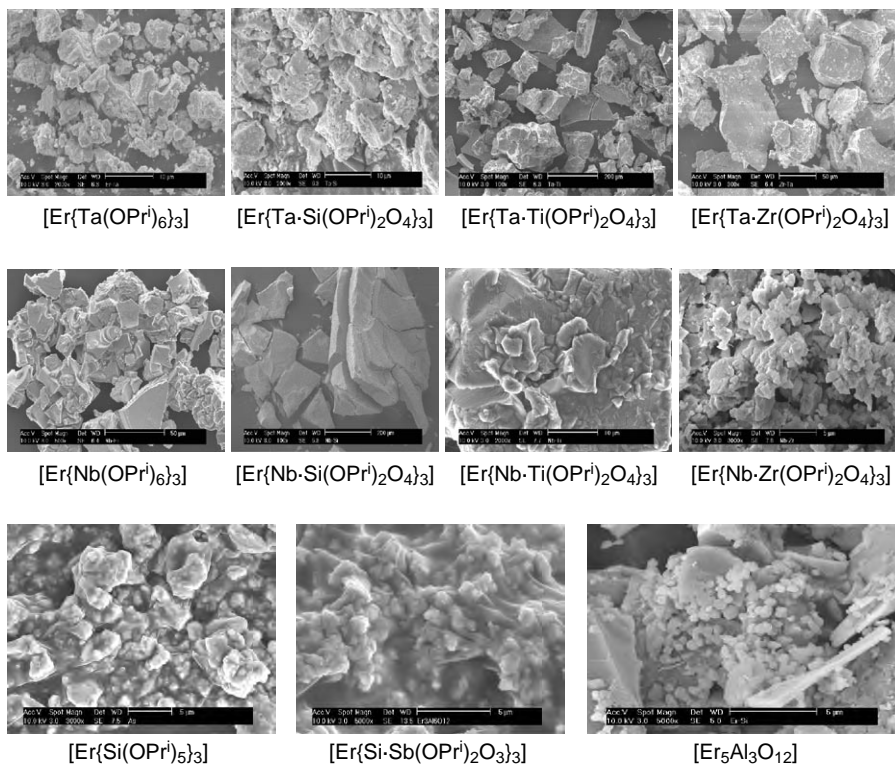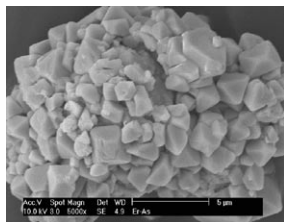


[Er{Ta(OPr$^i$)$_6$}$_3$]    [Er{Ta·Si(OPr$^i$)$_2$O$_4$}$_3$]    [Er{Ta·Ti(OPr$^i$)$_2$O$_4$}$_3$]    [Er{Ta·Zr(OPr$^i$)$_2$O$_4$}$_3$]

[Er{Nb(OPr$^i$)$_6$}$_3$]    [Er{Nb·Si(OPr$^i$)$_2$O$_4$}$_3$]    [Er{Nb·Ti(OPr$^i$)$_2$O$_4$}$_3$]    [Er{Nb·Zr(OPr$^i$)$_2$O$_4$}$_3$]

[Er{Si(OPr$^i$)$_5$}$_3$]    [Er{Si·Sb(OPr$^i$)$_2$O$_3$}$_3$]    [Er$_5$Al$_3$O$_{12}$]

$[Er\{As(OPr^i)_4\}_3]$



$[Er\{As·Sn(OPr^i)_2O_2\}_3]$



$[Er\{As·Zn(OPr^i)_2O_2\}_3]$



$[Er\{Sb(OPr^i)_4\}_3]$
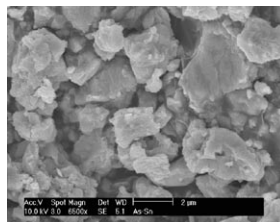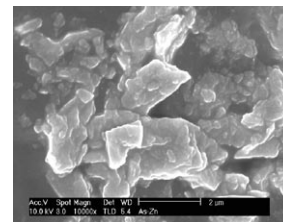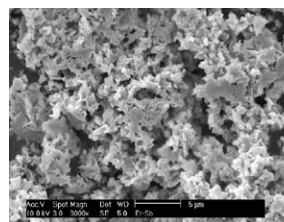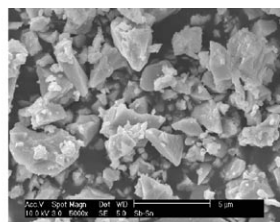


$[Er\{Sb·Sn(OPr^i)_2O_2\}_3]$
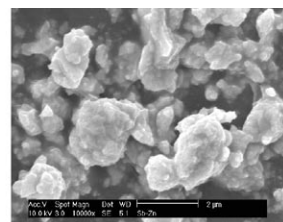


$[Er\{Sb·Zn(OPr^i)_2O_2\}_3]$
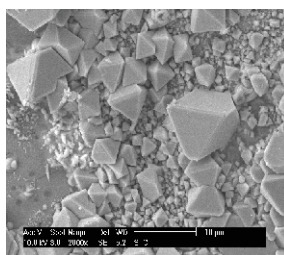


Diamond shape $[Er_2SiO_5]$



$[Er_2ZrO_5]$



$[Er_2TiO_5]$

M = Ta, Nb
R = i–C$_3$H$_7$

M′ = Si, Ti, Zr
R = i–C$_3$H$_7$
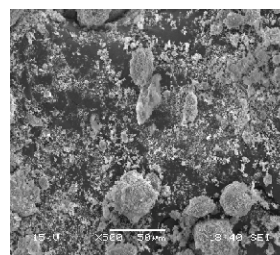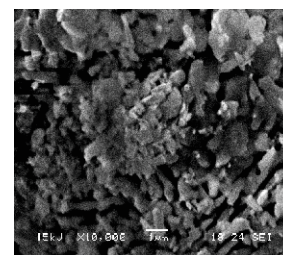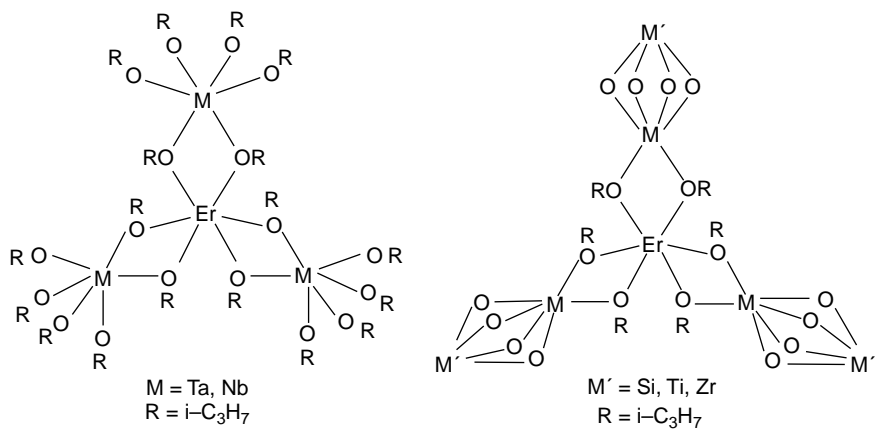
*Change in molecular structure from molecular precursor to metal oxide.*
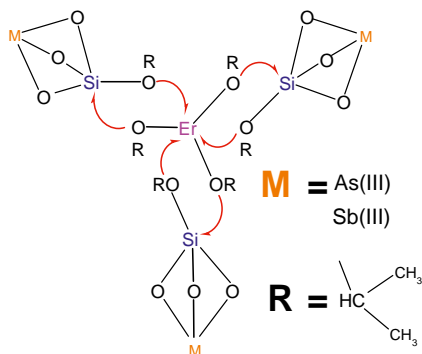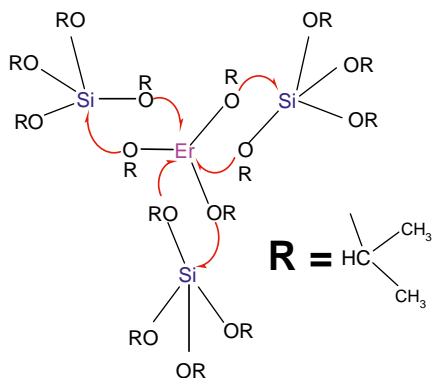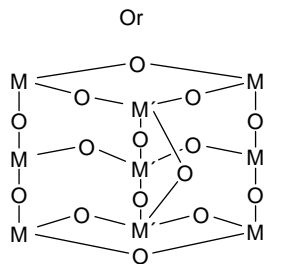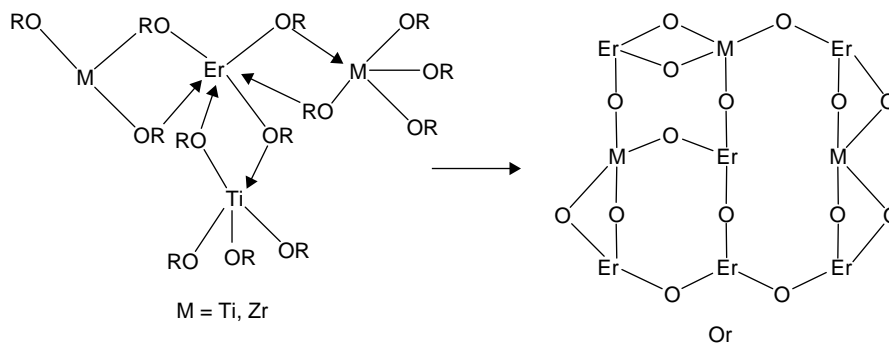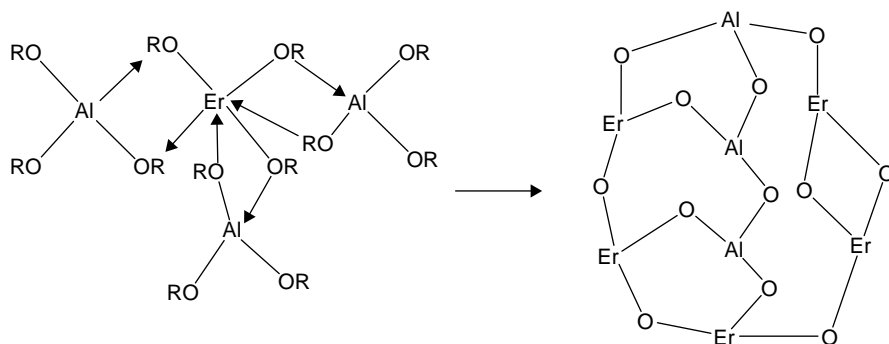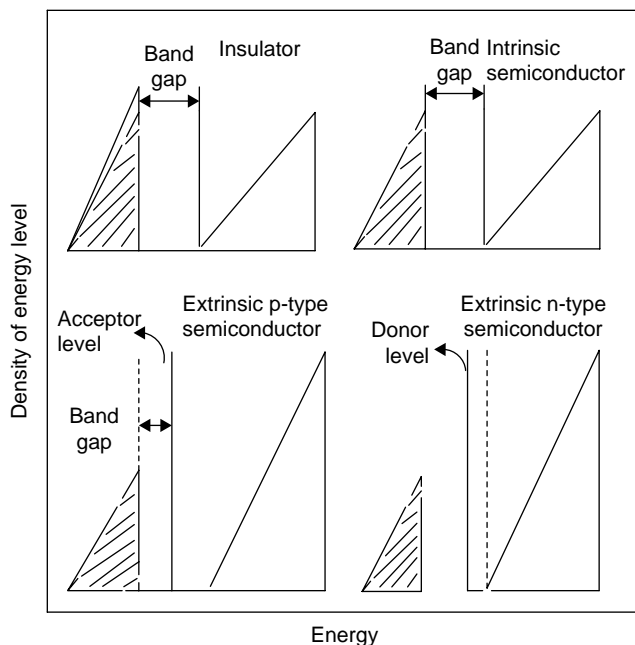
**FIGURE 14.21**   *Band gap of the nanocrystalline materials tuned to a desired energy level by controlling the particle size.*
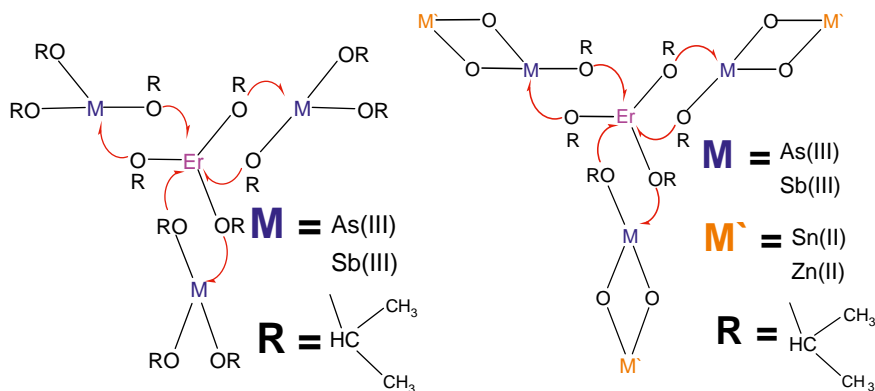


## 14.8  APPLICATIONS OF METAL OXIDE FOR PHOTOLUMINESCENCE

There is currently an increasing interest for fabricating good luminescent devices based on controlled particle properties. For luminescent systems,

it is necessary to synthesize homogeneous ultra pure particle with a good dispersity and with a well-passivated surface area[98–101]. Photoluminescence is a powerful tool for providing important information about the physical properties of materials at the molecular levels, including shallow and deep level defects and band gap state for energy level[101]. The cation of oxide can change the oxidation state to show extrinsic or semiconductor behaviour. Oxide with large band gap between the filled valence band and the vacant conduction bands acts as insulator. In intrinsic semiconductors, the band gap is narrow and some electrons have the ability to jump from the filled to the empty band due to heat or light exhibiting low level of conductivity. In extrinsic semiconductors, the vacant acceptor acts as a conducting band which can receive the electron from the filled valence band acting as donor band or the valance band can induce sufficient degree of incomplete occupation or semiconducting[102–106]. The band gap of the nanocrystalline materials can be tuned to a desired energy level by controlling the particle size as in Figure 14.21.

Doping corresponds to the deliberate introduction of elements (such as atoms, ions or molecules) in a luminescent material with **homogeneous** miscibility under soft reaction condition which helps to improve its properties by controlling the surface functionality[105, 106] which are as follows:

- The functionality of materials depends on the properties of the particles and is directly associated with doping and dispersibility.

- Doping provides a structural control in the powder.

- Doping increases unexpected structural modifications due to band gap.

Sol–gel process provides an ideal way for better dispersion of doping metal ions. The systematic doping studies were carried out by varying the nature and the concentration of the doping species. f→f electron transition takes place within the transition to produce the sharp absorption and emission depending on the matching properties of surface-to-volume ratio within the electronic surface area[105–114].

Capping of nanoparticles with organic ligands has several advantages. Coating helps to prevent aggregation and controls the growth. Capped particle has a potential to modify the surface properties for their use in application-based chemistry and to protect the particles from harsh reaction conditions.

Dispersion quality for photoluminescence depends on the following factors:

- *Particle size* – helps to create consistency for nanodispersion in solvent medium.

- *Dispersant* – high loading of nanopowder.

- *Medium* – aqueous or non-aqueous.

- The pH of the medium.

The stability of nanopowder depends on the electrostatic repulsion and steric factor in a solvent/host matrix. By following the aforementioned conditions, the commercial-grade nanopowder can be synthesized which has resistance towards temperature, oxidation, and durability towards environment and pH of the solvents.

In order to investigate the presence of OH groups in 2 mol% $Er^{3+}$ doped $Al_2O_3$–$SiO_2$ and $TiO_2$–$SiO_2$ samples, the FTIR absorption spectra are measured. In the spectral range of 3000/cm–4000/cm, the broad band due to stretching vibrations of OH groups was observed in the case of $Er^{3+}$ doped $Al_2O_3$–$SiO_2$ system. The amount of OH groups was gradually reduced with an increment of the annealing temperature. After annealing at 1100°C, the OH groups were almost removed within the sensitivity range of the FTIR spectrometer. While in the case of $Er^{3+}$ doped $TiO_2$–$SiO_2$ system, the FTIR absorption spectra shows the same tendency for all samples as a function of annealing temperature[107, 108].
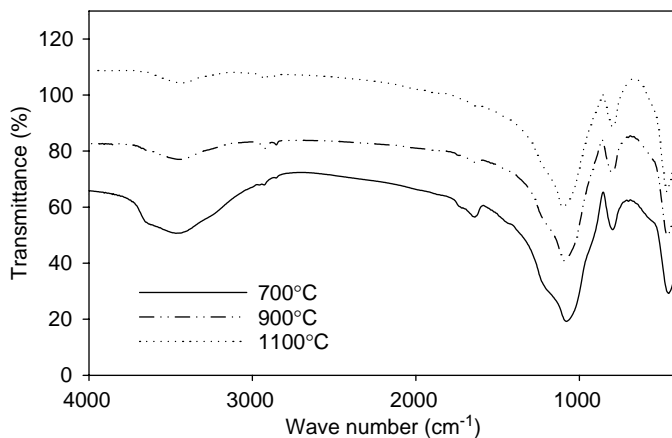


The above figure shows the X-ray diffraction curves of 2 mol% $Er^{3+}$ doped $Al_2O_3$–$SiO_2$ and $TiO_2$–$SiO_2$ samples obtained by annealing gel powders at 700°C, 900°C and 1100°C for 1h, respectively, under $O_2$ atmosphere. In the case of $Er^{3+}$ doped $Al_2O_3$–$SiO_2$ system, no sharp peaks were observed even after annealing at 1100°C. This clearly means that all the materials consist of amorphous phase below the heat-treatment temperature of 1100°C. However, in $Er^{3+}$ doped $TiO_2$–$SiO_2$ system, the small diffraction peaks, due

to the crystalline nature of erbium titanium oxide ($Er_2Ti_2O_7$), were observed in the case of the sample annealed at 900°C. Moreover, the crystallization of erbium titanium oxide is increased more after heat-treatment at 1100°C. From these XRD profiles, it could be presumed that the structure of Er–O–Ti isopropoxide orderly arranged at precursor stage might be destroyed as the samples were annealed above 900°C[107, 108].
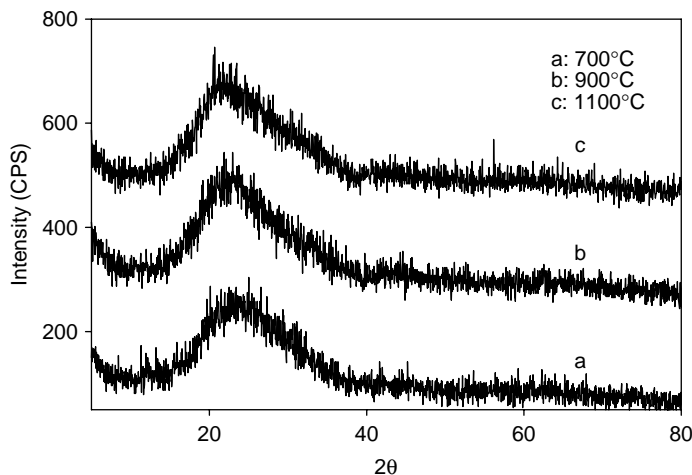


The photoluminescence spectra of 2 mol% $Er^{3+}$ doped $Al_2O_3$–$SiO_2$ and $TiO_2$–$SiO_2$ heat-treated at 1100°C for gel materials is prepared from different bimetallic alkoxides. The emission band due to the $^4I_{13/2} \rightarrow {}^4I_{15/2}$ transition of $Er^{3+}$ ion was observed at $1.55\mu s$ at room temperature by using the excitation of 980-nm laser diode. The photoluminescence intensity of $Er^{3+}$ doped $Al_2O_3$–$SiO_2$ was higher than that of $Er^{3+}$ doped $TiO_2$–$SiO_2$. It was also observed that the emission band of the latter system prepared using Er–O–Ti isopropoxide consisted of several sharp peaks. These phenomena are related to the crystalline phase generated in $Er^{3+}$ doped $TiO_2$–$SiO_2$ system. Namely, it can be explained that the crystalline phase formed in $Er^{3+}$ doped $TiO_2$–$SiO_2$ system prevents uniform distribution of $Er^{3+}$ ion in the matrix and eventually it has influence on the emission intensity and peak shape of $Er^{3+}$ doped $TiO_2$–$SiO_2$. On the other hand, an emission broadening of $Er^{3+}$ doped $Al_2O_3$–$SiO_2$ system is induced by the Stark effect due to the splitting of degenerate energy levels of $Er^{3+}$ embedded in an amorphous structure. The full width at half maximum (FWHM) measured for 2 mol% $Er^{3+}$ doped $Al_2O_3$–$SiO_2$ is about 100 nm and this value is broader than those observed in $Er^{3+}$ doped silica-based systems prepared by other methods[100–108].
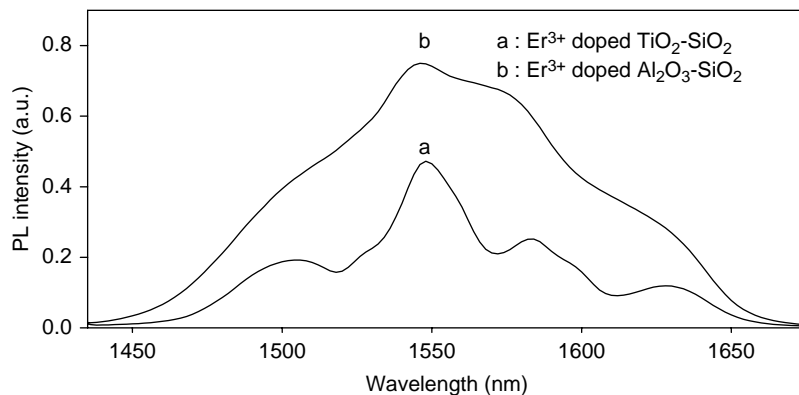
The spectral half width of the emission band from the maximum is about 60 nm and is due to **homogeneous broadening** plus additional Stark splitting of the excited and ground states. The emission results from the recombination of a photo generated hole with a single ionized charged state with specific surface defects. When the lanthanide ions are coordinated, the emission energy of the ligands' broad bands is altered. The lifetime of these complexes was in the range of 2.0–4.5 μs. It is assumed that the lifetime can be greatly improved by removing the residual organic solvent and impurities, which are responsible for the luminescence quenching. The photoluminescence properties can be controlled by the size and composition of the particles[107, 108].
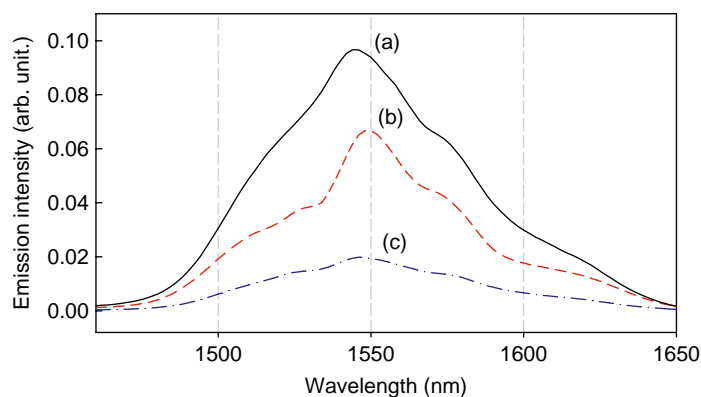


*Zirconia prepared by thermal process*: It was observed that the maximum photoluminescence was observed at 400°C. On further heating at 450°C, the luminescence curve reduces drastically. It is assumed that some impurities from organic ligands contribute to the photoluminescence behaviour. In microwave synthesis, the photoluminescence behaviour

exhibits different fashion as shown in page XXX. The luminescence properties depend on dopant, composition, host stoichiometry and processing conditions. However, the controversy exists on the origin of photoluminescence in zirconia. It is assumed that oxygen vacancy contributes to the photoluminescence (see Athar, unpublished).
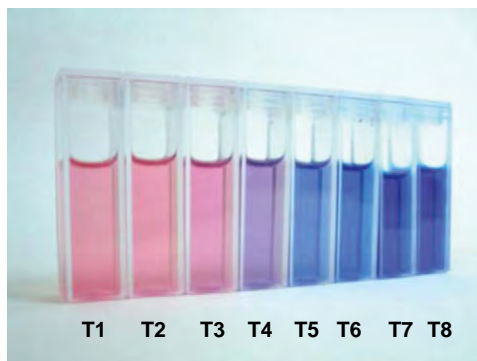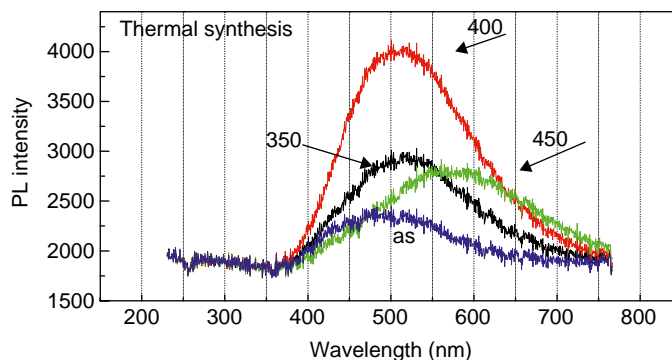




Real picture of the eight temperature sensors prepared of $SiO_2$ doped with $CoCl_2$.

## 14.9 CONCLUSIONS

A facile route based on precursor chemistry has been emphasized with low cost, easiness and sustainability for technological applications. The evaluation of suitable molecular precursor plays a very important role to produce wide spectrum of nanopowder with high purity with well-defined properties without any contaminations. The application of nanopowder takes place with uniform size distribution of nanoparticles in the matrix with compatible dispersion. The success in nanoscience depends on the symbiotic relationship between the molecular chemistry and new materials. The syn-

thesis of nanopowder with low energy consumption, convenient manipulation and large operational compatibility with controlled particle properties is still a challenge for synthetic chemists.

## 14.10  FUTURE PROSPECTS

A future direction of nanomaterials depends on the cultural development of advanced society. The application of a cost-effective molecular precursor for the fabrication of green-based nanotechnology with better understanding of the application of colloidal chemistry and particle–solution interface relationship within the framework of structure–property relationship still continues to be a challenge to the synthetic chemist. The technology-based light harvesting applications depend on the following parameters:

1. The investigation of nanomaterials, methods for their production and processing in bulk production.

2. Significant success to be achieved in the synthesis of nanomaterials with a narrow size and shape dispersion by retaining the pre-defined metal stoichiometry for their applications in nanodevices.

3. Synthetic methodology has to be designed for the novel precursor to change into technological-grade materials via solution or gas phase method with controlled properties for their future use in magnetic fluids, ultrafine abrasive, biomaterials, etc.

4. To devise environmental-friendly technosphere with new innovative steps based on nanosynthesis for their daily use.

## ACKNOWLEDGEMENT

## DEDICATION

Dedicated to my beloved father M. Athar Ali and father-in-law Mahmood Ahmad Farroqin.

## REFERENCES

[1] A.R. West, Solid State Chemistry and its Applications, Wiley, Chichester, J and Sons, 488, 1984.

[2] J.H. Fendler (Ed.), Nanoparticles and Nanostructured Films, Wiley-VCH, Weinheim, 1998.

[3] J.P. Jolivet, Metal Oxide Chemistry and Synthesis: From Solution to Solid State, Wiley, Chichester, 2000.

[4] U. Schubert, N. Hüsing, Synthesis of Inorganic Materials, Wiley-VCH, Weinheim, 2000.

[5] S. Sapra, D.D. Sarma, in: C.N.R. Rao, A. Muller, A.K. Cheetham (Eds.), The Chemistry of Nanomaterials: Synthesis Properties and Applications, Wiley-VCH, Weinheim, 2004.

[6] S. Mathur, H. Shen, H.S. Nalwa, Inorganic nanomaterials from molecular templates, Encyclopedia of Nanoscience and Nanotechnology 4 (2004) 131.

[7] F. Wells, Structural Inorganic Chemistry, Clarendon Press, Oxford, 1975.

[8] C.N.R. Rao, and A. Govindaraj, Nanotubes and nanowires, Nanoscience & nanotechnology series, R. Soc. Chem., London (monograph) 2005.

[9] C.C. Koch, Nanostructured Materials, William Andrew Publishing, New York, 2002.

[10] S. Pasko, L.G.H. Pfalzgraf, A. Abrutis, Mater. Lett. 59 (2005) 1836.

[11] R. Bhakta, R. Thomas, F. Hipler, H.F. Bettinger, J. Muller, P. Ehrhart, A. Devi, J. Mater. Chem. 14 (2004) 3231.

[12] A.C. Jones, J. Mater. Chem. 12 (2002) 2576.

[13] O. Masala, R. Seshadri, Annu. Rev. Mater. Sci. 34 (2004) 41.

[14] U. Schubert, J. Mater. Chem. 15 (2005) 3701.

[15] N. Pinna, G. Garnweitner, M. Antonietti, M. Niederberger, J. Am. Chem. Soc. 127 (2005) 5608.

[16] N. Pinna, G. Garnweitner, M. Antonietti, M. Niederberger, Adv. Mater. 16 (2004) 23–24 2196.

[17] N. Pinna, G. Neri, M. Antonietti, M. Niederberger, Angew. Chemie. 43 (2004) 33. 4345.

[18] M. Niederberger, G. Garnweitner, F. Krumeich, R. Nesper, H. Colfen, M. Antonietti, Chem. Mater. 16 (2004) 7. 1202.

[19] R. Papiernik, H.L.G. Pfalzgraf, J. Vaissermann, M.C.H.B. Goncalves, J. Chem. Soc. Dalton Trans. (1998) 2285.

[20] J.V. Barkley, J.C. Cannadine, I. Hannaford, M.M. Harding, A. Steiner, J. Tallon, R. Whyman, Chem. Commun. (1997) 1653.

[21] R. Fleischer, H. Wanderlich, M. Braun, Eur. J. Org. Chem. (1998) 1063.

[22] S.P.O. Brien, M. Yin, C.H. Wu, Y. Lou, C. Burda, J.T. Koberstein, Y. Zhu, J. Am. Chem. Soc. 127 (2005) 9506.

[23] D.C. Bradley, Philos. Trans. R. Soc. London A330 (1990) 167.

[24] R.C. Mehrotra, J. Non-Cryst. Solid 100 (1988) 9.

[25] M.J. McGeary, P.S. Coan, K. Folting, W.E. Streib, K.G. Caulton, Inorg. Chem. 30 (1991) 1723.

[26] U. Schubert, S. Tewinkel, F. Moller, Inorg. Chem. 34 (1995) 995.

[27] L.G.H. Pfalzgraf, Polyhedron 13 (1994) 1181.

[28] H. Fric, U. Schubert, New J. Chem. 29 (2005) 232.

[29] D.C. Bradley, Chem. Rev. 89 (1989) 1317.

[30] J. Livage, M. Henry, C. Sanchez, Prog. Solid State Chem. 18 (1988) 259.

[31] V.G. Kessler, S. Gohil, S. Parola, Dalton Trans. 544 (2003).

[32] V.G. Kessler, Chem. Commun. 11 (2003) 1213.

[33] L.G.H. Pfalzgraf, Mater. Res. Soc. Symp. Proc. 271 (1992) 15.

[34] E. Scolan, C. Sanchez, Chem. Mater. 10 (1998) 3217.

[35] D.C. Bradley, R.C. Mehrotra, D.P. Gaur, Metal Alkoxides, Academic Press, London, 1978.

[36] N.Y. Turova, E.P. Turevslaya, V.G. Kessler, M.I. Yanovskaya, The Chemistry of Metal Alkoxides, Kluwer, London, 2002.

[37] D.C. Bradley, R.C. Mehrotra, I.P. Rothwell, A. Singh, Alkoxo and Aryloxo Derivatives of Metals, Academic Press, London, 2001.

[38] R.C. Mehrotra, R. Bohra, D.P. Gaur, Metal $\beta$-diketonates and Allied Derivatives, Academic Press, London, 1978.

[39] R.C. Mehrotra, A. Singh, Chem. Soc. Rev. 25 (1996) 1.

[40] D.F. Shriver, M.A. Drezdzon, The Manipulation of Air-Sensitive Compounds, second ed., Wiley Interscience, New York, 1986.

[41] U. Schubert, E. Arpac, W. Glaubitt, A. Helmerich, C. Chau, Chem. Mater. 4 (1992) 291.

[42] J.H. Thurston, K.H. Whitmore, Inorg. Chem. 41 (16) (2002) 94.

[43] C. Sanchez, B. Julian, P. Belleville, M. Popall, J. Mater. Chem. 15 (2006) 3559.

[44] T.J. Boyle, C.A. Zechmann, T.M. Alam, M.A. Rodrigues, Inorg. Chem. 41 (4) (2002) 946.

[45] M. Puchberger, F.R. Kogler, M. Jupa, S.H. Gross, H. Fric, G. Kickelbick, U. Schubert, Eur. J. Inorg. Chem. (2006) 3283.

[46] G. Kickelbick, U. Schubert, Eur. J. Inorg. Chem. (1998) 159.

[47] L.D. Gelb, K.E. Gubbins, Langmuir 14 (1998) 2097–2111.

[48] P.C. Andrews, J.G. MacLellan, R.E. Mulvey, P.J. Nichols, Dalton Trans. (2002) 1651.

[49] J.H. Schattka, E.H.M. Wong, M. Antonietti, R.A. Caruso, J. Mater. Chem. 16 (2006) 1414.

[50] R. Tamaki, Y. Tanaka, M.Z. Asuncion, J. Choi, R.M. Laine, J. Am. Chem. Soc. 123 (2001) 12416.

[51] S. Doeuff, M. Henry, C. Sanchez, J. Livage, Non-Cryst. Solids 89 (1987) 206.

[52] P.I. Gouma, Rev. Adv. Mater. Sci. 5 (2003) 147.

[53] C.J. Brinker, G.W. Scherer, Sol–Gel Science: The Physics and Chemistry of Sol–Gel Processing, Academic Press, San Diego, 1990, p. 108.

[54] P. Gomez-Romero, C. Sanchez (Eds.), Functional Hybrid Materials, Wiley–VCH Interscience, New York, 2004.

[55] K.J. Edler, Sol–Gel Processing, Kluwer, London, 2004.

[56] L. Klein (Ed.), Sol-Technology, Noyes, Park Ridge, 1988.

[57]    D. Trevor, J. Sakka (Eds.), Handbook of Sol–Gel Science and Technology: Processing, Characterization and Applications, Kluwer Academic Publishers, Norwell, 2004.

[58]    U. Schubert, J. Sol–Gel Sci. Technol. 26 (2003) 47.

[59]    M. Henry, in: N.H. Nalwa (Ed.), Handbook of Organic–Inorganic Hybrid Materials and Nano Composites, vol. 1, American Scientific Publishers, USA, 2003.

[60]    J. Polleux, A. Gurlo, N. Barsan, U. Weimar, M. Antonietti, M. Niederberger, Angew. Chem. Int. Ed. 45 (2006) 261–265.

[61]    S. Pavasupreea, Y. Suzukia, S. Pivsa-Artb, S. Yoshikawa, Sci. Technol. Adv. Mater. 6 (2005) 224.

[62]    Z.R.R. Tian, J.A. Voigt, J. Liu, B. Mckenzie, H.F. Xu, J. Am. Chem. Soc. 125 (2003) 12384.

[63]    S.J. Limmer, G.Z. Cao, Adv. Mater. 15 (2003) 427.

[64]    M. Niederberger, G. Garnweitner, N. Pinna, M. Antonietti, J. Am. Chem. Soc. 126 (2004) 9120.

[65]    J.N. Hay, H.M. Raval, J. Sol–Gel Sci. Technol. 13 (1998) 109.

[66]    J.N. Hay, D. Porter, H.M. Raval, Mater. Chem. 10 (2000) 1811.

[67]    N.B. Clothup, L.H. Daly, S.E. Wiberley, Introduction to Infrared and Raman Spectroscopy, Academic Press, New York, 1964.

[68]    K. Nakamoto, Infrared and Raman Spectra of Inorganic and Coordination Compounds, fourth ed., Wiley, New York, 1986.

[69]    R.M. Silvestein, G.C. Bessler, T.C. Morril, Spectrometric Identification of Organic Compounds, John Wiley & Sons, New York, 1981.

[70]    A. Davydov, Molecular Spectroscopy of Oxide for Catalyst Surface, John Wiley and Sons, New York, 2003.

[71]    R.C. Mehrotra, in: R. Reisfeld, C.K. Jorgensen (Eds.), Chemistry, Spectroscopy and Applications of Sol–Gel Glasses, Springer-Verlag, Berlin, Heidelberg, 1992.

[72]    P. Gabbott, Principles and Applications of Thermal Analysis, Wiley-Blackwell Publishing, USA, 2007.

[73]    R.B.M. Schasfoort, A.J. Tudos, Handbook of Surface Plasmon Resonance, first ed., The Royal Society of Chemistry, Springer, Cambridge, 2008.

[74]    B.D. Cullity, Elements of X-ray Diffraction, Addison-Wesley Publishing Company, Inc., London, 1978.

[75]    A. Guinier, X-ray Diffraction in Crystals, Imperfect Crystals and Amorphous Bodies, Dover publications, New York, 1994.

[76]    I.M. Watt, The Principles and Practice of Electron Microscopy, second ed., Cambridge University Press, Cambridge, 1997.

[77]    J.J. Bozzola, L.D. Russell, Electron Microscopy, second ed., Jones & Bartlett Publishers, 1998, 2nd Edn. Jones and Bartlett, Publishers, Sudbury, MA.

[78]    B.M. Choudary, K. Mahendar, M.K. Lakshmi, V.S. Ranganath, T. Athar, Adv. Synth. Catal. 348 (2006) 1977.

[79]    E. Hosono, S. Fujihara, K. Kakiuchi, H. Imai, J. Am. Chem. Soc. 126 (2004) 7790.

[80]    X.C. Jiang, T. Herricks, Y.N. Xia, Adv. Mater. 15 (2003) 1205.

[81] Y. Zhou, M. Antonietti, J. Am. Chem. Soc. 125 (2003) 14960.

[82] N.R. Jana, L. Gearhart, and C.J. Murphy, Chem. Commun. 617–618, 2001.

[83] R. Backov, Soft Matter 2 (2006) 452.

[84] F. Carn, A. Colin, M.F. Achard, H. Deleuze, E. Sellier, M. Birot, R. Backov, J. Mater. Chem. 14 (2004) 1370.

[85] S. Kitagawa, R. Kitaura, S. Noro, Angew. Chem. Int. Ed. 43 (2004) 2334.

[86] M. Groenewolt, T. Brezesinki, H. Schlaad, M. Antonietti, P.W. Groh, B. Ivan, Adv. Mater. 17 (2005) 1158.

[87] T.H. Lee, J.H. Kim, B.S. Bae, J. Mater. Chem. 16 (2006) 1657.

[88] T. Athar, R. Reddy, Chin. J. Chem. 26 (2008) 1.

[89] S. Jeong, J.D. Budai, D.P. Norton, Thin Solid Films 422 (1–2) (2002) 166.

[90] J.P. Kim, K. An, N.K. Yang, J.G. Park, T. Hyeon, J. Am. Chem. Soc. 129 (2007) 5812.

[91] M.H. Chisholm, J.P. Rothwell, Comprehensive Coordination Chemistry, Pergamon Press, London, 1987.

[92] M.H. Chisholm, Inorganic Chemistry: Towards the 21st Century ACS Symposium Series 211, American Chemical Society, Washington, D.C., 1983.

[93] T. Athar, O.H. Jeong, S. Sang II, J. Solid State Chem. 178 (2005) 1464.

[94] T. Athar, O.H. Jeong, S. Sang II, Appl. Organomet. Chem. 19 (2005) 964.

[95] T. Athar, O.H. Jeong, S. Sang II, Chin. J. Chem. 25 (7) (2007) 998.

[96] T. Athar, O.H. Jeong, S. Sang II, Inorg. Chim. Acta. 358 (2005) 4541.

[97] X.L. Duan, C.F. Song, Y.C. Wu, F.P. Yu, X.F. Cheng, D.R. Yuan, J. Non-Cryst. Solids 354, (2008) 3516–3519.

[98] M. Grätzel, Nature 414 (2001) 338.

[99] P. Gaucher, J. Hector, J.C. Kurfiss, in: O. Auciello, R. Waser (Eds.), Science and Technology of Electroceramic Thin Films, vol. 147, Kluwer, Netherlands, 1995.

[100] M. Leskata, M. Ritala, in: H.S. Nalwa (Ed.), Handbook of Thin Film Materials, vol. 1, Academics, New York, 2002.

[101] G. Blasse, B.C. Grabmaier, Luminescent Materials, Springer-verlag Berlin and New York, 1994.

[102] S.M. Sze, K. Ng, K. Wok, Physics of Semiconductor Devices, third ed., Wiley, New York, 2006.

[103] P.Y. Yu, M. Cardona, Fundamentals of Semiconductors: Physics and Materials Properties, Springer-New York, 2004.

[104] D.K. Schroder, Semiconductor and device characterization, John Wiley, New York, 1990.

[105] E.D. Palik, Handbook of Optical Constants of Solids, Academic Press, Orlando, FL, 1985, p. 719.

[106] E.F. Schubert, Doping in III–V Semiconductors, Cambridge University Press, Cambridge, 1993.

[107] Mi.Ae. Lim, T. Athar, M.H. Lee, I.H. Seok, J.J. Ju, S. Sang II, J. Mater. Sci. Lett. 41 (4) (2006) 1285.

# Index